Transactions of the ASME®

Technical Editor, LEON M. KEER

The Technological Institute
Northwestern University
Evanston, IL 60201

APPLIED MECHANICS DIVISION

Chairman, THOMAS L. GEERS
Secretary, S. LEIBOVICH
Associate Editors,
R. M. CHRISTENSEN
C. O. HORGAN
R. L. HUSTON
D. J. INMAN
W. D. IWAN
W. G. KNAUSS
F. A. LECKIE
J. T. C. LIU
R. M. McMEEKING
A. K. NOOR
J. W. NUNZIATO
R. H. PLAUT
J. W. RUDNICKI
J. G. SIMMONDS
P. D. SPANOS
K. R. SREENIVASAN
Z. WARHAFT
L. T. WHEELER

BOARD ON COMMUNICATIONS
Chairman and Vice-President
R. NICKELL

Members-at-Large
J. LLOYD
R. REDER
F. SCHMIDT
M. FRANKE
M. KUTZ
T. MIN
F. LANDIS
R. ROCKE
W. WINER
R. GENTILE
B. ZIELS
R. MATES

President, E. L. DAMAN
Exec. Dir.
D. L. BELDEN
Treasurer, ROBERT A. BENNETT

PUBLISHING STAFF
Mng. Dir., Publ., JOS. SANSONE
Managing Editor,
CORNELIA MONAHAN
Production Editor, JUDY SIERANT
Prod. Asst., MARISOL ANDINO

Transactions of the ASME, Journal of Applied Mechanics (ISSN 0021-8936) is published quarterly (Mar., June, Sept., Dec.) for $120 per year by The American Society of Mechanical Engineers, 345 East 47th Street, New York, NY 10017. Second class postage paid at New York, NY and additional mailing offices. POSTMASTER: Send address changes to The Journal of Applied Mechanics, c/o THE AMERICAN SOCIETY OF MECHANICAL ENGINEERS, 22 Law Drive, Box 2300, Fairfield, NJ 07007-2300.
CHANGES OF ADDRESS must be received at Society headquarters seven weeks before they are to be effective. Please send old label and new address.

PRICES: *To members, $29.00, annually; to* nonmembers, $120.00.
Add $15.00 for postage to countries outside the United States and Canada.

STATEMENT from By-Laws. The Society shall not be responsible for statements or opinions advanced in papers or . . . printed in its publications (B7.1, Par. 3).

COPYRIGHT © 1989 by the American Society of Mechanical Engineers. Reprints from this publication may be made on condition that full credit be given the TRANSACTIONS OF THE ASME, JOURNAL OF APPLIED MECHANICS, and the author, and date of publication be stated.

INDEXED by Applied Mechanics Reviews and Engineering Information, Inc.

Journal of Applied Mechanics

Published Quarterly by The American Society of Mechanical Engineers

VOLUME 56 • NUMBER 1 • MARCH 1989

TECHNICAL PAPERS

1 Dynamic Shear Band Development in Plane Strain
A. Needleman

10 A Generalization of the Upper Bound Method With Particular Reference to the Problem of a Ploughing Indenter (89-APM-7)
A. Azarkhin and O. Richmond

15 Analysis of Steady Compaction Waves in Porous Materials
J. M. Powers, D. S. Stewart, and H. Krier

25 A Constitutive Model for a Jointed Rock Mass With Orthogonal Sets of Joints
E. P. Chen

33 An Asympotic Analysis of Cold Sheet Rolling
R. P. Smet and R. E. Johnson

40 Growth of an Infinitesimal Cavity in a Rate-Dependent Solid
R. Abeyaratne and H.-S. Hou

47 Melting From a Horizontal Rotating Disk
C. Y. Wang

51 A Mesomechanical Model for Brittle Deformation Processes: Part I (89-WA/APM-1)
D. Krajcinovic and D. Sumarac

57 A Mesomechanical Model for Brittle Deformation Processes: Part II (89-WA/APM-2)
D. Sumarac and D. Krajcinovic

63 Analysis of a Vertical Crack in a Multilayered Medium (89-APM-24)
W. Lin and L. M. Keer

70 The Hemispheroidal Inhomogeneity at the Free Surface of an Elastic Half Space (89-APM-2)
D. Kouris, E. Tsuchida, and T. Mura

77 A Test Specimen for Determining the Fracture Resistance of Bimaterial Interfaces
P. G. Charalambides, J. Lund, A. G. Evans, and R. M. McMeeking

83 An Examination of the Mori-Tanaka Effective Medium Approximation for Multiphase Composites
A. N. Norris

89 Magnetic Fields Generated by a Mechanical Singularity in a Magnetized Elastic Half Plane
C.-S. Yeh

96 A Theoretical and Experimental Study of a Curved Strip Compressed by a Flat Plate
H. Iseki, R. Sowerby, D. Bhattacharyya, and P. Gatt

105 Self-Equilibrated Singular Solutions of a Complete Spherical Shell: Classical Theory Approach
N. Simos and A. M. Sadegh

113 Axial Crushing of Multicorner Sheet Metal Columns
W. Abramowicz and T. Wierzbicki

121 Buckling of Edge Damaged, Cylindrical Composite Shells
M. Sabag, Y. Stavsky, and J. B. Greenberg

127 Deflection and Snapping of Ring-Loaded Spherical Caps
C. W. Brodland and H. Cohen

133 Rigid Body Collisions (89-APM-3)
R. M. Brach

139 An Historical Note on Finite Rotations
H. Cheng and K. C. Gupta

146 On Standard Eigenvalues of Variable-Coefficient Heat and Rod Equations
H. P. W. Gottlieb

149 An Alternating Frequency/Time Domain Method for Calculating the Steady-State Response of Nonlinear Dynamic Systems
T. M. Cameron and J. H. Griffin

155 On the Stability Behavior of Bifurcated Normal Modes in Coupled Nonlinear Systems (89-APM-1)
C. H. Pak

162 Order and Chaos in a Discrete Duffing Oscillator: Implications on Numerical Integration (89-APM-6)
P. G. Reinhall, T. K. Caughey, and D. W. Storti

168 The Onset of Chaos in a Two-Degree-of-Freedom Impacting System
J. Shaw and S. W. Shaw

175 Almost-Sure Stability of Some Linear Stochastic Systems
S. T. Ariaratnam and B. L. Ly

179 Methods and Gaussian Criterion for Statistical Linearization of Stochastic Parametrically and Externally Excited Nonlinear Systems
R. J. Chang and G. E. Young

(Contents continued on Inside Back Cover)

Downloaded 04 May 2010 to 171.66.16.49. Redistribution subject to ASME license or copyright; see http://www.asme.org/terms/Terms_Use.cfm

CONTENTS (Continued)

186 **Statistical Identification of Nonlinear Random Vibration Systems**
T. Ozaki

192 **Response and Stability of a Random Differential Equation: Part I—Moment Equation Method**
H. Benaroya and M. Rehak

196 **Response and Stability of a Random Differential Equation: Part II—Expansion Method**
H. Benaroya and M. Rehak

202 **Probability Distribution of the Eigenvalues of the Random String Equation**
R. N. Iyengar and C. S. Manohar

208 **In Integral Variational Equation for Transport Processes in a Moving Fluid**
E. S. Geskin

211 **Boundary Integral Analysis of the Creeping Flow of Long Bubbles in Capillaries**
M. J. Martinez and K. S. Udell

218 **A Similar Flow Between Two Disks in the Presence of a Magnetic Field**
E. A. Hamza

BRIEF NOTES

On Immobile Kinematic Chains and a Fallacious Matrix Analysis **E. N. Kuznetsov** 222

A Way of Accurately Estimating Eigenvalues **R. Schmidt** 224

Thermodynamical Inequalities, Reciprocal Relations, and Mixtures **A. E. Green and P. M. Naghdi** 226

228 Vibration of Beams and Plate Strips With Three-Dimensional Flexibility **M. Stein**

231 Two-Dimensional Singularity Solutions in the Presence of an Elliptical Hole **M. Denda**

DISCUSSION

234 **Discussion on a previously published paper by M. S. Willet and W. L. Poesch**

BOOK REVIEWS

236 ***Propagation of Transient Elastic Waves in Stratified Anisotropic Medium*** **by J. H. M. T. Van der Hijden** . . . Reviewed by **S. K. Datta**

235 ***Dynamics of Multibody Systems*** **by R. E. Roberson and R. Schwertassek** . . . Reviewed by **R. L. Huston**

236 ***Die Methode der Finiten Elemente, Band III*** **by J. Argyris and H.-P. Miejnek** . . . Reviewed by **K. Appa**

237 Books Received by the Office of the Technical Editor

238 Worldwide Mechanics Meeting List

217 *Change of Address Form*

32, 46, 50, 95
148,191,201 Applied Mechanics Symposium Proceedings

Downloaded 04 May 2010 to 171.66.16.49. Redistribution subject to ASME license or copyright; see http://www.asme.org/terms/Terms_Use.cfm

Dynamic Shear Band Development in Plane Strain

A. Needleman
Division of Engineering,
Brown University,
Providence, R.I. 02912
Mem. ASME

Plane strain compression of a rectangular block is used as a model problem to investigate the dynamics of shear band development from an internal inhomogeneity. The material is characterized as a von Mises elastic-viscoplastic solid, with a hardness function that exhibits a local maximum. Regardless of whether the material is hardening or softening, plastic strain development involves the evolution of fingerlike contours emanating from the inhomogeneity at 45 deg to the compression axis. Once a given strain contour crosses the specimen, it fans out about its initial direction of propagation. For a softening solid, this fanning out ceases for some strain level greater than the strain at the hardness maximum and further straining takes place in an ever narrowing band. Many of the qualitative features of shear band development under dynamic loading conditions are the same as under quasi-static loading conditions, but a significant retardation of shear band development due to inertial effects is found.

1 Introduction

Large inelastic deformations are frequently accompanied by the formation of intense bands of localized shearing. Often the large localized strains in a shear band precipitate a shear fracture. In other circumstances shear bands do not lead to fracture, but localized shearing becomes an important mechanism for subsequent plastic deformation. Hence, shear bands have a dual significance; as a precursor to fracture and as a mechanism of large strain plastic response.

When the solid is considered to be deforming quasi-statically and isothermally, shear band localizations can be analyzed as a "material instability," within a framework due to Hadamard (1903), Thomas (1961), Hill (1962), Mandel (1966), and Rice (1977). Within this framework, a material element is considered subject to all around displacement boundary conditions consistent with homogeneous deformations; different homogeneous deformations states prevail outside and inside the band and the analysis determines the jumps in field quantities across the band interface. For rate independent solids, the onset of a shear band localization can occur as a bifurcation corresponding to a loss of ellipticity of the rate equilibrium equations (Hill (1962), Rice (1977)). For rate sensitive solids a bifurcation is effectively excluded and the governing rate equations remain elliptic, although in the presence of initial band type imperfections shear band localizations do emerge (e.g., Pan et al., 1983).

The analysis of shear band development in nonhomogeneously deforming solids requires a full boundary value problem solution. Such solutions have been obtained for the quasi-static development of shear bands (see, e.g., Tvergaard et al. (1981), Triantafyllidis et al. (1982), LeMonds and Needleman (1986), and the review of Needleman and Tvergaard (1983)), and have shown that shear bands do initiate with the orientation given by the "material instability" analysis. Shear band propagation, however, is greatly affected by the inhomogeneity of the surrounding fields.

The physical mechanisms responsible for triggering shear bands can vary widely. At low strain rates, a key feature of plastic material response for localization is the yield surface vertex structure implied by the discrete nature of crystallographic slip. The significance of a vertex lies in the reduced stiffness to a change in loading path which permits shear bands to emerge in strain hardening materials (see, e.g., Rice (1977)). At higher strain rates, thermal softening appears to play a major role in shear band formation, as originally suggested by Zener and Holloman (1944). An overview of conditions for high rate shear band formation in simple shear and correlation with experiments is given by Clifton et al. (1984).

Profusions of internal shear bands are sometimes observed (e.g., Anand and Spitzig (1980)), and these bands appear to originate at internal inhomogeneities. Analyses of shear localization from internal strain concentrators have been carried out by Abeyaratne and Triantafyllidis (1981), Tvergaard (1982, 1987), Freund, Wu and Toulios (1985), and LeMonds and Needleman (1986). Abeyaratne and Triantafyllidis (1981) investigated shear band initiation in quasi-statically deforming hypo-elastic and hyper-elastic solids in plane strain. LeMonds and Needleman (1986) also considered plane strain quasi-static deformations but analyzed the course of shear band development in elastic-viscoplastic solids, accounting for strain hardening, rate dependence, thermal softening, and heat conduction. Tvergaard (1982, 1987) has studied the quasi-static response of porous plastic solids having two size scales of void nucleating particles and where early nucleation at relatively

Contributed by the Applied Mechanics Division of THE AMERICAN SOCIETY OF MECHANICAL ENGINEERS for publication in the JOURNAL OF APPLIED MECHANICS.

Discussion on this paper should be addressed to the Editorial Department, ASME, United Engineering Center, 345 East 47th Street, New York, N.Y. 10017, and will be accepted until two months after final publication of the paper itself in the JOURNAL OF APPLIED MECHANICS. Manuscript received by ASME Applied Mechanics Division, December 1, 1987; final revision, July 13, 1988.

Copyright © 1989 by ASME

Downloaded 03 May 2010 to 171.66.16.31. Redistribution subject to ASME license or copyright; see http://www.asme.org/terms/Terms_Use.cfm

large particles triggers localization into a void sheet. In Freund, Wu and Toulios (1985) the dynamics of shear band propagation was analyzed for a nonlinear elastic solid in antiplane strain.

Here, the dynamics of shear band development from internal material inhomogeneities under plane strain compressive loading is used as a model problem for investigating shear band propagation in a rate-sensitive solid under plane strain conditions. The material is characterized as an elastic-viscoplastic von Mises solid. In order to simulate the phenomenon of thermal softening due to adiabatic heating, the material is taken to be strain softening. Although attention is focused on circumstances where such softening is responsible for shear band development, it is important to emphasize that for more general constitutive descriptions of plastic flow, strain softening is not necessary to precipitate a shear band localization (Rudnicki and Rice (1975); Rice (1977)). Due to the viscoplastic formulation, wave speeds remain real even in the softening regime; in fact, regardless of the plastic prestrain, wave speeds are set by the elastic moduli. Furthermore, as a consequence, the pathological mesh size effects encountered in localization analyses for rate independent solids are eliminated (Needleman, 1988).

2 Problem Formulation

The analysis is based on a convected coordinate Lagrangian formulation of the field equations with the initial unstressed state taken as reference. All field quantities are considered to be functions of convected coordinates, y^i, which serve as particle labels, and time t. The position, relative to a fixed Cartesian frame, of a material point in the initial configuration is denoted by $\mathbf{x}$. In the current configuration the material point initially at $\mathbf{x}$ is at $\bar{\mathbf{x}}$. The displacement vector $\mathbf{u}$ and the deformation gradient $\mathbf{F}$ are defined by

$$\mathbf{u}=\bar{\mathbf{x}}-\mathbf{x}, \quad \mathbf{F}=\frac{\partial \bar{\mathbf{x}}}{\partial \mathbf{x}}. \tag{1}$$

Base vectors in the reference configuration (unbarred) and in the current configuration (barred) are given by

$$\mathbf{g}_i=\frac{\partial \mathbf{x}}{\partial y^i}, \ \bar{\mathbf{g}}_i=\frac{\partial \bar{\mathbf{x}}}{\partial y^i} \tag{2}$$

$$\mathbf{g}^i=g^{ij}\mathbf{g}_j, \quad \bar{\mathbf{g}}^i=\bar{g}^{ij}\bar{\mathbf{g}}_j \tag{3}$$

where g^{ij} and $\bar{g}^{ij}$ are, respectively, the inverses of the metric tensors $g_{ij}=\mathbf{g}_i\cdot\mathbf{g}_j$ and $\bar{g}_{ij}=\bar{\mathbf{g}}_i\cdot\bar{\mathbf{g}}_j$.

The momentum balance can be expressed either in terms of the symmetric Cauchy stress tensor σ or the nonsymmetric nominal stress tensor $\mathbf{s}$. These are related to the force, $\mathbf{df}$, transmitted across a material element by

$$\mathbf{df}=\bar{\nu}\cdot\sigma d\bar{S}=\nu\cdot\mathbf{s}dS \tag{4}$$

Here, $d\bar{S}$ and $\bar{\nu}$ give the area and orientation, in the current configuration, of a material element that had area dS and orientation ν in the reference configuration and the stress measures $\mathbf{s}$ and σ are related by

$$\mathbf{s}=\mathbf{F}^{-1}\cdot\tau \quad \tau=\det(\mathbf{F})\sigma. \tag{5}$$

The dynamic principle of virtual work is written as

$$\int_V s^{ji}\delta F_{ij}dV=\int_S T^i\delta\, u_i dS-\int_V \rho\frac{\partial^2 u^i}{\partial t^2}\delta u_i\, dV \tag{6}$$

where V, S, and ρ are the volume, surface and mass density, respectively, of the body in the reference configuration, and

$$T^i=s^{ji}\nu_j. \tag{7}$$

The specific problem considered is plane strain compression of an initially square block of dimension $2h_0 \times 2h_0$. The y^1-y^2 plane is taken to be the plane of deformation and the compression axis is aligned with the y^2 direction. The origin of the coordinate system is placed at the center of the block and identical displacement histories are imposed at $y^2=\pm h_0$ and the sides $y^1=\pm h_0$ remain traction-free. Attention is restricted to deformations that remain symmetric about both $y^1=0$ and $y^2=0$. The boundary conditions for the quadrant analyzed numerically are

$$\dot{u}_1=0 \quad \dot{T}^2=0 \qquad \text{at } y^1=0 \tag{8}$$

$$\dot{u}_2=0 \quad \dot{T}^1=0 \qquad \text{at } y^2=0 \tag{9}$$

$$\dot{T}^1=0 \quad \dot{T}^2=0 \qquad \text{at } y^1=h_0 \tag{10}$$

$$\dot{T}^1=0 \ \dot{u}^2=\dot{U}(t) \qquad \text{at } y^2=h_0 \tag{11}$$

where $\dot{(\ )}$ is $\partial(\ )/\partial t$.

The function $\dot{U}(t)$ in (11) is taken as

$$\dot{U}(t)=\begin{cases} V_1 t/t_1, & \text{for } t\le t_1; \\ V_1, & \text{for } t>t_1 \end{cases} \tag{12}$$

with V_1 being a prescribed velocity.

The material is characterized as an elastic-viscoplastic von Mises solid. The total rate of deformation, $\mathbf{D}$, is written as the sum of an elastic part, $\mathbf{D}^e$, and a plastic part $\mathbf{D}^p$, with

$$\mathbf{D}^e=\frac{1+\nu}{E}\hat{\tau}-\frac{\nu}{E}(\hat{\tau}:\mathbf{I})\mathbf{I} \tag{13}$$

$$\mathbf{D}^p=\frac{3\dot{\bar{\epsilon}}}{2\bar{\sigma}}\tau'=\dot{\bar{\epsilon}}\mathbf{p} \tag{14}$$

where $\hat{\tau}$ is the Jaumann rate of Kirchhoff stress, $\mathbf{I}$ is the identity tensor, $\hat{\tau}:\mathbf{I}$ is the trace of $\hat{\tau}$, $\dot{\bar{\epsilon}}$ is the effective plastic strain rate, E is Young's modulus, ν is Poisson's ratio, and

$$\tau'=\tau-\frac{1}{3}(\tau:\mathbf{I})\mathbf{I} \quad \bar{\sigma}^2=\frac{3}{2}\tau':\tau' \tag{15}$$

with $\tau':\tau'=\tau_{ij}\tau^{ji}$.

Combining equations (13) and (14) and inverting to express $\hat{\tau}$ in terms of $\mathbf{D}$, gives a relation of the form

$$\hat{\tau}=\mathbf{L}:\mathbf{D}-\mathbf{P} \quad \mathbf{P}=\dot{\bar{\epsilon}}\mathbf{L}:\mathbf{p}=\dot{\bar{\epsilon}}\mathbf{p}:\mathbf{L} \tag{16}$$

where $\mathbf{L}$ is the tensor of elastic moduli and the dyadic product $\mathbf{L}:\mathbf{p}$ denotes $L^{ijkl}p_{lk}$. On the current base vectors, (16) has the form

$$\hat{\tau}^{ij}=L^{ijkl}\dot{E}_{lk}-P^{ij}. \tag{17}$$

The Lagrangian strain rate appears in (17) via the identity $\dot{E}_{ij}=\bar{\mathbf{g}}_i\cdot\mathbf{D}\cdot\bar{\mathbf{g}}_j$ and its components on the reference base vectors are given by

$$\dot{E}_{ij}=\frac{1}{2}(\mathbf{F}^k_{,i}\dot{F}_{kj}+F^k_{,j}\dot{F}_{ki}). \tag{18}$$

The constitutive relation (17) can be expressed in terms of the convected derivative of Kirchhoff stress on the current base vectors, i.e., $\dot{\tau}^{ij}=\bar{\mathbf{g}}^i\cdot\dot{\tau}^c\cdot\bar{\mathbf{g}}^j$, as

$$\dot{\tau}^{ij}=C^{ijkl}\dot{E}_{lk}-P^{ij} \tag{19}$$

where

$$C^{ijkl}=L^{ijkl}-\frac{1}{2}\left[\bar{g}^{ik}\tau^{jl}+\bar{g}^{il}\tau^{jk}+\bar{g}^{jk}\tau^{il}+\bar{g}^{jl}\tau^{ik}\right]. \tag{20}$$

The uniaxial response is represented by the power law rate relation

$$\dot{\bar{\epsilon}}=\dot{\epsilon}_0[\bar{\sigma}/g(\bar{\epsilon})]^{1/m}. \tag{21}$$

The hardness function $g(\bar{\epsilon})$, with $\bar{\epsilon}=\int\dot{\bar{\epsilon}}dt$, represents the effective stress versus effective strain response in a tensile test carried out at a strain rate such that $\dot{\bar{\epsilon}}=\dot{\epsilon}_0$ and $\bar{\sigma}$ is the effective

Downloaded 03 May 2010 to 171.66.16.31. Redistribution subject to ASME license or copyright; see http://www.asme.org/terms/Terms_Use.cfm

stress defined in (15). In (21), $m > 0$ is the strain rate hardening exponent.

On quite general grounds, for metals undergoing plastic deformation due to dislocation motion, the plastic strain rate is appropriately taken as a function of the stress and the current state (Rice, 1970). The relation (21) employs the idealization of a single-parameter characterization of the current state. A fundamental distinction between rate-dependent material behavior as embodied in (21) and rate-independent behavior is that the plastic strain rate in (21) does not depend on incremental quantities. For structural metals at room temperature, values of m in the range 0.002 to 0.02 are representative (see, for example, data collected by Ghosh (1977)). Even though there is no explicit plastic yielding condition in the constitutive formulation, for this range of m, there is an apparent rate-dependent yield strength and an "unloading"-like response on strain rate reversal (see e.g. Needleman, 1988).

The power law description of material strain rate sensitivity in (21) is not a fundamental physical relation, but it can provide a reasonable representation of the strain rate sensitivity of common structural metals over several decades of strain rate. The physical background for power law viscoplasticity, and its limitations, are discussed by Asaro (1983) and Klopp, Clifton, and Shawki (1985).

The hardness function $g(\bar{\epsilon})$ is taken to have the form

$$g(\bar{\epsilon}) = \sigma_0 \frac{(1+\bar{\epsilon}/\epsilon_0)^N}{1+(\bar{\epsilon}/\epsilon_1)^2}. \tag{22}$$

In (22), σ_0 is a reference strength and for $\epsilon_1 \to \infty$, (22) reduces to a power law hardening relation. As ϵ_1 decreases, $g(\bar{\epsilon})$ exhibits strain softening at decreasing values of $\bar{\epsilon}$. Figure 1 shows curves of $g(\bar{\epsilon})$ versus $\bar{\epsilon}$ with $N = 0.1$ and $\epsilon_0 = 0.00218$ and for $\epsilon_1 = 10^4 \times \epsilon_0$, $200 \times \epsilon_0$ and $100 \times \epsilon_0$. The finite element calculations to be discussed subsequently are based on the three hardness functions shown in Fig. 1.

Since the plastic strain rate in (21) depends on the current state and not on incremental quantities, the propagation of disturbances depends on the elastic stiffness, which is consistent with observation (see, e.g., Clifton, 1972). In particular, the speed at which incremental disturbances propagate does not depend explicitly on whether the material is hardening or softening. Over the range of stress and deformation states arising in the numerical examples here, the maximum $\|\tau\| < 0.01 \times E$ and maximum principal logarithmic strains less than 0.5, wave speeds remain nearly constant at their linear elastic values, even in the softening regime.

3 Numerical Method

The discretization is carried out in the reference configuration with the convected coordinates, y^i, being the independent variables. Linear displacement triangular elements are used arranged in a quadrilateral pattern consisting of "crossed" triangles. The "crossed" triangular quadrilaterals are used both because of their ability to represent incompressible deformations without mesh locking (Nagtegaal et al., 1974), and because of their ability to reproduce localized deformation modes that are oblique to the quadrilateral mesh (Tvergaard et al., 1981; Needleman and Tvergaard, 1983). A lumped mass matrix is used instead of the consistent mass matrix in (28), since this has been found preferable for explicit time integration procedures, from the point of view of accuracy as well as computational efficiency (Krieg and Key, 1973). When the finite element approximations of the displacement components u^i are substituted into (6) and the integrations are carried out, the discretized equations of motion are obtained

$$\mathbf{M}\frac{\partial^2 \mathbf{U}}{\partial t^2} = \mathbf{R} \tag{23}$$

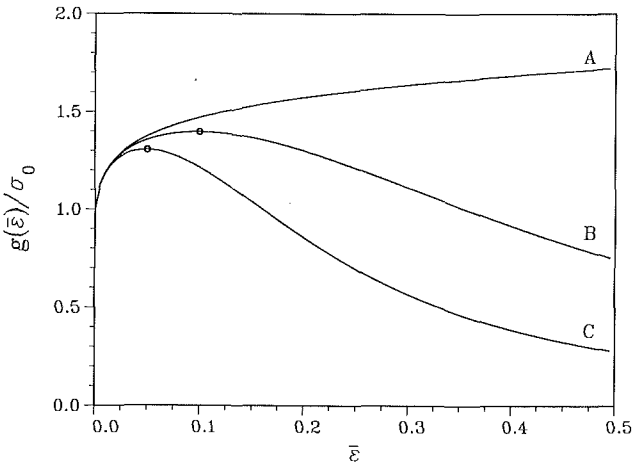


Fig. 1 Curves of hardness g versus effective plastic strain, $\bar{\epsilon}$, from (2.22) with $N = 0.1$, $\epsilon_0 = 0.00218$ and (A) $\epsilon_1 = 10^4 \times \epsilon_0$, (B) $\epsilon_1 = 200 \times \epsilon_0$ and (C) $\epsilon_1 = 100 \times \epsilon_0$

where $\mathbf{M}$ is a mass matrix, $\mathbf{U}$ is a nodal displacement vector and $\mathbf{R}$ is a nodal force vector.

An initial inhomogeneity is specified that corresponds to a local reduction in flow strength, σ_0 in (22) of the form

$$\sigma_0(y^1, y^2) = \bar{\sigma}_0[1 - \alpha \exp\{-[(y^1 - y_0^1)^2 + (y^2 - y_0^2)^2]/r_0^2\}] \tag{24}$$

where y_0^1 and y_0^2 specify the location of the inhomogeneity and r_0 and α give the inhomogeneity size and magnitude, respectively.

At $t = 0$, the rectangular block under consideration is taken to be stress-free and motionless. The equations of motion (23) are integrated using a central difference scheme that can be regarded as a member of the Newmark family of time stepping algorithms (Hughes and Belytschko, 1983).

At each time increment, the stress state is updated using the rate tangent method of Peirce et al. (1984). This combination of a central difference time-stepping scheme, in conjunction with the tangent modulus stress updating algorithm, is discussed by Moran (1987) and has also been used in Needleman (1988) and Tvergaard and Needleman (1988). For the present problem, the basic equations take the form

$$\mathbf{U}_{n+1} = \mathbf{U}_n + \Delta t \mathbf{V}_n + \frac{1}{2}(\Delta t)^2 \frac{\partial \mathbf{V}_n}{\partial t} \tag{25}$$

$$\frac{\partial \mathbf{V}_{n+1}}{\partial t} = -\mathbf{M}^{-1}\mathbf{R}_{n+1} \tag{26}$$

$$\mathbf{V}_{n+1} = \mathbf{V}_n + \frac{1}{2}\Delta t \left[\frac{\partial \mathbf{V}_n}{\partial t} + \frac{\partial \mathbf{V}_{n+1}}{\partial t}\right]. \tag{27}$$

Here, $\mathbf{U}$ is the vector of nodal displacements, $\mathbf{V}$ is the vector of nodal velocities, $\mathbf{M}^{-1}$ denotes the inverse of the mass matrix and the subscripts n and $n+1$ refer to quantities evaluated at t_n and t_{n+1}, respectively.

At each integration point, the stress tensor is updated via

$$\tau_{n+1}^{ij} = \tau_n^{ij} + \Delta t \dot{\tau}^{ij}. \tag{28}$$

The stress rate components, $\dot{\tau}^{ij}$, are computed from (19) and (20) with $\mathbf{L}$ and $\mathbf{P}$ replaced by the corresponding rate tangent quantities,

$$\mathbf{L}^{\tan} = L - \frac{\xi}{1+\xi}\frac{1}{h}(\mathbf{L}:\mathbf{p}) \otimes (\mathbf{L}:\mathbf{p}) \quad \mathbf{P}^{\tan} = \frac{\dot{\bar{\epsilon}}_t}{1+\xi}\mathbf{L}:\mathbf{p} \tag{29}$$

where $\mathbf{A} \otimes \mathbf{B}$ denotes the tensor product $A^{ij}B^{kl}$ and

$$\dot{\bar{\epsilon}}_t = \dot{\epsilon}_0[\bar{\sigma}/g(\bar{\epsilon})]^{1/m} \qquad \xi = (\theta \Delta t)h \frac{\partial \dot{\bar{\epsilon}}}{\partial \bar{\sigma}} \tag{30}$$

$$h = \mathbf{p}:\mathbf{L}:\mathbf{p} - \left(\frac{\partial \dot{\bar{\epsilon}}}{\partial \bar{\epsilon}}\right)\left(\frac{\partial \dot{\bar{\epsilon}}}{\partial \bar{\sigma}}\right)^{-1}. \tag{31}$$

Downloaded 03 May 2010 to 171.66.16.31. Redistribution subject to ASME license or copyright; see http://www.asme.org/terms/Terms_Use.cfm

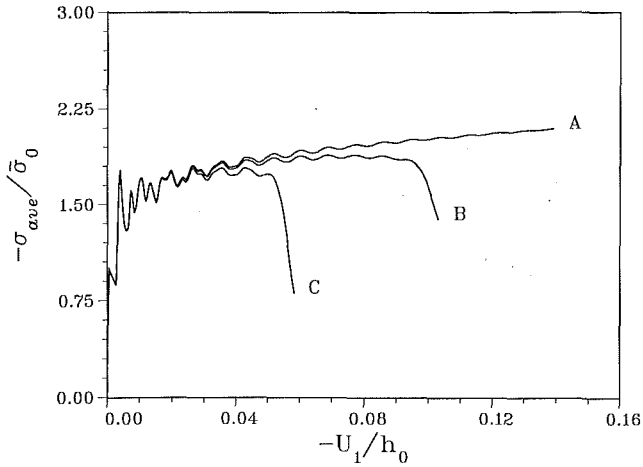


Fig. 2 Average stress versus end displacement curves with a prescribed velocity of $V_1 = -10$ m/s. The fixed material properties and initial inhomogeneity are specified in the text and curves (A), (B), and (C) correspond to the three hardness functions shown in Fig. 1.

In the second of (30), θ is a parameter of the integration scheme that is taken to be unity in the numerical calculations here.

The effective plastic strain is updated using $\bar{\epsilon}_{n+1} = \bar{\epsilon}_n + \Delta t \dot{\bar{\epsilon}}$ with

$$\dot{\bar{\epsilon}} = \frac{\Delta \bar{\epsilon}}{\Delta t} = \frac{\dot{\bar{\epsilon}}_t}{1+\xi} + \frac{\xi}{(1+\xi)h} (\mathbf{L}:\mathbf{p}):\mathbf{D}. \tag{32}$$

The constitutive updating calculations use $(\mathbf{U}_{n+1} - U_n)/\Delta t$ to represent the displacement rate components in (18).

In the limit $\xi \to \infty$, (29) through (32) reduce to their rate-independent counterparts. On the other hand, for $\xi = 0$, which results from setting $\theta = 0$ in the second of (30), the Euler integration scheme is recovered.

4 Results

In the calculations here, all material parameters are kept fixed except for ϵ_1 which governs the rate of softening. Although the aim here is not to model any particular material, the fixed property values are taken to be representative of structural steels; $E = 211$ GPa, $\bar{\sigma}_0 = 460$ MPa, $\epsilon_0 = \bar{\sigma}_0/E = 0.00218$, $\nu = 0.3$, $N = 0.1$, $m = 0.01$ and $\dot{\epsilon}_0 = 0.002\ s^{-1}$. The initial inhomogeneity in (24) is specified by $y_0^1 = y_0^2 = 0$, $\alpha = 0.2$ and $r_0 = 0.1$ mm. With $\rho = 7800\ kg/m^3 = 7.8 \times 10^{-3} MPa/(m/s)^2$, the elastic wave speeds are

$$c_0 = \sqrt{\frac{G}{\rho}} = 3.23 \times 10^3 m/s$$

$$c_1 = \sqrt{\frac{2G(1-\nu)/(1-2\nu)}{\rho}} = 6.03 \times 10^3 m/s \tag{33}$$

where $2G = E/(1+\nu)$.

Three values of the imposed velocity are considered; $V_1 = -3$ m/s, $V_1 = -10$ m/s and $V_1 = -30$ m/s, which correspond to $|V_1|/c_0 = 0.929 \times 10^{-3}$, $|V_1|/c_0 = 3.10 \times 10^{-3}$ and $|\mathbf{V}_1|/c_0 = 9.29 \times 10^{-3}$, respectively. In each case the rise time, t_1 in (12), is 0.1×10^{-6} s. Also, the block size h_0 is taken to be 1 mm, so that the nominal strain rates for the three imposed velocities are 3×10^3, 10^4, and 3×10^4, respectively.

A uniform finite element mesh is used, with the elements arranged so that at a strain a little larger than when the peak hardness is attained, the element diagonals are oriented for 45 deg shear bands. For the majority of calculations, with $\epsilon_1 = 200 \times \epsilon_0$, a 26×20 element mesh is used (the deformed mesh is shown subsequently in Fig. 8), while with $\epsilon_1 = 100 \times \epsilon_0$ a 24×20 mesh is used. In each case the 20 element division is in the y^2 direction. A variable time-step method is used with one criterion limiting the time step being the requirement that the time step be no greater than the time for a wave traveling at velocity c_1 to traverse half the smallest element side. With the ratio of wave speeds in (33), this is about 94 percent of the time for a wave traveling at the shear wave speed c_0 to traverse the smallest element side. Other time step limits are set by stability requirements for the rate tangent modulus integration of the constitutive relations. However, in the problems considered here these are rarely operative and the time step limits set by stability requirements for the explicit integration of the equations of motion determine the maximum permissible time step.

Figure 2 shows curves of average stress versus end displacement, with an imposed velocity of 10 m/s, for each of the hardening relations in Fig. 1. The average stress (per unit out-of-plane thickness) is given by

$$\sigma_{ave} = \frac{1}{h} \int_0^{h_0} [T^1]_{y^2 = h_0} dy^1 \tag{34}$$

where h is the current width at $y^2 = h_0$ and the end displacement is $U_1 = \int_0^t V_1 dt$.

The initial response is identical for the three hardening relations. Once extensive plastic deformation occurs, dynamic effects are rapidly damped. For the softening solids there is an abrupt stress drop that is associated with shear band formation.

Before considering shear band propagation, the dynamics of strain development for the hardening solid is shown in Fig. 3. Strain contours originate at the inhomogeneity and evolve as fingerlike contours at 45 deg to the compression axis. Once a given contour crosses the specimen, it fans out about its initial direction of propagation. This process continues and a shear band does not form for this strain hardening solid. In Fig. 3, the propagation speed along the 45 deg direction is 830 m/s for the 0.08 contour and 1100 m/s for the 0.09 contour.

For the softening solid in Fig. 4, strain development initially follows the pattern shown in Fig. 3. A shear band bifurcation occurs for the underlying rate-independent solid at the attainment of the maximum hardness and the 45 deg shear band orientation is the most critical one. Eventually, for a strain level beyond the peak in Fig. 1, spreading in the direction perpendicular to the initial propagation direction slows down and further straining occurs in a band. The ultimate course of events is essentially determined at the stage of loading shown in Fig. 4(*b*); continually increasing strain in a shear band with very little change in strain outside the band. Between Figs. 4(*a*) and 4(*b*), the speeds of propagation of the 0.07 and 0.08 contours are 2200 m/s and 1600 m/s, respectively. Between Figs. 4(*b*) and 4(*c*), the propagation speed of the 0.09 contour along the band is 2900 m/s, which is approaching the shear wave speed. For the case in Fig. 2 with $\epsilon_1 = 200 \times \epsilon_0$, plastic strain contour speeds at a similar stage of band development are somewhat slower, around 1300 m/s.

Figure 5 shows the effect of prescribed velocity on the average stress versus end displacement response for a material characterized by the hardness function with $\epsilon_1 = 200 \times \epsilon_0$. With $V_1 = -3$ m/s, corresponding to an average strain rate of 3000/s, the response is essentially quasi-static as soon as there is any significant plasticity. When the velocity is increased to -10 m/s, (this is the same case as B in Fig. 2) dynamic effects persist much longer, but have been essentially damped out by the time localization initiates. At $V_1 = -30$ m/s, significant inertial effects are evident trough localization initiation. If the imposed velocity were increased much beyond -30 m/s, the average stress would change sign at the first trough, indicating a separation event, subsequent to which imposition of (11) would not be the physically appropriate boundary condition.

Downloaded 03 May 2010 to 171.66.16.31. Redistribution subject to ASME license or copyright; see http://www.asme.org/terms/Terms_Use.cfm

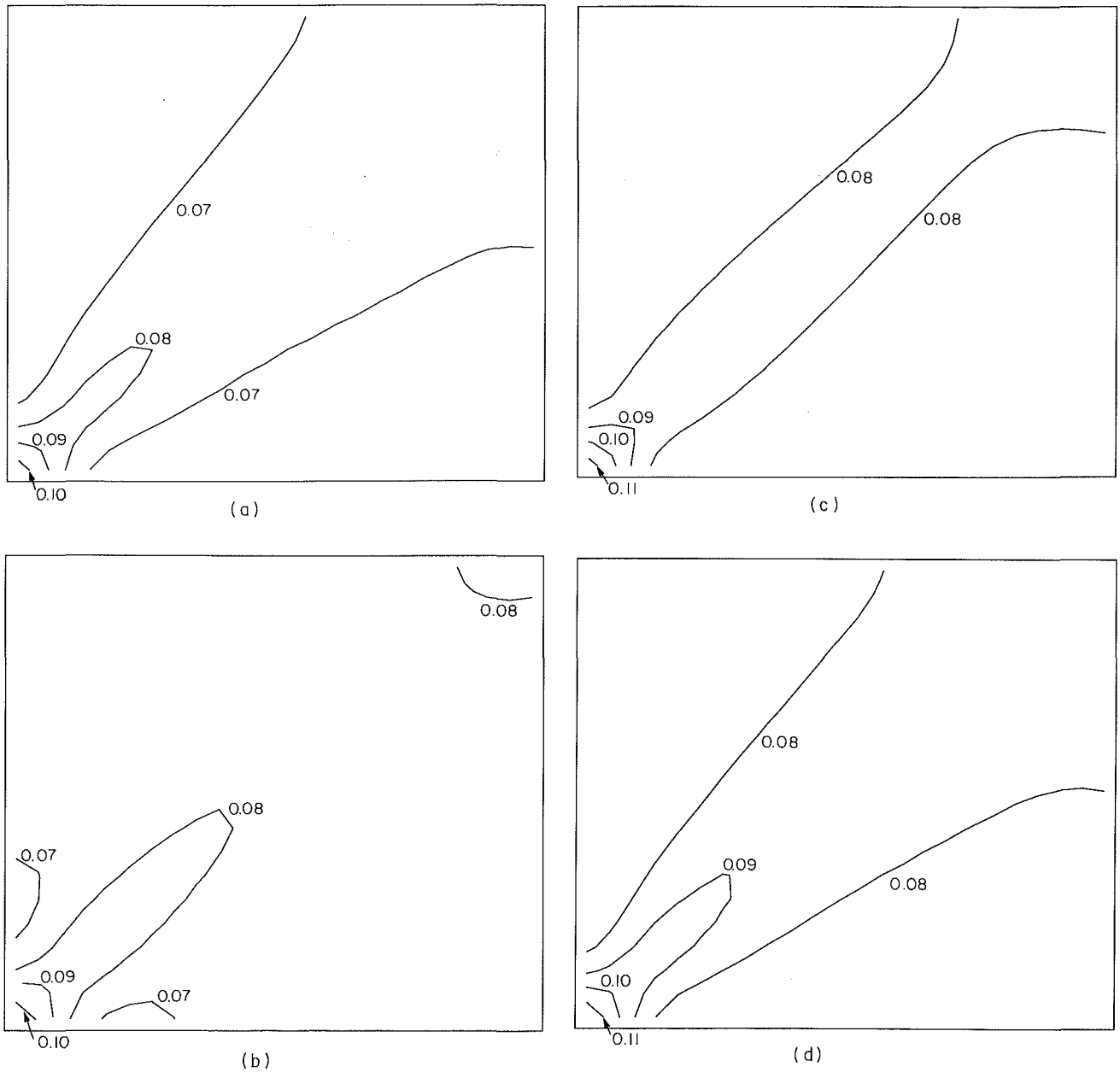
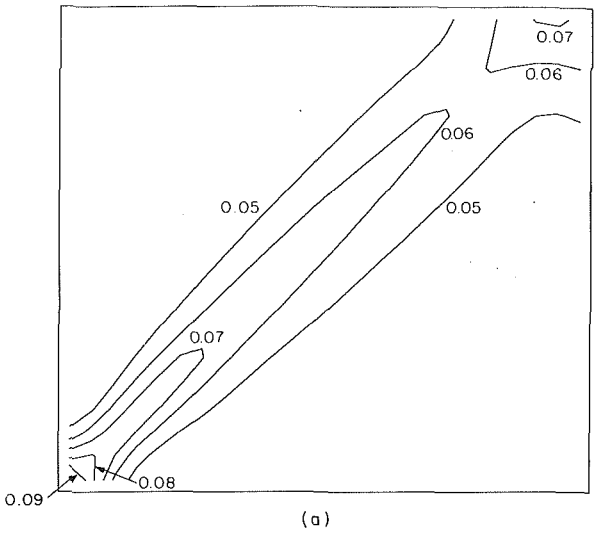


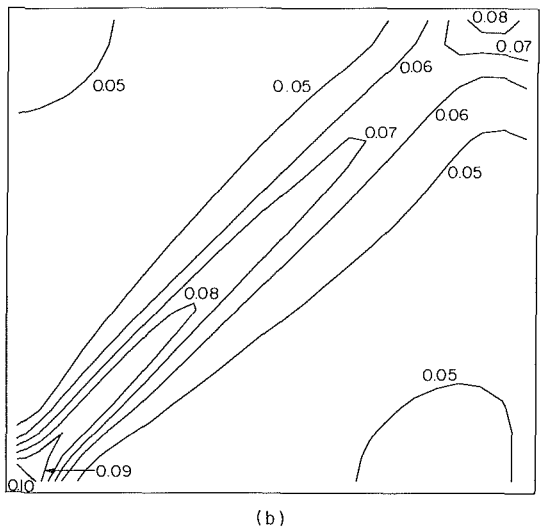
Fig. 3 Contours of constant effective plastic strain, $\bar{\epsilon}$, for a hardening solid, $\epsilon_1 = 10^4 \times \epsilon_0$. The fixed material properties and initial inhomogeneity are specified in the text and the prescribed end velocity is $V_1 = -10$ m/s; (*a*) $t = 6.44 \times 10^{-6}$ s, (*b*) $t = 6.71 \times 10^{-6}$ s, (*c*) $t = 6.98 \times 10^{-6}$ s, and (*d*) $t = 7.25 \times 10^{-6}$ s.

Quasi-static calculations were carried out using the same material properties and using an identical finite element mesh for the cases in Fig. 5 with $V_1 = -3$ m/s and $V_1 = -30$ m/s. With $V_1 = -3$ m/s, except for the lack of "wiggles," the quasi-statically computed stress strain curve coincides with that in Fig. 5 up to the drop due to shear localization. The quasi-static calculation gives localization at a strain 0.0006 smaller than given by the dynamic calculation in Fig. 5, but other than this small shift, the quasi-static postlocalization response is indistinguishable from the dynamic response shown. The case analyzed here is one for which there are equilibrium solutions with increasing end displacement during shear band development. In some circumstances (see, e.g., Tvergaard et al., 1981), there may be no equilibrium solutions having increasing end displacement as localization proceeds, and in such cases, dynamic effects may be significant for localization development even at very low imposed velocities.

In the quasi-static analysis with a prescribed velocity of -30 m/s, the order of magnitude increase in the nominal applied strain rate, from 3×10^3 to 3×10^4, gives an increase in stress level due to material rate sensitivity of about 2 percent ($10^{0.01} \approx 1.02$), but shear localization, as signaled by the drop in the overall stress-strain curve, occurs at nearly the same end displacement value as with $V_1 = -3$ m/s. This behavior is expected, since analyses of the effect of rate sensitivity on plastic instabilities in rigid-plastic power law rate hardening materials, e.g. Hutchinson and Neale (1977), show that while the instability strain depends sensitively on the strain rate hardening exponent, it is independent of the rate. Hence, the delay in shear band initiation with increasing imposed velocity evident in Fig. 5 is a consequence of material inertia and not of material strain rate sensitivity.

Downloaded 03 May 2010 to 171.66.16.31. Redistribution subject to ASME license or copyright; see http://www.asme.org/terms/Terms_Use.cfm





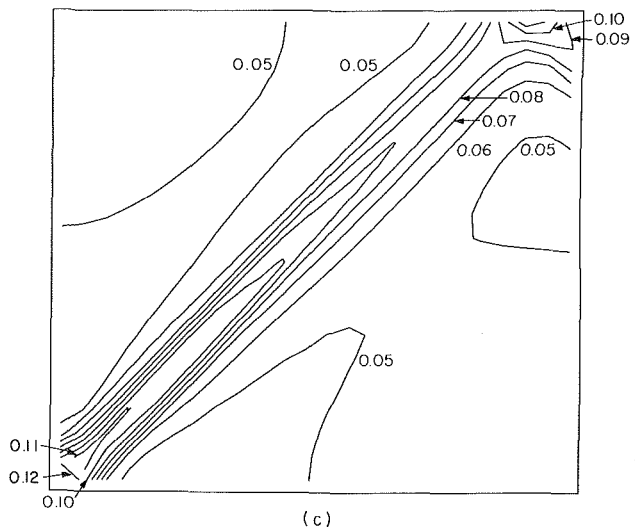


Fig. 4 Contours of constant effective plastic strain, $\bar{\epsilon}$, for a softening solid, $\epsilon_1 = 100 \times \epsilon_0$. The fixed material properties and initial inhomogeneity are specified in the text and the prescribed end velocity is $V_1 = -10$ m/s; (a) $t = 4.75 \times 10^{-6}$ s, (b) $t = 5.02 \times 10^{-6}$ s, and (c) $t = 5.28 \times 10^{-6}$ s.

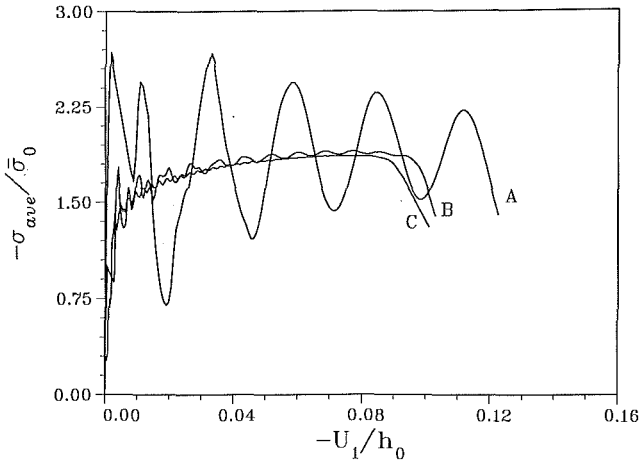


Fig. 5 Average stress versus end displacement curves for a softening solid, $\epsilon_1 = 200 \times \epsilon_0$ with (A) $V_1 = -30$ m/s, (B) $V_1 = -10$ m/s, and (C) $V_1 = -3$ m/s.

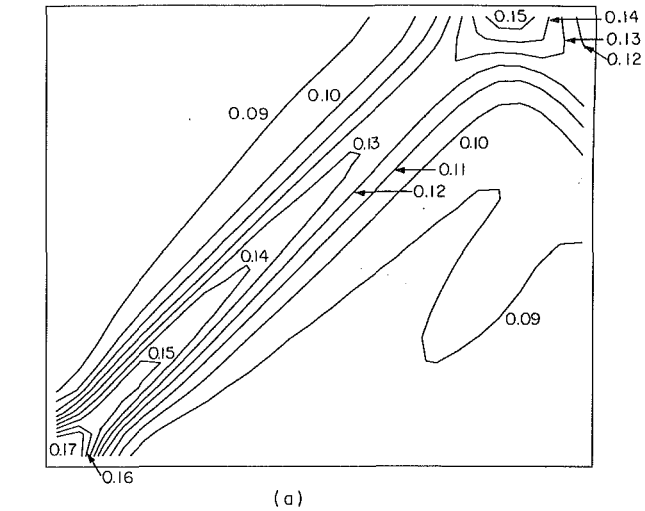
There is a significant distinction between the dynamic and quasi-static formulations regarding characteristic time scales. In the quasi-static formulation there is a single material time scale, $1/\dot{\epsilon}_0$, while in the dynamic formulation there are two; $1/\dot{\epsilon}_0$ and a problem-dependent time scale that is a wave speed divided by a characteristic length, e.g., c_0/h_0. The rate of strain development scales with $V_1/\dot{\epsilon}_0 h_0$ in the quasi-static formulation, but not in the dynamic analyses, due to inertial effects.

Figures 6 and 7 show the course of shear band development for $V_1 = -3$ m/s and $V_1 = -30$ m/s, respectively. There is a clear effect of imposed velocity on the speed of propagation of the strain contours. For example, in Fig. 6 the 0.15 contour propagates along the band at a speed between 590 m/s and 680 m/s, while in Fig. 7, the corresponding propagation speed is 2500 m/s. The qualitative features of shear band development do not depend on the imposed rate, but it is evident in Figs. 6 and 7, as well as in Fig. 5, that there is a delay in shear band initiation with increasing rate.

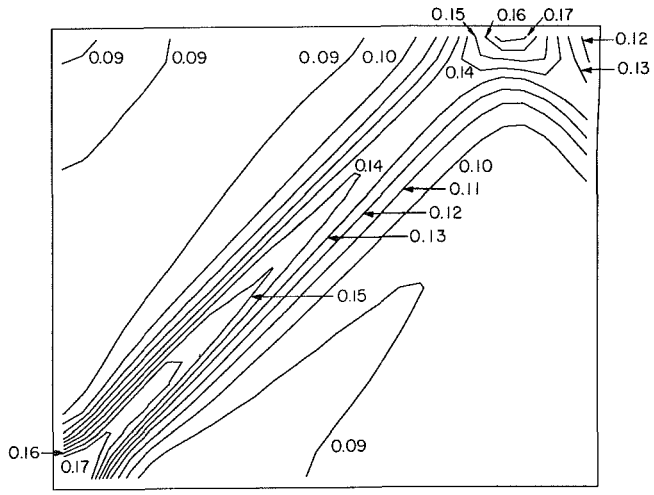
Figure 8 shows deformed finite element meshes at two stages of deformation. Figure 8(*a*) corresponds to the stage of deformation in Fig. 7(*c*). Even though the shear band has already formed, this is difficult to ascertain from the deformed mesh. At the stage of deformation in Fig. 8(*b*), the mesh is incapable of resolving the sharp strain gradients across the band and the discreteness of the mesh significantly affects the computed response. This figure is included to illustrate the ability of the mesh to develop a narrow shear band, which confirms, for example, that the initial thickness of the band evident in Figs. 3, 4, 6, and 7 is an actual reflection of the inhomogeneity size and is not a mesh artifact.

Several calculations were carried out to explore the effect of discretization parameters on the computed response. First, calculations were carried out for the case with $V_1 = -30$ m/s and $\epsilon_1 = 200 \times \epsilon_0$ using $\theta = 1$, $\theta = 0.5$ and $\theta = 0$ (the Euler integration scheme) in the rate tangent modulus constitutive update (equations (29) to (32)). The three calculations were continued to $U_1/h_0 = -0.107$ and the computed overall stress-strain curves were indistinguishable on the scale of Fig. 5. The computed field quantity distributions were also in excellent agreement; the difference in effective strain values at $U_1/h_0 = -0.107$ being at most one digit in the third significant figure. For numerical stability, with $\theta = 0$, smaller time steps were used than were used for the other two values of θ. Next, calculations were carried out using two additional meshes for the case with $V_1 = -10$ m/s and $\epsilon_1 = 100 \times \epsilon_0$. In one case the mesh aspect ratio was varied, while in the other case the aspect ratio was kept fixed, but a finer mesh was used.

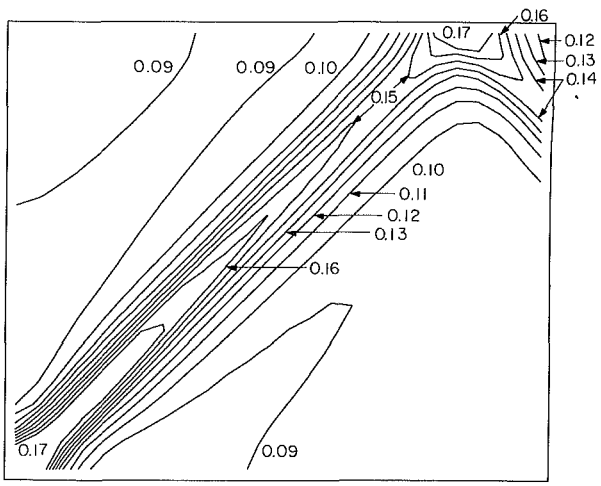
Downloaded 03 May 2010 to 171.66.16.31. Redistribution subject to ASME license or copyright; see http://www.asme.org/terms/Terms_Use.cfm



(a)

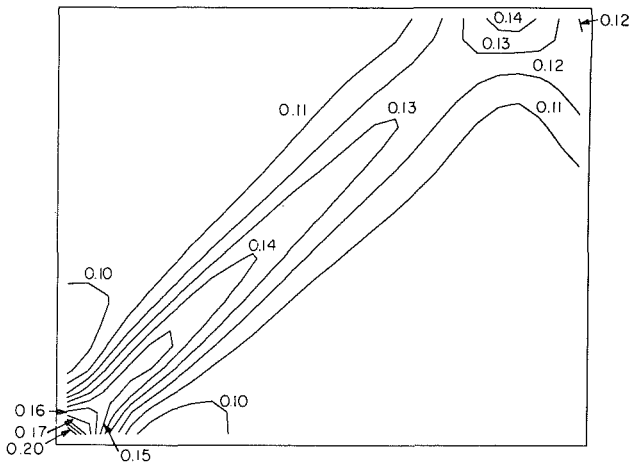


(b)

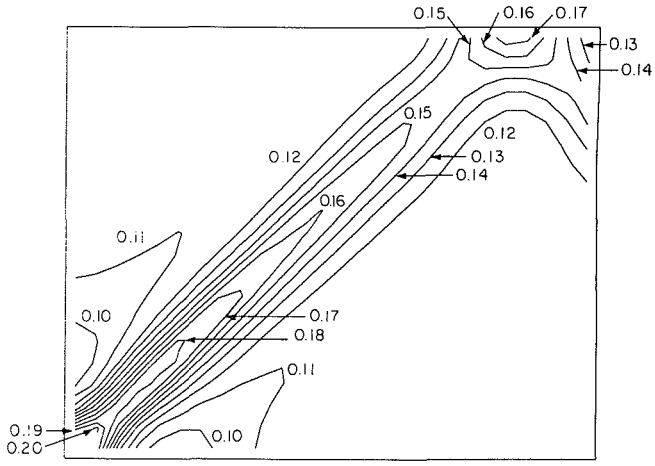


(c)

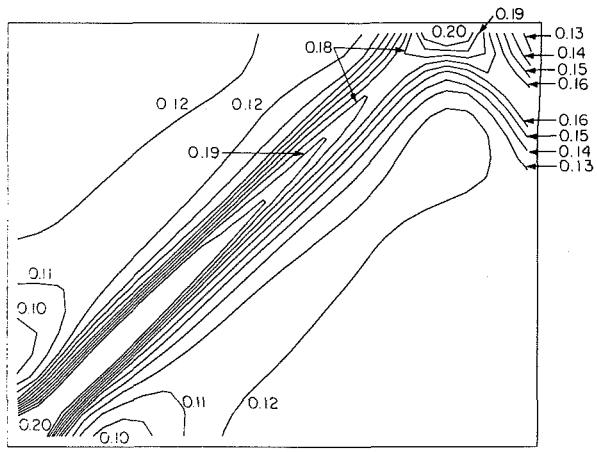
Fig. 6 Contours of constant effective plastic strain, $\bar{\epsilon}$, for a softening solid, $\epsilon_1 = 200 \times \epsilon_0$. The fixed material properties and initial inhomogeneity are specified in the text and the prescribed end velocity is $V_1 = -3$ m/s; (a) $t = 28.67 \times 10^{-6}$ s, (b) $= 29.19 \times 10^{-6}$ s, and (c) $t = 29.71 \times 10^{-6}$ s.



(a)



(b)

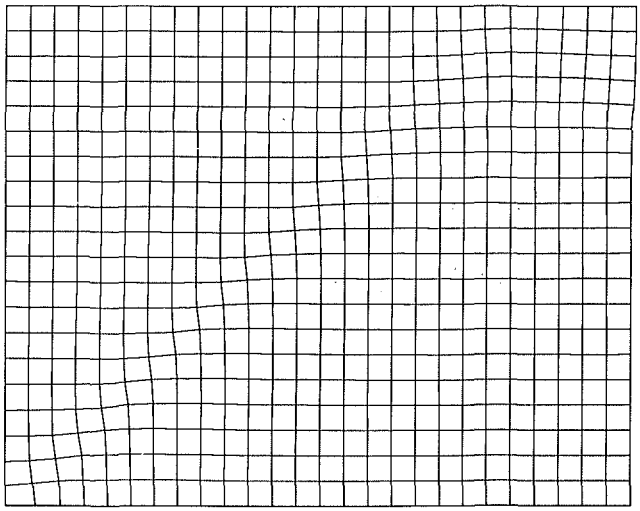


(c)

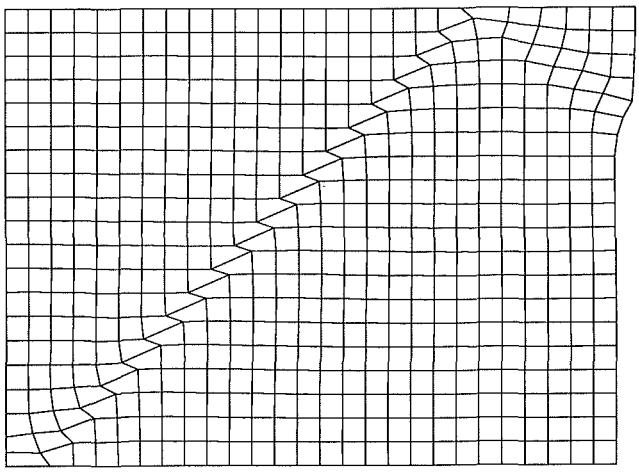
Fig. 7 Contours of constant effective plastic strain, $\bar{\epsilon}$, for a softening solid, $\epsilon_1 = 200 \times \epsilon_0$. The fixed material properties and initial inhomogeneity are specified in the text and the prescribed end velocity is $V_1 = -30$ m/s; (a) $t = 3.24 \times 10^{-6}$ s, (b) $t = 3.50 \times 10^{-6}$ s, and (c) $t = 3.76 \times 10^{-6}$ s.

The computed average stress versus end displacement curves are shown in Fig. 9. The consequences of a nonoptimal mesh orientation have been discussed by Tvergaard et al. (1981) and, consistent with their observations, the band in the nonoptimally oriented 29 × 20 mesh is spread across two rows of quadrilaterals. This gives rise to a significant mesh-induced delay in the onset of shear band formation even though this mesh has more elements than the reference mesh. Increasing the number of elements, but keeping a fixed aspect ratio leads

Downloaded 03 May 2010 to 171.66.16.31. Redistribution subject to ASME license or copyright; see http://www.asme.org/terms/Terms_Use.cfm



(a)



(b)

Fig. 8 Deformed finite element meshes for a softening solid, $\epsilon_1 = 200 \times \epsilon_0$. Each quadrilateral consists of four "crossed" triangular elements. The fixed material properties and initial inhomogeneity are specified in the text and the prescribed end velocity is $V_1 = -30$ m/s; (a) $t = 3.76 \times 10^{-6}$ s and (b) $t = 4.79 \times 10^{-6}$ s.

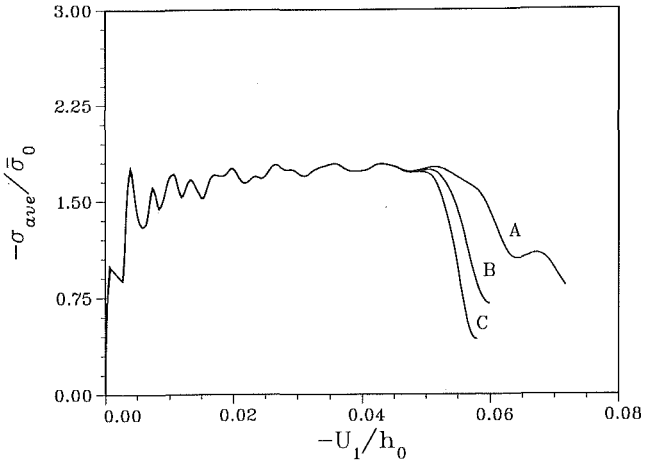


Fig. 9 Stress versus end displacement for a softening solid, $\epsilon_1 = 100 \times \epsilon_0$, with a prescribed velocity $V_1 = -10$ m/s using three meshes; (A) 29 × 20, (B) 24 × 20, and (C) 36 × 30

to a slightly earlier onset of localization, which is due in part to a better resolution of the strain concentration at the inhomogeneity. The finer mesh can also resolve larger gradients and so exhibits a greater stress drop before mesh-induced stiffening occurs. The postlocalization rise in the stress versus end displacement curve for the 29 × 20 mesh is a consequence of mesh-induced stiffening when gradients in the band become very large. A similar stiffening occurs for the other two meshes in Fig. 9, but occurs later in the deformation history with improved resolution of the band.

The speed of propagation of the constant plastic strain contours does not differ much between these three meshes. For the 24 × 20 mesh in Fig. 4, the propagation speed along the band of the 0.08 plastic strain contour is 1600 m/s. At a similar stage of deformation with the 36 × 30 mesh the 0.08 contour is propagating at 1900 m/s and at 1600 m/s with 29 × 20 mesh. The difference in propagation speed found for the 36 × 30 mesh is attributable more to variations in speed as the contour propagates along the band than to the increased resolution; with the 24 × 20 mesh in Fig. 4, a propagation speed of 2200 m/s is found for the 0.07 contour.

5 Discussion

Key features of the phenomenology of shear band development under dynamic loading conditions are the same as under quasi-static loading conditions. Shear bands do not occur for the strain hardening solid but, with softening, develop at 45 deg from the compression axis, as expected based on a quasi-static "material instability" analysis. Under quasi-static loading conditions, for the softening viscoplastic solids considered here, the strain at which shear bands initiate is an outcome of the competition between the destabilizing influence of the inhomogeneity and the stabilizing effect of material strain rate sensitivity. Under dynamic loading conditions, a delay in shear band development arises due to inertial effects. Also, since wave effects induce nonhomogeneous deformations, an inhomogeneity is not required to initiate localization, but, in the circumstances analyzed here, the inhomogeneity plays the major role in triggering the onset of shear localization.

The key to the development of shear bands in the calculations here is the reduction in speed of propagation of plastic strain contours in the direction normal to the eventual band. This is consistent with what would be expected based on a rate-independent shear band bifurcation analysis, where, at bifurcation, the propagation velocity of shear waves normal to the band vanishes. The vanishing of this wave speed is also the shear band initiation criterion that emerges from the perturbation analysis of Freund, Wu, and Toulios (1985). By way of contrast for the hardening solid in Fig. 3, a shear band does not form and strain contours continue to "fan out." The process of band formation, a cascade of fingerlike plastic strain contours emanating from the inhomogeneity and from a small region where the band intersects the impacted surface, in a continually sharpening band, is one that makes defining a band propagation speed somewhat arbitrary. Although there is no single event that can be identified with shear band initiation, there is a reasonably well identifiable strain in Figs. 4, 6, and 7 above which all further straining occurs within a narrowing band. A band propagation speed can be identified with propagation speed of some particular strain contour along the band, but this speed is not associated with some sharp gradient propagation through the material.

The main strain gradients occur across the band and large strain gradients do not develop along most of the band; substantial strain gradients in the band direction are confined to very near the inhomogeneity, and to a small region where the band intersects the impacted surface. This can be seen in Figs. 4, 6, and 7; for example, even in Fig. 7(*c*), the element in the center of the inhomogeneity has an effective plastic strain

Downloaded 03 May 2010 to 171.66.16.31. Redistribution subject to ASME license or copyright; see http://www.asme.org/terms/Terms_Use.cfm

of 0.33, while in the adjacent element in the shear band the effective plastic strain value is 0.25 (clearly, the mesh used here does not resolve the details of field distributions around the inhomogeneity). The continually steepening strain gradient across the band is much like that in one-dimensional simple shear calculations (e.g., Wada et al., 1978; Wu and Freund, 1984; Shawki, Clifton, and Majda, 1988; Needleman, 1988). Such narrowing shear bands are observed (Marchand and Duffy, 1988). In actuality, of course, under the conditions of temperature, strain, and strain rate that prevail in a narrow shear band, material behavior is not described by the sort of simple phenomenological constitutive relation used in this investigation. Also, some material-dependent length scale ultimately sets a minimum band thickness.

The situation analyzed in this investigation is one where, just prior to shear band formation, the stress and deformation fields are rather uniform. When shear band development takes place from a more nonuniform deformation state, the gradients in the background field retard shear band growth, as is shown in quasi-static analyses (Tvergaard et al., 1981; Triantafyllidis et al., 1982). Under dynamic loading conditions, when there are strong unfavorable gradients, shear bands are likely to propagate in a more cracklike fashion that in the cases analyzed here.

A strain softening constitutive relation has been used as a simple model for a thermal softening solid. For an actual thermal softening solid, the softening response varies with the imposed strain rate and increased thermal softening could accompany an increase in imposed strain rate, which would tend to counteract the delay in localization due to inertial effects.

Acknowledgments

The support of this work through ARO Grant DAA G29-85-K-0003 is gratefully acknowledged. The computations reported here were carried out on an Alliant FX-8 computer at the Brown University, Division of Engineering, Computational Mechanics Facility. I am pleased to acknowledge helpful discussions with Prof. R. J. Clifton of Brown University.

References

Abeyaratne, R., and Trintafyllidis, N., 1981, "The Emergence of Shear Bands in Plane Strain," *Int. J. Solids Struct.*, Vol. 17, pp. 1113–1134.

Anand, L., and Spitzig, W. A., 1980, "Initiation of Localized Shear Bands in Plane Strain," *J. Mech. Phys. Solids*, Vol. 28, pp. 113–128.

Asaro, R. J., 1983, "Mechanics of Crystals and Polycrystals," *Adv. Appl. Mech.*, Vol. 23, pp. 2–115.

Clifton, R. J., 1972, "Plastic Waves: Theory and Experiment," *Mechanics Today*, Vol. 1, S. Nemat-Nasser ed., Pergamon Press, Oxford, U.K., pp. 102–167.

Clifton, R. J., Duffy, J., Hartley, K. A., and Shawki, T. G., 1984, "On Critical Conditions for Shear Band Formation at High Rates," *Scripta Metall.*, Vol. 18, pp. 443–448.

Freund, L. B., Wu, F. H., and Toulios, M., 1985, "Initiation and Propagation of Shear Bands in Antiplane Shear Deformation," *Proc.* Considére Memorial Symposium, ed. J. Salençon ed., Ecole Nationale des Ponts et Chaussées, Paris, pp. 125–134.

Ghosh, A. K., 1977, "The Influence of Strain Hardening and Strain-Rate Sensitivity on Sheet Metal Forming," *J. Eng. Matl. Tech.*, Vol. 99, pp. 264–274.

Hadamard, J. J., 1903, *Leçons sur la Propagation des Ondes et Equations de L'Hydrodynamique*. Libraire Scientifique A. Hermann, Paris.

Hill, R., 1962, "Acceleration Waves in Solids," *J. Mech. Phys. Solids*, Vol. 10, pp. 1–16.

Hughes, T. J. R., and Belytschko, T., 1983, "A Precis of Developments in Computational Methods for Transient Analysis," ASME JOURNAL OF APPLIED MECHANICS, Vol. 50, pp. 1033–1041.

Hutchinson, J. W., and Neale, K. W., 1977, "Influence of Strain Rate Sensitivity on Necking under Uniaxial Tension," *Acta Met.*, Vol. 25, pp. 839–846.

Klopp, R. W., Clifton, R. J., and Shawki, T. G., 1985, "Pressure-Shear Impact and the Dynamic Viscoplastic Response of Metals," *Mech. Matl.*, Vol. 4, pp. 375–385.

Krieg, R. D., and Key, S. W., 1973, "Transient Shell Response by Numerical Time Integration," *Int. J. Numer. Meth. Engng.*, Vol. 7, pp. 273–286.

LeMonds, J., and Needleman, A., 1986, "Finite Element Analysis of Shear Localization in Rate and Temperature Dependent Solids," *Mech. Matl.*, Vol. 5, pp. 339–361.

Mandel, J., 1966, "Conditions de Stabilité et Postulat de Drucker," *Rheology and Soil Mechanics*, J. Krautchenko and P. M. Sirieys ed., Springer-Verlag, Berlin, pp. 58–68.

Marchand, A., and Duffy, J., 1988, "An Experimental Study of the Formation Process of Adiabatic Shear Bands in a Structural Steel," *J. Mech. Phys. Solids*, Vol. 36, pp. 251–283.

Moran, B., 1987, "A Finite Element Formulation for Transient Analysis of Viscoplastic Solids with Application to Stress Wave Propagation Problems," *Comp. Struct.*, Vol. 27, pp. 241–247.

Nagtegaal, J. C., Parks, D. M., and Rice, J. R., 1974, "On Numerically Accurate Finite Element Solutions in the Fully Plastic Range," *Comp. Meth. Appl. Mech. Eng.*, Vol. 4, pp. 153–177.

Needleman, A., 1988, "Material Rate Dependence and Mesh Sensitivity in Localization Problems," *Comp. Meth. Appl. Mech. Eng.*, Vol. 67, pp. 69–85.

Needleman, A., and Tvergaard, V., 1983, "Finite Element Analysis of Localization in Plasticity," *Finite Elements—Special Problems in Solid Mechanics*, Vol. 5, J. T. Oden and G. F. Carey ed., Prentice-Hall, Englewood Cliffs, N.J. pp. 94–157.

Pan, J., Saje, M., and Needleman, A., 1983, "Localization of Deformation in Rate Sensitive Porous Plastic Solids," *Int. J. Fracture*, Vol. 21, pp. 261–278.

Peirce, D., Shih, C. F., and Needleman, A., 1984, "A Tangent Modulus Method for Rate Dependent Solids," *Comp. Struct.*, Vol. 18, pp. 875–887.

Rice, J. R., 1970, "On the Structure of Stress-Strain Relations for Time-Dependent Plastic Deformation in Metals," *J. Appl. Mech.*, Vol. 37, pp. 728–737.

Rice, J. R., 1977, "The Localization of Plastic Deformation," *Theoretical and Applied Mechanics*, Proc. 14th Int. Congr. Theoret. Appl. Mech., W. T. Koiter ed., North-Holland, Amsterdam, pp. 207–220.

Rudnicki, J. W., and Rice, J. R., 1975, "Conditions for the Localization of Deformation in Pressure-Sensitive Dilatant Materials," *J. Mech. Phys. Solids*, Vol. 23, pp. 371–394.

Shawki, T. G., Clifton, R. J., and Majda, G., 1988, "Shear Band Formation in Thermal Viscoplastic Materials," to be published.

Thomas, T. Y., 1961, *Plastic Flow and Fracture of Solids*, Academic Press, New York.

Triantafyllidis, N., Needleman, A., and Tvergaard, V., 1982, "On the Development of Shear Bands in Pure Bending," *Int. J. Solids Struct.*, Vol. 187, pp. 121–138.

Tvergaard, V., 1982, "Ductile Fracture by Cavity Nucleation Between Larger Voids," *J. Mech. Phys. Solids*, Vol. 30, pp. 265–286.

Tvergaard, V., 1987, "Effect of Anisotropic Hardening on Ductile Failure of a Material Containing Two Size-Scales of Particles," DCAMM Report 354, The Technical University of Denmark.

Tvergaard, V., and Needleman, A., 1988, "Temperature and Rate Dependence of Charpy V-Notch Energies for a High Nitrogen Steel," *Int. J. Fracture*, Vol. 37, pp. 197–215.

Tvergaard, V., Needleman, A., and Lo, K. K., 1981, "Flow Localization in the Plane Strain Tensile Test," *J. Mech. Phys. Solids*, Vol. 29, pp. 115–142.

Wada, M., Nakamura, T., and Kinoshita, N., 1978, "Distribution of Temperature, Strain Rate and Strain in Plastically Deforming Metals at High Strain Rates," *Phil. Mag. A*, Vol. 38, pp. 167–185.

Wu, F. H., and Freund, L. B., 1984, "Deformation Trapping Due to Thermoplastic Instability in One-Dimensional Wave Propagation," *J. Mech. Phys. Solids*, Vol. 32, pp. 119–132.

Zener, C., and Holloman, J. H., 1944, "Effect of Strain Rate upon Plastic Flow of Steel," *J. Appl. Phys.*, Vol. 15, pp. 22–32.

Downloaded 03 May 2010 to 171.66.16.31. Redistribution subject to ASME license or copyright; see http://www.asme.org/terms/Terms_Use.cfm

A Generalization of the Upper Bound Method With Particular Reference to the Problem of a Ploughing Indenter

A. Azarkhin
Mem. ASME

O. Richmond
Mem. ASME

Alcoa Laboratories,
Alcoa Center, PA 15069

An algorithm based on a combination of the upper bound method and finite element repesentation has been developed. The algorithm is applied to the problem of a rigid indenter ploughing through a rigid/perfectly-plastic material. Numerical examples are given and the results are compared with previous approximate solutions. Limitations of the upper bound method are discussed.

1 Introduction

It is well established that friction and wear in macroscopically elastic contacts are directly related to local plastic deformation on the scale of surface asperities in the area of intimate contact between two sliding surfaces (Bowden and Tabor, 1950; Rabinowicz, 1965; Suh, 1986). Understanding of deformations on this scale is also important for optimization of metal forming processes (Wanheim, 1978; Rowe, 1977). A way to investigate the surface ploughing by an asperity is to represent the asperity in one of the major shapes—pyramid, cone, or spherical cap—and then to use the upper bound technique to evaluate the ploughing forces. Upper bound applications usually assume that a rigid/perfectly-plastic material moves around the asperity by rigid blocks, creating discontinuities of velocities at the interfaces between the blocks. Forces acting on the asperity are then estimated by minimization of power, taking into account additional constraints imposed by conservation of mass/volume and kinematic boundary conditions. The problem is nonlinear, and it is customary to take a small number of parameters and impose some additional simplifying assumptions to make the calculations tractable (De Vathire et al., 1981; Avitzur et al., 1984; Abildgaard, 1984). Often, only one free parameter is left to vary after all the others have been eliminated using constraints. This seems to justify doubts about the accuracy achieved. Thus, in this paper we suggest a combination of the upper bound method with finite difference/finite element representations. In contrast to the traditional representations, the elements (blocks) are plastically deformable and there are no discontinuities of velocities across the sides of the elements. We develop an algorithm for solving the corresponding equations with many parameters.

We present more accurate solutions for some previously solved examples to evaluate accuracy of the assumptions used. We also present a limited number of new examples to demonstrate some features of the suggested algorithm and to discuss limitations of the upper bound method itself. A systematic study of parameters for different types of asperities and conditions related to metal forming (elastic-plastic contact) will be given in a subsequent publication.

2 Discretization

2.1 Rates of Deformation. The problem is discretized by subdividing the domain into many elements with arbitrary shapes and numbers of sides so as to fit conveniently the shape of the asperity and the boundary of the domain. Expressions for the derivatives of velocities and, hence, rates of deformation, can be found from

$$\int_{\Delta V} \frac{\partial u_x}{\partial x} dV = \int_{\Delta S} u_x dS_x \cong \frac{\partial u_x}{\partial x} \Delta V \cong \sum_{i=1}^{L} (\bar{u}_x)_i (\Delta S_x)_i \qquad (1)$$

where ΔV is the volume of the element surface ΔS. Summation is performed over all L sides of the element. The bar denotes the velocity averaged over the side (i) using the node values, and the notation S_x indicates the projection of the surface onto the plane perpendicular to the x-axis. Then,

$$\epsilon_x = \frac{\partial u_x}{\partial x} \cong \frac{1}{\Delta V} \sum_{i=1}^{L} (\bar{u}_x)_i (\Delta S_x)_i. \qquad (2)$$

The derivatives $\partial u_y/\partial x$ and $\partial u_z/\partial x$ are obtained by replacing u_x in (2) by u_y and u_z, respectively. All other derivatives can be written in a similar manner. This version is convenient in that any shape of the element can be taken, and knowledge of the shape function is not required. But, of course, any other finite element/finite difference representation would do.

2.2 Boundary Conditions. We assume, throughout the

Contributed by the Applied Mechanics Division of THE AMERICAN SOCIETY OF MECHANICAL ENGINEERS for presentation at the Joint ASCE/ASME Applied Mechanics, Biomechanics, and Fluids Engineering Conference, San Diego, CA, July 9–12, 1989.

Discussion on this paper should be addressed to the Editorial Department, ASME, United Engineering Center, 345 East 47th Street, New York, N. Y., 10017, and will be accepted until two months after final publication of the paper itself in the JOURNAL OF APPLIED MECHANICS. Manuscript received by ASME Applied Mechanics Division, September 22, 1987; final revision, February 29, 1988.

Paper No. 89-APM-7.

Copyright © 1989 by ASME

Downloaded 03 May 2010 to 171.66.16.31. Redistribution subject to ASME license or copyright; see http://www.asme.org/terms/Terms_Use.cfm

paper, that the coordinate system is fixed with the indenter so that the indenter is stationary and the metal is moving. At infinity, velocities are prescribed. Numerically, infinity is modeled by considering a domain which is substantially larger than the size of the indenter. A sufficient size is found by trials; that is, the size is considered sufficient if further increase of the domain produces only small changes in the results. On the surface, which could be the free surface, or the surface of a confining lid, or the surface of the indenter, we require that

$$\mathbf{u}(s)\cdot\mathbf{n}=0 \tag{3}$$

where $\mathbf{u}$ is a velocity vector and $\mathbf{n}$ is the normal unit vector. One way to implement condition (3) is to write it down for each node of the surface. We, however, will use a milder form of condition (3), namely, the absence of flux across the surface of the element:

$$g=\bar{\mathbf{u}}\cdot\mathbf{n}\Delta S=0. \tag{4}$$

3 Upper Bound Method Formulation

In the upper bound method, the problem is posed as the minimization of the functional for the rate of energy. In our case, the functional is defined by

$$f(\mathbf{u})=\frac{\sqrt{3}\sigma_0}{2}\sum_{n=1}^{N}(\dot{\epsilon}_{ij}\dot{\epsilon}_{ij})_n^{1/2}\Delta V_n+\frac{1}{\sqrt{3}}\sum_{n=1}^{M}m\sigma_0|\mathbf{u}_n(s)|dS_n \tag{5}$$

where the rates of deformation $\dot{\epsilon}_{ij}$ are defined in terms of the velocity $\mathbf{u}$, by equation (2). In expression (5), N is the number of elements, M is the number of surfaces in contact with the indenter, m is the friction factor which can take values between 0 and 1 depending on lubrication and other surface conditions, σ_0 is the Mises yield stress, and velocities for minimization are chosen from a kinematically admissible set.

A remark related to the last term in equation (5) should be made. For the employed model of friction, commonly used for plastic problems, Hill's limit theorem is valid. Indeed, if shear tractions were known in both directions and values, we could have stated the theorem as

$$\int_v\left|\sigma'^{*}_{ij}\right|\left|d\epsilon^{*}_{ij}\right|dv$$

$$+\int_s F_i du_i^{*}ds\geq\int\left|\sigma'_{ij}\right|\left|d\epsilon_{ij}\right|dv+\int_s F_i du_i ds \tag{6}$$

where trial values are denoted by asterisks. In the present formulation, the directions are unknown, and we replace the scalar product $F_i du_i^{*}$ with the product of moduli

$$|F||du^{*}|=\frac{m\sigma_0}{\sqrt{3}}|du^{*}| \tag{7}$$

which can only exaggerate the inequality. Compare this with the case of Coulomb friction when the theorem does not apply (Drucker, 1954).

Besides the kinematic boundary conditions up- and downstream, the conditions of nonpenetration/separation at the interface in the form (3) or (4) should be maintained. Form (4), however, gave better stability for our examples.

Additional constraints follow from the condition of incompressibility. These can be written in differential form,

$$\dot{\epsilon}_{ii}=0 \tag{8}$$

or in integral form for each element

$$r=\sum_{i=1}^{L}\bar{\mathbf{u}}_i\cdot\mathbf{n}_i\Delta s_i=0. \tag{9}$$

In (9), $\bar{\mathbf{u}}_i$ is the average velocity vector for a side (i), $\mathbf{n}_i$ and Δs_i are, respectively, unit normal and the area of the side, and L is the number of sides. Strictly speaking, conditions (8) and (9) are identical. This is not necessarily so numerically. In usual finite element representations (see Zienkiewicz, 1983, for instance), because of the isoparametric mapping, say, expressions (8) and (9) give slightly different results. If (8) is used, some oscillations in the solution appear when the sizes of the elements are not small enough. Our major motivation for use of the formulation (1) and (2) was that (8) and (9) are then identical, since the derivatives are defined through fluxes for the given elements directly without mapping.

4 Numerical Implementation

4.1 Unconstrained Functional Formulation. Minimization of the functional (5) with constraints (4), (9) and with many parameters creates serious numerical difficulties. It is more convenient to restate the problem in terms of minimization of an unconstrained functional using the penalty approach (Bracken and McCormic, 1968). A generalized functional including constraints (4) and (9) is

$$F(\mathbf{u})=f(\mathbf{u})+A\left[\sum_{(j)}r_j^2+\sum_{(j)}g_j^2\right] \tag{10}$$

The first sum in (10) is taken over all elements, the second sum is taken over all interface surfaces of the elements. A is a large positive number so as to discourage attempts to violate constraints (4), (9). It should not be excessively large, however, or there may be problems of stability and convergence. An appropriate number is found by trial. Further details can be found in Bracken and McCormic (1968). A motivation for inclusion of ΔS in (4) is now apparent. It is a scaling factor to make dimensions of the two sums in (8) equal.

4.2 A Procedure for Minimization. There are several powerful techniques for minimization of unconstrained functionals (Brent, 1971; Fletcher and Powell, 1963; Fletcher and Reeves, 1964; Goldstein and Price, 1967). A few subroutines are also available in any scientific software. However, our experience with the present problem shows that they are too slow for practical purposes. The reason probably is that they are too general and do not consider the particular structure of the functional (10). After trying several versions of the procedures of minimization, we finally adopted the following one which seems to be straightforward. We start the iterative process by giving some increment to the first variable so that the functional is minimized with respect to that variable while keeping all other variables unchanged. Then we repeat this procedure with the second variable, the third, etc., until all have been adjusted. This completes the first iteration. The next iteration is then performed in the same manner. We abort the process when the change of the functional between the two iterations is less than some prescribed value. Each minimization of the functional (10) with respect to a variable is achieved by computing the functional for three values of the variable, $u_i-\Delta u$, u_i and $u_i+\Delta u$. The functional is then represented by a parabola fitting these values, and the minimum found.

We do not allow the increment to exceed some specified value because otherwise the behavior of the functional may deviate so much from a curve of the second order that a decrease of the functional is not achieved. This algorithm was used to obtain all results discussed next. Although convergence of the algorithm varied depending on the specific problem, $2N-3N$ iterations were required for a solution of 0.1 percent accuracy, with N being the number of variables.

Although the number of iterations is large, each iteration is fast. We note that when the increment Δu is given to a component velocity at some point (i, j, k), only energy and penalty terms for elements adjacent to that point change. All the other terms of the functional (10) do not change and need not be recomputed. This feature provides noticeable savings in com-

Downloaded 03 May 2010 to 171.66.16.31. Redistribution subject to ASME license or copyright; see http://www.asme.org/terms/Terms_Use.cfm

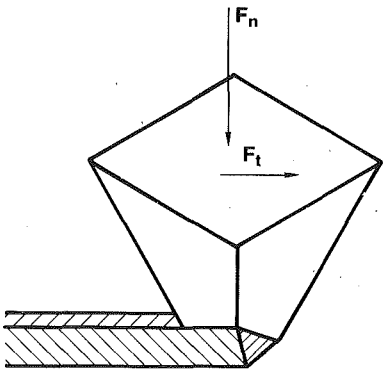


Fig. 1 A general view of a rigid pyramid ploughing through an indented material

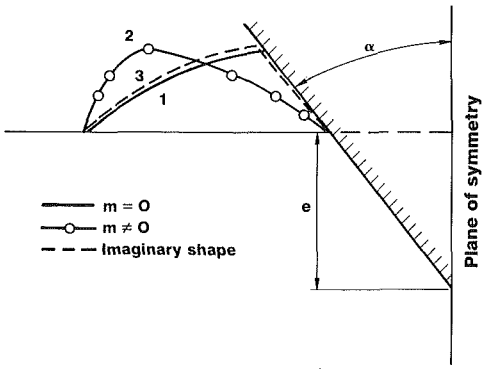


Fig. 2 Pile-up shapes and view normal to velocity V_0

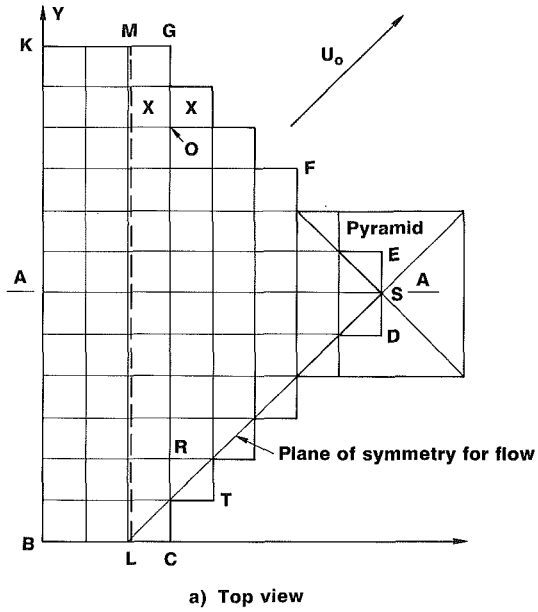
puting time, and would not be retained if we used a general purpose subroutine.

More details on the iterative process will be given later with particular examples.

5 Examples

5.1 Pile-Up Shape. Can It Be Determined? Let us consider an indenter with the shape of a pyramid ploughing through a rigid/perfectly-plastic material, as shown in Fig. 1. This particular problem was chosen because it has already been solved (DeVathire et al., 1981) by the usual upper bound technique, and because it presents a good example for testing the proposed approach. It also provides an opportunity to evaluate the previously used assumptions.

The upper bound method is based on the upper bound theorem (Gvozdev, 1960; Drucker et al., 1951; Drucker et al., 1952; Prager, 1959; Hill, 1952; Hill, 1957) which assumes that the configuration of the domain, including the free surface, is prescribed. Although this limitation of a prescribed free surface has been pointed out by several authors (e.g., DeVathire et al., 1981; Avitzur et al., 1984; and Oh and Kobayashi, 1975), they still attempted to use the method to obtain the shape of the free surface by the process of minimization. We tried the same, but the consequences were disastrous. In some cases, with $m=0$, the solution seemed reasonable, like the solid curve in Fig. 2. In other cases, like the curve with circles, it was unbelievable. The following example shows that the requirement that the surface must be prescribed is more than a mathematical formality needed to accomplish the proof. Suppose that the true solution with $m\neq 0$ looks like the solid line in Fig. 2. Consider some neighboring state which deviates from the previous one just enough to separate from the pyramid, curve 3 in Fig. 2. The energy of friction is then reduced to zero and the total power decreases. Further



a) Top view

Fig. 3 Top view of treated domain and mesh

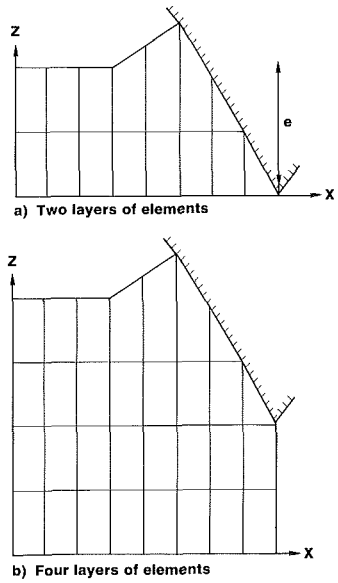


Fig. 4 Transverse section through indenter and mesh (Section AA of Fig. 3)

minimization begun from this state would lead us away from the true solution toward the curve with circles. We suggest the following explanation of the fact that in other works the use of minimization process has led to believable results. Too few parameters were used for minimization. The system was so stiff that in the process of minimization it could only move in the preassigned direction.

5.2 Verification of Some Other Assumptions. Other common assumptions in treating ploughing problems are:

(1) The deformation of the material below the tip of the indenter is negligible; and,

(2) The rate of energy is zero as soon as the material passes the maximum section of the indenter.

In order to evaluate these assumptions, we will compare our results with those of DeVathire et al., 1981. To do this, we preserve the shape of the pile-up as it is found in that paper keeping in mind, however, the remarks of the previous Sec-

Downloaded 03 May 2010 to 171.66.16.31. Redistribution subject to ASME license or copyright; see http://www.asme.org/terms/Terms_Use.cfm

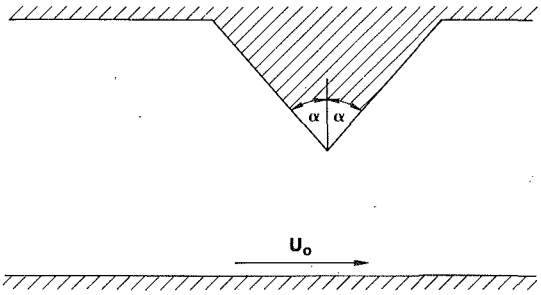


Fig. 5 Evaluation of the tangential forces as predicted by different models for $\alpha = 45$ deg

tion, 5.1. First, we keep these two assumptions, but introduce many parameters. Our mesh is shown in Figs. 3 and 4(*a*). It has 130 elements, 306 unknown components of velocity u_x, u_y and u_z, and 200 constraints.

To reduce the number of unknowns, the symmetry of the system was used. On boundaries *BC*, *BK*, *KG*, *GF*, *FE*, *ES* and at the bottom, velocities were prescribed. On the plane of symmetry for the flow, *LS*, one of the unknown velocities u_x was eliminated and replaced by u_y. For the points of type *T* on the boundary *CD*, all unknowns were eliminated and replaced by the unknowns at point *R* according to the rule

$$(u_x)_T = (u_y)_R$$

$$(u_y)_T = (u_x)_R$$

$$(u_z)_T = (u_z)_R$$

Results of calculations for power (or dimensionless tangential force) for a pyramid with the angle $\alpha = 45$ deg, are shown in Fig. 5. The solid curve reproduces the results of DeVathire et al., 1981. The present results are given by the broken curve. We can seen that the previous upper bound calculation was reduced by 10-20 percent by adding many parameters to the system.

A further decrease in power was observed when the deformation of the material below the tip of the pyramid was taken into account by adding two more layers of elements as shown in Fig. 4(*b*). The results are given by the curve with circles in Fig. 5. This curve shows that the subsurface deformation can play an important role in the deformation process and should not be neglected.

We will now evaluate the second assumption mentioned at the beginning of this subsection. There are two versions of implementing it. One version, which was employed in obtaining curves 2 and 3 of Fig. 5, is to assign the velocity on the boundary KGFES equal to that at infinity. This makes the system stiffer than it is in reality and gives an evaluation of the power from above. Another version is to include the velocities on the boundary KGFES in the parameters for minimization and assume that there is nothing behind the pyramid to obstruct the flow. That is, exit into an orifice is modeled. This model also was implemented and the results are given by the curve with triangles in Fig. 5. These two curves, with circles and with triangles, give the range for the evaluation of the rate of energy. If there were only one free parameter to minimize, like in DeVathire et al., 1981, the two versions would be identical.

We will now discuss one difficulty of the first version. It is obvious that the configuration of the surface and the velocities on the boundary KGFES are not completely independent. The area of the cross-section of the pile-up should be equal to that of the material replaced by the pyramid. This is not the only restriction on the configuration and velocities. Suppose the domain is truncated to LMGFEDCL as shown in Fig. 3. All node velocities of the corner element adjacent to MG and the

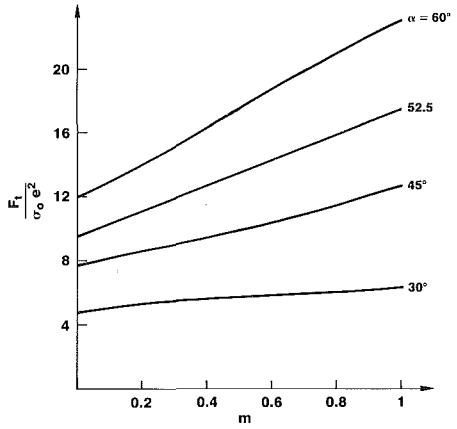


Fig. 6 Pyramid sliding in a confined volume

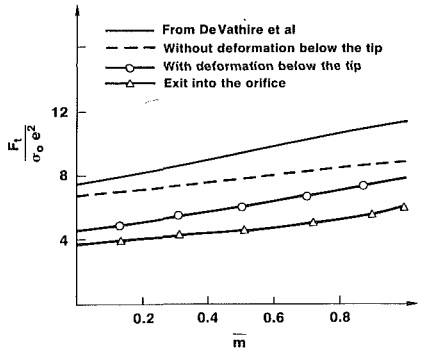


Fig. 7 Evaluation of the tangential force for the problem of Fig. 6 for different angles α, frictionless top

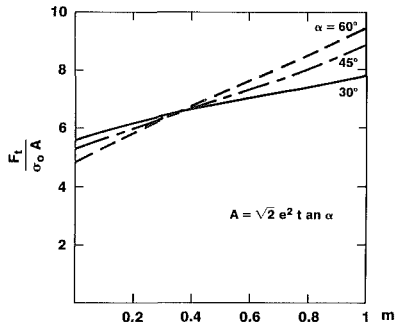


Fig. 8 Tangential force per unit area of projection for different angles α

element adjacent to LC are prescribed. But they cannot be prescribed arbitrarily because then conservation of volume could be violated. There is a less obvious problem with the truncated domain. To clarify it, let us assume that only one layer of elements is given. Then consider the two elements shown by the crosses in Fig. 3. Only three components of velocity for point 0, (u_x, u_y, and u_z) are available for minimization. All others are prescribed by the boundary conditions. But there are four constraints here: two conditions of conservation of volume (one for each element); and, two conditions that the fluxes across the top surfaces are equal to zero. The problem can be cured by expanding the domain, for example, to those which actually were considered before the truncation by ML.

Fortunately, this difficulty cannot be overlooked since the user will have a clear indication of the problem during the execution of the program. If there is a problem, one of several penalty terms in expression (10) will not be suppressed and a

Downloaded 03 May 2010 to 171.66.16.31. Redistribution subject to ASME license or copyright; see http://www.asme.org/terms/Terms_Use.cfm

large difference between $F(\mathbf{u})$ and $f(\mathbf{u})$ will be obtained. In addition, the flow of the metal will develop a strange pattern. We note that the other option, exit of the flow into an orifice, does not have this difficulty.

5.3 The Intenter in a Confined Volume-Fully Embedded Asperity. We now will study the case of sliding of a pyramid in a volume confined by a flat top surface as shown in Fig. 6. The pyramid is oriented with respect to the flow as before and as shown in Fig. 3.

The rate of work (or tangential force) is shown in Fig. 7 for different angles, α, of the pyramid and different friction factors, m. The data were obtained by considering the domain LMGEDC in Fig. 3 with four layers of elements, as shown in Fig. 4(b). Once again, the symmetry of the system was used.

We also assumed that the imposed hydrostatic pressure was sufficiently high to prevent the separation of the material at the back of the pyramid, hence, the velocities u_x, u_y, and u_z at a point in front of the pyramid were, respectively, equal to the velocities u_x, $-u_y$, and u_z for the corresponding points behind the pyramid.

As we should expect, the tangential force grows as the angle α increases, since the area obstructing the flow increases. Results for different angles are much closer if we evaluate the tangential force per unit area of projection of the pyramid on the plane perpendicular to the flow, Fig. 8.

6 Conclusions

It has been shown in the sample problems that the combination of a small number of parameters and usual assumptions; e.g., neglecting deformations below the tip of the indenter, do not give a good evaluation for the rate of energy. The proposed approach seems to provide a feasible alternative for cases when better acuracy is required. It is understood, however, that this option retains other shortcomings of the upper bound method, such as the fact that the configuration of an unknown surface cannot be found within the framework of the method. Another is that the local pressure on the surface of the tool/asperity cannot be found.

References

Abildgaard, T., 1984, "Prediction of the Force Components Acting on a Ploughing Cone by Means of Three-Dimensional Upper Bound Theory," *Advanced Technology of Plasticity*, vol. 1, pp. 121–126.

Avitzur, B., Huang, C. K., and Zhu, Y. D., 1984, "A Friction Model Based on the Upper Bound Approach to the Ridge and Sublayer Deformation," *Wear*, Vol. 95, pp. 59–77.

Bowden, F. P., and Tabor, D., 1950, *The Friction and Lubrication of Solids, Part I*, Clarendon Press, Oxford.

Bracken, J., and McCormic, G. P., 1968, "Selected Applications of Non-Linear Programming," J. Wiley and Sons, New York.

Brent, R. P., 1971, "Algorithms for Finding Zeros and Extremes of Functions without Calculation Derivatives," Stanford University, Technical Report CS-71-198.

DeVathire, M., Delamare, F., and Felder, E., 1981, "An Upper Bound Model of Ploughing by a Pyramidal Indenter," *Wear*, Vol. 66, pp. 51–64.

Drucker, D. C., 1954, "Coulomb, Friction, Plasticity, and Limit Loads," ASME JOURNAL OF APPLIED MECHANICS, Vol. 21, pp. 71–74.

Drucker, D. C., Greenberg, H. J., and Prager, W., 1951, "The Safety Factor of an Elastic-Plastic Body in Plane Strain," ASME JOURNAL OF APPLIED MECHANICS, Vol. 18, pp. 371–378.

Drucker, D. C., Prager, W., and Greenberg, H. J., 1952, "Extended Limit Design Theorems for Continuous Media," *Quart. Appl. Math.*, pp. 381–389.

Fletcher, R., and Powell, M. J., 1963, "A Rapidly Convergent Descent Method for Minimization," *Computer*, Vol. 6, No. 2, pp. 163–168.

Fletcher, R., and Reeves, C. M., 1964, "Function Minimization by Conjugate Gradient," *Computer J.*, Vol. 7, No. 2, pp. 149–154.

Goldstein, A., and Price, J. F., 1967, "An Effective Algorithm for Minimization," *Numer. Math.*, Vol. 10, pp. 184–189.

Gvozdev, A. A., 1938, "The Determination of the Value of the Collapse Load for Statically Indeterminate Systems Undergoing Plastic Deformation," *Proceedings of the Conference on Plastic Deformation, Acad. of Sci. USSR*, 1938, Moscow, pp. 19–33 (in Russian), English Translation in *Intern. J. Mech. Sci*, 1960, Vol. 1, pp. 322–355.

Hill, R., 1957, "On the State of Stress in a Plastic-Rigid Body at the Yield Point," *Phil. Mag.*, Vol. 42, pp. 868–875.

Hill, R., "A Note on Estimating the Yield-Point Loads in a Plastic-Rigid Body," *Phil. Mag.*, Vol. 43, pp. 353–355.

Oh, S. I., and Kobayashi, S., 1975, "An Approximate Method for a Three-Dimensional Analysis in Rolling," *Intern. J. Mech. Sci.*, Vol. 17, pp. 293–305.

Prager, W., 1959, *An Introduction to Plasticity*, Addison-Wesley, Reading, MA.

Rabinowicz, E., 1965, *Friction and Wear of Materials*, John Wiley and Sons, New York.

Rowe, J. W., 1977, *Principles of Industrial Metal Working Processes*, E. Arnold, Ltd., London.

Suh, N. P., 1986, *Tribophysics*, Prentice-Hall, Englewood Cliffs, N.J.

Wanheim, T., 1978, "A Model for Friction in Metal Forming Processes," *Ann CIRP*, Vol. 27, pp. 189–196.

Zienkiewicz, O. C., 1983, *The Finite Element Method*, 3rd ed., McGraw-Hill Book Company, Ltd., UK.

Downloaded 03 May 2010 to 171.66.16.31. Redistribution subject to ASME license or copyright; see http://www.asme.org/terms/Terms_Use.cfm

J. M. Powers
Visiting Assistant Professor,
Department of Mechanical and
Industrial Engineering.

D. S. Stewart
Associate Professor,
Department of Theoretical and
Applied Mechanics.

Herman Krier
Professor,
Department of Mechanical and
Industrial Engineering,
Mem. ASME

University of Illinois at
Urbana-Champaign,
Urbana, IL 61801

Analysis of Steady Compaction Waves in Porous Materials[1]

A two-phase continuum mixture model is used to analyze steady compaction waves in porous materials. It is shown that such a model admits both subsonic and supersonic steady compaction waves in response to a piston-driven boundary condition when a Tait equation is used to describe a solid matrix material and a generic static compaction relation is used to describe collapse of the matrix. Parameters for the Tait equation are chosen to match shock and compaction wave data. The model is able to predict compaction wave speed, final pressure, and final volume fraction in porous HMX. The structure of the compaction wave is also studied. A shock preceding the compaction wave structure is predicted for compaction waves travelling faster than the ambient sound speed of the solid. For subsonic compaction waves no leading shock is predicted. The compaction zone length is studied as a function of initial volume fraction, piston velocity, and compaction viscosity.

Introduction

It has been established by experiments with granular high energy solid propellants (Bernecker and Price, 1974; Price and Bernecker; 1975) and by numerical solution of unsteady two-phase reactive flow models (Bulter and Krier, 1986; Baer and Nunziato; 1986) that deflagration to detonation transition (DDT) in a confined column of such granular energetic material involves material compaction and heat release. In many cases the origin of such a DDT can be traced to the influence of a compaction wave, defined as a propagating disturbance of the solid volume fraction of the granular material. Steady compaction waves in porous HMX (cyclic nitramine) were observed by Sandusky and Liddiard (1985) and Sandusky and Bernecker (1985) arising from the impact of a constant velocity piston (piston velocity < 300 m/s). Compaction waves in these experiments travel at speeds less than 800 m/s, well below the ambient solid sound speed, which is near 3000 m/s. To understand compaction waves it is necessary to explain why this nonclassical result is obtained.

The first step in modeling compaction waves is to study steady compaction waves. With understanding gained from steady waves, it is easier to understand the time-dependent development of a compaction wave and how such a compaction wave can further evolve into a detonation wave. Although it is possible to numerically solve the coupled unsteady partial differential equations which model such dynamic compaction processes (including the formation of shock waves) (Krier and Stewart, 1985), it is difficult to interpret from such models what physical properties dictate the speed, pressure changes, and porosity changes of compaction waves. It is the goal of this paper to provide a simple method to predict these parameters as a function of material properties with a representative model.

We simulate the experiments of Sandusky and Liddiard by studying steady solutions to two-phase flow model equations. Without considering wave structure, Kooker (1986) has used an algebraic end state analysis to predict compaction wave speed as a function of piston velocity for full two-phase model equations. It is possible to extend this analysis in the limit where the effect of one of the phases is dominant. This approach was first used by Baer (1988) in his study of steady compaction wave structure. Here we provide a more detailed discussion of steady structure and basic parameter dependencies. Throughout this paper, we will compare our assumptions and results to those of Baer.

Our results show a continuous dependence of compaction wave structure with supporting piston velocity; depending on the piston velocity, two broad classes of compaction zone structure exist. At low piston velocities the compaction wave travels at speeds less than the ambient solid sound speed. We call such waves subsonic compaction waves. The structure is characterized by a smooth rise in pressure from the ambient to a higher pressure equal to the static pore collapse stress level. Subsonic compaction waves have been observed in experiment (though compaction zone widths have not been measured) and predicted by Baer. Above a critical piston velocity the compaction wave travels at speeds greater than the ambient solid sound speed. A discontinuous shock wave leads a relaxation zone where the pressure adjusts to its equilibrium static pore

[1]This work was supported by the Air Force Office of Scientific Research under Grant AFOSR-85-0311 and Los Alamos National Laboratory DOE-LANL-9XR6-5128C1.

Contributed by the Applied Mechanics Division for publication in the JOURNAL OF APPLIED MECHANICS.

Discussion on this paper should be addressed to the Editorial Department, ASME, United Engineering Center, 345 East 47th Street, New York, N.Y. 10017, and will be accepted until two months after final publication of the paper itself in the JOURNAL OF APPLIED MECHANICS. Manuscript received by ASME Applied Mechanics Division, July 10, 1987; final revision, March 8, 1988.

Copyright © 1989 by ASME

Downloaded 03 May 2010 to 171.66.16.31. Redistribution subject to ASME license or copyright; see http://www.asme.org/terms/Terms_Use.cfm

collapse value. We call such waves supersonic compaction waves. Supersonic compaction waves with leading shocks have not been observed nor predicted in previous studies.

A shock wave in compaction wave structure is admitted because the model equations are hyperbolic. Our model ignores the effects of diffusive momentum and energy transport. If included, these effects would define the width of the shock structure. Here it is assumed that the length scales on which these processes are important are much smaller than the relaxation scales which define compaction zone structure.

As mentioned by a reviewer, compaction wave phenomena predicted here have analogies in gas dynamics. As described by Becker and Bohme (1969), gas dynamic models which include thermodynamic relaxation effects predict a dispersed wave to result from the motion of a piston into a cylinder of gas. Steady solutions with and without discontinuous jumps are identified. These solutions have features which are similar to those predicted by our compaction wave model.

Here we comment on the differences and similarities of the original Baer study and the present study. We have relaxed Baer's incompressibility assumption and assume a fully compressible solid. We give a complete characterization of compaction wave structure as a function of piston speed including an analysis of the supersonic case. With our analysis many new results are obtained. We obtain a unique algebraic equilibrium condition for a generic static pore collapse function. As does Baer, we demonstrate that the problem of determining compaction wave structure can be reduced to solving one ordinary differential equation for volume fraction. We show that other thermodynamic quantities (pressure, density, etc.) are algebraic functions of volume fraction. An analytic solution in the strong shock limit is given.

Compaction Wave Model

We write two-phase continuum mixture equations to describe the motion of a mixture of solid particles and gas. The model, discussed in more detail by Powers, Stewart, and Krier (1987), describes two-phase flow with interphase mass, momentum, and energy transport. A density, ρ_i; pressure, P_i; energy, e_i; temperature, T_i; velocity, u_i; and volume fraction, ϕ_i, is defined for each phase (for the gas $i=1$, for the solid $i=2$). We define the volume fraction as the ratio of the volume of a constituent to the total volume. It is assumed that at each point in space both phases simultaneously exist; each phase may possess a distinct pressure, velocity, temperature, etc. For each phase mass, momentum, and energy evolution equations are written. A thermal and caloric state relation is assumed for each phase. To close the system, a compaction equation similar to that of Baer and Nunziato is utilized. The compaction equation models the time-dependent pore collapse of a porous matrix and is based on the dynamic pore collapse theory of Carroll and Holt (1972). Details about the rationale for the model are given by Baer and Nunziato and Gokhale and Krier (1982). Compaction work is assumed to be negligible.

Unsteady Model. The unsteady two-phase equations are

$$\frac{\partial}{\partial t}(\rho_i\phi_i)+\frac{\partial}{\partial x}(\rho_i\phi_i u_i)=A_i \tag{1}$$

$$\frac{\partial}{\partial t}(\rho_i\phi_i u_i)+\frac{\partial}{\partial x}(P_i\phi_i+\rho_i\phi_i u_i^2)=B_i \tag{2}$$

$$\frac{\partial}{\partial t}(\rho_i\phi_i[e_i+u_i^2/2])+\frac{\partial}{\partial x}(\rho_i\phi_i u_i[e_i+u_i^2/2+P_i/\rho_i])=C_i \tag{3}$$

$$\frac{\partial\phi_2}{\partial t}+u_2\frac{\partial\phi_2}{\partial x}=\frac{\phi_1\phi_2}{\mu_c}(P_2-P_1-f(\phi_2)) \tag{4}$$

$$P_i=P_i(\rho_i, T_i) \tag{5}$$

$$e_i=e_i(P_i, \rho_i) \tag{6}$$

$$\phi_1+\phi_2=1. \tag{7}$$

Equations (1), (2), and (3) describe the evolution of mass, momentum, and energy, respectively, of each phase. Interphase transport is represented in these equations by the terms A_i, B_i, and C_i, which are assumed to be algebraic functions of P_i, u_i, ρ_i, etc. These terms are specified such that the following conditions hold:

$$\sum_{i=1}^{2}A_i=0,\quad \sum_{i=1}^{2}B_i=0,\quad \sum_{i=1}^{2}C_i=0. \tag{8}$$

This insures that the mixture equations obtained by adding the constituent mass, momentum, and energy equations are conservative.

For each phase we define an initial temperature, density, velocity, and volume fraction. The subscript 0 is taken to represent an initial condition.

$$T_i=T_{i0},\quad \rho_i=\rho_{i0},\quad u_{i0}=0,\quad \phi_2=\phi_{20} \tag{9}$$

Other variables are determined by the algebraic relations (5), (6), and (7).

Equation (4) is the compaction equation. A similar model equation has been used by Butcher, Carroll, and Holt (1974) to describe time-dependent (dynamic) pore collapse in porous aluminum. The parameter μ_c is defined as compaction viscosity, not to be confused with the viscosity associated with momentum diffusion. The compaction viscosity defines the only length scale in this problem. The existence of such a parameter is still a modeling assumption and its value has not been measured. There is, however, a theoretical justification for the dynamic pore collapse model. It has been shown (Baer and Nunziato) that when dynamic compaction is incorporated into two-phase model equations, the equations are hyperbolic. We require the initial value problem to be hyperbolic in order to insure a stable solution.

In the compaction equation (4) f represents the intragranular stress in the porous medium. It is assumed to be a function of the volume fraction. Baer has estimated f from Elban and Chiarito's (1986) empirical quasi-static data obtained by measuring the static pressure necessary to compact a porous media to a given volume fraction. Carroll and Holt have suggested an analytical form for f for three regimes of pore collapse, an elastic phase, an elastic-plastic phase, and a plastic phase. In this work we will model f with an equation similar to Carroll and Holt's plastic phase equation. Here we make two *a priori* assumptions about f. First, we assume f is a monotonically increasing function of volume fraction so that an increasing hydrostatic stress is necessary to balance the increased intragranular stress which arises due to an increasing solid volume fraction. Second, we assume that at the initial state f must equal the difference of the solid and gas pressures so that the system is initially in equilibrium. Our results show that with these assumptions, compaction wave phenomena are relatively insensitive to the particular functional form of f.

Equations (5) and (6) are state relations for each phase. Equation (7) arises from the definition of volume fraction. It states that all volume is occupied by either solid or gas. Using standard techniques it can be shown that these equations are hyperbolic; thus, initial value problems are well posed. The characteristic wave speeds are u_1, u_2, $u_1\pm c_1$, and $u_2\pm c_2$, where c_i represents the sound speed of phase i.

Dimensionless Steady Model. To study compaction waves in the context of this model, we make the following assumptions: (1) a steady wave travelling at speed D exists, (2) gas phase equations may be neglected, (3) interphase transport

Downloaded 03 May 2010 to 171.66.16.31. Redistribution subject to ASME license or copyright; see http://www.asme.org/terms/Terms_Use.cfm

terms may be neglected, and (4) the solid phase is described by a Tait equation of state. As a result of Assumption 1, equations (1) through (4) may be transformed to ordinary differential equations under the Galilean transformation $\xi = x - Dt$, $v = u - D$. By examining the dimensionless form of equations (1) through (7), it can be shown that in the limit as the ratio of initial gas density to initial solid density goes to zero, that we are justified in neglecting gas phase equations and interphase transport. To prove this contention, one can integrate the steady mixture mass, momentum, and energy equations formed by adding the component equations to form algebraic mixture equations. By making these equations dimensionless (as shown by Powers, Stewart, and Krier), it is seen that all gas phase quantities are multiplied by the density ratio ρ_{10}/ρ_{20}. As long as dimensionless gas phase properties are less than $O(\rho_{20}/\rho_{10})$, we are justified in neglecting the effect of the gas phase.

As the gas phase is neglected, the subscripts 1 and 2 are discarded. All variables are understood to represent solid phase variables. The caloric Tait equation (Bdzil et al., 1981) for the solid is

$$e = \frac{P + \rho_0 s}{(\gamma - 1)\rho}. \tag{10}$$

Here γ and s are parameters that define the Tait state equation. The value of γ is chosen to match shock Hugoniot data (Marsh, 1980). It is analogous to the specific heat ratio for an ideal equation of state. We define s as the nonideal solid parameter. In this study we view s as an adjustable parameter which allows us to vary the equation of state in a simple way in order to show how the results are sensitive to nonideal state effects. When $s = 0$, the state equation is an ideal state equation. For this study a value of s was chosen to match the compaction wave data of Sandusky and Liddiard.

To determine the ambient solid sound speed, an important term in this analysis, it is necessary to specify a thermal equation of state. By assuming a constant specific heat at constant value c_v, a thermal equation of state consistent with equation (10) can be derived:

$$P = (\gamma - 1)c_v \rho T - \rho_0 s/\gamma. \tag{11}$$

Based on equations (10) and (11) an equation for the solid sound speed c is easily derived by using the thermodynamic identity $Td\eta = de - P/\rho^2 d\rho$, where η is the entropy.

$$c^2 = \frac{\partial P}{\partial \rho}\bigg|_{\eta} = \gamma(\gamma - 1)c_v T \tag{12}$$

To simplify the analysis, dimensionless variables are denoted by an asterisk subscript and are defined as follows

$$\rho_* = \rho/\rho_0,\ v_* = v/D,\ e_* = e/D^2,\ T_* = c_v T/D^2,$$
$$P_* = P/(\rho_0 D^2),\ \xi_* = \xi \rho_0 D/\mu_c.$$

With this choice of dimensionless variables four dimensionless parameters arise.

$$\gamma = \text{Tait Solid Parameter}, \qquad \frac{s}{D^2\gamma} = \sigma = \text{Nonideal Solid Parameter}$$

$$\frac{\gamma(\gamma - 1)c_v T_0 - s}{\gamma D^2} = \pi = \text{initial pressure},$$

$$\phi_0 = \text{initial volume fraction}$$

For materials of interest ϕ_0 and γ are of order 1. Interesting limiting cases can be studied when $s \to 0$, corresponding to the strong shock or weak nonideal effect limit, or when $\pi \to 0$, corresponding to the strong shock limit.

With the assumptions made, we can write steady dimensionless equations to describe the compaction of an inert solid porous material as follows:

$$\frac{d}{d\xi_*}(\rho_* \phi v_*) = 0 \tag{13}$$

$$\frac{d}{d\xi_*}(P_* \phi + \rho_* \phi v_*^2) = 0 \tag{14}$$

$$\frac{d}{d\xi_*}(\rho_* \phi v_* [e_* + v_*^2/2 + P_*/\rho_*]) = 0 \tag{15}$$

$$\frac{d\phi}{d\xi_*} = \frac{\phi(1 - \phi)}{v_*}(P_* - f_*(\phi)) \tag{16}$$

$$e_* = \frac{P_* + \gamma\sigma}{(\gamma - 1)\rho_*}. \tag{17}$$

Initial conditions are specified as

$$\rho_* = 1,\ \phi = \phi_0,\ v_* = -1,\ P_* = \pi. \tag{18}$$

Equations (13)–(17) are equivalent to Baer's steady model except a term Baer calls "compaction work" is not included and a simpler state equation is used. Equations (13), (14), and (15) may be integrated subject to initial conditions (18) resulting in the following set of equations:

$$\frac{d\phi}{d\xi_*} = \frac{\phi(1 - \phi)}{v_*}(P_* - f_*(\phi)) \tag{19}$$

$$\rho_* \phi v_* = -\phi_0 \tag{20}$$

$$P_* \phi + \rho_* \phi v_*^2 = \phi_0(\pi + 1) \tag{21}$$

$$\rho_* \phi v_*(e_* + v_*^2/2 + P_*/\rho_*) = -\phi_0\left(\frac{\pi + \gamma\sigma}{\gamma - 1} + 1/2 + \pi\right) \tag{22}$$

$$e_* = \frac{P_* + \gamma\sigma}{(\gamma - 1)\rho_*} \tag{23}$$

From equations (20) through (23), equations for pressure and velocity as functions of volume fraction can be written. Equation (23) is used to eliminate energy from equation (22). Velocity is eliminated from equations (21) and (22) by using equation (20). Then density is eliminated from equation (22) by using equation (21). What remains is a quadratic equation involving only pressure and volume fraction. It is possible to solve this equation for pressure explicitly in terms of volume fraction. The solution is

$$P_* = \frac{\phi_0}{\phi(\gamma + 1)}\left(\frac{\gamma\sigma\phi}{\phi_0} - 1 - \pi\right)\left[-1 \pm \sqrt{1 + \frac{(\gamma + 1)\left[2\gamma\sigma\left(\frac{\phi}{\phi_0}(1 + \pi) - 1\right) - \pi(2 - \pi(\gamma\text{-}1))\right]}{\left(\frac{\gamma\sigma\phi}{\phi_0} - 1 - \pi\right)^2}}\right]. \tag{24}$$

The solution corresponding to the positive branch is the physically relevant one. The negative branch is associated with negative pressure. Equations (20) and (21) may be simultaneously solved for velocity as a function of pressure and volume fraction. The velocity is given by

$$v_* = \frac{P_* \phi - \phi_0(1 + \pi)}{\phi_0}. \tag{25}$$

By using equation (24) to substitute for pressure in equation (25), velocity is available as a function of volume fraction alone. The mass equation (20) can be used to give density as a function of volume fraction and then the state equation (17) can be used to give energy as a function of volume fraction.

Downloaded 03 May 2010 to 171.66.16.31. Redistribution subject to ASME license or copyright; see http://www.asme.org/terms/Terms_Use.cfm

Thus all variables in the compaction equation (19) can be expressed as functions of volume fraction; the compaction wave problem is reduced to solving one ordinary differential equation (19) for volume fraction subject to the condition $\phi = \phi_0$ at $\xi = 0$.

Next we describe the technique for determining wave speed as a function of piston velocity. This calculation is algebraic and can be made without regard to structure. The solution is parameterized by the wave velocity through the definitions of π and σ. Instead of using a piston velocity as an input condition, it is easier to consider the wave speed to be known and from that wave speed calculate a piston velocity. By assuming static pressure equilibrium end state in equation (19) ($P_*(\phi) = f_*(\phi)$), it is possible to determine the equilibrium volume fraction and thus, from equations (24) and (25), the final velocity v_*. The piston velocity (u_p) is found by transforming the final velocity to the lab frame by using the transformation $u_p = D(v_* + 1)$.

Pressure equilibrium end states are found when a volume fraction is found such that the pressure given by equation (24) matches the intragranular stress predicted by f. In the initial state, equation (24) predicts a pressure of π, the dimensionless initial pressure. But assumption f also yields a value of π in the initial state so that the undisturbed material is stationary. In Fig. 1, dimensional pressure in HMX is plotted as a function of volume fraction from equation (24) for a series of wave speeds and an initial volume fraction of 0.73. Parameters used to model HMX are listed in Table 1. (We use c_v, μ_c, and ρ_0 of Baer and Nunziato and estimate the parameters γ and s from shock and compaction data.) All curves pass through the point of initial pressure and volume fraction.

Table 1 HMX Material Properties and Initial Conditions

Parameter	Description	Value
γ	Tait Solid Parameter	5
c_v	Constant Volume Specific Heat	1500 J/(kg K)
s	Nonideal Solid Parameter	8.976×10^6 m^2/s^2
T_0	Initial Temperature	300 K
ρ_0	Initial Density	1900 kg/m^3
μ_c	Compaction Viscosity	1000 kg/(ms)

The curve on Fig. 1 for the ambient sonic wave speed ($D = 3000$ m/s) has a special property whose importance will be apparent in the following paragraph. For this curve a volume fraction minimum exists at the initial volume value. It can be proven for a sonic wave speed, that the discriminant in equation (24) is identically zero for $\phi = \phi_0$ and $D = \gamma(\gamma - 1) c_v T_0$ (the ambient solid sonic wave speed).

The positive pressure branch of equation (24) is a double-valued function of volume fraction for wave velocities that exceed the ambient solid sound speed and single-valued for wave velocities less than or equal to the ambient solid sound speed. For subsonic wave speeds, small increases from the initial volume fraction cause small positive perturbations in pressure. For supersonic wave speeds a positive increase of the initial volume fraction is only acceptable if the pressure jumps discontinuously to a shocked value of the upper portion of the double-valued $P_* - \phi$ curve. Because the governing equations are hyperbolic, these shocks jump are admissible. From equation (19) the shock jump condition for volume fraction is

$$[\phi]_0^s = 0 \tag{26}$$

where "0" denotes the initial state and "s" the shock state. Thus the shock volume fraction is always equal to the initial volume fraction.

From equations (24) and (25) the shock pressure and particle velocity can be determined. The shocked values are independent of the initial solid volume fraction.

$$P_s = \frac{2 - (\pi + \sigma)(\gamma - 1)}{\gamma + 1} - \sigma \tag{27}$$

$$v_s = -\frac{(\gamma - 1) + 2\gamma(\pi + \sigma)}{\gamma + 1}. \tag{28}$$

The combination of parameters $\pi + \sigma$ is independent of the nonideal solid parameter s. So from equations (27) and (28) it is deduced that nonideal effects lower the shock pressure by a constant, σ, and do not affect the shock particle velocity.

Based on the implications of equation (24), the structure analysis is thus conveniently split in two classes, subsonic and supersonic. As wave speed increases from subsonic values, the initial pressure at the wave front is the ambient pressure until

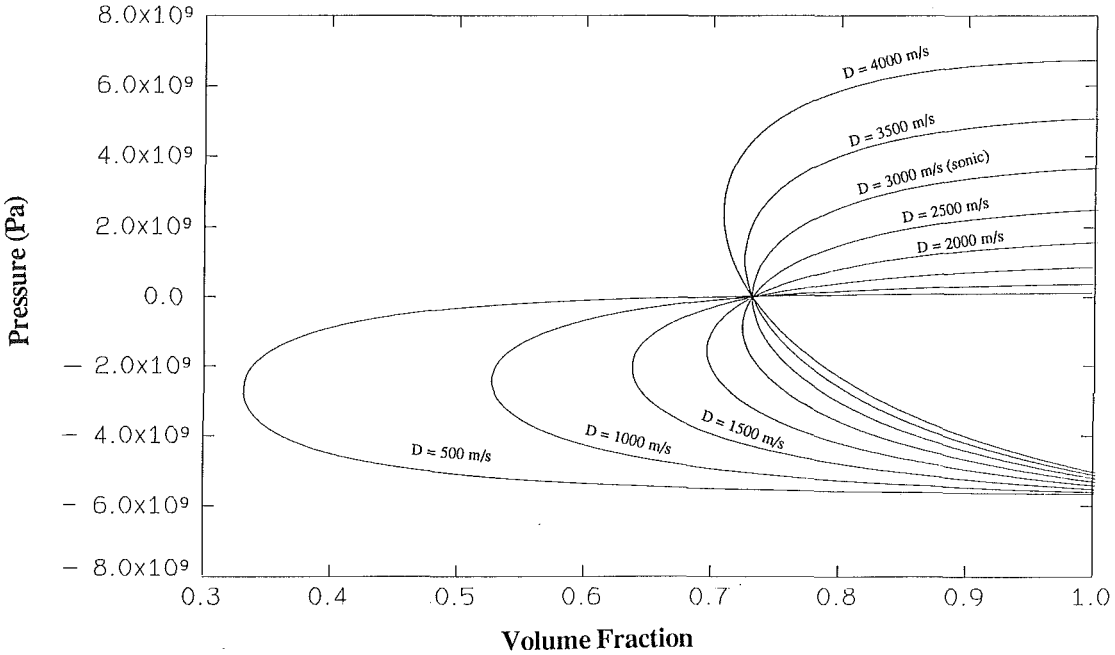


Fig. 1 Pressure versus volume fraction from conservation and state equations for subsonic, sonic, and supersonic wave speeds

Downloaded 03 May 2010 to 171.66.16.31. Redistribution subject to ASME license or copyright; see http://www.asme.org/terms/Terms_Use.cfm

the compaction wave speed is sonic. For wave speed greater than the ambient solid sound speed the initial pressure jumps are dictated by equation (27). A plot of the leading pressure versus compaction wave speed is shown in Fig. 2.

As an aside, we note that a criterion for a solid equation of state is that the candidate equation along with the Rankine-Hugoniot jump conditions be able to match experimental piston impact data. For voidless HMX ($\phi = 1$) observations of shock wave speed as a function of piston velocity are reported by Marsh (1980). By rewriting equation (28) in dimensional form, we solve for D as a function of piston velocity.

$$D = \frac{1+\gamma}{4} u_p + \sqrt{\left(\frac{1+\gamma}{4} u_p\right)^2 + \gamma(\gamma-1)c_v T_0}. \qquad (29)$$

From equation (12), the term $\gamma(\gamma-1)c_v T_0$ is the square of the ambient sound speed for the nonideal solid. In a result familiar from gas dynamics, it can be deduced from equation (29) that the minimum steady shock wave speed admitted in response to a piston boundary condition is the ambient sonic speed. For values of γ, c_v, and T_0 listed in Table 1, we plot shock wave speed D as a function of piston velocity u_p and data from Marsh in Fig 3. We fixed γ such that there is agreement between the data and the model predictions. In the range of piston velocities shown, equation (29) approximates a linear D versus u_p relation used by other modelers to match this data.

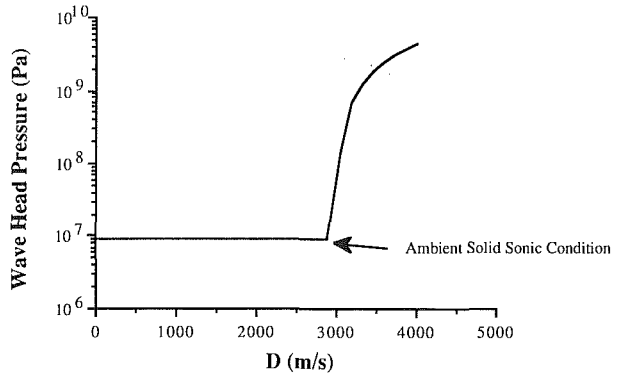


Fig. 2 Wave head pressure versus wave speed

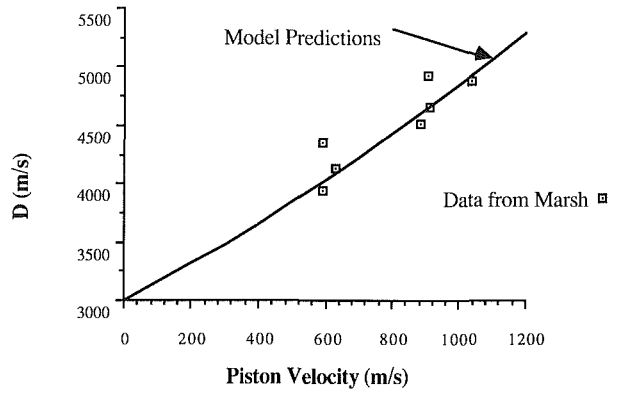


Fig.3 Predictions and observations of shock wave speed

Subsonic Compaction Waves

Subsonic End States. To study subsonic compaction waves admitted by equation (19), we choose a form for f_*:

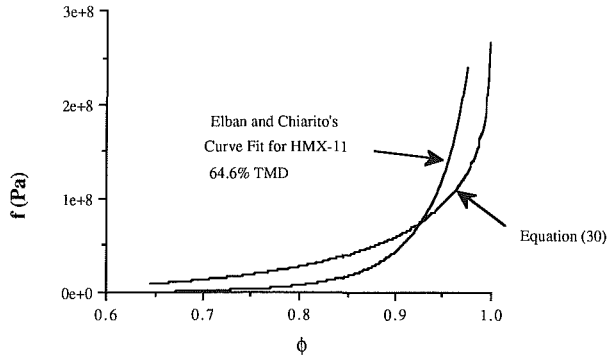


Fig. 4 Comparison of Elban's static pore collapse data with equation (30)

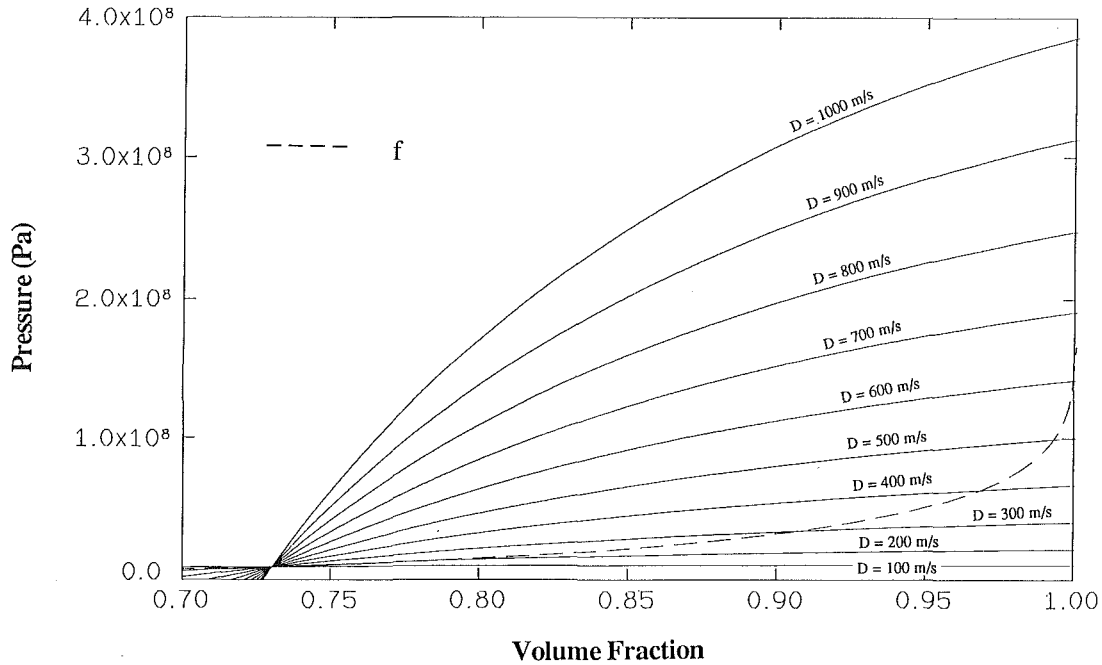


Fig. 5 Pressure versus volume fraction from conservation and state equations for subsonic wave speeds and static pore collapse function, f

Downloaded 03 May 2010 to 171.66.16.31. Redistribution subject to ASME license or copyright; see http://www.asme.org/terms/Terms_Use.cfm

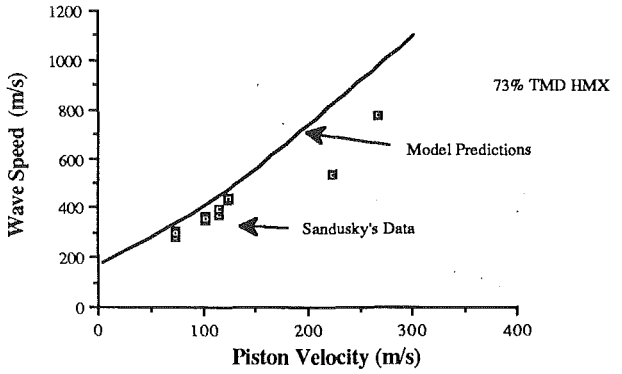


Fig. 6 Compaction wave speed versus piston velocity for subsonic compaction

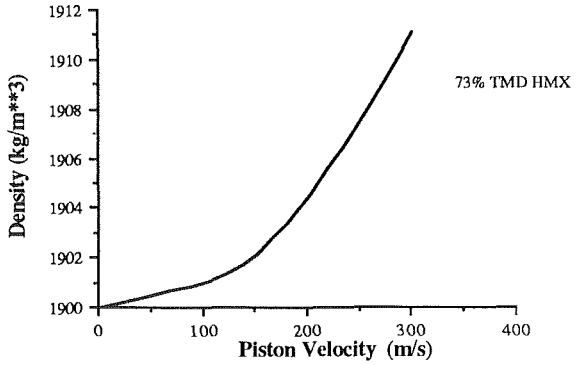


Fig. 7 Final density versus piston velocity for subsonic compaction

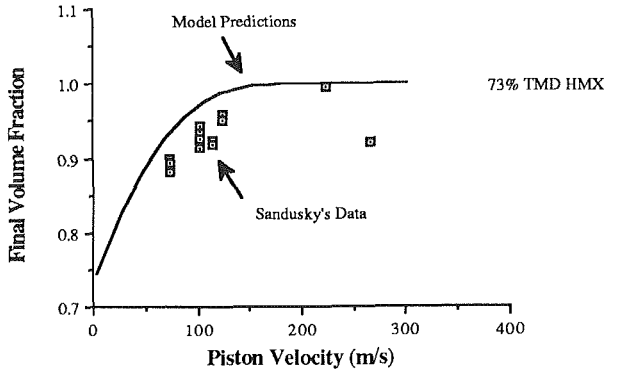


Fig. 8 Final volume fraction versus piston velocity for subsonic compaction

$$f_*(\phi) = \pi \frac{\phi^2}{\phi_0^2} \frac{(2-\phi_0)^2}{(2-\phi)^2} \frac{\ln\left[\frac{1}{1-\phi}\right]}{\ln\left[\frac{1}{1-\phi_0}\right]}. \tag{30}$$

This function satisfes the requirements described earlier, namely, it is a monotonically increasing function of volume fraction and is constructed such that the system is in equilibrium in the initial state. It has the same form as the plastic phase static pore collapse relation given by Carroll and Holt. It is not the Carroll and Holt relation as the leading coefficent in the Carroll and Holt relation is the yield stress of the solid. In equation (30) the leading coefficient is a function of initial volume fraction. Predictions of equation (30) approximately match the experimental results of Elban and Chiarito. Figure 4 compares a curve fit of Elban and

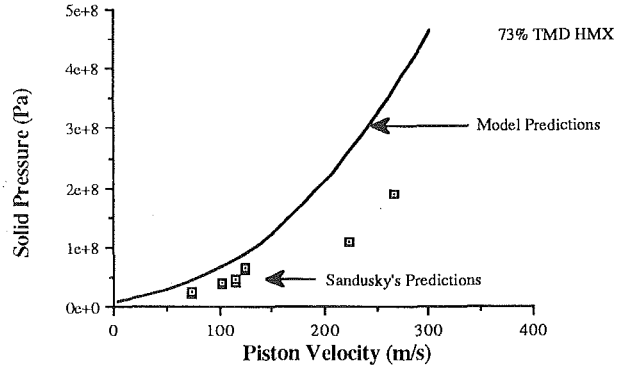


Fig. 9 Pressure versus piston velocity for subsonic compaction

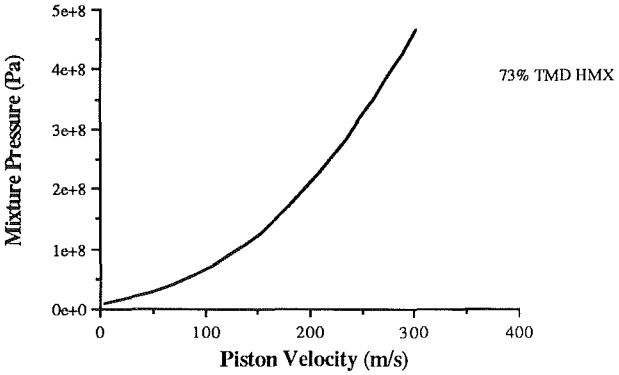


Fig. 10 Mixture pressure versus piston velocity for subsonic compaction

Chiarito's data for HMX with the approximation given by equation (30).

To locate an end state we use equations (24) and (30) to set $P_*(\phi) = F_*(\phi)$ and solve for ϕ. For 73 percent theoretical maximum density (TMD) HMX (volume fraction = 0.73) and a variety of subsonic wave speeds, curves of pressure versus volume fraction from equations (24) and (30) are plotted in Fig. 5. As wave speed increases, the final volume fraction increases. For wave speeds above 600 m/s nearly complete compaction is predicted. For wave speeds of about 200 m/s or lower, no steady compaction wave is predicted. This is solely a consequence of the assumed form of f. The form of f chosen crosses through the initial point with a positive slope and fails to intersect the pressure-volume fraction curves for low wave speeds.

For 73 percent TMD HMX Figs. 6 through 10 shows plots of compaction wave speed, final density, final volume fraction, final pressure, and final mixture pressure (mixture pressure = pressure * volume fraction) versus piston velocity. Also shown are the observations of Sandusky and Liddiard and Sandusky and Bernecker of wave speed and final volume fraction and their predictions of pressure. The relatively small density changes verify that Baer's incompressibility assumption is a good approximation. Figures 11 through 13 show predictions of compaction wave speed, final volume fraction, and final mixture pressure as a function of initial volume fraction for a constant piston velocity of 100 m/s along with Sandusky's predictions as reported by Kooker (1987).

Equation (19) has been numerically integrated to determine the structure of the subsonic compaction zone. In the numerical integrations we use pressure, velocity, and f as given by equations (24), (25), and (30), respectively. The integrations were performed on the University of Illinois at Urbana-Champaign's Cyber 175 computer using the IMSL routine DVERK. A step size was chosen such that approximately fifty points described the compaction zone. Negligible changes results from using more points. The integration was per-

Downloaded 03 May 2010 to 171.66.16.31. Redistribution subject to ASME license or copyright; see http://www.asme.org/terms/Terms_Use.cfm

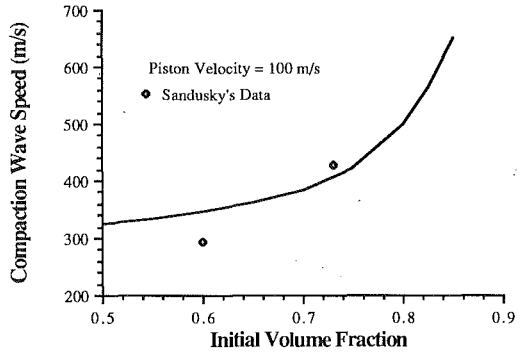


Fig. 11 Compaction wave speed versus initial volume fraction

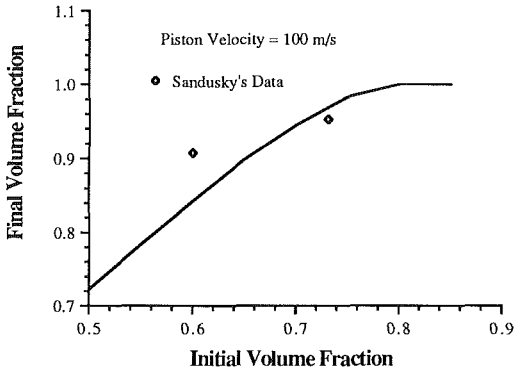


Fig. 12 Final volume fraction versus initial volume fraction

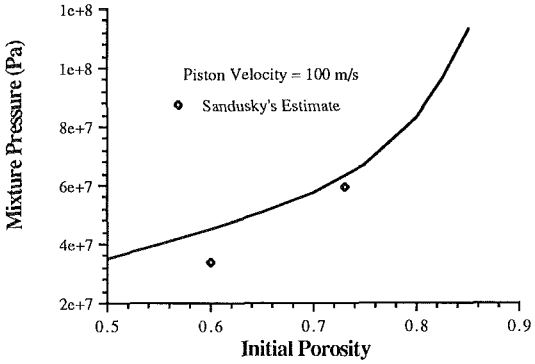


Fig. 13 Mixture pressure versus initial volume fraction

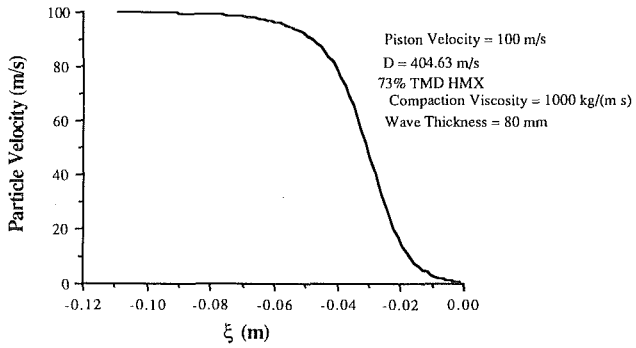


Fig. 14 Particle velocity versus distance for subsonic compaction

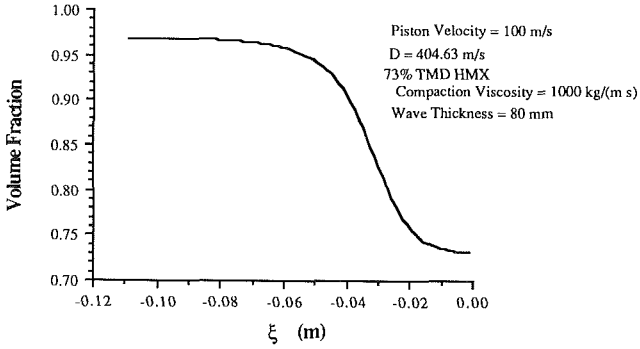


Fig. 15 Volume fraction versus distance for subsonic compaction

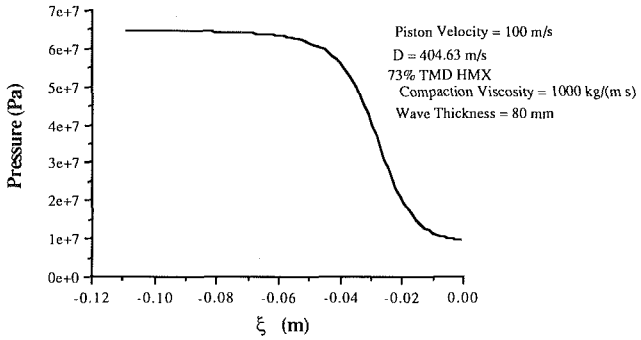


Fig. 16 Pressure versus distance for subsonic compaction

formed starting at $\xi_* = 0$ and integrating towards $\xi_* \to -\infty$. To initiate the integration, a small positive perturbation of volume fraction was introduced which, in this case, causes a small positive perturbation in pressure.

Figures 14, 15, and 16 show the particle velocity, volume fraction, and pressure in the compaction zone for a subsonic compaction wave. Here the piston velocity is 100 m/s and the initial volume fraction is 0.73. The compaction wave speed is 404.63 m/s. For an assumed compaction viscosity of 1000 kg/(ms) a compaction wave thickness of 80 mm is predicted. Because compaction viscosity defines the only length scale in this problem, compaction viscosity only serves to define the compaction wave thickness. For the same value of compaction viscosity Baer reports a compaction wave thickness of 31.9 mm. The discrepancy could be due to many effects including our definition of compaction zone length. It is important to note that the length is of the same order of magnitude. Final pressure, wave speed, and final volume fraction are unchanged by the value chosen for compaction viscosity. By measuring a compaction wave thickness, an estimate could be made for the compaction viscosity.

Supersonic Compaction Waves

End States. At 0.73 initial porosity for piston velocities greater than 884 m/s, supersonic compaction waves are also admitted. Figures 17 through 21 show plots of compaction wave speed, final density, final volume fraction, final pressure, and final mixture pressure as a function of piston velocity. These curves encompass both the subsonic and supersonic compaction wave end states. It is seen that the end states are a continuous function of piston velocity. Also plotted on Fig. 17 is the shock wave speed as a function of piston velocity. For large wave speeds the predicted shock velocity converges with the compaction wave velocity. It is demonstrated next that this is a consequence of nonideal effects having little importance at supersonic wave speeds. Furthermore, it will be demonstrated that the existence of subsonic compaction waves can be attributed solely to nonideal effects.

Supersonic Structure. Equations (24) and (25) can be simplified in the limit as $\sigma \to 0$. The limit of small σ corresponds either to negligible nonideal effects or large wave

Downloaded 03 May 2010 to 171.66.16.31. Redistribution subject to ASME license or copyright; see http://www.asme.org/terms/Terms_Use.cfm

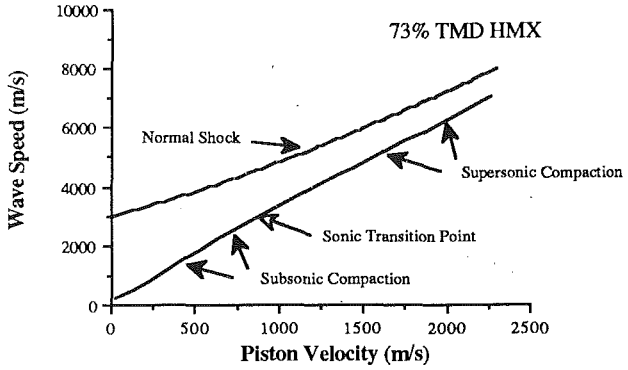


Fig. 17 Shock and compaction wave speeds versus piston velocity for subsonic and supersonic compaction

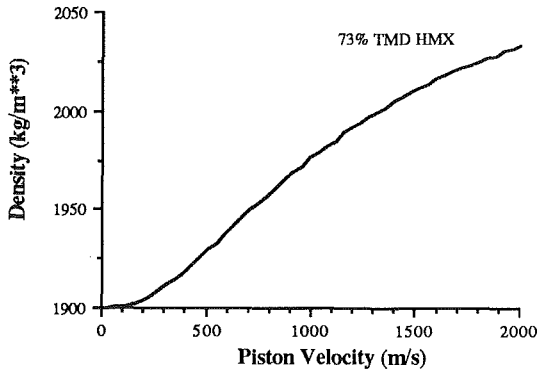


Fig. 18 Density versus piston velocity for subsonic and supersonic compaction

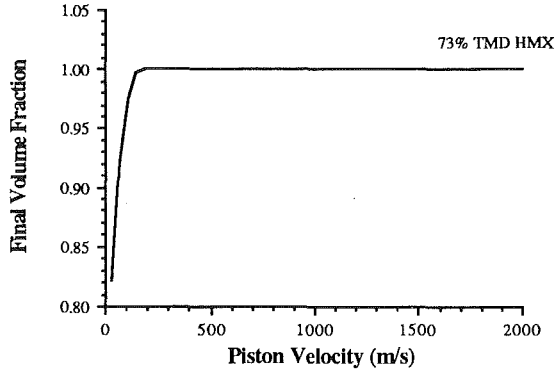


Fig. 19 Final volume fraction versus piston speed for subsonic and supersonic compaction

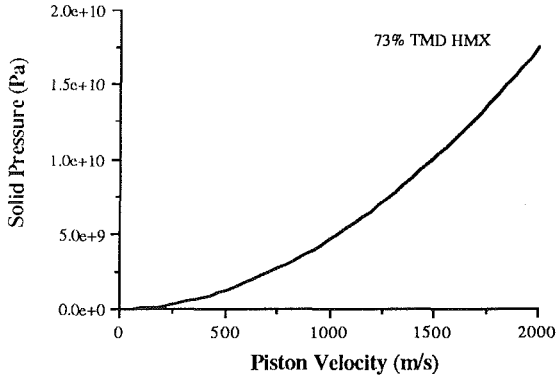


Fig. 20 Pressure versus piston velocity for subsonic and supersonic compaction

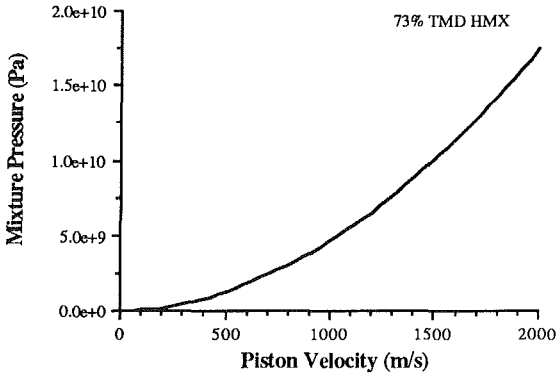


Fig. 21 Mixture pressure versus piston velocity for subsonic and supersonic compaction

speed. In the limit as $\sigma \to 0$ equations (24), (25), and (19) can be written as

$$P_* = \frac{P_s \phi_0}{\phi} \tag{31}$$

$$v_* = v_s \tag{32}$$

$$\frac{d\phi}{d\xi_*} = \frac{1-\phi}{v_s}\,(P_s\phi_0 - \phi f_*(\phi)). \tag{33}$$

Equation (32) holds that in this limit the velocity is constant in the relaxation zone and is equal to the shocked particle velocity. For $s \equiv 0$ (that is for an ideal state relation) equation (32) is equivalent to equation (29); thus, for an ideal state relation the minimum compaction wave speed is the ambient sonic speed. *Any subsonic compaction wave admitted by the model (equations (19)-(23)) is a direct consequence of nonideal state effects.*

In the strong shock limit $D \to \infty$, and both π and $\sigma \to 0$. Equation (33) has a simple solution in this limit, assuming f_* to be sufficiently bounded. (Note that because of the logarithmic singularity at $\phi = 1$, (30) does not meet this criterion. We do not, however, restrict ourselves to functions of this form.) In this limit equation (33) becomes

$$\frac{d\phi}{d\xi_*} = -\frac{2\phi_0}{\gamma - 1}\,(1-\phi) \tag{34}$$

whose solution is

$$\phi = 1 - (1-\phi_0)\exp\left(\frac{2\phi_0}{\gamma-1}\,\xi_*\right). \tag{35}$$

In terms of dimensional parameters, the compaction zone thickness found by equating the exponent in equation (35) to one and substituting the expression for piston velocity for wave speed is estimated as

$$L_{\text{comp}} = O\left(\frac{2(\gamma-1)\mu_c}{(\gamma+1)\rho_0\phi_0 u_p}\right). \tag{36}$$

The length is proportional to compaction viscosity and inversely proportional to piston velocity and the product of density and volume fraction.

An example of supersonic structure arising from the impact of a 1000 m/s piston is now given. Figures 22, 23, and 24 show the particle velocity, volume fraction, and pressure in the compaction zone for a supersonic compaction wave. Here, the initial volume fraction is 0.73. The compaction wave speed is 3353.67 m/s and the wave thickness is 2.9 mm. It is seen that pressure and particle velocity undergo shock jumps. Volume fraction does not undergo a shock jump; however, its derivative does jump at the initial point.

Compaction Zone Thickness

It is possible to study the parametric dependence of compac-

Downloaded 03 May 2010 to 171.66.16.31. Redistribution subject to ASME license or copyright; see http://www.asme.org/terms/Terms_Use.cfm

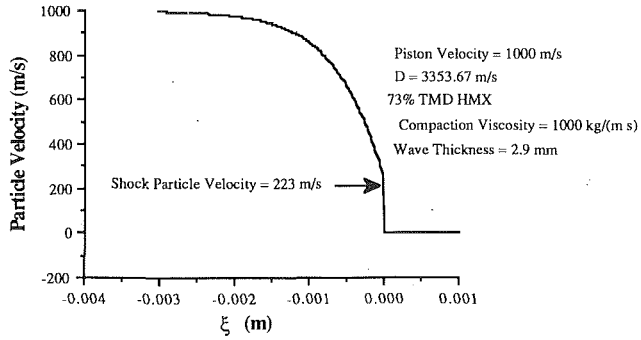


Fig. 22 Particle velocity versus distance for supersonic compaction

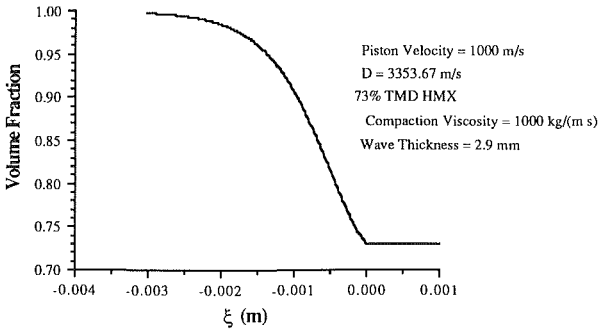


Fig. 23 Volume fraction versus distance for supersonic compaction

tion zone thickness. Given a constant compaction viscosity, our model can predict compaction zone thickness as a function of initial volume fraction and piston velocity. Should experiments be devised to measure the compaction zone thickness, the experiments could provide a means to verify the theory.

The thickness is defined as the distance at which the ratio of the difference of instantaneous volume fraction, and initial volume fraction to the difference of final volume fraction, and initial volume fraction, is equal to 0.99. The final volume fraction is available from the algebraic end state calculation. Figure 25 shows the compaction zone length versus initial volume fraction for a piston velocity of 100 m/s and compaction viscosity of 1000 kg/(ms). We do not understand why the peak in this curve occurs. We do note that for high initial volume fraction, the zone length decreases as initial volume fraction increases in accordance with the predictions of equation (36) for supersonic compaction. We speculate that for low porosity a different mechanism dictates the subsonic compaction zone length than supersonic length. Figure 26 shows compaction zone length versus piston velocity for 73 percent TMD HMX and compaction viscosity of 1000 kg/(ms). The compaction zone length decreases with increasing piston velocity in accordance with the predictions of equation (36) for supersponic compaction. Figure 27 shows a compaction zone length as a function of compaction viscosity for a 100 m/s piston velocity and 0.73 initial volume fraction. As no estimates are available for compaction viscosity, compaction zone lengths for a wide range of compaction viscosity have been plotted. Though plotted on a log scale, the relationship is truly linear with the compaction zone length equal to a constant mutiplied by the compaction viscosity.

Discussion

The piston impact problem for a compressible porous solid has been solved in the context of a steady two-phase model

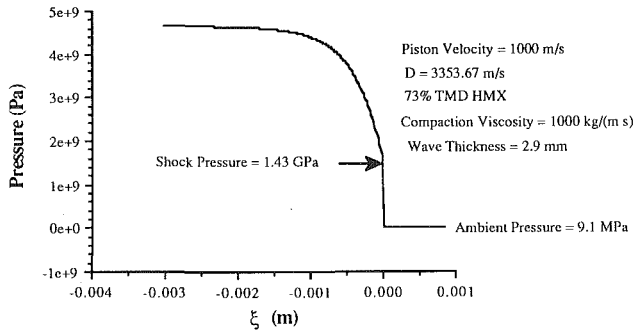


Fig. 24 Pressure versus distance for supersonic compaction

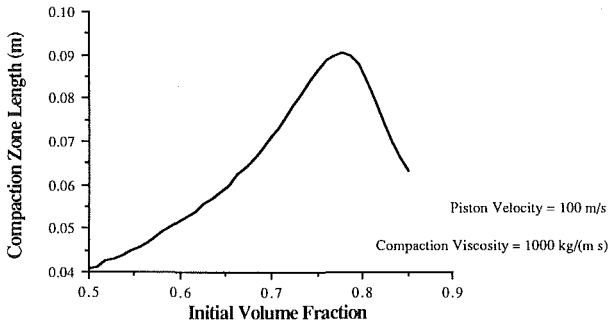


Fig. 25 Compaction zone length versus initial volume fraction

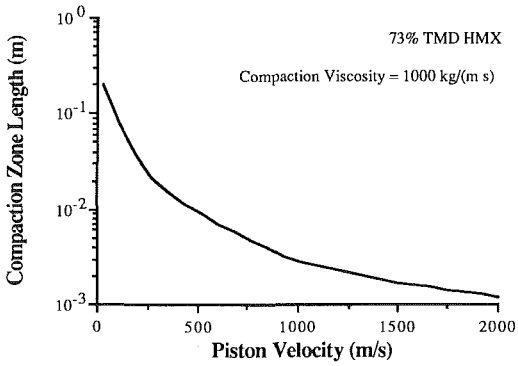


Fig. 26 Compaction zone length versus piston velocity

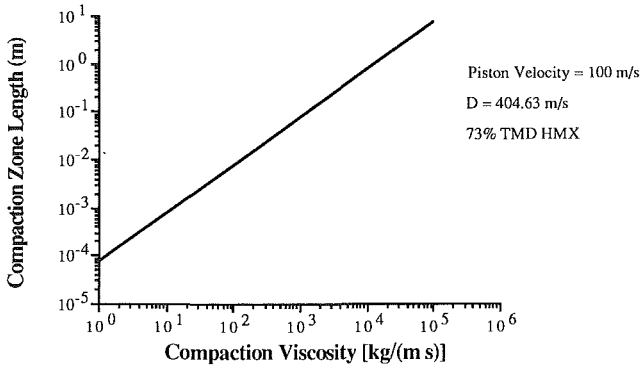


Fig. 27 Compaction zone length versus compaction viscosity

neglecting gas phase effects. With this model, it is possible to obtain an exact solution for the compaction wave speed, final porosity, and final pressure. The degree of accuracy of our predictions can be attributed to the ad hoc estimates for the nonideal solid parameter and the assumed form of the static

Downloaded 03 May 2010 to 171.66.16.31. Redistribution subject to ASME license or copyright; see http://www.asme.org/terms/Terms_Use.cfm

pore collapse function, f. We do not claim that our model is truly representative of porous HMX, only that its functional form is essentially correct. Within the framework of this model it is possible to understand the general features of a compaction wave.

As summarized by Kooker (1987), many compaction wave models do not consider dynamic pore collapse; rather, they enforce static pore collapse ($P=f$) throughout the flow field. In the context of the zero gas density limit, such as assumption results in a compaction wave without structure. The pressure discontinuously adjusts to a static equilibrium value. However, it it not established whether two-phase models with static pore collapse are hyberbolic, a necessary condition if jumps are to be admitted. For two-phase models assuming pressure equilibrium between phases but not incorporating quasi-static compaction data, Lyczkowski et al. (1978) have identified regimes in which unsteady two-phase equations are not hyperbolic.

There are many ways to extend this work. By including the effects of the gas phase, it should be possible to determine how the gas phase's presence modifies the compaction wave structure. By including the effect of particle size in f, it should be possible to model the experiments of Elban, et al. (1987) which show that the static pore collapse stress level is a function of both volume fraction and particle size. By considering the solid to be composed of particles, it may be possible to model the effect of particle breakup on the results when f is assumed to be a function of particle size.

Acknowledgments

The authors acknowledge the helpful discussions with Drs. M. R. Baer and J. W. Nunziato, Sandia National Laboratories, who suggested to us that the problem could be addressed in the limits we have studied. We also acknowledge the assistance of Mr. Mark Miller, graduate student, M/IE, University of Illinois at Urbana-Champaign.

References

Baer, M. R., 1988, "Numerical Studies of Dynamic Compaction of Inert and Energetic Granular Materials," ASME JOURNAL OF APPLIED MECHANICS, Vol. 55, pp. 36–43.

Baer, M. R., and Nunziato, J. W., 1986, "A Two-Phase Mixture Theory for the Deflagration-to-Detonation Transition (DDT) in Reactive Granular Materials," *Int. J. Mulitphase Flow*, Vol. 12, pp. 861–889.

Bdzil, J. B., Engelke, R., and Christenson, D. A., 1981, "Kinetics Study of a Condensed Detonating Explosive," *J. Chem. Phys.*, Vol. 74, pp. 5694–5699.

Becker, E., and Bohme, G., 1969, "Steady One-Dimensional Flow; Structure of Compression Waves," *Nonequilibrium Flows*, P. P. Wegener, ed., Marcel Dekker, New York.

Bernecker, R. R., and Price, D., 1974, "Studies in the Transition from Deflagration to Detonation in Granular Explosives—I. Experimental Arrangement and Behavior of Explosives Which Fail to Exhibit Detonation," *Combust. Flame*, Vol. 22, pp. 111–118.

Bernecker, R. R., and Price, D., 1974, "Studies in the Transition from Deflagration to Detonation in Granular Explosives—II. Transitional Characteristics and Mechanisms Observed in 91/9 RDX/wax," *Combust. Flame*, Vol. 22, pp. 119–129.

Butcher, B. M., Carroll, M. M., and Holt, A. C., 1974, "Shock-Wave Compaction of Porous Aluminum," *J. Appl. Phys.*, Vol. 45, pp. 3864–3875.

Butler, P. B., and Krier, H., 1986, "Analysis of Deflagration to Detonation Transition in High-Energy Solid Propellants," *Combust. Flame*, Vol. 63, pp. 31–48.

Butler, P. B., Lembeck, M. F., and Krier, H., 1982, "Modeling of Shock Development and Transition to Detonation Initiated by Burning in Porous Propellant Beds," *Combust. Flame*, Vol. 46, pp. 75–93.

Carroll, M. M., and Holt, A. C., 1972, "Static and Dynamic Pore-Collapse Relations for Ductile Porous Materials," *J. Applied Physics*, Vol. 43, pp. 1626–1635.

Elban, W. L., and Chiarito, M. A., 1986, "Quasi-Static Compaction Study of Coarse HMX Explosive," *Powder Technology*, Vol. 46, pp. 181–193.

Elban, W. L., Coyne, P. J., and Chiarito, M. A., 1987, "The Effect of Particle Size on the Quasi-Static Compaction Behavior of Granular HMX Beds," 1987 JANNAF Propulsion Systems Hazards Subcommittee Meeting, CPIA Publication 464, pp. 61–75.

Gokhale, S. S., and Krier, H., 1982, "Modeling of Unsteady Two-Phase Reactive Flow in Porous Beds of Propellant," *Prog. Energy Combust. Sci.*, Vol. 8, pp. 1–39.

Kooker, D. E., 1986, "A Numerical Study of Compaction Waves in Class D HMX, 1986 JANNAF Propulsion Systems Hazards Subcommittee Meeting, CPIA Publication 446, Vol. 1, pp. 213–238.

Kooker, D. E., 1987, "A Workshop Summary of Compaction Waves in Granular Material: Numerical Predictions," 1987 JANNAF Propulsion Systems Hazards Subcommittee Meeting, CPIA Publication 464, Vol. 1, pp. 127–138.

Krier, H., and Stewart, J. R., 1985, "Prediction of Detonation Transition in Porous Explosives from Rapid Compression Loadings," UILU-ENG-85-4007, Department of Mechanical and Industrial Engineering, Univ. of Illinois at Urbana-Champaign.

Lyczkowski, R. W., Gidaspow, D., Solbrig, C., and Hughes, E. D., 1978, "Characteristics and Stability Analyses of Transient One-Dimensional Two-Phase Flow Equations and Their Finite Difference Approximations," *Nuclear Science and Engineering*, Vol. 66, pp. 378–396.

Marsh, S. P., ed., 1980, *LASL Shock Hugoniot Data*, University of California Press, Berkeley, CA.

Powers, J. M., Stewart, D. S., and Krier, H., 1987, "Two-Phase Steady Detonation Analysis," presented at the 11th International Colloquium on Dynamics of Explosions and Reactive Systems, Warsaw, Poland, to appear in AIAA Progress Series.

Powers, J. M., 1988, "Theroy of Detonation Structure for Two-Phase Materials," Ph.D. Dissertation, Univ. of Illinois at Urbana-Champaign.

Price, D., and Bernecker, R. R., 1975, "Sensitivity of Porous Explosives to Transition from Deflagration to Detonation," *Combust. Flame*, Vol. 25, pp. 91–100.

Sandusky, H. W., and Bernecker, R. R., 1985, "Compressive Reaction in Porous Beds of Energetic Materials," *Proceedings-Eighth Symposium (International) on Detonation*, NSWC MP 86-194, Naval Surface Weapons Center, White Oak, Md., pp. 881–891.

Sandusky, H. W., and Liddiard, T. P., 1985, "Dynamic Compaction of Porous Beds," NSWC TR 83-256, Naval Surface Weapons Center, White Oak, Md.

Downloaded 03 May 2010 to 171.66.16.31. Redistribution subject to ASME license or copyright; see http://www.asme.org/terms/Terms_Use.cfm

A Constitutive Model for Jointed Rock Mass With Orthogonal Sets of Joints[1]

E. P. Chen
Sandia National Laboratories,
Albuquerque, NM 87185
Fellow, ASME

The development and numerical implementation of a constitutive model for jointed rock media is the subject of investigation in this paper. The constitutive model is based on the continuum assumption of strain-partitioning among the elastic rock matrix and joint sets with nonlinear normal and shear responses. Rate equations for the stress-strain response of the jointed media have been formulated. A numerical incremental solution scheme to these equations has been developed. It has been implemented into the finite element code JAC as an additional material model. Several sample problems have been solved for demonstration purposes. Interpretation and discussion of these results are presented.

Introduction

This investigation involves the development and numerical implementation of a two-dimensional continuum model for the description of jointed rock mass. Following terminology given in Jaeger and Cook (1979), joints are defined in this work as cracks or fractures in rock along which there has been little or no displacement. Joints usually occur in sets that are more or less parallel and regularly spaced. There are usually several sets in rock in very different directions so that the rock mass is broken up into a blocky structure. Specific application of the model is for the potential geological disposal of radioactive waste in the layered sequence of fractured volcanic tuffs under Yucca Mountain, Nev. This is currently being considered by the Nevada Nuclear Waste Storage Investigations Project, administered by the Nevada Operations Office of the U.S. Department of Energy. Analysis of the drilled core samples from Yucca Mountain suggests that the rock mass in the mountain can be described reasonably in terms of a jointed medium with orthogonal sets of joints (Scott and Castellanos, 1984). Continum description of a jointed medium captures the gross response of the rock by smearing the individual responses of the joints. Hence, its applicability is best suited to cases where the least dimension of the representative rock volume is approximately an order of magnitude larger than the joint spacings so that enough joints exist in the rock to validate the averaging process.

The specific continuum model to be discussed follows the development by Chen (1986) based on previous studies by Thomas (1982) and Morland (1974). The main feature of this model includes two parts: a continuum approximation based on average discontinuous displacements across jointing planes within a representative elementary volume, and a material constitutive description based on linear elastic matrix material behavior and nonlinear normal and hsear joint behavior between jointing planes. The deformation response normal to the joint is assumed to be nonlinear elastic. Joint shear response was treated as linear elastic in the shear stress versus shear displacement relationship prior to attaining a critical stress level governed by the Coulomb friction criterion. Beyond the critical stress value, a linear relationship, analogous to strain hardening plasticity, governs the remainder of the shear stress versus slip displacement relationship. All material constants can be obtained through laboratory experiments on single joint specimens.

The constitutive model has been formulated mathematically in terms of a set of rate equations governing the stress-strain response of a jointed medium. Rate equations are derived to facilitate the solution by incremental analysis schemes. The solution to these equations can be manipulated to reduce to that of a fourth-order algebraic equation. This solution scheme has been coded and implemented into the finite element code JAC (Biffle, 1984). JAC is a two-dimensional finite element computer program for analyzing the nonlinear quasi-static response of solids using the conjugate gradient method. It is vectorized to perform on the CRAY computers and solves nonlinear problems efficiently. Moreover, the various options in JAC, such as element birth-death and contact surfaces, make it a very versatile code for geological computations.

Verifications of the correctness of code implementation is accomplished by comparing JAC and analytical results for a few sample problems. Additional examples have also been included for demonstration purposes. Experiment work is underway (US DOE, 1985) to provide data to validate the code predictions. Code validation through comparisons between analytical predictions and experimental data involves extensive analysis and warrants a report in its own right. Therefore,

[1]This work was supported by the Nevada Nuclear Waste Storage Investigations Project of the U.S. Department of Energy.

Contributed by the Applied Mechanics Division for publication in the JOURNAL OF APPLIED MECHANICS.

Discussion on this paper should be addressed to the Editorial Department, ASME, United Engineering Center, 345 East 47 Street, New York, N.Y. 10017, and will be accepted until two months after final publication of the paper itself in the JOURNAL OF APPLIED MECHANICS. Manuscript received by ASME Applied Mechanics Division, June 16, 1987; final revision, March 15, 1988.

Copyright © 1989 by ASME

Downloaded 03 May 2010 to 171.66.16.31. Redistribution subject to ASME license or copyright; see http://www.asme.org/terms/Terms_Use.cfm

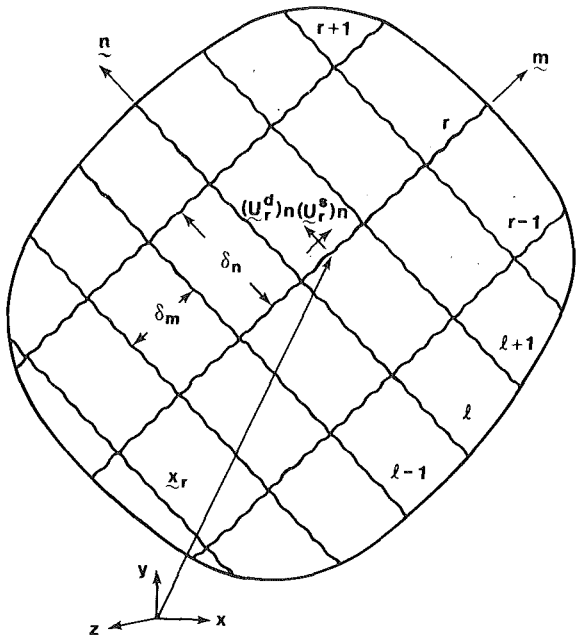


Fig. 1 A jointed rock medium

a separate discussion on code validation will be issued in the future, and the subject of validation will not be included in the present paper.

Bazant and Tsubaki (1980) developed a model to account from the systems of cracks in reinforced concrete. The slip behavior of the cracks in Bazant and Tsubaki (1980) is similar to the current joint model; however, the dilation behavior used in the two models is quite different. An implicit finite element scheme was used in Bazant and Tsubaki (1980) to obtain numerical results. Because of the normal joint stress-displacement relationship (equation (7)) used in the current model, the rate equations possess multiple roots. The current solution procedure is preferred since it allows the consistent selection of the roots to the rate equations.

Constitutive Model Formulation

The formulation of the constitutive model is briefly described here for completeness. More theoretical details can be found in Chen (1986), Thomas (1982), and Morland (1974) and will not be repeated.

Let us consider a representative element of a jointed medium containing orthogonal sets of joints (Fig. 1). On Fig. 1, the two joint sets are characterizied, respectively, by their unit normal vectors (**m**, **n**), where **m** and **n** are mutally perpendiculation, and by spacing parameters (δ_m, δ_n). The joints in a given set are assumed to be regularly spaced and parallel.

Under these assumed conditions continum assumptions, which attempt to capture the gross responses at the expense of detailed information on joint location and actual discontinuities across each joint, can be made to simplify the analysis. Consider a single joint set with orientation **n**. In view of the usual constitutive descriptin of joint properties, the displacement discontinuity is separated into the dilation discontinutiy $(\mathbf{u}_r^d)_n$ $(\mathbf{x}_r)$ and the slip discontinuity $(\mathbf{u}_r^s)_n$ $(\mathbf{x}_r)$ at position $\mathbf{x}_r$ on the rth joint, Fig. 1. The net dilation and slip along the common normal **n** and passing through the R joints of a represenative element are

$$R(\bar{u}^{d,s})_n(\mathbf{x}) = \sum_{r=1}^{R} (u_r^{d,s})_n(\mathbf{x}_r) \tag{1}$$

where $(\bar{u}^{d,s})_n$ **(x)** are the mean dilation and slip discontinuties on the common normal through each $\mathbf{x}_r$ defined by the postion **x**. On length scales, large compared with the element dimension $R\delta_n$, the actual discontinuties and the joint locations will be unimportant, provided that the correct net displacements (1) are represented. Thus, continuous dilation and slip displacement fields $(u^{d,s})_n$ **(x)** are introduced for the joint set with normal **n** such that

$$(u^{d,s})_n(+R\delta_n\mathbf{n}) - (u^{d,s})_n = R(\bar{u}^{d,s})_n(\mathbf{x}). \tag{2}$$

It follows from equation (2) that the dilation and slip strains can be expressed in terms of the mean displacements as

$$e^d_{nn} = \frac{(\bar{u}^d)_n}{\delta_n},\quad e^d_{ss} = e^d_{zz} = e^d_{mm} = e^d_{nz} = e^d_{mz} = 0 \tag{3}$$

$$e^s_{mn} = e^s_{nm}\frac{(\bar{u}^s)_n}{2\delta_n},\quad e^s_{nn} = e^s_{mm} = e^s_{zz} = e^s_{nz} = e^s_{mz} = 0 \tag{4}$$

Expressions similar to equations (1) through (4) can be derived for the joint set with normal **m**. Consequently, the total displacement and strain field at any point **x** can be expressed in the decomposition as

$$\mathbf{u}(\mathbf{x}) = \mathbf{u}^b(\mathbf{x}) + (u^d)_m(\mathbf{x})\mathbf{m} - (u^s)_m(\mathbf{x})\mathbf{n} + (u^d)_n\mathbf{n} + (u^s)_n\mathbf{m} \tag{5}$$

$$\underset{\sim}{e}(x) = \underset{\sim}{e}^b(\mathbf{x}) + \sum_{k=m}^{n}[(\underset{\sim}{e}^d)_k(\mathbf{x}) + (\underset{\sim}{e}^s)_k(\mathbf{x})] \tag{6}$$

where $\mathbf{u}^b$ and $\underset{\sim}{e}^b$ are, respectively, a continuous displacement and strain field characterizing the deformation of the rock matrix. In the absence of the joint sets, the displacement and strain field reduces to that of the rock matrix, as it should. This decomposition ignores the shear coupled-dilation displacement. Hence, within the framework of this model, normal and shear deformations are not directly related. The above equations completely characterize a contiuum model approximating the behavior of the discontinuities. Given the stress-displacement response of representative sets, this model will predict the gross behavior of jointed media containing two orthogonal sets of joints under applied loads.

Motivated by the generally low level of thermal and mechanical stresses expected in the field applications, the intact material is taken to behave as a linear elastic solid. The normal stress-displacement relationship for joints is taken to follow the empirical approach by Goodman (1976). In terms of the quantities shown on Fig. 2, the relationship is defined as follows:

$$T_{nn} = 0,\ \bar{u}^d \geqq 0, \tag{7a}$$

$$T_{nn} = -A_n\left(\frac{\bar{u}^d}{\bar{u}^d_{\max} - \bar{u}^d}\right),\ \text{otherwise} \tag{7b}$$

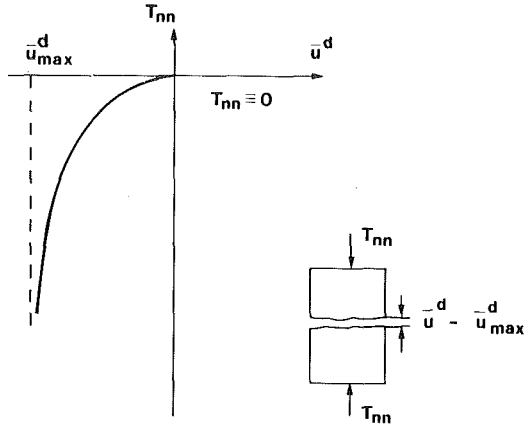


Fig. 2 Nonlinear elastic normal joint behavior

Downloaded 03 May 2010 to 171.66.16.31. Redistribution subject to ASME license or copyright; see http://www.asme.org/terms/Terms_Use.cfm

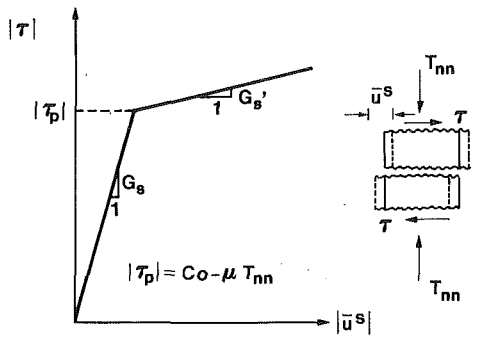


Fig. 3 Nonlinear shear behavior of joints

where T_{nn} and $\bar{u}^d$ are, respectively, the normal stress component and the corresponding displacement across the joint. For the sign convention, tensile stresses and displacements are taken to be positive. Physically, equation (7*a*) expresses that joints have no tensile strength and (7*b*) indicates that there is a limit to the amount of compression possible. The constants $\bar{u}^d_{\max}$ and A_n are the maximum closure of the joint and half-closure stress, respectively. These constants are determined from laboratory experiments on single joint specimens (e.g., see Olsson (1987)).

A bilinear shear stress-displacement response with slopes G_s and G_s' has been assumed for the slip behavior of joints (Fig. 3). The onset of nonlinear response is assumed to be governed by a linear Mohr-Coulomb criterion. A scalar slip function is given as

$$F = |\tau| - \mu T_{nn} - C_0 \tag{8}$$

where T_{nn} and τ are, respectively, the normal and shear stress across the joint. In equation (7), μ is the coefficient of friction and C_0 is the cohesion. Again, the constants G_s, G_s', μ and C_0 are found from laboratory experiments on single joint specimens. The joint behavior is elastic if $F \le 0$ and is inelastic for $F > 0$ and $\partial F/\partial \tau \cdot \dot{\tau} \le 0$. Note that there is not limit to the amount of shear deformation in this constitutive model. Thus, although the constitutive description conceptualizes the blocky structures for the rock, the joint block interference or interlock is not included in the present model. If the interlock effect is deemed important, it may be included in future work in the further refinement of the continuum model.

Derivation of Rate Equations and Code Implementation

Combining equation (6), Hooke's Law for isotropic elastic materials, and the normal and shear joint behavior expressions (7)–(8), one can derive the strain-stress relationships for the jointed solid. Owing to the nonlinear joint responses, it is customary to solve this class of problems by incremental analysis procedures, in which the known stresses and strains at the previous load step are used to find the current stresses and strains once the strain rates have been determined. Therefore, it is advantageous to express the strain-stress relationships in their rate forms. These expressions have been derived in the local joint (m, n) coordinate system as

$$\dot{e}_{mm} = \frac{\dot{T}_{mm}}{2G} - \left(\frac{K - 2G/3}{6KG}\right) tr\,\underset{\sim}{\dot{\mathbf{T}}} + \frac{\beta_m \dot{T}_{mm}}{(A_m - T_{mm})^2} \tag{9}$$

$$\dot{e}_{nn} = \frac{\dot{T}_{nn}}{2G} - \left(\frac{K - 2G/3}{6KG}\right) tr\,\underset{\sim}{\dot{\mathbf{T}}} + \frac{\beta_n \dot{T}_{nn}}{(A_n - T_{nn})^2} \tag{10}$$

$$\dot{e}_{zz} = \frac{\dot{T}_{zz}}{2G} - \left(\frac{K - 2G/3}{6KG}\right) tr\,\underset{\sim}{\dot{\mathbf{T}}} \tag{11}$$

$$\dot{e}_{mn} = \left(\frac{1}{2G} + \frac{1}{2\delta_n (G_s)_n} + \frac{1}{2\delta_m (G_s)_m}\right) \dot{T}_{mn} \tag{12}$$

where

$$\beta_k = -A_k (\bar{u}^d_{\max})_k / \delta_k, \quad k = m,n. \tag{13}$$

In the above equations, K and G are, respectively, the bulk and shear modulus of the rock matrix. The subscripts m and n associated with the joint properties A, G_s, δ, $\bar{u}^d_{\max}$, etc., identify the joint sets through corresponding normals. The normal stress rates are coupled in equations (9) through (11) and are not directly separable. Combining equations (9) through (11) and substituting the resulting equation into equations (9) and (10) renders

$$\frac{d}{dt}\left(-T_n + \frac{\alpha_1 \beta_n}{T_n} + \frac{\alpha_2 \beta_m}{T_m}\right) = \alpha_2 tr\,\underset{\sim}{\dot{\mathbf{e}}} + 2G\dot{e}_{nn} \tag{14}$$

$$\frac{d}{dt}\left(-T_m + \frac{\alpha_1 \beta_m}{T_n} + \frac{\alpha_2 \beta_n}{T_n}\right) = \alpha_2 tr\,\underset{\sim}{\dot{\mathbf{e}}} + 2G\dot{e}_{mm} \tag{15}$$

where

$$T_k = A_k - T_{kk}, \; k = m,n \tag{16}$$

and

$$\alpha_1 = K + 4G/3, \; \alpha_2 = K - 2G/3. \tag{17}$$

The left side of equations (13) and (14) are total differentials and can be integrated directly. Integrating equations (13) and (14) from the beginning to the end of load step one obtains

$$-T_n^{t+1} + \alpha_1 \beta_n (T_n^{t+1})^{-1} + \alpha_2 \beta_m (T_m^{t+1})^{-1} = \gamma_1 \tag{18}$$

$$-T_m^{t+1} + \alpha_1 \beta_m (T_m^{t+1})^{-1} + \alpha_2 \beta_n (T_n^{t+1})^{-1} = \gamma_2 \tag{19}$$

where

$$\gamma_1 = -T_n^t + \alpha_1 \beta_n (T_n^t)^{-1} + \alpha_2 \beta_m (T_m^t)^{-1} + \alpha_2 (tr\,\underset{\sim}{\mathbf{e}}^{t+1} - tr\,\underset{\sim}{\mathbf{e}}^t) + 2G\left(e_{nn}^{t+1} - e_{nn}^t\right) \tag{20}$$

$$\gamma_2 = -T_m^t + \alpha_1 \beta_m (T_m^t)^{-1} + \alpha_2 \beta_n (T_n^t)^{-1} + \alpha_2 (tr\,\underset{\sim}{\mathbf{e}}^{t+1} - tr\,\underset{\sim}{\mathbf{e}}^t) + 2G\left(e_{mm}^{t+1} - e_{mm}^t\right) \tag{21}$$

In equations (18) through (21), the superscripts t and $t+1$ indicate the end of the load steps at which the quantities are evaluated. Note that in an indirect conjugate gradient procedure as in the JAC code, the solution algorithm is iterative in nature. Therefore, a trial strain increment is provided to the constitutive model to obtain the trial stress increment. Then the stress and strain increments are evaluated for global equilibrium. If equilibrium is satisfied, the trial strain and stress increments are indeed the solution to the problem. Otherwise, another trial strain increment is provided and the process repeated. Given trial strain increments $\underset{\sim}{\mathbf{e}}^{t+1}$, γ_1, and γ_2 are completely determined at the beginning of the load step. Then equations (18) and (19) provide two algebraic equations for the solution of the normal stresses at the end of the load step. Combining equations (18) and (19) one obtains a fourth-order equation for the evaluations of the stress T_n^{t+1}:

$$\alpha_1 (T_n^{t+1})^4 + (\alpha_1 \gamma_1 + \gamma_3)(T_n^{t+1})^3 + [\gamma_1 \gamma_3 + \alpha_2^2 (\beta_n - \beta_m) - 2\alpha_1^2 \beta_n](T_n^{t+1})^2 + [\beta_n (\alpha_2^2 - \alpha_1^2)\gamma_1 - \alpha_1 \beta_n \gamma_3](T_n^{t+1}) - \alpha_1 \beta_n^2 (\alpha_2^2 - \alpha_1^2) = 0 \tag{22}$$

Downloaded 03 May 2010 to 171.66.16.31. Redistribution subject to ASME license or copyright; see http://www.asme.org/terms/Terms_Use.cfm

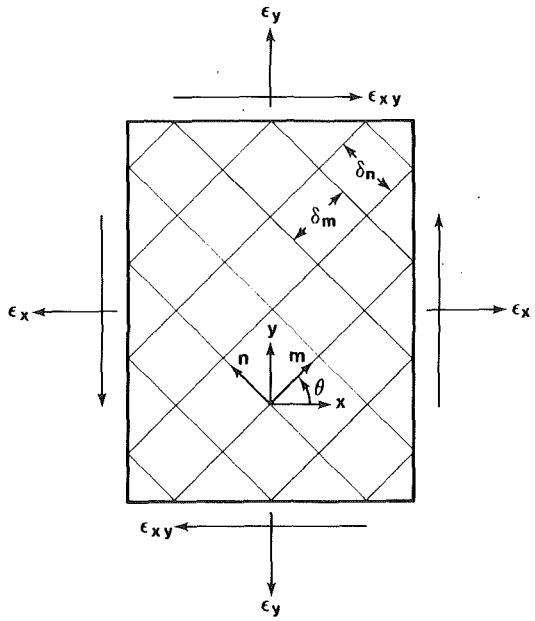


Fig. 4 Jointed rock block geometry and loading condition

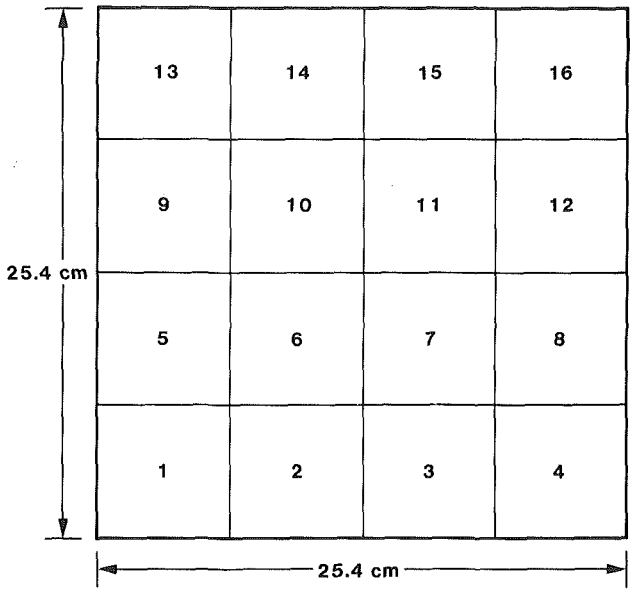


Fig. 5 Sixteen-element test problem geometry

where $\gamma_3 = \alpha_1\ \gamma_1 - \alpha_2\ \gamma_2$. It can be shown that only the maximum root is applicable; the other roots are either associated with the undefined tensile branch of the normal stress-displacement relationship for joints or provide results inconsistent with applied loading conditions. Once T_n^{t+1} is determined, T_m^{t+1} is found from

$$\alpha_2 T_m^{t+1} = \alpha_1 T_n^{t+1} + (\alpha_2^2 - \alpha_1^2)\beta_1 / T_n^{t+1} + \gamma_3 \qquad (23)$$

and the current stresses T_{mm}^{t+1} and T_{nn}^{t+1} are easily obtained from equation (16). The stress rates $\dot{T}_{mm} = T_{mm}^{t+1} - T_{mm}^{t}$ and $\dot{T}_{nn} = T_{nn}^{t+1} - T_{nn}^{t}$ are then determined, and the remaining normal stress rate component $\dot{T}_{zz}$ is obtained from equation (11) as

$$\dot{T}_{zz} = (3KG/\alpha_3)\dot{e}_{zz} + (\alpha_2/2\alpha_3)(\dot{T}_{mm} + \dot{T}_{nn}) \qquad (24)$$

where $\alpha_3 = K + G/3$. With the aid of equation (3), explicit expressions for the normal displacement rates for the joints can be calculated from

$$(\dot{\tilde{u}}^d)_k = \delta_k[\dot{e}_{kk} - \dot{T}_{kk}/2G + (\alpha_2/6KG)tr\dot{\underset{\sim}{\mathbf{T}}}],\ k = m,n \qquad (25)$$

and from which the current joint normal displacements can be obtained.

The shear stress rate is calculated directly from equation (12) once the shear strain rate is known. However, equation (12) governs only elastic behavior of the joints. Since the slip behavior is assumed to be nonlinear and obeys the Mohr-Coulomb criterion, the slip function F in equation (8) is checked after all the stresses have been updated. If $F \leq 0$ for both sets of joints, the system behaves linear elastically. Thus, the current stresses are indeed given by the updated ones, and the joint slip displacements are obtained from equation (3). The calculation for this load step is then concluded. If $F > 0$ and $\partial F/\partial\tau \cdot \tau \leq 0$ for either set of joints, joint nonlinearity has been achieved. In the nonlinear range, it is assumed that the joint behavior dominates, and the rock matrix contribution is ignored. Beyond the linear range the shear stress and, in turn, the joint slip displacement is calculated from the shear stress versus slip displacement relationship from Fig. 3. This can be done easily since it is essentially a one-dimensional operation. For equilibrium considerations, the magnitude of the shear stresses acting on the two joint sets are necessarily equal. Therefore, initiation of the slip nonlinearity for one set will affect the shear behavior of the other. This interaction is included in the current orthogonal joint set model.

The previous equations have been implemented as an additional material type in the material model library of the finite element code JAC (Biffle, 1984). This is accomplished on the vectorized update version of JAC for the CRAY computer. Input formats and a FORTRAN correction set that can be used to modify the existing JAC UPDATE Program Library are reported in Chen (1987).

It is noted that equations (9) through (12) may be integrated numerically using the standard tangent stiffness method. However, as can be seen in the above solution procedure, these rate equations posses multiple roots owing to the contitutive behavior of the joints. The current solution procedure allows the consistent selection of the root to the rate equations. To use the numerical integration method, additional criteria must be built-in to the solution procedure to guarantee the consistent selection of the roots.

Sample Calculations

Several examples have been provided here for verification and demonstration purposes. All JAC calculations are done on the Sandia CRAY-1/S computer with the implemented joint model. The following rock properties, taken from the work of Thomas (1982) are used for all examples:

Intact rock

$K = 4.59$ GPa (667.0 ksi), $G = 2.76$ GPa (400.0 ksi).

Reference joint set

$A_n = 6.89$ MPa (1.0 ksi), $(\tilde{u}^d_{\max})_n = 0.00762$ cm (-0.003 in.)

$(G_s)_n = 0.27$ GPa/cm (100.0 ksi/in),

$$(G_s')_n = 2.71 \text{ MPa/cm (1.0 ksi/in)}$$

$\mu_n = 0.7$, $C_0 = 1.72$ MPa (0.25 ksi), $\delta_n = 1.27$ cm (0.5 in.).

For convenience, the joint set orthogonal to the reference set is assumed to have the same properties as the reference set. Alignment angle of the reference joint set to the loading directions, the initial stress state, and boundary conditions are the variables in these examples.

The first sample involves a rock block which occupies the xy-plane under the condition of plane strain shown on Fig. 4.

Downloaded 03 May 2010 to 171.66.16.31. Redistribution subject to ASME license or copyright; see http://www.asme.org/terms/Terms_Use.cfm

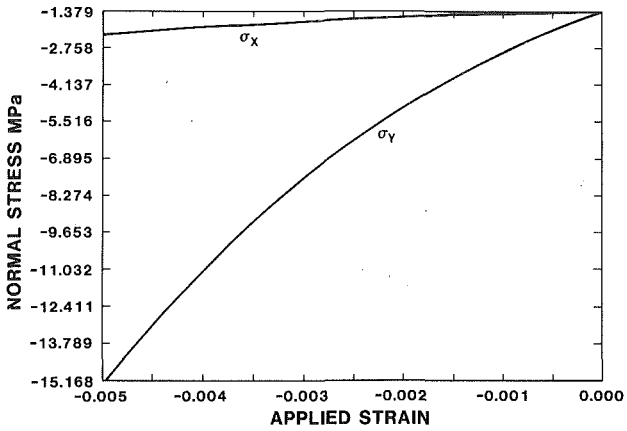


Fig. 6 Applied strain versus normal stress for sample Problem 1

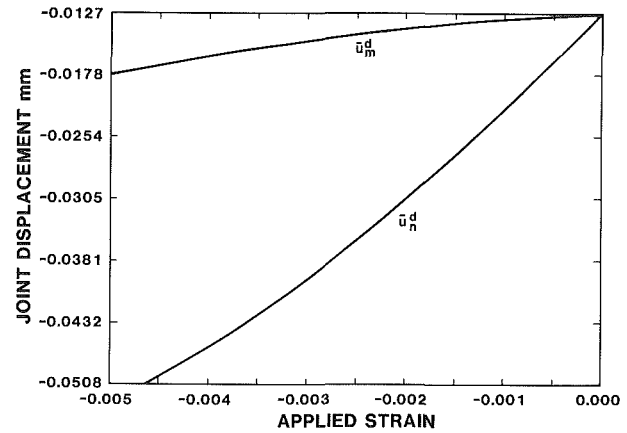


Fig. 7 Applied strain versus joint displacement for sample Problem 1

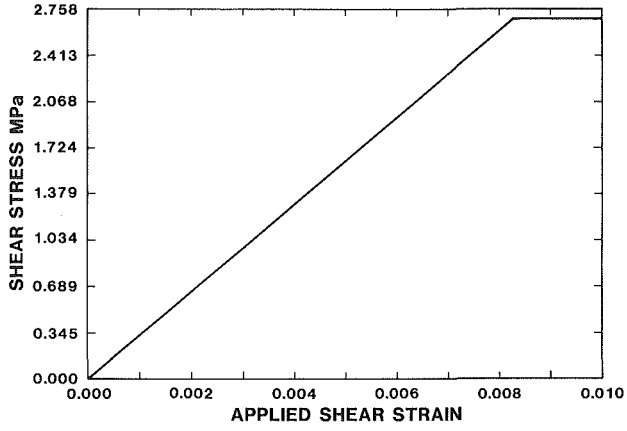


Fig. 8 Applied shear strain versus shear strain for sample Problem 2

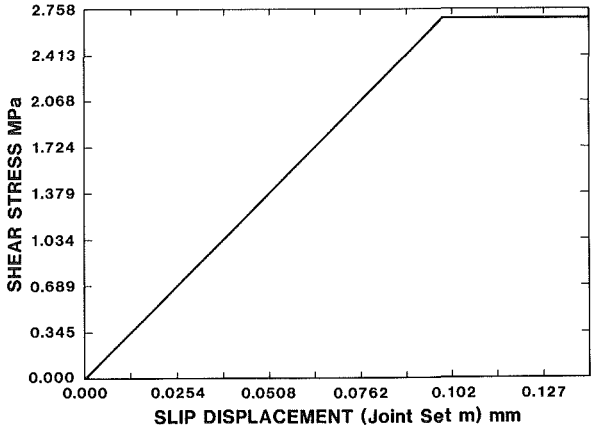


Fig. 9 Slip displacement versus shear stress for joint set m (sample Problem 2)

The reference joint set n is assumed to align with the x-axis, i.e., $\theta = 0$, and the block is loaded by uniaxial strain along the y-direction from $\epsilon_y = 0$ to $\epsilon_y = -0.005$. The block is constrained such that $\epsilon_x = \epsilon_z = \epsilon_{xy} = 0$ during this straining process. An initial stress state of $\sigma_x = \sigma_y = \sigma_z = -1.379$ MPa (-200.0 psi), $\tau_{xy} = 0.0$ is assumed to prevail in the rock block. Both analytical and finite element solutions have been obtained for this problem. The finite element idealization for the geometry and loading conditions for this example is shown in Fig. 5. The infinitely large rock in the analytical solution is replaced by a 25.4 by 25.4 cm (10 by 10 in.) block divided into 16 elements. The vertical as well as the bottom edges of the block are roller supported, and the to edge is given a downward displacement of 0.127 cm (0.05 in.) to simulate the applied loading and boundary conditions. The same initial stress state exists in the finite element model. Finite element results indicate that a uniform stress state exists in the four middle elements, suggesting minimal edge effects. If the jointed rock model is implemented correctly into the JAC code, one would expect the solutions of this problem from both the analytical treatement and the middle elements of the finite element method to agree very well. This is indeed the case. The results of the normal stresses and joint normal displacements as functions of the applied strain are given, respectively, on Figs. 6 and 7. On Figs. 6 and 7, the analytical and finite element solutions are virtually the same and cannot be distinguished from each other based on the scale used. The stress versus strain curves on Fig. 6 exhibit the nonlinear characteristics of the jointed rock model. As shown on Fig. 7, the orthogonal joint set model accounts for joint displacements in two directions according to their corresponding stress levels. This represents an additional capability over the single joint set model developed previously (Thomas, 1982).

The second sample problem involves the pure shear of the same rock block on Fig. 4, again with $\theta = 0$. The loading condition is such that the shearing strain ϵ_{xy} is increased from 0 to 0.01 while all the normal strains are held at zero. An initial stress state of $\sigma_x = \sigma_z = -1.379$ MPa ($-200.$ C psi), $\sigma_y = -3.447$ MPa (-500.0 psi), and $\tau_{xy} = 0$ is assumed for this case. The 16-element mesh on Fig. 5 is again used for the finite element idealization for this problem. For boundary and loading conditions in the finite element model, the bottom edge is fixed, the top edge is roller-supported and given a uniform displacement of 0.508 cm (0.2 in.) to the right, while the vertical edges are free surfaces and constrained to remain straight. This set of conditions produces a pure shear deformation and uniform stress state for the finite-size block. Thus, if the shear aspect of the code implementation is performed correctly, finite element and analytical solutions should agree. Again, this is proven to be the case. Figure 8 shows a plot of shear stress versus applied shear strain for both the analytical and the finite element solution. The two curves are exactly the same and thus merge into one in the figure. The onset of nonlinearity in the shear stress occurs at 2.689 MPa (390 psi), as determined from the Mohr-Coulomb criterion for the joint set m with a corresponding stress normal to the joint of -1.379 MPa (-200 psi). Beyond this point, stress increases following the stiffness specified by G_s' and reaches approximately 2.744 MPa (398 psi) when fully displaced. At this stress level, joint set n remains elastic because of its high normal stress level of -3.447 MPa (-500 psi). These characteristics are shown on Fig. 9 and 10. Variations of the slip displacement for the two joint sets as a function of the applied shear strain are depicted on Figs. 11 and 12. For joint set n (Fig. 12), the slip displacement increases linearly until the

Downloaded 03 May 2010 to 171.66.16.31. Redistribution subject to ASME license or copyright; see http://www.asme.org/terms/Terms_Use.cfm

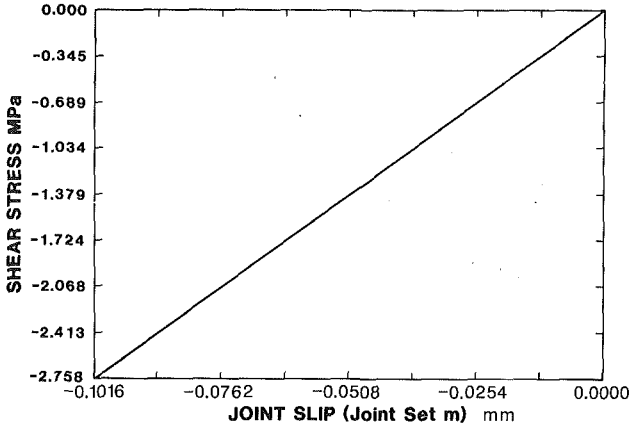


Fig. 10 Slip displacement versus shear stress for joint set *n* (sample Problem 2)

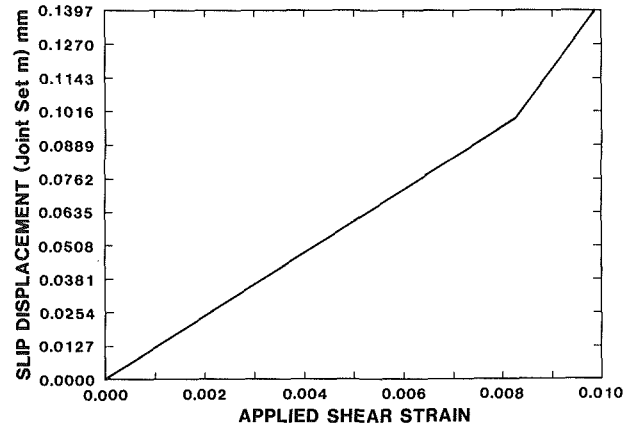


Fig. 11 Applied shear strain versus slip displacement for joint set *m* (sample Problem 2)

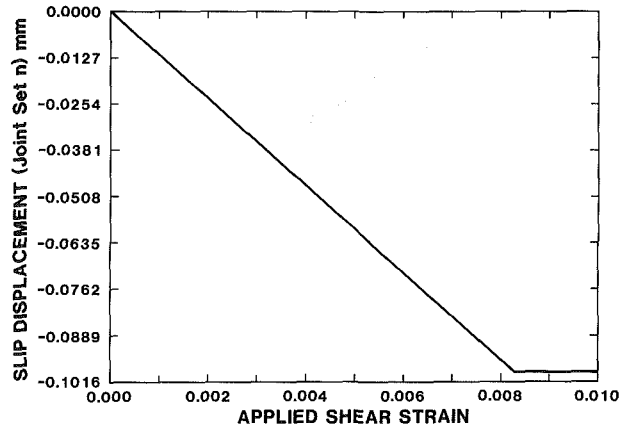


Fig. 12 Applied shear strain versus slip displacement for joint set *n* (sample Problem 2)

applied shear strain reaches the level that triggers the onset of nonlinearity for the joint set *m*. The joint set remains elastic; however, stress, and thus slip displacement, increases very slowly beyond this point. Therefore, a bend in the curve is observed. The same is true for joint set *m* except that beyond the triggering applied strain level, this joint behaves nonlinearly. Therefore, although the stress increases slowly, slip displacement is accumulated at a much faster rate than in the other joint set (Fig. 11). The analytical and finite element solution are exactly the same, and therefore, only one curve is distinguishable on Figs. 9 through 12. Thus, the correctness of the code implementation is considered verified.

The remaining sample calculation has been performed for

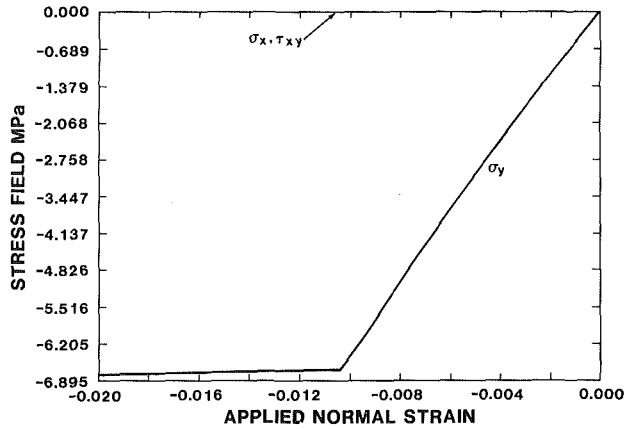


Fig. 13 Applied normal strain versus stress field in the *xy* plane (sample Problem 3)

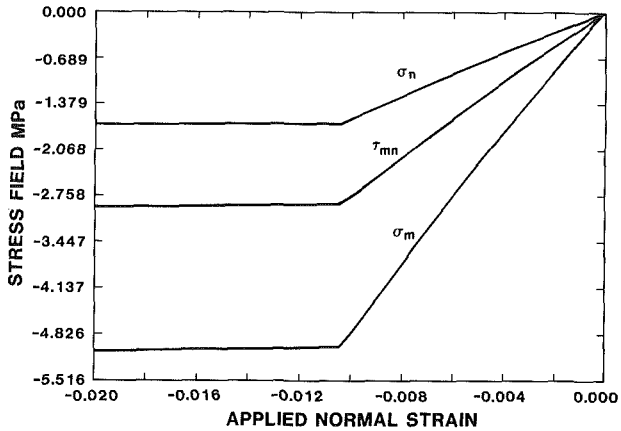


Fig. 14 Applied normal strain versus stress field in the plane of the joints (sample Problem 3)

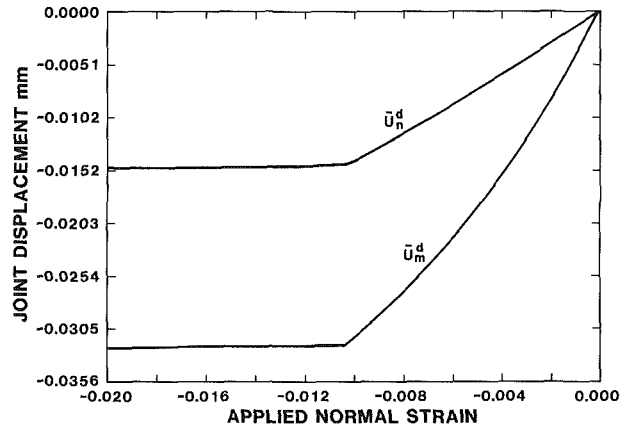


Fig. 15 Applied normal strain versus joint displacement (sample Problem 3)

the finite element method only. The rock block on Fig. 4, as idealized by the 16-element finite mesh on Fig. 5, is used in this example. The orientation of the joint sets does not align with the global *xy* system, and the angle θ on Fig. 4 is assumed to be 60°. The boundary and loading conditions are such that the bottom edge of the block is on roller support, the vertical edges are free surfaces, and the top edge is given a uniform downward displacement of 0.508 cm (0.2 in.). The rock is initially stress-free. This provides a case where the joints are subjected to the combined actions of normal and shear stresses resulting from the applied load condition. The inclined joint sets interact with the finite boundaries, resulting in

Downloaded 03 May 2010 to 171.66.16.31. Redistribution subject to ASME license or copyright; see http://www.asme.org/terms/Terms_Use.cfm

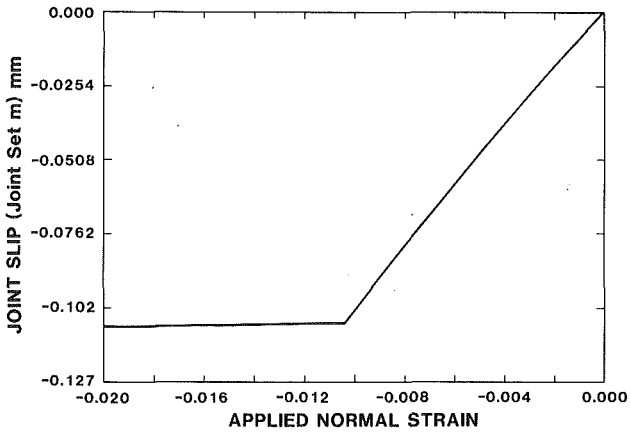


Fig. 16 Applied normal strain verus joint slip for joint set m (sample Problem 3)

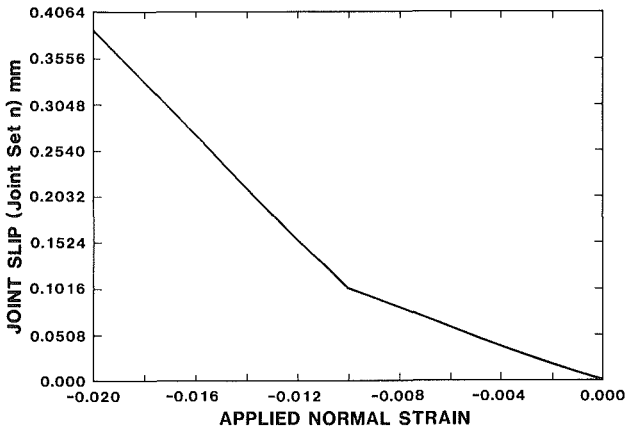


Fig. 17 Applied normal strain versus joint slip for joint set n (sample Problem 3)

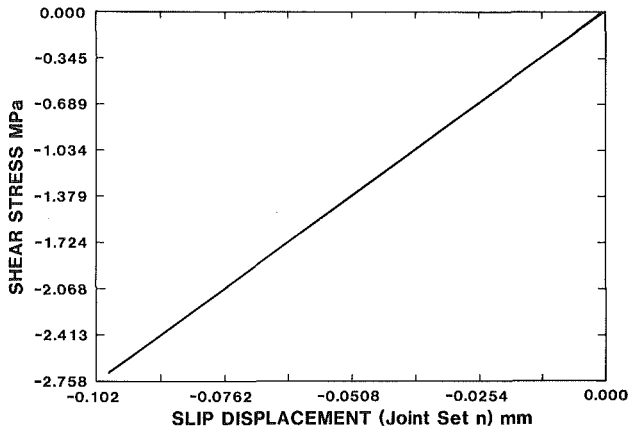


Fig. 18 Joint slip versus shear stress for joint set m (sample Problem 3)

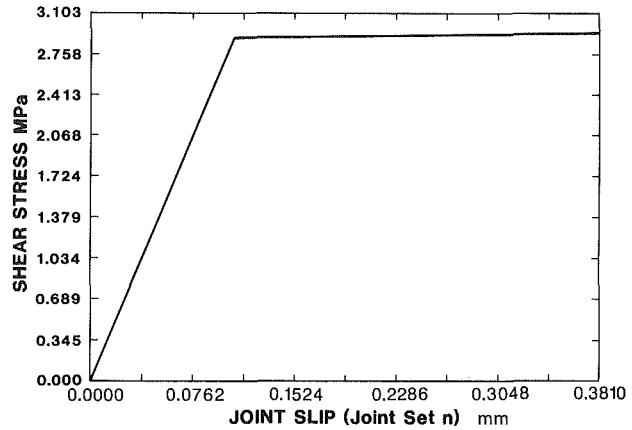


Fig. 19 Joint slip versus shear stress for joint set n (sample Problem 3)

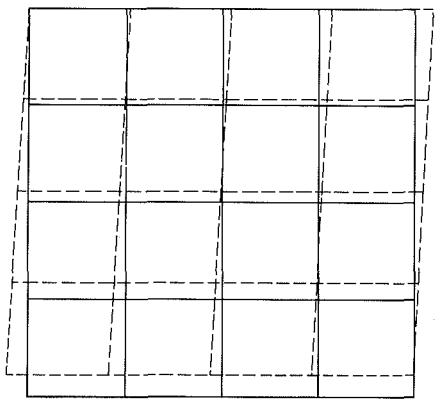


Fig. 20 Deformed versus undeformed mesh geometry (sample Problem 3)

nonuniform stress distribution in the rock block. However, the qualitative behavior of the joints in each element is similar, and it suffices to discuss the results by focusing on the information from a single element. Henceforth, it is understood that all information presented is for element 10, whose location is indicated on Fig. 5. The stress field in the orientation of the reference xy-system is shown on Fig. 13 as functions of the applied strain. Since the applied loading is uniaxial along the y-direction and the vertical edges are free, $\sigma_x = \tau_{xy} = 0$ during the entire loading process and only σ_y is generated. σ_y increases nonlinearly with the applied strain until the strain level at which the onset of joint slip has occurred. Beyond this level, the stress increases slowly because of the constraint of the joint shear behavior. The same is true for the stress distribution in the mn joint coordinate system (Fig. 14). Through Mohr-Circle transformation, no stress component vanishes in this orientation. The corresponding joint displacements to the stresses are given on Figs. 15 through 17. Figure 15 exhibits the variation of the normal joint displacements as a function of the applied normal strain ϵ_y. Because the absolute value of the stress σ_m is greater than σ_n, larger displacement is developed for joint set m. Also because of this higher normal stress, the magnitude of the shear stress level to trigger the onset of nonlinearity is higher for joint set m than for n. Hence, larger joint slip is observed (Fig. 17) for joint set n than for joint set m (Fig. 16). Indeed, joint set m remains linear in shear while joint set n attains nonlinearity for the prescribed loading condition. These are shown on Figs. 18 and 19, respectively, in terms of the shear stress versus slip displacement plots. Finally, it is interesting to observe the deformed mesh patterns on Fig. 20 at the end of the loading process. (The displacements have been magnified three times to exaggerate the deformation pattern.) It is seen that global shearing deformation occurs as a result of uniaxial straining. Analogous behavior has been observed for anisotropic elastic solids (Lekhnitskii, 1963) and this similarity between the jointed rock model and anisotropic material is noted.

Downloaded 03 May 2010 to 171.66.16.31. Redistribution subject to ASME license or copyright; see http://www.asme.org/terms/Terms_Use.cfm

Summary

The numerical implementation of a constitutive model for jointed rock media into the finite element code JAC (Biffle, 1984) has been presented. Detailed expressions used for implementation have been included herein. Example problems have been solved to verify the correctness of the code implementation and to demonstrate the utility of the constitutive model.

It is emphasized that the present model is a continuum description of the real material that measures the gross response rather than giving detailed individaul joint information. As such, the model is applicable to situations in which the least dimension of the representative rock volume is approximately an order of magnitude larger than the joint spacings so as to allow a valid averaging process. Moreover, the model is limited to two-dimensional calculations, orthogonal joint sets, and noninterfering block responses. Work is underway to relax these restrictions. These extensions of the model will be reported in future documentation.

Acknowledgment

The many helpful discussions with the author's colleagues, notably R. K. Thomas, C. H. Conley, and R. S. Chambers, during the course of this investigation, are gratefully acknowledged.

References

Bazant, Z. P., and Tsubaki, T., 1980, "Slip-Dilatancy Model for Cracked Reinforced Concrete," *Journal of the Structural Division*, ASCE, Vol. 106, pp. 1947–1966.

Biffle, J. H., 1984, "JAC—A Two-Dimensional Finite Element Computer Program for the Non-Linear Quasi-static Response of Solids with the Conjugate Gradient Method," Sandia National Laboratories Report SAND81-0998, Albuquerque, NM.

Chen, E. P., 1986, "Two-Dimensional Continuum Model for Jointed Media with Orthogonal Set of Joints," *Proceedings of the 27th U.S. Symposium on Rock Mechanics*, H. L. Hartman, ed., Society of Mining Engineers, Inc., Littletown, CO, pp. 862–867.

Chen, E. P., 1987, "A Computational Model for Jointed Media with Orthogonal Sets of Joints," Sandia National Laboratories Report SAND86-1122, Albuquerque, NM.

Goodman, R. E., 1976, *Methods of Geological Engineering*, West Publishing Co., St. Paul, MN.

Jaeger, J. C., and Cook, N. G. W., 1979, *Fundamentals of Rock Mechanics*, 3rd Ed., Halsted Press, New York.

Lekhnitskii, S. G., 1963, *Theory of Elasticity of an Anisotropic Elastic Body*, Holden-Day, Inc., San Francisco, CA.

Morland, L. W., 1974, "Continuum Model of Regularly Jointed Medium," *Journal of Geophysical Research*, Vol. 79, No. 2, pp. 357–362.

Olsson, W. A., 1987, "Rock Joint Compliance Studies," Sandia National Laboratories Report SAND86-0177, Albuquerque, NM.

Scott, R. B., and Castellanos, M., 1984, "Stratigraphic and Structural Relations of Volcanic Rocks in Drill Holes USW GU-3 and USW G-3, Yucca Mountain, Nye Country, Nevada," USGS Report USGS-OFR-8-491, Denver, CO.

Thomas, R. K., 1982, "A Continuum Description for Jointed Media," Sandia National Laboratories Report SAND81-2615, Albuquerque, NM.

U.S. Department of Energy, 1985, "Nevada Nuclear Waste Storage Investigations Exploratory Shaft Test Plan Draft Document," Revision 1, US DOE Nevada Operations Office, Las Vegas, NV.

Downloaded 03 May 2010 to 171.66.16.31. Redistribution subject to ASME license or copyright; see http://www.asme.org/terms/Terms_Use.cfm

An Asymptotic Analysis of Cold Sheet Rolling

Robert P. Smet
S-Cubed,
San Diego, CA 92121-1095

Robert E. Johnson
Department of Theoretical and Applied Mechanics,
University of Illinois at Urbana-Champaign,
Urbana, IL 61801

We examine the plane strain cold rolling problem of thin strip implementing a perturbation scheme upon the governing equations. The analysis accounts for transverse variations in the flow and inhomogeneous work hardening. We establish deformation regimes based upon the parameters μ, the friction coefficient, τ, the ratio of the initial yield stress and the maximum roll pressure, and δ, a measure of the small gap reduction. We see that the inclusion of these inhomogeneous effects gives mildly different results for values of $\mu/\tau > O(1)$ or $\tau\,\delta/\mu = O(1)$. We gauge these effects by examining the roll pressure, shear stress, longitudinal stress, yield stress, front and back tensions and torque to see how they are affected by the inclusion of inhomogeneous flow effects.

Introduction

The analysis of the cold rolling of thin strip is well documented, dating back to the pioneering works of Siebel (1924), von Karman (1925) and Orowan (1943). The majority of the analytical work since that time has, in fact, been based on the slab type of analysis developed by those pioneers. Noteworthy studies in this area include: Bland and Ford (1948), Sims (1954), Ford (1957), Ford and Alexander (1964), Alexander (1972) and Venter and Abd-Rabbo (1980a, 1980b), to mention only a few of the many excellent studies. A detailed review of each author's work shall not be made here but it may suffice to examine the table presented by Venter, et al. in their paper.

Here we will examine the two-dimensional inhomogeneous plastic deformation (plane strain) of an isotropic work hardening metal in a rolling mill. To do this, we will depart from the traditional slab type of analysis and examine this problem using modern asymptotic methods starting from the equilibrium equations for plane strain. The asymptotic expansions will be based on the generally small one-pass reduction parameter δ, i.e., the ratio of the change in sheet thickness to the length of the gap. In contrast, slab analysis is basically a one-dimensional theory which is modified in a somewhat ad hoc way to account for inhomogeneous deformation (i.e., variations in the plastic flow transverse to the rollling direction). As a result, slab analysis has not been able to rigorously account for the inhomogeneous character of the deformation present in rolling operations and, in particular, the effect of inhomogeneous compression on work hardening. Previous analytical work on rolling of a work hardening material has assumed that the material could be modeled as one which was experiencing homogeneous compression (Venter and Abd-Rabbo, 1980a, 1980b). This assumption was necessary due to the one-dimensional character of the traditional slab analysis. In an attempt to account for the actual inhomogeneous compression of the material, for which there will be a greater amount of cold work imparted to the material, Venter and Abd-Rabbo made an ad hoc adjustment to the strain hardening exponent (i.e., they artificially increased the exponent appearing in the power law, work hardening expression). Except for previous applications of the finite element method the present analytical work will, for the first time, directly account for the effect of inhomogeneous compression on the work hardening of the metal because the true two-dimensional nature of the deformation is maintained throughout the analysis. An asymptotic analysis similar to that presented here has been used by Johnson (1987) to examine conical extrusion. We might add that the basic methods proposed here have also been very useful in analyzing compression molding (Johnson, 1984) and in studying the gravity driven flow of glaciers (Johnson and McMeeking, 1984).

We shall see that the introduction of inhomogeneous work hardening will invalidate the need for the boundary condition of sticking on the rolls, since in slab analysis it was possible for the shear stress at the roll surface to reach the yield stress. Consequently, in slab analysis it is necessary to change the roll surface boundary condition beyond the point where the shear stress first reaches the yield stress from a friction condition to a condition in which the material is yielded in pure shear. In the present treatment, it will not be necessary to change boundary conditions because the shear stress can never exactly equal the yield stress (except possibly at only one point). This difference between the present work and previous works is found to have a mildly significant effect on the output parameters in those situations up to the point where sticking previously was assumed to occur.

Our goal has been to incorporate inhomogeneous work hardening effects into the analysis of rolling to determine the subsequent effect upon the roll pressure, shear stress,

Contributed by the Applied Mechanics Division for publication in the JOURNAL OF APPLIED MECHANICS.

Discussion on this paper should be addressed to the Editorial Department, ASME, United Engineering Center, 345 East 47th Street, New York, N.Y. 10017, and will be accepted until two months after final publication of the paper itself in the JOURNAL OF APPLIED MECHANICS. Manuscript received by ASME Applied Mechanics Division, October 29, 1987; final revision, May 26, 1988.

Copyright © 1989 by ASME

Downloaded 03 May 2010 to 171.66.16.31. Redistribution subject to ASME license or copyright; see http://www.asme.org/terms/Terms_Use.cfm

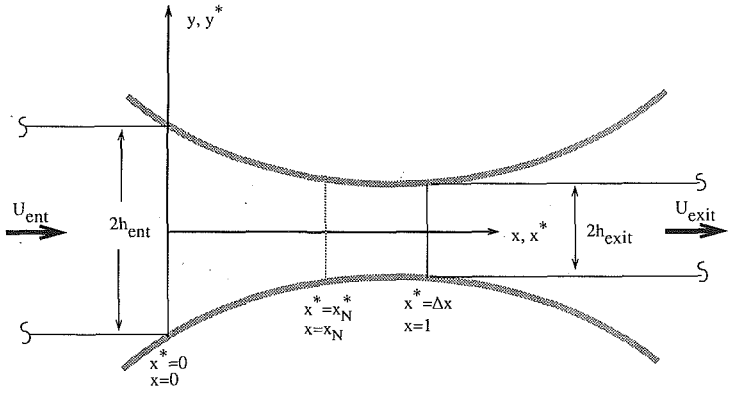


Fig. 1 A diagram of the rolling geometry including the coordinate systems for the dimensional and nondimensional quantities

longitudinal deviatoric stress, yield stress, roll torque, and front and back tensions. Clearly the inclusion of roll efficiency, roll force, elastic effects, and other various aspects of the rolling problem could well have been done without much further effort but we felt that emphasizing the roll pressure and stresses would be the most expedient means of demonstrating the effects of inhomogeneous deformation.

Description

Although the rolling geometry is no different from that of previous analyses (see Fig. 1), we shall adopt a different approach to the solution. The material enters at location $x^*_{ent} = 0$ at a velocity U_{ent} and a thickness $2h_{ent}$ between two identical rollers of undeformed radius R which are rotating with angular speed ω. The material gets squeezed between the rolls and exits at a location $x^*_{exit} = \Delta x$ at a thickness $2h_{exit}$. Within the gap of the undeformable rolls the thickness is given by $2h(x^*) = 2[R - \sqrt{R^2-(x^*-\Delta x)^2}] + 2h_{exit}$ and since the material typically enters at a velocity below that of the rolls, a point is generally reached within the gap region where the velocity of the material is equal to that of the rolls. This location x^*_N is known as the neutral point (plane); before the neutral point the shear stress exerted by the rolls on the material drives the material and beyond the neutral point the shear stress retards the material. These locations are known as the entry side and exit side of the neutral point, respectively. In the usual study of the rolling problem, forces are applied to the entrance and exit, respectively, referred to as the back and front tensions. The location of the neutral point is established by an iterative process of matching roll pressures at the neutral plane which are calculated separately on the entrance and exit side of x^*_N. For this value of x^*_N one could find the entrance velocity for a given roll rotation speed ω by way of mass conservation. However, we shall assume that we know x^*_N, which is equivalent to prescribing the entrance velocity and rotation speed, and we then determine the front and back tensions as part of the solution.

Analysis

We begin the analysis by first presenting the nondimensionalized governing equations for plane strain, viz., equilibrium, continuity, constitutive laws and flow rule plus boundary conditions. Each variable is made dimensionless as follows: the coordinate x^* by Δx = length of the gap; the coordinate y^* by Δh = half the change in strip thickness; the shear, longitudinal, and transverse stresses, S^*_{xy}, σ^*_{xx} and σ^*_{yy}, by $|\sigma^*_{yy}|_{max}$; the x^* and y^* components of velocity, u^* and v^*, by U_{ent} = entrance material velocity; the longitudinal and transverse deviatoric stresses, S^*_{xx} and S^*_{yy}, by σ_o = initial yield stress of the material at the entrance to the mill; time, t^*, by $\Delta x/U_{ent}$; and plastic multiplier, λ^*, by $U_{ent}/\sigma_o\Delta h$. We also introduce the parameters, $\tau = \sigma_o/|\sigma^*_{yy}|_{max}$, which is the ratio of the yield stress and maximum roll pressure, and $\delta = \Delta h/\Delta x \ll 1$, which is a measure of the small reduction in one pass. We must bear in mind that we prescribe $|\sigma^*_{yy}|_{max}$ at $x^* = x^*_N$ by letting τ and x_N be input parameters and determine the corresponding front and back tensions. Although this may not be the best approach in practice, it is certainly a convenient approach if the primary goal is to explore the qualitative character of the solution.

The dimensionless governing equations are the equilibrium equations,

$$\delta \frac{\partial \sigma_{xx}}{\partial x} + \frac{\partial S_{xy}}{\partial y} = 0, \tag{1}$$

$$\delta \frac{\partial S_{xy}}{\partial x} + \frac{\partial \sigma_{yy}}{\partial y} = 0, \tag{2}$$

the mass conservation equation for an incompressible material,

$$\delta \frac{\partial u}{\partial x} + \frac{\partial v}{\partial y} = 0, \tag{3}$$

the constitutive equations,

$$\lambda S_{xx} = \delta \frac{\partial u}{\partial x}, \quad \lambda S_{yy} = \frac{\partial v}{\partial y}, \quad \frac{2}{\tau}\lambda S_{xy} = \frac{\partial u}{\partial y} + \delta \frac{\partial v}{\partial x} \tag{4a,b,c}$$

and the flow rule, whereby we assume that the flow stress increases at a rate proportional to a power of the total plastic strain, i.e.,

$$S^2_{xx} + \left(\frac{S_{xy}}{\tau}\right)^2 = \frac{1}{3}\left\{1 + \frac{2}{\sqrt{3}}\frac{B}{\delta}\int_0^t \lambda\left[S^2_{xx} + \left(\frac{S_{xy}}{\tau}\right)^2\right]^{1/2} dt\right\}^{2n}. \tag{5}$$

Note that to obtain (5), we have used (4) and the dimensional flow rule

$$\sqrt{\frac{1}{2}S^*_{ij}S^*_{ij}} = \frac{\sigma_o}{\sqrt{3}}\left(1 + \frac{2}{\sqrt{3}}B\epsilon_p\right)^n,$$

where the total plastic strain is

$$\epsilon_p = \int_0^{t^*} \sqrt{\frac{2}{3}D^*_{ij}D^*_{ij}}\, dt^*$$

and the strain rates are given by

$$D^*_{ij} = \frac{1}{2}(u^*_{i,j} + u^*_{j,i}).$$

Here B and n are given material parameters and the integral of the plastic strain rate is to be evaluated following a material

Downloaded 03 May 2010 to 171.66.16.31. Redistribution subject to ASME license or copyright; see http://www.asme.org/terms/Terms_Use.cfm

point. Also, for plane strain, with the present nondimensionalization, $\sigma_{xx} = \sigma_{yy} + 2\tau S_{xx}$ and we have $S_{xx} = -S_{yy}$ due to incompressibility.

For the nondimensional boundary conditions we have the friction condition on the roll surfaces,

$$\mathbf{t}\cdot\boldsymbol{\lambda} = \mp\mu\mathbf{t}\cdot\mathbf{n} \quad \text{on} \quad y = h(x),$$

where μ is the friction coefficient, $h(x) = C_1 + C(x-1)^2$, $C_1 = h_{\text{exit}}/\Delta h$ and $C = (\Delta x)^2/2R\Delta h$; and the symmetry condition

$$S_{xy}(x, y=0) = 0;$$

where, due to symmetry, we need only consider the solution between $y = 0$ and $y = h(x)$. Note that in the previous equation $\mathbf{t} = \boldsymbol{\sigma}\cdot\mathbf{n}$ is the roll surface traction, $\mathbf{n}$ = unit inward normal to the roll surface, and $\boldsymbol{\lambda}$ = unit tangent to the roll surface. The $-$ and $+$ signs in the first boundary condition are for points before and after the neutral point, respectively. We should explain that the different dimensional scalings of the stresses is motivated by the nature of the boundary condition and the flow rule. The boundary condition $\mathbf{t}^*\cdot\boldsymbol{\lambda} = \mp\mu\mathbf{t}^*\cdot\mathbf{n}$ would indicate that $\mathbf{t}^*\cdot\boldsymbol{\lambda} \simeq S^*_{xy}$ should be scaled by the same stress as $\mathbf{t}^*\cdot\mathbf{n} \simeq \sigma^*_{yy}$, namely the maximum roll pressure, $|\sigma^*_{yy}|_{\max}$. However, the flow rule would indicate that the characteristic stress for S^*_{xx} is the yield stress σ_o.

We now establish the appropriate expansions for the previously mentioned scaled variables. Clearly, to enforce conservation of mass (3), we make the expansions of u and v in powers of $\delta \ll 1$ as follows:

$$u = u^{(0)} + \delta u^{(1)} + \ldots,$$
$$v = \delta v^{(0)} + \delta^2 v^{(1)} + \ldots.$$

We shall make the following expansions for the stresses and plastic multiplier λ:

$$\sigma_{yy} = \sigma^{(0)}_{yy} + \delta\sigma^{(1)}_{yy} + \ldots,$$
$$S_{xy} = \mu(S^{(0)}_{xy} + \delta S^{(1)}_{xy} + \ldots),$$
$$S_{xx} = S^{(0)}_{xx} + \delta S^{(1)}_{xx} + \ldots,$$
$$\lambda = \lambda^{(0)} + \delta\lambda^{(1)} + \ldots.$$

We again note that $\sigma_{xx} = \sigma_{yy} + 2\tau S_{xx}$ and $S_{xx} = -S_{yy}$. Substituting the above expansions into the governing equations (1)–(5) and boundary conditions, we obtain to leading order,

$$\delta\left(\frac{\partial\sigma^{(0)}_{yy}}{\partial x} + 2\tau\frac{\partial S^{(0)}_{xx}}{\partial x}\right) + \mu\frac{\partial S^{(0)}_{xy}}{\partial y} = 0, \tag{6}$$

$$\frac{\partial\sigma^{(0)}_{yy}}{\partial y} = 0, \tag{7}$$

$$\frac{\partial u^{(0)}}{\partial x} + \frac{\partial v^{(0)}}{\partial y} = 0, \tag{8}$$

$$\lambda^{(0)}S^{(0)}_{xx} = 0, \quad \lambda^{(0)}S^{(0)}_{yy} = 0, \quad 2\frac{\mu}{\tau}\lambda^{(0)}S^{(0)}_{xy} = \frac{\partial u^{(0)}}{\partial y} \tag{9a,b,c}$$

$$S^{(0)2}_{xx} + \left(\frac{\mu}{\tau}S^{(0)}_{xy}\right)^2 = \frac{1}{3}\left\{1 + \frac{2B}{\sqrt{3}\,\delta}\int_0^t (\lambda^{(0)} + \delta\lambda^{(1)})\left[S^{(0)2}_{xx} + \left(\frac{\mu}{\tau}S^{(0)}_{xy}\right)^2\right]^{1/2} dt\right\}^{2n}, \tag{10}$$

B.C.: $$S^{(0)}_{xy}(x, y=0) = 0, \tag{11a}$$

$$S^{(0)}_{xy} - 2\delta\frac{\tau}{\mu}S^{(0)}_{xx}\frac{dh}{dx} = \mp\sigma^{(0)}_{yy} \quad \text{on} \quad y = h(x). \tag{11b}$$

Note that we have kept the $\delta\,\partial\sigma^{(0)}_{xx}/\partial x$ term in the first equilibrium equation. We do this because we know that the shear stress must balance the longitudinal stress gradient. Hence, we expect and can later verify that $\delta\,\partial\sigma^{(0)}_{xx}/\partial x$ is of the same order as $\mu\,\partial S^{(0)}_{xy}/\partial y$. From (9) we find $\lambda^{(0)} = 0$ since the boundary condition $S^{(0)}_{xy}(x, 0) = 0$ makes it impossible to have $S^{(0)}_{xx} = S^{(0)}_{yy} = 0$. With $\lambda^{(0)} = 0$ we find from (9c) that $u^{(0)} = u^{(0)}(x)$. Consequently, from mass conservation $u^{(0)}(x) = Q/h(x)$, where $Q = h_{\text{ent}}/\Delta h$ is the dimensionless net flux through the rolls (i.e., $Q^* = 2U_{\text{ent}}h_{\text{ent}}$), and equation (8) gives $v^{(0)} = -y\,du^{(0)}/dx$. Also, from (7), $\sigma^{(0)}_{yy} = \sigma^{(0)}_{yy}(x)$ and, therefore, from (6),

$$S^{(0)}_{xy} = -y\frac{\delta}{\mu}\frac{d\sigma^{(0)}_{yy}}{dx} - 2\tau\frac{\delta}{\mu}\int_0^y \frac{\partial S^{(0)}_{xx}}{\partial x}(x,\xi)\,d\xi. \tag{12}$$

Applying the boundary conditions on the shear stress at the rolls (11b), we obtain a differential equation for $\sigma^{(0)}_{yy}$ on each side of the neutral point $x = x_N$, namely

$$\frac{d\sigma^{(0)}_{yy}}{dx} \mp \frac{\mu}{\delta}\frac{\sigma^{(0)}_{yy}}{h(x)} = -\frac{2\tau}{h(x)}\left[\frac{dh}{dx}S^{(0)}_{xx}(x, h(x)) + \int_0^{h(x)}\frac{\partial S^{(0)}_{xx}}{\partial x}\,dy\right] = -\frac{2\tau}{h(x)}\frac{d}{dx}\left[\int_0^{h(x)} S^{(0)}_{xx}\,dy\right]. \tag{13}$$

Observing that the maximum value of σ^*_{yy} occurs at $x^* = x^*_N$, we apply the condition that $\sigma_{yy} = -1$ at the neutral point x_N and we find

$$\sigma^{(0)}_{yy}(x) = \exp\left(-\frac{\mu}{\delta}\int_x^{x_N}\frac{d\eta}{h(\eta)}\right)\left\{-1 + 2\tau\int_x^{x_N} d\zeta\,\frac{\exp\left(\frac{\mu}{\delta}\int_\zeta^{x_N}\frac{d\eta}{h(\eta)}\right)}{h(\zeta)}\,\frac{d}{d\zeta}\left[\int_0^{h(\zeta)} S^{(0)}_{xx}(\zeta,\xi)\,d\xi\right]\right\} \tag{14a}$$

for $x \le x_N$ and

$$\sigma^{(0)}_{yy}(x) = \exp\left(-\frac{\mu}{\delta}\int_{x_N}^{x}\frac{d\eta}{h(\eta)}\right)\left\{-1 - 2\tau\int_{x_N}^{x} d\zeta\,\frac{\exp\left(\frac{\mu}{\delta}\int_{x_N}^{\zeta}\frac{d\eta}{h(\eta)}\right)}{h(\zeta)}\,\frac{d}{d\zeta}\left[\int_0^{h(\zeta)} S^{(0)}_{xx}(\zeta,\xi)\,d\xi\right]\right\} \tag{14b}$$

for $x \ge x_N$. From equations (12) and (13), we obtain,

$$S^{(0)}_{xy} = \mp\frac{y}{h(x)}\sigma^{(0)}_{yy} + 2\tau\frac{\delta}{\mu}\left\{\frac{y}{h(x)}\frac{d}{dx}\left[\int_0^{h(x)} S^{(0)}_{xx}(x,\xi)\,d\xi\right] - \int_0^y \frac{\partial S^{(0)}_{xx}}{\partial x}(x,\xi)\,d\xi\right\} \tag{15}$$

where the upper sign applies to the entry side, i.e., ahead of the neutral point. The second term in (15) has not previously appeared in the literature and represents a nonlinear effect within the shear stress due to transverse variations within the flow. Note that if $S^{(0)}_{xx}$ does not vary in the transverse direction, as in homogeneous compression, then (15) would yield a shear stress which varies linearly in the y-direction, viz., $S^{(0)}_{xy} = y/h(x)\,[\mp\sigma^{(0)}_{yy} + 2\tau\,\delta/\mu\,S^{(0)}_{xx}\,dh/dx]$. We will find later, however, that the integral terms in (15) have only a modest ef-

Downloaded 03 May 2010 to 171.66.16.31. Redistribution subject to ASME license or copyright; see http://www.asme.org/terms/Terms_Use.cfm

fect on inhomogeneous deformation from the assumed situation of $S_{xy}^{(0)} \approx \mp\, y/h(x)\ \sigma_{yy}^{(0)}$, typical of all previous analyses. We retain these terms because they represent the first manifestations of inhomogeneous compression and at this point we assume that $\tau\delta/\mu \leq 0(1)$.

We now simplify the flow condition by first noting from (4*a*) that $\lambda^{(1)} = 1/S_{xx}^{(0)}\ du^{(0)}/dx$, and then inserting this along with $\lambda^{(0)} = 0$ into the flow rule (10), we obtain,

$$S_{xx}^{(0)^2} + \left(\frac{\mu}{\tau}\, S_{xy}^{(0)}\right)^2 = \frac{1}{3}\left\{1 + \frac{2}{\sqrt{3}}\, B \int_0^t \frac{du^{(0)}}{dx}\left[1 + \left(\frac{\mu}{\tau}\,\frac{S_{xy}^{(0)}}{S_{xx}^{(0)}}\right)^2\right]^{1/2} dt\right\}^{2n}.$$

Changing integration variables using the pathline of a material particle $s = s(t)$ whereby

$$\frac{ds}{dt} = \left[\left(\frac{dx}{dt}\right)^2 + \left(\delta\,\frac{dy}{dt}\right)^2\right]^{1/2} \quad \text{or} \quad \frac{ds}{dt} \approx \frac{dx}{dt} = u^{(0)},$$

$$\text{gives } S_{xx}^{(0)^2} + \left(\frac{\mu}{\tau}\, S_{xy}^{(0)}\right)^2 = \frac{1}{3}\left\{1 + \frac{2}{\sqrt{3}}\, B \int_0^x \frac{dlnu^{(0)}}{dx}\left[1 + \left(\frac{\mu}{\tau}\,\frac{S_{xy}^{(0)}}{S_{xx}^{(0)}}\right)^2\right]^{1/2} dx\right\}^{2n}. \tag{16}$$

which is to be evaluated along the curves $dy/dx \simeq -\, v^{(0)}/u^{(0)}$ or $\xi = y/h(x) =$ constant. The term $(\mu/\tau\ S_{xy}^{(0)}/S_{xx}^{(0)})^2$ under the radical sign represents the hardening due to the shear strain rate, i.e., the inhomogeneous deformation. In fact, if one were to look at the $0(\delta)$ contribution to the velocity, one would find that $\partial u^{(1)}/\partial y = 2\,\mu/\tau\ S_{xy}^{(0)}/S_{xx}^{(0)}\ du^{(0)}/dx$, and that this term appearing under the radical is actually the first manifestation of transverse hardening due to shear strain rate. Note also that μ/τ, the significance of which shall be examined later, is equal to $\mu\,|\sigma_{yy}^{*}|_{\max}/\sigma_o$, which is a measure of the shear stress relative to the yield stress. To help clarify this investigation from those previous to this, we study in the following section how the theory of Orowan will fall out automatically from our current development under his assumptions.

The flow rule expression has an interesting feature embedded within it. We can write (16) as

$$\frac{dY^{\left(\frac{1}{n}-1\right)}}{dx} = \frac{2(1-n)}{\sqrt{3}^{1+1/n}}\, B\, \frac{dlnu^{(0)}/dx}{S_{xx}^{(0)}} \tag{17a}$$

where

$$Y = Y^{(0)}(x,\xi) = \left\{S_{xx}^{(0)^2} + \left(\frac{\mu}{\tau}\, S_{xy}^{(0)}\right)^2\right\}^{1/2}. \tag{17b}$$

Note that when $S_{xx}^{(0)} = 0$, i.e., the stress being yielded wholly in shear, the flow stress Y experiences an infinite derivative which is unsatisfactory since it would result in an infinite yield stress. The only exception to this would be if $S_{xx}^{(0)}$ vanished at only one point and was in fact an integrable singularity in (16) or (17*a*).

So, we see that equations (14), (15), and (16) (or (17)) represent a set of triply coupled equations in $\sigma_{yy}^{(0)}$, $S_{xy}^{(0)}$ and $S_{xx}^{(0)}$. We solve these equations via an iterative process started by assuming that $S_{xy}^{(0)} \approx -\,(y/h(x))\ \exp\,(-(\mu/\delta)\int_x^{x_N} d\eta/h(\eta))$ for $x < x_N$ and $S_{xy}^{(0)} \approx y/h(x)\ \exp\,(-(\mu/\delta)\int_{x_N}^{x} d\eta/h(\eta))$ for $x > x_N$. Solving (17*a*) using a fourth order Runge-Kutta scheme enables us to march downstream from $x = 0$ to $x = x_N$ (and onward to the exit $x = 1$) to obtain values of the yield stress and, hence, values of $S_{xx}^{(0)}$ for the first iteration pass. These values of $S_{xx}^{(0)}$ are then inserted into equation (14) and then (15) and in turn into the Runge-Kutta scheme of equation (17*a*) to obtain the next iteration values of the yield or flow stress. Using these flow stresses and the shear stresses from (15), we use (17*b*) to get the new values of $S_{xx}^{(0)}$. We continue this process utilizing relaxation parameters on $S_{xy}^{(0)}$ and $S_{xx}^{(0)}$ until the residuals of the dimensional stresses divided by the dimensional flow stress are less than 10^{-3}.

There are limitations to this theory, the thin strip assumption notwithstanding. Note from equations (4*a*) and (4*c*) that we could factor out the λ term by writing them together as

$$2\,\frac{\delta}{\tau}\,\frac{S_{xy}}{S_{xx}}\,\frac{\partial u}{\partial x} = \frac{\partial u}{\partial y} + \delta\,\frac{\partial v}{\partial x}. \tag{18}$$

We would find that, to order δ, the correction to $u^{(0)}(x)$ is given by

$$\delta u^{(1)}(x,y) = 2\delta\,\frac{\mu}{\tau}\,\frac{du^{(0)}}{dx}\int_0^y \frac{S_{xy}^{(0)}(x,\xi)}{S_{xx}^{(0)}(x,\xi)}\, d\xi. \tag{19}$$

This can give us some indication of when the analysis is no longer valid, viz., if $\delta u^{(1)}(x,y)$ becomes of the same order as $u^{(0)}(x)$. Our previous asymptotic analysis assumed that $S_{xx} = 0(1)$ to leading order, but if S_{xx} were small, say $0(\delta)$, then our analysis breaks down, implying that the full governing equations would have to be dealt with. This would necessitate implementation of the finite element method on the full governing equations. We suspect that for large values of μ (e.g., $\mu = .4$) this situation would be predominant and, hence, our theory is not likely usable. However, it should be feasible to use the FEM on the full problem along with the friction boundary condition. We shall henceforth consider those cases where $S_{xx} = 0(1)$ and compare our results with typical cases studied in the literature.

A Comparison to the Orowan Theory

When a systematic comparison is made of the current asymptotic theory to the Orowan inhomogeneous deformation theory (for small ϕ), one finds that, although the ordinary differential equation for the roll pressures would be equivalent, the expressions for the deviatoric stresses would be quite different. More precisely, when one takes Orowan's equation for the horizontal force f (see Orowan (1943) p. 150), namely

$$\frac{df}{d\phi} = 2\mathrm{Rs}\,\cos\phi\,(\tan\phi \pm \mu) \tag{20}$$

and subsequently converts this into current asymptotic variables (using $f \equiv -\int_{-\hat{h}(\hat{x})}^{\hat{h}(\hat{x})} \hat{\sigma}_{xx}\, d\hat{y}$, $R\sin\phi \equiv \Delta x - \hat{x}$, $h(\phi) \equiv 2\hat{h}(\hat{x})$ and $s \cong -\hat{\sigma}_{yy}$, one finds that equation (13) is recovered. However, when one converts Orowan's $f(\phi)$ for slipping, viz.,

$$f(\phi) = h\left[s\left\{1 \pm \mu\left(\frac{1}{\phi} - \frac{1}{\tan\phi}\right)\right\} - kw\right] \tag{21}$$

(where $k = k(\phi)$ is the yield stress in homogeneous compression and

$$w(\phi,a) = \frac{1}{\sin\phi}\int_0^{\phi} \sqrt{1 - a^2\left(\frac{\theta}{\phi}\right)^2}\,\cos\theta\ d\theta,\ a = \frac{\mu s}{k/2}\Big),$$

to the equivalent nondimensional asymptotic horizontal force, $-\int_{-h(x)}^{h(x)} \sigma_{xx} dy$, one would find that Orowan had employed deviatoric stresses of the form

$$S_{xx}^{(0)} = \sqrt{k^2 - \left(\frac{\mu\sigma_{yy}^{(0)}}{\tau}\right)^2\left(\frac{y}{h(x)}\right)^2} \tag{22}$$

and

$$S_{xy}^{(0)} = \mp\,\frac{y}{h(x)}\,\sigma_{yy}^{(0)}, \tag{23}$$

with a yield stress $k(x)$. Furthermore, the asymptotic theory

Downloaded 03 May 2010 to 171.66.16.31. Redistribution subject to ASME license or copyright; see http://www.asme.org/terms/Terms_Use.cfm

would show directly that the contribution to the horizontal force of the shear in (21), $\pm h\mu s\ (1/\phi - 1/\tan\phi) \cong 1/3\ \phi$ (for small ϕ), is actually $0(\delta)$ and should be neglected. Lastly, the asymptotic equivalent to Orowan's inhomogeneity function $w(\phi, a)$, which is $1/hk \int_{-h(x)}^{h(x)} S_{xx}^{(0)}(x, \xi)d\xi$, has no x (or ϕ) dependence and can, by use of (22), be written in closed form as

$$w(a) = \sqrt{1-a^{*2}} + \frac{1}{a^*} \sin^{-1} a^*, \quad a^* = \frac{\mu\sigma_{yy}^{(0)}}{\tau k(x)}.$$

The curve of this function falls upon Orowan's curve exactly.

In summary, one can conclude that Orowan's theory shares the same ODE for the roll pressure as the asymptotic theory, but the deviatoric stresses are fundamentally different. Orowan assumed a shear term linear in $y/h(x)$, viz., $S_{xy}^{(0)} \sim y/h(x)\ \sigma_{yy}^{(0)}$, whereas the systematic asymptotic analysis gave an additional nonlinear term (bracketed in (15)) as well. Likewise, Orowan had assumed a simple homogeneous compression flow rule (with no transverse hardening), but the current scheme automatically incorporates transverse hardening through the $(\mu/\tau\ S_{xy}^{(0)}/S_{xx}^{(0)})^2$ term under the radical in (16). For a more complete comparison of the two theories, refer to Smet (1988).

Results and Discussion

We wish to make comparisons of our theory with that of Orowan as implemented by Venter et al. (1980a). To make these comparisons, a computer code representing Venter-Abd-Rabbo (VA) results was written separately apart from the Smet-Johnson (SJ) code which has been described earlier. We shall find that since the present approach prescribes the maximum roll pressure (i.e., through τ) as an input parameter, the roll pressures we obtain will coincide closely with those of Venter and Abd-Rabbo. However, the increase in work hardening will show up within the deviatoric stresses and hence manifest itself in the front and back tensions as well as the torque. So, essentially we have worked the problem so as to produce a nearly identical roll pressure as Venter and then find the corresponding tensions that produce that pressure. Although the longitudinal stress $S_{xx}^{(0)}$ varies transversely by virtue of the inhomogeneous deformation, its effect on the roll pressure, through the $d/dx \int_0^{h(x)} S_{xx}^{(0)}\, d\xi$ term in (14), becomes minor overall in relation to that of Venter's roll pressure.

We study parameter regimes of varied μ, τ and δ for the materials soft copper and steel. Table 1 gives the material and input/output parameters for the two cases we had studied. In case (*i*), for soft copper, the values of μ and τ have been chosen so as to show the effect of the $\mu\ S_{xy}^{(0)}/\tau S_{xx}^{(0)}$ term in the flow rule equation (16) and enables us to observe the difference this makes in relation to homogeneous compression. This amounts to taking μ sufficiently large so as to produce considerable shear. The other input parameters were taken directly from Venter's paper. In case (*ii*), for steel, we have selected the input parameters (i.e., μ, τ, x_N, R, h_{ent} and h_{exit}) to illustrate features of the nonlinear shear stress inhomogeneity in (15), i.e., the integral terms. The output parameters which we show an interest in, outside of the roll pressure and roll stresses, are the maximum value of $\delta u^{(1)}/u^{(0)}$ within the flow field (recall that this indicates breakdown of the theory), and the front and back tensions (T_f^*, T_b^*) and roll torque. The front and back tensions are given by

$$\frac{T^*}{\Delta h\,|\sigma_{yy}^*|_{\max}} = 2\int_0^{h(x)} \sigma_{xx}^{(0)} dy = 2\left[\sigma_{yy}^{(0)}(x)h(x) + 2\tau\int_0^{h(x)} S_{xx}^{(0)}(x,\xi)d\xi\right]$$

where $T^* = T_b^*$ at $x^* = 0$, $T^* = T_f^*$ at $x^* = \Delta x$ and the torque by

Table 1 Material and input/output parameters to stress equations

	Case (*i*)	Case (*ii*)
Material:	Soft copper	Steel
Materials parameters[a]:		
n	.23	.295
B	727.651	16.65
σ_o(MN/m^2)	85.46	324.24
Input parameters:		
μ	.215	.25
τ	.098	.15
x_N	.592	.80
h_{ent}(mm)	1.27	5.08
h_{exit}(mm)	.762	.341
R (m)	.1778	.0650
Output parameters:		
C_1	1.50	.072
C	.9986	.964
δ	.038	.194
	SJ[†]/VA[††]	SJ/VA
T_b^*(MN/m^2)	71.02/61.76	47.09/41.22
T_f^*(MN/m^2)	186.52/178.49	1166.36/1162.34
G^*(KNm/m)	25.61/26.80	183.74/184.13
$(\delta u^{(1)}/u^{(0)})_{\max}$, percent	7.44/5.96	1.22/16.89

[a]The material parameters for soft copper were taken from Venter et al. (1980a) and those for steel from Li and Kobayashi (1982).
[†]Smet-Johnson
[††]Venter-Abd-Rabbo

$$G^* = R\Delta x\,|\sigma_{yy}^*|_{\max}\left\{\int_0^{x_N} \mu S_{xy}^{(0)} dx + \int_{x_N}^1 \mu S_{xy}^{(0)} dx\right\}.$$

In examining soft copper in case (*i*), we took $\mu = .215$ and $\tau = .098$, which is the upper limit of μ and lower limit of τ before which $S_{xx}^{(0)}$ becomes vanishingly small at $x = x_N$. Figures 2(*a*)–(*d*) demonstrate the comparison of our theory to that of Venter et al. In Fig. 2(*a*) we see that the roll pressures for both theories are virtually the same, differing by roughly one percent at entrance and exit. Because of the transverse variation of $S_{xx}^{(0)}$, $S_{xy}^{(0)}$ and $Y^{(0)}$ (see Figs. 2(*b*)–2(*d*)), the back tension differs by 15.0 percent and the front tension by about 4.5 percent from those of Venter. Likewise, the roll torque changes by 4.5 percent between the two theories. We see that these variations in the tensions and the torque can be attributed strongly to the hardening due to shear in the flow rule and to a much lesser degree to the nonlinear effect upon the shear stress itself. We can see this for case (*i*) by examining the $0(\mu/\tau)$ term in (16) in relation to the $0(\tau\,\delta/\mu)$ term in (15). The $0(\mu/\tau)$ term is a measure of the effect of the $(\mu\ S_{xy}^{(0)}/\tau\ S_{xx}^{(0)})$ term in the flow rule and the $0(\tau\delta/\mu)$ term measures the effect of the nonlinear term in the shear stress. Since $\mu/\tau = 2.19$ and $\tau\,\delta/\mu = .017$, we can obviously assert that any inhomogeneity will virtually all be due to a transverse variation in strain hardening.

Whereas Venter and Abd-Rabbo model the effect of inhomogeneous deformation by an ad hoc change of the strain hardening exponent within the flow condition, we find that this comes about systematically within our theory by the $\mu/\tau\ S_{xy}^{(0)}/S_{xx}^{(0)}$ term in (16). Figure 2(*d*) shows the yield stress at the wall for our theory as well as the Orowan yield stress which does not vary in the transverse direction and coincides with the yield stress predicted by the present theory along the centerline. The yield stress for our theory varies between the two curves within the transverse direction because of the increase in hardening from the centerline to the wall. Note that the largest deviation occurs beyond the neutral point due to the nature of the $1/S_{xx}^{(0)}$ term in (17*a*) and the subsequent behavior of $S_{xx}^{(0)}$ at the wall.

For case (*ii*) of steel, the values of μ, τ, and δ were chosen to exhibit significant shear effect for a relatively large reduction, e.g., a value of $\delta \sim .2$. After examining Figs. 3(*a*)–(*d*), the roll

Downloaded 03 May 2010 to 171.66.16.31. Redistribution subject to ASME license or copyright; see http://www.asme.org/terms/Terms_Use.cfm

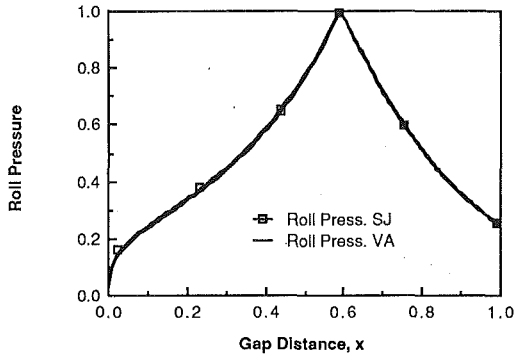


Fig. 2(*a*) Graphs of roll pressure $-\sigma_{yy}^{(0)}$ as a function of the gap distance x for the theories of Smet-Johnson (SJ) and Venter Abd-Rabbo (VA)

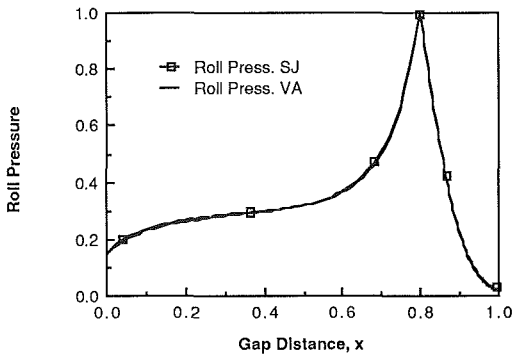


Fig. 3(*a*) Graphs of roll pressure $-\sigma_{yy}^{(0)}$ as a function of x

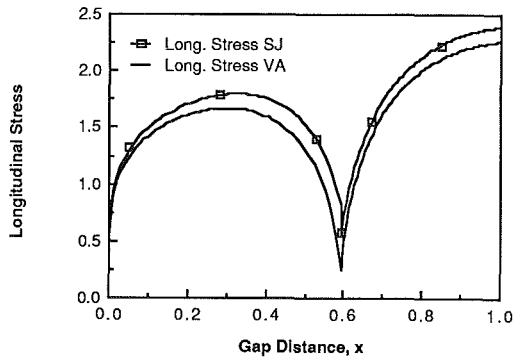


Fig. 2(*b*) Graphs of $S_{xx}^{(0)}$ at $y = h(x)$ as a function of the gap distance x for both theories

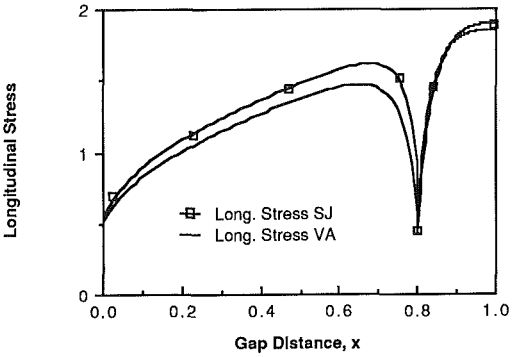


Fig. 3(*b*) Graphs of $S_{xx}^{(0)}$ at $y = h(x)$ as a function of x

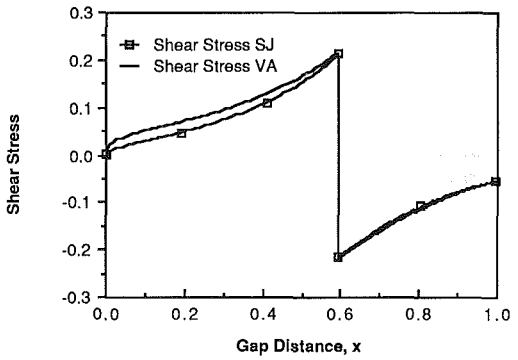


Fig. 2(*c*) Graphs of $S_{xy}^{(0)}$ at $y = h(x)$ as a function of the gap distance x for both theories

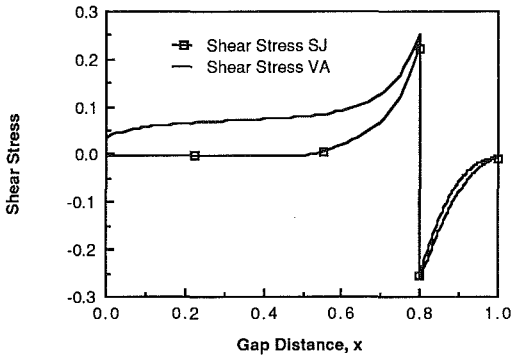


Fig. 3(*c*) Graphs of $S_{xy}^{(0)}$ at $y = h(x)$ as a function of x

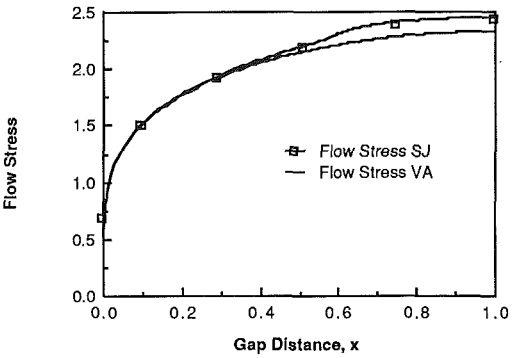


Fig. 2(*d*) Graphs of $Y^{(0)}(x, \xi) = \sqrt{S_{xx}^{(0)2} + \left(\frac{\mu}{\tau} S_{xy}^{(0)}\right)^2}$

at $\xi = y/h(x) = 1$ for both theories. Note that $Y^{(0)}$ for VA is the same at all y locations and at the centerline, $y = 0$, $Y^{(0)}$ for SJ is the same as the VA result.

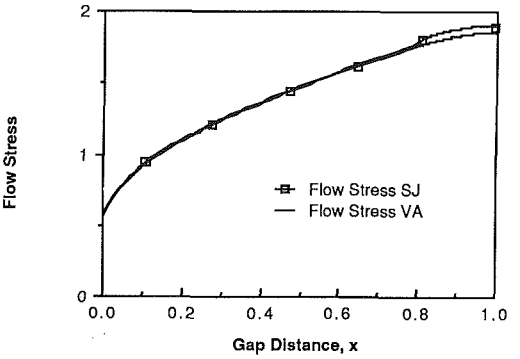


Fig. 3(*d*) Graphs of $Y^{(0)} = \sqrt{S_{xx}^{(0)2} + \left(\frac{\mu}{\tau} S_{xy}^{(0)}\right)^2}$

at $\xi = y/h(x) = 1$ for both theories

Downloaded 03 May 2010 to 171.66.16.31. Redistribution subject to ASME license or copyright; see http://www.asme.org/terms/Terms_Use.cfm

pressures for the two theories are the same, but note the acute peak at the neutral plane, evidence of nonuniform behavior. That is, the perturbation scheme begins to break down in a small neighborhood of the neutral plane. Also from Fig. 3(*b*) observe for $S_{xx}^{(0)}$ at the wall, the same type of behavior near the neutral point. Although the yield stress at the wall is virtually that for homogeneous compression (see Fig. 3(*d*)), notice in Fig. 3(*c*) that the shear stresses for the two theories are quite different. This is a case where $\mu/\tau = 1.7$ and $\tau\,\delta/\mu = .12$. This latter value is large enough to provide a demonstration of the nonlinear effect upon the shear stress in equation (15). However, because $\mu/\tau = 1.7$ we see that this effect, in regard to the roll pressure and yield stress, is virtually masked by the still more prominent transverse variation in strain hardening. There is a 14.2 percent difference in the back tension no doubt due to this latter effect. We see that for larger values of δ a significant shear effect will occur although the yield stress may not deviate greatly from homogeneous compression.

It should be stressed that as μ increases and τ decreases the value of $S_{xx}^{(0)}$ at both the wall and neutral plane goes to zero with a derivative approaching $\pm\infty$ at each side of $x = x_N$. This indicates the region where the theory begins to break down, as shown by equation (18), because u will no longer be just a function of x alone to leading order. Hence, plane sections no longer remain plane. For case (*i*) this occurs at values of $\mu \geq .215$ and $\tau \leq .098$. Thus, the theory of Orowan and implemented by Venter is no longer valid beyond this point. Consequently the case $\mu = .3$ considered by Venter is rendered questionable since the full governing equations should then have to be solved throughout the whole flow field.

Venter et al. believing that inhomogeneous deformation would be manifested, have concluded that the very close agreement for the roll pressure between their work and that of Alexander for the case of $\mu = .07$ was due to the particular choice of input parameters. We find, however, that to reproduce that roll pressure we would require $\tau = .28$ (recall $\tau = \sigma_o/|\sigma_{yy}^*|_{\max}$) and thus $\mu/\tau = .25$. Likewise, $\tau\,\delta/\mu = .15$, so with (15) and (16) as a guide we see that although there may be some inhomogeneous deformation due to transverse variation, its overall effect on the hardening is not significant because μ/τ is rather small. Hence, this is simply a case of homogeneous compression thus making the effect of shear, which is linear in y in this case, insignificant.

Summary

We can say that although our theory may predict roll pressures no different than for Venter's theory, due to appropriate inclusion of inhomogeneous deformation, the front and back tensions may differ by up to 10–20 percent depending upon the material and input parameters. This results from increased hardening of the material in the transverse direction. There are also cases of larger δ whereby the nonlinear effect on the shear stress increases. Although two types of inhomogeneous effects may arise, the more prominent effect will be that due to the increase in strain hardening, usually at small δ. We can see this by examining the magnitude of the $0(\mu/\tau)$ term in (16) and the $0(\tau\,\delta/\mu)$ term in (15). If μ/τ is small and $\delta \ll \mu/\tau$ then very little overall inhomogeneous deformation will arise. When $\mu/\tau = 0(1)$, then strain hardening effects will be more predominant than any nonlinear effects in the shear stress, since $\tau\,\delta/\mu = 0(\delta)$. If one's primary purpose is to calculate the degree of hardening and the roll pressure but not necessarily to predict the shear stress then it is our belief that one should only keep the $0(\mu/\tau)$ term in the flow rule and neglect the $0(\tau\,\delta/\mu)$ term in the shear stress. This is because the effect of the $0(\tau\,\delta/\mu)$ term in the shear stress upon work hardening is weak.

We also assert that the use of the boundary condition which assumes that the material is yielded fully in shear, i.e., $\mathbf{t}\cdot\boldsymbol{\lambda} = k$ at $y = \pm h(x)$ in slab analysis is not usable in our theory since when $S_{xx}^{(0)}$ nears zero, the full governing equations must be solved, still using the boundary condition of $\mathbf{t}\cdot\boldsymbol{\lambda} = \mp\mu(\mathbf{t}\cdot\mathbf{n})$. We have determined that results obtained from slab analysis for moderate values of μ, say $\mu = 0.3$, which rely on this ad hoc boundary condition change are of questionable validity.

Acknowledgments

This work was sponsored in part by a grant from the National Science Foundation (NSF MSM 85-13795). We would also like to acknowledge the helpful comments of Robert M. McMeeking during the early stages of this work.

References

Alexander, J. M., 1972, "On the theory of rolling," *Proceedings of the Royal Society of London*, Vol. A326, pp. 535–563.

Bland, D. R., and Ford, H., 1948, "The calculation of roll force and torque in cold strip rolling with tensions," *Proceedings of the Institution of Mechanical Engineers*, Vol. 159, pp. 144–163.

Ford, H., 1957, "The theory of rolling," *Metallurgical Reviews*, Vol. 2, pp. 1–28.

Ford, H., and Alexander, J. M., 1964, "Simplified Hot-Rolling Calculations," *Journal of the Institute of Metals*, Vol. 92, pp. 397–404.

Johnson, R. E., 1987, "Conical extrusion of a work-hardening material: an asymptotic analysis," *J. Eng. Math.*, Vol. 21, pp. 295–329.

Johnson, R. E., 1984, "Power-law creep of a material being compressed between parallel plates: a singular perturbation problem," *Journal of Engineering Mathematics*, Vol. 18, pp. 105–117.

Johnson, R. E., and McMeeking, R. M., 1984, "Near-surface flow in glaciers obeying Glen's law," *Quarterly Journal of Mechanics and Applied Mathematics*, Vol. 37, Part 2, pp. 273–291.

Karman, T. von, 1925, "Beitrag zur Theorie des Walzvorganges," *Zeitschrift für Angewandte Mathematik und Mechanik*, Vol. 5, pp. 139–141.

Li, G. J., and Kobayashi, S., 1982, "Rigid-Plastic Finite-Element Analysis of Plane Strain Rolling," *Journal of Engineering for Industry*, Vol. 104, pp. 55–64.

Orowan, E., 1943, "The calculation of Roll Pressure in Hot and Cold Flat Rolling," *Proceedings of the Institution of Mechanical Engineers*, Vol. 150, pp. 140–167.

Siebel, E., 1924, "Berichte des Walzwerkausschusses," *Verein deutscher Eisenhüttenleute*, No. 37.

Sims, R. B., 1954, "The Calculation of Roll Force and Torque in Hot Rolling Mills," *Proceedings of the Institution of Mechanical Engineers of London*, Vol. 168, pp. 191–214.

Smet, R. P., 1988, "The Asymptotic Analysis of Cold Rolling with Inhomogeneous Deformation," Ph.D. Thesis, University of Illinois.

Venter, R., and Abd-Rabbo, A., 1980, "Modelling of the rolling process – I. Inhomogeneous Deformation Model," *International Journal of Mechanical Sciences*, Vol. 22, pp. 83–92.

Venter, R., and Abd-Rabbo, A., 1980, "Modelling of the rolling process – II. Evaluation of the stress distribution in the rolled material," *International Journal of Mechanical Sciences*, Vol. 22, pp. 93–98.

Downloaded 03 May 2010 to 171.66.16.31. Redistribution subject to ASME license or copyright; see http://www.asme.org/terms/Terms_Use.cfm

Growth of an Infinitesimal Cavity in a Rate-Dependent Solid[1]

Rohan Abeyaratne
Assoc. Mem. ASME

Hang-sheng Hou

Department of Mechanical Engineering,
Massachusetts Institute of Technology,
Cambridge, MA 02139

This study examines the effect of rate dependence on growth of an infinitesimal cavity in a homogeneous, isotropic, incompressible material. Specifically, a sphere containing a traction-free void of infinitesimal initial radius is considered, its outer surface being subjected to a prescribed uniform radial nominal stress p, *which is suddenly applied and then held constant. The sphere is composed of a particular class of rate-dependent materials. The large strains which occur in the vicinity of the void are accounted for in the analysis, and the problem is reduced to a nonlinear initial value problem, which is then studied qualitatively through a phase plane analysis. The principal results of this paper consist of two equations that are derived between the applied stress* p *and the cavity radius* b: $p = \hat{p}(b)$ *and* $p = \bar{p}(b)$. *The first of these describes a curve which separates the* (p, b)*-plane into regions where cavitation does and does not occur. The second describes a curve which further subdivides the former subregion—the post-cavitation region—into domains where void expansion occurs slowly and rapidly.*

1 Introduction

The phenomenon of void growth has been studied extensively in view of the critical role played by internal cavities in the failure of solids, (e.g., Gent and Lindley (1958), Rogers (1960), McClintock (1968), Rice and Tracey (1969), Budiansky et al. (1982)). Recently, Ball (1981, 1982) carried out a bifurcation analysis within the theory of finite elasticity of a *solid* sphere which was subjected to a uniform radial tensile traction on its outer surface. For certain materials, he showed that no matter how large the load, the sphere would simply undergo a homogeneous deformation and expand into a larger solid sphere. However, for other materials, the deformation remains homogeneous only at sufficiently small loads, and at a critical value of load, a second nonhomogeneous deformation bifurcates from the homogeneous one; in this latter deformation, the body contains a traction-free void at its center. As noted by Ball (1982) and Horgan and Abeyaratne (1986), an alternative interpretation for the phenomenon being modeled here is that it describes the growth of a preexisting void of *infinitesimal* initial size. Hill (1950) has examined an equivalent problem for a cavity in an elastic-plastic solid; using a finite strain theory, he shows that the hoop strain at the cavity wall becomes infinite at a finite value of the remotely applied radial tensile load. In any case, a feature of Ball's instability analysis is that it automatically determines the critical load at which "cavitation" occurs without the use of an additional "failure" criterion; consequently, one may view the critical stress at cavitation as being, in some sense, the "ideal dilatational strength" of the material. Certain extensions of this work have been carried out by Horgan and Abeyaratne (1986), Podio-Guidugli et al. (1986), Sivaloganathan (1986), Chung et al. (1987), and Ertan (1987).

It is essential to account for the effects of finite strain in an analysis of cavitation. The corresponding problem in linearized elasticity, or even in the infinitesimal strain theory of plasticity, exhibits no bifurcation of this sort. If one considered a spherical body containing a void of infinitesimal initial size, then according to either of these theories, the void continues to remain infinitesimal no matter how large a radial load is applied to the outer surface of the sphere.

The phenomenon of cavitation may be viewed as an intrinsic material instability, which is intimately related to the constitutive description of the material. In the present investigation, we examine the effect of rate dependence on cavitation. We consider a sphere, composed of an incompressible rate-dependent material, which contains a traction-free infinitesimal void situated at its center. The growth of this void, due to a uniform radial traction which is suddenly applied at the outer surface of the sphere and then held constant, is examined. The effects of inertia are neglected. While other loading histories could equally well be studied, we do not do so in this paper. It should be noted that even though we do not consider a bifurcation problem for a solid sphere in this paper, it will be convenient for us to refer to the phenomenon being studied as cavitation; the equivalence between these two problems has only been established in the rate-independent case.

The constitutive law which will be used here to characterize an incompressible rate-dependent solid is essentially that proposed by Anand (1985), and Anand et al. (1987), for describing the viscoplastic response of metals at high temperature. Within the context of the present problem, it reduces to a single scalar equation which in turn may be viewed as a

[1]The results reported here were obtained in the course of an investigation supported in part by the U.S. Army Research Office.

Contributed by the Applied Mechanics Division for publication in the JOURNAL OF APPLIED MECHANICS.

Discussion on this paper should be addressed to the Editorial Department, ASME, United Engineering Center, 345 East 47th Street, New York, N.Y. 10017, and will be accepted until two months after final publication of the paper itself in the JOURNAL OF APPLIED MECHANICS. Manuscript received by ASME Applied Mechanics Division, October 22, 1987; final revision, March 22, 1988.

Copyright © 1989 by ASME

Downloaded 03 May 2010 to 171.66.16.31. Redistribution subject to ASME license or copyright; see http://www.asme.org/terms/Terms_Use.cfm

generalization of the classical Kelvin-Voigt model for viscous solids. In a particular limit, it specializes to an elastic material while in a second special case we recover a non-Newtonian fluid.

The problem at hand is first reduced to a nonlinear initial value problem for the cavity radius $b(t)$. We then study the qualitative behavior of its solutions by examining its phase plane. First, we determine all equilibrium solutions of the differential equation. In general, we find that corresponding to every value of the applied stress p, $b(t)=0$ is one such state; in addition, for certain materials we find other equilibrium solutions $b(t)=\text{constant}>0$ when the applied stress lies in a suitable range. These latter solutions describe configurations in which the cavity is open. The phase portraits are then used to study the stability of these various configurations. In this manner we are able to decide whether or not the cavity will grow and if it does, to examine the rate at which this happens. Furthermore, we find that for certain materials the void grows without bound while in others, it eventually converges to an equilibrium state in which the cavity remains open.

In the particular limiting case of pure creep, the material behaves like a viscous fluid; $b(t)=0$ is the only equilibrium solution and it is a repeller, irrespective of the value of p. Thus, no matter how small the applied load (>0), the void will grow without bound.

The principal results of this paper consist of two equations that we derive between the applied stress and the cavity radius: $p=\hat{p}(b)$ and $p=\bar{p}(b)$. The first of these describes a curve which separates the (p, b)-plane into regions where cavitation does and does not occur. The second describes a curve which further subdivides the former subregion—the post-cavitation region—into domains where void expansion occurs slowly and rapidly.

In Section 2 we formulate the problem to be addressed, and then in Section 3, reduce it to a problem for the cavity radius. When rate dependency is absent, instead of the differential equation, an algebraic equation is obtained, and this is analyzed in Section 4. The analysis for rate-dependent materials is carried out in Section 5.

2 Preliminaries

Consider a hollow sphere of incompressible material with its center situated at the origin of a spherical coordinate system. The undeformed inner radius of the sphere is taken to be zero, while without loss of generality, the outer radius may be assumed to be unity. It should be emphasized that this is *not* the same as a solid sphere, since we will be imposing a *traction-free* boundary condition at the origin. (One could equivalently consider a hollow sphere with a traction-free internal cavity of radius $B>0$, and at the end of the analysis, let $B\to 0+$, which leads to the same results as those obtained here; a brief discussion of the case $B>0$ is included at the end of Section 5.) Let (R, Θ, Φ) denote the spherical coordinates of a point in the reference undeformed configuration, and (r, θ, ϕ), the corresponding coordinates in the current deformed configuration. Boldface letters represent tensor or vector quantities.

We restrict attention to spherically symmetric motions of the form

$$\begin{cases} r=\hat{r}(R, t), \\ \theta=\Theta, \\ \phi=\Phi, \end{cases} \tag{1}$$

on the time interval $0\le t<\infty$. The deformation gradient tensor corresponding to (1) is

$$\mathbf{F}=\frac{\partial \hat{r}}{\partial R}\,\mathbf{e}_R\otimes\mathbf{e}_R+\frac{\hat{r}}{R}\,(\mathbf{e}_\Theta\otimes\mathbf{e}_\Theta+\mathbf{e}_\Phi\otimes\mathbf{e}_\Phi), \tag{2}$$

where $\mathbf{e}_R$, $\mathbf{e}_\Theta$ and $\mathbf{e}_\Phi$ form an orthonormal basis for the spherical coordinate system. The incompressibility of the material requires the motion to be *isochoric*, so that

$$\frac{\hat{r}^2}{R^2}\,\frac{\partial \hat{r}}{\partial R}=1, \tag{3}$$

which, upon integration, leads to

$$r=\hat{r}(R, t)=(R^3+b^3(t))^{1/3} \qquad \text{for } 0\le R\le 1,\ t\ge 0; \tag{4}$$

since $r\to b$ as $R\to 0$, $b(t)$ denotes the *current cavity radius* and is to be determined. Since the sphere is assumed to be undeformed at the initial instant,

$$b(0)=0. \tag{5}$$

From (1), the velocity field is $\mathbf{v}=\dot{r}(r, t)\mathbf{e}_r\equiv\partial\hat{r}/\partial t\,\mathbf{e}_r$, so that the stretching tensor $\mathbf{D}=1/2(\mathbf{L}+\mathbf{L}^T)$ where $\mathbf{L}=\text{grad}\,\mathbf{v}$, is

$$\mathbf{D}=\frac{\partial \dot{r}}{\partial r}\,\mathbf{e}_r\otimes\mathbf{e}_r+\frac{\dot{r}}{r}\,(\mathbf{e}_\theta\otimes\mathbf{e}_\theta+\mathbf{e}_\phi\otimes\mathbf{e}_\phi). \tag{6}$$

Since, by (4)

$$\dot{r}(r, t)=\frac{b^2\dot{b}}{r^2}, \tag{7}$$

(6) becomes

$$\mathbf{D}=-\frac{2\dot{r}}{r}\,\mathbf{e}_r\otimes\mathbf{e}_r+\frac{\dot{r}}{r}\,(\mathbf{e}_\theta\otimes\mathbf{e}_\theta+\mathbf{e}_\phi\otimes\mathbf{e}_\phi). \tag{8}$$

Next, we define $\dot{\gamma}(r, t)$ by

$$\dot{\gamma}(r, t)=2\sqrt{3}\,\frac{\dot{r}}{r}, \tag{9}$$

so that the principal values of $\mathbf{D}$ are $\dot{\delta}_1=-\dot{\gamma}/\sqrt{3}$, $\dot{\delta}_2=\dot{\delta}_3=\dot{\gamma}/2\sqrt{3}$, and $|\dot{\gamma}|=\sqrt{2\mathbf{D}\cdot\mathbf{D}}$. If $V(t)=4/3\,\pi b^3$ denotes the current volume of the cavity, then the rate of volume change is

$$\frac{\dot{V}}{V}=\frac{\sqrt{3}}{2}\,\dot{\gamma}(b, t)=\frac{3\dot{b}}{b} \text{ provided } b>0. \tag{10}$$

Integrating (9) with the help of (7) and (4), and taking γ to vanish when $\hat{r}=R$, yields

$$\gamma=\int_0^t\dot{\gamma}(\hat{r}(R, \xi), \xi)\,d\xi=2\sqrt{3}\int_0^t\frac{b^2(\xi)\dot{b}(\xi)}{R^3+b^3(\xi)}\,d\xi$$

$$=2\sqrt{3}\ln\frac{r}{R}. \tag{11}$$

If the sphere is composed of an isotropic material, then by symmetry, the Cauchy stress tensor τ must have the form

$$\tau(r, t)=\tau_r(r, t)\mathbf{e}_r\otimes\mathbf{e}_r+\tau_\theta(r, t)\,(\mathbf{e}_\theta\otimes\mathbf{e}_\theta+\mathbf{e}_\phi\otimes\mathbf{e}_\phi). \tag{12}$$

Thus, the deviator of the Cauchy stress tensor, $\mathbf{S}=\tau-(1/3\,tr\tau)\mathbf{I}$, is

$$\mathbf{S}=\frac{-2\tau}{\sqrt{3}}\,\mathbf{e}_r\otimes\mathbf{e}_r+\frac{\tau}{\sqrt{3}}\,(\mathbf{e}_\theta\otimes\mathbf{e}_\theta+\mathbf{e}_\phi\otimes\mathbf{e}_\phi) \quad \text{where } \tau=\frac{1}{\sqrt{3}}\,(\tau_\theta-\tau_r). \tag{13}$$

Observe that $|\tau|=\sqrt{1/2\mathbf{S}\cdot\mathbf{S}}$.

In the absence of body force, the equation of equilibrium $div\,\tau=0$ during a quasistatic motion of the form (1) reduces, in view of (12), $(13)_2$, to

$$\frac{\partial \tau_r}{\partial r}-\frac{2}{r}\sqrt{3}\tau=0 \qquad \text{for } b<r<a,\ t\ge 0; \tag{14}$$

$a(t)$ is the current outer radius of the sphere, which by (4), is

$$a(t)=(1+b^3(t))^{1/3}. \tag{15}$$

Suppose that the outer surface of the sphere is subjected to a uniform *nominal* radial tensile stress $p(t)\,(\ge 0)$ and that the interior cavity surface is *traction-free*. Then

Downloaded 03 May 2010 to 171.66.16.31. Redistribution subject to ASME license or copyright; see http://www.asme.org/terms/Terms_Use.cfm

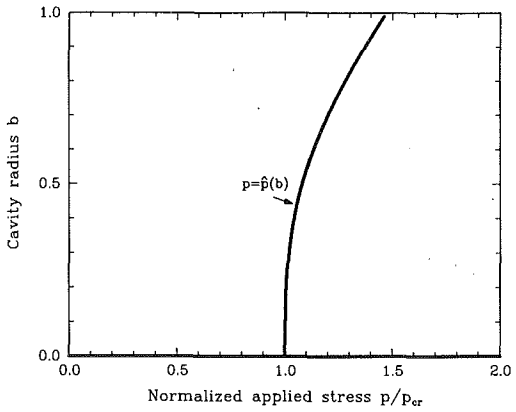


Fig. 1 Schematic graph of cavity size versus applied stress for a rate-independent material

$$\tau_r(a, t) = \frac{p(t)}{a^2}, \quad \tau_r(b, t) = 0 \quad \text{for } t \geq 0. \tag{16}$$

Finally we turn to the *constitutive description* of the incompressible rate-dependent material at hand. In view of incompressibility, it is only the deviatoric part of the Cauchy stress that is determined by the motion. We assume that

$$\mathbf{S} = \lambda \mathbf{D}, \tag{17}$$

where $\lambda = \lambda(\dot{\delta}_1, \dot{\delta}_2, \dot{\delta}_3, \delta_1, \delta_2, \delta_3)$ is a function determined by the material; the $\dot{\delta}_i$'s are the principal values of $\mathbf{D}$, and are the material time derivatives of the δ_i's. A general discussion of constitutive relations of this form may be found in Anand (1985), (see also Anand et al. (1987)). The specific form (17) is a slight generalization of the isothermal version of the viscoplastic law proposed by him for metals at high temperature.

By (8), and (9), in the present problem, $2\dot{\delta}_2 = 2\dot{\delta}_3 = -\dot{\delta}_1 = \dot{\gamma}/\sqrt{3}$ and $2\delta_2 = 2\delta_3 = -\delta_1 = \gamma/\sqrt{3}$. Therefore, it is convenient to define a function $g(\dot{\gamma}, \gamma)$ for all $\dot{\gamma}$ and γ by

$$g(\dot{\gamma}, \gamma) = \frac{\dot{\gamma}}{2} \lambda\left(-\frac{\dot{\gamma}}{\sqrt{3}}, \frac{\dot{\gamma}}{2\sqrt{3}}, \frac{\dot{\gamma}}{2\sqrt{3}}, -\frac{\gamma}{\sqrt{3}}, \frac{\gamma}{2\sqrt{3}}, \frac{\gamma}{2\sqrt{3}}\right). \tag{18}$$

Then, in view of $(13)_1$, (8), and (9), the constitutive law (17) in the context of the present problem, is equivalent to the single scalar equation

$$\tau = g(\dot{\gamma}, \gamma), \tag{19}$$

where τ, γ, and $\dot{\gamma}$ are given by $(13)_2$, (11), and (9), respectively. In the special case $g = g(\gamma)$, the response of the sphere according to (19) is rate-independent; for $g = g(\dot{\gamma})$ it behaves like a non-Newtonian fluid.

In this paper we restrict attention to a particular subclass of the materials (17); for these materials g has the form

$$g(\dot{\gamma}, \gamma) = g_1(\gamma) + \text{sgn}(\dot{\gamma})\, |\dot{\gamma}|^m g_2(\gamma), \quad g_1(0) = 0, \; g_2(\gamma) \geq 0, \; m > 0, \tag{20}$$

where g_1 and g_2 are arbitrary constitutive functions and the strain rate exponent m is strictly positive. The response of the sphere according to (19) is rate-independent if we take $g_2(\gamma)$ to be zero. In particular, if $g_1(\gamma) = \mu\gamma^n$, $g_2 = 0$, (20) specializes to the rate-independent, pure power law form

$$g(\dot{\gamma}, \gamma) = \mu\gamma^n. \tag{21}$$

(It should be emphasized that the constitutive law (17) with $\lambda = \lambda(\delta_1, \delta_2, \delta_3)$ does not, in general, lead to rate-independent response even though it does so for deformations of the type encountered here.) Next, when $g_1(\gamma) = \mu\gamma$, $g_2(\gamma) = \eta = \text{constant}$ and $m = 1$, (20) is of the so-called Kelvin-Voigt form. If $g_1 \equiv 0$

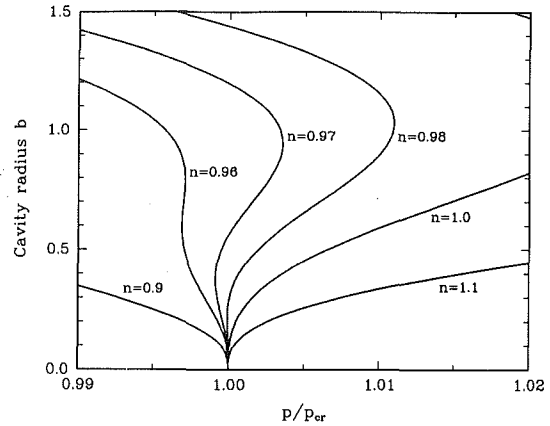


Fig. 2 Post-cavitation behavior for rate-independent power law materials showing different turning directions

we say that the material exhibits *pure creep*; in particular, when $g_1(\gamma) = 0$, $g_2(\gamma) = \mu\gamma^n$, (20) takes the power-law form

$$g(\dot{\gamma}, \gamma) = \mu\dot{\gamma}^m\gamma^n. \tag{22}$$

Constitutive relations of the form (22) have been used in studies on viscoplasticity, e.g., Shawki et al. (1983), Wright (1987), and Anand et al. (1987). For example, based on their experimental results, Klopp et al. (1985) have suggested that the mechanical response of aluminum at a temperature of 295° K can be described by (22), with μ, n, and m taken to be 6.793 (MPa•s^m), 0.04 and 0.254, respectively.

Returning to the problem at hand, if we use (4), (9), and (11) in (19), we find τ in terms of $b(t)$ and r. The field equations $(13)_2$, (14), and (19) then involve the three quantities τ_r, τ_θ, and b. They are to be solved subject to the boundary conditions (16), (17) and the initial condition (5).

3 Formulation of the Mathematical Problem

Integrating the equilibrium equation (14) with respect to r and using the boundary condition $(16)_1$ yields

$$\tau_r(r, t) = \frac{p(t)}{a^2} - 2\sqrt{3}\int_r^a \frac{\tau(\xi, t)}{\xi}\, d\xi, \tag{23}$$

which on imposing the remaining boundary condition $(16)_2$ and the constitutive law (19) provides

$$p(t) = 2\sqrt{3}a^2 \int_b^a \frac{g(\dot{\gamma}(r, t), \gamma(r, t))}{r}\, dr. \tag{24}$$

Equation (24) may be written out explicitly by substituting the known expressions for $\dot{\gamma}$, γ and a from (9), (11), (15), (4), and (7). This leads to

$$p(t) = 2\sqrt{3}(1 + b^3)^{2/3} \int_b^{(1+b^3)^{1/3}} g\left(2\sqrt{3}\frac{b^2\dot{b}}{r^3}, \frac{2}{\sqrt{3}} \ln \frac{r^3}{r^3 - b^3}\right)\frac{dr}{r}. \tag{25}$$

Finally, it is convenient to change variables in (25) by setting $u = (r^3 - b^3)/r^3$ so that

$$p(t) = \frac{2}{\sqrt{3}}(1 + b^3)^{2/3} \int_0^{\frac{1}{1+b^3}} \frac{g\left(2\sqrt{3}(1-u)\frac{\dot{b}}{b}, \frac{2}{\sqrt{3}} \ln \frac{1}{u}\right)}{1-u}\, du, \quad t \geq 0. \tag{26}$$

This is an implicit differential equation for the void radius $b(t)$.

The separable form of the particular class of constitutive

Downloaded 03 May 2010 to 171.66.16.31. Redistribution subject to ASME license or copyright; see http://www.asme.org/terms/Terms_Use.cfm

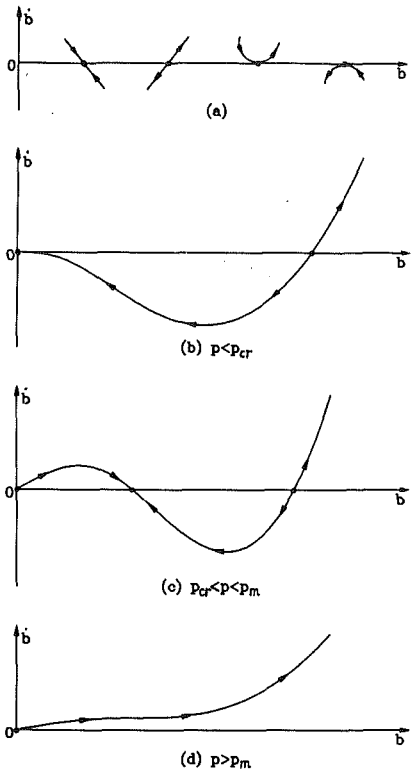


Fig. 3 Phase portraits

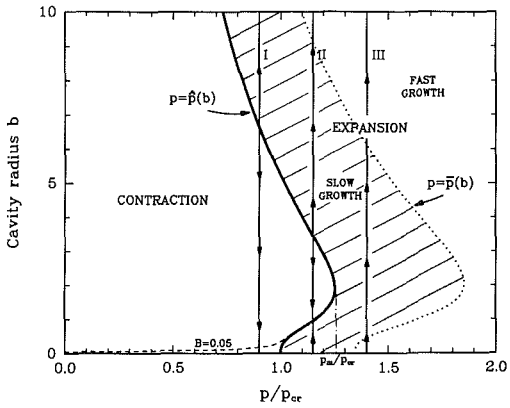


Fig. 4 Void expansion and contraction domains; rate-dependent material (20) with $g_1(\gamma)=\mu\gamma^n$, $n>1$

laws (20) makes it especially attractive for use in our analysis since, (26) may now be explicitly solved for $\dot{b}(t)$. Substituting (20) into (26) gives

$$pb^m = \frac{2}{\sqrt{3}}(1+b^3)^{2/3}\left[\operatorname{sgn}(\dot{b})(2\sqrt{3}\,|\dot{b}|)^m \int_0^{\frac{1}{1+b^3}} \frac{g_2\left(\frac{2}{\sqrt{3}}\ln\frac{1}{u}\right)}{(1-u)^{1-m}}\,du + b^m\int_0^{\frac{1}{1+b^3}} \frac{g_1\left(\frac{2}{\sqrt{3}}\ln\frac{1}{u}\right)}{1-u}\,du\right], \tag{27}$$

which when solved for $\dot{b}$ yields the following first-order differential equation for $b(t)$:

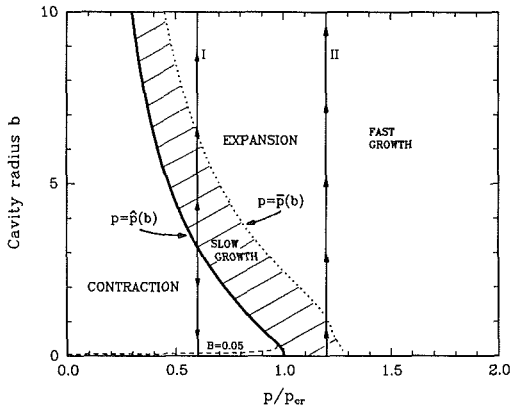


Fig. 5 Void expansion and contraction domains; rate-dependent material (20) with $g_1(\gamma)=\mu\gamma^n$, $n<n^*$

$$\dot{b} = \frac{b}{2\sqrt{3}}\operatorname{sgn}(h)\left(\frac{|h(b,t)|}{\int_0^{\frac{1}{1+b^3}} \frac{g_2\left(\frac{2}{\sqrt{3}}\ln\frac{1}{u}\right)}{(1-u)^{1-m}}\,du}\right)^{1/m}, \tag{28}$$

where

$$h(b,t) = \frac{\sqrt{3}p(t)}{2(1+b^3)^{2/3}} - \int_0^{\frac{1}{1+b^3}} \frac{g_1\left(\frac{2}{\sqrt{3}}\ln\frac{1}{u}\right)}{1-u}\,du. \tag{29}$$

Given the constitutive functions $g_1(\gamma)$ and $g_2(\gamma)$, (28) subjected to $b(0)=0$ constitutes the initial value problem to be studied.

The integrals appearing in (28) and (29) must of course be convergent and in order to ensure this, the constitutive functions g_1 and g_2 must be such that

$$\int_0^1 \frac{g_1\left(\frac{2}{\sqrt{3}}\ln\frac{1}{u}\right)}{1-u}\,du, \quad \int_0^1 \frac{g_2\left(\frac{2}{\sqrt{3}}\ln\frac{1}{u}\right)}{(1-u)^{1-m}}\,du, \tag{30}$$

exist. The necessary and sufficient condition on the constitutive law which ensures cavitation in the rate-independent case ($g_2\equiv 0$) is that the first of these integrals exist, and this is closely related to the condition derived by Ball; (set $u=\lambda^{-3}$ in $(30)_1$ and compare with equations (1.9), (1.10) of Ball (1982)). Since $g_1(0)=0$, $g_2(0)$ is finite and $m>0$, the upper limits in (30) cause no difficulty. Convergence requirements at the lower limits impose restrictions on the constitutive functions g_α at severe strains. Note, in particular, that if $g_\alpha(\gamma)=O(\gamma^n)$ as $\gamma\to\infty$, $n>0$, these integrals do exist.

4 The Rate-Independent Case

It turns out that the results in the rate-independent case ($g_2\equiv 0$) are closely related to those in the rate-dependent case and, therefore, it is useful to begin by briefly examining the former circumstance.

Setting $g_2=0$ in (27) yields *either* $b=0$ *or*

$$p=\hat{p}(b)\equiv\frac{2}{\sqrt{3}}(1+b^3)^{2/3}\int_0^{\frac{1}{1+b^3}} \frac{g_1\left(\frac{2}{\sqrt{3}}\ln\frac{1}{u}\right)}{1-u}\,du, \tag{31}$$

the latter of which is an algebraic equation relating the applied load p to the cavity radius b. Equation (31) defines a curve on

Downloaded 03 May 2010 to 171.66.16.31. Redistribution subject to ASME license or copyright; see http://www.asme.org/terms/Terms_Use.cfm

the (p, b)-plane. The coordinates $(p_{cr}, 0)$ of the point at which this curve intersects the p-axis may be found by sending b to zero in (31); this yields

$$p_{cr} = \frac{2}{\sqrt{3}} \int_0^1 \frac{g_1\left(\frac{2}{\sqrt{3}} \ln \frac{1}{u}\right)}{1-u}\, du. \tag{32}$$

Figure 1 shows a schematic graph of b versus p. The graph consists of two branches, viz. the curve defined by (31) and the straight line $b=0$, and represents the collection of all possible equilibrium states. *Assuming* that the states corresponding to $b=0$ are stable for $p \le p_{cr}$, and that those associated with (31) are stable for $p \ge p_{cr}$, it then follows from Fig. 1 that as the load p is increased from zero, the cavity radius will remain infinitesimal until p reaches the critical value p_{cr}; thereafter, the void would begin to grow.

The graph between b and p according to (31) does not of course necessarily have the simple appearance shown in Fig. 1. For example, Fig. 2 shows these graphs for the pure power law materials, where each curve is drawn for a different value of the hardening exponent n. Observe that the curves may turn right or left according to the value of n. A Taylor expansion of (31) about $b=0$ gives $p = p_{cr} + (2/3)\ b^3 p_{cr} - \mu/n(2/\sqrt{3})^{n+1}\ b^{3n} \ldots$. It follows from this that in the immediate vicinity of the bifurcation point $(p_{cr}, 0)$, the curves are right turning for $n>1$ and left turning for $n<1$. Moreover, all curves which initially turn right eventually turn left when b becomes sufficiently large. Finally, numerical calculation indicates that for $n^* < n < 1$, where $n^* \simeq 0.955$, the curves first turn left, then right, and finally left again.

5 The Rate-Dependent Case

We now return to the rate-dependent case, and consider a step loading history $p(t)=0$ for $t<0$, $p(t)=p=$ *constant* for $t>0$. In order to analyze the governing differential equation

$$\dot{b} = \frac{b}{2\sqrt{3}}\, \mathrm{sgn}(H) \left(\frac{|H(b)|}{\int_0^{\frac{1}{1+b^3}} \frac{g_2\left(\frac{2}{\sqrt{3}} \ln \frac{1}{u}\right)}{(1-u)^{1-m}}\, du} \right)^{1/m}, \tag{33}$$

where

$$H(b) = \frac{\sqrt{3}p}{2(1+b^3)^{2/3}} - \int_0^{\frac{1}{1+b^3}} \frac{g_1\left(\frac{2}{\sqrt{3}} \ln \frac{1}{u}\right)}{1-u}\, du, \tag{34}$$

we begin by considering its phase plane. Since (33) is a first-order equation, all of its trajectories are *confined to a single curve* in the $(b, \dot{b})$-plane. The equation of this curve is given by (33).

The equilibrium solutions of (33) are found by setting $b(t) =$ *constant*: this yields as equilibrium points, $b=0$ and $b=$ the zeros of the function $H(b)$. Note from (34) and (31) that the roots of $H(b)=0$ are precisely the same as those of $\hat{p}(b) - p = 0$ and so the equilibrium solutions of the rate-dependent theory are precisely the solutions according to the underlying rate-independent theory ($g_2 \equiv 0$) at the same stress p.

Next, in order to examine the stability of an equilibrium point, we consider the details of the phase plane in its vicinity. In particular, as shown in Fig. 3(*a*), there are four possibilities, only the first of which is stable. Since, by (33), $\dot{b}$ and H have the same sign, we can argue that an equilibrium point b_* is locally stable if and only if $H'(b_*) < 0$. From (31) and (34), this is equivalent to $\hat{p}'(b_*) > 0$. Thus, an equilibrium solution of the rate-dependent theory is stable provided the b versus p curve for the underlying rate-independent theory is right turning at the appropriate point.

In order to illustrate this further, consider a material whose underlying rate-independent portion is of the pure power-law form, i.e., $g_1(\gamma) = \mu\gamma^n$. Suppose first that $n>1$. Then, from our discussion of the rate-independent case (see Fig. 2), we know that for $0<p<p_{cr}$, where p_{cr} is given by (32), (33) has one other equilibrium point as shown in Fig. 3(*b*). On the other hand, for $p_{cr}<p<p_m$, it has two other equilibrium points as shown in Fig. 3(*c*). Figure 3(*d*) corresponds to the remaining case $p>p_m$ in which event $b=0$ is the unique equilibrium solution.

Next, in order to construct the complete trajectory, we recall that $\dot{b}$ and H have the same sign. Now consider a value of applied stress in the range $0<p<p_{cr}$ and let $b_*>0$ be the associated nonzero equilibrium point. Since $H(0)<0$, $H(b) \to 0+$ as $b \to \infty$, and b_* is the unique zero of H, we conclude that $H(b)<0$ for $b<b_*$ and $H(b)>0$ for $b>b_*$. Thus, it follows that the trajectory is as shown in Fig. 3(*b*). The orientation of the trajectory may be read off from the figure and is shown by the arrows there. The remaining cases $p_{cr}<p<p_m$ and $p>p_m$ may be examined similarly; the results are displayed in Figs. 3(*c*), and 3(*d*).

The preceding conclusions, for all values of p, may be displayed on a single (p, b)-plane as shown in Fig. 4. The bold curve in this figure denotes the equilibrium states, i.e., it is the curve with equation $p=\hat{p}(b)$; for the moment, ignore the dotted and dashed curves in the figure. (The figure has been drawn for $n=1.2$.) The phase portraits for each load level p correspond to a vertical line in this plane; line I corresponds to $p<p_{cr}$, line II to $p_{cr}<p<p_m$ and line III to $p>p_m$. Observe that the solution curve $p=\hat{p}(b)$ associated with the equilibrium states marks the border between the *void expansion* domain ($\dot{b}>0$) and the *void contraction* domain ($\dot{b}<0$). Figure 4 clearly exhibits the *stable* and *unstable* manifolds.

Figure 5 displays the corresponding results for the case $n<n^*$. (The figure has been drawn for $n=0.8$). The results for the remaining case $n^*<n<1$ can, of course, be similarly displayed.

When the initial condition $b(0)=0$ is taken into consideration, we see from (33) that $b(t)=0$ for $t \ge 0$ is a solution to the initial value problem at hand. From ordinary differential equation theory, e.g., Coddington and Levinson (1955), we know that this is in fact the *only* solution since the right-hand side of (33) is Lipschitz with respect to b on a convex region of the (b, t)-plane. However, we see from Figs. 4 and 5 that this solution is *stable* only when $0 \le p \le p_{cr}$, in which case the equilibrium point acts as an *attractor*; for $p>p_{cr}$, it is unstable.

Observe from the preceding discussion that the specific form of the constitutive function $g_2(\gamma)$ and the value of the

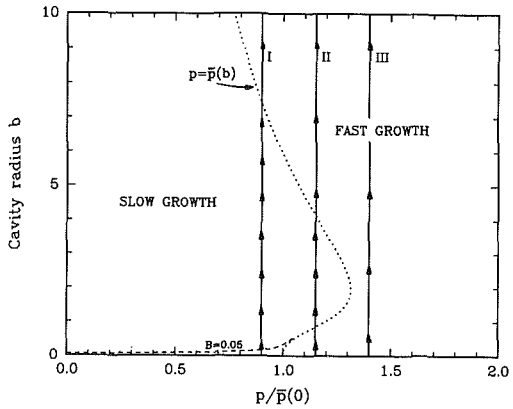


Fig. 6 Fast and slow growth domains; pure creep material (20) with $g_1 = 0$, $g_2(\gamma) = \mu\gamma^n$, $n>1$

Downloaded 03 May 2010 to 171.66.16.31. Redistribution subject to ASME license or copyright; see http://www.asme.org/terms/Terms_Use.cfm

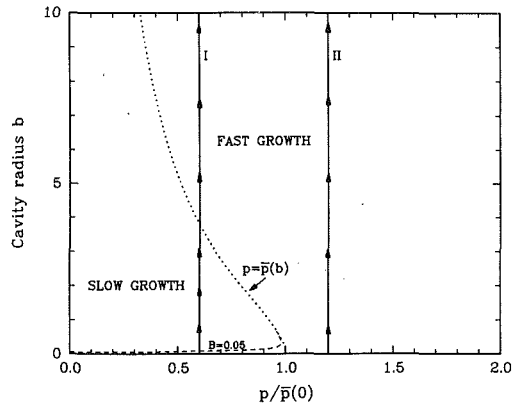


Fig. 7 Fast and slow growth domains; pure creep material (20) with $g_1 = 0$, $g_2(\gamma) = \mu\gamma^n$, $n < n^*$

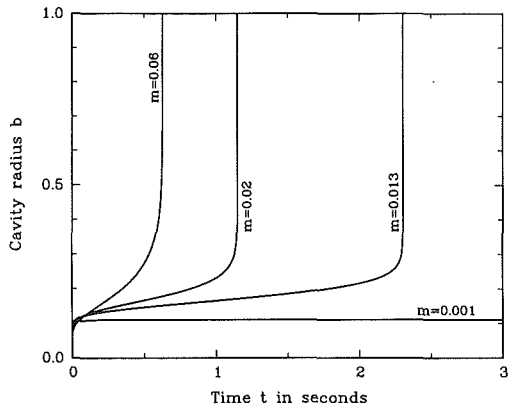


Fig. 8 Cavity radius as a function of time for a cavity of initial radius $B = 0.05$; pure creep material (20) with $g_1 = 0$, $g_2(\gamma) = \mu\gamma^n$, $n = 0.5$, $p = 2.5\mu$

strain rate exponent $m > 0$ only affect the rate at which the solution approaches the stable manifold or leaves the unstable one, but not the qualitative behavior of the solution. In particular, the values and stability of the equilibrium solutions are unaffected by these quantities.

Consider next the region of the (p, b)-plane where void *expansion* takes place and focus attention on the *rate* of void growth $\dot{b}$. We will assume that the amount of rate dependency m is small (but nonzero). Since the exponent $1/m$ in (33) is then large, it follows that $\dot{b}$ will be small when the term in the parenthesis in (33) is less than unity, and vice versa. Thus, the condition which signals the onset of *rapid* void expansion is when this term becomes unity, which from (33), (34) and $\dot{b} > 0$ is

$$p = \bar{p}(b) \equiv \frac{2}{\sqrt{3}}\,(1+b^3)^{2/3} \int_0^{\frac{1}{1+b^3}} \left(\frac{g_1\left(\frac{2}{\sqrt{3}} \ln \frac{1}{u}\right)}{(1-u)} + \frac{g_2\left(\frac{2}{\sqrt{3}} \ln \frac{1}{u}\right)}{(1-u)^{1-m}} \right) du. \quad (35)$$

Therefore, the void expands slowly when $p < \bar{p}$ and rapidly when $p > \bar{p}$. The dotted curves in Figs. 4 and 5 are graphs of b versus $\bar{p}(b)$, where for purposes of the figure we have used $g_1 = 2g_2 = \mu\gamma^n$ and $m = 0.1$. This curve separates the (p, b)-plane into regions where slow and rapid void expansion take place. Equation (35) may be viewed as a formula for the critical value of applied stress, corresponding to a given value of current void size b, at which rapid void expansion takes place. (A similar study of the void contraction domain can of course be carried out, leading to (35) with a negative sign separating the g_1 and g_2 terms.)

Next we consider the somewhat exceptional special case of pure creep. Setting $g_1(\gamma) \equiv 0$ in (33) and (34) leads to the following differential equation for $b(t)$:

$$\dot{b} = \frac{b}{2\sqrt{3}} \left(\frac{p}{\bar{p}(b)} \right)^{1/m}, \quad (36)$$

where the function $\bar{p}(b)$ is given by (35) with $g_1 = 0$. Note that in the particular case of the power-law model (22), $\bar{p}$ differs from $\hat{p}$ in (31) only by the presence of the term m. Clearly, the only equilibrium solution (for all values of p) in this case is $b = 0$ and Figs. 6 and 7 show the phase portraits. Note that the equilibrium state $b = 0$ is unstable at *all* levels of load $p > 0$, which simply means that after application of the load, the body will continue to creep forever. The *rate* of creep $\dot{b}$ may be examined as before, through the graph of b versus $\bar{p}(b)$. The results are displayed in Figs. 6 and 7. (The former has been drawn for $n = 1.2$, $m = 0.1$ and the latter for $n = 0.8$, $m = 0.1$.)

Finally, suppose that instead of a void with zero undeformed radius, we had considered an internal cavity of undeformed radius $B(>0)$. One can readily formulate the analogous problem in this case leading to

$$\dot{b} = \frac{b^3 - B^3}{2b^2\sqrt{3}}\,\mathrm{sgn}(h) \times \left(\frac{|h(b,t)|}{\int_{B^3/b^3}^{(1+b^3-B^3)^{-1}} \frac{g_2\left(\frac{2}{\sqrt{3}} \ln \frac{1}{u}\right)}{(1-u)^{1-m}}\, du} \right)^{1/m}, \quad (37)$$

where

$$h(b,t) = \frac{\sqrt{3}p(t)}{2(1+b^3-B^3)^{2/3}} - \int_{B^3/b^3}^{(1+b^3-B^3)^{-1}} \frac{g_1\left(\frac{2}{\sqrt{3}} \ln \frac{1}{u}\right)}{1-u}\, du. \quad (38)$$

The equilibrium solutions in this case are shown by the dashed curves in Figs. 4 and 5 (drawn for $B = 0.05$); note that they are hardly distinguishable from the solid curves at even moderate values b. The dashed curves in Figs. 6 and 7 denote the boundaries between the regions of rapid and slow void expansion; they coincide with the dotted curves in those figures over most of their length. The phase portraits are similar to before and, therefore, so is the behavior of the void. The initial value problem (37), (38) subject to $b(0) = B$ was solved numerically for the pure creep case. The results are displayed in Fig. 8 which clearly shows the stages of slow and rapid growth. Observe from the dashed curve in Fig. 7, that for $B > 0$, the rapid growth region extends to the entire p-axis; the vertical line I begins by passing through a narrow fast growth domain, then through a slow growth domain, and finally returns to the fast growth domain. This is confirmed by Fig. 8.

Acknowledgments

The authors gratefully acknowledge helpful discussions with Lallit Anand.

References

Anand, L., 1985, "Constitutive Equations for Hot-working of Metals," *International Journal of Plasticity*, Vol. 1, pp. 213-231.

Downloaded 03 May 2010 to 171.66.16.31. Redistribution subject to ASME license or copyright; see http://www.asme.org/terms/Terms_Use.cfm

Anand, L., Kim, K. H., and Shawki, T. G., 1987, "Onset of Shear Localization in Viscoplastic Solids," *Journal for the Mechanics and Physics of Solids*, Vol. 35, pp. 407–429.

Ball, J. M., 1981, "Existence of Solutions in Finite Elasticity," *Proceedings of the IUTAM Symposium on Finite Elasticity*, D. E. Carlson and R. T. Shield, eds., Martinus Nijhoff, The Hague, pp. 1–12.

Ball, J. M., 1982, "Discontinuous Equilibrium Solutions and Cavitation in Nonlinear Elasticity," *Philosophical Transactions of the Royal Society, London*, Vol. A306, pp. 557–611.

Budiansky, B., Hutchinson, J. W., and Slutsky, S., 1982, "Void Growth and Collapse in Viscous Solids," *Mechanics of Solids*, H. G. Hopkins and M. J. Sewell, eds., Pergamon Press, London, pp. 13–45.

Chung, D-T., Horgan, C. O., and Abeyaratne, R., 1987, "A Bifurcation Problem in Finite Plasticity Related to Void Nucleation," *International Journal of Solids and Structures*, Vol. 23, pp. 983–988.

Coddington, E. A., and Levinson, N., 1955, *Theory of Ordinary Differential Equations*, McGraw-Hill, New York.

Ertan, N., 1988, "Influence of Compressibility and Hardening on Cavitation," *ASCE Journal of Engineering Mechanics*, Vol. 114, pp. 1231–1244.

Gent, A. N., and Lindley, P. B., 1958, "Internal Rupture of Bonded Rubber Cylinders in Tension," *Proceedings of the Royal Society, London*, Vol. A249, pp. 195–205.

Horgan, C. O., and Abeyaratne, R., 1986, "A Bifurcation Problem for a Compressible Nonlinearly Elastic Medium: Growth of a Micro-Void," *Journal of Elasticity*, Vol. 16, pp. 189–200.

Klopp, R. W., Clifton, R. J., and Shawki, T. G., 1985, "Pressure-Shear Impact and the Dynamic Viscoplastic Response of Metals," *Mechanics of Materials*, Vol. 4, pp. 375–385.

McClintock, F. A., 1968, "A Criterion for Ductile Fracture by Growth of Holes," ASME JOURNAL OF APPLIED MECHANICS, Vol. 35, pp. 363–371.

Podio-Guidugli, P., Caffarelli, G. V., and Virga, E. G., 1986, "Discontinuous Energy Minimizers in Nonlinear Elastostatics: An Example of J. Ball Revisited," *Journal of Elasticity*, Vol. 16, pp. 75–96.

Rice, J. R., and Tracey, D. M., 1969, "On the Ductile Enlargement of Voids in Tri-axial Stress Fields," *Journal of the Mechanics and Physics of Solids*, Vol. 17, pp. 201–217.

Rogers, H. C., 1960, "Tensile Fracture of Ductile Materials," *Transactions of the Metallurgical Society of the AIME*, Vol. 218, pp. 498–506.

Shawki, T. G., Clifton, R. J., and Majda, G., 1987, "Analysis of Shear Strain Localization in Thermal Visco-plastic Materials," Brown University Technical Report.

Sivaloganathan, J., 1986, "A Field Theory Approach to Stability of Radial Equilibria in Nonlinear Elasticity," *Mathematical Proceedings of the Cambridge Philosophical Society*, Vol. 99, pp. 589–604.

Wright, T. W., 1987, "Steady Shearing in a Visco-plastic Solid," *Journal of the Mechanics and Physics of Solids*, Vol. 35, pp. 269–282.

Downloaded 03 May 2010 to 171.66.16.31. Redistribution subject to ASME license or copyright; see http://www.asme.org/terms/Terms_Use.cfm

C. Y. Wang
Departments of Mathematics and Mechanical Engineering, Michigan State University, East Lansing, Mich. 48824
Mem. ASME

Melting From a Horizontal Rotating Disk

Melting of a disk is facilitated by rotation. The problem is governed by a nondimensional parameter α which represents the relative importance of injection (melt) rate and rotation times viscosity. The nonlinear governing equations are solved by perturbations for small α and numerical integration for arbitrary α. Torque and heat transfer rates are found. The solution is one of the rare exact similarity solutions of the Navier-Stokes equations.

Introduction and Formulation

If a horizontal solid surface melts, a thin film of fluid will be formed on the surface. Further melting is retarded due to the thickening of the liquid film which serves as a barrier to heat transfer. Now suppose the solid surface is rotated. Centrifugal forces would cause the fluid to move radially outwards and facilitate melting. Eventually an equilibrium state is reached. This paper studies the fluid dynamics and heat transfer of such a state. The problem is fundamental not only to melting, but also to ablation cooling, forced mass transfer, and surface chemical reactions. The only relevant previous work is due to Dorfman (1967) who briefly considerd the fluid film caused by injection through a porous rotating plate. Dorfman's work, however, is primarily about numerical solution of the film on a nonporous rotating plate.

Figure 1 shows the situation. The free surface of the liquid film is at $z = 0$ and the solid surface is at $z = h$. The density of the layer ρ is assumed to be larger than ambient density ρ_0 such that static stability is assured. To model melting, fluid is injected through the wall with velocity W. The solid surface is also rotated with angular velocity Ω. We assume the radius of the disk R is much larger than the film thickness h such that end effects can be neglected. We also assume the ambient "air" has little effect on the dynamics of the film.

Let (u, v, w) be the velocity components in the directions (r, θ, z), respectively. The axisymmetric Navier-Stokes equations are

$$uu_r + wu_z - \frac{v^2}{r} = -\frac{1}{\rho} p_r + \nu\left(u_{rr} + \frac{1}{r} u_r + u_{zz} - \frac{u}{r^2}\right) \quad (1)$$

$$uv_r + wv_z + \frac{uv}{r} = \nu\left(v_{rr} + \frac{1}{r} v_r + v_{zz} - \frac{v}{r^2}\right) \quad (2)$$

$$uw_r + ww_z = -\frac{1}{\rho} p_z + \nu\left(w_{rr} + \frac{1}{r} w_r + w_{zz}\right) + g \quad (3)$$

$$(ru)_r + (rw)_z = 0 \quad (4)$$

Contributed by the Applied Mechanics Division of THE AMERICAN SOCIETY OF MECHANICAL ENGINEERS for publication in the JOURNAL OF APPLIED MECHANICS.

Discussion on this paper should be addressed to the Editorial Department, ASME, United Engineering Center, 345 East 47th Street, New York, N.Y. 10017, and will be accepted until two months after final publication of the paper itself in the JOURNAL OF APPLIED MECHANICS. Manuscript received by ASME Applied Mechanics Division, May 28, 1987; final revision, July 29, 1988.

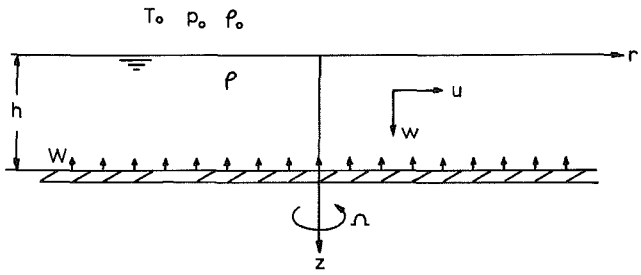


Fig. 1 The coordinate system

where p is the pressure ν is the kinematic viscosity, and g is the gravitational constant. We make the following transform

$$u = r\Omega F'(\eta), \quad v = r\Omega G(\eta), \quad w = -2\sqrt{\nu\Omega}\, F, \quad (5)$$

where $\eta \equiv \sqrt{\Omega/\nu}\, z$ is a normalized variable. The Navier-Stokes reduce to

$$(F')^2 - 2FF'' - G^2 = F''' \quad (6)$$

$$2(F'G - G'F) = G''. \quad (7)$$

From equation (3) the pressure can be integrated. Applying the condition that the normal stress $(p - 2\mu w_z)$ is equal to the ambient pressure p_0, we find

$$p = p_0 + \rho(\nu w_z + gz + \nu w_z|_0 - w^2/2). \quad (8)$$

The boundary conditions are zero shear on the free surface

$$F(0) = 0, \quad F''(0) = 0, \quad G'(0) = 0 \quad (9)$$

and injection and rotation on the solid surface

$$F(\beta) = \alpha, \quad F'(\beta) = 0, \quad G(\beta) = 1 \quad (10)$$

where $\beta = \sqrt{\Omega/\nu}\, h$ and $\alpha \equiv W/2\sqrt{\Omega\nu}$ is the nondimensional parameter representing the relative importance of injection rate to rotation and viscosity.

Perturbation Solution for Small α

When α is small, we expect the film to be thin. Since from equation (10) $F = 0(\alpha)$, $G = 0(1)$, equation (6) shows that the proper stretched variable is

$$\eta = \alpha^{\frac{1}{3}} \zeta. \quad (11)$$

Copyright © 1989 by ASME
Downloaded 03 May 2010 to 171.66.16.31. Redistribution subject to ASME license or copyright; see http://www.asme.org/terms/Terms_Use.cfm

Then equations (6), (7) dictate the following expansions (see, e.g., Van Dyke, 1964)

$$F=\alpha f_0(\zeta)+\alpha^{\frac{7}{3}} f_1(\zeta)+0\left(\alpha^{\frac{11}{3}}\right) \tag{12}$$

$$G=1+\alpha^{\frac{4}{3}} g_0(\zeta)+\alpha^{\frac{8}{3}} g_1(\zeta)+0(\alpha^4). \tag{13}$$

The successive orders are

$$-1=f_0''', \quad 2f_0'=g_0'' \tag{14}$$

$$(f_0')^2-2f_0f_0''-2g_0=f_1''' \tag{15}$$

$$2(f_1'+f_0'g_0-f_0g_0')=g_1''. \tag{16}$$

The boundary conditions at $\zeta=0$ are

$$f_0(0)=f_0''(0)=g_0'(0)=0 \tag{17}$$

$$f_1(0)=f_1''(0)=g_1'(0)=0. \tag{18}$$

However, the film thickness β is unknown. Let

$$\alpha^{-\frac{1}{3}}\beta\equiv\lambda=\lambda_0+\alpha^{\frac{4}{3}}\lambda_1+0\left(\alpha^{\frac{8}{3}}\right). \tag{19}$$

Expanding equations (10) in a Taylor series about $\zeta=\lambda_0$ yields

$$f_0(\lambda_0)=1, \quad f_0'(\lambda_0)=0, \quad g_0(\lambda_0)=0 \tag{20}$$

$$f_1(\lambda_0)+\lambda_1 f_0'(\lambda_0)=0, \quad f_1'(\lambda_0)+\lambda_1 f_0''(\lambda_0)=0 \tag{21}$$

$$g_1(\lambda_0)+\lambda_1 g_1'(\lambda_0)=0. \tag{22}$$

The zeroth order solution, also obtained by Dorfman (1967) is

$$f_0=-\frac{\zeta^3}{6}+\frac{3^{2/3}}{2}\zeta \tag{23}$$

$$g_0=-\frac{\zeta^4}{12}+\frac{3^{2/3}}{2}\zeta^2-\frac{5}{4}3^{1/3} \tag{24}$$

$$\lambda_0=3^{1/3}. \tag{25}$$

These are substituted into equations (15), (16). After some work, the first-order solution is

$$f_1=\frac{\zeta^7}{2520}-\frac{3^{2/3}}{120}\zeta^5+\frac{13}{24}3^{1/3}\zeta^3-\frac{87}{56}\zeta \tag{26}$$

$$g_1=\frac{\zeta^8}{2520}+\frac{3^{1/3}}{4}\zeta^4-\frac{24}{7}\zeta^2+\frac{589}{840}3^{2/3} \tag{27}$$

$$\lambda_1=\frac{104}{105}3^{2/3}. \tag{28}$$

Thus

$$F'(0)=\alpha^{2/3}f_0'(0)+\alpha^2 f_1'(0)+\ldots$$

$$=\frac{3^{2/3}}{2}\alpha^{2/3}-\frac{87}{56}\alpha^2+0(\alpha^{10/3}) \tag{29}$$

$$G(0)=1-\frac{5}{4}3^{1/3}\alpha^{4/3}+\frac{589}{840}3^{2/3}\alpha^{8/3}+0(\alpha^4) \tag{30}$$

$$G'(\beta)=2\alpha-\frac{136}{35}3^{1/3}\alpha^{7/3}+0(\alpha^{11/3}) \tag{31}$$

$$\beta=3^{1/3}\alpha^{1/3}+\frac{104}{105}3^{2/3}\alpha^{5/3}+0(\alpha^3). \tag{32}$$

Nonexistence of a Boundary Layer at Large α

For large injection rates α we intuitively expect uniform vertical flow for the interior and a boundary layer near the top surface. The proper stretching in the boundary layer is

$$F=\alpha\bar{f}(\bar{\zeta}), \quad G=\bar{g}(\bar{\zeta}), \quad \eta=\frac{1}{\alpha}\bar{\zeta} \tag{33}$$

where the barred quantities are of order unity. Equation (6) gives

$$(\bar{f}')^2-2\bar{f}\bar{f}''=\bar{f}''' \tag{34}$$

$$\bar{f}(0)=0, \quad \bar{f}''(0)=0, \quad \bar{f}(\infty)=\alpha. \tag{35}$$

We integrate equation (34) to obtain

$$-2\bar{f}\bar{f}'\Big|_0^\infty+3\int_0^\infty(\bar{f}')^2d\eta=\bar{f}''\Big|_0^\infty \tag{36}$$

or

$$\int_0^\infty(\bar{f})^2d\eta=0. \tag{37}$$

The only solution is $\bar{f}\equiv 0$ which contradicts $\alpha>0$. Thus, we conclude boundary layer type solutions do not exist.

Exact Numerical Integration and Results

For arbitrary α numerical integration is necessary. By choosing any $0<G(0)<1$, and guessing $F'(0)$, equations (6), (7), (9) can be integrated as an initial value problem using the fifth-order Runge-Kutta-Fehlberg algorithm. The integration

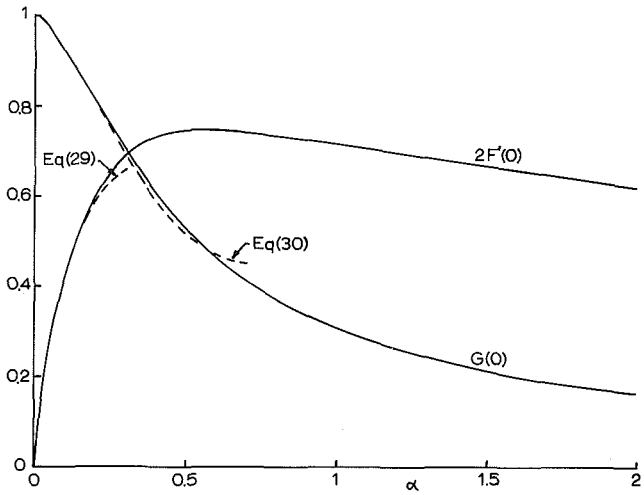


Fig. 2 The initial values: $F'(0)$ is the normalized radial surface velocity, $G(0)$ is the normalized azimuthal surface velocity

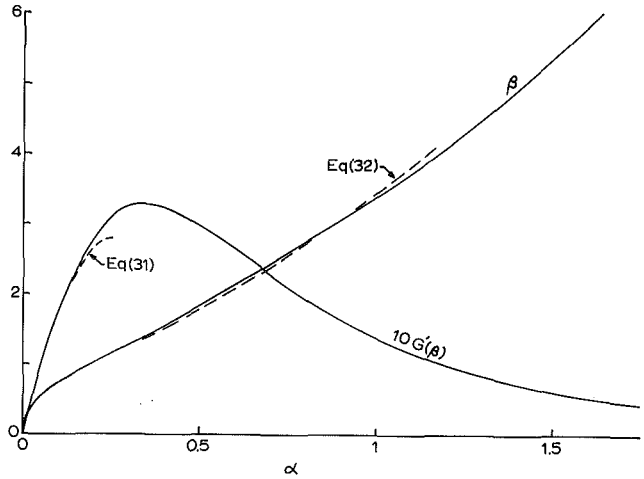


Fig. 3 The normalized torque $G'(\beta)$ and the film thickness β

Downloaded 03 May 2010 to 171.66.16.31. Redistribution subject to ASME license or copyright; see http://www.asme.org/terms/Terms_Use.cfm

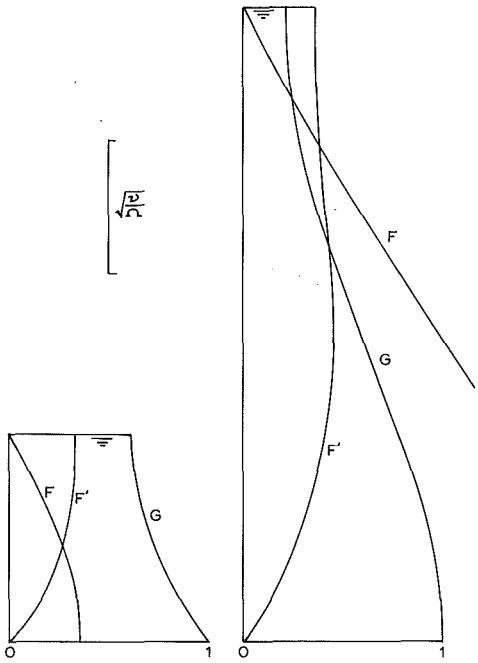


Fig. 4 Normalized velocity distributions: Left: α = 0.4, Right: α = 1.5. $F(\eta)$ vertical component, $F'(\eta)$ radial component, $G(\eta)$ azimuthal component

proceeds until $G=1$, say, at $\eta=\eta^*$. A solution is found if $F'(\eta^*)$ is zero, then $\eta^* = \beta$. If not, $F'(0)$ is adjusted. The initial values obtained by a one-dimensional shooting method are plotted in Fig. 2 as a function of α. Our approximate results compare well with the exact numerical solutions for small α.

$F'(0)$ and $G(0)$ represent the surface velocities in the radial and azimuthal directions, respectively. We see that as α increases, $G(0)$ decreases monotonically, but $F'(0)$ increases to a maximum of 0.374 near $\alpha = 0.55$. As α is further increased, $F'(0)$ decreases more slowly than $G(0)$, making the surface velocity more radial.

Of interest is the torque τ required for the rotation

$$\tau=\int_0^R \rho\nu \frac{\partial v}{\partial z}\bigg|_{z=\beta} 2\pi r^2 dr=\frac{1}{2}\pi\rho\,\Omega\sqrt{\Omega\nu}\,R^4 G'(\beta). \quad (38)$$

The normalized torque $G'(\beta)$ and the film thickness β are plotted in Fig. 3. Note that $G'(\beta)$ reaches a maximum of 0.33 at $\alpha = 0.34$. The thickness β increases indefinitely with injection α. Some normalized velocity distributions are shown in Fig. 4. The radial velocity F' is semi-parabolic only at small α. Maximum F' shifts from the free surface to the interior when $\alpha > 0.794$.

The Thermal Problem

The energy equation is

$$uT_r + wT_z = \frac{\nu}{\mathrm{Pr}}\left(T_{rr}+\frac{1}{r}T_r+T_{zz}\right) \quad (39)$$

where T is the temperature and Pr is the Prandtl number. Set

$$\theta\equiv\frac{T-T_0}{T_w-T_0} \quad (40)$$

where T_0 is the temperature on the free surface and T_w is the temperature of the solid surface. Equation (39) becomes

$$\theta''(\eta)+2\mathrm{Pr}\,F\theta'=0 \quad (41)$$

$$\theta(0)=0, \quad \theta(\beta)=1. \quad (42)$$

The solution can be expressed in terms of an integral

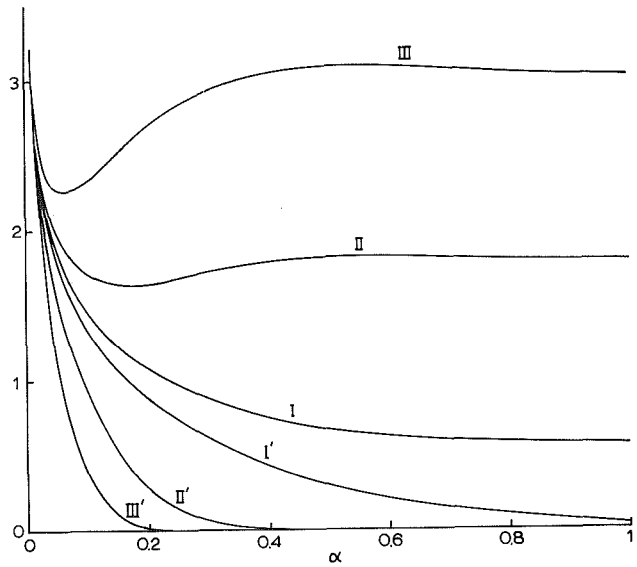


Fig. 5 Normalized heat transfer as a function of α and Pr: I, II, III, values of $\theta'(0)$ at Pr = 0.7, 7, and 20, respectively, I′, II′, III′ values of $\theta'(\beta)$ at Pr = 0.7, 7, 20, respectively

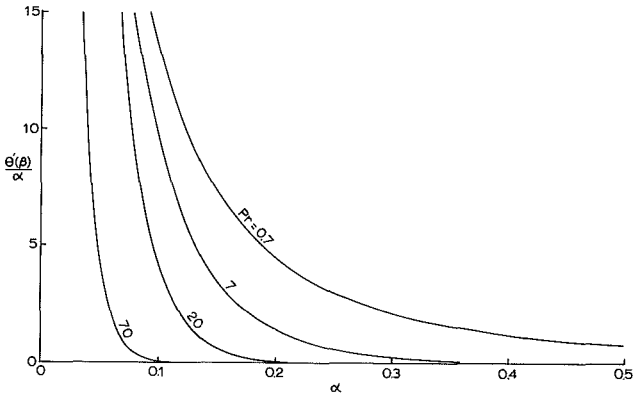


Fig. 6 Normalized latent heat $2\nu H/\kappa(T_0 - T_w) = \theta'(\beta)/\alpha$ as a function of α

$$\theta=\frac{1}{C}\int_0^\eta \exp\left[-2\mathrm{Pr}\int_0^\eta F\,d\eta\right]d\eta,$$

$$C\equiv\int_0^\beta \exp\left[-2\mathrm{Pr}\int_0^\eta F\,d\eta\right]d\eta. \quad (43)$$

Since $F(\eta)$ and β are known, the function θ can be found by quadratures or direct numerical integration of equation (41). The heat transfer per unit area q is

$$q=-\kappa\frac{\partial T}{\partial z}=\kappa\sqrt{\frac{\Omega}{\nu}}\,(T_0-T_w)\theta'(\eta) \quad (44)$$

where κ is the thermal conductivity. On the boundaries,

$$\theta'(0)=\frac{1}{C}, \quad \theta'(\beta)=\frac{1}{C}\exp\left[-2\,\mathrm{Pr}\int_0^\beta F\,d\eta\right]. \quad (45)$$

For small α, it can be shown

$$C\sim 3^{1/3}\alpha^{1/3}+0(\mathrm{Pr}\alpha^{4/3}). \quad (46)$$

Figure 5 shows the numerical results. Both $\theta'(0)$ and $\theta'(\beta)$ approach infinity when α is small. As α is increased, $\theta'(\beta)$ decays exponentiallly while $\theta'(0)$ seems to approach a constant.

In the case of continuous melting, the latent heat per unit mass H is a given physical number

Downloaded 03 May 2010 to 171.66.16.31. Redistribution subject to ASME license or copyright; see http://www.asme.org/terms/Terms_Use.cfm

$$H = q/W = \frac{\kappa}{2\nu} (T_0 - T_w) \frac{\theta'(\beta)}{\alpha} . \quad (47)$$

The value $\theta'(\beta)/\alpha$ is plotted in Fig. 6. Thus, from H and the temperature difference, one can find α representing the rate of melting.

Discussion

The melting problem is important in chemical engineering processes. Traditionally gravity is utilized to remove the melted fluid from an inclined surface. Removal by centrifugal forces is more efficient, since the rotation rate can be increased and controlled. The melting is also more evenly distributed since the heat transfer and the thickness of the film is constant. For a given melting material, one can adjust the temperature T_0 and the rotation rate Ω for optimum torque and melt rate W. As in all film flows, the free surface may become unstable for larger velocities.

Our result is also a rare exact similarity solution of the Navier-Stokes. Note that in order for the solution to exist, rotation and wall injection need to be both nonzero. In this respect the problem differs distinctly from that of the Von Karman (1921) rotating plate.

References

Dorfman, L. A., 1967, "Flow and Heat Transfer in a Film of Viscous Liquid on a Rotating Disk," *Journal of Engineering Physics*, Vol. 12, pp. 309–316.

Van Dyke, M., 1964, *Perturbation Methods in Fluid Mechanics*, Academic Press, New York, Chap. 3.

Von Karman, Th., 1921, "Über laminare und turbulente Reibung," *Zeit. Angew. Math. Mech.*, Vol. 1, pp. 233–252.

Downloaded 03 May 2010 to 171.66.16.31. Redistribution subject to ASME license or copyright; see http://www.asme.org/terms/Terms_Use.cfm

Dusan Krajcinovic
Department of Civil Engineering, Mechanics, and Metallurgy, University of Illinois at Chicago, Chicago, Ill. 60680
Fellow, ASME

Dragoslav Sumarac
Civil Engineering Department, University of Belgrade, Belgrade, Yugoslavia

A Mesomechanical Model for Brittle Deformation Processes: Part I

The discussion centers on the formulation of a constitutive model for brittle solids satisfying two conflicting requirements: simplicity and accuracy. Owing to the inherent complexity oif the problem, stemming from the random distribution of interacting defects, analytical expressions relating macrofields are possible only under some restrictive conditions emphasizing modest levels of defect concentrations.

Introduction

The title continuum damage mechanics (CDM) is ofen used to label a loose agglomeration of analytical models formulated with an express purpose of dealing with brittle response of solids. The continuing reliance of these models on the macro observations resulted in a bevy of different and often contradicting theories. With a generous helping of "material" parameters, these phenomenological models are shown to a fit a particular set of experimental data with an often suspicious accuracy. The ensuing controversy, related to the selection of the "best" or even most appropriate model for a particular problem, was typically approached using clever little artifices emphasizing unrealistic assumptions regarding crack distribution.

This state of affairs (summarized briefly in Krajcinovic, 1984), typical of infancy of most branches of continuum mechanics, has nevertheless ran its course. The recently emerging micromechanical models (M. Kachanov 1982, 1987; Horri and Nemat-Nasser 1983, 1986; Krajcinovic and Fanella, 1986; Krajcinovic and Sumarac, 1987, 1987a; Sumarac and Krajcinovic, 1987; etc.) suggest in no uncertain manner that most of the existing phenomenological models stand on a very shaky ground. This, of course, just proves that every attempt to model an irreversible process on the basis of macro observations presents a risky venture having a modest chance of successful outcome.

The objective of this paper is to examine the essential structure of the micromechanical (or, more accurately, mesomechanical) models outlining the assumptions needed to ensure their tractability and, consequently, their practical utility. Roughly speaking, the structure of these theories emphasizes a model of the dominant mode of irreversible changes of the mesostructure embedded, via an appropriate homogenization algorithm, into a constitutive relation mapping macrostresses on macrostrains in a homogenized solid.

Damage Variable

In order to define the damage, it is necessary to consider two scales: macroscale on which the solid is regarded as continuum and the damage is represented by a continuous function of coordinates and the mesoscale on which the solid is inhomogeneous and some of the field discontinuous. The introduction of two scales implies existence of the unit cell, or representative volume (Hill 1967) which, loosely speaking, presents the smallest volume of material which in a given sense responds as a macrocontinuum. Mathematically, a unit cell maps on the material point of the continuum. The configurational space (recoored history H) attached to each point of the continuum must, therefore, contain necessary information defining:

- number, type, position, size and orientation of defects,
- number and orientation of cleavage and slip planes, and
- morphology of energy barriers (such as grain boundaries),

within the unit cell.

In contradistinction to ductile deformation, during which the material "slips through" the crystalline lattice, the damage can be defined as a process during which the material remains "in place" while the lattice degrades through the loss of bonds. Since the elastic compliance of a solid locally depends on the type, distribution and density of primary bonds, it is not surprising that it changes only in the course of brittle processes. In fact, in a complete accord with the original Kachanov (1958) model, the extent of damage can be measured by the change in the elastic macrocompliance of the solid (Chaboche, 1979; Lemaitre and Chaboche, 1985). This characterization is also suggested by Hart et al. (1975) who argues that the change in compliance being a readily identifiable and measurable property of the specimen is a natural choice for the internal variable.

On the mesoscale the ruptured bonds cluster into cracks along cleavage planes or grain boundaries. Assuming that

Contributed by the Applied Mechanics Division of THE AMERICAN SOCIETY OF MECHANICAL ENGINEERS for presentation at the Winter Annual Meeting, San Francisco, Calif., December 10–15, 1989.

Discussion of this paper should be addressed to the Editorial Department, ASME, United Engineering Center, 345 East 47th Street, New York, N.Y. 10017, and will be accepted until two months after final publication of the paper itself in the JOURNAL OF APPLIED MECHANICS. Manuscript received by ASME Applied Mechanics Division, February 2, 1988; final revision, July 25, 1988.
Paper No. 89-WA/APM-1.

Copyright © 1989 by ASME

Downloaded 03 May 2010 to 171.66.16.31. Redistribution subject to ASME license or copyright; see http://www.asme.org/terms/Terms_Use.cfm

each of N planar cracks within a unit cell mapping on a point $\mathbf{x}$ can be regarded as elliptical, the configurational space (or history H) defining the "damage" in the point contains $8N$ variables: three scalars defining position, three Euler angles defining orientation, and two scalars defining size of each crack.

A much less ambitious description of damage involves only $4N$ variables assuming cracks to be circular and disregarding their exact position within the unit cell. The "damage" in $\mathbf{x}$ is then described by N doublets $(A, \mathbf{n})$, where A is the relative void area in the plane with normal $\mathbf{n}$ through the point $\mathbf{x}$ (Krajcinovic, 1985; Ilankamban and Krajcinovic, 1987).

An even simpler characterization is possible when the crack distribution and orientations are perfectly random rendering the solid isotropic. In that case a single scalar "crack density parameter" (Budiansky and O'Connell, 1976; Lemaitre and Chaboche, 1985) suffices. Every successive approximation enhances the tractability at the expense of the rigor and possibly accuracy.

Thermodynamic Considerations

Consider a perfectly elastic material in a completely inert environment. Restricting discussions to perfectly brittle deformation processes, the current state is defined locally by the temperature T, elastic strain tensor, and a history parameter H.

According to the first law of thermodynamics, the sum of rates of changes in the mechanical work dW and heat energy dQ must be balanced by the sum of rates of changes of the internally stored energy du and the energy needed for the creation of new, internal surfaces (rupture of bonds) dD, i.e.,

$$dW + dQ = du + dD \tag{1}$$

where all terms in (1) are taken per unit of volume.

Introducing the dual (Gibbs) potential density function

$$\psi(\sigma, T, H) = \sigma : \epsilon - u + T\eta \tag{2}$$

where η is the entropy density, the entropy production (Clausius-Duhem) inequality can be, for $dT = \text{grad } T = 0$, written as

$$d\psi - \epsilon : d\sigma - dD \geq 0. \tag{3}$$

Since

$$d\psi = \frac{\partial \psi}{\partial \sigma} : d\sigma + \frac{\partial \psi}{\partial H}\, dH = \frac{\partial \psi}{\partial \sigma} : d\sigma + d^I\psi \tag{4}$$

and

$$\epsilon = \frac{\partial \psi}{\partial \sigma} \quad (H \text{ fixed}) \tag{5}$$

the entropy production inequality (3) reduces to

$$d^I\psi - dD \geq 0. \tag{6}$$

The energy dissipated on the creation of new internal surfaces is proportional to the increase in the crack surfaces. Thus, denoting by $\delta l(L)$ advance of the crack front L in the direction of its normal, the energy dissipated on the creation of new surfaces can be written in the form (Rice, 1975)

$$dD = \int_L 2\gamma \delta l \, dL \tag{7}$$

where γ is the surface energy.

Finally, since the energy release rate G (Rice, 1978) is defined as

$$G = -(\partial \psi / \partial l) \tag{8}$$

the inequality (6) can be rewritten in a more familiar form (Rice, 1975) as

$$\int_L (G - 2\gamma)\delta l \, dL \geq 0 \tag{9}$$

where $G = J$ is the energy release rate density. The inequality (9) is typically assumed to be satisfied pointwise on L, leading to the more common form of the stability criterion

$$(G - 2\gamma)\delta l > 0 \tag{10}$$

valid both for rapid cracking and healing. In the language of thermodynamics, δl is the flux, G the affinity (driving force), and 2γ the resistive force. Consideration of a more general crack growth pattern will result in the increase of the number of fluxes and their conjugate forces (Chudnovsky, 1987).

Single Crack Embedded in Elastic Matrix

Compliance Tensor. Consider first the case of a single crack embedded in a perfectly elastic matrix. Since this discussion focuses on the cracks which are very small when compared to the dimensions of a solid specimen, the elastic matrix can be considered as being infinitely extended. For the case of infinitesimal strains, the Gibbs potential is a homogeneous quadratic function of strains

$$\psi(\sigma, H) = \tfrac{1}{2}\, \sigma : \mathbf{S}(H) : \sigma \tag{11}$$

where $\mathbf{S}(H)$ is a fourth rank compliance tensor serving as a repository of the recorded history H.

Within the domain of validity of linear elastic fracture mechanics, the stress and strain fields in an infinitely extended solid containing a crack and subjected to a far field stress can be determined through the superposition of solutions of two elementary problems: problem of a body subjected to far field stresses σ^o at boundaries and a problem of a body with a crack loaded by self-equilibrated stresses over its surfaces. Consequently, the total energy of the system can be written as a sum of two terms

$$\psi(\sigma, H) = \psi^o(\sigma) + \psi^*(H) \tag{12}$$

where the superscripts (o) corresponds to the first problem (virgin state of the material) and $(*)$ to the second problem (presence of a crack). The overall compliance tensor $S(H)$ can be also written as a sum of two terms

$$\mathbf{S}(\mathbf{x}, H) = \mathbf{S}^o(\mathbf{x}) + \mathbf{S}^*(\mathbf{x}, H) \tag{13}$$

where $\mathbf{S}^o$ is the compliance of the virgin (undamaged, $H = 0$) material, while $\mathbf{S}^*$ is the perturbation caused by the defect localized in a small region (unit cell) V (Kunin, 1983).

Thus, from (5), with (11) and (13),

$$\epsilon = (\mathbf{S}^o + \mathbf{S}^*) : \sigma = \mathbf{S} : \sigma \tag{14}$$

where

$$\mathbf{S} = \mathbf{S}^o + \mathbf{S}^* = \frac{\partial^2 \psi}{\partial \sigma \partial \sigma} \tag{15}$$

and

$$\mathbf{S}^o = \frac{\partial^2 \psi^o}{\partial \sigma \partial \sigma}\,; \quad \mathbf{S}^* = \frac{\partial^2 \psi^*}{\partial \sigma \partial \sigma}\,. \tag{16}$$

Since the processes for which $dH \neq 0$ are inherently path-dependent (especially in the case of unilateral constraints imposed by cracks), the stress-strain relationship (14) must be cast into an incremental form

$$d\epsilon = \mathbf{S} : d\sigma + d^I\mathbf{S} : \sigma = \mathbf{S} : d\sigma + d^I\epsilon \tag{17}$$

where

$$d^I\mathbf{S} = \frac{\partial \mathbf{S}}{\partial H}\, dH = [\mathbf{S}(\sigma, H + dH) - \mathbf{S}(\sigma, H)] \tag{18}$$

using the notation from Rice (1975).

Consequently, from (5) and (12)

$$d^I\epsilon = \frac{\partial}{\partial \sigma}\, (d^I\psi) \tag{19}$$

Downloaded 03 May 2010 to 171.66.16.31. Redistribution subject to ASME license or copyright; see http://www.asme.org/terms/Terms_Use.cfm

and

$$d^I\mathbf{S}=\frac{\partial^2}{\partial\sigma\partial\sigma}(d^I\psi). \tag{20}$$

Consider now a representative volume V containing a statistically valid sample of grains, defects, and other inhomogeneities. For convenience, this representative volume can be identified with the unit cell mapping on a material point of an effective continuum. In the case of macroscopically homogeneous deformation of this volume, the macroscopic values of stresses and strains are related to the volume averages of the corresponding local (inhomogeneous) fields (Hill, 1967; Rice, 1971).

During an isothermal process at fixed H

$$\epsilon=\frac{1}{V}\frac{\partial\Psi}{\partial\sigma} \tag{21}$$

where $\Psi = V\psi$ is the Gibbs energy of the volume V.

The change in the recorded history dH can be defined by a set of fluxes $d\xi_i$ ($i = 1$ to N) representing in the considered case the change in the size of cracks (bond density) within the volume V. The irreversible change in the Gibbs energy of the volume can be written as a product of fluxes and their affinities such that

$$\sum_k f_j(\sigma,H)d\xi_j\equiv d^I\Psi \tag{22}$$

such that

$$d^I\epsilon=\frac{1}{V}\sum_k\frac{\partial f_k(\sigma,H)}{\partial\sigma}d\xi_k \tag{23}$$

with summation extended over all N operative cracks.

In view of (6) and (8), with $dl = d\xi$ and $f = (G-2\gamma)$, the inelastic change in the strain (averaged over volume V) is

$$d^I\epsilon=\frac{1}{V}\int_L\left[\frac{\partial G}{\partial\sigma}\delta l\right]dL. \tag{24}$$

The energy release rate density is a homogeneous quadratic function of the stress intensity factors k_i ($i = 1, 2, 3$). Following Rice (1975), the energy rate density can be written as

$$G=C_{ij}k_ik_j \tag{25}$$

where the components of the symmetric second-order tensor $\mathbf{C}$ are functions of the overall compliance (i.e., recorded history H). Since the stress intensity factors are homogeneous linear functions of the stress tensor, the expressions (19) and (20) can be, in conjunction with (21) and (25), rewritten as

$$d^I\epsilon_{ij}=\frac{2}{V}\int_L\left[C_{mn}k_m\frac{\partial k_n}{\partial\sigma_{ij}}\delta l\right]dL \tag{26}$$

$$d^IS_{ijmn}=\frac{2}{V}\int_L\left[C_{rp}\frac{\partial k_r}{\partial\sigma_{ij}}\frac{\partial k_p}{\partial\sigma_{mn}}\delta l\right]dL. \tag{27}$$

The expressions (26) and (27) are consistent with the adopted definition of damage. In other words, the process is elastic if $\delta l = 0$ (since no energy is dissipated) even though the crack opening displacement may change with load. In a complete analogy to plasticity, the measurements of compliance, stress and strain components will yield only the informations regarding the increments of damage. The initial state of material is typically considered as "virgin" even though some damage is invariably present.

Kinetics of the Crack Growth. The final step in the formulation of the constitutive law consists of the determination of a functional relationship (damage law) between dl and $d\sigma$ in (24). Typically, a damage law is deduced on the basis of hypothetical arguments based almost exclusively on macro observations. However, as shown by Krajcinovic and Fanella (1986), a constitutive relationship can actually be derived considering stochastic distributions of weak planes and energy barriers on the mesoscale.

In determination of the crack growth pattern of a mesocrack, the stochastic distribution of surface energies (geometry of cleavage planes and grain boundaries) plays a major role. In principle, as the stress levels are gradually raised, a crack can grow (penetrate successive energy barriers) either in a steady (smooth) mode consisting of an infinite number of continuously changing values (σ, l) satisfying (10) or in a jerky manner emphasizing long periods of languor ($\delta l = 0$) interspersed by short, almost instantaneous bursts of rapid changes in the crack size Δl. The latter case appears to be more common in the case of brittle and semibrittle solids in predominantly tensile regimes. The acoustic signature of the energy ΔD (7) released during the rapid increase in the crack size is readily recorded in tests (Holcomb and Costin, 1986).

The crack stability criterion is derivable directly from the entropy production inequality (10). The crack growth is stable if

$$\frac{\partial G}{\partial l}\delta l<0 \tag{28}$$

and unstable when

$$\frac{\partial G}{\partial l}\delta l>0. \tag{29}$$

In the first of the two cases (28), a crack will grow in a steady mode as the stress increases. The second case (29) is characteristic of jerky changes in the crack size.

As an example of arguments leading to the formulation of kinetic equations (Krajcinovic and Fanella, 1986, etc.) consider a specimen weakened by an already existing circular crack small enough to be trapped by the crystalline lattice (Lawn and Wilshaw, 1975). Assuming further, for simplicity, that the loading is proportional, i.e., that $\sigma = q\sigma^r$ (where σ^r is some reference state of stress) the energy release rate can be for the case of jerky changes of crack length written in form

$$G=q^2af(\mathbf{S},\mathbf{n},\beta) \tag{30}$$

where a is the crack radius. The exact form of the function f depends on the overall compliance of the solid, orientation of the crack normal (three Euler angles), and the shape factor β.

A crack will retain its size and shape until the inequality (10) becomes satisfied. Consequently, the cracking condition is in view of (10) and (29)

$$F_c=q^2af-2\gamma>0. \tag{31}$$

The surface energy is randomly distributed within the representative volume.

Assuming, for example, that a crack remains planar and that it grows in a self-similar fashion ($f = f_o$ = const.), and that the surface energies γ_i of equal strengths are separated by distances $2a_i$ the conditions (31) represent a family of hyperbolas in the (a, q) space (Fig. 1). The loads at which a crack changes its size from a_{i-1} to a_i are from (31)

$$q_i=\left\{\frac{2\gamma_i}{a_if}\right\}^{1/2}=q_{i-1}\left\{\frac{\gamma_ia_{i-1}}{\gamma_{i-1}a_i}\right\}^{1/2} \tag{32}$$

where it was assumed that $\gamma_i > \gamma_{i-1}$ and $a_i > a_{i-1}$.

A good example is provided by a brittle polycrystalline solid. A crack of size a_o originally occupies only a part of the cleavage plane of a grain with surface energy γ_o. At some stress level q_o, the crack extends over the entire cleavage plane a_1 before it gets trapped by the grain boundary (with surface energy γ_1). At this point, additional energy input is needed for the crack to penetrate the grain boundary and twist and tilt into the cleavage plane of the adjacent grain (which, incidentally, involves the change in the function f as well). Thus the crack size indeed changes in a stepwise manner with a proviso

Downloaded 03 May 2010 to 171.66.16.31. Redistribution subject to ASME license or copyright; see http://www.asme.org/terms/Terms_Use.cfm

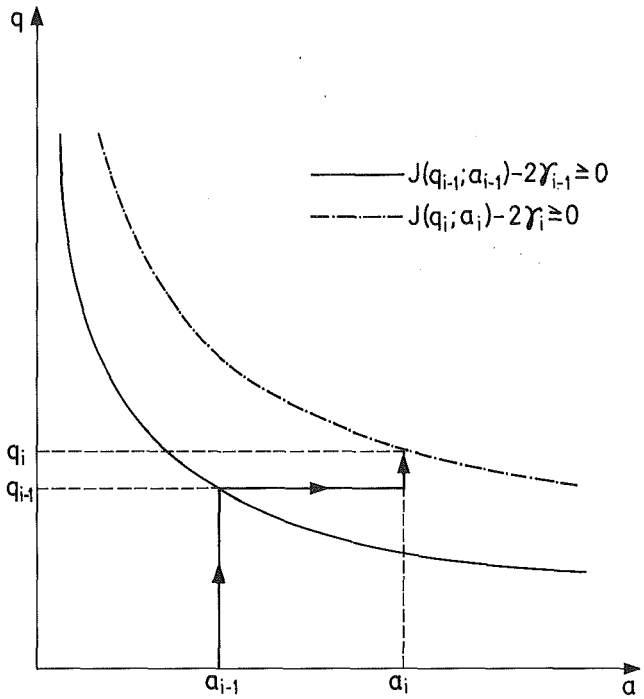


Fig. 1 Spasmodic growth of cracks trapped by successive energy barriers of increasing magnitude

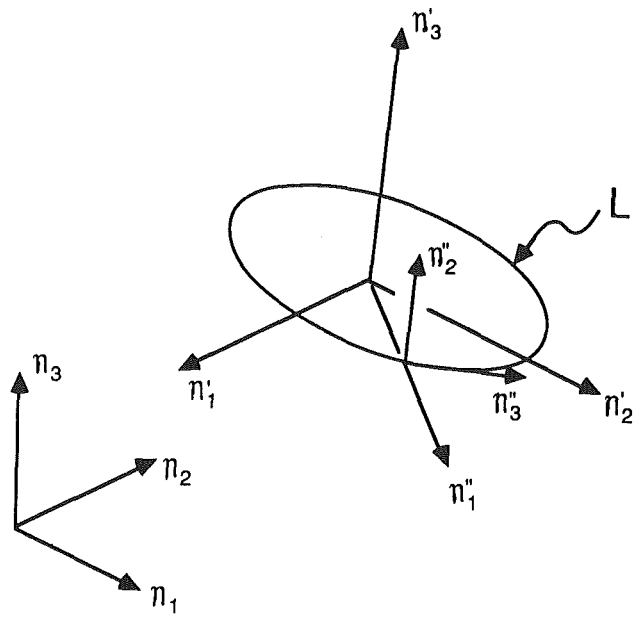


Fig. 2 Global and local (primed and double-primed) coordinate systems defining the orientation of an elliptical crack

that in certain conditions $q_i = q_{i-1}$ which, in most cases, leads to instantaneous splitting.

Solid Weakened by an Ensemble of Cracks

Compliance Tensor. Consider now a case of a perfectly elastic and brittle matrix containing an ensemble of microcracks permeating a large part of its volume. The size of the specimen is considered to be an order or two of magnitude in excess of the size of cracks justifying again the assumption that the solid is infinitely large.

As shown in Kunin (1983), the problem of a solid weakened by N cracks reduces to a system of N integral equations interrelating the external fields $\sigma^{(k)}(\mathbf{x})$ of all N interacting cracks to each other and to the far field stress σ^o. Since the number of cracks N is typically very large (and changing), the "exact" solutions of such a problem are possible only for some simple (and physically unrealistic) en-echelon crack configurations. A parallel approach would involve description of a crack field by means of an infinite set of its many points statistical momenta. The situation is further exacerbated in view of the unilateral constraints imposed by cracks.

Finally, every microcrack, being by definition smaller than the unit cell, is surrounded by a medium characterized by the crack induced anisotropy. The determination of the stress intensity factors **k**, components of the tensor **C** and/or crack opening displacements **b** (see, Barnett and Asaro, 1972; Mura, 1982; Kanninen and Popelar, 1985, etc.) for a crack in an anisotropic solid requires a nontrivial computational effort. Hence, it is obvious that a string of simplifying assumptions is necessary to ensure the tractability of the problem.

Some of the simplifying assumptions are rather easily justified. For example, since the ellipticity of a crack, except in some extreme cases has little influence on the results (Budiansky and O'Connell 1976), assumption that all cracks are circular in shape at all times should not have an adverse effect on the results. A much more radical and far reaching assumption relates to the applicability of the effective field theories. The application of the frequently used and popular self-consistent method (SCM) implies (Kunin, 1983) that:

- the external field of each crack weakly depends on the exact configuration of adjacent cracks, and that
- the external field of each crack is equal to the external field imposed by the far field stresses.

The first two assumptions leads to approximation of the inhomogeneous solid weakened by discrete defects surrounding the observed crack by an effective and homogeneous continuum of unknown compliance **S**. The second assumption obviates the necessity to solve the governing system of integral equations since $\sigma^{(k)} = \sigma^o$. The final fields are obtained via the juxtaposition of perturbations attributed to individual cracks. The solution is, therefore, always possible when the analytical expressions for the stress intensity factor **k**, tensor **C**, and/or crack opening displacement **b** of a single crack embedded into an effective medium are available. Unfortunately, this is the case only when the solid is either isotropic or transversely isotropic (Hoenig, 1978).

Assuming that the conditions warrant an appropriate, effective, medium approximation, consider a single penny-shaped crack embedded into an infinitely extended continuum subjected to far-field macrostresses σ. Conceiving of the crack as an ellipsoid of vanishing thickness h, the eigenstrains within the Eshelby's inclusion (void – see, Hoenig, 1978; Mura, 1982) are

$$\lim_{h\to 0}(h\epsilon^*_{ij}) = \frac{1}{2}\beta'_p(\delta_{ip}\delta_{j3}+\delta_{jp}\delta_{i3}) \tag{33}$$

where

$$b'_p = \beta'_p\sqrt{1-(r/a)^2} \quad (r\leq a) \tag{34}$$

is one-half of the crack opening displacement.

Since the eigenstrains are linear in stresses (Hoenig, 1978)

$$\beta'_n = M_{nm}\sigma'_{3m} \tag{35}$$

where $\mathbf{M} = \mathbf{M}(\mathbf{S})$. In reference to Fig. 2

$$\beta''_n = g'_{nm}\beta'_m \tag{36}$$

where $[g']$ is the rotation matrix with trigonometric functions of the angle θ subtended by axes n'_1 and n''_1 for elements. Also,

$$k'_i = Q_{ij}\beta''_j = Q_{ij}g'_{jk}\beta'_k = Q_{ij}g'_{jk}M_{km}\sigma'_{3m} \tag{37}$$

Downloaded 03 May 2010 to 171.66.16.31. Redistribution subject to ASME license or copyright; see http://www.asme.org/terms/Terms_Use.cfm

where $k_i' = \{K_1, K_{11}, K_{111}\}$ is the vector of stress intensity factors, while $\mathbf{Q} = \mathbf{Q}(\mathbf{S})$.

In the case of isotropic solid (with μ being the shear modulus)

$$Q_{ij} = \frac{\mu}{1-\nu}\sqrt{\frac{\pi}{a}}\ (\delta_{ij} - \nu\delta_{i3}\delta_{j3})$$
$$M_{ij} = \frac{4a}{\mu\pi}\ \frac{1-\nu}{2-\nu}\left(\delta_{ij} - \frac{\nu}{2}\ \delta_{i3}\delta_{j3}\right) \tag{38}$$

while

$$C_{ij} = \frac{1-\nu}{2\mu}\left(\delta_{ij} + \frac{\nu}{1-\nu}\ \delta_{i3}\delta_{j3}\right).$$

After some reasonably simple manipulations from (26),

$$d^I\epsilon_{i3}' = 8\ \frac{1-\nu^2}{VE(2-\nu)}\int_L a(2\sigma_{3i}' - \nu\sigma_{33}'\delta_{i3})\delta a\ dL. \tag{39}$$

In order to rewrite the expression (39) in terms of global coordinates (Fig. 2), it is necessary to use the transformation

$$n_i' = g_{ij}n_j \tag{40}$$

(Krajcinovic and Fanella, 1986) leading to

$$d^I\epsilon_{ij} = \frac{3}{V}\sum_k\int_{L_k} ab_{ijpr}\sigma_{pr}\delta a\ dL \tag{41}$$

where

$$b_{ijpr} = h_{ijpr} + h_{ijrp} \tag{42}$$

and

$$h_{ijpr} = \frac{8(1-\nu)^2}{3E(2-\nu)}\ (\delta_{ip}g_{3j}g_{3r} + \delta_{ir}g_{3j}g_{3p} + \delta_{jp}g_{3r}g_{3i} + \delta_{jr}g_{3i}g_{3p} - 2\nu g_{3i}g_{3j}g_{3r}g_{3p}). \tag{43}$$

The expression for the compliance $\mathbf{S}$ derived by Wu (1985), and later by Krajcinovic and Fanella (1986), can be recovered directly from (41) assuming that $\delta a \neq \delta a(L)$, i.e., self-similar growth of circular cracks. The incremental expressions (26) and (27) are obviously much more general since they allow considerations of nonproportional loads and arbitrary crack shapes.

The expressions (42) and (43) can be readily extended to the case of elliptical cracks and transversely isotropic solids. In all other cases, the analytical expressions for $\mathbf{C}$ and $\mathbf{k}$ are not available. Consequently, the determination of the inelastic strain rate will entail nontrivial numerical effort.

The expression (27) for $d^I\mathbf{S}$ can in view of (41) be rewritten in form

$$d^I\mathbf{S} = \frac{3N}{V}\langle a^2\delta a\mathbf{b}(\phi,\beta)\rangle \tag{44}$$

where the angular brackets stand for the average value. The elements of the $\mathbf{b}(\phi, \beta)$ tensor are functions of the crack orientation. If the crack size and orientation are not correlated,

$$d^I\mathbf{S} = \left(\frac{N}{V}\langle 3a^2\delta a\rangle\right)\langle\mathbf{b}(\phi,p)\rangle \tag{45}$$

where the term in parentheses is the increment of the Budiansky, O'Connell (1976) crack density parameter (for the case of circular cracks).

The utility of the preceding formulas is contingent on the availability of functional relationships between N and δa on one and $d\sigma$ on the other side. Naturally, the form of these relationships, discussed in the preceding section of this paper, depends on the mesostructure of the solid and the state of stress.

In the case of brittle "cleavage 1" response, the number of cracks (introduced during the manufacturing and solidification processes) N is constant. Assuming a monotonically increasing, homogeneous state of macrostresses, the cracks can grow only in the spasmodic, jerky mode. Thus, instead of (41)

$$d^I\boldsymbol{\epsilon} = \frac{1}{V}\ [N_o\langle 3a_o^2\delta a_o\mathbf{b}\rangle + N_1\langle 3a_1^2\delta a_1\mathbf{b}\rangle + \ \ldots\ ]:\boldsymbol{\sigma} \tag{46}$$

where

$$N = N_o + N_1 + \ldots$$

with N_i standing for the number of cracks with radius a_i.

In view of the stochastic morphology of the mesostructure, the initial crack radii a_o, distances separating the energy barriers a_1, a_2, etc., are defined by appropriate probability density functions $p(a_i)$. Consequently, the sums in (42) can be recast into integrals as shown in Krajcinovic and Fanella (1986), Krajcinovic and Sumarac (1987, 1987a), etc.

The derivation of the inelastic strain rate (41) for larger crack concentrations (involving crack interaction) presents a much more difficult problem. Formally, using the higher order effective field theories (or even approximate expressions for the direct interaction of cracks, Kachanov (1987)), it is not very difficlut to rederive the expressions similar to (41) and (44). However, since the components of the tensor $\mathbf{b}$ are both explicit and implicit functions of the overall compliance, the computations by necessity involve an iterative, predictor-corrector numerical algorithm (Sumarac and Krajcinovic, 1987).

In contrast to the previously suggested models, the proposed formulation utilizes stress concentration factors rather than eigenstrains. Since the exact and approximate expressions for the former are much more readily available in the literature, the proposed formulation (while formally equal to the older) is more suitable for applications.

Summary and Conclusions

The principal objective of this paper was to explore the least restrictive set of assumptions and simplifications leading to a constitutive theory for brittle deformation processes which: (*i*) will reflect the salient aspects of the physical phenomenon, and (*ii*) still be simple enough for practical applications. These conflicting requirements are found to be satisfied by a model which completely ignores the crack interaction but, in return, admits a closed-form, analytical solution.

In the case of uniaxial tension, compression or pure bending of unconfined brittle solids, the ultimate failure emphasizes runaway propagation of a single, critical defect at relatively low crack density. Consequently, the simplest model, based on (39) and (41), should be expected to be of adequate accuracy.

In the presence of lateral confinement above the transition point (Horii and Nemat-Nasser, 1986) at incipient localization (just ahead of the apex of the stress-strain curve), the crack interaction cannot be any more neglected. Within this relatively short phase of the deformation process, the simplest model will underestimate the inelastic strain. The ensuing increase in accuracy in the determination of the inelastic strains will not justify the attendant increase in complexity. However, a rational estimate of the macrofailure must obviously incorporate direct interaction of closely-spaced defects.

Acknowledgments

The authors of this paper gratefully acknowledge the financial support for this work rendered by the Air Force Office of Scientific Research, Directorate of Aerospace Sciences, Civil Engineering Program to the University of Illinois at Chicago.

References

Barnett, D. M., and Asaro, R. J., 1972, "The Fracture Mechanics of Slit-Like Cracks in Anisotropic Elastic Media," *J. Mech. Phys. Solids*, Vol. 20, pp. 353-366.

Downloaded 03 May 2010 to 171.66.16.31. Redistribution subject to ASME license or copyright; see http://www.asme.org/terms/Terms_Use.cfm

Budiansky, B., and O'Connell, R. J., 1976, "Elastic Moduli of a Cracked Solid," *Int. J. Solids Struct.*, Vol. 12, pp. 81-97.

Chaboche, J. L., 1979, "Le concept de contraint effective applique a l'elasticite et la viscoplasticite en presence d'un endommagement anisotrope," Report Colloq. Euromech 115, Grenoble, France.

Hart, E. W., Li, C. Y., and Wire, G. L., 1975, "Phenomenological Theory A Guide to Constitutive Relations and Fundamental Deformation Properties," *Constitutive Equations in Plasticity*, A. Argon, ed., MIT Press, Cambridge, Mass.

Hill, R., 1967, "The Essential Structure of Constitutive Laws for Metal Composites and Polycrystals," *J. Mech. Phys. Solids*, Vol. 15, pp. 79-95.

Hoenig, A., 1978, "The Behavior of a Flat Elliptical Crack in an Anisotropic Body," *Int. J. Solids Struct.*, Vol. 14, pp. 925-934.

Hoenig, A., 1979, "Elastic Moduli of a Non-randomly Cracked Body," *Int. J. Solids Struct.*, Vol. 15, pp. 137-154.

Holcomb, D. J., and Costin, L. S., 1986, "Detecting Damage Surfaces in Brittle Materials using Acoustic Emissions," ASME JOURNAL OF APPLIED MECHANICS, Vol. 53, pp. 536-544.

Horii, H., and Nemat-Nasser, S., 1983, "Overall Moduli of Solids with Microcracks: Load Induced Anisotropy," *J. Mech. Phys. Solids*, Vol. 31, pp. 155-171.

Horii, H., and Nemat-Nasser, S., 1986, "Brittle Failure in Compression: Splitting, Faulting and Brittle-Ductile Transition," *Phil. Trans. Royal Soc. London*, Vol. A319, pp. 337-374.

Ilankamban, R., and Krajcinovic, D., 1987, "A Constitutive Theory for Progressively Deteriorating Brittle Solids," *Int. J. Solids Structures*, Vol. 23, pp. 1521-1534.

Kachanov, L. M., 1958, "On the Creep Rupture Time," *Izv. AN SSSR*, Otd. Tekhn. Nauk, Vol. 8, pp. 26-31.

Kachanov, M., 1982, "A Microcrack Model of Rock Inelasticity – Part I," *Mech. of Materials*, Vol. 1, pp. 19-27.

Kachanov, M., 1987, "Elastic Solids with Many Cracks: A Simple Method of Analysis," *Int. J. Solids Structures*, Vol. 23, pp. 23-35.

Kanninen, M. F., and Popelar, C. H., 1985, *Advanced Fracture Mechanics*, Oxford University Press, New York.

Krajcinovic, D., 1984, *Continuous Damage Mechanics*, ASME *Appl. Mech. Rev.*, Vol. 37, pp. 1-6.

Krajcinovic, D., 1985, "Continuum Damage Mechanics Revisited: Basic Concepts and Definitions," ASME JOURNAL OF APPLIED MECHANICS, Vol. 52, pp. 892-834.

Krajcinovic, D., and Fanella, D., 1986, "A Micromechanical Damage Model for Concrete," *Eng. Fracture Mech.*, Vol. 5/6, pp. 585-596.

Krajcinovic, D., and Sumarac, D., 1987, "Micromechanically Based Damage Models," *Proc. 10th US National Congress of Applied Mechanics*, J. P. Lamb, ed., ASME, New York.

Krajcinovic, D., and Sumarac, D., 1987a, "Micromechanics of the Damage Processes," *Continuum Damage Mechanics: Theory and Application*, D. Krajcinovic and J. Lemaitre, eds., Springer-Verlag, Wien, Austria, 1987.

Kunin, I. A., 1983, *Elastic Media with Microstructure II, Three-Dimensional Models*, Springer-Verlag, Berlin.

Lawn, B. R., and Wilshaw, T. R., 1975, *Fracture of Brittle Solids*, Cambridge Univ. Press, Cambridge, UK.

Lemaitre, J., and Chaboche, J.-L., 1985, *Mecanique des materiaux solides*, Dunod, Paris, France.

Mura, T., 1982, *Micromechanics of Defects in Solids*, M. Nijhoff Publ., The Hague, The Netherlands.

Rice, J. R., 1975, "Continuum Mechanics and Thermodynamics of Plasticity in Relation to Microscale Deformation Mechanisms," *Constitutive Equations in Plasticity*, A. Argon, ed., MIT Press, Cambridge, Mass.

Sumarac, D., and Krajcinovic, D., 1987, "A Self-Consistent Model for Microcrack-Weakened Solids," *Mech. of Mater.*, Vol. 6, pp. 39-52.

Wu, C. H., 1985, "Tension-Compression Test of a Concrete Specimen via Damage Theory," *Damage Mechanics and Continuum Modeling*, N. Stubbs and D. Krajcinovic, eds., ASCE, New York, pp. 1-12.

Downloaded 03 May 2010 to 171.66.16.31. Redistribution subject to ASME license or copyright; see http://www.asme.org/terms/Terms_Use.cfm

Dragoslav Sumarac
Civil Engineering Department,
University of Belgrade,
Belgrade, Yugoslavia

Dusan Krajcinovic
Department of Civil Engineering, Mechanics,
and Metallurgy,
University of Illinois at Chicago,
Chicago, IL 60680
Fellow, ASME

A Mesomechanical Model for Brittle Deformation Processes: Part II

The approximate, closed-form solutions for the inelastic strain and compliances are derived for some simple plane stress and plane strain cases. The computations are performed for a model-ignoring crack interaction as well as for the case of the self-consistent model.

Introduction

The expressions for the inelastic strains and compliances derived in Part I of this paper are directly applicable whenever the conditions and circumstances render the self-consistent method (SCM) an adequate approximation of the physical phenomena. The utility of these expressions is contingent on the availability of the analytical (exact or approximate) expressions for the stress intensity factors (SIF), energy release rate or the crack opening displacements. Within these limitations, the proposed model provides an exact solution for the brittle "cleavage 1" processes characterized by the relatively modest crack concentrations and the splitting macrofailure mode. Consequently, the proposed model applies to a wide class of materials such as concrete, rocks, ceramics, etc., subjected to loads in absence of large lateral confinements.

For simplicity and economy of space, the discussion will, in the sequel, focus on the plane stress and strain conditions. For each case, the governing equations will be derived for two levels of approximation:

- Taylor's model (TM) assuming no interaction at all, i.e., considering that each crack is embedded in the virgin (undamaged) continuum, and
- SCM assuming that the external field of each crack weakly depends on the exact position of the surrounding defects.

In both cases the actual, defect weakened, solid surrounding a crack is approximated by an effective continuum. In the case of the TM, the effective continuum is identical to the undamaged solid. In the case of SCM, the effective continuum acknowledges the existence of the adjacent cracks (using only the first statistical moment as a measure) assuming, additionally, that the stress on each crack is equal to the macro (far field) stress.

Contributed by the Applied Mechanics Division of THE AMERICAN SOCIETY OF MECHANICAL ENGINEERS for presentation at the Winter Annual Meeting, San Francisco, Calif., December 10–15, 1989.

Discussion of this paper should be addressed to the Editorial Department, ASME, United Engineering Center, 345 East 47th Street, New York, N.Y. 10017, and will be accepted until two months after final publication of the paper itself in the JOURNAL OF APPLIED MECHANICS. Manuscript accepted by ASME Applied Mechanics Division, February 8, 1988.

Paper No. 89-WA/APM-2.

Compliance Tensor

In two-dimensional problems, it is often convenient to use the Voigt notation

$$\{\tau_1,\tau_2,\tau_6\} \equiv \{\sigma_{11},\sigma_{22},\sigma_{12}\}$$
$$\{e_1,e_2,e_6\} \equiv \{\epsilon_{11},\epsilon_{22},2\epsilon_{12}\}. \quad (1)$$

Single Slit in Isotropic Continuum. Consider first a single open slit of length $2a$ in an infinitely extended, isotropic, and perfectly elastic solid. The SIF are

$$k_1 = K_I = \tau_2'\sqrt{\pi a}$$
$$k_2 = K_{II} = \tau_6'\sqrt{\pi a} \quad (2)$$

where primes indicate reference to the local coordinate system embedded in the slit and oriented as shown in Fig. 1. Knowing the expressions for the strain energy release rate (Kanninen and Popelar, 1985), the tensor **C** (I.38) is an identity tensor

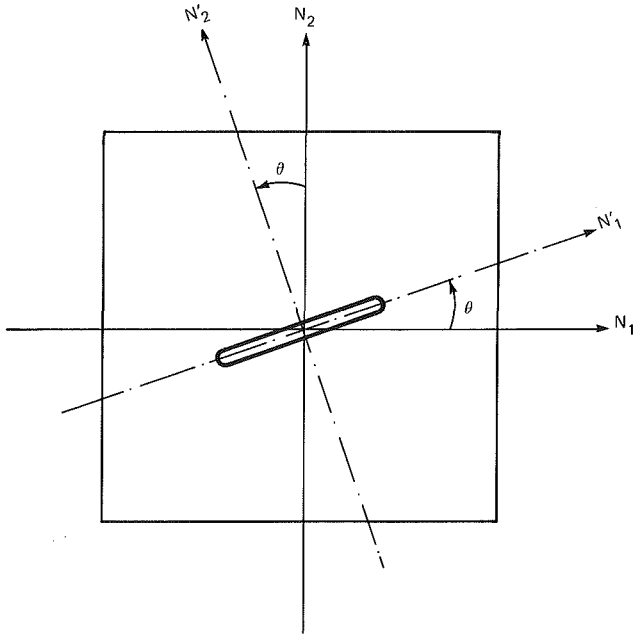


Fig. 1 Global and local coordinate systems of a two-dimensional slit

Copyright © 1989 by ASME

Downloaded 03 May 2010 to 171.66.16.31. Redistribution subject to ASME license or copyright; see http://www.asme.org/terms/Terms_Use.cfm

$$C_{pq} = \frac{1}{E'}\,\delta_{pq} \tag{3}$$

where

$$E' = \begin{cases} E & \text{(plane stress)} \\ E/(1-\nu^2) & \text{(plane strain)} \end{cases} \tag{4}$$

Consequently, from (I.25) the strain energy release rate averaged over the area A of the representative (unit cell) surface is

$$G = J = C_{mn}k_m k_n = \frac{\pi a}{AE'}\,[(\tau_2')^2 + (\tau_6')^2]. \tag{5}$$

The strain energy associated with the presence of an open slit is

$$\Psi^* = \frac{2}{A}\int_o^a G\,da = \frac{\pi a^2}{AE'}\,[(\tau_2')^2 + (\tau_6')^2] \tag{6}$$

Thus, the compliance associated with the open slit is from (I.16)

$$S_{ij}^{(k)'} = \frac{4}{a}\int_o^a C_{pq}\,\frac{\partial k_p}{\partial \tau_i'}\,\frac{\partial k_q}{\partial \tau_j'}\,da = \frac{2\pi a^2}{AE'}\,(\delta_{2i}\delta_{2j} + \delta_{6i}\delta_{6j}). \tag{7}$$

In order to sum the contributions of all slits, the expression (7) for the compliance must be rewritten in terms of the global coordinate system. This is accomplished by a simple orthogonal transformation (Horii and Nemat-Nasser, 1983)

$$S_{ij}^{(k)} = S_{mn}^{(k)'}\,g_{mi}g_{nj} = \frac{2\pi a^2}{AE'}\,(g_{2i}g_{2j} + g_{6i}g_{6j}) \tag{8}$$

where the matrix of the rotation tensor $[g]$ is

$$[g] = \begin{bmatrix} \cos^2\theta & \sin^2\theta & \sin 2\theta \\ \sin^2\theta & \cos^2\theta & -\sin 2\theta \\ -\frac{1}{2}\sin 2\theta & \frac{1}{2}\sin 2\theta & \cos 2\theta \end{bmatrix} \tag{9}$$

with θ being the angle subtended by n_i' and n_i''(Fig. 1).

Single Slit in Anisotropic Continuum. The corresponding expressions can be also derived for the case of an anisotropic continuum weakened by a sharp, straight slit of length $2a$. The derivation is facilitated by the fact that the anisotropy has no influence (Sih et al., 1965) on the SIF which are, again, given by (2). However, the determination of the tensor $\mathbf{C}$ (I.25) requires lengthy derivation (Sumarac, 1987).

The strain energy release rates for the slit associated with Mode I and Mode II (Sih et al., 1965) are

$$\begin{aligned} J_1 &= -\frac{k_1}{2}\,S_{22}'\,Im\left[\frac{k_1(\lambda_1'+\lambda_2')+k_2}{\lambda_1'\lambda_2'}\right] \\ J_2 &= \frac{k_2}{2}\,S_{11}'\,Im[k_2(\lambda_1'+\lambda_2')+k_1\lambda_1'\lambda_2'] \end{aligned} \tag{10}$$

where

$$\begin{aligned} \lambda_j' &= r_j + is_j' \\ \bar{\lambda}_j &= r_j - is_j' \end{aligned} \qquad (j=1,2;\ r_j'\geq 0,\ s_j'\geq 0) \tag{11}$$

are the roots of the characteristic equation

$$S_{11}'(\lambda')^4 - 2S_{16}(\lambda')^3 + (2S_{12}' + S_{66}')(\lambda')^2 - 2S_{26}'\lambda' + S_{22}' = 0. \tag{12}$$

Substituting (11) into (10), the strain energy release rate can be written as

$$G = J_1 + J_2 = C_{pq}^a k_p k_q \tag{13}$$

where the components of the tensor $\mathbf{C}$ are derived in the form

$$C_{ij}^a = \frac{1}{2}\begin{bmatrix} S_{22}\left(\frac{s_1}{r_1^2+s_1^2} + \frac{s_2}{r_2^2+s_2^2}\right) & S_{22}\,\frac{r_1s_2 + r_2s_1}{(r_1^2+s_1^2)(r_2^2+s_2^2)} \\ S_{11}(r_1s_2 + r_2s_1) & S_{11}(s_1+s_2) \end{bmatrix}' \tag{14}$$

Finally, the strain energy attributable to the presence of a single open slit in an anisotropic two-dimensional solid is

$$\Psi^* = \frac{\pi a^2}{2A}\left\{S_{22}\left(\frac{s_1}{r_1^2+s_1^2} + \frac{s_2}{r_2^2+s_2^2}\right)\tau_2^2 + \left[S_{11}(r_1s_2 + r_2s_1) + S_{22}\,\frac{r_1s_2 + r_2s_1}{(r_1^2+s_1^2)(r_2^2+s_2^2)}\right]\tau_2\tau_6 + S_{11}(s_1+s_2)\tau_6^2\right\}' \tag{15}$$

where all terms in (14) and (15) are primed (i.e., refer to the crack coordinate system). The second of the three terms on the right-hand side of (15) presents the interaction of the Mode I and Mode II characteristic of anisotropic solids.

Ensemble of Slits. Consider now a problem of N open slits within the representative surface area A. The compliance of the effective continuum at $\mathbf{x} = \mathbf{x}_o$ is obtained simply by superposition of individual compliances computed for each of N open slits, i.e.,

$$\mathbf{S}(\mathbf{x}_o, H) = \mathbf{S}^o(\mathbf{x}_o) + \mathbf{S}^*(\mathbf{x}_o, H) = \mathbf{S}^o + \sum_k \mathbf{S}^{(k)} \tag{16}$$

where $\mathbf{s}^o(\mathbf{x}_o)$ is the compliance of the undamaged (virgin) solid. The compliance attributable to a single open crack is given by expressions (7) or (8).

Assuming, for simplicity, that the slit length $2a$ is constant, the second term on the right-hand side of (16) after averaging is

$$\mathbf{S}^* = \frac{2\pi a^2 N}{E'A} < \mathbf{g}(\theta) > = \frac{2\pi a^2 N}{E'A}\int_{\theta_1}^{\theta_2} \mathbf{g}(\theta)\,d\theta \tag{17}$$

where

$$g_{ij}(\theta) = g_{2i}g_{2j} + g_{6i}g_{6j} \tag{18}$$

is a function of θ only in the case of TM (8) or of $\mathbf{S}$ and θ in the case of SCM

$$g_{ij}(\theta, \lambda) = E' C_{pq}^a g_{pi} g_{qj}. \tag{19}$$

The limits θ_1 and θ_2 in (17) define the fan $\theta_1 \leq \theta < \theta_2$ of all open slits in A.

For example, if the damage is isotropic (Lemaitre and Chaboche, 1986) $\theta_1 = 0$ and $\theta_2 = 2\pi$ the nonzero components of the compliance tensor are for the case of plane stress

$$S_{11}^* = S_{22}^* = \frac{\omega}{E} \qquad S_{66}^* = 2\,\frac{\omega}{E} \tag{20}$$

where

$$\omega = \frac{N\pi a^2}{A} \tag{21}$$

is the nondimensional damage parameter (Budiansky and O'Connell, 1976). For the case of plane strain, the expressions (20) are premultiplied by $(1-\nu^2)$ where E and ν are the elastic parameters of the slit-weakened solid.

In the cae of small slit concentration (TM)

$$\frac{E}{E_o} = \frac{\nu}{\nu_o} = \frac{1}{1+\omega} \qquad \text{(plane stress)} \tag{22}$$

and

Downloaded 03 May 2010 to 171.66.16.31. Redistribution subject to ASME license or copyright; see http://www.asme.org/terms/Terms_Use.cfm

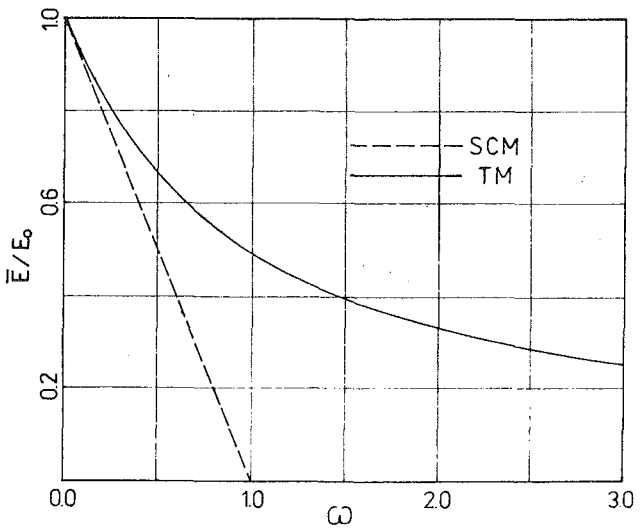


Fig. 2 The elastic modulus of a brittle solid specimen weakened by a random (isotropic) slit distribution (SCM—self-consistent model, TM—Taylor model)

$$\frac{E}{E_o} = \frac{(1-\nu_o\omega)^2-\nu_o^2}{(1+\omega)(1-\nu_o\omega)^2(1-\nu_o^2)}\,; \quad \frac{\nu}{\nu_o} = \frac{1}{1-\nu_o\omega} \tag{23}$$

for the case of plane strain.

In the SCM approximation, solving (16) in conjunction with (19) leads to the following expressions

$$\frac{E}{E_o} = \frac{\nu}{\nu_o} = 1-\omega \qquad \text{(plane stress)} \tag{24}$$

and

$$\frac{E}{E_o} = \frac{(1-\omega)(1+\nu_o-2\nu_o\omega)}{(1+\nu_o)(1-\nu_o\omega)^2}\,; \quad \frac{\nu}{\nu_o} = \frac{1-\omega}{1-\nu_o\omega} \tag{25}$$

for the case of plane strain. The elastic modulus of the effective continuum is plotted versus the "damage" parameter ω in Fig. 2 for the case of plane stress. It is interesting that the SCM breaks down if $\omega>1$ since the effective moduli acquires negative values. This is not the case for TM which, therefore, lacks an inherent indication that the method ceases to be valid for larger slit densities.

A comprehensive study of the elastic moduli of a brittle solid weakened by specific patterns of microcracks was just published in an excellent paper by Laws and Brockenbrough (1987). Their work can, if desired, be incorporated into the process model to be developed in the sequel.

Kinetic Equations

The condition which must be satisfied for a crack (slit) to commence growing has been derived in Part I from the thermodynamic considerations as

$$F_c^{(k)} = (G-2\gamma)_{(k)} \geq 0 \tag{26}$$

where the subscript (k) identifies a specific crack within A. Application of (26) necessitates rewritting G (5) in terms of the stresses defined in the global coordinate system. Using again the transformation rule

$$(\tau_m')^2 = g_{mi}g_{mj}\tau_i\tau_j \qquad (m=2,6) \tag{27}$$

the expression (26) can be cast in form

$$F_c^{(k)} = \tau_i\tau_j(g_{2i}g_{2j}+g_{6i}g_{6j})_{(k)} - \tau_o^2 \geq 0 \tag{28}$$

where

$$\tau_o^2 = 2\frac{\gamma_o E'}{\pi a_o}\,. \tag{29}$$

Geometrically, the condition (28) represents an ellipse in the space of stresses. For all points within the ellipse (28), the kth crack retains its size $2a_o$. When $F_c^{(k)}$ becomes equal to zero, the slit becomes unstable and commences growing. The inner envelope of all ellipses computed for each of N open slits represents the flow potential separating the locus of all points which can be reached without irreversible changes in the mesostructure of the solid from the rest of the stress space.

As an illustration, consider the case of a perfectly brittle specimen subjected to monotonically increasing uniaxial tension associated with tractions q applied in the direction of the n_2-axis

$$\tau_i = q\delta_{2i}. \tag{30}$$

The Griffith criterion (28) can be rewritten as

$$F_c^{(k)} = q^2\cos^2\theta - q_o^2 = 0 \tag{31}$$

where $q_o=\tau_o$.

As already pointed out, the pattern in which a crack grows through the mesostructure depends not only on the stresses but even more so on the geometry of the weak planes (planes with minimum surface energy such as cleavage planes in crystals, phase interfaces in composites, etc.). Thus, instead of (26), it appears more reasonable, and certainly simpler, to use the maximum stress criterion (Krajcinovic and Fanella, 1986; Sumarac and Krajcinovic, 1987)

$$F_c^{(k)} = K_I^{\{k\}} - K_{IC}^{o(k)} = 0 \tag{32}$$

where $K_{IC}^{o(k)}$ is the critical stress intensity factor for the given crystalline cleavage plane (or phase interface). Consequently, with (2a)

$$F_c^{(k)} = q\,\cos^2\theta\sqrt{\pi a_o} - K_{IC}^o = 0. \tag{33}$$

The first crack which will become critical (33) must be perpendicular to the tensile axis $\theta=0$. The onset of the nonlinear response occurs, therefore, at

$$q_o = K_{IC}^o(\pi a_o)^{-1/2}. \tag{34}$$

As the externally applied load q is increased beyond q_o, the slits of less preferential orientation will also become critical. The limits of the fan containing all slits which will increase in size $\theta_1 \leq \theta \leq \theta_2$ can be determined from (33) as

$$\theta_{1,2} = \pm\cos^{-1}[(q_o/q)^{1/2}]. \tag{35}$$

Since the slits are obviously unstable in the considered case, once the equality (33) is satisfied, they will keep growing (I.29) until trapped by an energy barrier (grain boundary or any other region of large enough K_{IC}). Assuming that the energy barriers are separated by distance $2a_1$ (for example, the grain diameter, size of the aggregate) at any point $q>q_o$, all N open slits will belong to one of the two sets

$$\begin{aligned} &\{a,\theta,q;\ a=a_o;\ F_c<0\}\in H_o \\ &\{a,\theta,q;\ a=a_1;\ F_c>0\}\in H_1. \end{aligned} \tag{36}$$

If N is the number of all open cracks which are initially randomly distributed over the representative area A, then from (35)

$$N_1 = \frac{2\theta_1}{\pi}N \qquad N_o = N-N_1 \tag{37}$$

are the number of cracks in sets H_1 and H_o, respectively.

If the mesostructure contains even higher energy barriers, the procedure will have to be repeated once again. All cracks will then be classified with respect to their size into three sets similar to (36).

Process Model

Once the expressions for the compliances and the stability criteria are established, it is possible to combine them into a complete process model enabling the determination of

Downloaded 03 May 2010 to 171.66.16.31. Redistribution subject to ASME license or copyright; see http://www.asme.org/terms/Terms_Use.cfm

macrostrains for any load level. For simplicity, discussion will be, at this point, limited to: monotonically increasing uniaxial tension, "cleavage 1" processes (Ashby, 1979) and TM and SCM approximations. The restriction to TM and SCM approximations is justified in view of the fact that most of the brittle ceramics and concretes are indeed characterized by "cleavage 1" (N=const.) response. In that case, the macrofailure is traceable to the runaway propagation of a single, preferentially-oriented crack (Horii and Nemat-Nasser, 1986; Rudnicki, 1977) occurring at reasonably modest damage levels. For simplicity, the initial crack distribution will be regarded as isotropic and the grain size a constant.

Taylor's Model. The individual slits change their size spasmodically in finite increments $\Delta a = a_1 - a_o$. The sequence in which they become critical (and change their size) is governed by their orientation (33). Thus, from (8)

$$\Delta^I S_{ij}^{(k)} = S_{ij}^{(k)}(a_1) - S_{ij}^{(k)}(a_o) = \frac{2\pi}{AE'}(a_1^2 - a_0^2)(g_{2i}g_{2j} + g_{6i}g_{6j}). \tag{38}$$

In the case of monotonically-incremented tensile loading, the strain energy release rate of each slit will be a nondecreasing function of loads. Consequently, slits will not heal ($\Delta a > 0$) and the compliance attributable to the presence of open cracks at a particular load level can be written as

$$S_{ij}^{*} = N_1 < S_{ij}^{(k)}(a_1) > + (N - N_1) < S_{ij}^{(k)}(a_o) > \tag{39}$$

assuming existence of only two classes of energy barriers (with surface energies γ_o and γ_1). This situation is typical of concrete (Zaitsev, 1982). The aggregate-cement paste has the smallest surface energy which is approximately two times smaller than that of the cement paste. The toughness of the aggregate is at least an order of magnitude higher precluding any cracking through the aggregate. The same situation exists in polycrystalline ceramics having different surface energies of cleavage planes and grain boundaries.

From (39), with (17) and (37),

$$S_{ij}^{*} = \frac{2Na_1^2}{AE'}\left[\frac{2\theta_1}{\pi}\int_0^{\theta_1} g_{ij}(\theta)d\theta + \rho^2\left(1 - \frac{2\theta_1}{\pi}\right)\int_{\theta_1}^{\pi/2} g_{ij}(\theta)\, d\theta\right] \tag{40}$$

where

$$\rho = a_o/a_1 < 1 \tag{41}$$

is an aspect ratio defining the mesostructure.

In the case of TM, the quadratures in (41) are trivial allowing derivation of analytical expression for the components of the compliance tensor. Since a_o and a_1 are constant in the case of plane stress, the axial compliance is

$$E_o S_{11}^{T} = 1 + \omega_1\left\{\left(1 - \frac{2}{\pi}p_1\right)\rho^2 + \left[\frac{2}{\pi}p_1 - \left(1 - \frac{2}{\pi}p_1\right)\rho^2\right]\frac{2}{\pi}[p_1 - p(1-p^2)^{1/2}]\right\} \tag{42}$$

where

$$\omega_1 = \frac{N\pi a_1^2}{A} \qquad p = \sqrt{q_o/q} \quad p_1 = \cos^{-1}p \tag{43}$$

with superscript T standing for the TM. The expression for the lateral compliance is obtained from (42) changing the sign in front of the second term in the last bracket on the right-hand side.

In the case of plane strain, the expressions (42) are simply premultiplied by $(1-\nu_o^2)$. The upper and lower bound for the TM compliances (42) are obtained assuming isotropic distribution of slits with lengths $2a_o$ and $2a_1$, respectively. Thus,

$$\begin{aligned} S_{11}^{o}(1+\omega_o) \le S_{11}^{T} \le S_{11}^{o}(1+\omega_1) \\ S_{22}^{o}(1+\omega_o) \le S_{22}^{T} \le S_{22}^{o}(1+\omega_1) \end{aligned} \tag{44}$$

with

$$\omega_o = \frac{N\pi a_o^2}{A}. \tag{45}$$

Self-Consistent Model. The determination of the compliances attributable to the existence of an ensemble of open slits in an anisotropic solid is replete with computational difficulties. Not the least of these consists of finding the roots of the characteristic equation (12). The situation is considerably simpler in the case of transverse isotropy which would indeed occur if an originally isotropic solid is subjected to uniaxial tension. In principal coordinates **n**, the overall compliance tensor has in a two-dimensional case the following form

$$\mathbf{S} = \begin{bmatrix} S_{11} & S_{12} & 0 \\ S_{12} & S_{22} & 0 \\ 0 & 0 & 2(S_{11} - S_{12}) \end{bmatrix}. \tag{46}$$

The characteristic equation (12) reduces to a biquadratic form

$$\lambda^4 + 2\lambda^2 + m = 0 \tag{47}$$

where

$$m = S_{22}/S_{11}. \tag{48}$$

The roots of the biquadratic algebraic equation (47) are

$$\lambda_{1,2}^2 = -1 \pm \sqrt{1-m}. \tag{49}$$

In the considered case $m > 1$ rendering the roots complex conjugate

$$\begin{aligned} \lambda_1, \bar{\lambda}_1 &= r_1 \pm is_1 \\ \lambda_2, \bar{\lambda}_2 &= r_2 \pm is_2 \end{aligned} \tag{50}$$

where

$$\begin{aligned} r_1 = -r_2 = r = \sqrt{\frac{1}{2}(m^{1/2} - 1)} \\ s_1 = s_2 = s = \sqrt{\frac{1}{2}(m^{1/2} + 1)} \end{aligned} \tag{51}$$

for principal planes.

For all other planes, the matrix (47) is full and the attendant characteristic equation is not amenable to a closed-form solution. However, the roots $\lambda_k'(\theta)$ for a plane subtending an angle θ with the isotropy axis are provided by means of the transformation (Lekhnitski, 1981)

$$\lambda_k' = \frac{\lambda_k \cos\theta - \sin\theta}{\lambda_k \sin\theta + \cos\theta} \tag{52}$$

where λ given by (50) are solutions of (47). The form identical to (52) applies to the complex conjugates $\bar{\lambda}_i$.

The expressions for the components of the compliance tensor are derived after rather arduous derivation in form

$$S_{ij}^{(k)} = \frac{2\pi a^2}{A} C_{pq}^{a} g_{pi} g_{qj} \quad (p,q = 2,6;\ i,j = 1,2,6) \tag{53}$$

where C_{pq}^{a} is given by (14) with

$$\begin{aligned} r_1' &= w_1 r(r\sin 2\theta + \cos 2\theta) & s_1' &= s w_1 \\ r_2' &= w_2 r(r\sin 2\theta - \cos 2\theta) & s_2' &= s w_2 \end{aligned} \tag{54}$$

$$w_{1,2} = (m^{1/2}\sin^2\theta + \cos^2\theta \pm r\sin 2\theta)^{-1}.$$

Proceeding in the same manner as before, the expressions for the compliances attributed to the presence of N open slits with lengths $2a_o$ and $2a_1$ within area A are derived in form

$$S_{ij}^{*} = \frac{2Na_1^2}{A}\left\{\frac{2\theta_1}{\pi}\int_0^{\theta_1} C_{pq}^{a}(\theta,m) g_{pi} g_{qj} d\theta + \left(1 - 2\frac{\theta_1}{\pi}\right)\rho^2 \times \int_{\theta_1}^{\pi/2} C_{pq}^{a}(\theta,m) g_{pi} g_{qj} d\theta\right\} \quad (p,q = 2,6;\ i,j = 1,2,6) \tag{55}$$

Downloaded 03 May 2010 to 171.66.16.31. Redistribution subject to ASME license or copyright; see http://www.asme.org/terms/Terms_Use.cfm

It is important to note that the components of the tensor $\mathbf{S}^*$ are both implicit (through m) and explicit functions of $\mathbf{S}$. Using the matrix notation from (16) and (55), it follows that

$$\{S\} = \{S^o\} + [c(m)]\{S\}. \tag{56}$$

Thus, the components of the overall compliance tensor can be computed solving the matrix equation (Krajcinovic and Sumarac, 1987)

$$\{S\} = [I - c(m)]^{-1}\{S^o\}. \tag{57}$$

Since the matrix $[c]$ (obtained through quadratures in (55)) depends on the ratio of two principal overall compliances $\mathbf{S}$, the solution of (57) obviously entails an iterative, predictor-corrector algorithm at each load increment. Generally, the algorithm is rather simple consisting of predicting m (48), computing $\mathbf{S}$ from (57), and checking whether the predicted value of m is sufficiently accurate to proceed to the next loading increment.

The iterations converged rapidly in all of the considered cases of proportional loading during which the crack patterns change in the orderly fashion (characterized by a monotonic increase of the fan of destabilized slits (35)). In the case of nonproportional loadings, the fan (35) will, in general, change its shape in an abrupt manner making predictions of m a much more venturesome proposition.

The final failure is assumed to occur when a slit of size $2a_1$ becomes critical, i.e., when the stress intensity factor exceeds K_{IC}^m characterizing the energy barriers (say, the energy needed to extend the slit through the grain boundary). Knowing a specific value of K_{IC}^m, it is rather straightforward to determine on the basis of (33) the load intensity

$$q_n = K_{IC}^m (\pi a_1)^{-1/2} \tag{58}$$

at which the slit at the preferential orientation ($\theta = 0$) becomes critical and breaks through the energy barrier. At this point it is unlikely that the slit can be arrested, i.e., the macro failure occurs in the splitting mode.

Numerical Results

For both of the considered models, the deformation develops in a succession of two phases:

(a) $q < q_o$, the response is linearly elastic and isotropic,

(b) $q > q_o$, the process becomes dissipative and the response transversely isotropic and nonlinear.

In unloading ($\delta a = 0$), the compliance is constant (I.27) and the inelastic rate of change of strains is zero as well (I.26). The stress-strain relationship along the unloading segment of the path is from (I.17) then

$$d\epsilon = (\mathbf{S}^o + \mathbf{S}^*) : d\sigma. \tag{59}$$

Note that the compliance is different from the original compliance of the undamaged solid since it reflects already accumulated damage. Hence, as suggested by Lemaitre and Chaboche (1981), the slope of the unloading path can be used as a measure of the accumulated damage. This, of course, is in complete accord with the proposed definition of damage since the changes in the damage and the compliance depend on the relative loss of primary bonds in the solid.

In contrast to the ductile behavior upon unloading ($\sigma = 0$), the strain in the specimen vanishes as well. Naturally, in actual materials some residual strain is typically present as a result of interlock forces and rough crack surfaces. This residual strain has, however, nothing in common with ductility.

The temptation of using a closed-form, analytical solution whenever available is difficult to resist. Consequently, it seems resonable to concentrate the computational effort on the assessment of the error associated with the application of TM. To accomplish this task, the results of TM are compared with the corresponding results obtained using SCM.

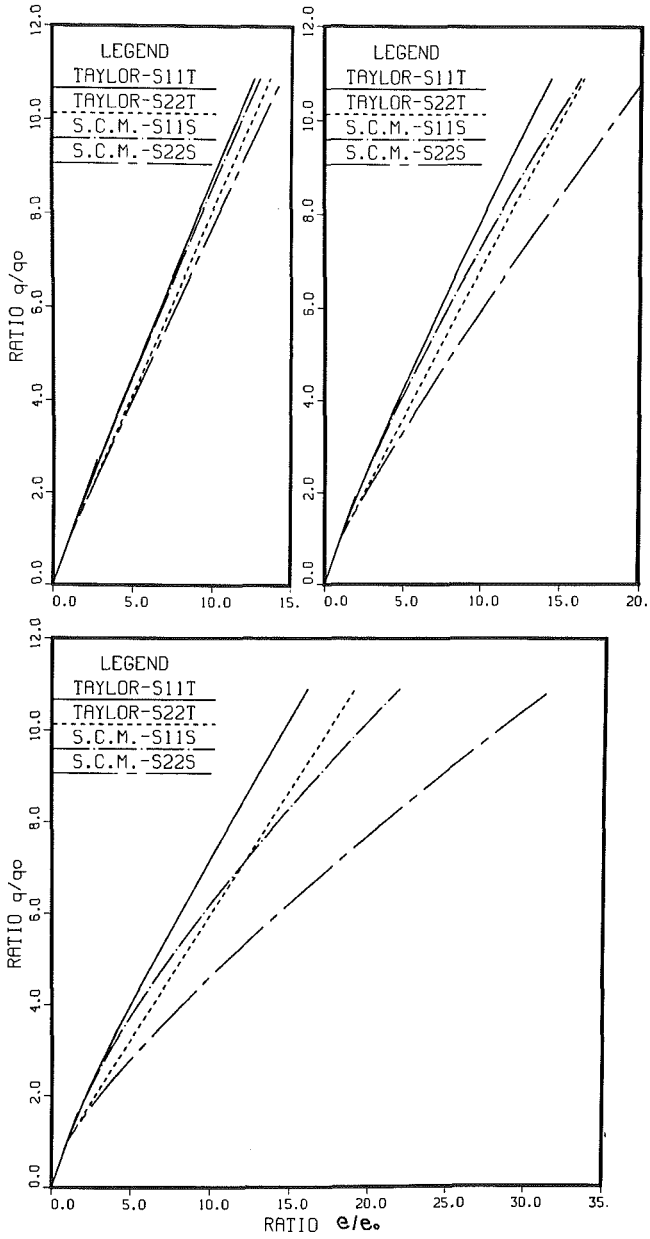


Fig. 3 The normalized stress-strain curve (for three damage ratios $ND^2 = 0.1$, 0.2, and 0.3) for a specimen in uniaxial tension

The normalized stress versus the normalized strain in both axial and lateral direction are computed for three values of ω and plotted in Fig. 3. The disparity between results obtained using TM and SCM appears to be substantial for large values of q. However, the errors are typically not very large since, in the case of the observed class of responses, the ultimate load seldom exceeds the load q at the onset of nonlinear behavior by a factor larger than 2 to 2.5 (Zaitsev, 1982, etc.). At $q/q_o \approx 2.5$, the results differ by approximately 10 percent which is well within the range of experimental accuracy.

The ratio m is plotted versus the externally applied traction in Fig. 4. The response is originally isotropic ($m = 1$) only to become anisotropic as the cracking intensifies ($m > 1$). However, as q/q_o exceeds 2 to 2.5, the degree of anisotropy declines since more and more cracks change their length from $2a_o$ to $2a_1$. This trend (Ortiz, 1987) is quite obvious from curves plotted in Fig. 3. For high stresses, the stress-strain curves flatten out approaching asymptotically a straight line defined by the limiting compliance $\mathbf{S}^o/(1-\omega_1)$ at which all

Downloaded 03 May 2010 to 171.66.16.31. Redistribution subject to ASME license or copyright; see http://www.asme.org/terms/Terms_Use.cfm

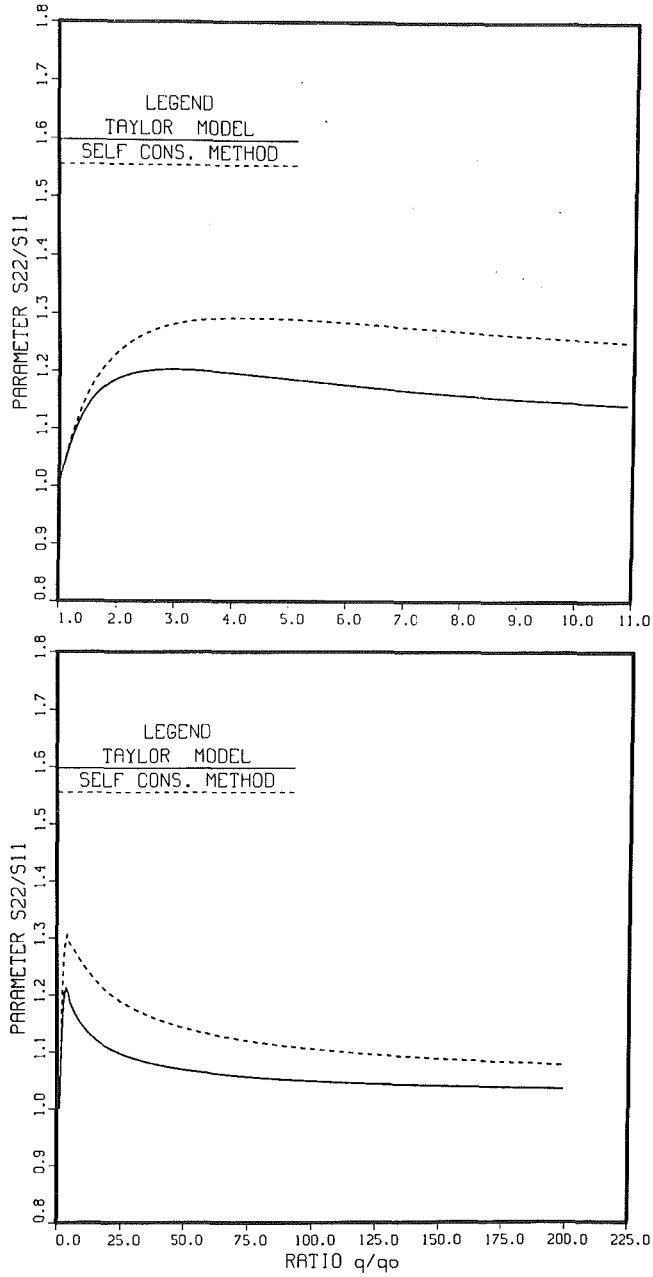


Fig. 4 Anisotropy measure of a specimen in uniaxial tension as a function of the eternally applied tensile traction

slits are of the size $2a$. However, even at an unrealistic value of $q/q_o = 200$, the value of m is still 1.1 and decreasing rather slowly (see Fig. 5 in which the peak appears as a result of compressed scale). The complete recovery of isotropy occurs only at an infinite value of q and is, therefore, impossible in view of the finite magnitude of the energy barrier in (58). The stress-strain curves plotted in this paper do not contain the macro failure point.

All numerical results are given in terms of the damage parameter ω which depends on the mesostructure of the solid. Once the mesostructure is defined, the parameter ω can be determined in a manner shown in Krajcinovic and Fanella, 1986; or Stojimirovic et al., 1987.

The presented computations are intended solely as an illustration of the proposed model and its ability in duplicating experimentally observed trends. The assumption of equal grain size ($a_i = \text{const.}$) will, for example, introduce a discontinuity in the first derivative of S since a finite number of cracks will become activated at $q = q_o$. This somewhat aberrant behavior (localized in the narrow vicinity of q_o) can be readily eliminated introducing a realistic distribution of grain sizes.

Summary and Conclusions

The proposed constitutive theory for the mechancial response of perfectly brittle, "cleavage 1" solids is believed to be an appealing blend of rigor and simplicity. The formulation combines the rigor of thermodynamics with the simplicity of closed-form solutions. The absence of physically unidentifiable parameters is another attractive point of the theory.

The proposed formulation is based on a relatively simple model of the mesostructural kinetics which captures the salient aspects of the physical phenomenon blurring the nonessential details. In its present form, the model is directly applicable to the "cleavage 1" response typical of a large class of brittle materials. The subsequent extensions and modifications of the present basic model are expected to widen the application spectrum to brittle ductile phenomena exhibited under an even wider set of circumstances.

The numerical computatons were concentrated on the validation of the simpler of two approximation levels allowing solutions in a closed, analytical form. It was found that the so-called Taylor model (Krajcinovic and Fanella, 1986) leads to results of surprisingly good accuracy for the entire range of parameters typical of the considered class of materials subjected to uniaxial tension. This is an encouraging signal for future development since the higher order theories are normally associated with a rather formidable computational effort.

Acknowledgment

The authors gratefully acknowledge the financial support for this work rendered by the U.S. National Science Foundation, Division of Engineering, Solid Mechanics Program research grant to the University of Illinois at Chicago.

References

Ashby, M. F., 1979, "Micromechanics of Fracture in Static and Cyclic Failure," *Fracture Mechanics*, R. A. Smith, ed., Pergamon Press, Oxford, UK, pp. 1–27.

Budiansky, B., and O'Connell, R. J., 1976, "Elastic Moduli of a Cracked Solid," *Int. J. Solids Structures*, Vol. 12, pp. 81–97.

Horii, H., and Nemat-Nasser, S., 1983, "Overall Moduli of Solids with Microcracks: Load Induced Anisotropy," *J. Mech. Phys. Solids*, Vol. 31, pp. 155–171.

Kanninen, M. F., and Popelar, C. H., 1985, *Advanced Fracture Mechanics*, Oxford Univ. Press, New York.

Krajcinovic, D., and Fanella, D., 1986, "A Micromechanical Damage Model for Concrete," *Eng. Fracture Mech.*, Vol. 25, pp. 585–596.

Krajcinovic, D., and Sumarac, D., "Micromechanics of Damage Processes," *Continuum Damage Mechanics: Theory and Application*, D. Krajcinovic and J. Lemaitre, eds., Springer-Verlag, Wien, Austria, 1987.

Laws, N., and Brockenbrough, J. R., 1987, "The Effect of Microcrack Systems on the Loss of Stiffness of Brittle Solids," *Int. J. Solids and Structures*, Vol. 23, pp. 1247–1268.

Lekhnitski, S. G., 1981, *Theory of Elasticity of an Anisotropic Body*, Mir Publ. Moscow.

Lemaitre, J., and Chaboche, J. L., 1985, *Mechanique des Materiaux Solides*, Dunod, Paris.

Ortiz, M. A., 1987, "A Continuum Theory of Crack Shielding in Ceramics," ASME JOURNAL OF APPLIED MECHANICS, Vol. 54, pp. 55–61.

Rudnicki, J. W., 1977, "The Inception of Faulting in a Rock Mass with Weakened Zone," *J. Geophys. Res.*, Vol. 82, pp. 844–854.

Sih, G. C., Paris, P. C., and Irwin, G. R., 1965, "On Cracks in Rectilinearly Anisotropic Bodies," *Int. J. Fracture Mech.*, Vol. 1, pp. 189–203.

Stojimirovic, A., Krajcinovic, D., and Sadowski, T., 1987, "Constitutive Model for Polycrystalline MgO Ceramics," *Constitutive Modelling for Non-traditional Materials*, V. Stokes and D. Krajcinovic, eds. ASME, New York.

Sumarac, D., 1987, "Self-consistent Model for the Brittle Response of Solids," Ph.D. Thesis, Univ. of Illinois at Chicago.

Zaitsev, Yu. V., 1982, *Deformation and Strength; Models for Concrete based on Fracture Mechanics*, Stroiizdat, Moscow.

Downloaded 03 May 2010 to 171.66.16.31. Redistribution subject to ASME license or copyright; see http://www.asme.org/terms/Terms_Use.cfm

W. Lin

L. M. Keer
Fellow ASME

Department of Civil Engineering,
Northwestern University,
Evanston, IL 60208

Analysis of a Vertical Crack in a Multilayered Medium

A general mathematical formulation to analyze cracks in a multilayered medium is constructed. First, a matrix for a single layer is formed in the Hankel transformed domain. Then a global matrix is formed by assembling together each layer matrix. The displacement and stress fields are obtained by inverting the Hankel transform. Finally, the planar crack problem is solved by the boundary integral method. The results given are the crack opening displacement and the stress intensity factors.

1 Introduction

Hydraulically-induced fracture is a technique being developed in the petroleum industry. The basic idea in the hydraulic fracture process is to use a highly pressurized fluid to break the rock so that the resources, oil or natural gas, can be more easily extracted. One of the difficult analytical problems for such fracturing processes is how to calculate the important quantities of physical interest when the process zone extends from the pay zone into upper and lower barriers. The methodology applied in this article, which studies one layer having upper and lower half space barriers, can also be applied to more general multilayered structures.

Multilayered structures are often encountered in many science and engineering branches such as geophysics, laminated composite materials, and highway pavements. The first systematic approach to multilayered media may be traced back to the Thompson (1950) -Haskell (1953) methods. Later, Gilbert and Backus (1966) introduced the propagator matrix method; Fuchs (1968, 1971) introduced the reflectivity method, and Pao and Gajewski (1977) have written a long article about generalized ray method.

The Green's functions in a multilayered media were derived by Luco and Apsel (1983). Xu and Mal (1987) give a simpler formulation and show that the problem can be solved by a personal computer. Kundu and Mal (1985) discussed the difficulty associated with the numerical integration in the transformed domain. Small and Booker (1986) solved a multilayered system by the flexibility matrix method. In Section 2, a general scheme to analyze the multilayered system is developed.

For the three-dimensional crack analysis in an unbounded medium, the boundary integral method is still preferred since the unknowns and equations occur only on the crack surfaces. The unknowns in the boundary integral method can be the crack opening displacement, Murakami and Nemat-Nasser (1983), the first derivatives of crack opening displacement, Weaver (1977), or the second derivatives of the crack opening displacement. The choice depends on whether or not it is more convenient to avoid the high order singularity. Recent articles by Lee and Keer (1986) and Lin and Keer (1987) use the triangular element in the same manner as Murakami and Nemat-Nasser. Although the triangular element is somewhat easier for mesh generation, a four node element which may be generated via conformal mapping, can evaluate the finite part integral more easier. Other articles such as Krenk and Schmidt (1982), Martin and Wickmen (1983), Lin and Keer (1986), etc., are concerned with the scattering due to a crack in the frequency domain.

An extra difficulty encountered for analyzing a vertical crack in the multilayered medium is the point singularity that occurs at the intersection of the crack edge and the interface. Several articles, Benthem (1977), Bazant and Estenssoro (1979), and Somaratna and Ting (1986), have discussed this type of point singularity.

In Section 3, the boundary integral equation will be constructed by a Green's function approach. Triangular elements and a square root singularity along the crack edge will be adopted. Although, the point singularity at interfaces is not considered in this article due to complexity, the interfacial phenomenon is discussed in the numerical results.

2 Mathematical Formulation for Multilayered Medium

To analyze a multilayered medium systematically, there are three basic principles involved. First, the matrix for a single layer is formed in such a way that the same formula can be applied to every layer. Next, the interfacial continuity conditions are executed in the transformed domain instead of in the spatial domain, since the mathematical operation required in the transformed domain is algebraic. The complexity of executing continuity conditions in the spatial domain can be found in Chan et al. (1974). Finally, to reduce the computational work, the solution is obtained by inverting the Hankel transform instead of inverting the double Fourier transform. Using these principles, the methodology to analyze the multilayered medium is constructed. Essentially, three types of matrices can be formed, namely the flexibility matrix, stiffness matrix, and propagator matrix. However, only the flex-

Contributed by the Applied Mechanics Division of THE AMERICAN SOCIETY OF MECHANICAL ENGINEERS for presentation at the Joint ASCE/ASME Applied Mechanics, Biomechanics, and Fluids Engineering Conference, San Diego, CA, July 9 to 12, 1989.

Discussion of this paper should be addressed to the Editorial Department, ASME, United Engineering Center, 345 East 47th Street, New York, N.Y. 10017, and will be accepted until two months after final publication of the paper itself in the JOURNAL OF APPLIED MECHANICS. Manuscript received by ASME Applied Mechanics Division, February 4, 1988; final revision, June 8, 1988.

Paper No. 89-APM-24.

Copyright © 1989 by ASME

Downloaded 03 May 2010 to 171.66.16.31. Redistribution subject to ASME license or copyright; see http://www.asme.org/terms/Terms_Use.cfm

ibility matrix is considered in detail. The other two methods are described in Appendix A.

First, consider a linear elastic isotropic layer which occupies the spatial domain $0 \le z \le H$. Although initially there is no body force, such forces will be introduced later into the system. The displacement field in this case may be expressed in terms of Papkovich-Neuber potentials in rectangular coordinates. However, these potentials lead, unavoidably, to a double Fourier transform; therefore, the following alternative forms in cylindrical coordinates, Green and Zerna (1954), are considered:

$$u_z = \phi_{z,z} + z\phi_{r,z} - \kappa\phi_r \tag{1a}$$

$$u_r = \phi_{z,r} + z\phi_{r,r} + 2\phi_{\theta,\theta}/r \tag{1b}$$

$$u_\theta = \phi_{z,\theta}/r + z\phi_{r,\theta}/r - 2\phi_{\theta,r}. \tag{1c}$$

Here $\kappa = 3 - 4\nu$, ν is Poisson's ratio, ϕ_z, ϕ_r and ϕ_θ satisfy Laplace equations, and the comma denotes differentiation. These forms are particularly useful when the applied body force is a vertical or a horizontal point force since only the constant term or the first term in Fourier series expansion is needed. Next, the axially symmetric and asymmetric cases are considered.

(A) Axially Symmetric Case. In the axially symmetrical case, $u_\theta = \phi_\theta = 0$ and ϕ_z and ϕ_r have no angular dependence. Thus, the potentials can be solved by using the zeroth order Hankel transform. The results are exponential functions with unknown coefficients in the transformed domain. The displacement field is obtained by replacing the potentials in equation (1) with the Hankel integrals, and the stress field is obtained by further application of Hooke's law. Explicitly, the results are:

$$(u_z, \sigma_{zz}) = \int_o^\infty (U_{zz}, S_{zz}) \xi J_o(\xi r) d\xi \tag{2a}$$

$$(u_r, \sigma_{rz}) = \int_o^\infty (U_r, S_{rz}) \xi J_1(\xi r) d\xi \tag{2b}$$

and

$$\begin{Bmatrix} U_{zz} \\ U_r \\ S_{zz}/2\mu\xi \\ S_{rz}/2\mu\xi \end{Bmatrix} = (1/\alpha) \begin{bmatrix} -1 & -2\alpha - \xi z & -1 & 2\alpha - \xi z \\ -1 & 1 - \xi z & 1 & 1 + \xi z \\ 1 & \alpha + \xi z & -1 & \alpha - \xi z \\ 1 & -1 + \alpha + \xi z & 1 & 1 - \alpha + \xi z \end{bmatrix} \times \begin{Bmatrix} A_1 \exp(-\xi z) \\ A_2 \exp(-\xi z) \\ A_3 \exp[\xi(z-H)] \\ A_4 \exp[\xi(z-H)] \end{Bmatrix} \tag{3}$$

Here, μ is the shear modulus, $\alpha = 1 - 2\nu$, and $A_i(\xi)$ are functions to be determined from the boundary conditions. It should be noted that symbol U_{zz}, instead of U_z, is used in equation (2a); U_z will be reserved for the more lengthy asymmetric case.

To form the flexibility matrix, three vectors are defined as:

$$\{\mathbf{u}\}^T = \{-U_{zz}(H), -U_r(H), U_{zz}(0), U_r(0)\} \tag{4a}$$

$$\{\sigma\}^T = \{S_{zz}(H), S_{rz}(H), S_{zz}(0), S_{rz}(0)\} \tag{4b}$$

$$\{\mathbf{A}\}^T = \{A_1, A_2, A_3, A_4\}. \tag{4c}$$

To form the stiffness matrix or propagator matrix, $\{\mathbf{u}\}$ and $\{\sigma\}$ are defined in other forms. Details about the two other matrix methods are given in Appendix A. After defining $\{\mathbf{u}\}$, $\{\sigma\}$, and $\{\mathbf{A}\}$, the $\{\mathbf{u}\} - \{\mathbf{A}\}$ and $\{\sigma\} - \{\mathbf{A}\}$ relationships are constructed by substituting $z = 0$ and $z = H$ into equation (3) in the form of equations (4a)–(4b). The results are written as:

$$\{\mathbf{u}\} = [\mathbf{f}_1]\{\mathbf{A}\} \tag{5a}$$

$$\{\sigma\} = [\mathbf{f}_2]\{\mathbf{A}\}. \tag{5b}$$

The flexibility matrix for the layer is:

$$[\mathbf{f}_v] = [\mathbf{f}_1][\mathbf{f}_2]^{-1} \tag{6a}$$

$$[\mathbf{f}_v]\{\sigma\} = \{\mathbf{u}\}. \tag{6b}$$

If a body force is applied in the layer, the total displacement and the stress fields can be written as:

$$\{\mathbf{u}\}_T = \{\mathbf{u}\}_F + \{\mathbf{u}\} \tag{7a}$$

$$\{\sigma\}_T = \{\sigma\}_F + \{\sigma\}. \tag{7b}$$

Here, the subscript "F" denotes that the field is due to the same body force as applied in the "full" space case, and "T" denotes that the field is contributed from both the body forces and the boundary conditions. By substituting equations (7a) and (7b) into equation (6b), one obtains the result:

$$[\mathbf{f}_v]\{\sigma\}_T = \{\mathbf{u}\}_T + [\mathbf{f}_v]\{\sigma\}_F - \{\mathbf{u}\}_F. \tag{8}$$

Next, the displacement and stress fields, $\{\mathbf{u}\}_F$ and $\{\sigma\}_F$, due to a unit vertical point force applied at $\mathbf{x}_o$ will be constructed. In this case, the displacement field in the spatial domain is

$$u_{zF} = C[\kappa/R + (z - z_o)^2/R^3] \tag{9a}$$

$$u_{rF} = Cr(z - z_o)/R^3. \tag{9b}$$

Here,

$$C = 1/16\pi\mu(1-\nu),\ R = |\mathbf{x} - \mathbf{x}_o|,\ r = [R^2 - (z - z_o)^2]^{1/2}. \tag{9c}$$

The displacement and stress fields in the transformed domain are obtained by performing the related Hankel transforms as given in equations (2a)–(2b). The results are:

$$U_{zzF} = C[\kappa/\xi + |z - z_o|]\exp(-\xi|z - z_o|) \tag{10a}$$

$$U_{rF} = C(z - z_o) \quad \exp(-\xi|z - z_o|) \tag{10b}$$

$$S_{zzF} = -2\mu C[(2 - 2\nu)\mathrm{sgn}(z - z_o) + \xi(z - z_o)]\exp(-\xi|z - z_o|) \tag{11a}$$

$$S_{rzF} = -2\mu C[1 - 2\nu + \xi|z - z_o|] \quad \exp(-\xi|z - z_o|). \tag{11b}$$

Then $\{\sigma\}_F$ and $\{\mathbf{u}\}_F$ in equation (8) are obtained by substituting $z = 0$ and $z = H$ into equations (10a)–(11b) in the forms of equations (4a)–(4b).

If the layer is replaced by an upper half space, then $A_3 = A_4 = 0$ in equation (3), and there is no change in the formulation. Hence, the half space solution may be viewed as a special case of a layer solution.

For a multilayered system that contains N layers, the remaining procedure is to assemble the matrix of each single layer to form the global matrix. To demonstrate the assembly process, two consecutive layers i and $i+1$ are considered. If layer i is above layer $i+1$, the interfacial conditions are:

$$\{S_{zz}(0_i), S_{rz}(0_i)\}_T = \{S_{zz}(H_{i+1}), S_{rz}(H_{i+1})\}_T \tag{12a}$$

$$\{U_{zz}(0_i), U_r(0_i)\}_T = \{U_{zz}(H_{i+1}), U_r(H_{i+1})\}_T. \tag{12b}$$

Downloaded 03 May 2010 to 171.66.16.31. Redistribution subject to ASME license or copyright; see http://www.asme.org/terms/Terms_Use.cfm

The flexibility matrix after assembling is:

$$[\mathbf{F}_v] = [\mathbf{f}_v]_i + [\mathbf{f}_v]_{i+1}.$$

The transposed vector of $\{\sigma\}_T$ is:

$$\{S_{zz}(H_i), S_{rz}(H_i), S_{zz}(0_i), S_{rz}(0_i), S_{zz}(0_{i+1}), S_{rz}(0_{i+1})\}_T.$$

The transposed vector of $\{\mathbf{u}\}_T$ is:

$$\{-U_{zz}(H_i), -U_r(H_i), 0., 0., U_{zz}(0_{i+1}), U_r(0_{i+1})\}_T.$$

The forcing terms are:

$$([\mathbf{f}_v]\{\sigma\}_F - \{\mathbf{u}\}_F)_i + ([\mathbf{f}_v]\{\sigma\}_F - \{\mathbf{u}\}_F)_{i+1}.$$

(B) Asymmetric Case. After discussing the process to solve the axially symmetric case, the displacement and the stress fields due to a point "horizontal" force are considered. Similarly to equation (8), the layer equation is:

$$[\mathbf{f}_h]\{\sigma_h\}_T = \{\mathbf{u}_h\}_T + [\mathbf{f}_h]\{\sigma_h\}_F - \{\mathbf{u}_h\}_F \tag{13}$$

Here, the goal is to construct the matrix $[\mathbf{f}_h]$, and vectors $\{\sigma_h\}_F$ and $\{\mathbf{u}_h\}_F$ in equation (13). It should be kept in mind that $[\mathbf{f}_h]$ depends on the definition of $\{\mathbf{u}_h\}$ and $\{\sigma_h\}$.

It is well known that the displacement field due to a unit horizontal point force applied at $\mathbf{x}_o$ in the full space is:

$$u_{zF} = Cr(z-z_o)\cos\theta/R^3 \tag{14a}$$

$$u_{rF} = C[\kappa/R + r^2/R^3]\cos\theta \tag{14b}$$

$$u_{\theta F} = -C\kappa\sin\theta/R \tag{14c}$$

where $r\cos\theta = x - x_o$, $r\sin\theta = y - y_o$. Thus, the angular dependence for the potentials in equations (1) are

$$(\phi_z, \phi_r, \phi_\theta) = (\Phi_z\cos\theta, \Phi_r\cos\theta, \Phi_\theta\sin\theta),$$

which are solved by the first order Hankel transform; the results are:

$$\Phi_j = \int_o^\infty \{B_j\exp(-\xi z) + B_{j+3}\exp[\xi(z-H)]\}\xi J_1(\xi r)d\xi \tag{15}$$

where $(\Phi_1, \Phi_2, \Phi_3) = (\Phi_z, \Phi_r, \Phi_\theta)$. By substituting equation (15) into equations (1), the displacements field in terms of B_j is obtained. The stress field is obtained by differentiating the displacement field. The results are in the following compact forms:

$$\{u_z/c, u_r/c + u_\theta/s, u_r/c - u_\theta/s,$$

$$\sigma_{zz}/c, \sigma_{rz}/c + \sigma_{\theta z}/s, \sigma_{rz}/c - \sigma_{\theta z}/s\}$$

$$= \int_o^\infty \{U_z J_1(\xi r), U_p J_2(\xi r), U_m J_0(\xi r),$$

$$S_z J_1(\xi r), S_p J_2(\xi r), S_m J_0(\xi r)\}\xi d\xi \tag{16}$$

where $c = \cos\theta$, $s = \sin\theta$ and

To obtain the flexibility matrix, $\{\mathbf{u}_h\}$, $\{\sigma_h\}$ and $\{\mathbf{B}_h\}$ are defined as:

$$\{\mathbf{u}_h\}^T = \{-U_z(H), -U_p(H), -U_m(H), U_z(0), U_p(0), U_m(0)\} \tag{18a}$$

$$\{\sigma_h\}^T = \{S_z(H), S_p(H), S_m(H), S_z(0), S_p(0), S_m(0)\} \tag{18b}$$

$$\{\mathbf{B}_h\}^T = \{B_1, B_2, B_3, B_4, B_5, B_6\}. \tag{18c}$$

Then, the $\{\mathbf{u}_h\} - \{\mathbf{B}_h\}$ and $\{\sigma_h\} - \{\mathbf{B}_h\}$ relationships are obtained by substituting $z = 0$ and $z = H$ into equations (17). The results are written as:

$$\{\mathbf{u}_h\} = [\mathbf{f}_3]\{\mathbf{B}_h\} \tag{19a}$$

$$\{\sigma_h\} = [\mathbf{f}_4]\{\mathbf{B}_h\} \tag{19b}$$

where the flexibility matrix is

$$[\mathbf{f}_h] = [\mathbf{f}_3][\mathbf{f}_4]^{-1}. \tag{20}$$

To obtain $\{\mathbf{u}_h\}_F$ and $\{\sigma_h\}_F$, the appropriate Hankel transforms as indicated in equation (16) are performed on equation (14). The results are:

$$\begin{aligned}
U_{zF} &= C \quad (z-z_o) && \exp(-\xi|z-z_o|)\\
U_{pF} &= C\ (1/\xi + |z-z_o|) && \exp(-\xi|z-z_o|)\\
U_{mF} &= C[(7-8\nu)/\xi - |z-z_o|] && \exp(-\xi|z-z_o|)\\
S_{zF}/2\mu &= C(1-2\nu-\xi|z-z_o|) && \exp(-\xi|z-z_o|)\\
S_{pF}/2\mu &= C[-\xi(z-z_o)] && \exp(-\xi|z-z_o|)
\end{aligned} \tag{21}$$

$$S_{mF}/2\mu = C[(-4+4\nu)\mathrm{sgn}(z-z_o) + \xi(z-z_o)]\exp(-\xi|z-z_o|).$$

Then, $\{\mathbf{u}_h\}_F$ and $\{\sigma_h\}_F$ in equation (13) are obtained by substituting $z = 0$ and $z = H$ into equation (21) in the forms of equations (18a)-(18c).

Generally speaking, when the loading or boundary conditions are more complex, more terms for the Fourier series expansion may be needed. However, the formulation is basically the same as the first term expansion, and the main differences between the mth term and the first term are in the replacement of $J_o(\xi r)$, $J_1(\xi r)$, $J_2(\xi r)$ by $J_{m-1}(\xi r)$, $J_m(\xi r)$, $J_{m+1}(\xi r)$.

3 Integral Equation and Numerical Scheme

To set up the integral equation, two symbols, $G_{ik}(\mathbf{x}, \mathbf{x}_o)$ and $\tau_{ijk}(x, x_o)$, are introduced, where $G_{ik}(\mathbf{x}, \mathbf{x}_o)$ is a representation for the ith direction displacement at x due to a unit point force applied along kth direction at $\mathbf{x}_o$ and $\tau_{ijk}(\mathbf{x}, \mathbf{x}_o)$ is the corresponding ij stress component. The processes required to derived the Green's functions have been described in Section 2. For a vertical planar crack with surface normal to x axis, the

$$\begin{Bmatrix} U_z \\ U_p \\ U_m \\ S_z/2\mu\xi \\ S_p/2\mu\xi \\ S_m/2\mu\xi \end{Bmatrix} = \begin{bmatrix} -1 & -\kappa-\xi z & 0 & 1 & -\kappa+\xi z & 0 \\ -1 & -\xi z & 2 & -1 & -\xi z & 2 \\ 1 & \xi z & 2 & 1 & \xi z & 2 \\ 1 & 2-2\nu+\xi z & 0 & 1 & -2+2\nu+\xi z & 0 \\ 1 & 1-2\nu+\xi z & -1 & -1 & 1-2\nu-\xi z & 1 \\ -1 & -1+2\nu-\xi z & -1 & 1 & -1+2\nu+\xi z & 1 \end{bmatrix} \begin{Bmatrix} B_1\xi\exp(-\xi z) \\ B_2\exp(-\xi z) \\ B_3\xi\exp(-\xi z) \\ B_4\xi\exp[\xi(H-z)] \\ B_5\exp[\xi(H-z)] \\ B_6\xi\exp[\xi(H-z)] \end{Bmatrix} \tag{17}$$

Downloaded 03 May 2010 to 171.66.16.31. Redistribution subject to ASME license or copyright; see http://www.asme.org/terms/Terms_Use.cfm

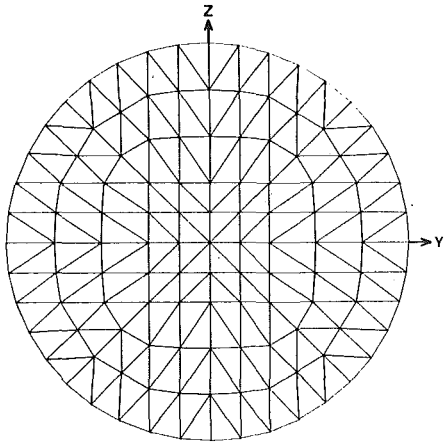


Fig. 1 The mesh and the coordinate system of the numerical examples

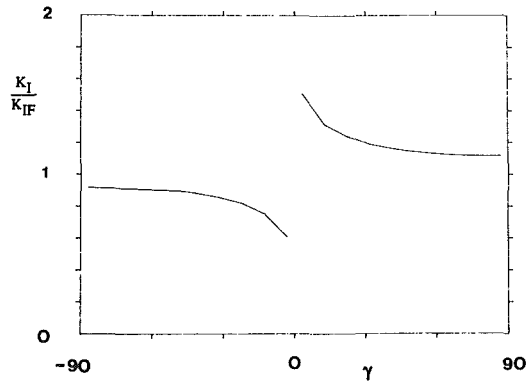


Fig. 2 The normalized stress intensity factor, K_I/K_{IF}, along the edge of the crack, angle $\gamma = \tan^{-1}$ (z/y) for bimaterials

integral representation for the displacement field due to the mode I crack opening displacement is:

$$u_k(\mathbf{x}_o) = \int \tau_{11k}(\mathbf{x}; \mathbf{x}_o)\, \Delta u_1(\mathbf{x})\, dA(\mathbf{x}). \tag{22}$$

In Appendix B, it is shown that equation (22) can be derived from the equivalent body force method.

The integral equation is obtained by applying Hooke's law to equation (22) and applying the pressure boundary condition along the crack surface. The result is:

$$-p(\mathbf{x}_o) = \sigma_{11}(\mathbf{x}_o) = \int K(\mathbf{x}, \mathbf{x}_o) \Delta u_1(\mathbf{x})\, dA(\mathbf{x}) \tag{23}$$

where

$$K(\mathbf{x}, \mathbf{x}_o) = 2\mu_o \{(1-\nu_o)\tau_{111,xo} + \nu_o[\tau_{112,yo} + \tau_{113,zo}]\}/(1-2\nu_o) \tag{24}$$

and $\mu_o = \mu(\mathbf{x}_o)$, $\nu_o = \nu(\mathbf{x}_o)$. Details concerning $K(\mathbf{x}, \mathbf{x}_o)$ are given in Appendix C. Numerically, equation (23) is written in discrete form as:

$$p(\mathbf{x}_o) = \int_o^\infty d\xi \left[\sum_{m=1}^{M} \int_{S_m} K(\mathbf{x}; \mathbf{x}_o; \xi) \Delta \bar{u}_1(\mathbf{x}) w(\mathbf{x}) dA(\mathbf{x}) \right] \tag{25}$$

where $w(\mathbf{x})$ is the weighting function for the crack opening displacement, i.e., $\Delta u_1(\mathbf{x}) = w(\mathbf{x}) \Delta \bar{u}_1(\mathbf{x})$, $K(\mathbf{x}, \mathbf{x}_o; \xi)$ is the kernel in ξ domain, and S_m is the subdomain. The numerical integration over the S_m domain is described by Lin and Keer (1987).

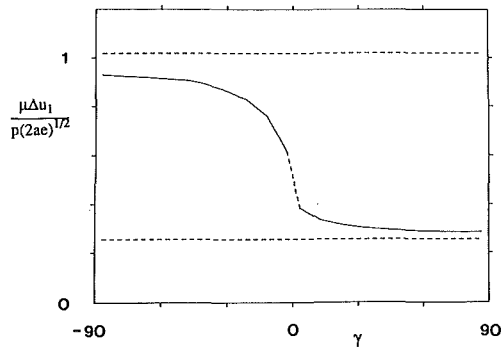


Fig. 3 The normalized crack opening, $\mu\Delta u_1/p(2ae)^{1/2}$, along the edge of the crack, angle $\gamma = \tan^{-1}$ (z/y) for bimaterials

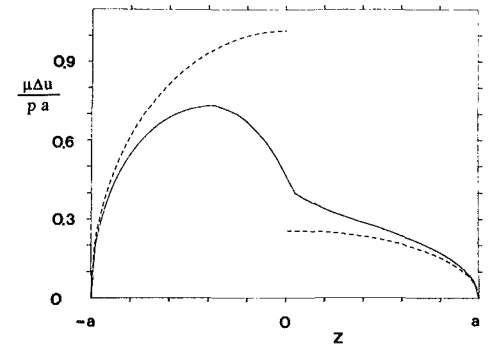


Fig. 4 The normalized crack opening, $\mu\Delta u_1/pa$, along the Z-axis for bimaterials

4 Numerical Examples and Discussions

The mesh and the coordinate system of the numerical examples are shown in Fig. 1. The crack is a penny-shaped crack, radius a, and the materials consist of an upper half space, a central layer, and a lower half space. The central layer represents the pay zone, while the upper and the lower half spaces represent barriers. The exact properties of the materials and the locations of the two interfaces are specified in the examples. The loading is by a constant fluid pressure p, applied on the crack surfaces.

In the first example, two interfaces are located at $z = 0$ and $z = 0.3a$. The shear moduli of the upper half space, the central layer and the lower half space are 4μ, 4μ, and μ, respectively. The Poisson's ratios are 0.2 for all materials. For this case, the kernel K has a closed form (Lee and Keer (1986)) which can be used to check the numerical integrations of the Hankel transforms. After checking, the Hankel transforms are performed by Simpson's rule with 400 integration points and with the maximum $\xi = 160/a$. In Fig. 2, the normalized stress intensity factor along the crack edge is plotted. The normalized factor $K_{IF} = 2p(a/\pi)^{1/2}$ corresponds to the stress intensity factor for a penny-shaped crack in fully space subjected to uniform tension. The result is same as in a previous paper by Lin and Keer (1988). It is noted that the stress intensity factor is greater than K_{IF} in the upper medium and is smaller than K_{IF} in the lower medium. The stress intensity factor at or near the interface is arguable because the point singularity at the intersection is not taken into account by the weighting function. In Fig. 3, the crack opening is plotted along the edge. The curved line gives the crack opening divided by the weighting function, $(2ae)^{1/2}$, where e is the distance from the collocation point in the boundary element to the crack edge. To understand this curve, two extreme cases are compared. When the shear modulus in the region $z > 0$ is replaced by μ, then, from the full space solution, $\mu\Delta u_1/p(2ae)^{1/2} = 4(1-\nu)\pi$, which is an

Downloaded 03 May 2010 to 171.66.16.31. Redistribution subject to ASME license or copyright; see http://www.asme.org/terms/Terms_Use.cfm

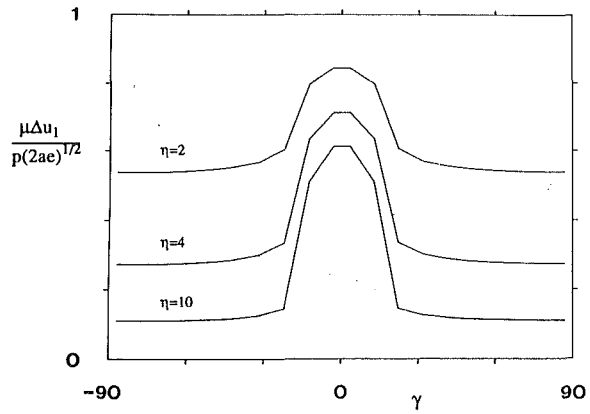


Fig. 5 The normalized crack opening, $\mu\Delta u_1/p\,(2ae)^{1/2}$, along the edge of the crack, angle $\gamma = \tan^{-1}(z/y)$ for trimaterials

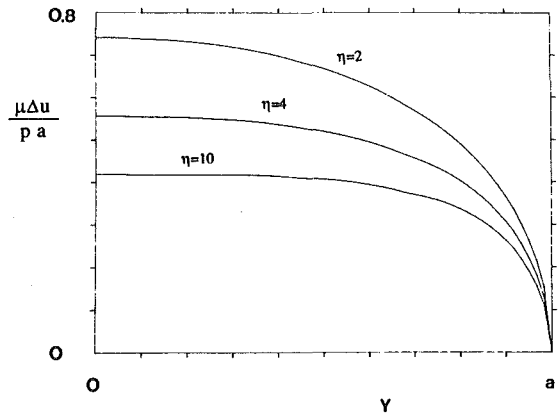


Fig. 7 The normalized crack opening, $\mu\Delta u_1/pa$, along the Y-axis for trimaterials

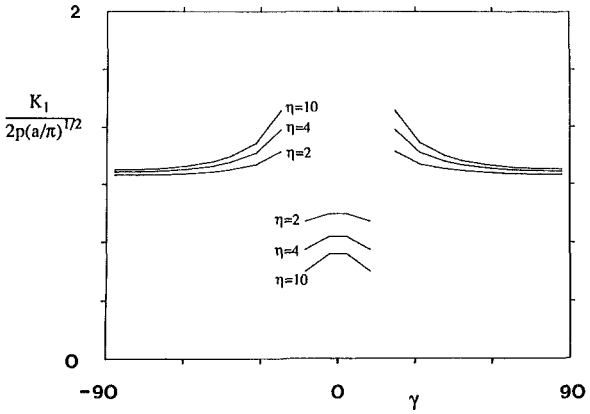


Fig. 6 The normalized stress intensity factors $K_1/[2p(a/\pi)^{1/2}$ along the edge of the crack, angle $\gamma = \tan^{-1}(z/y)$ for trimaterials

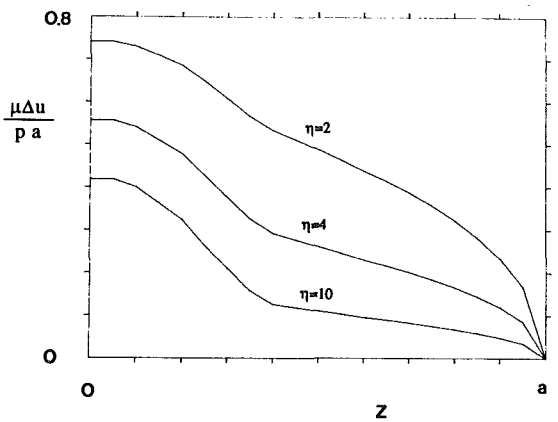


Fig. 8 The normalized crack opening, $\mu\Delta u_1/pa$, along the Z-axis for trimaterials

upper bound for the crack opening (upper dashed line). When the shear modulus for $z<0$ is replaced by 4μ, then, $\mu\Delta u_1/p(2ae)^{1/2} = (1-\nu)/\pi$, which is a lower bound for the crack opening (lower dashed line). The crack opening along the edge is decreasing from the lower medium to the upper medium because the upper medium is stiffer. Rapid changes occur near the interface. In Fig. 4, the crack opening along $y=0$ is plotted. The two dashed lines correspond to the upper bound, $\mu\Delta u_1/pa = 4(1-\nu)[1^2-(z/a)^2]^{1/2}/\pi$, and the lower bound, $\mu\Delta u_1/pa = (1-\nu)[1^2-(z/a)^2]^{1/2}/\pi$, of the crack opening as in the previous discussion.

In the second example, two interfaces are located at $z=0.3a$ and $z=-0.3a$. The shear modulus is μ for the central layer and $\eta\mu$ for the upper and lower half spaces. The Poisson's ratio is 0.2 for all materials. The three curves shown in Fig. 5 are the opening around the edge divided by the weighting function for $\eta=2$, 4, and 10. The lower bound for these curves are $\mu\Delta u_1/p(2ae)^{1/2} = 4(1-\nu)/\eta\pi = 1.02/\eta$. The three curves in Fig. 6 are the corresponding stress intensity factors. The conclusions are the same as the those obtained in the previous example: the opening in the softer medium is larger, rapid changes in crack opening occur around interfaces, and the stiffer region has a higher stress intensity factor. Figures 7 and 8 are the corresponding crack opening along Y axis and Z axis, respectively.

Remarks: First, if there are many layers in the system, the method of propagator matrices given in Appendix A is recommended. The flexibility matrix is used here only because there are only two interfaces. Second, the current approach can be applied in the frequency domain (see Xu and Mal (1987)). Even for the transversely isotropic medium, the current approach is also applicable (see Small (1986)).

5 Acknowledgment

The authors are grateful for the kind support by the Amoco Production Company. Helpful discussions with Drs. Z. A. Moschovidis and R. W. Veatch are acknowledged.

References

Bazant, Z. P., and Estenssoro, L. F., 1979, "Surface Singularity and Crack Propagation," *International Journal of Solids and Structures*, Vol. 15, pp. 405-426 and Vol. 16, pp. 479-481.

Benthem, J. P., 1977, "State of Stress at the Vertex of a Quarter-Infinite Crack in a Half-Space," *International Journal of Solids and Structures*, Vol. 13, pp. 479-492.

Chan, K. S., Karasudhi, P., and Lee, S. L., 1974, "Force at a Point in the Interior of a Layered Elastic Half Space," *International Journal of Solids and Structures*, Vol. 10, pp. 1179-1199.

Fuchs, K., 1968, "The Reflection of Spherical Waves from Transition Zone with Arbitrary Depth-Dependent Elastic Moduli and Density," *Journal of Physics of the Earth*, Special Issue, Vol. 16, pp. 27-41.

Fuchs, K., and Muller, G., 1971, "Computation of Synthetic Seismograms with the Reflectivity Method and Comparison of Observations," *Geophysical Journal of the Royal Astronomical Society*, Vol. 23, pp. 417-433.

Gilbert, F., and Backus, G. E., 1966, "Propagator Matrices in Elastic Wave and Vibration Problems," *Geophysics*, Vol. 31, pp. 326-332.

Green, A. E., and Zerna, W., 1954, *Theoretical Elasticity*, Oxford Univ. Press, pp. 169-171.

Haskell, N. A., 1953, "The Dispersion of Surface Waves on a Multilayered Media," *Bulletin of the Seismological Society of America*, Vol. 43, pp. 17-34.

Krenk, S., and Schmidt, H., 1982, "Elastic Wave Scattering by a Circular Crack," *Philosophical Transactions of the Royal Society of London*, Ser. A308, pp. 167-192.

Downloaded 03 May 2010 to 171.66.16.31. Redistribution subject to ASME license or copyright; see http://www.asme.org/terms/Terms_Use.cfm

Kundu, T., and Mal, A. K., 1985, "Elastic Waves in a Multilayered Solid Due to a Dislocation Source," *Wave Motion*, Vol. 7, pp. 459-471.

Lee, J. C., and Keer, L. M., 1986, "Study of a Three-Dimensional Crack Terminating at an Interface," ASME JOURNAL OF APPLIED MECHANICS, Vol. 53, pp. 311-316.

Lin, W., and Keer, L. M., 1987, "Scattering by a Planar Three-Dimensional Crack," *Journal of the Acoustical Society of America*, Vol. 82, No. 4, pp. 1442-1558.

Lin, W., and Keer, L. M., 1986, "Scattering by a Horizontal Subsurface Penny-Shaped Crack," *Proceedings of the Royal Society of London*, Ser. A408, pp. 277-294.

Lin, W., and Keer, L. M., 1988, "Growth of a Hydraulically Pressurized Fracture," *Engineering Fracture Mechanics*, Vol. 29, No. 4, pp. 473-481.

Luco, J. E., and Apsel, R. J., 1983, "On The Green's Functions For a Layered Half-Space, Part I," *Bulletin of the Seismological Society of America*, Vol. 73, No. 4, pp. 909-929.

Martin, P. A., and Wickham, G. R., 1983, "Diffraction of Elastic Waves by a Penny-Shaped Crack: Analytical and Numerical Results," *Proceedings of the Royal Society of London*, Ser. A390, pp. 91-129.

Mura, T., 1982, *Micromechanics of Defects in Solids*, Martinus Nijhoff, pp. 104-109.

Murakami, Y., and Nemat-Nasser, S., 1983, "Growth and Stability of Interacting Surface Flaws of Arbitrary Shape," *Engineering Fracture Mechanics*, Vol. 17, pp. 193-210.

Pao, Y. H., and Gajewski, R. R., 1977, "The Generalized Ray Theory and Transient Responses of Layered Elastic Solids," *Physical Acoustics*, Vol. 13, Academic Press, New York, pp. 183-265.

Small, J. C., and Booker, J. R., 1986, "Finite Layer Analysis of Layered Elastic Materials Using a Flexibility Approach. Part 2-Circular and Rectangular Loadings," *International Journal for Numerical Methods in Engineering*, Vol. 23, pp. 959-978.

Somaratna, N., and Ting, T. C. T., 1986, "Three-Dimensional Stress Singularities in Anisotropic Materials and Composites," *International Journal of Engineering Science*, Vol. 24, pp. 1115-1134.

Thomson, W. T., 1950, "Transmission of Elastic Waves Through a Stratified Solid Medium," *Journal of Applied Physics*, Vol. 21, pp. 89-93.

Weaver, J., 1977, "Three Dimensional Crack Analysis," *International Journal of Solids and Structures*, Vol. 13, pp. 321-330.

Xu, P. C., and Mal, A. K., 1987, "Calculation of the Inplane Green's Functions for a Layered Viscoelastic Solid," *Bulletin of the Seismological Society of America*, Vol. 77, No. 5, pp. 1823-1837.

APPENDIX A

Stiffness Matrix and Propagator Matrix

A1 Stiffness Matrix: To obtain the layer stiffness matrix, $\{\mathbf{u}\}$ and $\{\sigma\}$ are defined as:

$$\{\mathbf{u}\}^T = \{U_{zz}(H), U_r(H), U_{zz}(0), U_r(0)\} \quad (A1a)$$

$$\{\sigma\}^T = \{-S_{zz}(H), -S_{rz}(H), S_{zz}(0), S_{rz}(0)\}. \quad (A1b)$$

Then the $\{\mathbf{u}\}$-$\{\mathbf{A}\}$ and $\{\sigma\}$-$\{\mathbf{A}\}$ relationships are obtained by substituting $z=0$ and $z=H$ into equations (3). The results are written in the same forms as equations (5*a*) and (5*b*); the stiffness matrix is:

$$[s_v] = [\mathbf{f}_2][\mathbf{f}_1]^{-1}. \quad (A2)$$

If a body force is considered, the equation for the layer is:

$$[\mathbf{s}_v]\{\mathbf{u}\}_T = \{\sigma\}_T + [\mathbf{s}_v]\{\mathbf{u}\}_F - \{\sigma\}_F. \quad (A3)$$

Where $\{\mathbf{u}\}_F$ and $\{\sigma\}_F$ can be obtained from equations (10*a*)-(11*b*) and (*A*1*a*)-(*A*1*b*) by substituting $z=0$ and $z=H$.

For the case of applying a horizontal point force, the $\{\mathbf{u}_h\}$ and $\{\sigma_h\}$ are defined as:

$$\{\mathbf{u}_h\}^T = \{U_z(H), U_p(H), U_m(H), U_z(0), U_p(0), U_m(0)\} \quad (A4a)$$

$$\{\sigma_h\}^T = \{-S_z(H), -S_p(H), -S_m(H), S_z(0), S_p(0), S_m(0)\} \quad (A4b)$$

Then, the corresponding $[\mathbf{s}_h]$, $\{\sigma_h\}_F$ and $\{\mathbf{u}_h\}_F$ can be found by applying equations (17), (21) and (*A*4*a*)-(*A*4*b*).

A2 Propagator Matrix: To form the propagator matrix, two vectors $\{\mathbf{T}\}$ and $\{\mathbf{B}\}$ for the top and bottom surfaces of a layer are defined as follows:

$$\{\mathbf{T}\}^T = \{U_{zz}(H), U_r(H), S_{zz}(H), S_{rz}(H)\} \quad (A5a)$$

$$\{\mathbf{B}\}^T = \{U_{zz}(0), U_r(0), S_{zz}(0), S_{rz}(0)\}. \quad (A5b)$$

By substituting $z=0$ and $z=H$ into equation (3) to find the $\{\mathbf{T}\}$-$\{\mathbf{A}\}$ and $\{\mathbf{B}\}$-$\{\mathbf{A}\}$ relationship, the results are:

$$\{\mathbf{T}\} = [\mathbf{g}_1]\{\mathbf{A}\} \quad (A6a)$$

$$\{\mathbf{B}\} = [\mathbf{g}_2]\{\mathbf{A}\}. \quad (A6b)$$

The propagator matrix $[\mathbf{P}]$ is the relationship between $\{\mathbf{T}\}$ and $\{\mathbf{B}\}$, thus,

$$[\mathbf{P}]\{\mathbf{T}\} = \{\mathbf{B}\} \quad (A7a)$$

$$[\mathbf{P}] = [\mathbf{g}_2][\mathbf{g}_1]^{-1}. \quad (A7b)$$

To demonstrate how the propagator matrix works, two consecutive layers, i and $i+1$ are considered. Then,

$$[\mathbf{P}]_i\{\mathbf{T}\}_i = \{\mathbf{B}\}_i \quad (A8a)$$

$$[\mathbf{P}]_{i+1}\{\mathbf{T}\}_{i+1} = \{\mathbf{B}\}_{i+1}. \quad (A8b)$$

These two equations may be considered into one equation by applying the interfacial continuity condition,

$$\{\mathbf{B}\}_i = \{\mathbf{T}\}_{i+1}. \quad (A9)$$

The result is

$$[\mathbf{P}]_{i+1}[\mathbf{P}]_i\{\mathbf{T}\}_i = \{\mathbf{B}\}_{i+1}. \quad (A10)$$

Thus, if the system contains n layers, the relation between the top and the bottom surfaces are constructed as:

$$[\mathbf{P}(\text{system})]\{\mathbf{T}\}_1 = \{\mathbf{B}\}_n \quad (A11a)$$

$$[\mathbf{P}(\text{system})] = [\mathbf{P}]_n[\mathbf{P}]_{n-1} \cdots\cdots [\mathbf{P}]_2[\mathbf{P}]_1. \quad (A11b)$$

Now, applying boundary conditions on the top surface of the first layer and on the bottom surface of the last layer, the remaining unknowns in $\{\mathbf{T}\}_1$ and $\{\mathbf{B}\}_n$ can be solved. After $\{\mathbf{T}\}_1$ is solved, the remaining $\{\mathbf{T}\}_i$ are obtained by

$$\{\mathbf{T}\}_i = \{\mathbf{B}\}_{i-1} = [\mathbf{P}]_{i-1}\{\mathbf{T}\}_{i-1}.$$

In the above process, the $[\mathbf{P}]$ matrix is the downward propagator matrix. Alternatively, the upward propagator matrix in a layer also can be found by defining:

$$\{\mathbf{P}_u\}\{\mathbf{B}\} = \{\mathbf{T}\} \quad (A12a)$$

$$\{\mathbf{P}_u] = [\mathbf{g}_1][\mathbf{g}_2]^{-1}. \quad (A12b)$$

Then, the system upward propagation matrix is

$$[\mathbf{P}_u \text{ system}]\{\mathbf{B}\}_n = \{\mathbf{T}\}_1 \quad (A13a)$$

$$[\mathbf{P}_u \text{ system}] = [\mathbf{P}_u]_1[\mathbf{P}_u]_2 \cdots\cdots [\mathbf{P}_u]_{n-1}[\mathbf{P}_u]_n. \quad (A13b)$$

Now, consider the case that a body force is present in the jth layer, the equation for this layer is:

$$[\mathbf{P}]_j\{\mathbf{T}\}_{Tj} = \{\mathbf{B}\}_{Tj} + [\mathbf{P}]_j\{T\}_{Fj} - \{\mathbf{B}\}_{Fj}. \quad (A14)$$

The vectors $\{\mathbf{T}\}_{Fj}$ and $\{\mathbf{B}\}_{Fj}$ are easily obtained from equations (10*a*)-(11*b*). Next, both the downward and upward propagator matrices are applied to construct the relationships between the top and bottom surfaces. The result is:

$$[\mathbf{P}]_j[\mathbf{P}]_{j-1} \cdots [\mathbf{P}]_1\{\mathbf{T}\}_1 = [\mathbf{P}_u]_{j+1} \cdots [\mathbf{P}_u]_n\{\mathbf{B}\}_n + [\mathbf{P}]_j\{\mathbf{T}\}_{Fj} - \{\mathbf{B}\}_{Fj}. \quad (A15)$$

Downloaded 03 May 2010 to 171.66.16.31. Redistribution subject to ASME license or copyright; see http://www.asme.org/terms/Terms_Use.cfm

For the asymmetric case, the upward and downward propagator matrix are formed in the same manner. $\{\mathbf{T}\}$ and $\{\mathbf{B}\}$ are defined as;

$$\{\mathbf{T}\}^T = \{U_z(H), U_p(H), U_m(H), S_z(H), S_p(H), S_m(H)\} \tag{A16a}$$

$$\{\mathbf{B}\}^T = \{U_z(0), U_p(0), U_m(0), S_z(0), S_p(0), S_m(0)\} \tag{A16b}$$

From equations (17), (21), (A16a-b), the propagator matrices can be obtained.

APPENDIX B

Derivation of Integral Representation From Equivalent Body Force Method

When there is unbalanced strain, ϵ_{mn}, on a system, the equivalent body force on this system is $-C_{pqmn}\epsilon_{mn,q}$, where C_{pqmn} are elastic constants. This strain ϵ_{mn} is also called eigenstrain by Mura (1982). Hence, the displacement field due to this body force is:

$$u_k(\mathbf{x}_o) = -\int C_{pqmn}\epsilon_{mn,q}(\mathbf{x})G_{kp}(\mathbf{x}_o,\mathbf{x})dV(\mathbf{x}) \tag{B1}$$

where $G_{kp}(\mathbf{x}_o,\mathbf{x})$, (Section 3), is the displacement along the k direction at $\mathbf{x}_o$ due to a p direction unit force at $\mathbf{x}$. Because $G_{kp}(\mathbf{x}_o,\mathbf{x}) = G_{pk}(\mathbf{x},\mathbf{x}_o)$ due to Betti's reciprocal theorem and $C_{pqmn} = C_{mnpq}$ by the symmetry properties of the elastic constants, equation (B1) is written as:

$$u_k(\mathbf{x}_o) = \int \epsilon_{mn,q}(\mathbf{x})C_{mnpq}G_{pk}(\mathbf{x},\mathbf{x}_o)dV(\mathbf{x}). \tag{B2}$$

Integrating by parts, the result is:

$$u_k(\mathbf{x}_o) = -\int \epsilon_{mn}(\mathbf{x})C_{mnpq}G_{pkq}(\mathbf{x},\mathbf{x}_o)dV(\mathbf{x})$$

$$= \int \epsilon_{mn}(\mathbf{x})\tau_{mnk}(\mathbf{x},\mathbf{x}_o)dV(\mathbf{x}). \tag{B3}$$

The meaning of τ_{mnk} is also stated in Section 3. Finally, ϵ_{mn} is integrated along the normal of the crack surface to obtain the crack opening; the result is the integral representation in equation (22).

APPENDIX C

Kernel

To evaluate $K(\mathbf{x},\mathbf{x}_o)$ in equation (24), first consider $\tau_{113,zo}$. Since $x = x_o = 0$,

$$\tau_{113} = \tau_{\theta\theta 3} = 2\mu[(1-\nu)u_r/r + \nu(u_{r,r} + u_{z,z})]/(1-2\nu). \tag{C1}$$

Substituting u_r and u_z, equations (2a)-(3), the result is:

$$\tau_{\theta\theta 3} = \int_o^\infty [2\mu\xi^2/(1-2\nu)]\{2\nu[A_2\exp(-\xi z) + A_4\exp(\xi z - \xi H)]J_o(\xi r) + L_3 J_1(\xi r)/\xi r\}d\xi \tag{C2}$$

and

$$L_3 = [-A_1 + (1-\xi z)A_2]\exp(-\xi z) + [A_3 + (1+\xi z)A_4]\exp(\xi z - \xi H). \tag{C3}$$

To evaluate $\tau_{\theta\theta 3,zo}$, first evaluate $\{\mathbf{A}\}_{,zo}$. This evaluation is achieved by differentiating $\{\boldsymbol{\sigma}\}_F$ and $\{\mathbf{u}\}_F$ with respect to z_o in advance, see equations (4), (10a)-(11b).

The τ_{111} and τ_{112} terms are a bit more difficult. However, because the layers are horizontal and material is isotropic within each layer, $\tau_{111,xo} = -\tau_{111,x}$, $\tau_{112,yo} = -\tau_{112,y}$ and $\tau_{112}(0, y-y_o, z) = \tau_{221}(y-y_o, 0, z)$. Next, τ_{111} and τ_{221} are expressed in terms of τ_{rr1}, $\tau_{r\theta 1}$, $\tau_{\theta\theta 1}$. Then, performing the proper differentiation as indicated by equations (16)-(17), the results are:

$$\tau_{112,yo} = \int_o^\infty 2\mu\xi^3\{-U_p[J_1(\xi r)/\xi r - 3J_2(\xi r)/(\xi r)^2] + E_z[-J_o(\xi r) + J_1(\xi r)/\xi r]\}d\xi \tag{C4}$$

$$\tau_{111,xo} = \int_o^\infty 2\mu\xi^3\{-3U_p J_2(\xi r)/(\xi r)^2 + [2B_3\exp(-\xi z) + 2B_6\exp(-\xi H + \xi z) - E_z]J_1(\xi r)/\xi r\}d\xi \tag{C5}$$

where U_p is given in equation (17) and

$$E_z = 2\nu[B_2\exp(-\xi z) - B_5\exp(-\xi H + \xi z)]. \tag{C6}$$

When $\mathbf{x}$ and $\mathbf{x}_o$ are in the same layer, the kernel $K(\mathbf{x},\mathbf{x}_o)$ contains an extra term, the full space term, i.e.,

$$K_F(\mathbf{x},\mathbf{x}_o) = \mu/4\pi(1-\nu)R^3. \tag{C7}$$

Downloaded 03 May 2010 to 171.66.16.31. Redistribution subject to ASME license or copyright; see http://www.asme.org/terms/Terms_Use.cfm

D. Kouris
Department of Mechanical and Aerospace Engineering, Arizona State University, Tempe, Arizona 85287
Assoc. Mem. ASME

E. Tsuchida
Department of Mechanical Engineering, Saitama University, 255 Shimo-Okubo, Urawa 338, Japan

T. Mura
Department of Civil Engineering, Northwestern University, Evanston, Illinois 60208
Fellow ASME

The Hemispheroidal Inhomogeneity at the Free Surface of an Elastic Half Space

A series solution is presented for a hemispheroidal elastic inhomogeneity at the free surface of an elastic half space. The loading is either all around tension at infinity, perpendicular to the axis of symmetry of the inhomogeneity, or uniform, nonshear type eigenstrains sustained by the inhomogeneity. The displacement potentials of Boussinesq are used to represent the solution and several numerical calculations are performed to illustrate the results.

1 Introduction

The local mechanical behavior of composite materials that are loaded either mechanically or thermally is of major importance, due to local deviations from the average macroscopic properties. These disparities are derived from the fact that the elastic constants, and the coefficients of thermal expansion of the components in a composite, are usually very different. The reinforcements in composites under thermal or mechanical loading are usually modeled as inclusions (inhomogeneities).

In the present work, the local fields around a hemispheroidal inhomogeneity embedded at the free surface of an elastic material are investigated. The loading conditions considered are all-around tension at infinity, and nonshear type eigenstrains sustained by the inhomogeneity, introduced to model thermal expansion.

The problem of a semi-infinite elastic body having a hemispherical void under all around tension was studied by Eubanks (1954). Later, Fujita et al. (1980) solved the cases of hemiprolate and hemioblate void, and showed that the stress concentrations given by Eubanks were overestimated.

In this analysis, Boussinesq's displacement potentials are used and the solution is expressed in terms of five sets of prolate or oblate spheroidal harmonics, in series form. The harmonics chosen to represent the solution satisfy the boundary conditions at infinity and at the free surface automatically. In order to satisfy the boundary conditions at the interface, the "half range expansion" technique is employed. Due to the importance of the integrity of the interface, cases of both perfect bonding and sliding are considered. Several numerical calculations are performed for various shear moduli ratios and shape ratios. A special consideration is given to the surface displacements because of the availability of excellent experimental techniques for measuring differential strains.

The inclusion problem (shear moduli ratio equals unity) has been also solved by Cox (1988) for the perfectly bonded case.

2 Method of Solution

Consider a hemiprolate spheroidal inhomogeneity at the free surface of a semi-infinite, elastic, homogeneous, and isotropic material. The minor and major semi-axes of the inhomogeneity are denoted as a and b, respectively, and the center of the spheroid O is chosen as the origin of the coordinate system (see Fig. 1(a)). The problem is to determine the stress and displacement field under all-around tension applied at infinity or under constant, nonshear eigenstrains undergone by the inhomogeneity. The boundary conditions at the interface assume either perfect bonding or sliding. When sliding is allowed at the interface, shear tractions are specified to vanish and no debonding takes place. The slipping interface may be a realistic model as suggested by Head (1953), since sliding has been observed along the grain boundaries of polycrystals at high temperatures. The transformation equations relating Cartesian (x, y, z) and prolate spheroidal coordinates (α, β, γ) are given by:

$$\begin{aligned} x &= c\sinh\alpha\sin\beta\cos\gamma = \bar{cqp}\cos\gamma \\ y &= c\sinh\alpha\sin\beta\sin\gamma = \bar{cqp}\sin\gamma \\ z &= c\cosh\alpha\cos\beta = cqp \end{aligned} \tag{1}$$

where

$$q = \cosh\alpha, \quad \bar{q} = \sinh\alpha, \quad p = \cos\beta, \quad \bar{p} = \sin\beta$$

and c denotes the half-distance between foci.

Contributed by the Applied Mechanics Division of THE AMERICAN SOCIETY OF MECHANICAL ENGINEERS for presentation at the Joint ASCE/ASME Applied Mechanics, Biomechanics, and Fluids Engineering Conference, San Diego, Calif., July 9-12, 1989.

Discussion of this paper should be addressed to the Editorial Department, ASME, United Engineering Center, 345 East 47th Street, New York, N.Y. 10017, and will be accepted until two months after final publication of the paper itself in the JOURNAL OF APPLIED MECHANICS. Manuscript received by ASME Applied Mechanics Division, November 10, 1987; final revision, August 25, 1988.

Paper No. 89-APM-2.

Copyright © 1989 by ASME

Downloaded 03 May 2010 to 171.66.16.31. Redistribution subject to ASME license or copyright; see http://www.asme.org/terms/Terms_Use.cfm

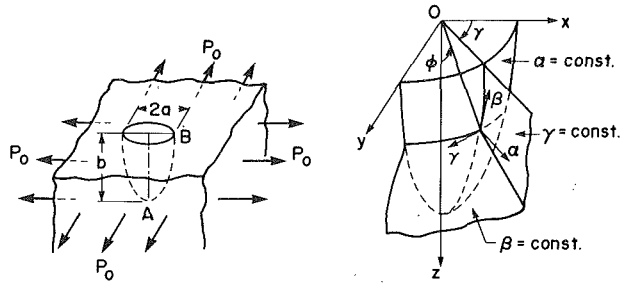


Fig. 1(a) Prolate inclusion

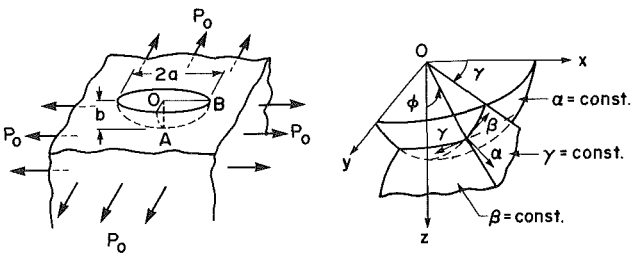


Fig. 1(b) Oblate inclusion

The surface of the inhomogeneity is given by $\alpha=\alpha_o=$ constant, and the free surface plane is given by $z=0$. The displacements are expressed in terms of the Boussinesq's potentials, and due to rotational symmetry they become:

$$2Gu_x=\frac{\partial\phi_o}{\partial x}+z\frac{\partial\phi_3}{\partial x}$$

$$2Gu_y=\frac{\partial\phi_o}{\partial y}+z\frac{\partial\phi_3}{\partial y} \tag{2}$$

$$2Gu_z=\frac{\partial\phi_o}{\partial z}+z\frac{\partial\phi_3}{\partial z}-(3-4\nu)\phi_3$$

where ϕ_o, ϕ_3 are arbitrary harmonic functions, G is the shear modulus, and ν is Poisson's ratio.

Transforming the displacements in (2) into the prolate spheroidal coordinate system, using the direction cosines of Table 1, we get:

$$2Gu_\alpha=h\bar{q}\frac{\partial\phi_o}{\partial q}+ch\bar{q}p\left\{q\frac{\partial\phi_3}{\partial q}-(3-4\nu)\phi_3\right\}$$

$$2Gu_\beta=-h\bar{p}\frac{\partial\phi_o}{\partial p}-chq\bar{p}\left\{p\frac{\partial\phi_3}{\partial p}-(3-4\nu)\phi_3\right\} \tag{3}$$

$$2Gu_\gamma=0$$

where $$\nabla^2=h^2\left\{\bar{q}^2\frac{\partial^2}{\partial q^2}+2q\frac{\partial}{\partial q}+\bar{p}^2\frac{\partial^2}{\partial p^2}-2p\frac{\partial}{\partial p}\right\}$$

$$h^2=\frac{1}{c^2(q^2-p^2)} \quad \text{and} \quad \nabla^2\phi_o=\nabla^2\phi_3=0.$$

Using Hooke's law, stresses are derived from strains as follows:

$$\sigma_\alpha=h^2\left\{\bar{q}^2\frac{\partial^2\phi_o}{\partial q^2}+c^2h^2\bar{p}^2\left(q\frac{\partial\phi_o}{\partial q}-p\frac{\partial\phi_o}{\partial p}\right)\right\}$$

$$+ch^2\left[q\bar{q}^2p\frac{\partial^2\phi_3}{\partial q^2}+\{c^2h^2q^2\bar{p}^2-2(1-\nu)\bar{q}^2\}p\frac{\partial\phi_3}{\partial q}\right.$$

$$\left.-(c^2h^2p^2+2\nu)q\bar{p}^2\frac{\partial\phi_3}{\partial p}\right]$$

$$\sigma_\beta=h^2\left\{\bar{p}^2\frac{\partial^2\phi_o}{\partial p^2}+c^2h^2\bar{q}^2\left(q\frac{\partial\phi_o}{\partial q}-p\frac{\partial\phi_o}{\partial p}\right)\right\}$$

Table 1 Direction cosines in the prolate spheroidal coordinate system

	x	y	z
α	$ch\bar{q}p\cos\gamma$	$ch\bar{q}p\sin\gamma$	$ch\bar{q}p$
β	$ch\bar{q}p\cos\gamma$	$ch\bar{q}p\sin\gamma$	$-ch\bar{q}p$
γ	$-\sin\gamma$	$\cos\gamma$	0

$$+ch^2\left[q\bar{p}p^2\frac{\partial^2\phi_3}{\partial p^2}-\{c^2h^2\bar{q}^2p^2+2(1-\nu)\bar{p}^2\}q\frac{\partial\phi_3}{\partial q}\right.$$

$$\left.+(c^2h^2p^2-2\nu)\bar{q}^2p\frac{\partial\phi_3}{\partial p}\right] \tag{4}$$

$$\sigma_\gamma=h^2\left(q\frac{\partial\phi_o}{\partial q}-p\frac{\partial\phi_o}{\partial p}\right)+ch^2\left\{(q^2-2\nu\bar{q}^2)p\frac{\partial\phi_3}{\partial q}\right.$$

$$\left.-(p^2+2\nu\bar{p}^2)q\frac{\partial\phi_3}{\partial q}\right\}$$

$$\tau_{\alpha\beta}=h^2\overline{qp}\left\{-\frac{\partial^2\phi_o}{\partial q\partial p}+c^2h^2\left(q\frac{\partial\phi_o}{\partial p}-p\frac{\partial\phi_o}{\partial q}\right)\right\}$$

$$-ch^2\overline{qp}\left[qp\frac{\partial^2\phi_3}{\partial q\partial p}+\{c^2h^2p^2-(1-2\nu)\}q\frac{\partial\phi_3}{\partial q}\right.$$

$$\left.-\{c^2h^2q^2+(1-2\nu)\}p\frac{\partial\phi_3}{\partial p}\right]$$

and all the other stress components are equal to zero.

The boundary conditions at the free surface are:

$$(\sigma_\beta)_{\beta=\pi/2}=(\tau_{\alpha\beta})_{\beta=\pi/2}=0$$
$$(\bar{\sigma}_\beta)_{\beta=\pi/2}=(\bar{\tau}_{\alpha\beta})_{\beta=\pi/2}=0 \tag{5}$$

where the stress components with the bar refer to the inhomogeneity. At infinity:

$$(\sigma_x)_{r\to\infty}=(\sigma_y)_{r\to\infty}=p_o$$
$$(\sigma_z)_{r\to\infty}=0 \tag{6}$$

for the all-around tension p_o case, and

$$(\sigma_{ij})_{r\to\infty}=0 \tag{7}$$

for the eigenstrain case.

At the interface $\alpha=\alpha_o$ and due to symmetry, the boundary conditions are:

α) for perfect bonding

$$(\sigma_\alpha)_{\alpha=\alpha_o}=(\bar{\sigma}_\alpha)_{\alpha=\alpha_o},\quad (\tau_{\alpha\beta})_{\alpha=\alpha_o}=(\bar{\tau}_{\alpha\beta})_{\alpha=\alpha_o},$$
$$(u_\alpha)_{\alpha=\alpha_o}=(\bar{u}_\alpha)_{\alpha=\alpha_o},\quad (u_\beta)_{\alpha=\alpha_o}=(\bar{u}_\beta)_{\alpha=\alpha_o} \tag{8}$$

β) for sliding

$$(\sigma_\alpha)_{\alpha=\alpha_o}=(\bar{\sigma}_\alpha)_{\alpha=\alpha_o},\quad (u_\alpha)_{\alpha=\alpha_o}=(\bar{u}_\alpha)_{\alpha=\alpha_o},$$
$$(\tau_{\alpha\beta})_{\alpha=\alpha_o}=0,\quad (\bar{\tau}_{\alpha\beta})_{\alpha=\alpha_o}=0 \tag{9}$$

where quantities denoted by a bar refer to the inhomogeneity.

When the eigenstrain is considered ($\epsilon_x^*=\epsilon_y^*$ and ϵ_z^*), the displacements in the inhomogeneity are expressed as the sum of the elastic displacements $\bar{u}_i$ given by (3) and the nonelastic displacements given by:

$$\bar{u}_x^*=\epsilon_x^*x$$
$$\bar{u}_y^*=\epsilon_y^*y \tag{10}$$
$$\bar{u}_z^*=\epsilon_z^*x$$

Using the direction cosines of Table 1, the displacements (10) are expressed in the prolate spheroidal coordinates:

Downloaded 03 May 2010 to 171.66.16.31. Redistribution subject to ASME license or copyright; see http://www.asme.org/terms/Terms_Use.cfm

$$2G\bar{u}^*_\alpha = 2G\, hc^2 q\bar{q}(\epsilon^*_x \bar{p}^2 + \epsilon^*_z p^2)$$
$$= h\bar{q}\left\{c^2 q\, \frac{2G}{3}\,[(2\epsilon^*_x + \epsilon^*_z)P_o(p) + 2(\epsilon^*_z - \epsilon^*_x)P_2(p)]\right\}$$
$$2G\bar{u}^*_\beta = 2G\, hc^2 p\bar{p}(\epsilon^*_x \bar{q}^2 - \epsilon^*_z q^2) \tag{11}$$
$$2G\bar{u}^*_\gamma = 0.$$

The displacement potentials chosen to represent the solution are

$$\text{[I]}\quad \begin{cases} \phi_o = -\dfrac{1-\nu}{2(1+\nu)}\, p_o (r^2 - 2z^2) \\ \qquad = \dfrac{1+\nu}{2(1+\nu)}\, p_o c^2 (\bar{q}^2\bar{p}^2 - 2q^2 p^2) \\ \phi_3 = -\dfrac{p_o}{1+\nu}\, z = -\dfrac{p_o}{1+\nu}\, cqp \end{cases}$$

$$\text{[II]}\quad \begin{cases} \phi_o = 2(1-\nu)c^2 p_o \displaystyle\sum_{n=0}^{\infty} A_n \{Q_{2n+2}(q)P_{2n+2}(p) \\ \qquad - Q_{2n}(q)P_{2n}(p)\} \\ \phi_3 = cp_o \displaystyle\sum_{n=0}^{\infty} A_n (4n+3) Q_{2n+1}(q)P_{2n+1}(p) \end{cases}$$

$$\text{[III]}\quad \begin{cases} \phi_o = (1-2\nu)c^2 p_o \displaystyle\sum_{n=0}^{\infty} B_n \{Q_{2n+3}(q)P_{2n+3}(p) \\ \qquad - Q_{2n+1}(q)P_{2n+1}(p)\} \\ \phi_3 = cp_o \displaystyle\sum_{n=0}^{\infty} B_n (4n+5) Q_{2n+2}(q)P_{2n+2}(p) \end{cases}$$

for the matrix ($\alpha > \alpha_o$), and

$$\text{[IV]}\quad \begin{cases} \phi_o = 2(1-\bar{\nu})c^2 p_o \displaystyle\sum_{n=0}^{\infty} \bar{A}_n \{P_{2n+2}(q)P_{2n+2}(p) \\ \qquad - P_{2n}(q)P_{2n}(p)\} \\ \phi_3 = cp_o \displaystyle\sum_{n=0}^{\infty} \bar{A}_n (4n+3) P_{2n+1}(q)P_{2n+1}(p) \end{cases}$$

$$\text{[V]}\quad \begin{cases} \phi_o = (1-2\bar{\nu})c^2 p_o \displaystyle\sum_{n=0}^{\infty} \bar{B}_n \{P_{2n+1}(q)P_{2n+1}(p) \\ \qquad - P_{2n-1}(q)P_{2n-1}(p)\} \\ \phi_3 = cp_o \displaystyle\sum_{n=0}^{\infty} \bar{B}_n (4n+1) P_{2n}(q)P_{2n}(p) \end{cases}$$

for the inclusion ($\alpha < \alpha_o$), where p_0 corresponds to the applied loading at infinity ($\sigma_x = \sigma_y = p_0$) and $p_o = 2G\epsilon^*_i$ for the eigenstrain case. The potential functions [I] are not necessary for the eigenstrain case. P_n and Q_n are Legendre functions of the first and second kind, respectively, and A_n, B_n, $\bar{A}_n$, $\bar{B}_n$ are unknown coefficients to be determined by the boundary conditions at the interface. Displacement function [I] corresponds to the applied load at infinity ($\sigma_x = \sigma_y = p_o$) and satisfies the boundary conditions (5) at the free surface.

The auxiliary displacement functions [II], [III], [IV], and [V] account for the disturbance due to the inhomogeneity and satisfy (5) identically, regardless of the coefficients A_n, B_n, $\bar{A}_n$, $\bar{B}_n$. These unknown coefficients are to be determined by the boundary conditions (8) or (9) at the interface. Deriving stresses and displacements from the displacement potentials [I]–[V] and enforcing (8), we arrive at the following equations:

$$\left(\frac{\sigma_\alpha}{p_o c^4 h^4}\right)_{\alpha=\alpha_o} = \left(\frac{\bar{\sigma}_\alpha}{p_o c^4 h^4}\right)_{\alpha=\alpha_o} \Rightarrow$$
$$\sum_{n=0}^{\infty} \{[S_{A1}A_{n-2} + S_{A2}A_{n-1} + S_{A3}A_n + S_{A4}A_{n+1}]$$
$$- [\bar{S}_{A1}\bar{A}_{n-2} + \bar{S}_{A2}\bar{A}_{n-1} + \bar{S}_{A3}\bar{A}_n + \bar{S}_{A4}\bar{A}_{n+1}]\} P_{2n}(p) \tag{12}$$
$$+ \sum_{n=0}^{\infty} \{[S_{B1}B_{n-2} + S_{B2}B_{n-1} + S_{B3}B_n + S_{B4}B_{n+1}]$$
$$- [\bar{S}_{B1}\bar{B}_{n-2} + \bar{S}_{B2}\bar{B}_{n-1} + \bar{S}_{B3}\bar{B}_n + \bar{S}_{B4}\bar{B}_{n+1}]\} P_{2n+1}(p) =$$
$$= -q_o^2\left(\frac{2}{3}\, q_o^2 - \frac{2}{15}\right)P_o(p) + q_o^2\left(\frac{2}{3}\, q_o^2 + \frac{2}{21}\right)P_2(p)$$
$$- \frac{8}{35}\, q_o^2 P_4(p)$$

$$\left(\frac{\tau_{\alpha\beta}}{p_o c^4 h^4 \overline{qp}}\right)_{\alpha=\alpha_o} = \left(\frac{\bar{\tau}_{\alpha\beta}}{p_o c^4 h^4 \overline{qp}}\right)_{\alpha=\alpha_o} \Rightarrow$$
$$\sum_{n=1}^{\infty} \{[t_{A1}A_{n-2} + t_{A2}A_{n-1} + t_{A3}A_n + t_{A4}A_{n+1}]$$
$$- [\bar{t}_{A1}\bar{A}_{n-2} + \bar{t}_{A2}\bar{A}_{n-1} + \bar{t}_{A3}\bar{A}_n + \bar{t}_{A4}\bar{A}_{n+1}]\} P'_{2n}(p) \tag{13}$$
$$+ \sum_{n=0}^{\infty} \{[t_{B1}B_{n-2} + t_{B2}B_{n-1} + t_{B3}B_n + t_{B4}B_{n+1}]$$
$$- [\bar{t}_{B1}\bar{B}_{n-2} + \bar{t}_{B2}\bar{B}_{n-1} + \bar{t}_{B3}\bar{B}_n + \bar{t}_{B4}\bar{B}_{n+1}]\} P'_{2n+1}(p) =$$
$$= -q_o\left(\frac{1}{3}\, q_o^2 - \frac{1}{7}\right)P'_2(p) + \frac{2}{35}\, q_o P'_4(p).$$

From the continuity of displacements, we have:

$$\left(\frac{u_\alpha}{p_o c^2 h\bar{q}}\right)_{\alpha=\alpha_o} = \left(\frac{\bar{u}_\alpha}{p_o c^2 h\bar{q}}\right)_{\alpha=\alpha_o} \Rightarrow$$
$$\sum_{n=0}^{\infty} \left\{[U_{A1}A_{n-1} + U_{A2}A_n] - \frac{1}{\Gamma}\,[\bar{U}_{A1}\bar{A}_{n-1} + \bar{U}_{A2}\bar{A}_n]\right\} P_{2n}(p) \tag{14}$$
$$+ \sum_{n=0}^{\infty} \left\{[U_{B1}B_{n-1} + U_{B2}B_n] - \frac{1}{\Gamma}\,[\bar{U}_{B1}\bar{B}_{n-1} + \bar{U}_{B2}\bar{B}_n]\right\} P_{2n+1}(p)$$
$$= -\frac{2q_o}{3(1+\nu)}\,[(1-2\nu)P_o(p) - (1+\nu)P_2(p)]$$

and

$$\left(\frac{u_\beta}{p_o c^2 h\bar{p}}\right)_{\alpha=\alpha_o} = \left(\frac{\bar{u}_\beta}{p_o c^2 h\bar{p}}\right)_{\alpha=\alpha_o} \Rightarrow$$
$$\sum_{n=1}^{\infty} \{[V_{A1}A_{n-1} + V_{A2}A_n]$$

Downloaded 03 May 2010 to 171.66.16.31. Redistribution subject to ASME license or copyright; see http://www.asme.org/terms/Terms_Use.cfm

$$-\frac{1}{\Gamma}\left[\bar{V}_{A1}\bar{A}_{n-1}+\bar{V}_{A2}\bar{A}_n\right]\Big\}P'_{2n}(p)$$

$$+\sum_{n=0}^{\infty}\Big\{[V_{B1}B_{n-1}+V_{B2}B_n]$$

$$-\frac{1}{\Gamma}\left[\bar{V}_{B1}\bar{B}_{n-1}+\bar{V}_{B2}\bar{B}_n\right]\Big\}P'_{2n+1}(p)$$

$$=\frac{1}{3(1+\nu)}[2\nu+(1+\nu)\bar{q}^2]P'_2(p) \tag{15}$$

where $P'_n(p)=\partial P_n(p)/\partial p$ and S_{Ai}, $\bar{S}_{Ai}$, S_{Bi}, $\bar{S}_{Bi}$, t_{Ai}, $\bar{t}_{Ai}$, t_{Bi}, $\bar{t}_{Bi}$, U_{Ai}, $\bar{U}_{Ai}$, U_{Bi}, $\bar{U}_{Bi}$, V_{Ai}, $\bar{V}_{Ai}$, V_{Bi}, and $\bar{V}_{Bi}$ are known functions of n and q_o, and they are given in the Appendix. The Legendre functions of odd order are expressed in terms of Legendre functions of even order by the use of "half-range expansion" technique. The "half-range expansion" equations are:

$$P_{2k+1}(p)=\sum_{n=0}^{\infty}w_k^{(n)}P_{2n}(p),\quad P'_{2k+1}(p)=\sum_{n=1}^{\infty}w_k^{(n)}P'_{2n}(p)$$

$$w_k^{(n)}=\frac{(4n+1)(2k+1)}{(2k+1-2n)(2k+2+2n)}P_{2n}(0)P_{2k}(0). \tag{16}$$

Equating the coefficients of $P_{2n}(p)$ and $P'_{2n}(p)$, we arrive at the following system of linear equations, from which A_n, B_n, $\bar{A}_n$, and $\bar{B}_n$ can be determined. Conditions (12) and (13) lead to

$$[S_{A1}A_{n-2}+S_{A2}A_{n-1}+S_{A3}A_n+S_{A4}A_{n+1}]$$
$$-[\bar{S}_{A1}\bar{A}_{n-2}+\bar{S}_{A2}\bar{A}_{n-1}+\bar{S}_{A3}\bar{A}_n+\bar{S}_{A4}\bar{A}_{n+1}]$$
$$+\sum_{k=0}^{\infty}\{S_{B1}B_{k-2}+S_{B2}B_{k-1}+S_{B3}B_k+S_{B4}B_{k+1}\}w_k^{(n)} \tag{16.1}$$
$$-\sum_{k=0}^{\infty}\{\bar{S}_{B1}\bar{B}_{k-2}+\bar{S}_{B2}\bar{B}_{k-1}+\bar{S}_{B3}\bar{B}_k+\bar{S}_{B4}\bar{B}_{k+1}\}w_k^{(n)}=$$

$$=-q_o^2\left(\frac{2}{3}q_o^2-\frac{2}{15}\right)\delta_o^{(n)}+q_o^2\left(\frac{2}{3}q_o^2+\frac{2}{21}\right)\delta_1^{(n)}-\frac{8}{35}q_o^2\delta_2^{(n)}$$
$$(n=0,1,2,\ldots)$$

$$[t_{A1}A_{n-2}+t_{A2}A_{n-1}+t_{A3}A_n+t_{A4}A_{n+1}]$$
$$-[\bar{t}_{A1}\bar{A}_{n-2}+\bar{t}_{A2}\bar{A}_{n-1}+\bar{t}_{A3}\bar{A}_n+\bar{t}_{A4}\bar{A}_{n+1}]$$
$$+\sum_{k=0}^{\infty}\{t_{B1}B_{k-2}+t_{B2}B_{k-1}+t_{B3}B_k+t_{B4}B_{k+1}\}w_k^{(n)} \tag{16.2}$$
$$-\sum_{k=0}^{\infty}\{\bar{t}_{B1}\bar{B}_{k-2}+\bar{t}_{B2}\bar{B}_{k-1}+\bar{t}_{B3}\bar{B}_k+\bar{t}_{B4}\bar{B}_{k+1}\}w_k^{(n)}=$$

$$=-q_o\left(\frac{1}{3}q_o^2-\frac{1}{7}\right)\delta_1^{(n)}+\frac{2}{35}q_o\delta_2^{(n)}\quad(n=1,2,\ldots)$$

condition (14) leads to

$$[U_{A1}A_{n-1}+U_{A2}A_n]-\frac{1}{\Gamma}[\bar{U}_{A1}\bar{A}_{n-1}+\bar{U}_{A2}\bar{A}_n]$$
$$+\sum_{k=0}^{\infty}\{U_{B1}B_{k-1}+U_{B2}B_k\}w_k^{(n)} \tag{16.3}$$
$$-\frac{1}{\Gamma}\sum_{k=0}^{\infty}\{\bar{U}_{B1}\bar{B}_{k-1}+\bar{U}_{B2}\bar{B}_k\}w_k^{(n)}=$$

$$=-\frac{2}{3}q_o\frac{1-2\nu}{1+\nu}\delta_o^{(n)}+\frac{2}{3}q_o\delta_1^{(n)}\quad(n=0,1,2,\ldots)$$

condition (15) leads to

$$[V_{A1}A_{n-1}+V_{A2}A_n]-\frac{1}{\Gamma}[\bar{V}_{A1}\bar{A}_{n-1}+\bar{V}_{A2}\bar{A}_n]$$
$$+\sum_{k=0}^{\infty}\{V_{B1}B_{k-1}+V_{B2}B_k\}w_k^{(n)}$$
$$-\frac{1}{\Gamma}\sum_{k=0}^{\infty}\{\bar{V}_{B1}\bar{B}_{k-1}+\bar{V}_{B2}\bar{B}_k\}w_k^{(n)} \tag{16.4}$$

$$=\frac{1}{3(1+\nu)}[2\nu+(1+\nu)\bar{q}^2]\delta_1^{(n)}\quad(n=1,2,3,\ldots)$$

where $\Gamma=\bar{G}/G$ is the ratio between the shear modulus of the inhomogeneity $\bar{G}$ and the shear modulus of the matrix G, and $\delta_i^{(n)}$ denotes Kronecker's delta.

Considering the sliding boundary conditions (9), we have

$$[t_{A1}A_{n-2}+t_{A2}A_{n-1}+t_{A3}A_n+t_{A4}A_{n+1}]$$
$$+\sum_{k=0}^{\infty}\{t_{B1}B_{k-2}+t_{B2}B_{k-1}+t_{B3}B_k+t_{B4}B_{k+1}\}w_k^{(n)}= \tag{16.5}$$

$$=-q_o\left(\frac{1}{3}q_o^2-\frac{1}{7}\right)\delta_1^{(n)}+\frac{2}{35}q_o\delta_2^{(n)}\quad(n=1,2,3,\ldots)$$

and

$$[\bar{t}_{A1}\bar{A}_{n-2}+\bar{t}_{A2}\bar{A}_{n-1}+\bar{t}_{A3}\bar{A}_n+\bar{t}_{A4}\bar{A}_{n+1}]$$
$$+\sum_{k=0}^{\infty}\{\bar{t}_{B1}\bar{B}_{k-2}+\bar{t}_{B2}\bar{B}_{k-1}+\bar{t}_{B3}\bar{B}_k+\bar{t}_{B4}\bar{B}_{k+1}\}w_k^{(n)}= \tag{16.6}$$
$$=0\qquad(n=1,2,3,\ldots)$$

From equations (16.1)–(16.4) for perfect bonding and (16.1), (16.3), (16.5), (16.6) for sliding, we can determine A_n, B_n, $\bar{A}_n$, and $\bar{B}_n$. In the numerical calculations, the infinite series are truncated at $n=N$, and N is chosen so that stresses and displacements in the continuity equations match.

After determining the coefficients A_n, B_n, $\bar{A}_n$, and $\bar{B}_n$, we can evaluate stresses and displacements everywhere in the matrix and the inhomogeneity.

2.1 Oblate Case ($a/b > 1.0$). When the inhomogeneity is of oblate shape (Fig. 1(*b*)), the oblate spheroidal coordinates are employed by the transformation:

$$x=c\cosh\alpha\sin\beta\cos\gamma=c\bar{\xi}\eta\cos\gamma$$
$$y=c\cosh\alpha\sin\beta\sin\gamma=c\bar{\xi}\eta\sin\gamma \tag{17}$$
$$z=c\sinh\alpha\cos\beta=c\xi\bar{\eta}$$

where

$$\xi=\sinh\alpha,\quad\bar{\xi}=\cosh\alpha,\quad\eta=\cos\beta,\quad\bar{\eta}=\sin\beta.$$

The displacement components $(u_\alpha, u_\beta, u_\gamma)$ are given in terms of (u_x, u_y, u_z) by:

$$u_\alpha=ch(\xi\bar{\eta}\cos\gamma u_x+\xi\bar{\eta}\sin\gamma u_y+\bar{\xi}\eta u_z)$$
$$u_\beta=ch(\bar{\xi}\eta\cos\gamma u_x+\bar{\xi}\eta\sin\gamma u_y+\xi\bar{\eta}u_z) \tag{18}$$
$$u_\gamma=-\sin\gamma u_z+\cos\gamma u_y$$

where

$$h^2=1/c^2(\xi^2+\eta^2).$$

The solution is formulated by the following sets of displacement potentials:

Downloaded 03 May 2010 to 171.66.16.31. Redistribution subject to ASME license or copyright; see http://www.asme.org/terms/Terms_Use.cfm

$$[\mathrm{I}]'\quad \begin{cases} \phi_o = \dfrac{1-\nu}{2(1+\nu)}\, p_o (r^2 - 2z^2) = \dfrac{1-\nu}{2(1+\nu)}\, p_o c^2 \\ \qquad (\bar{\xi}^2\bar{\eta}^2 - 2\xi^2\eta^2) \\ \phi_3 = -\dfrac{p_o}{1+\nu}\, z = -\dfrac{p_o}{1+\nu}\, c\xi\eta \end{cases}$$

$$[\mathrm{II}]'\quad \begin{cases} \phi_o = 2(1-\nu)c^2 p_o \displaystyle\sum_{n=0}^{\infty} A_n \{ q_{2n+2}(\xi) P_{2n+2}(\eta) \\ \qquad + q_{2n}(\xi) P_{2n}(\eta) \} \\ \phi_3 = -c p_o \displaystyle\sum_{n=0}^{\infty} A_n (4n+3) q_{2n+1}(\xi) P_{2n+1}(\eta) \end{cases}$$

$$[\mathrm{III}]'\quad \begin{cases} \phi_o = (1-2\nu)c^2 p_o \displaystyle\sum_{n=0}^{\infty} B_n \{ q_{2n+3}(\xi) P_{2n+3}(\eta) \\ \qquad + q_{2n+1}(\xi) P_{2n+1}(\eta) \} \\ \phi_3 = -c p_o \displaystyle\sum_{n=0}^{\infty} B_n (4n+5) q_{2n+2}(\xi) P_{2n+2}(\eta) \end{cases}$$

for the matrix ($\alpha > \alpha_o$), and

$$[\mathrm{IV}]'\quad \begin{cases} \phi_o = 2(1-\bar{\nu})c^2 p_o \displaystyle\sum_{n=0}^{\infty} \bar{A}_n \{ p_{2n+2}(\xi) P_{2n+2}(\eta) \\ \qquad + p_{2n}(\xi) P_{2n}(\eta) \} \\ \phi_3 = c p_o \displaystyle\sum_{n=0}^{\infty} \bar{A}_n (4n+3) p_{2n+1}(\xi) P_{2n+1}(\eta) \end{cases}$$

$$[\mathrm{V}]'\quad \begin{cases} \phi_o = (1-2\bar{\nu})c^2 p_o \displaystyle\sum_{n=0}^{\infty} \bar{B}_n \{ p_{2n+1}(\xi) P_{2n+1}(\eta) \\ \qquad + p_{2n-1}(\xi) P_{2n-1}(\eta) \} \\ \phi_3 = c p_o \displaystyle\sum_{n=0}^{\infty} \bar{B}_n (4n+1) p_{2n}(\xi) P_{2n}(\eta) \end{cases}$$

for the inhomogeneity ($\alpha < \alpha_o$), where $p_n(\xi)$ and $q_n(\eta)$ are modified Legendre functions of the first and second kind, respectively, and:

$$p_n(\xi) = (-i)^n P_n(i\xi)$$
$$q_n(\xi) = i^{n+1} Q_n(i\xi).$$

Following the same procedure as before, we have a system of equations to determine the unknown constants for the perfectly bonding case and the sliding case.

3 Numerical Calculations

In solving the simultaneous linear equations of infinite order for the unknown coefficients A_n, $\bar{A}_n$, B_n, and $\bar{B}_n$, the infinite series is truncated at the term where the tractions at the interface match up to three significant figures. The number of the necessary terms, varying between $N = 15$ and $N = 25$, depends on $s = a/b$, $\Gamma = \bar{G}/G$, and the boundary conditions. Several numerical calculations were performed for the cases of uniform all-around tension at infinity, or eigenstrain loading, for various shear moduli ratios and shape ratios and for constant Poisson's ratio $\nu = \bar{\nu} = 0.3$. The normal stress σ_α along the interface is shown in Fig. 2 for various s and a fixed $\Gamma = 2$ when the sliding inhomogeneity is loaded by a uniform all-around tension at infinity. It can be observed that σ_α exhibits high compressive values at the bottom of the inhomogeneity ($\varphi = 0^0$) for $s < 1.0$ (prolate). As the shape ratio s increases, the region of the interface under tension becomes smaller. A similar behavior can be observed with the distributions of the tangential stress $\bar{\sigma}_\beta$ and hoop stress $\bar{\sigma}_\gamma$ along the interface of the inhomogeneity. On the other hand, the stresses σ_β and σ_γ in the matrix at the interface show high tension at the bottom of the inhomogeneity for small s, although they are not shown in the figures.

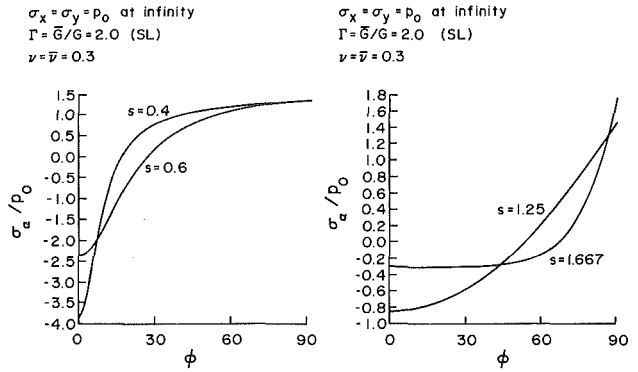


Fig. 2 Distribution of normal stress σ_α along the interface for sliding (SL) when $\Gamma = 2.0$, $\nu = \bar{\nu} = 0.3$, for various shape ratios $s = a/b$ ($\sigma_x = \sigma_y = p_o$)

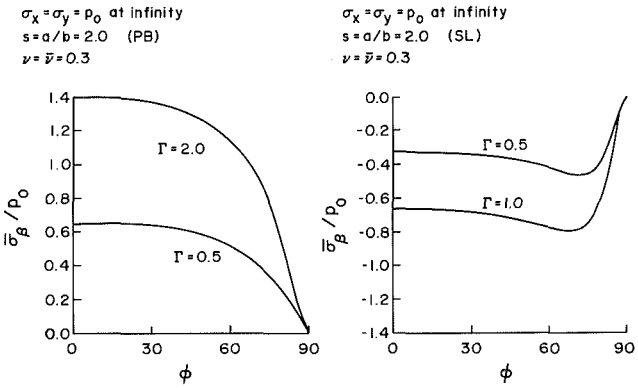


Fig. 3 Distribution $\bar{\sigma}_\beta$ along the interface, for various Γ when $s = 2.0$, $\nu = \bar{\nu} = 0.3$, for the cases of PB and SL ($\sigma_x = \sigma_y = p_o$)

In Fig. 3, $\bar{\sigma}_\beta$ in the inhomogeneity at the interface is given to show the difference between the perfect bonding case (PB) and the sliding case (SL). The tension at $\varphi = 0$ for (PB) changes to compression for (SL). Since $[u_\beta]$ in (SL) can be related to the shear stress $\tau_{\alpha\beta}$ in (PB), these quantities are shown in Fig. 4. In Fig. 5 tangential stresses σ_β and $\bar{\sigma}_\beta$ at the interface are shown and compared for perfect bonding and sliding. It can be observed that the stress fields around $\varphi = 0$ are completely different in the two cases. The effect of Γ and s on the displacement discontinuity $[u_\beta]$ is shown in Fig. 6 for eigenstrain loading in the z-direction. It can be observed that $[u_\beta]$ shows a small variation with Γ, while it strongly depends on the shape ratio s. Finally, the distribution of u_β along the free surface versus the normalized distance from the center of the inhomogeneity, is illustrated in Figs. 7 and 8. The long inhomogeneity ($s = 0.1$) is subjected to eigenstrain loading in the x- and y-directions and $\nu = \bar{\nu} = 0.3$. u_β is constant for sliding while it decays for perfect bonding. In both cases, higher values are obtained for "soft" inhomogeneity ($\Gamma = 0.5$). There is a discontinuity at the interface ($R = 1.0$) when sliding takes place, and u_β decays as R increases.

Downloaded 03 May 2010 to 171.66.16.31. Redistribution subject to ASME license or copyright; see http://www.asme.org/terms/Terms_Use.cfm

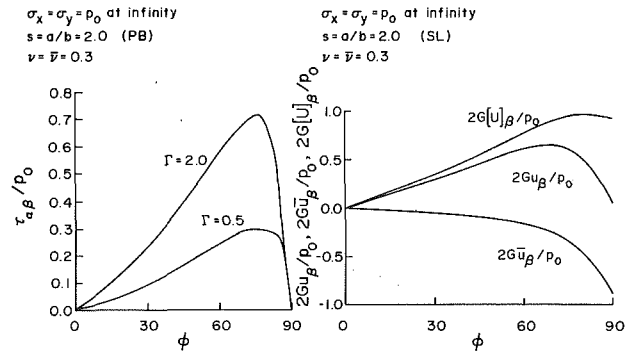


Fig. 4 Variation of shear stress $\tau_{\alpha\beta}$ (PB) and tangential displacement $2G[\bar{U}_\beta]$ (SL) versus φ

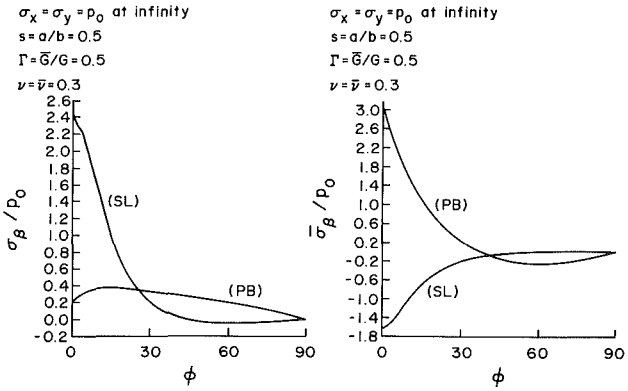


Fig. 5 Comparison between PB and SL for the tangential stresses σ_β and $\bar{\sigma}_\beta$ versus φ, when $s = 0.5, \Gamma = \bar{G}/G = 0.5$ and $\nu = \bar{\nu} = 0.3$ ($\sigma_x = \sigma_y = p_0$)

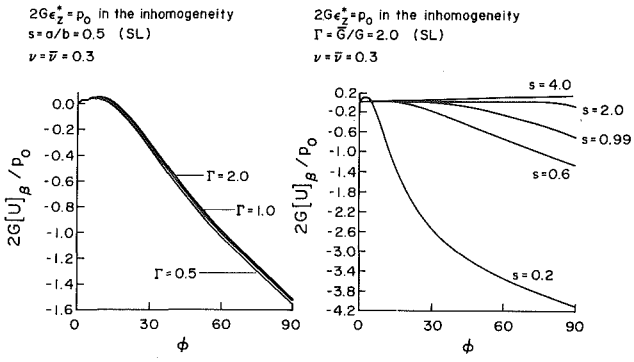


Fig. 6 The distribution of "slip" $2G[U_\beta]$ versus φ for various Γ and s when $\nu = \bar{\nu} = 0.3$ ($\epsilon_z^* \neq 0$)

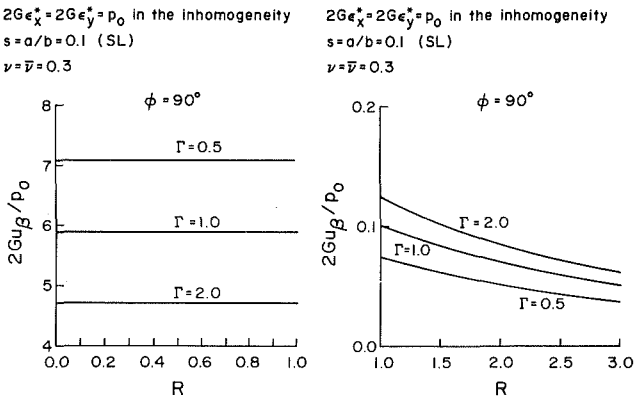


Fig. 7 The distribution of $2GU_\beta$ along the free surface when SL occurs and $s = 0.1, \nu = \bar{\nu} = 0.3$ ($\epsilon_x^* = \epsilon_y^*$)

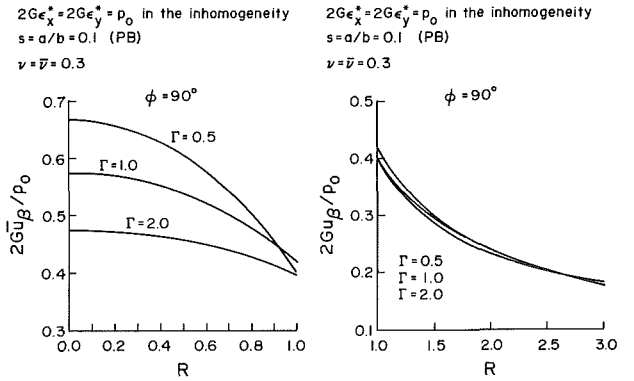


Fig. 8 $2GU_\beta$ along the free surface (PB with $s = 0.1, \nu = \bar{\nu} = 0.3$ ($\epsilon_x^* = \epsilon_y^*$)

References

Boussinesq, J., 1985, *Application des Potentiels*, Gauthier-Villars, Paris.

Cox, B., 1988, private communication.

Edwards, R. H., 1951, "Stress Concentrations Around Spheroidal Inclusion and Cavities," ASME JOURNAL OF APPLIED MECHANICS, Vol. 18, pp. 19–30.

Eshelby, J. D., 1957, "The Determination of the Elastic Fields of An Ellipsoidal Inclusion and Related Problems," *Proc. Roy. Soc., A* Vol. 241, pp. 376–296.

Eubanks, R. E., 1954, "Stress Concentration Due to a Hemispherical Pit at a Free Surface," ASME JOURNAL OF APPLIED MECHANICS, Vol. 21, pp. 57–62.

Eubanks, R. A., and Sternberg, E., 1956, "On the Completeness of the Boussinesq-Papkovich Stress Functions," *J. Rat. Mech. Anal.*, Vol. 5, pp. 735–746.

Fujita, T., and Tsuchida, E., 1981, "On the Stress Concentration Around Hemi-Oblate Spheroidal Pit in a Semi-Infinite Body," *Bull. Japan Soc. Mech. Engr.*, Vol. 24, pp. 15–21.

Fujita, T., Tsuchida, E., and Nakahara, I., 1980, "Stress Concentration due to a Hemi-Prolate Spheroidal Pit at a Free Surface of a Semi-Infinite Body Under All-Around Tension," *Bull. Japan Soc. Mech. Engr.*, Vol. 23, pp. 1048–1054.

Ghahremani, G., 1980, "Effect of Grain Boundary Sliding on an Elasticity of Polycrystals," *Int. J. Solids Structures*, Vol. 16, pp. 825–845.

Head, A. K., 1953, "Edge Dislocations in Inhomogeneous Media," *Proc. Phys. Soc.*, London, Vol. B66, pp. 793–801.

Hobson, E. W., 1931, *The Theory of Spheroidal and Ellipsoidal Harmonics*, University Press, Cambridge, England.

Mura, T., 1982, *Micromechanics of Defects in Solids*, Martinus Nijhoff Publishers, The Hague.

Mura, T., Jasiuk, I., and Tsuchida, E., 1985, "The Stress Field of a Sliding Inclusion," *Int. J. Solids Structures*, Vol. 21, pp. 1165–1179.

Sadowsky, M. A., and Sternberg, E., 1947, "Stress Concentration Around an Ellipsoidal Cavity in an Infinite Body Under Arbitrary Plane Stress Perpendicular to the Axis of Revolution of Cavity," ASME JOURNAL OF APPLIED MECHANICS, Vol. 14, No. 191–201.

Tsuchida, E., and Mura, T., 1983, "The Stress Field in an Elastic Half Space Having a Spheroidal Inhomogeneity Under All-Around Tension Parallel to the Plane Boundary," ASME JOURNAL OF APPLIED MECHANICS, Vol. 50, pp. 807–816.

Tsuchida, E., and Nakahara, I., 1967, "On the Stresses in a Semi-Infinite Solid Having a Hemispherical Pit Subjected to an Axisymmetric Pressure," *Trans. Japan Soc. Mech. Engr.* (in Japanese), Vol. 33, pp. 696–705.

Tsuchida, E., and Saito, Y., 1980, "Stresses in a Semi-Infinite Elastic Body Having an Oblate Spheroidal Cavity Under All-Around Tension," *3D, Theoretical and Applied Mechanics*, pp. 45–58.

Tsutsui, S., and Saito, K., 1973, "On the Effect of a Free Surface and a Spherical Inhomogeneity on Stress Fields of a Semi-Infinite Medium Under Axisymmetric Tension," *Proc. 23rd Japan Nat. Congr. Appl. Mech.*, Vol. 23, pp. 547–560.

Acknowledgment

This research was supported by the U.S. Army Research Contract No. DAAL 03-89-K-0019.

APPENDIX

Stress and Displacment Coefficients for the Spheroidal Inhomogeneity

$$S_{A1}(n,q) = \nu^* \frac{2n(2n-1)}{(4n-1)(4n-3)} \{qQ'_{2n-2}(q) - (2n-2)^2 Q_{2n-2}(q)\}$$

Downloaded 03 May 2010 to 171.66.16.31. Redistribution subject to ASME license or copyright; see http://www.asme.org/terms/Terms_Use.cfm

$$+\frac{2n(2n-1)(2n-2)}{(4n-1)(4n-3)}[\{(3-2\nu)q^2 - 2(1-\nu)\}Q'_{2n-3}(q) - (2n-3)(2n-3+2\nu)qQ_{2n-3}(q)]$$

$$S_{A2}(n,q) = -\nu^*\Big[2q^3Q'_{2n}(q) - 2n(2n+1)q^2Q_{2n}(q) - \frac{1}{(4n+3)(4n-1)}\times\{4(6n^2+3n-1)qQ'_{2n}(q) - 2(2n)^2(2n+1)^2Q_{2n}(q)\} + \frac{2n(2n-1)}{(4n-1)(4n-3)}\{qQ'_{2n-2}(q) - (2n-2)^2Q_{2n-2}(q)\}\Big] + 2nq^2[\{(3-2\nu)-(4-2\nu)q^2\}Q'_{2n-1}(q) + (2n-1)(2n+2\nu)q \times Q_{2n-1}(q)] + \frac{6n(4n^2-2)}{(4n+3)(4n-3)}[\{(3-2\nu)q^2 - 2(1-\nu)\}Q'_{2n-1}(q) - 2n(2n-1)qQ_{2n-1}(q)] + \frac{2n(2n-1)(4n^2-2n-3)}{(4n+3)(4n-3)}(1-2\nu)qQ_{2n-1}(q)$$

$$S_{A3}(n,q) = \nu^*\Big[2q^3Q'_{2n}(q) - 2nq^2(2n+1)Q_{2n}(q) - \frac{1}{(4n+3)(4n-1)}\times\{4(6n^2+3n-1)qQ'_{2n}(q) - 2(2n)^2(2n+1)^2Q_{2n}(q)\} + \frac{(2n+2)(2n+1)}{(4n+5)(4n+3)}\{qQ'_{2n+2}(q) - (2n+3)^2Q_{2n+2}(q)\}\Big] + (2n+1)q^2[\{(3-2\nu)-(4-2\nu)q^2\}Q'_{2n+1}(q) + (2n+2)(2n+1-2\nu) \times qQ_{2n+1}(q)] + \frac{3(2n+1)(4n^2+4n-1)}{(4n+5)(4n-1)}[\{(3-2\nu)q^2 - 2(1-\nu)\}Q'_{2n+1}(q) - (2n+1)(2n+2)qQ_{2n+1}(q)] - \frac{(2n+2)(2n+1)(4n^2+6n-1)}{(4n+5)(4n-1)} \times (1-2\nu)qQ_{2n+1}(q)$$

$$S_{A4}(n,q) = -\nu^*\frac{(2n+2)(2n+1)}{(4n+5)(4n+3)}\{qQ'_{2n+2}(q) - (2n+3)^2Q_{2n+2}(q)\} + \frac{(2n+1)(2n+2)(2n+3)}{(4n+3)(4n+5)}[\{(3-2\nu)q^2 - 2(1-\nu)\}Q'_{2n+3}(q) - (2n+4)(2n+4-2\nu)qQ_{2n+3}(q)]$$

$$t_{A1}(n,q) = \nu^*\frac{(2n-1)(2n-3)}{(4n-1)(4n-3)}Q'_{2n-2}(q) + \frac{(2n-1)(2n-2)}{(4n-1)(4n-3)}\{(2n-5+2\nu)qQ'_{2n-3}(q) - (2n-3)(1-2\nu)Q_{2n-3}(q)\}$$

$$t_{A2}(n,q) = -\nu^*\Big\{q^2Q'_{2n}(q) - \frac{(2n+2)(4n-2)}{(4n+3)(4n-1)}Q'_{2n}(q) - qQ_{2n}(q) + \frac{(2n-1)(2n-3)}{(4n-1)(4n-3)}Q'_{2n-2}(q)\Big\} + 2(1-\nu)(2n-1)q^2Q_{2n-1}(q) - (2n-2+2\nu)q^3Q'_{2n-1}(q) + \frac{3(2n-1)(4n^2-3)}{(4n+3)(4n-3)}\{qQ'_{2n-1}(q) - (1-2\nu)Q_{2n-1}(q)\} - 2\frac{4n^2+2n-3}{(4n+3)(4n-3)}(1-\nu)qQ'_{2n-1}(q)$$

$$t_{A3}(n,q) = \nu^*\Big\{q^2Q'_{2n}(q) - \frac{(2n+2)(4n-2)}{(4n+3)(4n-1)}Q'_{2n}(q) - qQ_{2n}(q) + \frac{(2n+4)(2n+2)}{(4n+3)(4n+5)}Q'_{2n+2}(q)\Big\} + 2(2n+2)(1-\nu)q^2Q_{2n+1}(q) - (2n+3-2\nu)q^3Q'_{2n+1}(q) + \frac{3(2n+2)(4n^2+4n-2)}{(4n-1)(4n+5)}\{qQ'_{2n+1}(q) - (1-2\nu)Q_{2n+1}(q)\} + 2\frac{4n^2+2n-3}{(4n-1)(4n+5)}(1-\nu)qQ'_{2n+1}(q)$$

$$t_{A4}(n,q) = -\nu^*\frac{(2n+4)(2n+2)}{(4n+5)(4n+3)}Q'_{2n+2}(q) + \frac{(2n+3)(2n+2)}{(4n+5)(4n+3)}\times\{(2n+6-2\nu)qQ'_{2n+3}(q) - (2n+4)(1-2\nu)Q_{2n+3}(q)\}$$

$$U_{A1}(n,q) = \nu^*Q'_{2n}(q) + 2nqQ'_{2n-1}(q) - 2n(3-4\nu)Q_{2n-1}(q)$$

$$U_{A2}(n,q) = -\nu^*Q'_{2n}(q) + q(2n+1)Q'_{2n+1}(q) - (2n+1)(3-4\nu)Q_{2n+1}(q)$$

$$V_{A1}(n,q) = -\nu^*Q_{2n}(q) - q(2n-4+4\nu)Q_{2n-1}(q)$$

$$V_{A2}(n,q) = \nu^*Q_{2n}(q) - q(2n+5-4\nu)Q_{2n+1}(q)$$

where $Q'_n(q) = \dfrac{dQ_n(q)}{dq}$ and $\nu^* = 2(1-\nu)$

The coefficients $S_{Bi}(n, q)$, $t_{Bi}(n, q)$ for $i = 1, 2, 3, 4$ and $U_{Bi}(n, q)$, $V_{Bi}(n, q)$ for $i = 1, 2$, can be obtained if the integer n is replaced by $n + \frac{1}{2}$ and ν^* is replaced by $\nu^{**} = 1 - 2\nu$ in the right side of the expressions given in this appendix.

The expressions for $\bar{S}_{Ai}(n, q)$, $\bar{t}_{Ai}(n, q)$, $\bar{U}_{Ai}(n, q)$ and $\bar{V}_{Ai}(n, q)$ are obtained by replacing $Q_n(q)$ and $Q'_n(q)$ with $P_n(q)$ and $P'_n(q)$, respectively, and ν with $\bar{\nu}$ in the expressions for S_{Ai}, t_{Ai}, U_{Ai}, and V_{Ai}. Finally, in order to obtain $\bar{S}_{Bi}$, $\bar{t}_{Bi}$, $\bar{U}_{Bi}$, and $\bar{V}_{Bi}$, we replace n by $n - \frac{1}{2}$ and $2(1-\bar{\nu})$ by $(1-2\bar{\nu})$ in the expressions for $\bar{S}_{Ai}$, $\bar{t}_{Ai}$, $\bar{U}_{Ai}$, and $\bar{V}_{Ai}$.

Downloaded 03 May 2010 to 171.66.16.31. Redistribution subject to ASME license or copyright; see http://www.asme.org/terms/Terms_Use.cfm

P. G. Charalambides

J. Lund

A. G. Evans

R. M. McMeeking
Mem. ASME

Materials Department,
College of Engineering,
University of California,
Santa Barbara, CA 93106

A Test Specimen for Determining the Fracture Resistance of Bimaterial Interfaces

A test specimen capable of measuring the fracture resistance of bimaterial interfaces has been devised. A finite element approach has been used to characterize trends in the stress intensities and center point displacement with specimen dimensions, elastic properties, and crack length. The utility of the specimen has been demonstrated by conducting experiments on the model system, Al/PMMA.

1 Introduction

Fracture at interfaces between dissimilar materials is a critical phenomenon in many multimaterial systems, ranging from composites (Rühle, Dalgleish, and Evans, 1987) to microelectronic devices (Hsueh and Evans, 1985). Yet, both the fundamental mechanics of this process and experimental techniques capable of systematically characterizing such fracture are incompletely developed. The principal intent of the present article concerns the development of a test procedure for purposes of systematic measurement of the interface fracture resistance.

Most of the important interface fracture problems involve combinations of normal and shear displacements along the crack, such that "mixed mode" conditions prevail. Typical problems include the debonding of fibers in composites (Rühle et al., 1987; Evans et al., 1987) and the decohesion of thin films (Drory, Thouless, and Evans, 1988). Emphasis is placed on a method capable of exploring the associated fracture locus.

An appropriate specimen is depicted in Fig. 1, consisting of a notched, bimaterial flexural beam. It will be demonstrated that this specimen provides fracture results for conditions of approximately equal normal and shear displacements on the interface crack far from the tip but in the K-dominated region. Consequently, when used in conjunction with other specimens, fracture resistance data could be obtained for the range of "mixed mode" space that has direct relevance to the aforementioned fracture problems.

The development of the test specimen involves analytical and finite element solutions of strain energy release rates and stress intensity factors, as well as experimental studies on a model system, consisting of Al bonded to PMMA. Comparisons between theory and experiment allow calibration of the technique and the development of experimental procedures for measuring the fracture resistance.

Contributed by the Applied Mechanics Division for publication in the JOURNAL OF APPLIED MECHANICS.

Discussion on this paper should be addressed to the Editorial Department, ASME, United Engineering Center, 345 East 47th Street, New York, N.Y. 10017, and will be accepted until two months after final publication of the paper itself in the JOURNAL OF APPLIED MECHANICS. Manuscript received by ASME Applied Mechanics Division, August 27, 1987; final revision, April 6, 1988.

2 The Mechanics of Interface Cracks

The small stain elasticity solution in the crack tip region (Fig. 2) can be developed using a bimaterial constant ϵ, which for plane strain is defined following Rice and Sih (1965) and Rice (1988) as

$$\epsilon=(1/2\pi)\ln\{[(3-4\nu_1)/G_1+1/G_2]\,[(3-4\nu_2)/G_2+1/G_1]^{-1}\} \quad (1)$$

where G and ν are the shear modulus and Poisson's ratio, respectively, and the subscripts 1 and 2 refer to the two bonded materials. The relative plane strain displacements of two points on the top and bottom crack surfaces, Δu_x and Δu_y (Fig. 2*a*) can then be expressed in terms of a complex stress intensity factor, K, as (Rice, 1988);

$$\Delta u_y+i\Delta u_x=\frac{2[(1-\nu_1)/G_1+(1-\nu_2)/G_2]K\sqrt{r/2\pi}r^{i\epsilon}}{(1+2i\epsilon)\cosh(\pi\epsilon)} \quad (2)$$

with r being the distance from the crack tip. In general, K can be expressed in terms of its real, Re, and imaginary, Im, parts, through the modulus $|K|$ and the phase angle, ψ,

$$K=|K|e^{i\psi} \quad (3)$$

The physical dimensions of K, as well as its behavior under change of either dimensions or absolute scale, and the ambiguous relationship between the real and imaginary parts of K, have been reviewed recently by Rice (1988). The crack surface displacements can also be written as,

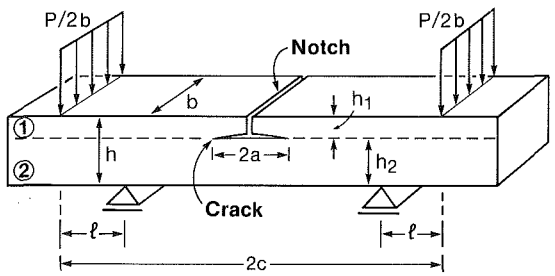


Fig. 1 A bimaterial, notched four-point bending specimen with symmetrical interfacial cracks

Copyright © 1989 by ASME

Downloaded 03 May 2010 to 171.66.16.31. Redistribution subject to ASME license or copyright; see http://www.asme.org/terms/Terms_Use.cfm

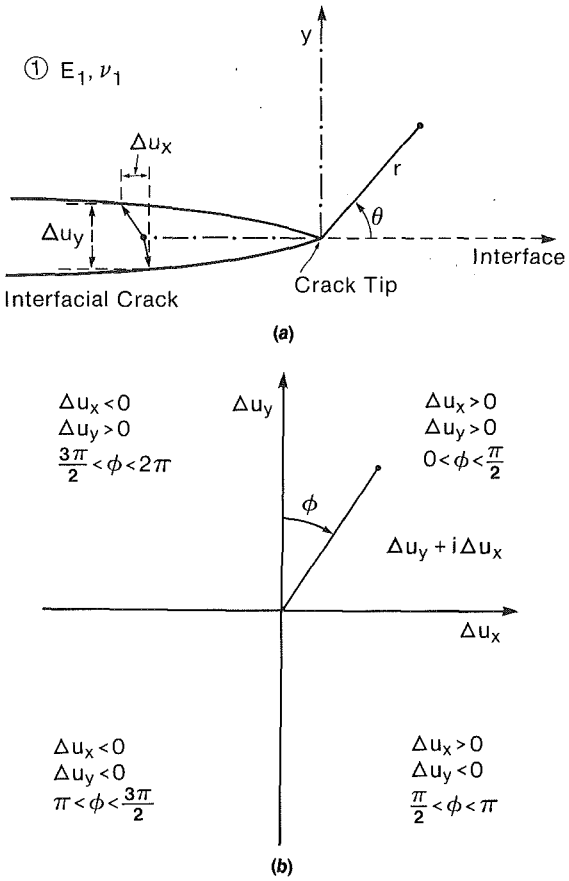


Fig. 2 *(a)* **The crack tip region for an interfacial macrocrack; *(b)* The rules for the phase angle ϕ in terms of Δu_x and Δu_y**

$$\Delta u_y + i\Delta u_x = [(\Delta u_x)^2 + (\Delta u_y)^2]^{1/2} e^{i\phi} \tag{4}$$

where ϕ is the phase angle depicted in Fig. 2(*b*). From equations (2) and (4)

$$[(\Delta u_x)^2 + (\Delta u_y)^2]^{1/2} e^{i\omega} = [q|K|\, r^{1/2} e^{i(\psi-\beta)}]/\sqrt{1+4\,\epsilon^2} \tag{5}$$

where

$$\beta = \text{Arc tan } (2\epsilon), \text{ and } \omega = \phi - \epsilon \ln r$$

and

$$q = \sqrt{2}\,[(1-\nu_1)/G_1 + (1-\nu_2)/G_2]/\sqrt{\pi}\,\cosh(\pi\epsilon).$$

Consequently, $|K|$ can be expressed in terms of the crack surface displacements as

$$|K| = [(1+4\epsilon^2)(\Delta u_x^2 + \Delta u_y^2)/r]^{1/2}/q \tag{6a}$$

and the phase angle becomes,

$$\psi = \omega + \beta. \tag{6b}$$

The modulus of K can also be related to the plane strain energy release rate $\mathcal{G}$ (Kanninen and Popelar, 1985), by

$$\mathcal{G} = [(1-\nu_1)/G_1 + (1-\nu_2)/G_2]\bar{K}K/4\cosh^2(\pi\epsilon) \tag{7}$$

Furthermore, since $K\bar{K} \equiv |K|^2$

$$|K| = \{4\cosh^2(\pi\epsilon)\mathcal{G}/[(1-\nu_1)/G_1 + (1-\nu_2)/G_2]\}^{1/2}. \tag{8}$$

The preceding results can be used in the following sequence to obtain the requisite interface crack quantities from numerical solutions. First, $\mathcal{G}$ can be explicitly determined either from a contour integral (Rice, 1968) or by a virtual crack extension procedure (Parks, 1974, 1978). The modulus $|K|$ can then be obtained directly from equation (8). Subsequently, the near tip crack surface displacement can be used to obtain an independent estimate of $|K|$, based on equation (6). A comparison provides an internal consistency check, as discussed elsewhere (Matos et al., 1988). Thereafter, the crack surface displacements can be fitted to equation (4), knowing ϵ, to obtain ω. Finally, the results can be expressed in terms of stress intensities

$$\text{Re}(K) = |K|\cos(\omega+\beta) \tag{9a}$$

$$\text{Im}(K) = |K|\sin(\omega+\beta). \tag{9b}$$

3 Analysis of the Specimen

The specimen (Fig. 1) consists of a bimaterial beam. A central notch exists through the thickness of the top layer and a symmetrical precrack is induced along the interface. The specimen is then loaded in four-point flexure. This situation constitutes a well-defined boundary value problem. The solution can be obtained numerically. In addition, an analytical estimate of the energy release rate can be obtained for cracks located between the inner loading points. For purpose of analysis, the subscript 1 indicates quantities relevant to the top layer, whereas the subscript 2 denotes the corresponding quantities for the bottom layer.

3.1 Analytical Solution for the Energy Release Rate. For the crack located between the inner loading lines, the cracked ligament is subject to constant moment conditions. Consequently, by analogy with other decohesion problems, (Drory et al., 1988; Thouless et al., 1987) the strain energy release rate should exhibit steady-state characteristics, at least when the interface crack length significantly exceeds the thickness of the upper layer of the beam. Furthermore, the steady-state value, $\mathcal{G}_{ss}$, can be deduced analytically by recognizing that it is simply the difference in the strain energy in the uncracked and cracked beam. Since there is negligible strain energy in the beam above the crack, $\mathcal{G}_{ss}$ can be deduced from consideration of the energies in the uncracked section, and in a section of the lower beam beneath the crack. From Euler-Bernoulli beam theory and plane strain conditions, these energies can be expressed in terms of the applied moment M as

$$U = (1-\nu^2)\,M^2/2EI \tag{9}$$

where U is the strain energy per unit cross-section and I is the second moment of area per unit width. Consequently,

$$\mathcal{G}_{ss} = \frac{M^2\,(1-\nu_2^2)}{2E_2}\left(\frac{1}{I_2} - \frac{\lambda}{I_c}\right) \tag{10}$$

where

$$\lambda = E_2(1-\nu_1^2)/E_1(1-\nu_2^2)$$

and the subscript c refers to the composite beam. Noting that the moment per unit width $M = Pl/2b$, with P being the total load and l the spacing between inner and outer load lines (Fig. 1),

$$I_c = h_1^3/12 + \lambda h_2^3/12 + \lambda h_1 h_2\,(h_1+h_2)^2/4(h_1+\lambda h_2) \tag{11}$$

and

$$I_2 = h_2^3/12.$$

All dimensions are shown in Fig. 1. The strain energy release rate thus becomes,

$$E_2\mathcal{G}_{ss}h^3b^2/P^2l^2\,(1-\nu_2^2) = (3/2)\,\{1/(h_2/h)^3 - \lambda/\{(h_1/h)^3 + \lambda(h_2/h)^3 + 3\lambda(h_1h_2/h^2)\,[h_1/h + \lambda h_2/h]^{-1}\}\}. \tag{12}$$

Trends in $\mathcal{G}_{ss}$ with relative dimensions h_1/h_2 and relative modulus, E_1/E_2 are depicted in Fig. 3. Evidently, the nondimensional $\mathcal{G}_{ss}$ increases monotonically with increase in relative upper beam thickness, h_1/h_2 and decreases as the relative modulus of the lower layer E_2/E_1, increases.

Downloaded 03 May 2010 to 171.66.16.31. Redistribution subject to ASME license or copyright; see http://www.asme.org/terms/Terms_Use.cfm

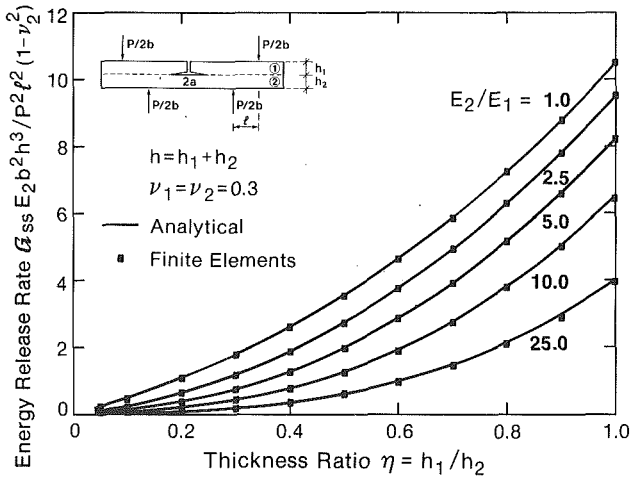


Fig. 3 The trends in the *steady-state* energy release rate with the thickness ratio h_1/h_2, and the modulus ratio E_2/E_1: comparison between analytical and finite element results

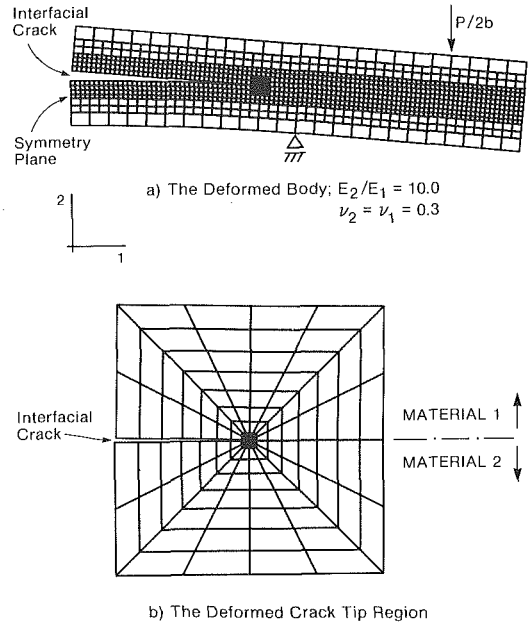


Fig. 4 (*a*) The mesh and the boundary conditions used in the finite element calculations; (*b*) the deformed finite element mesh in the near tip region

3.2 Numerical Solutions.

3.2.1 The Finite Element Procedure. Symmetry about the midsection of the beam depicted in Fig. 1 allows the requisite solutions to be obtained by considering one half of the beam (Fig. 4(*a*)). The finite elements[1] were 8-noded and isoparametric, with four stations used for integration of the stiffness matrix. The number of elements and nodes varied with the relative thickness, h_1/h_2, and with the dimensionless crack length a/l, such that a self-similar focused mesh was generated in the crack tip area having elements small enough to capture the features of the elastic crack tip solution (viz. $\sim h_1/100$ as shown in Fig. 4(*b*)). A roller support fixed the vertical displacement of the inner loading line, whereas symmetry was enforced by inhibiting horizontal displacements along the midsection of the lower layer. The crack surfaces were traction-free.

As noted in Section 2 the modulus of K can be calculated either from the displacement vector $\Delta u_y + i\Delta u_x$ at position r behind the crack tip or from the energy release rate $\mathcal{G}$, using the stiffness derivative method (Parks, 1974, 1978; Matos et al., 1988). The accuracy of $|K|$ computed using displacement magnitudes is subject to the numerical error introduced to the nodal displacements in the crack tip region. This error can be substantial for the first ring of elements around the crack tip. However, the two estimates for $|K|$ agree at a distance r_c from the crack tip (r_c/h is typically 10^{-2} to 10^{-3}) such that nodal displacements in the neighborhood of this region provide a good estimate of K and of the phase angle ψ (Matos et al., 1988). The $|K|$ and ψ estimates reported in this work were extracted from the finite element results, using both the displacement ratios determined at r_c and the energy approach (Matos et al., 1988). The results obtained via the two methods are in excellent agreement (maximum deviation less than 1 percent).

3.2.2 Fracture Mechanics Solutions. Elastic finite element solutions were obtained from various moduli ratios E_2/E_1 and for Poisson's ratios $\nu_1 = \nu_2 = 0.3$ The corresponding Dundurs' parameters α and β (Dundurs, 1969) are presented in Table 1. Elastically deformed meshes (Fig. 4) indicate that the top layer above the crack, being essentially stress-free, experiences rigid body motion determined by the deformation of the beam near the crack tip. Also, the upper beam experiences both opening and sliding relative to the lower beam, indicative of "mixed mode" conditions.

[1]Solved using the ABAQUS finite element program.

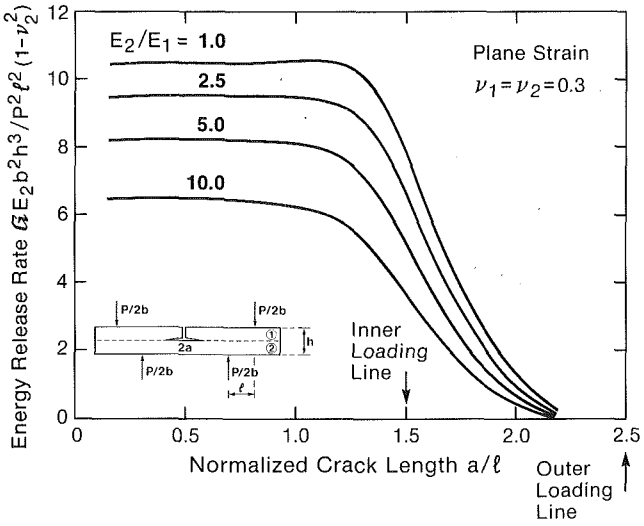
Table 1 The plain strain Dundurs' parameters α and β for materials combinations considered in the finite element calculations

Poisson's Ratio		Elastic Modulus Ratio,	Dundurs' Parameters	
ν_1	ν_2	E_2/E_1	α	β
0.3	0.3	1.0	0.0	0.0
0.3	0.3	2.5	− 0.429	− 0.122
0.3	0.3	5.0	− 0.667	− 0.190
0.3	0.3	10.0	− 0.818	− 0.234
0.3	0.3	25.0	− 0.923	− 0.264

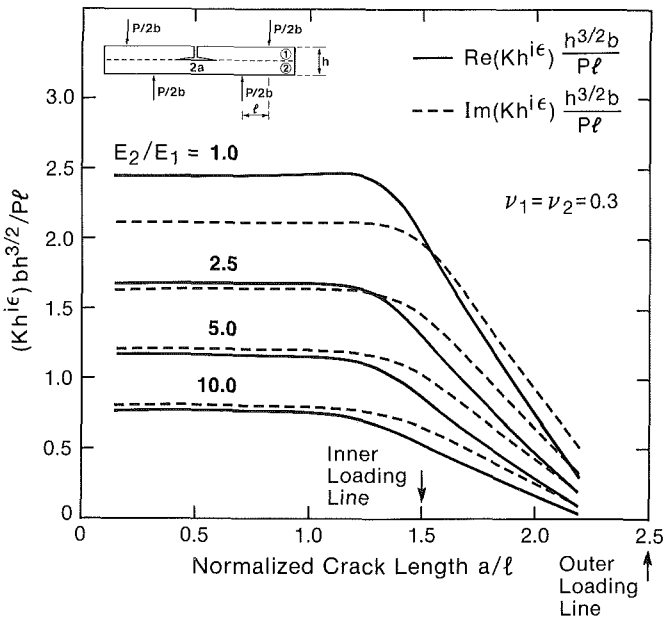
$$\alpha = \frac{\frac{G_1}{G_2}(1-\nu_2)-(1-\nu_1)}{\frac{G_1}{G_2}(1-\nu_2)+(1-\nu_1)} \qquad \beta = \frac{1}{2}\,\frac{\frac{G_1}{G_2}(1-2\nu_2)-(1-2\nu_1)}{\frac{G_1}{G_2}(1-\nu_2)+(1-\nu_1)}$$

The general trends in energy release rate, stress intensity factor and phase angle with crack length are shown in Fig. 5. The mechanics of the bimaterial crack problem (treated in the manner of Rice and Sih (1965)) make it necessary and desirable to normalize K by a typical specimen dimension, such as the full beam depth, $h = h_1 + h_2$. Furthermore, the normalization must include this dimension, raised to the power $i\epsilon$, to allow an unambiguous presentation of the phase relationship between the real and imaginary parts of K. (In the case, $E_2 = E_1$ and $\nu_2 = \nu_1$, $\epsilon = 0$ and $h^{i\epsilon} = 1$). These issues have been reviewed recently by Rice (1988). As expected, the energy release rate $\mathcal{G}$ and the stress intensity factor K attain an essentially constant, steady-state level within a distance from the

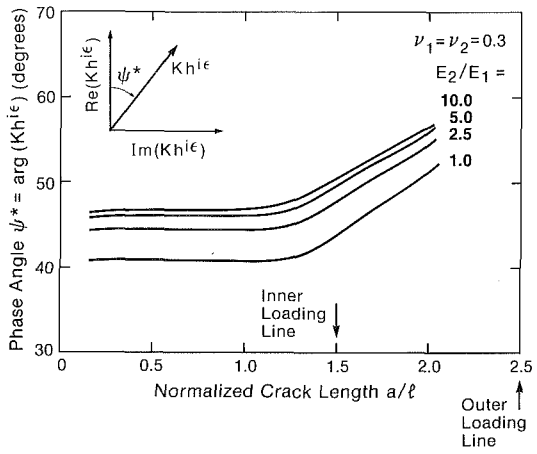
Downloaded 03 May 2010 to 171.66.16.31. Redistribution subject to ASME license or copyright; see http://www.asme.org/terms/Terms_Use.cfm



(a)

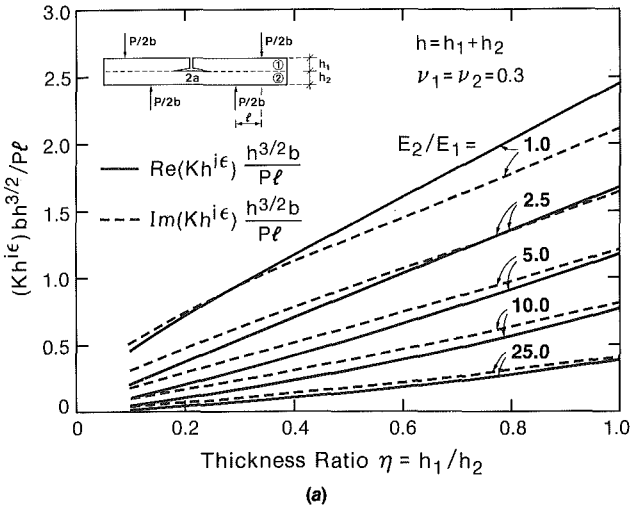


(b)

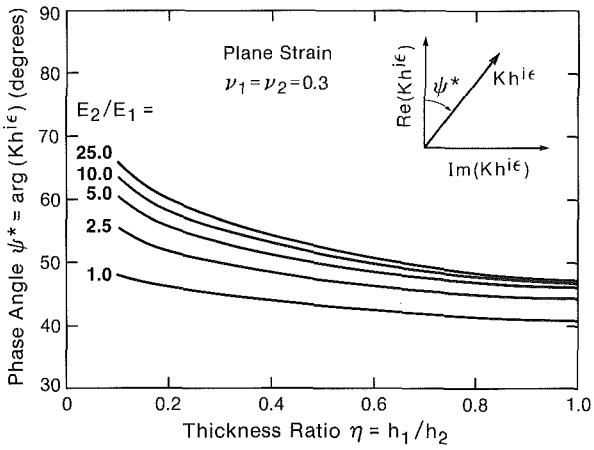


(c)

Fig. 5 *(a)* **The energy release rate with respect to crack length for $h_1/h_2 = 1$; *(b)* The stress intensity factors and their dependence on crack length for $h_1/h_2 = 1$; (c) The phase angle Ψ^*, with respect to crack length for $h_1/h_2 = 1$.**



(a)



(b)

Fig. 6 *(a)* **Trends in the *steady-state* real and imaginary stress intensity factors with the thickness ratio and the modulus ratio; *(b)* The *steady-state* phase angle Ψ^*, with respect to thickness ratio h_1/h_2 and modulus ratio E_2/E_1 for fixed Poisson's ratio, $\nu_1 = \nu_2 = 0.3$**

symmetry plane of the order of the smallest thickness of the two layers (Fig. 5(*b*)), and finally decreases linearly with the crack length beyond the inner load line to about zero at the outer supports. Note, also, that the phase angle, ψ^*, of the complex quantity $Kh^{i\epsilon}$ (Fig. 5(*b*)), is relatively insensitive to the modulus ratio in the constant moment region, but varies appreciably as the crack enters the transient moment region.

Within the *steady-state* region, the normalized finite element energy release rates (Fig. 3) are in excellent agreement with the analytical results. The corresponding stress intensities, (Fig. 6) Re $(Kh^{i\epsilon})$ and Im $(Kh^{i\epsilon})$, exhibit trends given by

$$\text{Re}(Kh^{i\epsilon}) = |K|\cos\psi^*$$
$$\text{Im}(Kh^{i\epsilon}) = |K|\sin\psi^* \qquad (13)$$

where $|K|$ is obtained analytically through equations (8) and (12), and the trends in ψ^* with respect to thickness ratio $(\eta = h_1/h_2)$ and modulus ratio are given in Fig. 6(*b*). It is worth noting, however, that for thickness ratios $\eta > 0.6$, the phase angle ψ^* is essentially invariant with modulus ratio. In particular, for beams with one relatively soft material $(E_2/E_1 > 3)$, the phase angle ψ^* deviates very little from 45 deg (Figs. 3 and 6(*b*)). Under these conditions, the phase angle can be set to $\psi^* \approx 45$ deg, for which the components of the complex stress intensity factor take the approximate form,

Downloaded 03 May 2010 to 171.66.16.31. Redistribution subject to ASME license or copyright; see http://www.asme.org/terms/Terms_Use.cfm

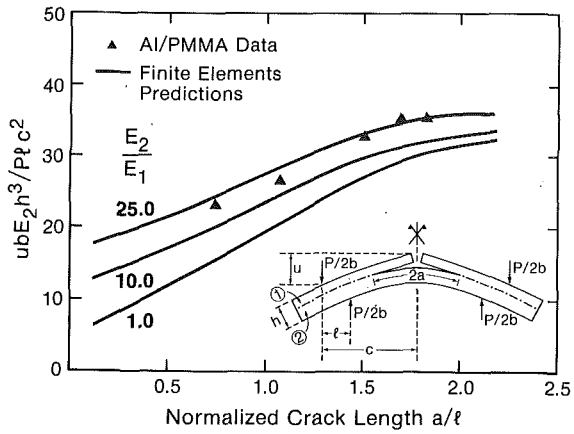


Fig. 7 The relative vertical displacement u of the midpoint of the beam with respect to the outer loading point as a function of the crack length. Also shown are experimental results for Al/PMMA ($E_2/E_1 \approx 25$).

$$\mathrm{Re}(Kh^{i\epsilon}) \simeq \mathrm{Im}\,(Kh^{i\epsilon})$$

$$\simeq \frac{Pl\cosh(\pi\epsilon)}{bh\dfrac{3}{2}\sqrt{1+\lambda}}\left[\frac{3}{2}\left(\frac{1}{\eta_2^3}-\frac{\lambda}{\eta_1^3+\lambda\eta_2^3+\dfrac{3\lambda\eta_1\eta_2}{\eta_1+\lambda\eta_2}}\right)\right]^{1/2} \tag{14}$$

where

$$\eta_i = h_i/h,\ i=1,2.$$

The vertical displacement at the specimen center, u, has also been calculated (Fig. 7) and expressed in terms of the nondimensional parameter, $ub\,E_2h^3/Pl\,c^2$, where $2c$ is spacing between the outer loading points. It is noted that u increases appreciably with increase in crack length, and has the expected linear dependence on a in the region between the inner loading points. This displacement is thus a relatively precise monitor of the crack length and will be used for this purpose in the experimental study (Section 4).

Finally, it is noted that for the material combinations chosen in this investigation, crack surface contact has not been observed even in the smallest element, consistent with the analytical predictions of first contact by Rice (1988). This condition of small scale contact has been used by Rice (1988) to justify the use of K to characterize bimaterial fracture mechanics.

4 Experimental Measurements

4.1 Procedure. An experimental assessment of the utility of the flexure specimen (Fig. 1) for determining interfacial fracture loci has been conducted, using Al/PMMA as a model material couple. Specifically, strips of these materials have been bonded using epoxy, with an initial interface debond created by placing a thin sheet of PTFE along the interface, at the specimen center, prior to bonding. A notch was then introduced through the upper layer, at the center. Erratic interfacial crack propagation from the initial debond, upon loading, was averted by causing controlled extension of the crack prior to testing. This was achieved by placing two thin clamps across the specimen and applying load until crack growth occurred. The clamps arrested the cracks and thus allowed the formation of a well-defined interfacial precrack. Specimen dimensions were selected to allow interface cracking prior to plastic deformation of the Al (Appendix). Suitable dimensions were determined to consist of equidimensional layers, having total thickness > 6 mm.

A displacement transducer was attached to the specimen adjacent to the notch, as needed to measure the vertical displacement, u, upon loading. Loads were imposed in a standard four-point flexure mode, subject to either fixed load or constant load point displacement rate conditions. Typically, with the cracks between the inner loading lines, the cracks extended at a constant rate, subject to constant load, as expected from the constant values of the stress intensities. Crack deceleration occurred when the cracks grew between the inner and outer load lines.

Crack lengths monitored from the displacement measurements were independently checked by means of direct optical observations of the crack front.

Table 2 The results of a typical test conducted at fixed displacement rate on a PMMA/Al specimen

Crack Length a(mm)	$\mathcal{G}_c$ (J/m2)	$\lvert K_c\rvert$ MPa$\sqrt{m}$	ψ (deg)
22.3	11.5	0.25	68
22.6	12.6	0.26	68
25.2	12.7	0.26	68
29.1	12.3	0.26	69
32.5	13.2	0.27	70
35.0	13.3	0.27	71
38.2	12.1	0.26	72
41.0	11.4	0.25	74

To obtain the phase angle, ψ, the units used for all dimensions were meters.

4.2 Results. Compliance measurements performed on specimens with interface cracks having various lengths are initially compared with computed values on Fig. 7. The good correlation in the region between the inner loading points consistent with $E_2/E_1 \approx 25$ for Al/PMMA validates the compliance characteristics of the specimen.[2] Fracture measurements performed using constant displacement rate conditions, with cracks between the inner loading points, reveal that cracks extend at essentially constant load and constant velocity. Consequently, by conducting experiments at different displacement rates and by measuring the load as a function of center point displacement, trends in fracture resistance can be generated by using equation (12) to obtain the critical value of the modulus, $|K_c|$ as well as the phase angle ψ. Results obtained for PMMA/Al using $|K_c|$ and ψ as the characterizing parameters are summarized in Table 2. The results are reproducible between specimens, provided that the bonding conditions are duplicated. The test approach thus seems capable of generating consistent mixed mode interfacial fracture information. The data are also within the general range expected for the Al/PMMA interface ($|K_c| \approx 0.4$ MPa $\sqrt{m}$ for $\psi \approx 0$; Hardwick et al., 1986) but should not be compared directly with the previous data, obtained at $\psi \approx 0$,

[2] Results for crack between the inner and outer loading points are invalid because the loads cause the stress to exceed the yield strength of the Al (Appendix).

Downloaded 03 May 2010 to 171.66.16.31. Redistribution subject to ASME license or copyright; see http://www.asme.org/terms/Terms_Use.cfm

because of the differing bonding procedures. A more comprehensive discussion of the crack growth data and the associated interpretation is presented elsewhere (Lund and Evans, 1987).

5 Concluding Remarks

A method for measuring the mixed-mode interfacial fracture resistance of bonded material couples has been devised and analyzed. The utility of the method has been demonstrated by conducting experiments on a model system consisting of PMMA bonded to Al. The results of the test are in a phase angle range typical of many practical interface decohesion problems: notably, thin film decohesion and fiber debonding in composites. The fracture resistance measurements thus have direct applicability to the interpretation and prediction of decohesion phenomena, albeit that scale effects associated with the differing crack geometries would require careful consideration (Rice, 1988).

The present test could also be used in conjunction with other tests to generate fracture loci $|K_c|$ versus ψ, that probe a larger range of phase angles.

Acknowledgment

The authors wish to thank Hibbitt, Karlsson and Sorensen Inc. of Providence, Rhode Island, for the provision of the ABAQUS code used for all the finite element calculations. Financial support was provided by the Defense Advanced Research Projects Agency through the University Research Initiative Program of UCSB under ONR Contract N-00014-86-K-0753.

References

Drory, M. D., Thouless, M. D., and Evans, A. G., 1988, "On The Decohesion of Thin Films," *Acta Met*, Vol. 36, pp. 2019–2028.

Dundurs, J., 1969, Discussion, ASME JOURNAL OF APPLIED MECHANICS, Vol. 36, Series E, pp. 650–652.

Evans, A. G., Rühle, M., Dalgleish, B. J., and Thouless, M. D., 1987, "On Prevalent Whisker Toughening Mechanisms in Ceramics," *Proc. M.R.S. Symposium on Advanced Structural Ceramics*, Vol. 78, pp. 259–271.

Hardwick, D. A., Ahearn, J. S., Desai, A., and Venables, J. D., 1986, "Environmental Durability of Phosphoric Acid Anodized Aluminium Adhesive Joints Protected With Hydration Inhibitors," *J. Mat. Sci.*, Vol. 21, pp. 179–187.

Hsueh, C. H., and Evans, A. G., 1985, "Residual Stresses and Cracking in Metal/Ceramic Systems for Microelectronics Packaging," *Journal of American Ceramic Society*, Vol. 68, No. 3, pp. 120–127.

Kanninen, M. F., and Popelar, 1985, *Advanced Fracture Mechanics*, Oxford University Press, New York.

Lund, J., and Evans, A. G., 1987, "Measurements of Mixed Mode Interfacial Fracture Resistance," to be published.

Matos, P. P. L., McMeeking, R. M., Charalambides, P. G., and Drory, M. D., 1988, "A Method for Calculating K_I^*, K_{II}^* and K_{III}^* in Mixed Mode Bimaterial Fracture," *Int. J. Fract.*, in press.

Parks, D. M., 1974, "A Stiffness Derivative Finite Element Technique for Determination of Elastic Crack Tip Stress Intensity Factors," *Int. J. Fract.*, Vol. 10, pp. 487–502.

Parks, D. M., 1978, "The Virtual Crack Extension Method for Nonlinear Materials Behavior," *Numerical Methods in Fracture Mechanics*, Eds, A. R. Luxmoore and D. R. Owen, eds., pp. 464–478.

Rice, J. R., 1968, "A Path Independent Integral and the Approximate Analysis of Strain Concentration by Notches and Cracks," ASME JOURNAL OF APPLIED MECHANICS, Vol. 35, pp. 379–386.

Rice, J. R., 1988, "Elastic Fracture Mechanics Concepts for Interfacial Cracks," ASME JOURNAL OF APPLIED MECHANICS, Vol. 55, pp. 98–103.

Rice, J. R., and Sih, G. C., 1965, "Plane Problems of Cracks in Dissimilar Media," ASME JOURNAL OF APPLIED MECHANICS, Vol. 32, pp. 418–423.

Rühle, M., Dalgleish, B. J., and Evans, A. G., 1987, "On the Toughening of Ceramics by Whiskers," *Scripta Met.*, Vol. 21, pp. 681–683.

Thouless, M. D., Evans, A. G., Ashby, M. F., and Hutchinson, J. W., 1987, "The Edge Cracking and Spalling of Brittle Plates," *Acta Metall.*, Vol. 35, No. 6, pp. 1333–1341.

APPENDIX

Specimen Design for Crack Growth Before Yield

The limiting elastic load P_y before yielding is given from simple bending theory as;

$$P_y = bh_2^2\sigma_y/3l \tag{A1}$$

where σ_y is the uniaxial yield strength, The critical load P_c for interfacial failure is given in terms of the ratio h_1/h_2 and a critical stress intensity K_c, as;

$$P_c = K_c h^{3/2} b/lA\,(h_1/h_2) \tag{A2}$$

where A is a constant obtained from the finite element solution presented in the text.

To avoid plasticity before crack extension,

$$P_c < P_y, \tag{A3}$$

which gives rise to the inequality,

$$K_c/\sigma_y\sqrt{h_2} < (A/3)\; h_1/h_2(1+h_2)^{3/2}. \tag{A4}$$

The above inequality suggests that, for a given material couple (given K_c and σ_y), plasticity is less likely to occur as the thickness h_2 increases and when $h_1 \approx h_2$.

Downloaded 03 May 2010 to 171.66.16.31. Redistribution subject to ASME license or copyright; see http://www.asme.org/terms/Terms_Use.cfm

An Examination of the Mori-Tanaka Effective Medium Approximation for Multiphase Composites

A. N. Norris
Department of Mechanics and Materials Science, Rutgers University, Piscataway, N.J. 08855-0909
Assoc. Mem. ASME

The Mori-Tanaka method is considered in the context of both scalar thermal conductivity and anisotropic elasticity of multiphase composites, and some general properties are deduced. Particular attention is given to its relation to known general bounds, and to the differential scheme. It is shown that the moduli predicted by the method always satisfy the Hashin-Shtrikman and Hill-Hashin bounds for two-phase composites. This property does not generalize to multiphase composites. A specific example illustrates that the method can predict moduli in violation of the Hashin-Shtrikman bounds for a three-phase medium. However, if the particle shapes are all spheres, then the prediction for the multiphase composite is coincident with the Hashin-Shtrikman bounds if the matrix material is either the stiffest or the most compliant phase. It is also shown that the generalized differential effective medium method yields the same moduli as the Mori-Tanaka approximation if certain conditions are satisfied in the differential scheme. Thus, it is required that at each stage in the differential process, and for each phase j (j = *1, 2, . . .* , n) *of new material, the average field in the incrementally added phase* j *material must be the same as the average field in the bulk phase* j. *For two phase media,* n = *1, this condition reduces to the less stringent requirement that the ratio of the field in the incrementally added material to the average field in the matrix material is the same as the dilute concentration ratio. The cumulative findings of this paper, particularly those concerning bounds, suggest that the Mori-Tanaka approximation be used with caution in multiphase applications, but is on firmer ground for two-phase composites.*

1 Introduction

Various approximate methods exist for predicting the effective thermal, electrical, and mechanical properties of composites. Among these are the self-consistent scheme, and the differential scheme (Cleary et al., 1980, McGlaughlin, 1977). These effective medium approximations do not require detailed statistical information of the microstructure, but can distinguish between different inclusion shapes. Therefore, such schemes can be useful for statistically homogeneous composites with known inclusion shapes. However, there is always some doubt as to their utility. For example, it is not obvious, a priori, whether the results will automatically satisfy known bounds on the moduli, such as those of Hashin and Shtrikman (1963). At the present time, several methods, including the differential scheme, are known to correspond to realizable media, and hence satisfy the bounds (Avellaneda, 1987).

The Mori-Tanaka approximation is another method that has received attention recently. It is based upon the original work of Mori and Tanaka (1973), and has been used to advantage by, for example, Taya and Mura (1981) and Taya and Chou (1981). Weng (1984) applied the Mori-Tanaka method to the effective medium problem for a two-phase composite with spherical inclusions. Further applications have been given by Benveniste (1986a,b; 1987a,b,c) for the thermal conductivity and mechanical properties of two-phase and multiphase media. Unlike most other approximate methods which require solving implicit equations numerically, the Mori-Tanaka method yields explicit, closed-form answers for the effective properties. As with all other effective medium methods, it hinges upon a mathematical approximation, explained in the following sections. A significant property was discovered by Weng (1984), who showed that the Mori-Tanaka method with spherical inclusions of the softer (harder) phase gives the Hashin-Shtrikman upper (lower) bounds for the bulk and shear moduli. Norris (1985) pointed out that randomly-oriented disk-shaped particles of the softer (harder) phase yields the lower (upper) bounds. Benveniste (1987c) has recently proved, using a clever argument, that the bulk and shear modulus predicted by Mori-Tanaka for a two-phase

Contributed by the Applied Mechanics Division of THE AMERICAN SOCIETY OF MECHANICAL ENGINEERS for publication in the JOURNAL OF APPLIED MECHANICS.

Discussion on this paper should be addressed to the Editorial Department, ASME, United Engineering Center, 345 East 47th Street, New York, N.Y. 10017, and will be accepted until 2 months after final publication of the paper itself in the JOURNAL OF APPLIED MECHANICS. Manuscript received by ASME Applied Mechanics Division October 27, 1987; final revision, February 5, 1988.

Copyright © 1989 by ASME

Downloaded 03 May 2010 to 171.66.16.31. Redistribution subject to ASME license or copyright; see http://www.asme.org/terms/Terms_Use.cfm

composite with randomly-oriented ellipsoidal particles will lie within the Hashin-Shtrikman bounds. This benign property had previously been noted from the numerical results of Tandon (1986) and Maewal and Dandekar (1987). However, as we show in this paper, the Mori-Tanaka method can give results for multiphase media that are in violation of the Haskin-Shtrikman bounds. It appears, therefore, that two-phase composites are a special case for the method.

The purpose of this paper is to examine the connection between the Mori-Tanaka approximation and known bounds. We also relate the approximation to the generalized differential scheme. One common consequence from both studies is that the two-phase medium is a special case. Both thermal and elastic properties are considered. The analysis is simpler for the scalar thermal conductivity problem, and is presented in Section 2. The theory for the elastic moduli is presented in Section 3, where the major results concerning bounds are derived. The connection with the differential scheme is explored in Section 4.

2 The Effective Thermal Conductivity of a Multiphase Isotropic Composite

2.1 General Equations and Definitions. Consider an $n+1$ phase composite made of isotropic constituents with thermal conductivities k_i, $i=0, 1, 2, \ldots, n$, and occupying total volume fractions c_i, such that $\sum_{i=0}^{n} c_i = 1$. Phase $i=0$ corresponds to the matrix material. The temperature field $\phi(\mathbf{x})$ and the normal component of the heat flux, $\mathbf{q}\cdot\mathbf{n}$, where $\mathbf{q}$ is the flux and $\mathbf{n}$ the unit normal, are both continuous across interfaces between the constituents. The heat flux and temperature field in phase i are related by

$$\mathbf{q}^{(i)} = k_i \mathbf{H}^{(i)}, \tag{1}$$

where

$$\mathbf{H}^{(i)} = -\nabla\phi^{(i)}. \tag{2}$$

Assuming an isotropic distribution of grains, the effective conductivity is isotropic and equal to $k^{(\mathrm{eff})}$, defined by the macroscopic relation

$$\bar{\mathbf{q}} = k^{(\mathrm{eff})}\bar{\mathbf{H}}. \tag{3}$$

An overbar denotes the spatial average of a quantity. Thus, $\bar{\mathbf{H}}$ is the average of $\mathbf{H}$ over the entire composite, and $\bar{\mathbf{H}}^{(i)}$ is the average of $\mathbf{H}^{(i)}$ in phase i. The average $\bar{\mathbf{H}}$ could be imposed, for example, by the boundary condition that $\phi = -\bar{\mathbf{H}}\cdot\mathbf{x}$ on the exterior surface of the composite. Under the assumption of macroscopic isotropy, the vectors $\bar{\mathbf{H}}$, $\bar{\mathbf{H}}^{(i)}$, can be replaced by scalar quantities $\bar{H}$, $\bar{H}^{(i)}$, where $\bar{H}^{(i)}$ is the component of $\bar{\mathbf{H}}^{(i)}$ in the direction of $\bar{\mathbf{H}}$. The effective conductivity follows from equations (1) and (3) as

$$k^{(\mathrm{eff})}\bar{H} = \sum_{i=0}^{n} k_i c_i \bar{H}^{(i)}. \tag{4}$$

Equation (4) can be rewritten

$$k^{(\mathrm{eff})} = k_0 + \frac{\sum_{j=1}^{n} (k_j - k_0) c_j \bar{H}^{(j)}/\bar{H}^{(0)}}{c_0 + \sum_{i=1}^{n} c_i \bar{H}^{(i)}/\bar{H}^{(0)}}. \tag{5}$$

This is an exact equation for the effective conductivity $k^{(\mathrm{eff})}$, but is complicated by the determination of the ratios $\bar{H}^{(j)}/\bar{H}^{(0)}$ for each of the added phases $j=1, 2, \ldots, n$.

2.2 The Mori-Tanaka Scheme and Hashin-Shtrikman Bounds. The Mori-Tanaka effective conductivity k is obtained from equation (5) by assuming that the ratio $\bar{H}^{(j)}/\bar{H}^{(0)}$ is equal to the ratio for a single, isolated grain of phase j embedded in uniform matrix material of infinite extent. Equivalently, the ratio $\bar{H}^{(j)}/\bar{H}^{(0)}$ is taken to be the ratio pertaining in the dilute limit of $c \ll 1$, where c is the total volume fraction of the added phases,

$$c = \sum_{j=1}^{n} c_j = 1 - c_0.$$

The ratio $\bar{H}^{(j)}/\bar{H}^{(0)}$ for randomly-oriented ellipsoidal particles of phase j is described by three depolarization coefficients β_1, β_2, and β_3 for each of the major axes (see Landau and Lifshitz (1960) for explicit formulae). These coefficients are between 0 and 1, and satisfy $\beta_1+\beta_2+\beta_3=1$. They each equal 1/3 for spherical particles; long circular cylinders (needles) have $\beta_1=0$, $\beta_2=\beta_3=1/2$, and thin, circular disks have $\beta_1=\beta_2=0$, $\beta_3=1$. In general,

$$\bar{H}^{(j)}/\bar{H}^{(0)} = \frac{1}{3}\sum_{i=1}^{3}\left(1+\frac{k_j-k_0}{\beta_i^{-1}k_0}\right)^{-1}. \tag{6}$$

Benveniste (1986a) observed that if k_0 is smaller (larger) than all of the other k_j, $j=1, 2, \ldots, n$, then the Mori-Tanaka method with $\bar{H}^{(j)}/\bar{H}^{(0)}$ for spherical particles $j=1, 2, \ldots, n$, gives the Hashin-Shtrikman lower (upper) bound on the effective conductivity.

On the other hand, if all the particles are in the shape of thin, circular disks, the Mori-Tanaka scheme gives, from equations (5) and (6),

$$k = k_0\left[\frac{1+2\bar{k}k_0^{-1}}{2+k_0\overline{k^{-1}}}\right], \tag{7}$$

where

$$\bar{k} = \sum_{j=0}^{n} c_j k_j \text{ and } \overline{k^{-1}} = \sum_{j=0}^{n} c_j k_j^{-1}.$$

For a two-phase composite, $n=1$, in which $k_0<k_1$ ($k_0>k_1$), the prediction of equation (7) corresponds to the Hashin-Shtrikman upper (lower) bound on the effective conductivity. This result does not generalize to the multiphase composite, $n>1$. In fact, equation (7) can violate the Hashin-Shtrikman bounds for $n>1$. For example, k of (7) exceeds the upper bound if $n=2$, $k_1=2k_0$, $k_2=3k_0$ and $c_1=c_2=0.4$. This violation indicates that the Mori-Tanaka scheme is not always realizable for multiphase composites.

It is possible to show for two-phase composites that the Mori-Tanaka k of equations (5) and (6) satisfies the Hashin-Shtrikman bounds. To see this, consider equation (5) with $n=1$ and $\alpha=\bar{H}^{(1)}/\bar{H}^{(0)}$. Then,

$$\frac{\partial k}{\partial \alpha} = \frac{c_0 c_1}{(c_0+c_1\alpha)^2} \geq 0. \tag{8}$$

Thus, k is maximum (minimum) for α maximum (minimum). Now consider α of equation (6) as a function of β_1, β_2, and β_3 constrained to the interior and surface of the tetrahedron $\beta_1+\beta_2+\beta_3=1$. It is easily shown that $\alpha(\beta_1, \beta_2, \beta_3)$ attains stationary values at the four vertices, corresponding to plate-like particles, at (1/3, 1/3, 1/3), which is a sphere, and at the points (1/2, 1/2, 0), (1/2, 0, 1/2), and (0, 1/2, 1/2) which are needles. If $k_1>k_0$, then α(sphere) < α(needles) < α(plate). But the sphere and plate values of α correspond to the Hashin-Shtrikman bounds on k, therefore, all other α give intermediate results.

3 The Effective Elastic Moduli of a Multiphase Composite

3.1 The Mori-Tanaka Approximation. Let $\mathbf{L}$ be the effective elastic modulus tensor for a multiphase composite, each

Downloaded 03 May 2010 to 171.66.16.31. Redistribution subject to ASME license or copyright; see http://www.asme.org/terms/Terms_Use.cfm

phase, $i=0, 1, 2, \ldots, n$ characterized by a fourth-order modulus tensor $\mathbf{L}_i$. The anisotropic Hooke's law for each phase is

$$\boldsymbol{\sigma}_i = \mathbf{L}_i \boldsymbol{\epsilon}_i, \tag{9}$$

where $\boldsymbol{\epsilon}_i = 1/2[\nabla \mathbf{u}_i + (\nabla \mathbf{u}_i)^T]$ is the strain. Let the average strain in phases i and 0 be related by

$$\bar{\boldsymbol{\epsilon}}_i = \bar{\mathbf{T}}_{i0} \bar{\boldsymbol{\epsilon}}_0, \qquad i=1, 2, \ldots, n, \tag{10}$$

then an exact expression for the effective moduli $\mathbf{L}^{(\text{eff})}$ follows in a manner analogous to the derivation of equation (6), as

$$\mathbf{L}^{(\text{eff})} = \mathbf{L}_0 + \left(\sum_{j=1}^{n} c_j (\mathbf{L}_j - \mathbf{L}_0) \bar{\mathbf{T}}_{j0} \right) \left[c_0 \mathbf{I} + \sum_{i=1}^{n} c_i \bar{\mathbf{T}}_{i0} \right]^{-1}. \tag{11}$$

Here $\mathbf{I}$ is the fourth-order isotropic indentity tensor, $\mathbf{I}=(1, 1)$ in the concise notation of Hill (1965). In the same notation, an isotropic stiffness tensor is $\mathbf{L}=(3\kappa, 2\mu)$, where κ and μ are bulk and shear moduli, the compliance tensor is $\mathbf{M}=\mathbf{L}^{-1}=(1/3\kappa, 1/2\mu)$, and tensor products are $\mathbf{L}_1\mathbf{L}_2=(9\kappa_1\kappa_2, 4\mu_1\mu_2)$.

In the Mori-Tanaka method $\bar{\mathbf{T}}_{i0}$ is approximated by the analogous quantity for an isolated particle of phase i in an infinite matrix of phase 0. Equivalently, the dilute limit value of $\bar{\mathbf{T}}_{i0}$ is taken. Then equation (1) provides an explicit equation for the Mori-Tanaka effective moduli $\mathbf{L}$. In particular, if the particles of phase i are ellipsoidally shaped and aligned. Eshelby's results provide $\bar{\mathbf{T}}_{i0}$ in the simple form

$$\bar{\mathbf{T}}_{i0} = [\mathbf{I} + \mathbf{S}_{i0}\mathbf{L}_0^{-1}(\mathbf{L}_i - \mathbf{L}_0)]^{-1}, \tag{12}$$

where $\mathbf{S}_{i0}$ depends only upon $\mathbf{L}_0$ and the aspect ratios of the particle of phase i (see, for example, Mura (1982)). The Mori-Tanaka method as defined by equation (11) and the approximation (12) has been called the "direct approach" by Benveniste (1987c). He showed it is identical for two-phase composites to the usual "equivalent inclusion–average stress" formulation of, for example, Weng (1984). The equivalence of the two formulations for multiphase composites is demonstrated in the Appendix.

3.2 Bounds on the Elastic Moduli. If all particle shapes are identical, and the particles are aligned, then the Eshelby tensor $\mathbf{S}_{i0}$ is the same for each phase $i=1, 2, \ldots, n$. Define L_0^0 by

$$\mathbf{L}_0^0 = \mathbf{L}_0 \mathbf{S}_{i0}^{-1} - \mathbf{L}_0. \tag{13}$$

Then the Mori-Tanaka effective moduli become

$$\mathbf{L} = \left(\sum_{j=0}^{n} c_j (\mathbf{L}_j + \mathbf{L}_0^0)^{-1} \right)^{-1} - \mathbf{L}_0^0. \tag{14}$$

Walpole (1966) obtained lower (upper) bounds on $\mathbf{L}^{(\text{eff})}$ in the form of equation (14) under the assumption that $(\mathbf{L}_i - \mathbf{L}_0)$ is positive (negative) definite for all $i=1, 2, \ldots, n$. The bounding modulus tensor is $\mathbf{L}^*$, defined by (14), with $\mathbf{L}_0^0 = \mathbf{L}_0^*$, where $\mathbf{L}_0^*$ depends upon the particular type of anisotropy of the composite.

If all the constituents are isotropic, then the well-known Hashin-Shtrikman (1963) bounds for a macroscopically isotropic composite are defined by

$$\mathbf{L}_0^* = (3\kappa_0^*, 2\mu_0^*), \tag{15}$$

where

$$\kappa_j^* = \frac{4}{3}\mu_j, \tag{16a}$$

$$\mu_j^* = \frac{\mu_j}{6}\left[\frac{9\kappa_j + 8\mu_j}{\kappa_j + 2\mu_j}\right]. \tag{16b}$$

The corresponding Eshelby tensor $\mathbf{S}_{i0}$ is for a spherical particle. Thus, we have that the Mori-Tanaka approximation for spherical particles coincides with the lower (upper) Hashin-Shtrikman bounds on κ and μ if $\kappa_j > \kappa_0$, and $\mu_j > \mu_0$, $j=1, 2, \ldots, n$ ($\kappa_j < \kappa_0$, $\mu_j < \mu_0$, $j=1, 2, \ldots, n$). This equivalence has been previously noted by Weng (1984) for a two-phase composite.

While still on the topic of isotropic constituents, we note that if all the particles are randomly-oriented disks, then $\bar{\mathbf{T}}_{i0}$ can still be expressed in the form of equation (12), but $\mathbf{S}_{i0}$ now depends upon $\mathbf{L}_i$,

$$\mathbf{S}_{j0} = (\mathbf{I} + \mathbf{L}_j^* \mathbf{L}_0^{-1})^{-1}. \tag{17}$$

The Mori-Tanaka effective moduli κ and μ reduce in the special case of a two-phase composite to the Hashin-Shtrikman lower (upper) bounds if $\kappa_1 < \kappa_0$ and $\mu_1 < \mu_0$ ($\kappa_1 > \kappa_0$, $\mu_1 > \mu_0$). As for the thermal conductivity, this result does not generalize to multiphase composites.

If all the constituents are aligned, transversely isotropic phases, the moduli tensors can be represented succinctly in the notation of Walpole (1969) as $\mathbf{L}=(2k, l, n, 2m, 2p)$, $\mathbf{M}=\mathbf{L}^{-1}=1/2(n/\gamma, -l/\gamma, 2k/\gamma, 1/m, 1/p)$, where $\gamma = kn - l^2 = kE$, and E is the axial Young's modulus. For example, if x_3 is the symmetry axis, then $k=C_{11}-C_{66}$, $l=C_{13}$, $n=C_{33}$, $m=C_{66}$, and $p=C_{44}$. Positive definiteness requires that k, m, p, and $n-l^2/k$ are each positive. The bounds of Hill (1964) and Hashin (1965) apply to composites made of aligned cylindrical fibers of arbitrary transverse geometry. These bounds have been phrased succinctly by Walpole (1969) for multiphase composites. In this case the tensor $\mathbf{L}_0^*$ is not well-defined, so it is necessary to work with the compliance tensor $\mathbf{M}$. The dual equation to (14) is

$$\mathbf{M} = \left(\sum_{j=0}^{n} c_j (\mathbf{M}_j + \mathbf{M}_0^0)^{-1} \right)^{-1} - \mathbf{M}_0^0, \tag{18}$$

where $\mathbf{M}_0^0 = \mathbf{L}_0^{0\,-1}$, when the latter is defined. If $(\mathbf{M}_i - \mathbf{M}_0)$ is positive (negative) definite for all $i=1, 2, \ldots, n$, then the lower (upper) bound, $\mathbf{M}^*$, on $\mathbf{M}^{(\text{eff})}$ is given by equation (18), with $\mathbf{M}_0^0 = \mathbf{M}_0^*$, where $\mathbf{M}_0^*$ is

$$\mathbf{M}_0^* = \frac{1}{2}\left(\frac{1}{m_0}, 0, 0, \frac{1}{m_0} + \frac{2}{k_0}, \frac{1}{p_0}\right). \tag{19}$$

Note that Walpole's (1969) $\mathbf{M}_0^*$ contains a typographical error: The correct expression follows from Laws (1974).

The Eshelby tensor $\mathbf{S}_{i0}$ corresponding to equation (19) is that of a circular, cylindrical particle. Therefore, the Hill-Hashin bounds for a multiphase tranversely isotropic fibrous composite of arbitrary transverse geometry corresponds to the Mori-Tanaka approximation with circularly cylindrical particles. This equivalence has been noted by Tandon (1986) for a two-phase composite.

We next develop general results relating the Mori-Tanaka method to the bounds discussed above. The procedure adopted is a generalization of Benveniste's (1987c). Returning to the general assumption that the particles are all identically shaped and aligned, then equation (14) is correct to first-order in c in the dilute limit of $c \ll 1$. Thus,

$$\mathbf{L}^{(\text{eff})} \sim \mathbf{L} = \mathbf{L}_0 + \sum_{j=1}^{n} c_j (\mathbf{L}_j - \mathbf{L}_0)(\mathbf{L}_j + \mathbf{L}_0^0)^{-1}(\mathbf{L}_0 + \mathbf{L}_0^0) + 0(c^2). \tag{20}$$

For a variation $\delta\mathbf{L}_0^0$ of $\mathbf{L}_0^0$ in this equation, the corresponding variation in $\mathbf{L}$ is

$$\delta\mathbf{L} = \sum_{j=1}^{n} c_j (\mathbf{L}_j - \mathbf{L}_0)(\mathbf{L}_j + \mathbf{L}_0^0)^{-1} \delta\mathbf{L}_0^0 (\mathbf{L}_j + \mathbf{L}_0^0)^{-1} \times (\mathbf{L}_j - \mathbf{L}_0) + 0(c^2). \tag{21}$$

Thus, a positive (negative) definite change in $\mathbf{L}_0^0$ yields a cor-

Downloaded 03 May 2010 to 171.66.16.31. Redistribution subject to ASME license or copyright; see http://www.asme.org/terms/Terms_Use.cfm

responding positive (negative) definite change in $\mathbf{L}$. By assumption, the dilute limit effective moduli satisfy the bounds for the particular type of microstructure considered. Therefore, if $\mathbf{L}^*$ represents the lower (upper) bounds, then both $\mathbf{L}-\mathbf{L}^*$ and $\mathbf{L}_0^0-\mathbf{L}_0^*$ are positive (negative) definite tensors of the same anisotropy class.

Now consider the finite concentration case. Variation of $\mathbf{L}_0^0$ in equation (14) yields

$$\delta\mathbf{L}=(\mathbf{L}+\mathbf{L}_0^0)\sum_{j=0}^{n}c_j[(\mathbf{L}_j+\mathbf{L}_0^0)^{-1}$$

$$-(\mathbf{L}+\mathbf{L}_0^0)^{-1}]\delta\mathbf{L}_0^0[(\mathbf{L}_j+\mathbf{L}_0^0)^{-1}-(\mathbf{L}+\mathbf{L}_0^0)^{-1}](\mathbf{L}+\mathbf{L}_0^0), \quad (22)$$

which is positive (negative) definite if $\delta\mathbf{L}_0^0$ is positive (negative) definite. It then follows from the dilute limit result for $\mathbf{L}_0^0-\mathbf{L}_0^*$ that $\mathbf{L}$ of equation (14) satisfies the bounds for finite concentrations. We have thus derived the result that the Mori-Tanaka approximation for multiphase composites, with all particles of the same shape and aligned, satisfies the appropriate Hashin-Shtrikman or Hill-Hashin bounds. This result is not as general as it may seem at first, since the only particle shapes that satisfy these criteria for the Mori-Tanaka approximation are spheres for isotropy, and circular cylinders for fiber-reinforced transverse isotropy. Also, these particular materials correspond to the Hashin-Shtrikman and Hill-Hashin bounds. Although there is no additional information here concerning multiphase composites, these results do have significant application to the particular case of two-phase composites.

The Mori-Tanaka approximation for a two-phase composite ($n=1$) can be written in the form of equation (14) with

$$\mathbf{L}_0^0=(\mathbf{L}_1-\mathbf{L}_0)(\bar{\mathbf{T}}_{10}^{-1}-\mathbf{I})^{-1}-\mathbf{L}_0, \quad (23)$$

where $\bar{\mathbf{T}}_{10}$ is the strain concentration ratio for dilute particulate concentration. Note that $\mathbf{L}_0^0$ of equation (23) is independent of c_1, and holds for any $\bar{\mathbf{T}}_{10}$. Therefore, by the same arguments as before, since the dilute limit moduli must satisfy the lower (upper) bounds on $\mathbf{L}^{(\mathrm{eff})}$, it follows that $\mathbf{L}_0^0-\mathbf{L}_0^*$ is positive (negative) definite. This in turn implies that $\mathbf{L}-\mathbf{L}^*$ is positive (negative) definite at all concentrations, $0<c_1<1$. Hence, the Mori-Tanaka moduli for two-phase composites satisfy the Hashin-Shtrikman or Hill-Hashin bounds, as appropriate. This general result is unique to two-phase composites, since it is not generally possible to write the Mori-Tanaka approximation for multiphase composites in the form of equation (14).

4 The Mori-Tanaka Approximation in Terms of the Differential Scheme

4.1 The Differential Scheme. The generalized differential scheme as understood here is a generalization of Bruggeman's (1935) method to multiphase composites. The present development is similar to that of Norris et al. (1985), where it was applied to a special type of three-phase medium in which one of the added phases was identical to the original matrix material. In order to understand the scheme, consider the scalar conductivity problem for a composite at some finite concentrations of the added phases $j=1, 2, \ldots, n$. Let V be the total volume of the composite, and as before, $\tilde{H}$ is the average of the field $H(\mathbf{x})$ in V. Infinitesimal, discrete volumes of the homogeneous composite material are then removed and replaced by homogeneous amounts of phases $j=1, 2, \ldots, n$. Thus, volume dv_j is replaced by phase j, such that the replaced volume is perfectly bonded to the composite, and dv_j contains a representative quantity of the existing composite of conductivity k. If $\tilde{H}^{(j)}$ is the average of H in dv_j, the incremental change in the effective conductivity is

$$dk=\sum_{j=1}^{n}(k_j-k)\frac{\tilde{H}^{(j)}}{\tilde{H}}\frac{dv_j}{V}. \quad (24)$$

It is preferable to work with the incremental volume fractions dc_j, rather than with the incremental volumes dv_j. Since the total volume V remains fixed, it is possible to show (Norris et al., 1985) that

$$\frac{dv_j}{V}=dc_j+c_j\frac{dc}{1-c}, \quad (25)$$

and hence,

$$dk=\sum_{j=1}^{n}(k_j-k)\frac{\tilde{H}^{(j)}(t)}{\tilde{H}(t)}\left[dc_j+c_j\frac{dc}{1-c}\right]. \quad (26)$$

This becomes an ordinary differential equation by introducing a parameter t to describe the evolution of the composite from homogeneous phase 0 with initial conditions $k(0)=k_0$, $c_j(0)=0, j=1, 2, \ldots, n$. The volume fraction c could be used as the parameter t, for example.

A rigorous justification for the differential equation (26) has been given by Avallaneda (1987). An explicit equation can be obtained, if, for example, the particles are assumed to be in the shape of randomly-oriented ellipsoids. Then $\tilde{H}^{(j)}/\tilde{H}$ is given by the right-hand side of equation (6) with k_0 replaced by $k(t)$. Bruggeman's (1935) scheme is contained in (26) as the special case of a two phase composite, $n=1$. The effective medium approximation for multicomponent composites is the limit of (26) as $c\to 1$. Discussions of these and other limiting cases are contained in Norris et al. (1985) and Norris (1985).

4.1 The Connection With the Mori-Tanaka Approximation. The field ratio in equation (26) can be written

$$\frac{\tilde{H}^{(j)}}{\tilde{H}}=\frac{\tilde{H}^{(j)}/\bar{H}^{(0)}}{1-c+\sum_{i=1}^{n}c_i\bar{H}^{(i)}/\bar{H}^{(0)}}. \quad (27)$$

Note that the averages $\tilde{H}^{(j)}$ and $\bar{H}^{(j)}$ are generally quite distinct and unrelated. The former is the average field in the incrementally added particles of phase j, while the latter is the average field in the entire volume of phase j in the composite.

Define $\check{A}$ and $\tilde{A}$ by

$$\check{A}(t)=\frac{1}{1-c}\sum_{j=1}^{n}c_j\tilde{H}^{(j)}/\bar{H}^{(0)}, \quad (28)$$

$$\tilde{A}(t)=\frac{1}{1-c}\sum_{j=1}^{n}c_j\bar{H}^{(j)}/\bar{H}^{(0)}, \quad (29)$$

An alternative form of the differential scheme follows from equations (27)–(29),

$$(1+\check{A})dk+kd\tilde{A}=d\left[\sum_{j=1}^{n}k_j\frac{c_j}{1-c}\tilde{H}^{(j)}/\bar{H}^{(0)}\right]$$

$$+\sum_{j=1}^{n}(k-k_j)\frac{c_j}{1-c}d[\tilde{H}^{(j)}/\bar{H}^{(0)}]. \quad (30)$$

This equation is integrable if it is *assumed* that

$$\tilde{H}^{(j)}(t)/\bar{H}^{(0)}(t)=\tilde{H}^{(j)}(0)/\bar{H}^{(0)}(0), \quad j=1, 2, \ldots, n, \quad (31)$$

and

$$\tilde{H}^{(j)}=\bar{H}^{(j)}, \qquad j=1, 2, \ldots, n. \quad (32)$$

Then $\check{A}=\tilde{A}$, and integration of equation (30) subject to the initial conditions $k(0)=k_0$, $c_j(0)=0$, $j\geq 1$, gives precisely equation (5) with $\tilde{H}^{(j)}/\bar{H}^{(0)}$ equal to its dilute concentration value. Thus, the differential scheme yields the Mori-Tanaka effective conductivity if equations (31) and (32) hold.

Equations (31) and (32) combined imply that the ratio $\tilde{H}^{(j)}(t)/\bar{H}^{(0)}(t)$ remains constant and equal to the dilute value

Downloaded 03 May 2010 to 171.66.16.31. Redistribution subject to ASME license or copyright; see http://www.asme.org/terms/Terms_Use.cfm

throughout the process. Thus, at each stage of the process, the effective k is given by the Mori-Tanaka method for that concentration. Equation (32) requires, in addition, that the average field in the incrementally added volumes be the same as the bulk average for that phase. It is interesting to note that (32) is not required a priori for two-phase composites, $n=1$, but follows as a consequence of assuming (31). To see this, consider the differential equation (26) for the two-phase composite, which becomes using (27),

$$dk=(k_1-k)\frac{\tilde{H}^{(1)}/\tilde{H}^{(0)}}{(1-c_1+c_1\tilde{H}^{(1)}/\tilde{H}^{(0)})}\frac{dc_1}{(1-c_1)}. \tag{33}$$

However, it follows from equation (4) with $k^{(\mathrm{eff})}\equiv k$, and $\tilde{H}=(1-c_1)\tilde{H}^{(0)}+c_1\tilde{H}^{(1)}$, that

$$\frac{\tilde{H}^{(1)}}{\tilde{H}^{(0)}}=\frac{(1-c_1)}{c_1}\left(\frac{k-k_0}{k_1-k}\right). \tag{34}$$

Substituting from equation (34) into equation (33) gives

$$dk=\frac{(k_1-k)^2}{(k_1-k_0)}\frac{\tilde{H}^{(1)}}{\tilde{H}^{(0)}}\frac{dc_1}{(1-c_1)^2}. \tag{35}$$

This equation can be integrated directly if (31) holds for $j=1$. The equality $\tilde{H}^{(1)}=\tilde{H}^{(1)}$ then follows by substituting the resulting k into (34).

4.3 Differential Effective Medium Theory for Multiphase Elastic Media. The differential equation for the effective moduli $\mathbf{L}(t)$ can be derived in a manner similar to the derivation of equation (26). Thus,

$$d\mathbf{L}=\sum_{j=1}^{n}(\mathbf{L}_j-\mathbf{L})\tilde{\mathbf{T}}_{j0}\Big[(1-c)\mathbf{I}+\sum_{i=1}^{n}c_i\tilde{\mathbf{T}}_{i0}\Big]^{-1}\left(dc_j+c_j\frac{dc}{1-c}\right), \tag{36}$$

where the initial conditions are $\mathbf{L}(0)=\mathbf{L}_0$, $c_j(0)=0$, $j=1, 2, \ldots, n$. The strain concentration tensors $\tilde{\mathbf{T}}_{j0}$, $j=1, 2, \ldots, n$ in equation (36) compare the strain in the currently added phase j to the strain in phase 0 throughout the composite. The tensors $\tilde{\mathbf{T}}_{j0}$ compare the bulk strain in phase j to the bulk strain in phase 0.

In the same way that the differential equation (26) was shown to be integrable if equations (31) and (32) hold, so it can be shown that equation (36) is exactly integrable if both

$$\tilde{\mathbf{T}}_{j0}(t)=\tilde{\mathbf{T}}_{j0}(0), \qquad j=1, 2, \ldots, n, \tag{37}$$

and

$$\tilde{\mathbf{T}}_{j0}=\bar{\mathbf{T}}_{j0}, \qquad j=1, 2, \ldots, n. \tag{38}$$

The case of a two-phase composite is again the exception. The strain concentration tensor $\bar{\mathbf{T}}_{10}$ can then be expressed in terms of the effective moduli as

$$\bar{\mathbf{T}}_{10}=\left(\frac{1-c_1}{c_1}\right)(\mathbf{L}-\mathbf{L}_0)(\mathbf{L}_1-\mathbf{L})^{-1}, \tag{39}$$

which when eliminated from equation (36) gives,

$$d\mathbf{L}=(\mathbf{L}-\mathbf{L}_1)\tilde{\mathbf{T}}_{10}(\mathbf{L}_1-\mathbf{L}_0)^{-1}(\mathbf{L}-\mathbf{L}_1)\frac{dc_1}{(1-c_1)^2}. \tag{40}$$

This differential equation depends only upon $\tilde{\mathbf{T}}_{10}$, and can be directly integrated if it is constant. The resultant moduli when substituted into equation (39) give $\bar{\mathbf{T}}_{10}=\tilde{\mathbf{T}}_{10}$, and the moduli themselves are identical to those of the Mori-Tanaka method. It has come to my attention that laws (1980) also derived the Mori-Tanaka effective medium equation for a two phase composite as a hybrid of the differential scheme and the self-consistent method.

5 Discussion and Conclusions

Our major findings concern the relationship of the Mori-Tanaka approximation to the Hashin-Shtrikman and Hill-Hashin bounds. These bounds will always be satisfied when the approximation is used for two-phase composites. However, this result does not generalize to multiphase media, as demonstrated by a counter example in Section 2.

We have shown that the Mori-Tanaka method can be formulated in terms of the generalized differential scheme provided certain conditions are satisfied by the average fields in the latter. The condition for two-phase media is that the ratio of the field in the incrementally added particles to that in the bulk matrix phase remains constant as the concentration of the added phase goes from zero to its final, finite value. The Mori-Tanaka method, in its "direct approach" formulation, requires that the ratio of the field in the *bulk* added phase to that in the matrix equals its dilute concentration value. It is perhaps surprising that the condition on the incremental field ratio produces the same results as the Mori-Tanaka condition for two-phase media. This is particularly so since the same condition does not suffice to yield the Mori-Tanaka results for multiphase media.

The relationship of the Mori-Tanaka method with the differential scheme offers an alternative way of looking at the former. However, it is not clear whether the relevant conditions, (31)–(32) or (37)–(38), can be realized by specific microgeometries. The answer is, in general, no, since we have shown that the Mori-Tanaka method for multiphase media can give moduli outside the limits of the Hashin-Shtrikman bounds. That it may be possible in two-phase composites is suggested by the fact that the Mori-Tanaka approximation satisfies the bounds, and also because the differential scheme condition (31) or (37) is simpler than that for multiphase media. It remains as an interesting and worthwhile challenge to provide a realization of the method for two phases.

Acknowledgments

Thanks to G. Milton and G. Weng for helpful discussions. This work was supported by the National Science Foundation through Grant No. MDM 85-16256.

References

Avellaneda, M., 1987, "Iterated Homogenization, Differential Effective Medium Theory and Applications," *Communications in Pure and Applied Mathematics*, Vol. 40, pp. 527–554.

Benveniste, Y., 1986a, "On the Effective Thermal Conductivity of Multiphase Composites," *Journal of Applied Mathematics and Physics (ZAMP)*, Vol. 37, pp. 696–713.

Benveniste, Y., 1986b, "On the Mori-Tanaka's Method in Cracked Bodies," *Mechanics Research Communications*, Vol. 13, pp. 193–201.

Benveniste, Y., 1987a, "A Differential Effective Medium Theory with a Composite Sphere Embedding," ASME JOURNAL OF APPLIED MECHANICS, Vol. 54, pp. 466–468.

Benveniste, Y., 1987b, "The Effective Thermal Conductivity of Composites with a Thermal Resistance Between the Constituents: Non-Dilute Case," *Journal of Applied Physics*, Vol. 61, pp. 2840–2843.

Benveniste, Y., 1987c, "A New Approach to the Application of Mori-Tanaka's Theory in Composite Materials," *Mechanics of Materials*, Vol. 6, pp. 147–157.

Bruggeman, D. A. G., 1035, "Berechnung Verschiedener Physikalischer Konstante von Heterogene Substanze," *Annalen der Physik*, Vol. 24, p. 636.

Budiansky, B., 1965, "On the Elastic Modulus of Some Heterogeneous Materials," *Journal of the Mechanics and Physics of Solids*, Vol. 13, pp. 223–227.

Cleary, M. P., Chen, I. W., and Lee, S. M., 1980, "Self-Consistent Techniques for Heterogeneous Solids," *ASCE Journal of Engineering Mechanics*, Vol. 106, pp. 861–887.

Hashin, Z., 1965, "On Elastic Behavior of Fibre Reinforced Materials of Arbitrary Transverse Phase Geometry," *Journal of the Mechanics and Physics of Solids*, Vol. 13, pp. 119–134.

Hashin, Z., and Shtrikman, S., 1963, "A Variational Approach to the Elastic Behavior of Multiphase Materials," *Journal of the Mechanics and Physics of Solids*, Vol. 11, pp. 127–140.

Hill, R., 1964, "Theory of Mechanical Properties of Fibre-Strengthened

Downloaded 03 May 2010 to 171.66.16.31. Redistribution subject to ASME license or copyright; see http://www.asme.org/terms/Terms_Use.cfm

Materials: I. Elastic Behaviour," *Journal of the Mechanics and Physics of Solids*, Vol. 12, pp. 199–212.

Hill, R., 1965, "Continuum Micromechanics of Elastoplastic Polycrystals," *Journal of the Mechanics and Physics of Solids*, Vol. 13, pp. 89–101.

Landau, L. D., and Lifshitz, E. M., 1960, *Electrodynamics of Continuous Media*, Pergamon Press, Oxford.

Laws, N., 1974, "The Overall Thermoelastic Moduli of Transversely Isotropic Composites According to the Self-Consistent Method," *International Journal of Engineering Science*, Vol. 12, pp. 79–87.

Laws, N., 1980, "A Note on the Prediction of Overall Moduli for Composite Materials," *Quarterly Journal of Mechanics and Applied Mathematics*, Vol. 33, pp. 43–45.

Maewal, A., and Dandekar, D. P., 1987, "Effective Thermoelastic Properties of Short-Fiber Composites," *Acta Mechanica*, Vol. 66, pp. 191–204.

McGlaughlin, R., 1977, "A Study of the Differential Scheme for Composite Materials," *International Journal of Engineering Science*, Vol. 15, pp. 237–244.

Mori, T., and Tanaka, K., 1973, "Average Stress in Matrix and Average Elastic Energy of Materials with Misfitting Inclusions," *Acta Metallurgica*, Vol. 231, pp. 571–574.

Mura, T., 1982, *Micromechanics of Defects in Solids*, Martinus Nijhoff, The Hague, Netherlands.

Norris, A. N., 1985, "A Differential Scheme for the Effective Moduli of Composites," *Mechanics of Materials*, Vol. 4, pp. 1–16.

Norris, A. N., Callegari, A. J., and Sheng, P., 1985, "A Generalized Differential Effective Medium Theory," *Journal of the Mechanics and Physics of Solids*, Vol. 33, pp. 525–543.

Tandon, G. P., 1986, "Micromechanical Determination of the Elasticity and Plasticity of Composites," Ph.D. Thesis, Rutgers University.

Taya, M., and Mura, T., 1981, "On Stiffness and Strength of an Aligned Short-Fiber Reinforced Composite Containing Fiber-End Cracks Under Uniaxial Applied Stress," ASME JOURNAL OF APPLIED MECHANICS, Vol. 48, pp. 361–367.

Taya, M., and Chou, T. W., 1981, "On Two Kinds of Ellipsoidal Inhomogeneities in an Infinite Elastic Body: An Application to a Hybrid Composite," *International Journal of Engineering Science*, Vol. 17, pp. 553–563.

Walpole, L. J., 1966, "On Bounds for the Overall Elastic Moduli of Inhomogeneous Systems—II," *Journal of the Mechanics and Physics of Solids*, Vol. 14, pp. 289–301.

Walpole, L. J., 1969, "On the Overall Elastic Moduli of Composite Materials," *Journal of the Mechanics and Physics of Solids*, Vol. 17, pp. 235–251.

Weng, G. J., 1984, "Some Elastic Properties of Reinforced Solids with Special Reference to Isotropic Ones Containing Spherical Inclusions," *International Journal of Engineering Science*, Vol. 22, pp. 845–856.

APPENDIX

Alternative Formulation of the Mori-Tanaka Method

For an average stress in the composite of $\bar{\sigma}$, define the corresponding strain $\hat{\epsilon}_0$ in pure matrix material,

$$\bar{\sigma} = \mathbf{L}_0 \hat{\epsilon}_0. \tag{A1}$$

The perturbed stress and strain in phase 0 in the composite are $\tilde{\sigma}$ and $\tilde{\epsilon}$, where

$$\bar{\sigma} + \tilde{\sigma} = \mathbf{L}_0(\hat{\epsilon}_0 + \tilde{\epsilon}). \tag{A2}$$

The additional perturbed stress and strain in phase i, $i>0$, are σ_i^{pt} and ϵ_i^{pt}, where

$$\begin{aligned} \bar{\sigma} + \tilde{\sigma} + \sigma_i^{pt} &= \mathbf{L}_i(\hat{\epsilon}_0 + \tilde{\epsilon} + \epsilon_i^{pt}), \\ &= \mathbf{L}_0(\hat{\epsilon}_0 + \tilde{\epsilon} + \epsilon_i^{pt} - \epsilon_i^*), \end{aligned} \tag{A3}$$

and ϵ_i^* is the transformation strain in phase i. Taking the average strain throughout the composite, and using (A1), gives

$$\tilde{\epsilon} = \sum_{i=1}^{n} c_i(\epsilon_i^* - \epsilon_i^{pt}). \tag{A4}$$

Equation (A4) then implies that the average strain is

$$\bar{\epsilon} = \hat{\epsilon}_0 + \sum_{i=1}^{n} c_i \epsilon_i^*. \tag{A5}$$

The effective moduli are defined by $\bar{\sigma} = \mathbf{L}\bar{\epsilon}$, or from (A1) and (A5),

$$\mathbf{L}\left(\hat{\epsilon}_0 + \sum_{i=1}^{n} c_i \epsilon_i^*\right) = \mathbf{L}_0 \hat{\epsilon}_0. \tag{A6}$$

Some relations between ϵ_i^* and $\hat{\epsilon}_0$ are necessary to solve (A6) for $\mathbf{L}$.

For each $i = 1, 2, \ldots, n$ let

$$\epsilon_i^{pt} = \mathbf{S}_{i0} \epsilon_i^*. \tag{A7}$$

The average strain in the matrix phase 0 is, from (A2)

$$\bar{\epsilon}_0 = \hat{\epsilon}_0 + \bar{\epsilon}. \tag{A8}$$

Equations (A3), (A7), (A8), and (12) imply, for each $i = 1, 2, \ldots, n$,

$$\epsilon_i^* = -\mathbf{L}_0^{-1}(\mathbf{L}_i - \mathbf{L}_0)\bar{\mathbf{T}}_{i0}\bar{\epsilon}_0. \tag{A9}$$

Then, equations (A4), (A7)-(A9), and (12) give

$$\hat{\epsilon}_0 = \left(c_0 \mathbf{I} + \sum_{i=1}^{n} c_i \mathbf{L}_0^{-1} \mathbf{L}_i \bar{\mathbf{T}}_{i0}\right) \bar{\epsilon}_0. \tag{A10}$$

Equations (A9) and (A10) can then be substituted into (A6) to given an explicit expression for $\mathbf{L}$ that is identical to equation (11). The Mori-Tanaka assumption is that $\mathbf{S}_{i0}$ is equal to the corresponding Eshelby tensor for a single inclusion of phase i in phase 0.

Downloaded 03 May 2010 to 171.66.16.31. Redistribution subject to ASME license or copyright; see http://www.asme.org/terms/Terms_Use.cfm

Chau-Shioung Yeh
Professor.
Department of Civil Engineering,
Institute of Applied Mechanics,
National Taiwan University,
Taipei, Taiwan 10764

Magnetic Fields Generated by a Mechanical Singularity in a Magnetized Elastic Half Plane

The induced magnetic fields generated by a line mechanical singularity in a magnetized elastic half plane are investigated in this paper. One version of linear theory for soft ferromagnetic elastic solids which has been developed by Pao and Yeh (1973) is adopted to analyze the plane strain problem undertaken. By applying the Fourier transform technique, the exact solutions for the generated magnetic inductions due to various mechanical singularities such as a single force, a dipole, and single couple are obtained in a closed form. The distributions of the generated inductions on the surface are shown with figures.

I Introduction

In recent years, the theory of magnetoelasticity, describing the interaction between the magnetic fields and elastic solids, has received considerable attention because of the possible applications in detection of flaws in ferrous metals, optical acoustics, levitation by superconductors, and many other electromechanical devices (Moon, 1984). The interaction between magnetic and elastic processes in ferromagnetic materials was thoroughly treated in a monograph by Brown (1966). He developed a rigorous phenomenological theory of magnetoelasticity on the basis of the large deformation theory of elasticity and the classical theory of ferromagnetism. An analogous theory based on a microscopic model was developed by Tiersten (1964) for obtaining a consistent set of field equations and boundary conditions. Since the general nonlinear theory is rather complicated, Pao and Yeh (1973) derived a set of linear equations and boundary conditions for soft ferromagnetic elastic materials with multidomain structure, which are widely used in electromechanical technology. The linear theory has been applied to investigate the magnetoelastic buckling of an isotropic plate in a transversally applied uniform magnetic induction (Pao and Yeh, 1973), and to investigate the intensification factors of cracks in ferromagnetic elastic solids (Shindo, 1977, 1978, 1980). Recently, as a possible applications in geophysics, Yeh (1987) has applied the same theory to investigate the induced magnetic fields in an infinite magnetized elastic space, which is generated by a tension fault normal to a uniform magnetic induction. The induced magnetic potential for several cases are obtained in closed form expressions.

In this paper, we investigate the magnetic inductions generated by the mechanical singularities in a magnetized elastic half plane, a two-dimensional plane strain problem. The solutions are expressed in a closed form and numerical results for several examples are presented.

Contributed by the Applied Mechanics Division of THE AMERICAN SOCIETY OF MECHANICAL ENGINEERS for publication in the JOURNAL OF APPLIED MECHANICS.

Discussion on this paper should be addressed to the Editorial Department, ASME, United Engineering Center, 345 East 47th Street, New York, N.Y. 10017, and will be accepted until two months after final publication of the paper itself in the JOURNAL OF APPLIED MECHANICS. Manuscript received by ASME Applied Mechanics Division, September 4, 1987; final revision, July 1, 1988.

II Linear Theory and Governing Equations

In the linearized theory (Pao and Yeh, 1973), all magnetic quantities such as magnetic induction B_i, magnetization M_i and magnetic intensity H_i are decomposed into two parts as

$$B_i = \bar{B}_i + b_i,\ M_i = \bar{M}_i + m_i,\ H_i = \bar{H}_i + h_i \tag{1}$$

where $\bar{B}_i$, $\bar{M}_i$, and $\bar{H}_i$ are the magnetic quantities in the rigid body state in which no mechanical source existed, and b_i, m_i, and h_i are those in the perturbation state generated by the mechanical singularities of stress or strain. This decomposition was also adopted by Pak and Herrmann (1986) to formulate a linear theory of the dielectric medium. All quantities in the perturbed state are assumed very small, that is,

$$|b_i|/|\bar{B}_i| < < 1,\ |m_i|/|\bar{M}_i| < < 1.$$

The gradient of displacements is also assumed small, $|\partial u_i/\partial x_j| < < 1$.

Rigid Body State. In the rigid body state, the static magnetic field satisfies the following equations

$$e_{ijk}\bar{H}_{k,j} = 0,\quad \bar{B}_{i,i} = 0 \tag{2}$$

where e_{ijk} is the permutation symbol and (,) denotes the partial differentiation with respect to the spatial variable. The constitutive law for the field is

$$\bar{H}_i = \chi\bar{H}_i,\ \bar{B}_i = \mu_0\,(\bar{H}_i + \bar{M}_i) = \mu_0\mu_r\bar{H}_i,\ \mu_r \equiv 1 + \chi \tag{3}$$

where χ is the magnetic susceptibility of the material, $\mu_0 = 4\pi \times 10^{-7}$ newton/ampere^2 is a universal constant and μ_r is the relative magnetic permeability. On the boundary of an undeformed body with an outward unit normal n_i, we have

$$\begin{aligned} e_{ijk}n_j[\bar{H}_k] &\equiv e_{ijk}n_j(\bar{H}_k^+ - \bar{H}_k^-) = 0 \\ n_i[\bar{B}_i] &\equiv n_i(\bar{B}_i^+ - \bar{B}_i) = 0 \end{aligned} \tag{4}$$

Copyright © 1989 by ASME
Downloaded 03 May 2010 to 171.66.16.31. Redistribution subject to ASME license or copyright; see http://www.asme.org/terms/Terms_Use.cfm

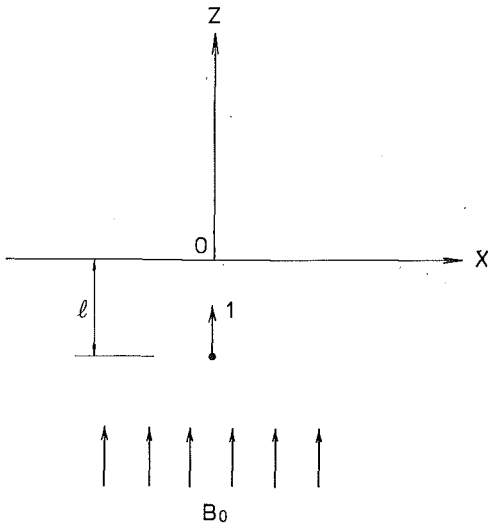


Fig. 1 A force normal to the boundary in the interior of a magnetized elastic half plane

where the quantities with the superscript + denote those outside the material. We should mention that any possible rigid body motion must be properly taken into account as discussed in Pao and Yeh, (1973), and the aforementioned system of equations forms a determinate set in evaluating $\bar{H}_i$, $\bar{M}_i$, and $\bar{B}_i$ if the external magnetic field and magnetic susceptibility are given. The material considered here is isotropic, cubic, or uniaxial in symmetry.

Perturbation State. In this investigation, we shall assume $|\bar{M}_j u_{i,j}| << |m_i|$ as is done by Shindo (1977, 1978, 1980). The equation of equilibrium under mechanical and magnetic body forces is

$$t_{ij,i} + \mu_0 (\bar{M}_i \bar{H}_{j,i} + \bar{M}_i h_{j,i} + m_i \bar{H}_{j,i}) + f_j = 0 \tag{5}$$

where t_{ij} is the magnetomechanical stress tensor and f_j the mechanical body force per unit volume. The perturbed magnetic fields satisfy the two static equations,

$$et_{ijk} h_{k,j} = 0, \quad b_{i,i} = 0. \tag{6}$$

Neglecting the effect of magnetostriction, the constitutive equations are

$$t_{ij} = \frac{\mu_0}{\chi} \bar{M}_i \bar{M}_j + \tau_{ij} + \mu_0 (\bar{H}_j m_i + \bar{H}_i m_j) \tag{7}$$

$$m_i = \chi h_i, \; b_i = \mu_0 (h_i + m_i) = \mu_0 \mu_r h_i \tag{8}$$

and

$$\tau_{ij} = \lambda u_{k,k} \delta_{ij} + G(u_{i,j} + u_{j,i}) \tag{9}$$

is the elastic stress tensor for a nonmagnetizable material. The λ and G are Lamé constants, and δ_{ij} is the Kronecker delta symbol. It should be mentioned that the stress tensor in the linear theory is symmetric.

The linearized boundary conditions are

$$e_{ijk} \{n_j [h_k] - u_{p,j} n_p [\bar{H}_k]\} = 0 \tag{10}$$

$$n_i [b_i] - u_{p,i} n_p [\bar{B}_i] = 0 \tag{11}$$

$$n_i [\tau_{ij}] = -\mu_0 n_i [\bar{M}_i \bar{M}_j / \chi] - \mu_0 n_i [\bar{H}_j \bar{m}_i + \bar{H}_i \bar{m}_j] + \frac{1}{2} \mu_0 n_j [\bar{M}_n{}^2] + \mu_0 n_j [\bar{M}_n m_n] \tag{12}$$

where $\bar{M}_n = \mathbf{n} \cdot \bar{\mathbf{M}}$, $m_n = \mathbf{n} \cdot \mathbf{m}$. Note that although $|\bar{H}_i u_{j,i}| < |h_i|$ within one material, the jumps of both quantities are still kept in equation (10) because $|\bar{H}_i u_{j,i}|$ on one side of the boundary may be of the same order of magnitude on the other side.

III Plane Problems of a Magnetized Half Space

Consider a magnetizable half plane occupying the region $z \leq 0$ as shown in Fig. 1. The applied magnetic induction $B_0 e_z$ is distributed in whole plane uniformly. By employing equations (2-4), the solutions for the rigid body state of the half plane are obtained as

$$\bar{B}_z^+ = B_0, \; \bar{H}_z^+ = B_0/\mu_0, \; \bar{M}_z^+ = 0, \; (z \geq 0). \tag{13}$$

$$\bar{B}_z = B_0, \; \bar{H}_z = B_0/\mu_0\mu_r, \; \bar{M}_z = \chi B_0/\mu_0\mu_r, \; (z \leq 0). \tag{14}$$

All other components of $\bar{\mathbf{B}}$, $\bar{\mathbf{H}}$, $\bar{\mathbf{M}}$, inside and outside the material are equal to zero.

The displacements and perturbed magnetic fields considered in this plane strain problem are

$$u_x = u(x, z), \; u_y = 0, \; u_z = w(x,z)$$
$$h_x^+ = h_x^+(x,z), \; h_y^+ = 0, \; h_z^+ = h_z^+(x,z)$$
$$h_x = h_x(x,z), \; h_y = 0, \; h_z = h_z(x,z).$$

The two magnetic equations (6) for the perturbation fields are satisfied by introducing a magnetic potential $\phi(x,z)$ such that

$$h_x^+ = \frac{\partial \phi^+}{\partial x}, \; h_z^+ = \frac{\partial \phi^+}{\partial x}, \tag{15}$$

$$h_x = \frac{\partial \phi}{\partial x}, \; h_z = \frac{\partial \phi}{\partial x}, \tag{16}$$

where the magnetic potentials ϕ^+ in $z \geq 0$ and ϕ in $z \leq 0$ satisfy the Laplace equations,

$$\nabla^2 \phi^+ = 0 \tag{17}$$

$$\nabla^2 \phi = 0 \tag{18}$$

where

$$\nabla^2 = \frac{\partial^2}{\partial x^2} + \frac{\partial^2}{\partial z^2}.$$

The substitution of equations (7), (8), (9), (14), and (16) into equation (5), omitting the body force, yields the equations of equilibrium as follows,

$$\nabla^2 u + \frac{1}{(1-2\nu)} \frac{\partial}{\partial x} \left(\frac{\partial u}{\partial x} + \frac{\partial w}{\partial z} \right) + \frac{2\chi B_0}{G\mu_r} \frac{\partial^2 \phi}{\partial x \partial z} = 0 \tag{19}$$

$$\nabla^2 w + \frac{1}{(1-2\nu)} \frac{\partial}{\partial z} \left(\frac{\partial u}{\partial x} + \frac{\partial w}{\partial z} \right) + \frac{2\chi B_0}{G\mu_r} \frac{\partial^2 \phi}{\partial z^2} = 0 \tag{20}$$

in which ν denotes Poisson's ratio of material. The boundary conditions (10)-(11) are reduced to

$$\frac{\partial \phi^+}{\partial x} - \frac{\partial \phi}{\partial x} = -\frac{\chi B_0}{\mu_0 \mu_r} \frac{\partial w}{\partial x}; \text{ on } z = 0 \tag{21}$$

$$\frac{\partial \phi^+}{\partial z} - \mu_r \frac{\partial \phi}{\partial z} = 0; \text{ on } z = 0. \tag{22}$$

Those for the stress-free boundary, equation (12), are reduced to

$$\frac{\partial u}{\partial z} + \frac{\partial w}{\partial x} = -\frac{\chi B_0}{G\mu_r} \frac{\partial \phi}{\partial x}; \text{ on } z = 0 \tag{23}$$

$$\nu \frac{\partial u}{\partial x} + (1-\nu) \frac{\partial w}{\partial z} = \frac{(1-2\nu)\chi(\chi-2)B_0}{2G\mu_r} \frac{\partial \phi}{\partial z}; \text{ on } z = 0. \tag{24}$$

We note that the contribution from the term $(1-2\nu)\chi(\chi-2)B_0{}^2/4\nu G\mu_0\mu_r{}^2$ in equation (24) is not counted since it generates the uniform stresses in the half plane. Equations (17)-(24) provide the governing equations associated with boundary conditions for investigating the magnetic induction generated by the mechanical singularities.

In view of equations (17) and (18), the mechanical singularities seem to have no effect on the magnetic potentials, however, their effects will become obvious through the

Downloaded 03 May 2010 to 171.66.16.31. Redistribution subject to ASME license or copyright; see http://www.asme.org/terms/Terms_Use.cfm

boundary conditions which couple the magnetic potentials with the deformations.

Employing Fourier transform with respect to x and its inversion theorem, we can obtain the solutions ϕ^+ and ϕ of equations (17) and (18), and the complementary solutions u_c are w_c of equations (19) and (20) (zero body forces) as follows,

$$\phi^+ = \frac{1}{2\pi}\int_{-\infty}^{\infty} A(\xi)e^{-|\xi|z+i\xi x}d\xi \tag{25}$$

$$\phi = \frac{1}{2\pi}\int_{-\infty}^{\infty} C(\xi)e^{|\xi|z+i\xi x}d\xi \tag{26}$$

$$u_c = \frac{1}{2\pi}\int_{-\infty}^{\infty}\left\{D_1(\xi)\frac{i\xi}{|\xi|}e^{|\xi|z} + D_2(\xi)\frac{i\xi}{|\xi|}\left((3-4\nu)+|\xi|z\right)e^{|\xi|z} + C(\xi)\frac{2(1-2\nu)\chi B_0}{G\mu_r}\frac{i\xi}{|\xi|}e^{|\xi|z}\right\}e^{i\xi x}d\xi \tag{27a}$$

$$w_c = \frac{1}{2\pi}\int_{-\infty}^{\infty}\left(D_1(\xi)e^{|\xi|z} + D_2(\xi)|\xi|ze^{|\xi|z}\right)e^{i\xi x}d\xi \tag{28a}$$

where $A(\xi)$, $C(\xi)$, $D(\xi)$, and $D_2(\xi)$ are arbitrary functions and will be determined by the boundary conditions. The solution (25) satisfies the condition of finiteness at $z \to \infty$ and the solutions (26), (27a) and (28a) satisfy those at $z \to -\infty$. The complete solutions of u and w must be supplemented with the contributions from the mechanical singularities, through the mechanical body forces, $u_p(x, z)$, i.e.,

$$u = u_c + u_p \tag{27b}$$

$$w = w_c + w_p. \tag{28b}$$

The substitutions of (25)–(28) into the boundary conditions (21)–(24) give rise to

$$\frac{1}{2\pi}\int_{-\infty}^{\infty} i\xi\left(A(\xi)-C(\xi)\right)e^{i\xi x}d\xi = -\frac{\chi B_0}{\mu_0\mu_r}\left(\frac{1}{2\pi}\int_{-\infty}^{\infty} i\xi D_1(\xi)e^{i\xi x}d\xi + \frac{\partial w_p}{\partial x}\Big|_{z=0}\right) \tag{29}$$

$$\frac{1}{2\pi}\int_{-\infty}^{\infty} i\xi\left(A(\xi)-\mu_r C(\xi)\right)e^{i\xi x}d\xi = 0 \tag{30}$$

$$\frac{1}{2\pi}\int_{-\infty}^{\infty}\left(2i\xi D_1(\xi)+4(1-\nu)i\xi D_2(\xi)\right)e^{i\xi x}d\xi + \left(\frac{\partial u_p}{\partial z}+\frac{\partial w_p}{\partial x}\right)\Big|_{z=0} = \frac{\chi B_0}{G\mu_r}\frac{1}{2\pi}\int_{-\infty}^{\infty}[(3-4\nu)i\xi C(\xi)]e^{i\xi x}d\xi \tag{31}$$

$$\frac{1}{2\pi}\int_{-\infty}^{\infty}\left(2|\xi|D_1(\xi)+2(1-2\nu)|\xi|D_2(\xi)\right)e^{i\xi x}d\xi + \frac{2}{(1-2\nu)}\left(\nu\frac{\partial u_p}{\partial x}+(1-\nu)\frac{\partial w_p}{\partial z}\right)\Big|_{z=0} = \frac{\chi B_0}{G\mu_r}\frac{1}{2\pi}\int_{-\infty}^{\infty}[(\chi-2+4\nu)|\xi|C(\xi)]e^{i\xi x}d\xi. \tag{32}$$

Equation (30) yields

$$A(\xi) = -\mu_r C(\xi). \tag{33}$$

Thus, equation (29) reduces to

$$\frac{1}{2\pi}\int_{-\infty}^{\infty} i\xi\left((\mu_r+1)C(\xi)-\frac{\chi B_0}{\mu_0\mu_r}D_1(\xi)\right)e^{i\xi x}d\xi = -\frac{\chi B_0}{\mu_0\mu_r}\frac{\partial w_p}{\partial x}\Big|_{z=0}. \tag{34}$$

Once u_p and w_p are given, equations (31)–(34) can be used to determine the arbitrary functions $A(\xi)$, the magnetic potentials ϕ^+ and ϕ and the displacements u and w can then be obtained by applying equations (25)–(28) accordingly.

IV Perturbation of Magnetic Fields by Mechanical Sources

Magnetic Fields Generated by a Line Force Normal to the Boundary of the Half Plane. When a unit line force is applied at $(0, -l)$ and acts in the positive z-direction, as shown in Fig. 1, the Kelvin solution for the displacements in an infinite plane is (Love, 1944)

$$u_p = \frac{1}{8\pi(1-\nu)G}\frac{x(z+l)}{r_1^2}$$
$$w_p = \frac{1}{8\pi(1-\nu)G}\left((3-4\nu)\ln r_1 + \frac{x^2}{r_1^2}\right) \tag{35}$$
$$r_1^2 = x^2 + (z+l)^2.$$

Thus, employing Fourier transform and its inversion theorem, we have

$$\frac{\partial w_p}{\partial x}\Big|_{z=0} = \frac{1}{8\pi(1-\nu)G}\left(\frac{(3-4\nu)x}{x^2+l^2}+\frac{2l^2x}{(x^2+l^2)^2}\right) = \frac{1}{2\pi}\int_{-\infty}^{\infty}\frac{1}{8(1-\nu)G}\frac{i\xi}{|\xi|}\left((3-4\nu)+|\xi|l\right)e^{-|\xi|l+i\xi x}d\xi,$$

$$\left(\frac{\partial u_p}{\partial z}+\frac{\partial w_p}{\partial x}\right)\Big|_{z=0} = \frac{1}{8\pi(1-\nu)G}\left(\frac{2(1-\nu)x}{x^2+l^2}+\frac{4l^2x}{(x^2+l^2)^2}\right) = \frac{1}{2\pi}\int_{-\infty}^{\infty}\frac{1}{8(1-\nu)G}\frac{i\xi}{|\xi|}\left((1-2\nu)+|\xi|l\right)e^{-|\xi|l+i\xi x}d\xi,$$

$$\frac{1}{(1-2\nu)}\left(\nu\frac{\partial u_p}{\partial x}+(1-\nu)\frac{\partial w_p}{\partial z}\right)\Big|_{z=0} = \frac{-1}{8\pi(1-\nu)G}\left(\frac{2(1-\nu)l}{x^2+l^2}+\frac{(l^2-x^2)l}{(x^2+l^2)^2}\right) = \frac{1}{2\pi}\int_{-\infty}^{\infty}\frac{-1}{8(1-\nu)G}\frac{i\xi}{|\xi|}\left((1-2\nu)-|\xi|l\right)e^{-|\xi|l+i\xi x}d\xi.$$

Substituting the above equations into equations (31)–(34), and with simple manipulation, we obtain

$$A = -\frac{\chi B_0}{2G\mu_0(\mu_r+1)\Delta}\frac{[|2(1-\nu)+|\xi|l]}{|\xi|}e^{-|\xi|l}$$

$$C = -\frac{A}{\mu_r}$$

$$D_1 = \frac{\gamma}{2G}\frac{[2(1-\nu)+|\xi|l]}{|\xi|}e^{-|\xi|l} + \frac{1}{8(1-\nu)G}\frac{[8(1-\nu)^2-(3-4\nu)+(3-4\nu)|\xi|l]}{|\xi|}e^{-|\xi|l}$$

Downloaded 03 May 2010 to 171.66.16.31. Redistribution subject to ASME license or copyright; see http://www.asme.org/terms/Terms_Use.cfm

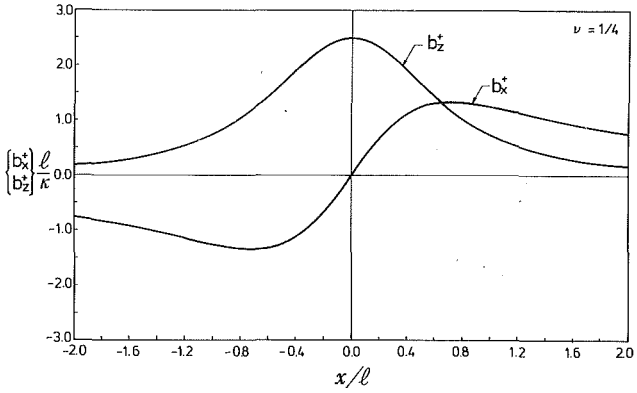


Fig. 2 The distribution of the generated magnetic induction on the surface due to the line force normal to the boundary

$$D_2 = \frac{-\beta}{2G} \frac{[2(1-\nu)+|\xi|l]}{|\xi|} e^{-|\xi|l} - \frac{1}{8(1-\nu)G} \frac{[(3-4\nu)+2|\xi|l]}{|\xi|} e^{-|\xi|l}$$

where

$$\beta = \frac{\chi^2}{2\mu_r(\mu_r+1)\Delta} \frac{{B_0}^2}{G\mu_0}$$

$$\gamma = \frac{\beta(1-\nu)(2\mu_r-3+4\nu)}{\mu_r}$$

$$\Delta = 1 - \frac{\chi^2 {B_0}^2 (1-\nu)[2\mu_r-(3-4\nu)]}{2G\mu_0{\mu_r}^2(\mu_r+1)}.$$

Thus, equations (25)–(28) give ϕ^+, ϕ, u, and w in a closed form as follows,

$$\phi^+ = \frac{\chi B_0}{2\pi G\mu_0(\mu_r+1)\Delta} \left[2(1-\nu)\ln r_1 + \frac{l(z+l)}{{r_1}^2}\right] \tag{38}$$

$$\phi = \frac{-\chi B_0}{2\pi G\mu_0\mu_r(\mu_r+)\Delta} \left[2(1-\nu)\ln r_2 + \frac{l(z-l)}{{r_2}^2}\right] \tag{39}$$

$$u = u_1 + u_2$$
$$w = w_1 + w_2 \tag{40}$$

with

$$u_1 = \frac{1}{8\pi(1-\nu)G} \left(4(1-\nu)(1-2\nu)\tan^{-1}\left(\frac{x}{l-z}\right) + (3-4\nu)\frac{(l+z)x}{{r_2}^2} + \frac{4lxz(l-z)}{{r_2}^4} + \frac{(l+z)x}{{r_1}^2}\right)$$

$$w_1 = \frac{1}{8\pi(1-\nu)G} \left(-8(1-\nu)^2\ln r_2 - (3-4\nu)\ln(r_1/r_2) - \frac{(3-4\nu)(z-l)^2+2lz}{{r_2}^2} - \frac{4lz(z-l)^2}{{r_2}^4} + \frac{(z+l)^2}{{r_1}^2}\right)$$

$$u_2 = \frac{-\beta}{2\pi G} \left\{\left(6(1-\nu)(1-2\nu) - \frac{2(1-\nu)^2(3-4\nu)}{\mu_r}\right)\tan^{-1} \times \left(\frac{x}{l-z}\right) + 3(1-2\nu)\frac{lx}{{r_2}^2} - 2(1-\nu)\frac{xz}{{r_2}^2} + \frac{2lxz(z-l)}{{r_2}^4} - \frac{(1-\nu)(3-4\nu)}{\mu_r}\frac{lx}{{r_2}^2}\right\}$$

$$w_2 = \frac{\beta}{2\pi G} \left(-4(1-\nu)^2\ln r_2 + 2(1-\nu)\frac{(z-l)^2}{{r_2}^2} + \frac{lz[x^2-(z-l)^2]}{{r_2}^4} + \frac{2(1-\nu)^2(3-4\nu)}{\mu_r}\ln r_2 + \frac{(1-\nu)(3-4\nu)}{\mu_r}\frac{l(z-l)}{{r_2}^2}\right), \quad r_2 = \sqrt{x^2+(z-l)^2}. \tag{41}$$

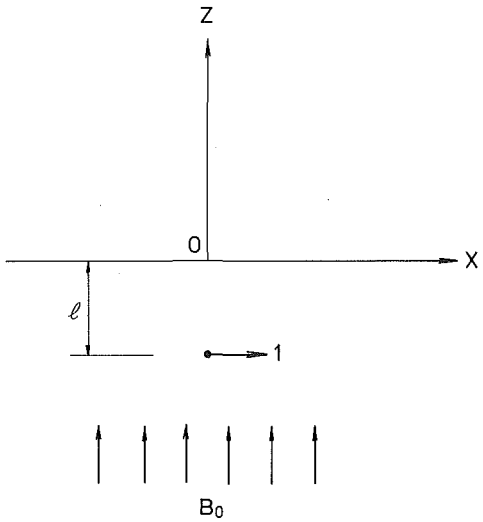


Fig. 3 A force parallel to the boundary in the interior of a magnetized elastic half plane

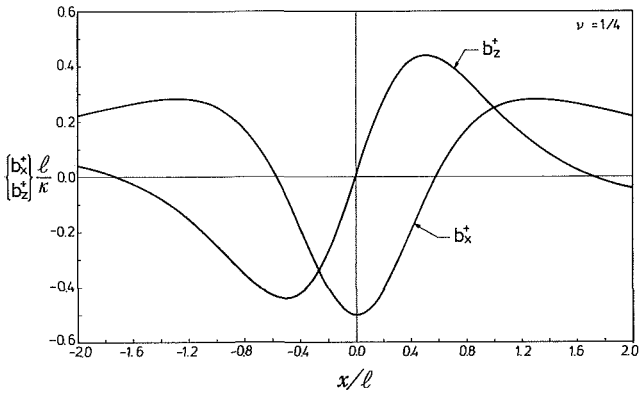


Fig. 4 The distribution of the generated magnetic induction on the surface due to the line force parallel to the boundary

Although only the magnetic fields generated by the mechanical singularities are interested in this investigation, the displacements for this case are also presented for the completeness of the problem. In the solutions, u_1 and w_1 are contributed from the single force only (Sneddon, 1951), and u_2 and w_2 are due to the effect of the external magnetic induction B_0. Since $\chi \approx \mu_r \approx 10^4$ for most ferromagnetic materials and $({B_0}^2/G\mu_0) << 1$ for usual B_0, it results in $\Delta \approx 1$ and then $\beta << 1$. Thus, we can see that the effect of B_0 on the displacements can be neglected. However, observing the expression for ϕ^+ in equation (34), it can be seen that $|\mathbf{b}^+|/B_0 = |\mu_0 \nabla\phi^+|/B_0 \propto$ force/Gl. If the applied force is large enough, $\mathbf{b}^+$ on the boundary may be measurable, even $B_0 \sim 1$ gauss. In the case considered, the generated magnetic induction in a vacuum can be expressed as

$$b_x{}^+ = \mu_0 \frac{\partial\phi^+}{\partial x} = \kappa\left(2(1-\nu)\frac{x}{{r_1}^2} + \frac{2lx(z+l)}{{r_1}^4}\right), \tag{43}$$

$$b_z{}^+ = \mu_0 \frac{\partial\phi^+}{\partial z} = \kappa\left\{2(1-\nu)\frac{(z+l)}{{r_1}^2} + \frac{l[(z+l)^2-x^2]}{{r_1}^4}\right\} \tag{44}$$

Downloaded 03 May 2010 to 171.66.16.31. Redistribution subject to ASME license or copyright; see http://www.asme.org/terms/Terms_Use.cfm

where $\kappa = \dfrac{\chi B_0}{2\pi G(\mu_r + 1)\Delta}$.

Figure 2 shows the distribution of the generated magnetic induction on the surface.

Magnetic Fields Generated by a Line Force Parallel to Boundary of the Half Plane. As the unit line force at $(0, -l)$ acts in the x-direction as shown in Fig. 3, the displacements are (Love, 1944)

$$u_p = \frac{-1}{8\pi(1-\nu)G}\left((3-4\nu)\ln r_1 + \frac{(z+l)^2}{r_1^2}\right),$$
$$w_p = \frac{1}{8\pi(1-\nu)G}\frac{x(z+l)}{r_1^2}. \tag{45}$$

Following the same procedure as that employed in the preceding case, we can obtain the magnetic potential and displacements. However, the effect of B_0 on the displacements is negligible as discussed in the preceding case, thus we only list the generated magnetic potentials for this case as follows,

$$\phi^+ = \frac{\kappa}{\mu_0}\left((1-2\nu)\tan^{-1}\left(\frac{x}{z+l}\right) - \frac{lx}{r_1^2}\right) \tag{46}$$

$$\phi = \frac{-\kappa}{\mu_0\mu_r}\left((1-2\nu)\tan^{-1}\left(\frac{x}{l-z}\right) - \frac{lx}{r_2^2}\right). \tag{47}$$

The generated magnetic induction in a vacuum can be obtained accordingly,

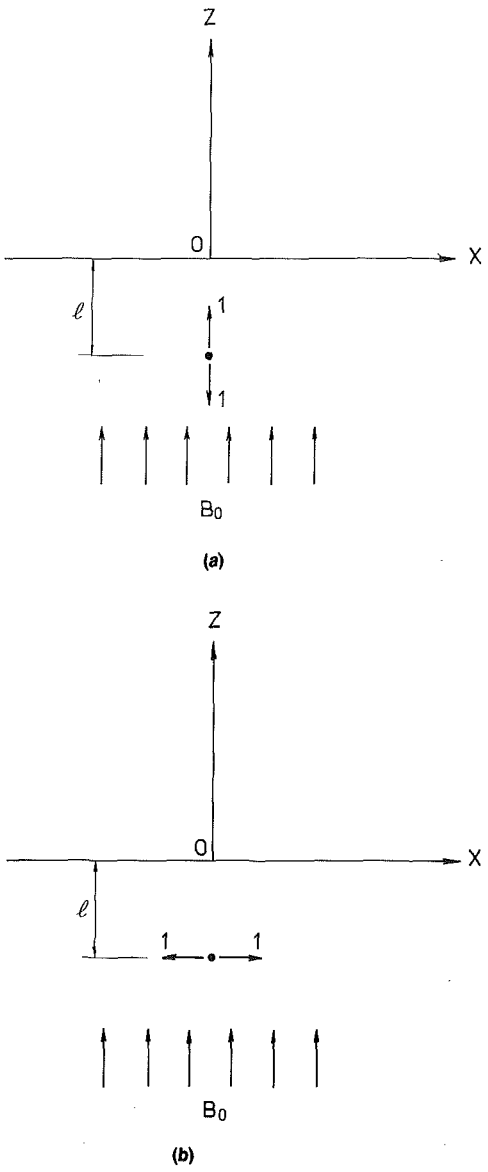
$$b_x^+ = \kappa\left(\frac{(1-2\nu)(z+l)}{r_1^2} - \frac{l(z+l)^2 - lx^2}{r_1^4}\right), \tag{48}$$

$$b_z^+ = \kappa\left(\frac{-(1-2\nu)x}{r_1^2} + \frac{2lx(z+l)}{r_1^4}\right). \tag{49}$$

Figure 4 shows the distribution of generated magnetic inductions on the surface.

V Magnetic Fields Generated by Line of Single-Couples

Once the magnetic inductions generated by the concentrated forces are obtained as equations (43), (44), (48), and (49), the magnetic inductions due to mechanical singularities such as a



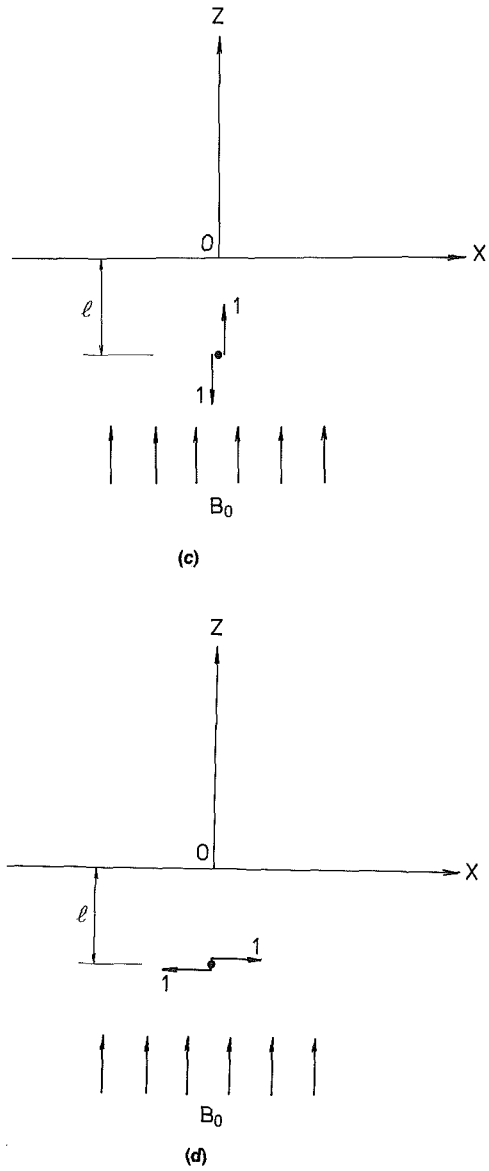
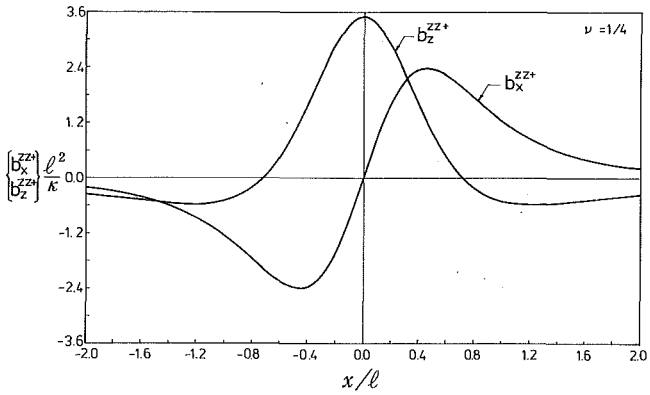
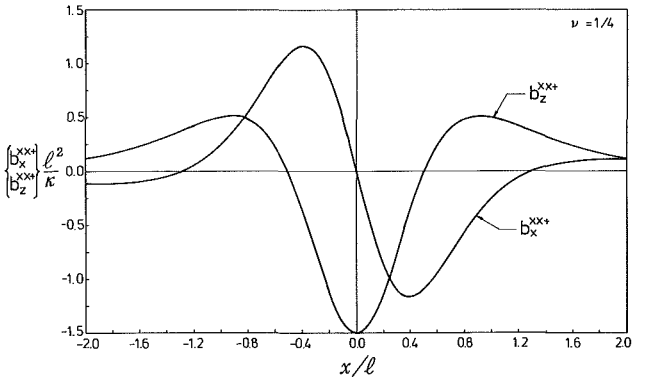


Fig. 5 A dipole or a single couple in the interior of a magnetized elastic half plane; (a) a dipole in the Z-direction, (b) a dipole in the X-direction, (c) a single couple whose arm is parallel to the X-axis, and (d) a single couple whose arm is parallel to the Z-axis.

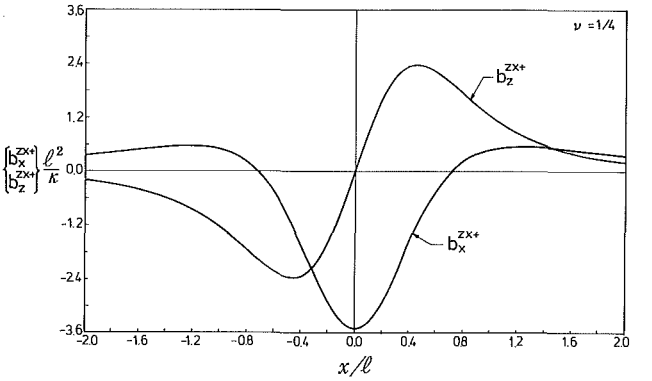
Downloaded 03 May 2010 to 171.66.16.31. Redistribution subject to ASME license or copyright; see http://www.asme.org/terms/Terms_Use.cfm



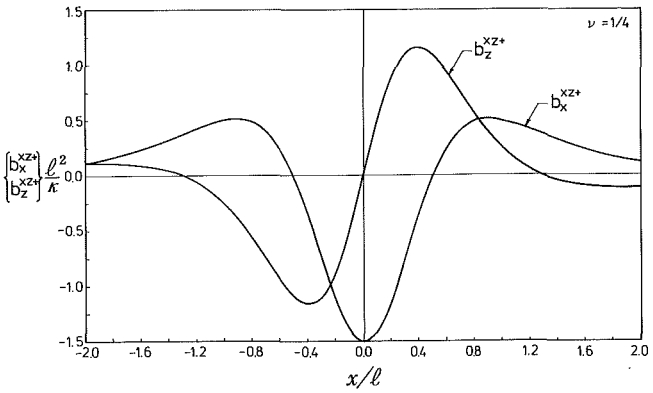
(a)



(b)



(c)



(d)

Fig. 6 The distribution of the generated magnetic induction on the surface due to the line dipole or line single couple; (*a*) Case (*I*): a line dipole in the Z-direction, (*b*) Case (*II*): a line dipole in the X-direction, (*c*) Case (*III*): a line single couple whose arm is parallel to X-axis, and (*d*) Case (*IV*): a single couple whose arm is parallel to Z-axis

dipole (Fig. 5) can be obtained by differentiations. In order to simplify the presentations, we use the symbols b_x^{z+} b_z^{z+}, b_x^{x+} and b_z^{x+} to replace b_x^+ in equation (43), b_z^+ in equation (44), b_x^+ in equation (48) and b_z^+ in equation (49), respectively. The superscript denotes the direction of unit line force. The generated magnetic inductions for each case shown in Fig. 5 can then be derived and presented as follows, Case (*i*):

$$b_x^{zz+} = -\frac{\partial b_x^{z+}}{\partial z} = \kappa \left\{ 2(1-\nu) \frac{2x(z+l)}{r_1^4} - \frac{2lx[x^2 - 3(z+l)^2]}{r_1^6} \right\} \tag{50}$$

$$b_z^{zz+} = -\frac{\partial b_z^{z+}}{\partial z} = \kappa \left\{ -2(1-\nu) \frac{[x^2 - (z+l)^2]}{r_1^4} - \frac{2l(z+l)[3x^2 - (z+l)^2]}{r_1^6} \right\}. \tag{51}$$

Case (*ii*):

$$b_x^{xx+} = -\frac{\partial b_x^{x+}}{\partial x} = \kappa \left\{ (1-2\nu) \frac{2x(z+l)}{r_1^4} + \frac{2lx[x^2 - 3(z+l)^2]}{r_1^6} \right\} \tag{52}$$

$$b_z^{xx+} = -\frac{\partial b_z^{x+}}{\partial x} = \kappa \left\{ -(1-2\nu) \frac{[x^2 - (z+l)^2]}{r_1^4} + \frac{2l(z+l)[3x^2 - (z+l)^2]}{r_1^6} \right\} \tag{53}$$

Case (*iii*):

$$b_x^{zx+} = -\frac{\partial b_x^{z+}}{\partial x} = \kappa \left\{ 2(1-\nu) \frac{[x^2 - (z+l)^2]}{r_1^4} + \frac{2l(z+l)[3x^2 - (z+l)^2]}{r_1^6} \right\}. \tag{54}$$

$$b_z^{zx+} = -\frac{\partial b_z^{z+}}{\partial x} = \kappa \left\{ 2(1-\nu) \frac{2x(z+l)}{r_1^4} - \frac{2lx[x^2 - 3(z+l)^2]}{r_1^6} \right\} \tag{55}$$

Case (*iv*):

$$b_x^{xz+} = -\frac{\partial b_x^{x+}}{\partial z} = \kappa \left\{ -(1-2\nu) \frac{[x^2 - (z+l)^2]}{r_1^4} + \frac{2l(z+l)[3x^2 - (z+l)^2]}{r_1^6} \right\} \tag{56}$$

$$b_z^{xz+} = -\frac{\partial b_z^{x+}}{\partial z} = \kappa \left\{ -(1-2\nu) \frac{2x(z+l)}{r_1^4} - \frac{2lx[x^2 - 3(z+l)^2]}{r_1^6} \right\} \tag{57}$$

where b_i^{jk+} denotes the x_i-component of the magnetic induction caused by a dipole in the x_j-direction as $j=k$; and denotes the x_i-component of the magnetic induction per unit moment resulting from a single couple whose forces are parallel to the x_j-direction and whose arm is parallel to the x_k-axis as $j \neq k$. We note that $b_i^{jk} \neq b_i^{kj}$.

Figures 6(*a*)–(*d*) presents the distributions of the generated magnetic induction on the surface for each case.

Downloaded 03 May 2010 to 171.66.16.31. Redistribution subject to ASME license or copyright; see http://www.asme.org/terms/Terms_Use.cfm

Acknowledgments

The author thanks Prof. Yih-Hsing Pao, Department of Theoretical and Applied Mechanics, Cornell University, for his helpful discussion and constructive criticism. The financial support from National Science Council, R. O. C. is also acknowledged.

References

Brown, Jr., W. F., 1966, *Magnetoelastic Interactions*, Springer-Verlag, New York.

Love, A. E. H., 1944, *A Treatise on the Mathematical Theory of Elasticity*, 4th Ed., Dover Pub., New York, p. 209.

Moon, F. C., 1984, *Magneto-Solid Mechanics*, John Wiley & Sons, Inc., New York.

Pak, Y. E., and Herrmann, G., 1986, "Crack Extension Force in a Dielectric Medium," *Int. J. Engng. Sci.*, Vol. 24, No. 8, pp. 1375–1388.

Pao, Y. H., and Yeh, C. S., 1973, "A Linear Theory for Soft Ferromagnetic Elastic Solids," *Int. J. Engng. Sci.*, Vol. 11, pp. 415–436.

Shindo, Y., 1977, "The Linear Magnetoelastic Problem for a Soft Ferromagnetic Elastic Solid with a Finite Crack," ASME JOURNAL OF APPLIED MECHANICS, Vol. 44, pp. 47–51.

Shindo, Y., 1978, "Magnetoelastic Interaction of a Soft Ferromagnetic Elastic Solid with a Penny-Shaped Crack in a Constant Axial Magnetic Field," ASME JOURNAL OF APPLIED MECHANICS, Vol. 45, pp. 291–296.

Shindo, Y., 1980, "Singular Stresses in a Soft Ferromagnetic Elastic Solid with Two Coplanar Griffith Cracks," *Int. J. Solids and Structures*, Vol. 16, pp. 537–543.

Sneddon, I. N., 1951, *Fourier Transform*, McGraw-Hill Co., Inc., New York, p. 419.

Tiersten, H. F., 1964, "Coupled Magnetomechanical Equations for Magnetically Saturated Insulators," *J. Math. Phys.*, Vol. 5, No. 9, pp. 1298–1318.

Yeh, C. S., 1987, "Magnetic Fields Generated by a Tension Fault," *Bull. of the College of Engng. National Taiwan University*, No. 40, March, pp. 47–56.

Downloaded 03 May 2010 to 171.66.16.31. Redistribution subject to ASME license or copyright; see http://www.asme.org/terms/Terms_Use.cfm

H. Iseki[1]

R. Sowerby

D. Bhattacharyya[2]

P. Gatt

Department of Mechanical Engineering
McMaster University
Hamilton, Ontario, Canada L85 4L7

A Theoretical and Experimental Study of a Curved Strip Compressed by a Flat Plate

The quasi-static loading of a curved strip compressed by a flat, rigid plate is considered, with particular reference to large deformations and the ensuing buckling behavior. Experiments were performed on curved strips of constant width but of different thickness. The strips were initially deformed to a fixed radius of curvature and stress relieved before pinning the ends. The span was held constant at about 305 mm. The deformation characteristics have been analyzed using an incremental finite element technique. Particular attention has been paid to modeling the situation when a node contacts the plate and the condition for separation of the strip from the plate. The predicted loads and deformation modes agreed well with experimental results from tests on steel and aluminum specimens. The experimental and theoretical procedures are pertinent to the study of dent resistance of sheet metal stampings, particularly automotive panels.

1 Introduction

The buckling of structural members under specified distributed or concentrated loads has been the subject of numerous investigations (see, for example, the work of Timoshenko, 1935; Witmer and Blamer, 1963; Sabir and Lock, 1973; Kondo, 1981; Alexander, 1984; Fujikake, 1985). When the load is applied to shells or curved thin-walled members by a flat rigid plate, the analysis is less tractable due to the difficulty in modeling the contact conditions. However, this type of loading mechanism is often analyzed, or utilized, in the theoretical, or experimental, studies of thin-walled members as energy absorbers (see Johnson and Reid, 1978). Some typical investigations in this area have been performed by Mutchler (1960) Reid and Reddy (1978), and Sugita (1985), but one shortcoming of the respective theoretical models was the failure to consider changes in length of the middle surface of the shell or tubular members.

Kitching et al., (1975) have studied the behavior of an open hemispherical shell loaded along its axis of symmetry by a rigid flat plate. The theoretical approach followed by Kitching et al., (1975) is essentially the same as that proposed earlier by Updike and Kalnins (1970 and 1972), and the shell is assumed to have three distinct phases of deformation, viz.:

i) Stage 1—where flattening of the dome of the shell occurs, once the rigid plate makes contact.

ii) Stage 2—at some critical stage in the deformation, a bifurcation occurs and the flat region of the shell snaps through to form an axisymmetric inward dimple.

iii) Stage 3—a further bifurcation which converts the axisymmetric inward dimple into a regular but nonaxisymmetric shape.

In the work of Updike and Kalnins (1970 and 1972), the material was assumed to remain elastic throughout all three stages of deformation. While a rigid plastic analysis for Stage 2 and the transition to Stage 3 has been given by Kitching et al., (1975) and Updike, (1972).

As demonstrated by Kitching et al. (1975), the theoretical models failed to reproduce the experimentally determined load-deflection characteristics, other than during the very early stages of deformation.

It will be apparent that it is a formidable task to predict the load-deflection characteristics of an arbitrarily shaped, elastic-plastic shell, compressed by a flat plate. At large deflections, geometric and (invariably) material nonlinearities arise and numerical procedures must be invoked to analyze the problem. In the present article, the load-deflection behavior of a curved metal strip compressed by a flat plate is studied both experimentally and theoretically; the experimental arrangement is shown schematically in Fig. 1(*a*). The strips were initially cold rolled in order to develop some initial curvature; they were then clamped between two thick curved plates which had been machined to a constant radius of curvature. The assembly was then placed in the furnace with an inert atmosphere; this procedure produced stress-free specimens of constant curvature. The ends of the strip were located in a notched plate, see Fig. 1(*b*), to simulate a pinned end condition.

As with the hemispherical shell, the strip starts to flatten when the platen makes contact. If the material exhibits elastic

[1]On leave from the Faculty of Engineering, Tokyo Institute of Technology, Tokyo, Japan.

[2]On leave from the Department of Mechanical Engineering, University of Auckland, Auckland, New Zealand.

Contributed by the Applied Mechanics Division of THE AMERICAN SOCIETY OF MECHANICAL ENGINEERS for publication in the JOURNAL OF APPLIED MECHANICS.

Discussion on this paper should be addressed to the Editorial Department, ASME, United Engineering Center, 345 East 47th Street, New York, N.Y. 10017, and will be accepted until two months after final publication of the paper itself in the JOURNAL OF APPLIED MECHANICS. Manuscript received by ASME Applied Mechanics Division, May 29, 1987; final revision, May 12, 1988.

Copyright © 1989 by ASME

Downloaded 03 May 2010 to 171.66.16.31. Redistribution subject to ASME license or copyright; see http://www.asme.org/terms/Terms_Use.cfm

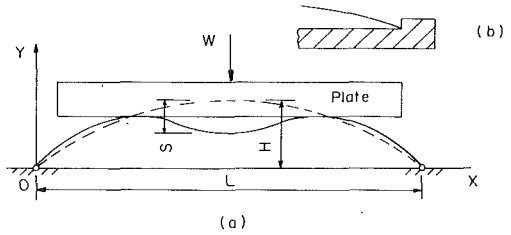


Fig. 1 *(a)* **Experimental arrangement; (*b*) Pinned end condition for the test piece**

behavior, a central portion of the strip can only remain horizontal, i.e., flat, if this region does not carry a bending moment. In effect, no normal forces are transmitted from the platen to this region of the strip, although in-plane forces are permitted. At some stage in the deformation process, the central portion of the strip can be seen to deflect inwards, away from the platen, to form a concave zone (see Fig. 1(*a*)). Separation can occur either in a gradual manner or by a sudden snap-through of the central region of the strip.

The deformation characteristics have been analyzed using an incremental finite element technique. Particular attention has been paid to modeling the situation where a node contacts the platen and also the conditions for separation of the strip from the plate.

The predicted load-deflection characteristics of the specimen along with shape of the strip in the pre- and post-buckled modes, agree well with experimental results from aluminum and steel test pieces.

Finally, it is worthwhile to note that the one area of concern in the automobile industry is the dent resistance of exterior body panels, and numerous publications dealing with this topic are available. The work of Johnson and Shaffit (1973), DiCello and George (1974), Painter and Pearce (1982), Mahmissa (1981), Yutori et al. (1980), Sakai et al. (1982), and Kojima and Hayashi (1980), provides a representative selection. A standard test to ascertain dent resistance has not yet been developed; consequently, it is difficult to assimilate experimental data which have been gathered from a variety of static and dynamic tests. Quasi-static tests have led to empirical expressions which relate proportionally the dent load to the quantity, $\sigma_y t^m$, where σ_y is the uniaxial yield strength of the material, t is the thickness, and m a material constant which lies between 1 and 2.

The present test, described above, may serve to differentiate between the dent resistance of different materials; in addition the span, curvature and thickness of the strip can be varied quite readily.

2 Notation

$O-x,y$; $O-X,Y$	local and global coordinate systems
$\{\mathbf{f}\}$, $\{\mathbf{F}\}$	vectors of nodal force in local and global coordinate systems
$\{\dot{\delta}\}$, $\{\dot{\Delta}\}$	vectors of displacement velocities of nodes in local and global coordinate systems
[T], [K]	transformation matrix and system stiffness matrix
l, b, t	length, width, and thickness of strip element
ϵ, $\dot{\epsilon}$, $d\epsilon$	true strain, strain rate, and incremental strain
σ, $\dot{\sigma}$, $d\sigma$	true stress, rate of stress, and incremental stress
E, ν, σ_y	Young's modulus, Poisson's ratio, and yield stress
W, S	punch force and stroke
R, L	initial radius and span of the curved strip.

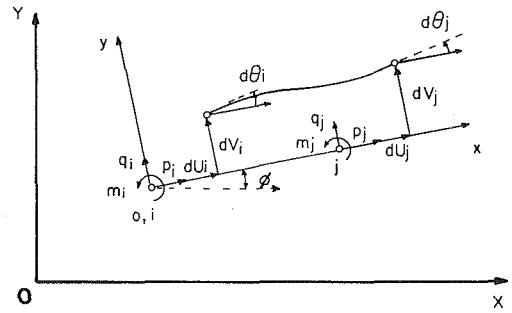


Fig. 2 Local and global coordinate systems

3 Theory

3.1 Velocity and Strain Rate of an Element. Figure 1(*a*) shows the experimental arrangement. The curved strip is divided into several beam-type elements, whose length, width and thickness are l, b, and t, respectively. The beam elements are further divided across their thickness into layers. It is assumed that the longitudinal stress is the only stress component, and that the width of the strip, b, remains unchanged. This is not strictly true, but in view of the small strains incurred in the present experiments the errors can be shown to be insignificant. The strain rate is calculated from equation (1) and the corresponding stress from equation (33) during a typical deformation increment, say, from step N to step $N+1$.

As is evident from equation (6) each deformation step will impose a slight curvature on each individual beam element, but this was found to be negligible. However, before proceeding with the calculation for the next increment, i.e., step $N+1$ to $N+2$, the middle surface of each beam element was assumed plane and the individual elements were remeshed in order to recommence with a rectangular beam element divided into layers across its thickness.

The entire curved strip is analyzed using an incremental, updated Langrangian, finite element technique, which allows for large strains and displacements.

The location of each element is specified by a global rectangular cartesian coordinate system OX, OY. In addition, a local rectangular cartesian system ox, oy is adopted, as shown in Fig. 2. In the latter system, a nodal point i on the middle surface of the element, ij, is considered as the origin o; the x-axis is directed along the middle surface of the element, and the y-axis is perpendicular to the surface.

If $\dot{u}$ and $\dot{v}$ are the velocities along the x and y directions, respectively, then in the local coordinate system,

$$\left.\begin{aligned}\dot{u} &= a_0 + a_1 x \\ \dot{v} &= b_0 + b_1 x + b_2 x^2 + b_3 x^3\end{aligned}\right\}. \tag{1}$$

The velocities at the nodes i and j are

$$\left.\begin{aligned}&\dot{u}=\dot{u}_i,\ \dot{v}=\dot{v}_i \text{ and } \frac{d\dot{v}}{dx}=\dot{\theta}_i \text{ at } x=0 \\ &\dot{u}=\dot{u}_j,\ \dot{v}=\dot{v}_j \text{ and } \frac{d\dot{v}}{dx}=\dot{\theta}_j \text{ at } x=l\end{aligned}\right\} \tag{2}$$

where θ represents the rate of rotation.

From equations (1) and (2), it follows that

$$\begin{Bmatrix}\dot{u}\\ \dot{v}\end{Bmatrix} = [\mathbf{A}]\{\dot{\delta}\} \tag{3}$$

$$[\mathbf{A}] = \begin{bmatrix} 1-x/l & 0 & 0 & x/l & 0 & 0 \\ 0 & \alpha & \beta & 0 & \gamma & \zeta \end{bmatrix} \tag{4}$$

Downloaded 03 May 2010 to 171.66.16.31. Redistribution subject to ASME license or copyright; see http://www.asme.org/terms/Terms_Use.cfm

where

$$\alpha = 1 - 3x^2/l^2 + 2x^3/l^3$$

$$\beta = x - 2x^2/l + x^3/l^2$$

$$\gamma = 3x^2/l^2 - 2x^3/l^3$$

$$\zeta = -x^2/l + x^3/l^2$$

and

$$\{\dot{\delta}\} = \{\dot{u}_i \dot{v}_i \dot{\theta}_i \dot{u}_j \dot{v}_j \dot{\theta}_j\}^T. \tag{5}$$

Assuming that Kirchhoff's hypothesis for plate bending applies to the velocities, and recognizing that the strip is thin, the strain rate $\dot{\epsilon}$ at a point y from the middle surface is calculated from

$$\dot{\epsilon} = \frac{d\dot{u}}{dx} - y\frac{d^2\dot{v}}{dx^2}. \tag{6}$$

From (3) and (6), the relationship between the strain rate $\dot{\epsilon}$ and the velocity $\{\dot{\delta}\}$ expressed in matrix form, is

$$\epsilon = [\mathbf{B}]\{\dot{\delta}\} \tag{7}$$

and

$$[\mathbf{B}] = \frac{1}{l^2}\left[-l \quad 6y\left(1-\frac{2x}{l}\right) \quad 2yl\left(2-\frac{3x}{l}\right) \right.$$

$$\left. l \quad -6y\left(1-\frac{2x}{l}\right) \quad 2yl\left(1-\frac{3x}{l}\right)\right]. \tag{8}$$

3.2 Equilibrium Between the Nodal Forces and Stress. The nodal forces and the stress acting on an element are denoted by $\{\mathbf{f}\}$ and σ, respectively, in the local coordinate system. The nodal force is made up of components p and q, acting in the x and y directions, respectively, along with a bending moment m; the positive directions are indicated in Fig. 2.

Upon applying the divergence theorem (see, Washizu, 1978) to a strip element, ij, it can be shown that

$$\{\dot{\delta}\}^T\{\mathbf{f}\} = \int_{-t/2}^{t/2}\int_0^l \dot{\epsilon}\sigma\, b\, dx\, dy \tag{9}$$

where

$$\{\mathbf{f}\} = \{p_i \quad q_i \quad m_i \quad p_j \quad q_j \quad m_j\}^T. \tag{10}$$

Upon substituting (7) into (9), the relationship between $\{\mathbf{f}\}$ and σ is obtained as

$$\{\mathbf{f}\} = \int_{-t/2}^{t/2}\int_0^l [\mathbf{B}]^T\sigma\, b\, dx\, dy \tag{11}$$

In a similar manner to the foregoing, the nodal force $\{\mathbf{F}\}$ in the global coordinate system is composed of components P, Q, and M. The nodal force $\{\mathbf{F}\}$ is calculated through the transformation $[\mathbf{T}]$ as follows:

$$\{\mathbf{F}\} = [\mathbf{T}]\{\mathbf{f}\} = [\mathbf{T}]\int_{-t/2}^{t/2}\int_0^l [\mathbf{B}]^T\sigma\, b\, dx\, dy \tag{12}$$

$$\{\mathbf{F}\} = \{P_i \quad Q_i \quad M_i \quad P_j \quad Q_j \quad M_j\}^T \tag{13}$$

$$[\mathbf{T}] = \begin{bmatrix}\lambda & 0\\ 0 & \lambda\end{bmatrix} \text{ and } [\lambda] = \begin{vmatrix}\cos\phi & -\sin\phi & 0\\ \sin\phi & \cos\phi & 0\\ 0 & 0 & 1\end{vmatrix} \tag{14}$$

where ϕ is the angle between the local and global coordinate systems. Now, define

$$X_{ji} = X_j - X_i \text{ and } Y_{ji} = Y_j - Y_i,$$

and it follows that

$$\cos\phi = X_{ji}/l \text{ and } \sin\phi = Y_{ji}/l$$

$$l = \left(X_{ji}^2 + Y_{ji}^2\right)^{1/2}. \tag{15}$$

3.3 The Stiffness Equation in the Global Coordinate System. The system stiffness equation is obtained by taking the material derivative of equation (12), allowing for the elastic compressibility of the curved shell. Hence,

$$\{\dot{\mathbf{F}}\} = [\dot{\mathbf{T}}]\int_{-t/2}^{t/2}\int_0^l [\mathbf{B}]^T\sigma\, b\, dx\, dy$$

$$+ [\mathbf{T}]\int_{-t/2}^{t/2}\int_0^l [\dot{\mathbf{B}}]^T\sigma\, b\, dx\, dy$$

$$+ [\mathbf{T}]\int_{-t/2}^{t/2}\int_0^l [\mathbf{B}]^T\dot{\sigma}\, b\, dx\, dy$$

$$+ \frac{1-2\nu}{E}[\mathbf{T}]\int_{-t/2}^{t/2}\int_0^l [\mathbf{B}]^T\sigma\dot{\sigma}\, b\, dx\, dy. \tag{16}$$

In the above expression,

$$\{\dot{\mathbf{F}}\} = \{\dot{P}_i \quad \dot{Q}_i \quad \dot{M}_i \quad \dot{P}_j \quad \dot{Q}_j \quad \dot{M}_j\}^T. \tag{17}$$

It now remains to generate the various matrices which comprise the stiffness matrix for the system.

3.3.1 The $[\mathbf{K}_T]$ *Matrix.* The material derivative $[\dot{T}]$ of the transformation matrix is obtained by differentiating equation (14) and it can be expressed in terms of the global nodal velocities $\{\dot{\Delta}\}$ as follows,

$$[\dot{\mathbf{T}}] = [\Lambda]\dot{\phi} = [\Lambda][\mathbf{B}_\phi]\{\dot{\Delta}\} \tag{18}$$

where

$$[\Lambda] = \begin{bmatrix}\lambda' & 0\\ 0 & \lambda'\end{bmatrix}, \quad [\lambda'] = \begin{vmatrix}-\sin\phi & -\cos\phi & 0\\ \cos\phi & -\sin\phi & 0\\ 0 & 0 & 0\end{vmatrix} \tag{19}$$

$$[\mathbf{B}_\phi] = \frac{1}{l}[\sin\phi \quad -\cos\phi \quad 0 \quad -\sin\phi \quad \cos\phi \quad 0] \tag{20}$$

$$\{\dot{\Delta}\} = \{\dot{U}_i \quad \dot{V}_i \quad \dot{\Theta}_i \quad \dot{U}_j \quad \dot{V}_j \quad \dot{\Theta}_j\}^T = [\mathbf{T}]\{\dot{\delta}\} \tag{21}$$

The first term on the right side of equation (16) is integrated assuming that the stress distribution within the element ij is approximately constant in $0 \le x \le l$, but the thickness is divided into a number of discrete layers. The numerical integration is performed on the following expression.

$$\int_{-t/2}^{t/2}\int_0^l [\mathbf{B}]^T\sigma\, b\, dx\, dy \doteq \int_{-t/2}^{t/2}\left(\int_0^l [\mathbf{B}]^T dx\right)\sigma\, b\, dy = \{\mathbf{f}'\} \tag{22}$$

where

$$\{\mathbf{f}'\} = \{-p' \quad 0 \quad m' \quad p' \quad 0 \quad -m'\}^T \tag{23}$$

$$p' = \int_{-t/2}^{t/2}\sigma\, b\, dy, \quad m' = \int_{-t/2}^{t/2}\sigma\, by\, dy. \tag{24}$$

Downloaded 03 May 2010 to 171.66.16.31. Redistribution subject to ASME license or copyright; see http://www.asme.org/terms/Terms_Use.cfm

The first term of equation (16) can be expressed as follows:

$$[\dot{\mathbf{T}}]\int_{-t/2}^{t/2}\int_0^l [\mathbf{B}]^T\sigma\, b\, dx\, dy \fallingdotseq [\dot{\mathbf{T}}]\{\mathbf{f}'\}$$

$$= [\Lambda]\{\mathbf{f}'\}\dot{\phi} = [\Lambda]\{\mathbf{f}'\}[\mathbf{B}_\phi]\{\dot{\Delta}\} = [\mathbf{K}_T]\{\dot{\Delta}\} \tag{25}$$

$$[\mathbf{K}_T] = [\Lambda]\{\mathbf{f}'\}[\mathbf{B}_\phi]. \tag{26}$$

3.3.2 The $[\mathbf{K}_B]$ *Matrix.* The material derivative $[\dot{\mathbf{B}}]^T$ arising in the second term of equation (16) is expressed by means of the following relationships,

$$\dot{x} = \dot{u}_i + (\dot{u}_j - \dot{u}_i)x/l \text{ and } \dot{l} = \dot{u}_j - \dot{u}_i$$

and

$$[\dot{\mathbf{B}}]^T = [\mathbf{B}_C]\{\dot{\delta}\} = [\mathbf{B}_C][\mathbf{T}]^T\{\dot{\Delta}\} \tag{27}$$

$$[\mathbf{B}_C] = \frac{1}{l^4}\begin{vmatrix} -l^2 & 0 & 0 & l^2 & 0 & 0 \\ -24xy & 0 & 0 & -12y(l-2x) & 0 & 0 \\ -2y(l^2+3lx) & 0 & 0 & -2y(2l^2-3lx) & 0 & 0 \\ l^2 & 0 & 0 & l^2 & 0 & 0 \\ 24xy & 0 & 0 & 12y(l-2x) & 0 & 0 \\ -2y(2l^2+3lx) & 0 & 0 & -2y(l^2-3lx) & 0 & 0 \end{vmatrix}. \tag{28}$$

Consequently, integration of the second term of equation (16) is given by

$$\int_{-t/2}^{t/2}\int_0^l [\dot{\mathbf{B}}]^T\sigma\, b\, dx\, dy = \left[\int_{-t/2}^{t/2}\int_0^l [\mathbf{B}_C]\sigma\, b\, dx\, dy\right][\mathbf{T}]^T\{\dot{\Delta}\}$$

$$\fallingdotseq \left[\int_{-t/2}^{t/2}\left(\int_0^l [\mathbf{B}_C]dx\right)\sigma\, b\, dy\right][\mathbf{T}]^T\{\dot{\Delta}\} = [\mathbf{B}_D][\mathbf{T}]^T\{\dot{\Delta}\} \tag{29}$$

$$[\mathbf{B}_E] = \frac{1}{l^3}\begin{vmatrix} l^2I_1 & 0 & -l^2I_2 & -l^2I_1 & 0 & l^2I_2 \\ & 12I_3 & 6lI_3 & 0 & -12I_3 & 6lI_3 \\ & & 4l^2I_3 & l^2I_2 & -6lI_3 & 2l^2I_3 \\ & & & l^2I_1 & 0 & -l^2I_2 \\ & & \text{SYM.} & & -12I_3 & -6lI_3 \\ & & & & & 4l^2I_3 \end{vmatrix}. \tag{36}$$

In the above

$$[\mathbf{B}_D] = \int_{-t/2}^{t/2}\left(\int_0^l [\mathbf{B}_C]dx\right)\sigma\, b\, dy$$

$$[\mathbf{B}_D] = \frac{1}{l^2}\begin{vmatrix} -lp' & 0 & 0 & lp' & 0 & 0 \\ -12m' & 0 & 0 & 0 & 0 & 0 \\ -5lm' & 0 & 0 & -lm' & 0 & 0 \\ lp' & 0 & 0 & -lp' & 0 & 0 \\ 12m' & 0 & 0 & 0 & 0 & 0 \\ -7lm' & 0 & 0 & lm' & 0 & 0 \end{vmatrix}. \tag{30}$$

Hence, the second term of equation (16) can be expressed as

$$[\mathbf{T}]\int_{-t/2}^{t/2}\int_0^l [\dot{\mathbf{B}}]^T\sigma\, b\, dx\, dy = [\mathbf{T}][\mathbf{B}_D][\mathbf{T}]^T\{\dot{\Delta}\} = [\mathbf{K}_B]\{\dot{\Delta}\} \tag{31}$$

$$[\mathbf{K}_B] = [\mathbf{T}][\mathbf{B}_D][\mathbf{T}]^T. \tag{32}$$

3.3.3 The $[\mathbf{K}_C]$ *Matrix.* In this study, anisotropy and Bauschinger effects of the shell material are neglected. To develop an expression between the stress and the strain, the bending theory of a beam is applied to each element and the following identity between the stress rate $\dot{\sigma}$ and strain rate $\dot{\epsilon}$ are as follows.

$$\dot{\sigma} = E_c\dot{\epsilon} = E_c[\mathbf{B}]\{\dot{\delta}\} = E_c[\mathbf{B}][\mathbf{T}]^T\{\dot{\Delta}\}, \tag{33}$$

and

$$\left.\begin{aligned} E_c &= E && (\sigma < \sigma_y \text{ when unloading}) \\ E_c &= \frac{H'}{1+H'/E} && (\sigma \geq \sigma_y \text{ when loading}) \end{aligned}\right\} \tag{34}$$

where

$$H' = d\sigma/d\epsilon^p.$$

The integration of the third term in equation (16) is denoted as follows:

$$\int_{-t/2}^{t/2}\int_0^l [\mathbf{B}]^T\dot{\sigma}\, b\, dx\, dy = \left(\int_{-t/2}^{t/2}\int_0^l [\mathbf{B}]^T E_c[\mathbf{B}] b\, dx\, dy\right)[\mathbf{T}]^T\{\dot{\Delta}\}$$

$$\fallingdotseq \left[\int_{-t/2}^{t/2}\left(\int_0^l [\mathbf{B}]^T[\mathbf{B}]dx\right)E_c b\, dy\right][\mathbf{T}]^T\{\dot{\Delta}\}$$

$$= [\mathbf{B}_E][\mathbf{T}]^T\{\dot{\Delta}\} \tag{35}$$

and

The $[\mathbf{B}_E]$ matrix is symmetric and the integration values I_1, etc., are defined as

$$I_1 = \int_{-t/2}^{t/2} E_c b\, dy$$

$$I_2 = \int_{-t/2}^{t/2} E_c by\, dy \tag{37}$$

$$I_3 = \int_{-t/2}^{t/2} E_c b\, y^2 dy.$$

The third term in equation (16) is then expressed as

$$[\mathbf{T}]\int_{-t/2}^{t/2}\int_0^l [\mathbf{B}]^T\dot{\sigma} b\, dx\, dy = [\mathbf{T}][\mathbf{B}_E][\mathbf{T}]^T\{\dot{\Delta}\} = [\mathbf{K}_C]\{\dot{\Delta}\} \tag{38}$$

Downloaded 03 May 2010 to 171.66.16.31. Redistribution subject to ASME license or copyright; see http://www.asme.org/terms/Terms_Use.cfm

$$[\mathbf{K}_C] = [\mathbf{T}][\mathbf{B}_E][\mathbf{T}]^T. \tag{39}$$

3.3.4 The $[\mathbf{K}_V]$ Matrix. The fourth term in equation (16) can be changed into a more convenient form as shown below

$$\frac{1-2\nu}{E}\int_{-t/2}^{t/2}\int_0^l [\mathbf{B}]^T\sigma\dot{\sigma}b\,dx\,dy = \frac{1-2\nu}{E}\int_{-t/2}^{t/2}\int_0^l [\mathbf{B}]^T\sigma E_c\dot{\epsilon}b\,dx\,dy$$

$$\doteq \frac{1-2\nu}{E}\left[\int_{-t/2}^{t/2}\left(\int_0^l [\mathbf{B}]^T[\mathbf{B}]dx\right)E_c\sigma b\,dy\right][\mathbf{T}]^T\{\dot{\Delta}\}$$

$$= [\mathbf{B}_V][\mathbf{T}]^T\{\dot{\Delta}\}. \tag{40}$$

In the above

$$[\mathbf{B}_V] = \frac{1-2\nu}{E}\int_{-t/2}^{t/2}\left(\int_0^l [\mathbf{B}]^T[\mathbf{B}]dx\right)E_c\sigma\, b\, dy$$

$$[\mathbf{B}_V] = \frac{1-2\nu}{l^3E}\begin{vmatrix} l^2J_1 & 0 & -l^2J_2 & -l^2J_1 & 0 & l^2J_2 \\ & 12J_3 & 6lJ_3 & 0 & -12J_3 & 6lJ_3 \\ & & 4l^2J_3 & l^2J_2 & -6lJ_3 & 2l^2J_3 \\ & & & l^2J_1 & 0 & -l^2J_2 \\ & \text{SYM.} & & & 12J_3 & -6lJ_3 \\ & & & & & 4l^2J_3 \end{vmatrix}. \tag{41}$$

and the integration values J_1, J_2, and J_3 are defined as:

$$J_1 = \int_{-t/2}^{t/2} E_c\sigma b\,dy$$

$$J_2 = \int_{-t/2}^{t/2} E_c\sigma by\,dy \tag{42}$$

$$J_3 = \int_{-t/2}^{t/2} E_c\sigma by^2 dy.$$

Consequently, the fourth term in equation (16) is finally expressed as

$$\frac{1-2\nu}{E}[\mathbf{T}]\int_{-t/2}^{t/2}\int_0^l [\mathbf{B}]^T\sigma\dot{\sigma}\, b\,dx\,dy$$

$$= [\mathbf{T}][\mathbf{B}_V][\mathbf{T}]^T\{\dot{\Delta}\} = [\mathbf{K}_V]\{\dot{\Delta}\} \tag{43}$$

$$[\mathbf{K}_V] = [\mathbf{T}][\mathbf{B}_V][\mathbf{T}]^T \tag{44}$$

From equation (16), and the foregoing expressions, the system stiffness matrix $[\mathbf{K}]$ can be determined as,

$$\{\dot{\mathbf{F}}\} = [[\mathbf{K}_T] + [\mathbf{K}_B] + [\mathbf{K}_C] + [\mathbf{K}_V]]\{\dot{\Delta}\} = [\mathbf{K}]\{\dot{\Delta}\} \tag{45}$$

$$[\mathbf{K}] = [\mathbf{K}_T] + [\mathbf{K}_B] + [\mathbf{K}_C] + [\mathbf{K}_V]. \tag{46}$$

3.4 Calculations for the Contacting Nodes and the Separation of the Strip from the Plate.

3.4.1 Determination of the Stress and Strain in Individual Elements. The curved strip is divided into 24 elements and each element is subdivided into 16 equal layers across the thickness. The incremental strain $d\epsilon$ and the incremental stress $d\sigma$ at the midpoint of each beam element, during the Nth step, are calculated as follows,

$$d\epsilon = \dot{\epsilon}d\tau = [\mathbf{B}]\{\dot{\delta}\}d\tau \qquad \text{at } x = l/2$$

$$= \frac{1}{l}(du_j - du_i) - \frac{y}{l}(d\theta_j - d\theta_i)$$

$$d\sigma_{x=l/2} = \dot{\sigma}d\tau = E_c d\epsilon_{x=l/2}. \tag{47}$$

Therefore, the total true strain ϵ, the true stess σ, and the equivalent plastic strain $d\epsilon^p$, at step $N+1$ are calculated as follows,

$$\epsilon_{N+1} = \epsilon_N + d\epsilon$$

$$\sigma_{N+1} = \sigma_N + d\sigma \tag{48}$$

$$\epsilon^{\mathrm{P}}_{N+1} = \epsilon^{\mathrm{P}}_N + (d\epsilon - d\sigma/E).$$

In the present calculation, the layers across the thickness are remeshed at each incremental step. The stress, the total strain, and the equivalent plastic strain are corrected in each step (see, Iseki and Murota (1986) for a more detailed discussion on the adjustment procedure).

3.4.2 Analysis of a Contacting Node. The contacting nodes are shown schematically in Fig. 3. For those nodes not touching the plate, the known boundary conditions are:

$$\dot{U} = \dot{V} = 0, \quad \dot{M} = 0, \text{ at } X = 0$$

$$\dot{U} = \dot{\Theta} = 0, \quad \dot{Q} = 0 \text{ at } X = L/2 \tag{49}$$

In the contact zone, the prevailing condition is $\dot{\Theta} = 0$ at a nodal point, and accordingly, the incremental moment M at a nodal point is generally not zero. Although the contact condition $\dot{\Theta} = 0$ is geometrically acceptable, the mechanical condition $\dot{M} \neq 0$ is not acceptable physically.

Therefore, it is assumed that a contacting node behaves like a frictionless needle bearing, with the following boundary conditions

$$\dot{V} = \dot{S}, \quad \dot{P} = \dot{M} = 0 \text{ for } X_{C1} \leq X \leq X_{C2} \tag{50}$$

3.4.3 Control of the Plate Stroke. It was recognized that some control had to be exercised over the size of the increment of plate displacement (or stroke), in order to account for the region of the strip in contact with the plate. This is vital to the calculation procedure since both the contacting nodes and the loads they carry change during the plate stroke. Relatively early in the deformation, material in the central region ceases to exert any force on the plate and begins to move away from it (see Figs. 6 and 7). At the same time, new nodes are coming into contact with the plate in region to the left of X_{C1} in Fig. 3. The following calculations were performed to assess the contact zone, yielding within an element and the onset of snap-through.

Downloaded 03 May 2010 to 171.66.16.31. Redistribution subject to ASME license or copyright; see http://www.asme.org/terms/Terms_Use.cfm

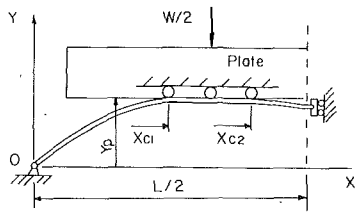


Fig. 3 Frictionless finite element nodes in contact with the plate (needle bearing model)

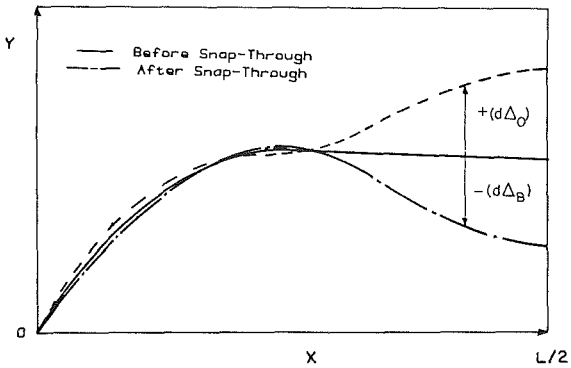


Fig. 4 Representation of the "snap-through" condition

(1) *A criterion for contact of a node:* Let Y_p specify the current position of the plate (see Fig. 4) and dS the displacement in the next increment, define Y_k and dV_k as corresponding quantities for a typical node, k, in the strip. If contact occurs, then $(Y_p + dS) \leq (Y_k + dV_k)$, and the contact control parameter η_c is defined as follows:

$$\eta_c = \frac{Y_p - Y_k}{dV_k - dS} \tag{51}$$

The positive minimum value is denoted as η_{cm}.

(2) *Separation condition for a node:* If Q_k is the calculated current force carried by a typical node in contact with the plate, and dQ_k is the calculated change in force in the next incremental, then if the quantity $(Q_k + dQ_k)$ becomes positive (physically it would drop to zero), this signifies separation. The control parameter is

$$\eta_s = \frac{-Q_k}{dQ_k} \tag{52}$$

and the minimum positive value is η_{sm}.

(3) *Test for yielding:* Elements can undergo either initial or subsequent (i.e., reloading) yielding, and obviously the representative stress increment, $d\sigma$, in a given step must equate the current stress state, σ, to at least the current flow stress, σ_f. The control parameter is

$$\eta_l = \frac{\bar{\sigma}_f - |\sigma|}{|d\sigma|} \text{ when } \sigma \cdot d\sigma > 0$$

$$\eta_l = \frac{\bar{\sigma}_f + |\sigma|}{|d\sigma|} \text{ when } \sigma \cdot d\sigma < 0 \tag{53}$$

for both initial and subsequent yielding and the minimum positive value is η_{lm}.

(4) *Control of the node at the mid-span:* At snap-through, the displacement of the central node, dV_c, can be large compared to the increment of plate displacement, dS. In the present calculation, it was found convenient to introduce a control parameter η_{dm} when dV_c exceeded $5\,|dS|$, namely

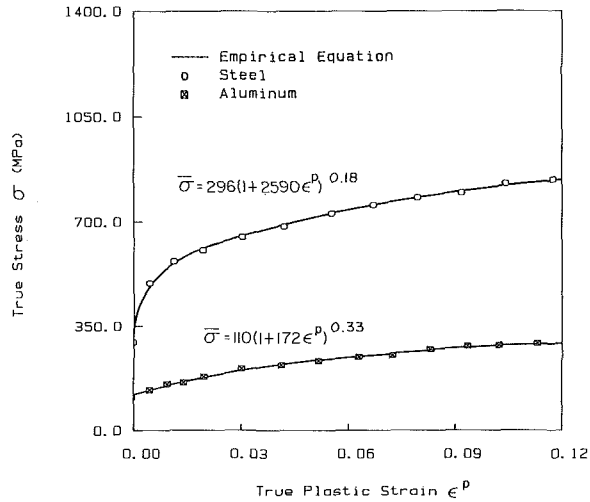


Fig. 5 Stress-strain curves for the test specimens

$$\eta_{dm} = \frac{5\,|dS|}{|dV_c|} \tag{54}$$

The minimum of the control parameters in equations (51)–(54) say, η_m, is then selected to regulate the stroke, viz., $\eta_{dm} \cdot dS$.

3.4.4 Snap-Through and Post-buckling Behavior. At a certain stage in the deformation, a sudden snap-through of the strip can occur. In the calculations, snap-through was always preceded by two nodes only contacting the plate (see Fig. 3). In the next incremental step, the force on the inner node dropped to zero while it still remained at the same level as the plate. During the subsequent increment, η_c in equation (51) is zero and under these conditions the only solution that the incremental numerical method provided was a prediction that the central region of the strip was raised sharply by $\{d\Delta_0\}$ (see Fig. 4). Since this is physically impossible, the actual shape of the central region was taken as the mirror image of the predicted profile, and this was considered to signify catastrophic buckling. Then, the simplest deformation mode $\{d\Delta_B\}$ which satisfies the contact condition is adopted as follows.

$$\{d\Delta_B\} = -\{d\Delta_0\} \tag{55}$$

The post-buckling deformation is calculated by means of this practical and easy procedure.

4 Calculated Results and Comparison With Experimental Results

4.1 Test Materials. Experiments were performed on test pieces prepared from a cold-rolled sheet of plain carbon steel (0.30 mm thick) and a sheet of 5182-0 aluminum alloy (1.07 mm thick). As alluded to earlier, strips 76.2 mm wide were cut from the sheets and rolled to a desired curvature. The samples were then clamped between a pair of thick plates which had been machined to a radius of curvature of approximately 921 mm. The assembly was placed in an electric furnace with an inert atmosphere and annealed.

Companion samples, which had experienced a similar amount of cold working (but had rolled flat) were annealed at the same time. Tensile tests were performed on specimens prepared from these latter samples and typical stress-strain curves are shown in Fig. 5. The experimental data were fitted by an empirical power hardening law of the form

$$\sigma = \sigma_y (1 + c\epsilon^p)^n \tag{56}$$

The coefficients σ_y, c, and n are given in Table 1, along with other pertinent material data.

Downloaded 03 May 2010 to 171.66.16.31. Redistribution subject to ASME license or copyright; see http://www.asme.org/terms/Terms_Use.cfm

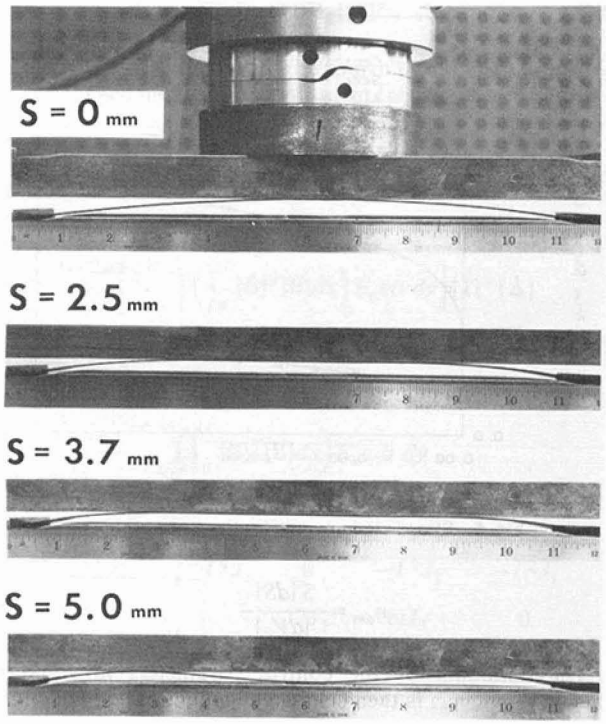


Fig. 6 Typical deformation sequence of a steel specimen

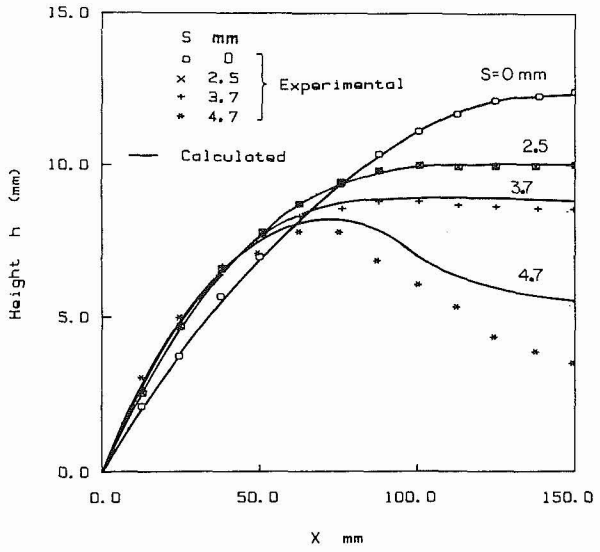
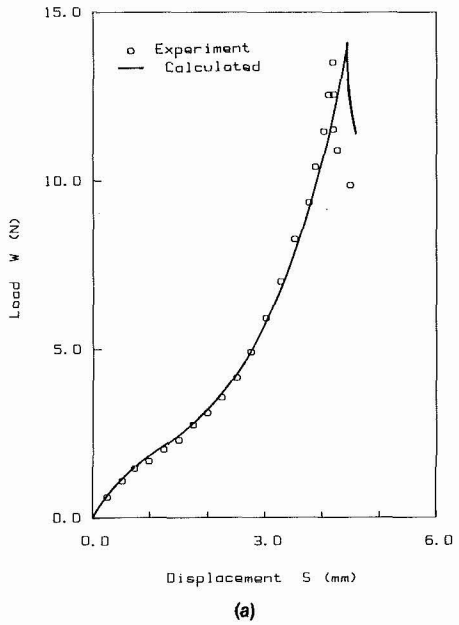


Fig. 7 Predicted and measured shape of a steel strip as a function of the plate displacement. Dimensions: $H = 12.7$ mm, $b = 76$ mm, $L = 305$ mm, $R = 920$ mm, $t = 0.30$ mm.



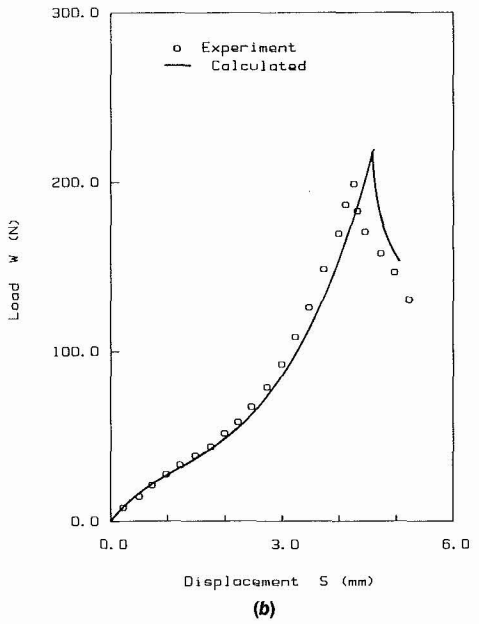


Fig. 8 A comparison between the measured and predicted plate load versus displacement relationship, $H = 12.7$ mm, $b = 76$ mm, $L = 305$ mm, $R = 920$ mm; (a) Steel specimen, $t = 0.30$ mm and (b) Aluminum specimen, $t = 1.07$ mm.

Table 1—Material Properties

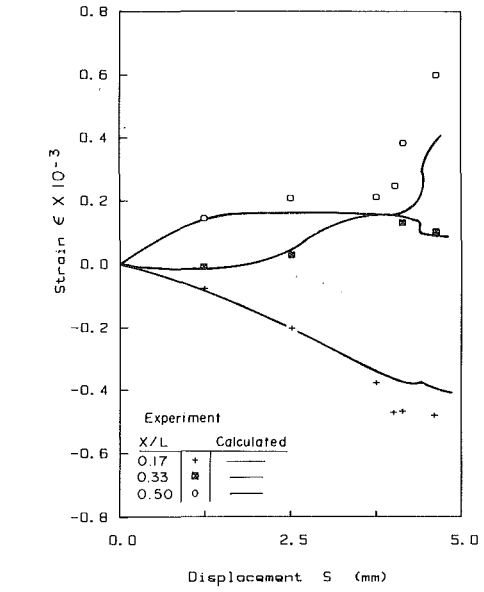
Material	t (mm)	E (GPa)	ν	σ_y (MPa)	ϵ_y	n	c
Steel	0.30	207	0.29	296	1.4×10^{-3}	0.18	2590
Aluminum	1.07	76	0.31	110	1.5×10^{-3}	0.33	172

4.2 Companion Tests of the Curved Strips. The annealed curved strips were trimmed to length and the ends located in a slotted plate as shown in Fig. 1(*b*). The design dimensions were a mid-height of $H_0 = 12.7$ mm, span $L = 304.8$ mm and radius of curvature 921 mm (see Fig. 1(*a*)); these dimensions could be adhered to with reasonable accuracy. As an illustration, Fig. 7 provides a comparison of the theoretical undeformed shape (the solid line at $S = 0$) and the experimentally determined profile, shown by the open circles for a steel strip.

The curved specimens were then compressed quasi-statically by a flat plate, as shown schematically in Fig. 1(*a*). To reduce friction at the point of contact, a polyethylene film, lubricated with machine oil, was placed between the test piece and the plate. Catastrophic buckling or "snap-through" is evident for the steel strip from Figs. 6 and 7.

Figures 8(*a*) and 8(*b*) are typical comparisons between the measured and predicted plate force-plate penetration characteristics, for the steel and aluminum samples, respec-

Downloaded 03 May 2010 to 171.66.16.31. Redistribution subject to ASME license or copyright; see http://www.asme.org/terms/Terms_Use.cfm



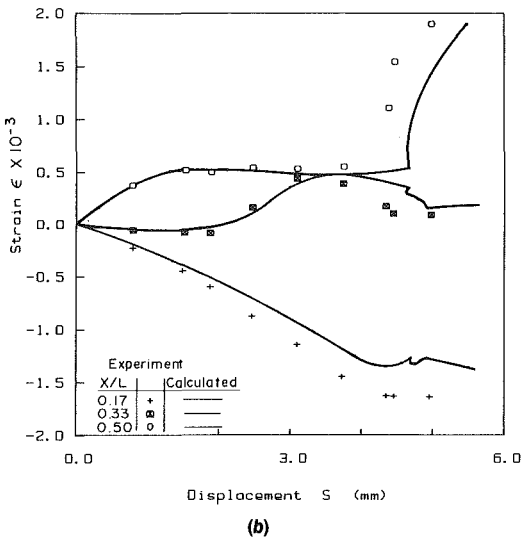


Fig. 9 A comparison between measured and calculated strain as a function of plate displacement, dimensions same as those given in Fig. 8; (*a*) Steel strip and (*b*) Aluminum strip

tively. Strain gauges were attached to the underside of some of the curved test pieces in order to assess the extent of the deformation; in terms of the span, the gauges were located at $L/6$, $L/3$, and $L/2$. The measured and predicted strains, as a function of platen displacement, are shown in Figs. 9(*a*) and 9(*b*) for the steel and aluminum specimens, respectively.

The finite element model is capable of predicting the stress and strain distribution across the thickness of the specimen at any location in the arch, and at any stage during the deformation. The program also predicts the contact length of the nodes, i.e., the distance $(X_{C1} - X_{C2})$ in Fig. 3. For brevity, results from these calculations are not shown here.

4.3 Influence of the Processing and Material Parameters on the Bifurcation Mode—Predicted Performance. It was found impracticable to perform experiments to investigate a wide range of processing and material parameters, and for this reason, the influence of certain variables were calculated. The material was assumed to have a stress-strain curve of the form given in (56), with Poisson's ratio and Young's modulus corresponding to a steel.

The influence of sheet thickness on the plate force-displacement characteristics is shown in Fig. 10(*a*), while the effect of yield stress, σ_y, and the strain hardening index, n, is illustrated in Figs. 10(*b*) and 10(*c*), respectively. In Figs. 10(*a*)–10(*c*), it was found convenient to represent the plate force as a nondimensional quantity by dividing the load, W, by the expression DbH/L^3, where D is the bending stiffness of the strip, i.e.,

$$D = Et^3/12(1-\nu^2)$$

5 Conclusions

As will be apparent from the results presented in the foregoing, the proposed finite element method is capable of predicting the load-deflection characteristics and the shape of the specimen, as a function of the plate stroke. Further evidence as to the accuracy of the predicted deformation mode is given in Figs. 9(*a*) and 9(*b*), which show the theoretical and measured strain paths at three locations on the underside of the specimens.

If the material remains elastic, as did the steel specimens, the snap-through phenomenon can be sudden and the plate load drops immediately (see Fig. 8). If the material yields, as did the aluminum test piece, the buckling occurs in a more gradual fashion. The same effect is also evident from the predicted curves in Figs. 10(*a*) to 10(*c*), which illustrates the influence of yield stress, strip thickness, and strain hardening index, respectively, on the buckling. If the material remains elastic throughout, then snap-through will occur at a constant value of the dimensionless parameter $W/(DbH/L^3)$.

Acknowledgments

The authors would like to thank their colleague Dr. N. Chandrasekaran for his contributions to this investigation. Thanks are also due to the Natural Sciences and Engineering Research Council of Canada for support under grant number A8120.

References

Alexander, T., 1984, "Postbuckling Resonance Analysis of Thin Shells," *Int. J. Numer. Methods. Eng.*, Vol. 20, pp. 2221–2234.

DiCello, J. A., and George, R. A., 1974, "Design Criteria for the Dent Resistance of Auto Body Panels," SAE Paper, No. 740081.

Fujikake, M., 1985, "A Simple Approach to Bifurcation and Limit Point Calculations," *Int. J. Numer. Methods Eng.*, Vol. 21, pp. 183–191.

Iseki, H., and Murota, T., 1986, "On the Determination of the Optimum Blank Shape of Non-Axisymmetric Cups by the Finite Element Method," *Bulletin of JSME*, Vol. 29, pp. 1033–1040.

Johnson, T. E., and Shaffit, W. O., 1973, "Dent Resistance of Cold Rolled Low-Carbon Steel Sheet," SAE Paper, No. 730528.

Johnson, W., and Reid, S. R., 1978, "Metallic Energy Dissipating Systems," ASME *Applied Mechanics Reviews*, Vol. 31, pp. 277–286.

Kitching, R., Houlston, R., and Johnson, W., 1975, "A Theoretical and Experimental Study of Hemispherical Shells Subjected to Axial Loads Between Flat Plates," *Int. J. Mech. Sci.*, Vol. 17, pp. 693–703.

Kojima, M., and Hayashi, Y., 1980, "A Study on the Selection of High Strength Steel Sheets for Auto-Body Panels," SAE Paper, No. 800369.

Kondo, K., 1981, "Large Deformations of Rigid-Plastic Shallow Spherical Shells," *Int. J. Mech. Sci.*, Vol. 23, pp. 69–76.

Mahmissa, H. F., 1981, "Dent Resistance of Surface Panel and Slam Area," SAE Paper, No. 810099.

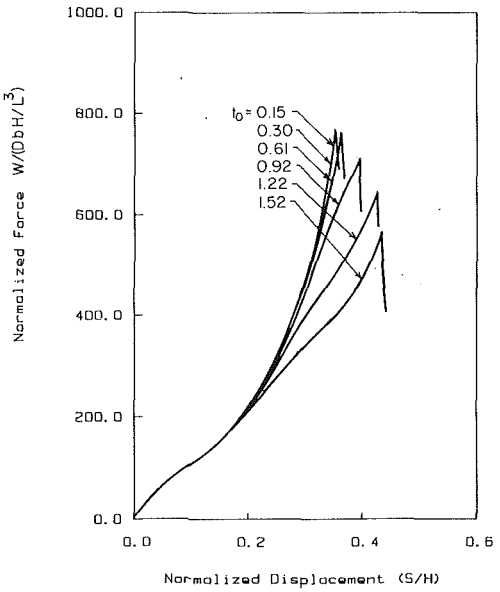
Mutchler, L. D., 1960, "Energy Absorption Aluminum Tubing," ASME JOURNAL OF APPLIED MECHANICS, Vol. 27, pp. 740–743.

Painter, M. J., and Pearce, R., 1982, "The Denting Behavior of Some Sheet Metals," *Proc. 12th Biennial Congress*, Int. Deep Drawing Res. Group, pp. 399–410.

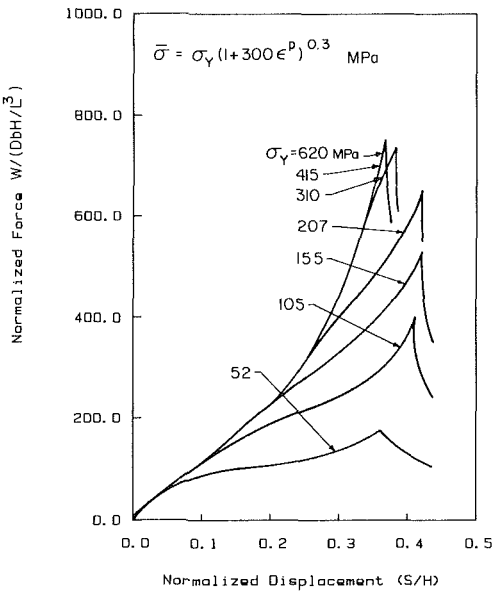
Reid, S. R., and Reddy, T. Y., 1978, "Effect of Strain Hardening on the Lateral Compression of Tubes Between Rigid Plates," *Int. J. Solids Structures*, Vol. 14, pp. 213–225.

Sabir, A. B., and Lock, A. C., 1973, "Large Deflection, Geometrically Non-Linear Finite Element Analysis of Circular Arches," *Int. J. Mech. Sci.*, Vol. 15, pp. 37–47.

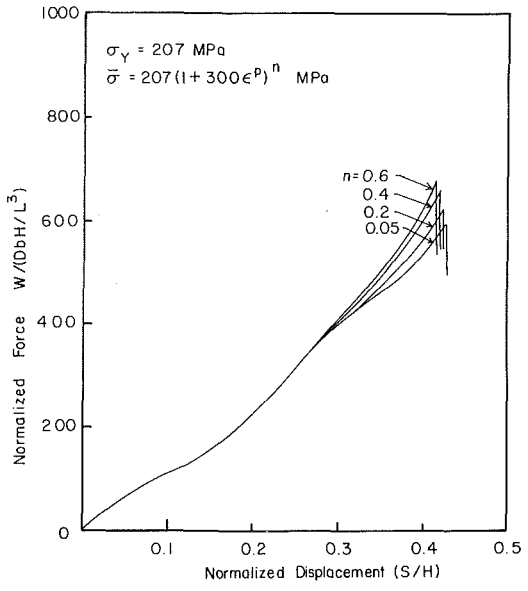
Downloaded 03 May 2010 to 171.66.16.31. Redistribution subject to ASME license or copyright; see http://www.asme.org/terms/Terms_Use.cfm



(a)



(b)



(c)

Fig. 10 Prediction of the influence of certain parameters on the normalized force versus plate displacement characteristics, $H = 12.7$ mm, $L = 305$ mm, $b = 76$ mm, $R = 920$ mm; (a) Effect of specimen thickness, $\sigma_y = 207$ MPa, $n = 0.3$, (b) Effect of yield stress, $n = 0.3$, $t = 1.22$ mm, and (c) Effect of strain hardening index, $\sigma_y = 207$ MPa, $t = 1.22$ mm

Sakai, H., Saito, K., and Tsukada, H., 1982, "Stiffness and Dent Characteristics of Body Outer Surface Panel," *JSAE Review*, March, pp. 62–67.

Sugita, Y., 1985, "Nonlinear Load-Deflection Relation of Toroidal Shells Subjected to Axisymmetric Compression Between Rigid Plates," *Int. J. Mech. Sci.*, Vol. 27, pp. 609–625.

Timoshenko, S., 1935, "Buckling of Flat Curved Bars and Slightly Curved Plates," ASME JOURNAL OF APPLIED MECHANICS, Vol. 2, pp. 17–20.

Updike, D. P., 1972, "On the Large Deformation of a Rigid-Plastic Spherical Shell Compressed by a Rigid Plate," *J. Eng. For Industry*, Vol. 94, pp. 949–955.

Updike, D. P., and Kalnins, A., 1970, "Axisymmetric Behavior of an Elastic Spherical Shell Compressed Between Rigid Plates," ASME JOURNAL OF APPLIED MECHANICS, Vol. 92, pp. 635–640.

Updike, D. P., and Kalnins, A., 1972, "Contact Pressure Between an Elastic Spherical Shell and a Rigid Plate," ASME JOURNAL OF APPLIED MECHANICS, Vol. 94, pp. 1110–1114.

Washizu, K., 1978, *Variational Methods in Elasticity and Plasticity*, Pergamon Press, New York.

Witmer, E. A., and Blamer, H. A., 1963, "Large Dynamic Deformations of Beams, Rings, Plates and Shells," *AIAA Journal*, Vol. 1, pp. 1848–1857.

Yutori, Y., Nomura, S., Kokubo, I., and Ishigai, H., 1980, "Studies on the Static Dent Resistance," *Proc. 11th Biennial Congress*, Int. Deep Drawing Res. Group (*Memoires Scientifiques, Revue Metallurgie*), pp. 561–569.

Downloaded 03 May 2010 to 171.66.16.31. Redistribution subject to ASME license or copyright; see http://www.asme.org/terms/Terms_Use.cfm

Self-Equilibrated Singular Solutions of a Complete Spherical Shell: Classical Theory Approach[1]

Nikolaos Simos
Postdoctoral Research Associate.
Earthquake Research Center
Assoc. Mem. ASME

Ali M. Sadegh
Associate Professor.
Department of Mechanical Engineering
Mem. ASME

The City College of the
City University of New York,
New York, N.Y. 10031

The elastic response of a complete spherical shell under the influence of concentrated loads (normal point loads, concentrated tangential loads, and concentrated surface moments) which apply in a self-equilibrating fashion is obtained. The mathematical analysis incorporates the classical uncoupled system of equations for the transverse displacement W *and a stress function* F. *The solution formulae for all three types of singular loading are in closed form and they are expressed in terms of complex Legendre and other elementary functions. The two latter portions of the analysis are associated with a multivalued stress function* F *which leads to a single-valued stress and displacement formulae. The intricacies of the solutions and their singular character are also discussed. Lastly, some representative shell problems are evaluated.*

Introduction

Despite the various mathematical descriptions of the shell element, the analysis of practical engineering shell problems remains complex and rigorous. Over the years a number of solutions, approximate or exact, have been presented in an effort to best describe the shell response near the loaded area. The behavior of the solution in the vicinity of the point load is the direct consequence of the particular mathematical description of the shell element. Singular solutions associated with a normal point load are also referred to as Green's functions or Fundamental solutions. Such solutions have been presented by Reissner (1947) for a spherial cap under different sets of edge conditions: Nordgren (1963) for thermoelastic problems, Flugge (1956, 1964, 1972) and Forsberg (1966) for different classes of shells, and also Simmonds and Tropf (1974) using the shallow theory approach on a hypar shell. In the work of Simmonds and Bradley (1976) fundamental solutions of arbitrary shallow shells were derived in the form of a power series. Derivation of the explicit form of the main singularities due to all types of surface loadings on shallow shells has been performed by Chernyshev (1963) and for spherical shallow shells by Lukasiewitz (1967, 1979). Concentrated forces on shallow shells were considered by Sanders (1970) and by Sanders and Simmonds (1970) for cylindrical shells. Reissner (1959), in his analysis of the unsymmetrical deformation of a shallow spherical shell, encountered a multivalued stress function. Singular solutions of a complete sphere subjected to two point loads at the poles have been introduced by Koiter (1963) while "free space" Green's functions for a closed sphere was obtained by Simmonds (1968). Berry (1955) obtained solutions of a hemispherical cap subjected to edge loads and moments by deriving an uncoupled system of equations and evaluating the Legendre functions with integration of their differential equation. In the works of Wilkinson and Kalnins (1966a,b), Green's functions for an open spherical shell were derived and the solution to the problem of a concentrated lateral force and moment at the appex of a similar shell was constructed.

The aim of this paper is the derivation of exact, closed-form singular solutions for a complete spherical shell subjected to point loads along the normal or tangential directions and concentrated surface moments. The mathematical formulation begins in the uncoupled system of differential equations which govern the transverse displacement function W and an auxiliary stress variable F of a nonshallow spherical shell. Our intention is to utilize the singular part of the solution of the governing differential equations and construct a set of solutions, fundamental or simply singular, that would correspond to the response of the domain of interest to the action of concentrated surface excitation. The solutions are meant to satisfy the overall equilibrium of the complete sphere and thus the application of the singular loads is of unique character. The fundamental solution for a normal point load will be the elastic response of a complete sphere under the action of a Delta function distribution accompanied by an axisymmetrically-distributed normal surface traction.The variable formulae are expressed in terms of complex Legendre functions as well as elementary functions. The closed-form solutions coincide with the ones of Koiter (1963) and Simmonds (1968). The action of an equilibrated unit tangential load is expressed in terms of two such unit loads acting in opposite directions at the two poles and an equilibrating moment applied in one of the poles. A multivalue stress variable F is participating in this part of the analysis but leading to single-valued stress and displacement functions. The field variable formulae reveal strong

[1] This paper is based on a part of the doctoral dissertation of N. Simos which was submitted to the Graduate School of the City University of New York in March 1988.

Contributed by the Applied Mechanics Division for publication in the JOURNAL OF APPLIED MECHANICS.

Discussion on this paper should be addressed to the Editorial Department, ASME, United Engineering Center, 345 East 47th Street, New York, N.Y. 10017, and will be accepted until two months after final publication of the paper itself in the JOURNAL OF APPLIED MECHANICS. Manuscript received by ASME Applied Mechanics Division, May 4, 1988; final revision, July 21, 1988.

Copyright © 1989 by ASME

Downloaded 03 May 2010 to 171.66.16.31. Redistribution subject to ASME license or copyright; see http://www.asme.org/terms/Terms_Use.cfm

singularities in the transverse shear resultants and weak singular behavior of the tangential displacement components. The action of a unit concentrated moment is evaluated in the form of two unit moments acting at the two poles. The corresponding solution can be viewed as the superposition of two appropriate tangential load solutions. In the last section, the present work is compared with the analogous work on shallow shells presented by Lukasiewicz (1967, 1979) focusing on the singular character of the kernels and, further, some representative classical shell problems are evaluated.

Fundamental Solutions of Normal Surface Traction

Consider a spherical shell defined by the coordinate system (ϕ,θ), Fig. 1, and having thickness h, middle surface radius R, Young's modulus E and Poisson's ratio μ. The govering differential equations of the shell subjected to normal surface load q_n are expressed in terms of the radial displacement function W and an auxiliary stress variable F. The decoupled form of the governing equations, derived by Berry (1955), can be written as

$$(\nabla^2+2)\left[\nabla^4+2\nabla^2+\frac{EhR^2}{D}\right]W=\frac{R^4}{D}\,[\nabla^2+1-\mu)q_n \tag{1}$$

$$(\nabla^2+2)F=\frac{D}{R}\left[\frac{R^4}{D}\,q_n-(\nabla^2+2)^2W\right] \tag{2}$$

where ∇^2 is the Laplacian operator and $D=Eh^3/12(1-\mu^2)$. The relations of F with the symmetric stress resultants $N_{\alpha\beta}$ were introduced by Berry (1955) and they are expressed in the form

$$N_\phi=\frac{1}{R^2}\left[\csc^2\phi\,\frac{\partial^2F}{\partial\theta^2}+\cot\phi\,\frac{\partial F}{\partial\phi}+F+\frac{D}{R}\,(\nabla^2+2)W\right]$$

$$N_\theta=\frac{1}{R^2}\left[\frac{\partial^2F}{\partial\phi^2}+F+\frac{D}{R}\,(\nabla^2+2)W\right] \tag{3}$$

$$N_{\phi\theta}=\frac{1}{R^2}\left[\cos\phi\,\csc^2\phi\,\frac{\partial F}{\partial\theta}-\csc\phi\,\frac{\partial^2F}{\partial\phi\partial\theta}\right].$$

One of the basic problems in the linear theory of elastic shells is the construction of the fundamental solutions or "free space" Green's functions. By definition, the Green's function, G, can be expressed in the form $G=G_s+G_r$ where G is a dependent variable while G_s and G_r correspond to the derivation of a fundamental singularity and regular solution, respectively. In the course of the derivation of a fundamental singularity, certain mathematical as well as physical conditions need to be satisfied. The conditions which require that the fundamental singularity must (*a*) be a solution of the governing system, (*b*) be singular at the pole, and (*c*) satisfy the reciprocal theorem everywhere in the domain of interest are not sufficient. For a spherical shell, G_s corresponds to an axisymmetric point load solution. As the load point is approached, such a solution should be expected to satisfy equilibrium along the normal to the middle surface and also $u=\beta=0$, where u and β are the surface displacement and the rotation of the normal, respectively. It should be remembered, however, that the latter requirements ought not to be imposed on the solution *a priori*. Such approach could lead to an incorrect form of the fundamental singularity.

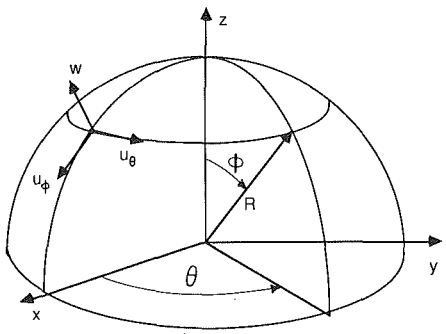


Fig. 1 Shell coordinates

Let a unit point load be applied at an arbitrary point $x'(\phi',\theta')$ in the form of a two-dimensional Dirac Delta distribution $\delta(\mathbf{n}-\mathbf{n}')$. $\mathbf{n}'$ is the unit normal vector at $\mathbf{x}'(\phi',\theta')$, $\mathbf{n}$ is the unit vector at an arbitrary point $\mathbf{x}(\phi,\theta)$ and they are related through the expression

$$\mathbf{n}\cdot\mathbf{n}'=\cos\gamma=\cos\phi\,\cos\phi'+\sin\phi\,\sin\phi'\,\cos(\theta-\theta'). \tag{4}$$

With the introducton of a geographical coordinate system (γ,η), where $\gamma=0$ coincides with $\mathbf{n}'$, the Delta distribution will take the axisymmetric form

$$\delta(\mathbf{n}-\mathbf{n}')=\frac{\delta(\gamma)}{2\pi R^2\sin\gamma}\,. \tag{5}$$

The equilibrating surface traction, denoted as q_n, and having overall resultant equal and opposite to the Delta function, will be expressed as

$$q_{n'}=-\frac{3}{4\pi R^2}\cos\gamma. \tag{6}$$

Considering $q_n=\delta(\mathbf{n}-\mathbf{n}')+q_n'$, and substituting into equation (1), the fundamental solution of the normal displacement function W will be the solution of

$$(\nabla^2+2)[\nabla^2+\nu(\nu+1)][\nabla^2+\lambda(\lambda+1)]W=\frac{R^2}{D}\,(\nabla^2+1-\mu)\left[\frac{\delta(\gamma)}{2\pi\sin\gamma}-\frac{3}{4\pi}\cos\gamma\right] \tag{7}$$

where ν and λ are complex conjugate parameters and they satisfy the relations

$$\nu(\nu+1)+\lambda(\lambda+1)=2,\quad \nu(\nu+1)\cdot\lambda(\lambda+1)=\frac{EhR^2}{D}$$

$$\nu(\nu+1)=1+i\tan\psi,\quad \lambda(\lambda+1)=1-i\tan\psi,$$

$$\chi\cos\psi=1,\quad \chi^2=\frac{EhR^2}{D} \tag{8}$$

while

$$\nabla^2=\frac{d^2}{d\gamma^2}+\cot\gamma\,\frac{d}{d\gamma}\,.$$

Let the normal displacement function $W(\mathbf{x};\mathbf{x}')$ be written in the equivalent form

$$W(\mathbf{x};\mathbf{x}')=W_1(\mathbf{x};\mathbf{x}')+W_2(\mathbf{x};\mathbf{x}') \tag{9}$$

such that

$$(\nabla^2+2)+[\nabla^2+\nu(\nu+1)][\nabla^2+\lambda(\lambda+1)\begin{pmatrix}W_1\\W_2\end{pmatrix}=\frac{R^2}{D}\,(\nabla^2+1-\mu)\begin{bmatrix}\dfrac{\delta(\gamma)}{2\pi\sin\gamma}\\[2ex]-\dfrac{3}{4\pi}\cos\gamma\end{bmatrix}. \tag{10, 11}$$

Solution of (11) leads to

$$W_2(\mathbf{x};\mathbf{x}')=-\frac{\mu+1}{4\pi Eh}\,[1+\cos\gamma\,\ln(1-\cos\gamma)]. \tag{12}$$

Let the scalar function $U_s(\mathbf{x};\mathbf{x}')$ satisfy

$$(\nabla^2+2)[\nabla^2+\nu(\nu+1)][\nabla^2+\lambda(\lambda+1)]U_s(\mathbf{x};\mathbf{x}')=\frac{\delta(\gamma)}{2\pi\sin\gamma} \tag{13}$$

Therefore, $W_1(\mathbf{x};\mathbf{x}')$ can now be written as

$$W_1(\mathbf{x};\mathbf{x}')=\frac{R^2}{D}\,(\nabla^2+1-\mu)\,U_s(\mathbf{x};\mathbf{x}'). \tag{14}$$

The fundamental singularity for $U_s(\mathbf{x};\mathbf{x}')$ will be con-

Downloaded 03 May 2010 to 171.66.16.31. Redistribution subject to ASME license or copyright; see http://www.asme.org/terms/Terms_Use.cfm

structed from the homogeneous solution of (13). Such solution can be expressed in the form

$$U_s(\mathbf{x};\mathbf{x}') = U_1(\mathbf{x};\mathbf{x}') + U_2(\mathbf{x};\mathbf{x}') + U_3(\mathbf{x};\mathbf{x}') \tag{15}$$

where the three components satisfy

$$(\nabla^2+2)U_1(\mathbf{x};\mathbf{x}')=0, \quad [\nabla^2+\nu(\nu+1)]U_2(\mathbf{x};\mathbf{x}')=0,$$
$$[\nabla^2+\lambda(\lambda+1)]U_3(\mathbf{x};\mathbf{x}')=0. \tag{16}$$

The singular part of $U_s(\mathbf{x};\mathbf{x}')$ that has poles at only one point on the complete sphere will constitute the fundamental singularity. Thus, the final form of the singular solution of (13) can be written as

$$U_s(\mathbf{x};\mathbf{x}') = A_2 P_\nu(-\cos\gamma) + A_3 P_\lambda(-\cos\gamma) \tag{17}$$

where A_2 and A_3 are complex conjugate arbitrary constants, while P_ν and P_λ are complex conjugate Legendre functions of the first kind. To evaluate the two constants, A_2 and A_3, so that the existence of the Delta function at $\gamma=0$ is satisfied, a scalar function $f(\mathbf{x};\mathbf{x}')$ is introduced such that

$$(\nabla^2+2)[\nabla^2+\lambda(\lambda+1)]U_s(\mathbf{x};\mathbf{x}') = f(\mathbf{x};\mathbf{x}') \tag{18}$$

is valid everywhere in the domain. Thus, $f(\mathbf{x};\mathbf{x}')$ satisfies

$$[\nabla^2+\nu(\nu+1)]f(\mathbf{x};\mathbf{x}')=0 \tag{19}$$

away from the pole, $\gamma=0$, and

$$[\nabla^2+\nu(\nu+1)]f(\mathbf{x};\mathbf{x}') = \frac{\delta(\gamma)}{2\pi\sin\gamma} \tag{20}$$

in the vicinity of the pole of the unit sphere. Substitution of (17) into (18) leads to

$$f(\mathbf{x};\mathbf{x}') = -2i\tan\psi(1-i\tan\psi)A_2 P_\nu(-\cos\gamma). \tag{21}$$

To evaluate the constant A_2, the divergence theorem is applied in a circular contour $C(\gamma=\gamma_0)$ around $\gamma=0$.

$$\int_\sigma\int \nabla^2 f(\mathbf{x};\mathbf{x}')d\sigma = \int_C \frac{\partial f(\mathbf{x};\mathbf{x}')}{\partial \mathbf{n}}\,dC. \tag{22}$$

From (20) one can write

$$\nabla^2 f(\mathbf{x};\mathbf{x}') = \frac{\delta(\gamma)}{2\pi\sin\gamma} - \nu(\nu+1)f(\mathbf{x};\mathbf{x}'). \tag{23}$$

Therefore,

$$\int_C \frac{\partial f(\mathbf{x};\mathbf{x}')}{\partial \mathbf{n}}\,dC = \int_\sigma\int \frac{\delta(\gamma)}{2\pi\sin\gamma}\,d\sigma - \nu(\nu+1)\int_\sigma\int f(\mathbf{x};\mathbf{x}')d\sigma. \tag{24}$$

In the limit as $\gamma\to 0$ the following relations hold

$$\lim_{\gamma\to 0}\int_\sigma\int \frac{\delta(\gamma)}{2\pi\sin\gamma}\,d\sigma = 1.$$

$$\lim_{\gamma\to 0} P_\nu(-\cos\gamma) = \frac{2}{\pi}\sin\nu\pi \lim_{\gamma\to 0}\left[\frac{1}{2}\log(1-\cos\gamma)+\text{const.}\right]$$

$$\lim_{\gamma\to 0} P_\nu^1(-\cos\gamma) = -\frac{2}{\pi}\sin\nu\pi \lim_{\gamma\to 0}\left[\frac{1}{\gamma} - \gamma\nu(\nu+1)\left[\frac{1}{2}\log(1-\cos\gamma)+\text{const.}\right]\right] \tag{25}$$

Therefore,

$$\lim_{\gamma\to 0}\int_\sigma\int f(\mathbf{x};\mathbf{x}')d\sigma = 0 \tag{26}$$

and

$$\lim_{\gamma\to 0}\int_C \frac{\partial f}{\partial \mathbf{n}}\,dC = \lim_{\gamma\to 0}\int_0^2 \frac{df}{d\gamma}\sin\gamma\,d\eta$$
$$= -8i\tan\psi(1-i\tan\psi)\sin\nu\pi. \tag{27}$$

Finally,

$$A_2 = -[8i\tan\psi(1-i\tan\psi)\sin\nu\pi]^{-1} \tag{28}$$

and, consequently, $A_3 = \text{CONJ}\,[A_2]$.
Further,

$$W_1(\mathbf{x};\mathbf{x}') = \frac{R^2}{D}(\nabla^2+1-\mu)U_s(\mathbf{x};\mathbf{x}')$$
$$= 2\frac{R^2}{D}\,\text{Re}[(1-\mu-i\tan\psi)A_2 P_\nu(-\cos\gamma)]. \tag{29}$$

The idea of the distributed normal traction $q_{n'}$ is connected to the Green's function of the Generalized form, which in turn is required to satisfy the orthogonality condition

$$\int_R\int W_2(\mathbf{x};\mathbf{x}')\cos\gamma\,dR = 0 \tag{30}$$

where R refers to the domain of interest. The evaluation of the integral leads to the following final form of the fundamental solution for the normal displacement function $W(\mathbf{x};\mathbf{x}')$

$$W(\mathbf{x};\mathbf{x}') = 2\text{Re}[AP_\nu(-\cos\gamma)] - \frac{1+\mu}{4\pi Eh}[1+\cos\gamma\ln(1-\cos\gamma)+B\cos\gamma] \tag{31}$$

where

$$A = \frac{R^2}{D}(1-\mu-i\tan\psi)A_2, \quad B = \frac{4}{3}-\ln(2).$$

The description of the complete field, however, requires the fundamental solution of the auxiliary stress variable $F(\mathbf{x};\mathbf{x}')$. We express $F(\mathbf{x};\mathbf{x}')$ in the from

$$F(\mathbf{x};\mathbf{x}') = F_1(\mathbf{x};\mathbf{x}') + F_2(\mathbf{x};\mathbf{x}') \tag{32}$$

such that

$$F_1(\mathbf{x};\mathbf{x}') = -\frac{D}{R}(\nabla^2+2)\,W(\mathbf{x};\mathbf{x}') \tag{33}$$

and

$$(\nabla^2+2)F_2(\mathbf{x};\mathbf{x}') = R^3 q_n \tag{34}$$

with q_n defined again as $q_n = \delta(\mathbf{n}-\mathbf{n}') + q_{n'}$. The function $F_1(\mathbf{x};\mathbf{x}')$ is obtained directly from (33) and can be written as

$$F_1(\mathbf{x};\mathbf{x}') = 2\text{Re}[A' P_\nu(-\cos\gamma)] + C_1\cos\gamma \tag{35}$$

where

$$A' = -\frac{D}{R}[2-\nu(\nu+1)]A, \quad C_1 = -\frac{3D(1+\mu)}{4\pi EhR}.$$

The generalized Green's function for the operator ∇^2+2 in (34) will also be required to satisfy the orthogonality condition of (29). The Green's function of (34) is the particular integral of

$$[\nabla^2+2]F_2(\mathbf{x};\mathbf{x}') = -\frac{3R}{4\pi}\cos\gamma \tag{36}$$

and which, after satisfying (29), leads to the final form

$$F_2(\mathbf{x};\mathbf{x}') = C_2[1+\cos\gamma\ln(1-\cos\gamma)+B\cos\gamma) \tag{37}$$

where $C_2 = \frac{R}{4\pi}$.

By utilizing the stress function-stress resultants relations, we arrive at the fundamental solutions for the stress resultants as seen by the surface coordinate system (γ, η)

$$N_\gamma = \frac{1}{R^2}\left[\cot\gamma[2\text{Re}\{-A' P_\nu^1(-\cos\gamma)\}] - C_1\cos\gamma + C_2\left(1+\frac{\cos^2\gamma}{1-\cos\gamma}\right)\right] \tag{38}$$

Downloaded 03 May 2010 to 171.66.16.31. Redistribution subject to ASME license or copyright; see http://www.asme.org/terms/Terms_Use.cfm

and

$$N_\eta = \frac{1}{R^2}\left[2\mathrm{Re}\left\{-A'\frac{d}{d\gamma}P_\nu^1(-\cos\gamma)\right\} - C_1\cos\gamma + C_2\left[1-2(1+\cot\gamma)-\frac{\cos\gamma}{1-\cos\gamma}\right]\right] \quad (39)$$

while due to axisymmetry $N_{\gamma\eta}=0$.
The surface displacement u_γ can consequently be derived from the stress displacement relations. We can appropriately write

$$u_\gamma = \frac{R}{Eh}\int (N_\gamma - \mu N_\eta)\,d\gamma - \int W\,d\gamma \quad (40)$$

which leads to

$$u_\gamma = \frac{1+\mu}{EhR}\left[2\mathrm{Re}\{A'P_\nu^1(-\cos\gamma)\} - C_2\left[-\sin\gamma\ln(1-\cos\gamma) + \frac{\cos\gamma\sin\gamma}{1-\cos\gamma} - B\sin\gamma\right]\right] - \frac{1}{EhR}[C_1(1-\mu)+3C_2]\sin\gamma \quad (41)$$

while $u_\eta = 0$.
The moment resultants M_γ and M_η can be deduced from the moment curvature relations with $M_{\gamma\eta}=0$

$$M_\gamma = D(k_\gamma^0 + \mu k_\eta^0) + \frac{h^2}{12R}N_\gamma, \quad M_\eta = D(k_\eta^0 + \mu k_\gamma^0) + \frac{h^2}{12R}N_\eta \quad (42)$$

where

$$k_\gamma^0 = -\frac{1}{R^2}\left(\frac{d^2W}{d\gamma^2}+W\right), \quad k_\eta^0 = -\frac{1}{R^2}\left(\cot\gamma\frac{dW}{d\gamma}+W\right). \quad (43)$$

Further, the transverse shear resultant Q_γ, which in the classical approach, has been accounted for the shell element equilibrium, can be derived from the relation

$$Q_\gamma\left(1+\frac{h^2}{12R^2}\right) = -\frac{D}{R^3}\frac{d}{d\gamma}[(\nabla^2+2)W] \quad (44)$$

which, after setting $1+h^2/12R^2 \approx 1$, leads to

$$Q_\gamma = \frac{D}{R^3}\left[2\mathrm{Re}\{[2-\nu(\nu+1)]AP_\nu^1(-\cos\gamma)\} + \frac{3(1+\mu)}{4\pi Eh}\sin\gamma\right]. \quad (45)$$

The true physical nature of the fundamental solutions stems from the character of the singularities in the stress and displacement kernel functions. Earlier we discussed the need for the fundamental singularity to satisfy certain physical conditions in the vicinity of the pole. Thus, we examine the complete solution in the limit as $\gamma\to 0$. We observe that it indeed satisfies the conditions $\lim_{\gamma\to 0} u_\gamma = \lim_{\gamma\to 0}\beta = 0$. Further, we study the behavior of the shear resultant Q_γ as $\gamma\to 0$ and note that

$$\lim_{\gamma\to 0} Q_\gamma = \frac{2D}{R^3}\lim_{\gamma\to 0}\left[\mathrm{Re}\left\{(2-\nu(\nu+1)A\left(-\frac{2}{\pi}\sin\nu\pi\right)\right\}\frac{1}{\gamma}\right] = -\frac{1}{2\pi R}\lim_{\gamma\to 0}\left(\frac{1}{\gamma}\right). \quad (46)$$

We also observe that the response of the shell in the vicinity of the point load along the radial direction is finite

$$\lim_{\gamma\to 0} W = \lim_{\gamma\to 0}\left(-\frac{1+\mu}{4\pi Eh}[1+(B+\ln 2)\cos\gamma] + \frac{1}{2\pi Eh}\mathrm{Re}\left(1+\mu+i\left(\frac{\tan^2\psi-\mu}{\tan\psi}\right)\left[\psi(\nu+1) + C + \frac{\pi}{2}\cot\nu\pi\right]\right)\right) \quad (47)$$

where $\psi(\,.\,.\,)$ is the logarithmic derivative of the Gamma function and C is the Euler's constant.

In addition, examination of the limiting values of the stress and moment resultants reveals that their kernels contain logarithmic singularities. We introduce the resulting expressions of the stress resultant kernels:

$$\lim_{\gamma\to 0} N_\gamma = \lim_{\gamma\to 0}[a_1\ln[\sin(\gamma/2)+b_1]$$

$$\lim_{\gamma\to 0} N_\eta = \lim_{\gamma\to 0}[a_1\ln[\sin(\gamma/2)+b_2] \quad (48)$$

where

$$a_1 = \frac{2}{R^2}\mathrm{Re}\left\{\frac{\sin\nu\pi}{\pi}\nu(\nu+1)A'\right\}$$

$$b_1 = -\frac{1}{R^2}\left[\mathrm{Re}\left\{\frac{\sin\nu\pi}{\pi}A'\nu(\nu+1)CP_1(\nu)\right\} + C_1 - C_2\right]$$

$$b_2 = \frac{1}{R^2}\left[4\,\mathrm{Re}\left\{\frac{\sin\nu\pi}{\pi}A'\nu(\nu+1)[CP_0(\nu) - CP_1(\nu) - C_1 - 3C_2]\right\}\right]$$

$$CP_0(\nu) = \psi(\nu+1) + C + \frac{\pi}{2}\cot\nu\pi - \frac{1}{2}\ln 2$$

$$CP_1(\nu) = [\pi\cot\nu\pi + \psi(\nu+2) + \psi(\nu) + 2C - 1 - \ln 2]/4.$$

It is interesting to note that an outward point load introduces compressive membrane stresses in the immediate area. Such behavior was also noted by Koiter (1963) and Wilkinson (1966) and it is believed to be the result of the incorporated postulates upon which the mathematical model has been established. Such postulates require that normals remain normals during deformation and the necessary forces to ensure that must be compressive in nature.

Evaluation of the equilibrium condition that the fundamental solution must automatically satisfy, proves that

$$\lim_{\gamma\to 0}\int_0^{2\pi}\left[Q_\gamma\cos\gamma + N_\gamma\sin\gamma\right]R\sin\gamma\,d\eta = \lim_{\gamma\to 0}\int_0^{2\pi} -\frac{1}{2\pi R}\left(\frac{1}{\gamma}\right)\cos\gamma + \sin\gamma\left[a_1\ln\left(\sin\frac{\gamma}{2}\right)+b_1\right]\Big)R\sin\gamma\,d\eta = -1 \quad (49)$$

which clearly indicates that equilibrium around the pole is satisfied.

Concentrated Tangential Load Solution

Let us consider a unit tangential load applied at an arbitrary point $x'(\phi';\theta')$ of the middle surface of a complete sphere and oriented arbitrarily. In order for the overall equilibrium to be preserved, surface equilibrating loads in the form of distributed traction or concentrated load arrangement must be introduced. In this analysis the former alternative will be evaluated. Thus, we return to the governing system of equations, (1) and (2), and we utilize the traction-free version of the uncoupled system, $q_n = q_s = q_t = 0$. We again introduce a geographical coordinate system (γ,η) with the north pole, $\gamma=0$, coinciding with the point of application of the unit load which, in the new system, is directed along $\eta=0$. We wish to construct a singular solution of the governing system that is symmetric with respect to $\eta=0$. This suggests the following general solution expressions for the radial displacement function $W(\mathbf{x};\mathbf{x}')$ and the auxiliary stress variable $F(\mathbf{x};\mathbf{x}')$

Downloaded 03 May 2010 to 171.66.16.31. Redistribution subject to ASME license or copyright; see http://www.asme.org/terms/Terms_Use.cfm

$$W(\mathbf{x};\mathbf{x}') = [h_1 P_\nu^1(\cos\gamma) + h_2 P_\nu^1(-\cos\gamma) + \bar{h}_1 P_\lambda^1(\cos\gamma) + \bar{h}_2 P_\lambda^1(-\cos\gamma) + C^1 Q_1^1(\cos\gamma)]\cos\eta \tag{50}$$

$$F(\mathbf{x};\mathbf{x}') = [H_1 P_\nu^1(\cos\gamma) + H_2 P_\nu^1(-\cos\gamma) + \bar{H}_1 P_\lambda^1(\cos\gamma) + \bar{H}_2 P_\lambda^1(-\cos\gamma) + D^1 Q_1^1(\cos\gamma)]\cos\eta \tag{51}$$

where h_1, h_2, H_1, etc. are arbitrary constants. A bar over a constant indicates complex conjugation while the following relations hold

$$H_1 = -\frac{D}{R}[2-\nu(\nu+1)]h_1, \quad H_2 = -\frac{D}{R}[2-\nu(\nu+1)]h_1$$

$$\bar{H}_1 = -\frac{D}{R}[2-\lambda(\lambda+1)]\bar{h}_1, \quad \bar{H}_2 = -\frac{D}{R}[2-\lambda(\lambda+1)]\bar{h}_1. \tag{52}$$

One may note that the independent solutions for $W(\mathbf{x};\mathbf{x}')$ and $F(\mathbf{x};\mathbf{x}')$ which are regular everywhere in the domain have been discarded. After utilizing the stress function-stress resultant relations, the stress resultant formulae are obtained and introduced into the stress displacement relations

$$\frac{1}{Eh}(N_\gamma - \mu N_\eta) = \frac{1}{R}\left(\frac{\partial u_\gamma}{\partial\gamma} + W\right)$$

$$\frac{1}{Eh}(N_\eta - \mu N_\gamma) = \frac{1}{R}\left(\csc\gamma\frac{\partial u_\eta}{\partial\eta} + u_\gamma\cot\gamma + W\right). \tag{53}$$

Integration of (53) leads to the expressions of the two tangential displacement components u_γ and u_η

$$u_\gamma = -\frac{1+\mu}{EhR}\left[\frac{d}{d\gamma}F(\gamma) + D^1 Q_1(\cos\gamma)\right]\cos\eta - C^1 Q_1(\cos\gamma) + f(\eta) \tag{54}$$

$$u_\eta = -\frac{1+\mu}{EhR}\csc\gamma\frac{\partial}{\partial\eta}F(\gamma,\eta) + \left(\cos\gamma\left[\frac{1+\mu}{EhR}D^1 Q_1(\cos\gamma) + C^1 Q A_1(\cos\gamma)\right] - \sin\gamma\left[\frac{1+\mu}{EhR}D^1 Q_1^1(\cos\gamma) + C^1 Q_1^1(\cos\gamma)\right]\right)\sin\eta - \cos\gamma\int f(\eta)d\eta + g(\gamma) \tag{55}$$

where $f(\eta)$ and $g(\gamma)$ are arbitrary functions of integration. In order to evaluate their form, the third of the stress displacement relations is employed

$$\frac{2(1+\mu)}{Eh}N_{\gamma\eta} = \frac{1}{R}\left[\frac{\partial u_\eta}{\partial\gamma} - \cot\gamma u_\eta + \csc\gamma\frac{\partial u_\gamma}{\partial\eta}\right]. \tag{56}$$

When the appropriate expressions of the variables are introduced in (56), it is observed that the following additional terms, expressed as Ω, remain with no counterparts

$$\Omega = -2\left[\frac{1+\mu}{EhR}D^1 + C^1\right]\csc\gamma\sin\eta + \csc\gamma\left[\frac{d}{d\eta}f(\eta) + \int f(\eta)d\eta\right] + \frac{d}{d\gamma}g(\gamma) - \cot\gamma g(\gamma). \tag{57}$$

Since $d/d\gamma\, g(\gamma) - \cot\gamma\, g(\gamma)$ is independent of η, without loss of generality, we can assume that

$$\frac{d}{d\gamma}g(\gamma) - \cot\gamma\, g(\gamma) = 0 \tag{58}$$

which leads to

$$g(\gamma) = a'\sin\gamma \tag{59}$$

where a' is an arbitrary constant. Further, by setting $f(\eta) = A_0\eta\sin\eta$, we observe that

$$\frac{d}{d\eta}f(\eta) + \int f(\eta)d\eta = 2A_0\sin\eta \tag{60}$$

and the expression Ω takes the form

$$\Omega = -2\left[\frac{1+\mu}{EhR}D^1 + C^1\right]\csc\gamma\sin\eta + 2A_0\csc\gamma\sin\eta = 0. \tag{61}$$

By setting $A_0 = 1 + \mu/EhR\, D^1 + C^1$, Ω vanishes and thus all the stress displacement relations are satisfied. However, the multivalued nature of $f(\eta)$ will lead to multivalued tangential displacements. Because such displacements cannot be allowed in the closed sphere domain, we require that

$$A_0 = 0, \quad \frac{1+\mu}{EhR}D^1 = C^1. \tag{62}$$

Hence, the components of the tangential displacements can now be written in the form

$$u_\gamma(\mathbf{x};\mathbf{x}') = -\frac{1+\mu}{EhR}\frac{\partial}{\partial\gamma}F(\mathbf{x};\mathbf{x}') \tag{63}$$

$$u_\eta(\mathbf{x};\mathbf{x}') = -\frac{1+\mu}{EhR}\csc\gamma\frac{\partial}{\partial\eta}F(\mathbf{x};\mathbf{x}'). \tag{64}$$

Note that $g(\gamma)$ represents rigid body displacement, since it is independent of η and, for that matter, it has been suppressed by setting $a' = 0$.

To this point, the description of the complete field has been obtained in its general form. We note that the kernel functions of the variables pose singular behavior at two points on the complete sphere, $\gamma = 0$ and $\gamma = \pi$. The unknown arbitrary constants, however, must be evaluated in a manner which will reflect a particular loading situation. In order to determine what these singularities correspond to at both poles, we obtain the resultant force and moment introduced by the state of stress around the edge of a circular contour that encloses each pole. The resultant force, along $\eta = 0$, can be expressed in the form of the integral

$$F_r = \lim_{\substack{\gamma\to 0\\ \gamma\to\pi}}\int_0^{2\pi}\left[(N_\gamma\cos\gamma + Q_\gamma\sin\gamma)\cos\eta - N_{\gamma\eta}\sin\eta\right]R\sin\gamma d\eta \tag{65}$$

while the resultant moment will be in the form

$$M_r = \lim_{\substack{\gamma\to 0\\ \gamma\to\pi}}\int_0^{2\pi} R\left[M_\gamma\cos\eta - M_{\gamma\eta}\cos\gamma\sin\eta - R\sin\gamma\cos\eta[Q_\gamma\cos\gamma - N_\gamma\sin\gamma]\right]\sin\gamma d\eta. \tag{66}$$

When the appropriate expressions are introduced into the two integrals above, we obtain the following interesting results:

$$F_r = -\frac{2\pi}{R}D^1 \tag{67}$$

and

$$M_r = \lim_{\substack{\gamma\to 0\\ \gamma\to\pi}}[2\pi D^1\cos\gamma]. \tag{68}$$

If the only surviving constant D^1 is given the value $D^1 = R/2\pi$, the general solution corresponds to the self-equilibrated system shown in Fig. 2(*a*). However, if we wish to examine the response of the shell due to the action of a unit tangential load in a self-equilibrated arrangement, the loading conditions of Fig. 2(*b*) should be incorporated. Obviously, a solution described in Fig. 2(*c*) must be superimposed on Fig. 2(*a*) in order for the desired arrangement of Fig. 2(*b*) to result.

The general solution, however, was only able to provide the physical problem of Fig. 2(*a*). Thus, it becomes inevitable to seek additional solutions of the governing system which are of forms different than the ones already utilized. We return to

Downloaded 03 May 2010 to 171.66.16.31. Redistribution subject to ASME license or copyright; see http://www.asme.org/terms/Terms_Use.cfm

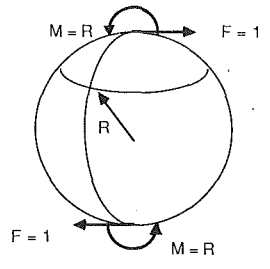


Fig. 2a

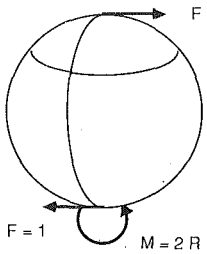


Fig. 2b

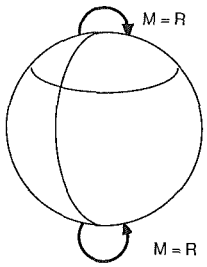


Fig. 2c

Fig. 2 Self-equilibrated tangential load and moment arrangements

$(\nabla^2+2)F^*(\mathbf{x};\mathbf{x}')=0$ and we seek a mutivalued form of $F^*(\mathbf{x};\mathbf{x}')$ that satisfies the operator. We should note that mutivalued stress functions are permitted in the analysis, provided they lead to single-valued stresses and displacements. Such form of the auxiliary stress variable is

$$F^*(\mathbf{x};\mathbf{x}')=A^*[\sin\gamma\,\eta\sin\eta-\csc\gamma\cos\eta]. \tag{69}$$

Accordingly, we obtain the following single-valued expressions

$$N_\gamma^*=\frac{2A^*}{R^2}\frac{\cos\eta}{\sin^3\gamma},\quad N_\eta^*=-\frac{2A^*}{R^2}\frac{\cos\eta}{\sin^3\gamma},$$

$$N_{\gamma\eta}^*=\frac{2A^*}{R^2}\frac{\cos\eta}{\sin^3\gamma}\sin\eta. \tag{70}$$

When equation (70) is introduced into the resultant force and moment integrals, and the arbitrary constant A^* takes the value $A^*=-D'$, the loading arrangement of Fig. 2(*c*) is obtained. Apparently, the additional stress resultants will introduce new components of the tangential displacement function, u_γ^* and u_η^*, of the form

$$u_\gamma^*=-\frac{2(1+\mu)}{EhR}D^1\left[\frac{1}{2}\ln\left[\tan\frac{1}{2}\gamma\right]-\frac{1}{2}\frac{\cos\gamma}{\sin^2\gamma}\right]\cos\eta \tag{71}$$

$$u_\eta^*=\frac{2(1+\mu)}{EhR}D^1\left[\cos\gamma\left(\frac{1}{2}\ln\left[\tan\frac{1}{2}\gamma\right]+\frac{1}{2}\frac{\cos\gamma}{\sin^2\gamma}\right)+1\right]\sin\eta. \tag{72}$$

Thus, the complete expressions of u_γ and u_η can be written as

$$u_\gamma=-\frac{1+\mu}{EhR}\frac{\partial}{\partial\gamma}F(\mathbf{x};\mathbf{x}')+u_\gamma^* \tag{73}$$

$$u_\eta=-\frac{1+\mu}{EhR}\csc\gamma\frac{\partial}{\partial\eta}F(\mathbf{x};\mathbf{x}')+u_\eta^*. \tag{74}$$

The remaining four arbitrary constants, h_1, h_2, $\bar{h}_1$ and $\bar{h}_2$, will be evaluated from physical requirements imposed at the two poles where the singular loads apply. First we consider the relation

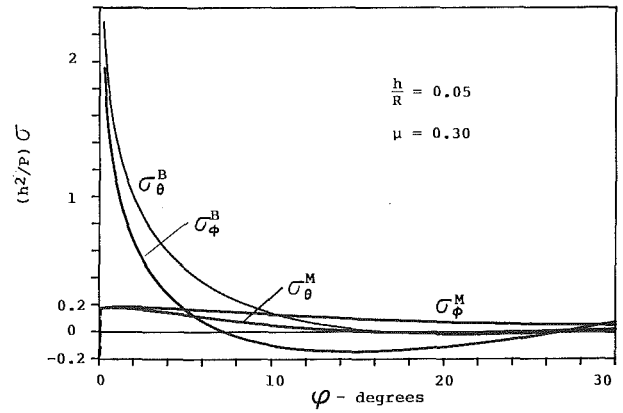


Fig. 3 Stress distribution in a spherical cap of 30 deg opening and fixed edge subjected to a normal point load *P* at the appex

$$\lim_{\substack{\gamma\to 0\\ \gamma\to\pi}}\int_0^{2\pi}[W\cos\gamma-u_\gamma\sin\gamma+R\sin\gamma\beta_\gamma]R\sin\gamma\cos\eta\,d\eta=0. \tag{75}$$

This implies that the net displacement in the normal direction at both poles vanishes since there is no net force acting in that direction. Evaluation of the integral leads to two relations between the arbitrary constants

$$\frac{2}{\pi}[\sin\nu\pi h_2+\sin\lambda\pi\bar{h}_2]+C^1=0 \tag{76}$$

$$\frac{2}{\pi}[\sin\nu\pi h_1+\sin\lambda\pi\bar{h}_1]-C^1=0. \tag{77}$$

The next requirement reflects the physical condition which implies that the net displacement component along the axis which lies on the horizontal tangent plane and is perpendicular to the direction of the unit tangent load must vanish. A similar limiting integral is introduced and it requires that

$$\lim_{\substack{\gamma\to 0\\ \gamma\to\pi}}[u_\gamma\cos\gamma+W\sin\gamma+u_\eta]\sin\gamma=0. \tag{78}$$

Equation (78) leads to two more relations between the constants

$$\sin\nu\pi H_2+\sin\lambda\pi\bar{H}_2=0 \tag{79}$$

$$\frac{\sin\nu\pi}{\pi}H_1+\frac{\sin\lambda\pi}{\pi}\bar{H}_1-\frac{D^1}{2}=0. \tag{80}$$

Careful evaluation of the singular character of the solution at the two poles reveals that while the normal displacement W is zero at the load point, both tangential displacement components, u_γ and u_η, pose logarithmic behavior. On the other hand, all stress and moment resultants experience a singularity which is of order $(1/\gamma)$ and, finally, the transverse shearing stress resultants Q_γ and Q_η demonstrate a very strong singular behavior of the order $(1/\gamma^2)$.

Unit Concentrated Moment Solutions

A unit moment is defined as the effect of a definite distribution of normal loading. It can be represented by the derivative of the Delta function with respect to the surface coordinate along which is to be acting. From the theory of generalized functions it is known that if Φ is a fundamental solution of the equation $L\Phi=\delta(\mathbf{n}-\mathbf{n}')$, where L is a differential operator, then $\partial\Phi/\partial\alpha$ is a solution of the equation $L\Phi=\partial\delta/\partial\alpha$. We should note, however, that the above simple differentiation holds only for the principal singularity or the principal part of the solution. Thus, such differentiation of the unit load kernels, which contain more than just the principal singulari-

Downloaded 03 May 2010 to 171.66.16.31. Redistribution subject to ASME license or copyright; see http://www.asme.org/terms/Terms_Use.cfm

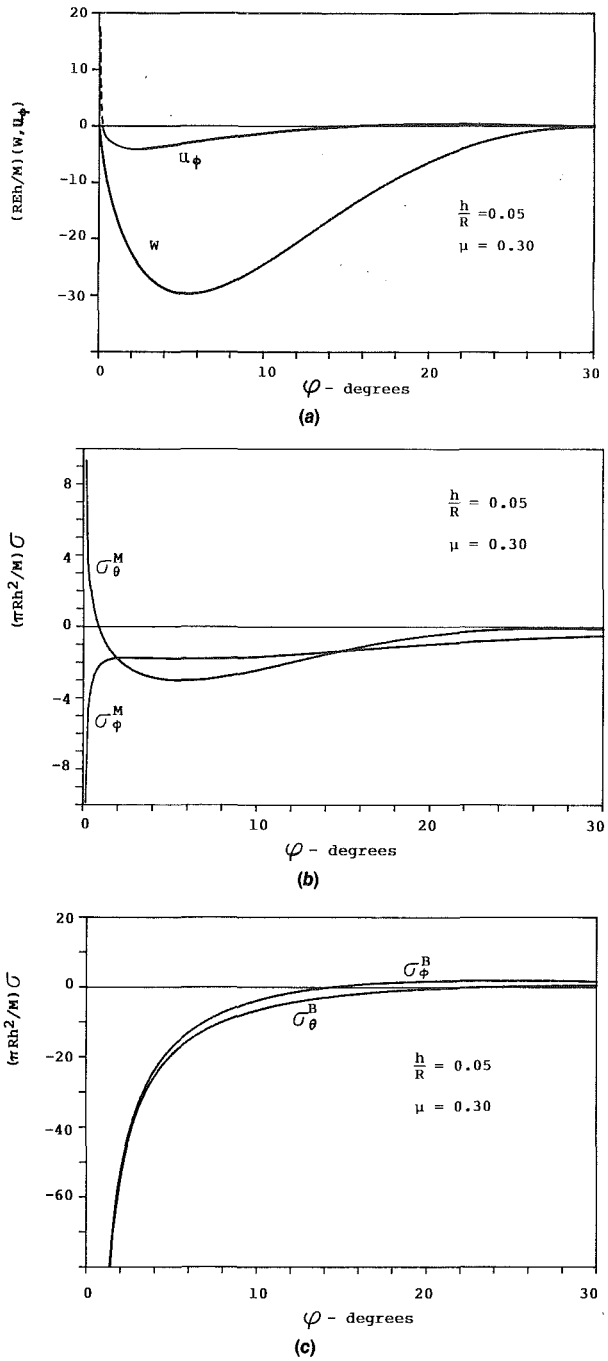


Fig. 4 Displacement and stress distribution in a spherical cap of 30 deg opening and fixed edge subjected to a concentrated moment M at its appex acting along the meridian passing through $\theta = 0$. Displacements and stresses and evaluated along the same meridian.

ty, could not lead to an accurate concentrated moment solution. A numerical evaluation of three different moment solutions was performed in order to best describe the action of a concentrated unit moment. These approaches include (*a*) differentiation of the normal load kernels, (*b*) appropriate superposition of two tangential load solutions derived in the latter section, and (*c*) a pair of two approaching opposite point loads corrected by an appropriate concentrated load. The evaluation revealed that (*b*) and (*c*) solutions coincide while (*a*) fails to represent the shell response in the vicinity of the pole. In conclusion, the closed form self-equilibrated moment solution is expressed in the form of two tangential load solutions derived in the previous section, i.e.,

$$W^m(\gamma,\eta) = \frac{1}{2R}\left[W^t(\gamma) + W^t(\pi-\gamma)\right]\cos\eta \qquad (81)$$

where W^m, W^t refer to the radial displacement due to unit moment and unit tangential load, respectively. Consequently, the singular character of this solution is similar to the one observed in the previous evaluation.

Evaluation and Discussion of the Solution

The solution formulae obtained in this paper represent the elastic response of a complete sphere under the influence of singular surface loads arranged in a particular manner. The importance of such solutions does not stem only from the fact that they are of closed form but also from their ability to represent the stress and deformation state in the point load vicinity. Within the postulates of the classical theory, the predictions of the singular character of the variable kernels agree with those obtained by Koiter (1963) and Wilkinson (1966). Since the singular character of the kernels represents the shell response in the vicinity of the applied singular load we attempt a comparison of the nonshallow solution presented here with the analogous complete work introduced by Lukasiewicz (1967, 1979) for shallow spherical shells. For the case of a normal point load applied in the outward direction the nonshallow theory predicts a singular state of membrane compression, i.e., $[N_\phi, N_\theta] \to -\infty$, while the shallow theory defines finite values for both membrane stress resultants. Both theories, however, predict singular behavior of logarithmic order for the bending state of stress, i.e, $[M_\phi, M_\theta] \to +\infty$. Similar conclusions were derived by the comparison of the works of Koiter (1963) and Reissner (1947). Evaluation of the predictions of the two theories for the cases of concentrated tangential load and moment leads to the following observations: For the shallow theory the application of a tangential load leads to vanishing moment resultants and, consequently, vanishing bending state of stress while a concentrated moment leads to vanishing membrane stress resultants. On the other hand, the nonshallow theory demonstrates a coupling between the membrane and bending stresses for both types of loading. Thus, we observe that in either case all stress resultants have a singular behavior in the vicinity of the singular load, Wilkinson and Kalnins (1986b) were led to the same conclusion, while Berry (1955) in his problem of a shell subjected to two concentrated moments at the edge obtained a similar behavior of the membrane stresses near the concentrated moment. The particular behavior of those stresses are shown in Figs. 4 and 5.

Simmonds (1968) concluded that the normal load case could be expressed as the sum of the part of the shallow solution that is rapidly decaying plus the membrane-inextensional nonshallow solution that stems from the part of the governing differential operator expressed as $\nabla^2 + 2$. To examine whether the same conclusion could hold for the concentrated tangential loads and moments we compared the rapidly varying parts of the two solutions. The two parts compared are the first term of (8.26) from Lukasiewicz (1979) that is of the form

$$W^* = (1+\mu)\frac{T1^3}{2\pi RD}\left(\frac{1}{r}\right) \qquad (82)$$

where 1, r represent characteristic lengths in the shallow theory, and the expression in (50) excluding the term $C^1 Q_1^1(\cos\gamma)$. The evaluation (numerical) indeed proves that the two terms are almost identical, while the complete nonshallow solution can safely be represented by equation (82) plus the membrane-inextensional solution $C^1 Q_1^1(\cos\gamma)$.

The variation of the displacements and stresses for the three load cases are presented in Figs. 3, 4, and 5. The particular problem studied involves a spherical cap of 30 deg opening and fixed boundary subjected to the concentrated loads at the appex. The effect of the boundary is introduced into the solu-

Downloaded 03 May 2010 to 171.66.16.31. Redistribution subject to ASME license or copyright; see http://www.asme.org/terms/Terms_Use.cfm

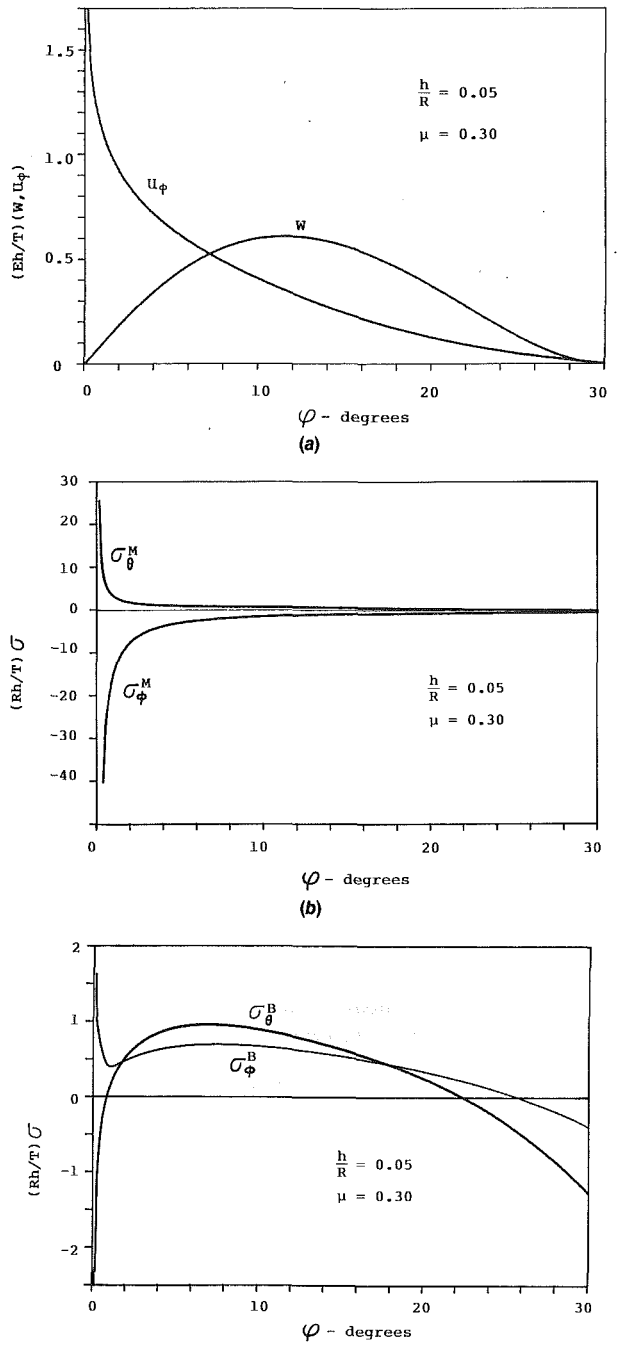


Fig. 5 Displacement and stress distribution in a spherical cap of 30 deg opening and fixed edge subjected to a concentrated tangential load T at the appex acting along the meridian passing through $\theta = 0$. Displacements and stresses and evaluated along the same meridian.

tion with the help of a boundary integral. The associated Legendre functions were evaluated from their Hypergeometric series expansions. As we should expect, the stresses are relatively small away from the applied load while the boundary effect is more noticable on the variation of bending stresses due to a concentrated tangential load shown in Fig. 5(*c*). We should also note that the variation of membrane stresses and bending stresses, shown in Figs. 4(*b*), 5(*c*), due to concentrated moments and tangential loads, respectively, display abrupt changes of direction in an area very close to the singular load. Lastly, on Table 1 the transverse displacement is compared against the same variable obtained from the classical shallow solution of Reissner (1947). We should note

Table 1 Transverse displacements $(Eh^2/PR)W$ of a spherical cap of 30 deg opening and fixed edge subjected to a point load P at the appex. Comparison of nonshallow and shallow solutions, ($\mu = 0.25$).

Degrees	Present nonshallow solution	Reissner's "exact" shallow solution
1	.3870	.3797
2	.3482	.3411
3	.3025	.3023
4	.2554	.2491
6	.1681	.1630
8	.0981	.0943
10	.0473	.0449
12	.0137	.0122
14	−.0065	−.0071
16	−.0169	−.0168
20	−.0199	−.0190
24	−.0116	−.0107
28	−.0018	−.0019
30	.0000	.0000

that despite the good agreement shown, Reissner's approximation is not a true representation beyond the shallow region and thus cannot be used in shells of opening angle that exceed the one used, i.e., $\phi > \pi/6$.

References

Berry, J. G., 1955, "On Thin Hemispherical Shells Subjected to Concentrated Edge Moments and Forces," *Proceedings of the 2nd Midwestern Conference on Solid Mechanics*, pp. 25–44.

Chernyshev, G. N., 1963, "On the Action of Concentrated Forces and Moments on an Elastic Thin Shell of Arbitrary Shape," *Journal of Applied Mathematics and Mechanics* (*Prikladnaya Matematika i Mekhanika*), Vol. 27, pp. 172–184.

Flugge, W., and Conrad, A. D., 1956, "Singular Solutions in the Theory of Shallow Shells," TR No. 101, Division of Engineering Mechanics, Stanford University.

Flugge, W., 1964, "Concentrated Forces on Shells," *Applied Mechanics—Proceedings of the Eleventh International Congress of Applied Mechanics*, Springer-Verlag, pp. 270–276.

Flugge, W., and Elling, R. E., 1972, "Singular Solutions for Shallow Shells," *International Journal of Solids and Structures*, Vol. 8, pp. 227–247.

Forsberg, K., and Flugge, W., 1966, "Point Load on a Shallow Elliptic Paraboloid," ASME Paper No. 66-APM-V, 1966.

Koiter, W. T., 1963, "A Spherical Shell Under Point at Its Poles," *Progress in Applied Mechanics—The Prager Anniversary Volume*, McMillan Company, pp. 155–169.

Lukasiewicz, S., 1967, "Concentrated Loads on Shallow Spherical Shells," *Quarterly Journal of Mechanics and Applied Mathematics*, Vol. 20. pp. 293–305.

Lukasiewicz, S., 1979, *Local Loads in Plates and Shells*, Sijthoff and Noordhoff.

Nordgren, R. P., 1963, "On the Method of Green's Functions in Thermoelastic Theory of Shallow Shells," *International Journal of Engineering Science*, Vol. 1, pp. 279–308.

Reissner, E., 1947, "Stresses and Small Displacements of Shallow Spherical Shells, I, and II." *Journal of Mathematics and Physics*, Vol. 25, pp. 80–85, Vol. 27, pp. 279–300.

Reissner, E., 1959, "On the Determination of Stresses and Displacements for Unsymmetrical Deformations of Shallow Spherical Shells," *Journal of Mathematical Physics*, Vol. 38, pp.16–35.

Sanders, Jr., J. L ., 1970, "Singular Solutions for Shallow Shell Equations," ASME Paper No. 70-WA/APM-1, Vol. 37, pp. 361–364.

Sanders, Jr., J. L., and Simmonds, J. G., 1970, "Concentrated Forces on Shallow Cylindrical Shells," ASME JOURNAL OF APPLIED MECHANICS, Vol. 92, pp. 367–373.

Simmonds, G. J., 1968, "Green's Functions for Closed Elastic Spherical Shells, Exact and Accurate Asymptotic Solutions," *Proceedings of the Koninklijke Nederlandse Academie van Weternschappen*, Series B, Vol. 71, No. 3, pp. 236–249.

Simmonds, G. J., and Bradley, M. R., 1976, "The Fundamental Solution for a Shallow Shell With an Arbitrary Quadratic Midsurface," ASME JOURNAL OF APPLIED MECHANICS, Vol. 98, No. 2, pp. 000–000.

Simmonds, J. G., and Tropf, C. G., 1974, "The Fundamental (Normal Point Load) Solution for a Shallow Hyperbolic Paraboloidal Shell," ASME JOURNAL OF APPLIED MECHANICS, Vol. 27, No. 1, pp. 102–120.

Wilkinson, J. P., and Kalnins, A., 1966, "On Nonsymmetric Dynamic Problem of Elastic Spherical Shells," ASME JOURNAL OF APPLIED MECHANICS, Vol. 87, Trans. ASME, Vol. 88, Series E, pp. 31–38.

Wilkinson, J. P., and Kalnins, A., 1966, "Deformation of Open Spherical Shells Under Arbitrary Located Concentrated Loads," ASME JOURNAL OF APPLIED MECHANICS, Series E, pp. 305–312.

Downloaded 03 May 2010 to 171.66.16.31. Redistribution subject to ASME license or copyright; see http://www.asme.org/terms/Terms_Use.cfm

Axial Crushing of Multicorner Sheet Metal Columns

W. Abramowicz
Visiting Professor.

T. Wierzbicki
Professor.

Department of Ocean Engineering,
Massachusetts Institute of Technology,
Cambridge, MA 02139

A method is developed for predicting crush behavior of multicorner prismatic columns subjected to an axial compressive load. The corner element of an arbitrary angle is analyzed first using rigorous methods of structural plasticity with finite deformations and rotations. On that basis, crush predictions are made for multicorner columns with an even number of corners. Static crush tests on square, hexagonal, and rhomboidal thin-walled columns are also reported here. Good correlation between the theory and experiments was obtained for the magnitude of a mean crushing force and kinematic parameters describing the process of progressive folding.

1 Introduction

The design of automobiles and other vehicles for crash have been traditionally based on destructive prototype testing. During the last decade, specialized finite element codes such as DYNA-3D or PAM-CRASH have been developed to assist efficient design of energy absorbing systems. These new tools are very promising, but they brought in their own problems such as modeling complexity, accuracy, and high computer costs. A third line of research in this general area is concerned with the development of simplified crush models of shells for rapid crashworthiness calculations. Such models have been successfully used to predict crash response of thin-walled members of a simple geometry such as axially compressed circular and rectangular columns (Ohokubo et al. (1979), Wierzbicki and Abramowicz (1983b), Abramowicz (1983a)). A comparison of the theoretical predictions with experimentally measured mean crushing force, reported among others by Abramowicz and Jones (1984, 1986) and Jones and Abramowicz (1985) show generally a good agreement.

One limitation of the above solutions which restrict their widespread use in the industry is the fact that they are restricted to columns consisting of right angle corner elements. The purpose of this paper is to present a complete analysis of the progressive crushing of thin-walled box columns with an arbitrary angle between the adjacent plates. The present analysis is based on the consideration of a generalized folding mode which combines features of the quasi-inextensional and extensional collapse mechanisms described earlier in the literature. The present problem poses a considerable modeling and computational challenge because the process of progressive crushing involves large plastic strains, curvatures, displacements, and rotation. In the present paper a highly desirable closed-form solution is obtained by making a set of assumptions regarding the kinematics of the problem and following rigorously the method of the plasticity theory.

2 Generalized Folding Mechanisms

An accurate prediction of the crushing strength of thin-walled members with an arbitrary central angle will be based on a new, generalized mixed folding mechanism (Fig. 2) which combines the features of the two simple folding modes described previously in the literature by Wierzbicki and Abramowicz (1983b), Hayduk and Wierzbicki (1984), and Abramowicz and Jones (1984). These are a quasi-inextensional (Fig. 1(a)) and extensional mode (Fig. 1(b)). The experimental observations suggest that during the progressive crushing of obtuse angle elements, a quasi-inextensional mode of deformation coexists with an extentional mode similar to that shown in Fig. 1(b). This suggests a "parallel elements" computational model of the column in which both mechanisms contribute simultaneously to the crushing resistance of the folding element. Such a model is interesting from the theoretical viewpoint, but leads to computational complexities which preclude the derivation of a desired closed-form solution. Instead, we shall consider a model with the "elements in a series" in which the quasi-inextensional mode persists during the first phase of deformation up to the intermediate configuration whereupon the extensional mode takes control of the crushing process.

The quasi-inextensional mode, shown in Fig. 1(a), consists of four trapezoidal elements (depicted as (1) in Fig. 1(a)), moving a rigid body, a section of toroidal surface (2) which accommodates extensional deformations in the circumferential directions, two sections of cylindrical surface with horizontal moving hinge lines (3), and two sections of cylindrical surface (4) in which material is bent and rebent again by moving inclined hinge lines. The current geometry of a folding mechanism can be conveniently described by the angle of rotation of the side plates α which is chosen to represent an independent variable of the process (timelike parameter). This collapse mode persists up to the configuration $\tilde{\alpha}$. At this point, the traveling hinge line LBO in Fig. 2, consisting of two

Contributed by the Applied Mechanics Division for publication in the JOURNAL OF APPLIED MECHANICS.

Discussion on this paper should be addressed to the Editorial Department, ASME, United Engineering Center, 345 East 47 Street, New York, N.Y. 10017, and will be accepted until two months after final publication of the paper itself in the JOURNAL OF APPLIED MECHANICS. Manuscript received by ASME Applied Mechanics Division, October 13, 1987; final revision, June 15, 1988.

Copyright © 1989 by ASME

Downloaded 03 May 2010 to 171.66.16.31. Redistribution subject to ASME license or copyright; see http://www.asme.org/terms/Terms_Use.cfm

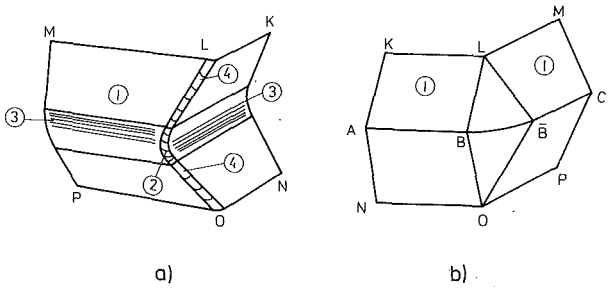


Fig. 1 Quasi-inextensional (*a*) and extensional (*b*) folding mechanisms

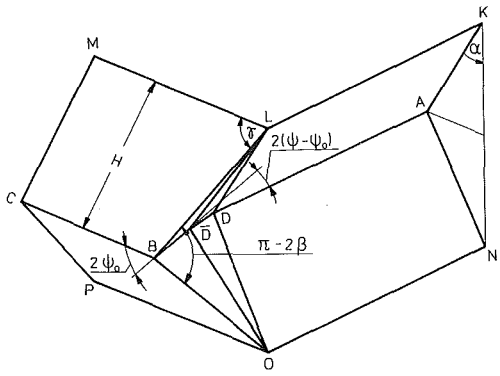


Fig. 2 New generalized folding mechanism

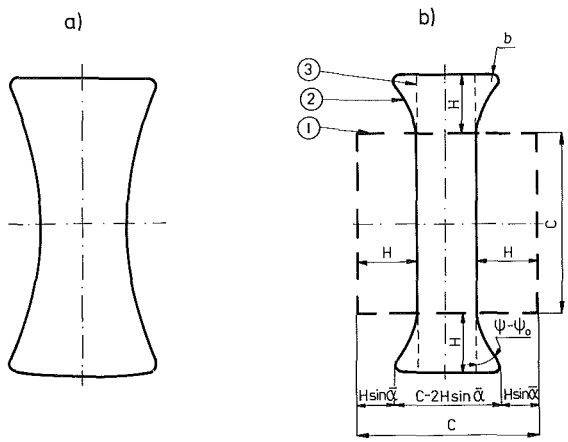


Fig. 3 Experimental (*a*) and theoretical (*b*) shapes of deformed cross-sections of a square column. (1) Undeformed cross-section. (2) Deformed cross-section as predicted by new generalized folding mode. (3) Deformed cross-section as predicted by quasi-inextensional mode.

sections of cylindrical surfaces and a section of toroidal surface, ceases to move and become fixed in the material coordinate system. From this point on, the hinge line is considered to be stationary. At the same time, initially straight lines LD and OD split into four separate lines LD, LD̄, etc., and rotate around the vertical axis LO as the deformation progresses, giving rise to the formation of two conical surfaces LDD̄ and ODD̄. Conical surfaces in Fig. 2 are stretched and flattened out during further deformation in a similar way to that shown in Fig. 1(*b*). The angle of intersection ($2\psi_o$) between lines AD and BC stays constant during the entire deformation process, due to the boundary condition imposed onto the free edges of the folding element while the angle ($<\bar{D}BC$) in Fig. 2 varies in the second phase of deformation and subsequently drives the bending about the stationary hinge lines LB and BO.

In the final configuration, points A, D̄, D, and B are no longer confined to the same straight line. Line AD is shifted inwardly with respect to point B, so as to accommodate the rotation of line BD̄. This new feature of the mixed folding mechanism agrees favorably with experimental observations reported by Abramowicz (1981) and Jones and Abramowicz (1985) (see Fig. 3(*a*)). In the limits $\bar{\alpha}=0$ or $\bar{\alpha}=\alpha_f$, and the new generalized folding mode reduces to the extensional and quasi-inextensional modes, respectively.

The simplified geometry of the folding pattern shown in Fig. 2 suggests that the final crushing distance of a mixed folding element equals $\delta_f=2H$ while the terminal value of the timelike parameter is $\alpha_f=\pi/2$. An actual folding element, however, can not be completely flattened because of the presence of the finite bending radii which diminish the expected crushing distance $2H$ by the sum $(a+b)$ of small and large radii of the toroidal surface and increase α_f beyond the right angle by a small amount $\Delta\alpha$.

The so-called "effective crushing distance" δ_{ef} can be calculated from the terminal shape of completely squeezed corner elements by assuming that the actual pattern of a deformed corner line is composed of alternating circular arcs. It can be shown through simple calculations performed for a right angle element that $\delta_f/2H=0.73$ and the additional rotation angle is $\Delta\alpha=0.279$ rad. These numbers are in surprisingly good agreement with the experimental observations and theoretical results obtained by Abramowicz (1983b, 1984) on the basis of computational models with linear strain hardening material.

The known input parameters for the present generalized folding mode are: the length of the cross-section C, the wall thickness h, and the angle ψ_o of a given element. In the abbreviated notation, these parameters can be represented by the vector:

$$\xi=\{C, h, \psi_o\}.$$

The timelike parameter α is considered to be an independent variable which controls the crushing process. The effective crushing distance, δ_{ef}, and the terminal value of timelike parameter α_f, were calculated separately and are also known parameters of the process. Finally, the length of the buckling wave $2H$, the small bending radius b, as well as the "switching" parameter $\bar{\alpha}$ are all unknown and will be determined as a part of the solution. For the sake of brevity, it is convenient to introduce the vector of unknown parameters:

$$\chi=\{b, H, \bar{\alpha}\}.$$

3 Basic Assumptions

We will consider materials whose response is rigid/perfectly plastic, isotropic and independent of time with a suitably adjusted flow stress σ_o to account for the work-hardening properties of the material. Assuming the usual normality-convexity properties of the yield function, the plastic dissipation $\sigma\cdot\dot{\epsilon}$ is uniquely defined by a strain rate tensor $\dot{\epsilon}$. It is assumed that the constitutive equations are not affected by the rotation of the shell element (the co-rotational yield condition). The Cauchy stress tensor, $\boldsymbol{\sigma}$, and velocity strain rate tensor, $\dot{\boldsymbol{\epsilon}}$, will be used to assure work conjugation of stress and strain rate measures. The effect of variable thickness is retained in the analysis of continuously deforming regions, but is neglected on stationary or moving hinge lines.

Velocity and Displacement Fields. A starting point in the present method is the selection of a suitable displacement field, for a given vector ξ:

$$\mathbf{u}^*=\mathbf{u}^*(\mathbf{x}, \chi, \alpha) \tag{1}$$

where * denotes kinematical admissibility of a given variable. The velocity field:

$$\dot{\mathbf{u}}^*=\dot{\mathbf{u}}^*(\mathbf{x},\chi,\alpha)\dot{\alpha} \tag{2}$$

Downloaded 03 May 2010 to 171.66.16.31. Redistribution subject to ASME license or copyright; see http://www.asme.org/terms/Terms_Use.cfm

which is obtained from the displacement field $\dot{\mathbf{u}}^*$ by time differentiation, is piecewise continuous with respect to this operation. Thus, the lines of the slope discontinuities, representing plastic hinge lines, are admitted by the theory. In addition, kinematic boundary conditions must also be satisfied by $\dot{\mathbf{u}}^*$.

In our solution, the displacement field will be represented by elementary functions. Therefore, time differentiation or integration operations will be performed here exactly and interchangeably without the need for introducing approximate time integration schemes. Thus, the present method provides for a convenient mechanism to continuously update the current deformed configuration of the folding element and to calculate strain rates.

Strain Displacement Relations. In the current deformed configuration α, the relations between the strain rate and the velocities are linear (equation (2)). In the continuously deforming regions, the strain rate is defined as a symmetric gradient of the velocity field (the so-called velocity strain). At the hinge lines, the rate of rotation is found from the kinematic continuity conditions (see equation ($A14$) in the Appendix).

Equilibrium. The equilibrium of the representative section of the tube is expressed via the principle of virtual velocities

$$P\dot{\delta}^* = \int_V \sigma\dot{\epsilon}^* dV \tag{3}$$

where the integration is performed over the plastically deformed part of the structure. The product $P\dot{\delta}$ represents the rate of work of external forces where the relative velocity of the uniformly shortened upper and lower edges of the basic folding mechanism is denoted by $\dot{\delta}$ while P is the instantaneous crushing force, i.e., the force necessary to deform the tube further from a given configuration. This force is equilibrated by the system of internal stresses σ.

If the class of considered velocity fields $\dot{\mathbf{u}}^*$ is sufficiently broad so as to include the actual velocity, equation (3) is equivalent to local equilibrium. In practice, however, the kinematically admissible velocity field may contain only a finite number of functions, so that local equilibrium is satisfied only to within a certain, acceptable error. For example, the accuracy of the FE method is related to the total number of degrees-of-freedom of the nodal points. In the Ritz or Galerkin method, accuracy is controlled by the number of terms in the Fourier expansion of the solution.

We are suggesting here a different approach to the construction of a set of approximating functions which appear to be particularly suited for the present class of problems. The structure, or, in our case, the basic folding element, is subdivided into a small number of "elements," (actually fourteen elements) whose boundaries are not fixed but *floating*. In such a formulation the velocity field with only three degrees-of-freedom $\chi = (b, H, \bar{\alpha})$ may result in an accuracy attainable by the FE method with a very dense mesh and hundreds or thousands of regular elements.

Minimum Principle. Consider a current configuration of the basic folding mechanism described by the parameter α. According to Hill-Markov's theorem of plasticity, the best set of parameters $\{H, b\}$ is obtained by extremizing the internal rate of energy dissipation

$$\frac{\partial}{\partial\chi}\int_v \sigma^*\dot{\epsilon}^* dv = 0. \tag{4}$$

The resulting optimum parameter of the velocity field will change from one configuration to the other, so that, in general, $\chi = \chi(\alpha)$. It has been observed in a number of tests that the length of the plastic folding wave $2H$, as well as the magnitude of the rolling radius b, undergo only slight changes in the advanced stage of the crushing process. Following the above observation, we will treat the vector of unknown parameters χ as independent of the process parameter α. The above assumption considerably simplifies the calculations and renders a closed-form solution possible.

Integrating equation (4) with respect to time (or α) from $t = \alpha = 0$ to the end of the process $t = t_f$, $\alpha = \alpha_f$ and changing the order of integration, we obtain:

$$\frac{\partial}{\partial\chi}\int_o^{\alpha_f} d\alpha \int_v \sigma^*\dot{\epsilon}^* dv = 0. \tag{5}$$

Thus, the best average values of χ is obtained by extremizing the total plastic work with respect to process parameters. The total plastic work is proportional to the mean crushing force P_m, defined by

$$P_m\delta_f = \int_o^{\alpha_f} d\alpha \int_v \sigma^*\dot{\epsilon}^* dv. \tag{6}$$

Therefore, the condition (5) is equivalent to the extremization of the mean crushing force $\partial/\partial\chi\ P_m(\chi, \alpha_f) = 0$. Several authors, including Duszek (1973), Martin (1975), and most recently Hill (1986) contributed to the understanding of the global minimum problem. However, a general proof of the minimum property of the functional (5) seems to be lacking.

4 Internal Energy Dissipation

The rate of internal energy dissipation comes, in general, from the continuous and discontinuous velocity fields (Wierzbicki and Abramowicz (1983b)).

$$\dot{E}_{\text{int}} = \int_S (M_{\alpha\beta}\dot{\kappa}_{\alpha\beta} + N_{\alpha\beta}\dot{\epsilon}_{\alpha\beta}) dS + \sum_{i=1}^{n} \int_{\mathfrak{L}^i} M_o{}^i[\dot{\theta}^i] dl^i \tag{7}$$

where S denotes the current shell midsurface, n is the total number of stationary or moving hinge lines, and $\mathfrak{L}^i$ is the length of the ith hinge. The symbol $[\dot{\theta}^i]$ denotes a jump of the rate of rotation across the moving hinge line. The components of the rotation rate and extension rate tensors are denoted, respectively, by $\dot{\kappa}_{\alpha\beta}$ and $\dot{\epsilon}_{\alpha\beta}$. The corresponding conjugate generalized stresses are the bending moments $M_{\alpha\beta}$ and the membrane forces $N_{\alpha\beta}$. The total internal plastic dissipation is obtained by integrating equation (7) in the interval $0 \le \alpha \le \alpha_f$. Since the total dissipation is obtained as a result of two different folding modes acting "in series," the expression for the rate of energy splits into two parts:

$$E_{\text{int}} = \int_o^{\bar{\alpha}} \dot{E}_{int}{}^{(1)} d\alpha + \int_{\bar{\alpha}}^{\alpha_t} \dot{E}_{\text{int}}{}^{(2)} d\alpha \tag{8}$$

where α denotes a configuration at which the extensional mode of deformation takes over the quasi-inextentional mode.

During the first phase of the deformation $0 \le \alpha \le \bar{\alpha}$, the crushing process is controlled by a quasi-inextensional folding mode and the corresponding dissipation is due to plastic flow over the toroidal surface, as well as the bending along stationary and traveling hinge lines.

Consider first the plastic flow over toroidal surfaces (Fig. $A1$). The integrand in the first integral of equation (7) has in general six components. In view of the rotational symmetry and the assumed radial plastic flow, all nondiagonal components of the strain rate tensor ($\dot{\kappa}_{\theta\Phi}$, $\dot{\epsilon}_{\theta\Phi}$) vanish identically. The stretching rate $\dot{\lambda}_{\theta\theta}$ in the meridional direction is zero in view of the assumed meridional inextensibility of plastic flow. The rate of curvature $\dot{\kappa}_{\theta\theta}$ equals zero under the assumption of central velocity, field Wierzbicki and Abramowicz (1983b). The generalized stresses $M_{\Phi\Phi}$ and $N_{\Phi\Phi}$ in the circumferential direction of a toroidal shell are related through the corotational yield condition for the shell $|M_\Phi/N_\Phi| = 1 - (N_\Phi/N_o)^2$. It follows from the flow rule, (Abramowicz

Downloaded 03 May 2010 to 171.66.16.31. Redistribution subject to ASME license or copyright; see http://www.asme.org/terms/Terms_Use.cfm

(1981)), that if $a/b \geq 2$, the stress profile is confined to the point $N_{\Phi\Phi} = N_o$, $M_{\Phi\Phi} = 0$, so that the rate of energy dissipation due to the plastic flow over the toroidal surface is reduced to

$$\dot{E}_1 = \int_S N_o \dot{\lambda}_{\Phi\Phi} dS \tag{9}$$

where $\dot{\lambda}_{\phi\phi}$ represents the stretch in the circumferential direction. The final expression for the energy E_1 is

$$E_1 = \int_o^{\bar{\alpha}} \dot{E}_1 = d\alpha = 16 M_o \frac{Hb}{h} I_1(\psi_o, \bar{\alpha}) \tag{10}$$

where I_1 is defined in the Appendix.

The rate of energy dissipated on the horizontal hinge lines $\dot{E}_2$ equals to the limit bending moment per unit length M_o times the rate of rotation α times the length of the hinge C. Because the hinge line is split, there will be two such hinge lines in the folding mechanisms as shown in Fig. 1(*a*).

$$\dot{E}_2 = 2 M_o C \dot{\alpha}. \tag{11}$$

The total energy dissipation, obtained by integrating equation (11) in the limits $(0, \bar{\alpha})$ is

$$E_2 = 2 M_o C \bar{\alpha}. \tag{12}$$

The rate of energy due to the inclined traveling hinge lines is equal to the fully plastic bending moment times the rate of rotation $\dot{\omega}$ equation (*A*7) times the variable length of the hinge line $l = 2H/\sin\gamma$. This gives

$$\dot{E}_3 = 4 M_o \frac{H^2}{b} \operatorname{ctg}\psi_o \cos\alpha \sqrt{(\operatorname{tg}^2\psi_o + \sin^2\alpha)}\,\dot{\alpha} \tag{13}$$

and

$$E_3 = 4 M_o \frac{H^2}{b} I_3(\psi_o, \bar{\alpha}) \tag{14}$$

where I_3 is a known function of ψ_o and $\bar{\alpha}$.

$$I_3(\psi_o, \bar{\alpha}) = \operatorname{ctg}\psi_o \int_o^{\bar{\alpha}} \cos\alpha \sqrt{\operatorname{tg}^2\psi_o + \sin^2\alpha}\, d\alpha. \tag{15}$$

In the second phase of the crushing process $\bar{\alpha} \leq \alpha \leq \alpha_f$, the initially straight line ADB in Fig. 2, is bent to accommodate the newly formed conical surface.

It is assumed that the material within the conical zone undergoes stretching in the meridional direction, θ, and is inextensible in the second principal direction. We define then $\dot{E}_4$

$$\dot{E}_4 = \int_S N_o \dot{\lambda}_{\theta\theta} dS \tag{16}$$

where S is a current area of the growing cone which uniquely depends on α. The final expression for $\dot{E}_4$, (see, Abramowicz and Jones (1984)) is

$$\dot{E}_4 = 2 M_o V_t \frac{H}{h} \tag{17}$$

where V_t corresponds to the rate of stretching of the arc $D\bar{D}$ in Fig. 2 and equals to

$$V_t = 2H\phi(\alpha, \bar{\alpha}, \psi_o)\dot{\alpha} \tag{18}$$

where

$$\phi(\alpha, \bar{\alpha}, \psi_o) = \frac{\sin\bar{\alpha}\operatorname{tg}\psi_o \sin 2\alpha}{2(\sin^2\bar{\alpha} + \operatorname{tg}^2\psi_o \sin^2\alpha)} + (\psi - \psi_o)\cos\alpha.$$

The total energy dissipation obtained by integrating equation (17) in the limits $(0, \bar{\alpha})$ is:

$$E_4 = 4 M_o \frac{H^2}{h} I_4(\psi_o, \bar{\alpha}) \tag{18}$$

where

$$I_4(\psi_o, \bar{\alpha}) = \int_{\bar{\alpha}}^{\alpha_f} \phi(\alpha, \bar{\alpha}, \psi_o) d\alpha \tag{19}$$

is again a known function of $\bar{\alpha}$ and ψ_o.

The rate of energy dissipation on the horizontal hinge line is the same as in phase I, equation (12). The total energy is

$$E_5 = 2 M_o C(\alpha_f - \bar{\alpha}) \tag{20}$$

provided we neglect the small amount of energy which will be dissipated by bending the common part $D\bar{D}$ of the conical surface, in Fig. 2.

During the second phase of deformation, the inclined hinge BL in Fig. 2 is fixed in a material coordinate system and has constant length. At the same time, the angle $2\theta_1$ between planes LBCM and LB$\bar{D}$ in Fig. 2, varies according to equation (*A*3) of the Appendix.

The corresponding contribution to the rate of energy dissipation comes from bending in the stationary hinge line BL and equals to the fully plastic bending moment M_o times the length of the hinge L times the rate of angular velocity $2\theta_1$ and equals to

$$\dot{E}_6 = 2 M_o \mathrm{H} \operatorname{ctg}\psi_o \frac{\sin\bar{\alpha}(\sin^2\bar{\alpha} + \operatorname{tg}^2\psi)_o}{\sin^2\bar{\alpha} + \operatorname{tg}\psi_o \sin^2\alpha}\dot{\alpha} \tag{21}$$

while the corresponding total energy, obtained by integrating (21) in the limits $(\bar{\alpha}, \alpha_f)$ is

$$E_6 = M_o H I_6(\psi_o, \bar{\alpha}) \tag{22}$$

where

$$I_6(\psi_o, \bar{\alpha}) = 2\operatorname{ctg}\psi_o \int_{\bar{\alpha}}^{\alpha_f} \frac{\sin\bar{\alpha}(\sin^2\bar{\alpha} + \operatorname{tg}^2\psi)_o}{\sin^2\bar{\alpha} + \operatorname{tg}^2\psi_o \sin^2\alpha} d\alpha. \tag{34}$$

For each given value of the angle ψ_o, the definite integrals I_1 through I_6 can be evaluated numerically if the magnitude of switching point $\alpha = \bar{\alpha}$ is known. In general, $\bar{\alpha}$ is defined by the optimality condition for a given structure and is unknown a priori. It is quite remarkable that the concept of elements with floating boundaries has effectively decoupled a complex calculations of the rate of internal energy dissipation equation (7) into a set of relatively simple "uniaxial" problems equations (9)–(22).

5 Crushing Strength of Arbitrary Multicorner Elements

The global energy balance equation (7) for a given assembly of corner elements can be obtained by summing up the contributions of plastic mechanisms in a single corner element and then adding the energies of individual corner elements. Each contributing term has a different functional dependence on unknown parameters b, H, and $\bar{\alpha}$, so that the governing equation (7) can finally be written in the form:

$$\frac{P_m}{M_o} = \left\{ A_1 \frac{b}{h} + (A_2 + A_5)\frac{C}{H} + A_3 \frac{H}{b} + A_4 \frac{H}{h} + A_6 \right\} \frac{2H}{\delta_{\mathrm{ef}}} \tag{23}$$

where the coefficients A_i depend on $\bar{\alpha}$ and ψ_o, and the coefficient $(A_2 + A_5)$ represents a total contribution of bending along horizontal hinge lines.

The mean crushing load P_m is thus a function of three unknown parameters H, b, and $\bar{\alpha}$ which are determined from the condition (6). The physically meaningful values of the parameter $\bar{\alpha}$ is restricted to the range $0 \leq \bar{\alpha} \leq \alpha_f$. If $\bar{\alpha}$ falls outside of this range, either of the limiting values should be assumed when calculating P_m.

6 Discussion of a Single Angle Element

Consider a representative folding element as shown in Fig.

Downloaded 03 May 2010 to 171.66.16.31. Redistribution subject to ASME license or copyright; see http://www.asme.org/terms/Terms_Use.cfm

2. Assuming the clamped boundary condition on horizontal planes in Fig. 2, the bending energy (E_2+E_5) should be doubled. Similarly, energies E_4 and E_6 should also be doubled because there are two conical surfaces and two inclined hinge lines in Fig. 2. Then, the energy balance equation (7) can be written in the form of equation (23) with corresponding constants equal to $A_1=8I_1$, $(A_2+A_5)=2\alpha_f$, $A_3=2I_3$, $A_4=4I_4$ and $A_6=I_6$, respectively. It should be pointed out that the basic folding elements with clamped boundary conditions represent only one possible deformation path to reach the final fully crushed configuation. Other paths are possible, as will be shown in the forthcoming publication.

The solution to equation (6) was found by means of the numerical iteration method. Results of the present calculations show that the mixed collapse mode of deformation controls the crushing process over the entire range of the C/h aspect ratios of practical significance. However, the magnitude of the switching point parameter $\bar{\alpha}$, which controls relative contributions of a quasi-inextensional and an extensional modes of deformations, depends strongly on the angle ψ_o and the aspect ratio C/h.

For small angles, $\psi_o=30$ deg, (one element of hexagonal column), the extensional mode of deformation controls most of the crushing and the inextensional mode is restricted only to relatively small angles 6 deg $\leq\bar{\alpha}\leq$ 40 deg, depending on the actual value of the C/h ratio. At the same time, the predicted value of the mean crushing load P_m is about 30 percent smaller compared to the value calculated on the basis of the quasi-inextensional mode only. For $\psi_o=45$ deg (a right angle element), the switching point parameter $\bar{\alpha}$ approaches 90 deg for $C/h>20$. As ψ_o increases to 60 degrees, the quasi-inextensional mode of deformation starts to control the crushing process up to $\alpha=\pi/2$ while the extensional mode takes over for α larger than $\pi/2$, and controls the terminal stage of crushing for all C/h ratios. Since the terminal stage of deformation gives only a small contribution to the entire energy dissipation, one can admit that a quasi-inextensional solution should provide a reasonable estimation of mean crushing force for all acute corner elements.

A pure quasi-inextensional mode can be obtained from the general case by setting $\bar{\alpha}=\alpha_f=\pi/2$. The energy balance equation, equation (23), can then be rewritten in the form:

$$\frac{P_m}{M_o}=\left\{A_1\frac{b}{h}+A_2\frac{C}{H}+A_3\frac{H}{b}\right\}\frac{2H}{\delta_{\text{ef}}}. \tag{24}$$

Note that coefficients A_4 and A_6 in equation (23) are vanishing because the lower and upper limits of integration in integrals I_4 and I_6 are the same. Solutions to equation (23) can now be obtained in a simple analytical form. Indeed, the minimization of equation (23) with respect to two free parameters H and b yield (Wierzbicki and Abramowicz (1983b)):

$$\frac{P_m}{M_o}=3(A_1A_2A_3)^{1/3}(C/h)^{1/3}\frac{2H}{\delta_{\text{ef}}}. \tag{25}$$

The present formulation is valid for a constant but otherwise arbitrary flow stress σ_o ($M_o=\sigma_o h^2/4$). For real materials the flow stress is not constant but depends on the current value of strain. It has been shown by the present authors (Wierzbicki and Abramowicz (1988)) that the energy equivalent flow stress σ_o for progressively collapsing prismatic columns made from mild steel equals approximately to: $\sigma_o=0.92\,\sigma_u$.

7 Crushing Resistance of Square, Hexagonal, and Rhomboidal Sections

The present method can be easily used to predict the crushing resistance of prismatic columns (square, hexagonal, etc.) composed of n identical elements. For such columns, the compatibility conditions on horizontal and vertical planes in Fig. 2 are always fulfilled and the final crushing resistance equals to the appropriate crushing force per one element times the number of corner elements, n.

Square Columns. The mean crushing strength equals to the force per one corner element times four. The present numerical solution for P_m/M_o has been approximated by the following function:

$$\frac{P_m}{M_o}=48.64(C/h)^{0.37}. \tag{26}$$

In the particular case of an inextensional mode of deformation ($\alpha_f=\pi/2$) the solution to equation (23) can be obtained in a simple analytical form, as discussed in the previous section. In this case, the coefficients A_1 through A_3 in equation (24) equal to $A_1=4.44$, $A_2=\pi$ and $A_3=2.30$, respectively, and the final result is:

$$\frac{P_m}{M_o}=52.22(C/h)^{0.33}. \tag{27}$$

This result has been derived in the earlier publication, Abramowicz and Jones (1984) and is valid for a quasi-inextensional, symmetric mode of deformation only. There is a small difference in the coefficients of equation (26) and (27). A higher fractional power in the present improved solution, equation (26), reflects a larger contribution of extensional deformation into the total energy dissipation. The difference between predictions of equations (26) and (27) is small and stays within four to eight percent, depending on the C/h ratio.

The final shape of the cross-section cut through the plane ABC (Fig. 2) of a collapsed element of the square column with $C/h=20$ corresponding to the present mixed mode solution and quasi-inextensional solution due to Wierzbicki and Abramowicz (1983b) is shown in Fig. 3. It is evident from this figure that the present solution better represents the experimentally observed shape of a deformed column.

Hexagonal Columns. Multiplying by six the mean crushing strength of an angle element with $\psi_o=30$ deg, the mean crushing force for a hexagonal column is obtained. Similarly as in the case of square columns, the nondimensional solution P_m/M_o for various C/h aspect ratios can be approximated by the function:

$$\frac{P_m}{M_o}=80.92(C/h)^{0.4} \tag{28}$$

which predicts a slightly higher fractional power than that obtained for square columns and thus emphasizes larger contribution of extensional deformations to the crushing resistance of hexagonal columns.

Rhomboidal Columns. Thus far, we have considered simple elements with equal central angles, that deform in regular symmetric modes with the same wave length H and radius of curvature, b. If the angles of a prismatic column are not identical, the solution can not be obtained just by summing up fractional contributions of all corners. The reason being that the wavelengths of subsequent modes may not be compatible and a full geometrical compatibility would require additional expenditure of energy. The global crushing resistance must then be calculated by minimizing equation (23) for the entire cross-section.

Let us consider the box column with a rhomboidal cross-section of the length $4C$ and an acute central angle α_1 ($\alpha_1=\pi-2\psi_o$, Fig. 2). Numerical calculations, described in the previous section, show that the greater the difference between acute and obtuse angles, the greater the difference between wavelengths of adjacent elements. Therefore, it is reasonable to admit that the optimum wave length for the entire cross-

Downloaded 03 May 2010 to 171.66.16.31. Redistribution subject to ASME license or copyright; see http://www.asme.org/terms/Terms_Use.cfm

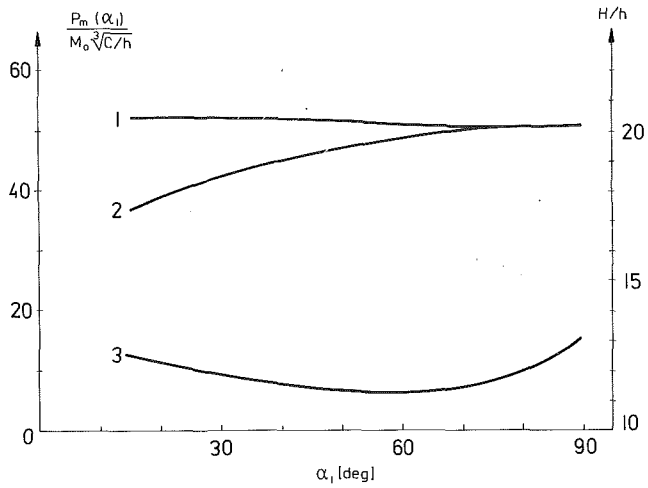


Fig. 4 Mechanical parameters of the crushing process of rhomboidal column with $C/h = 50$. (1) Mean crushing load P_m versus acute angle of column cross-section α_1. (2) Mean crushing load $P_m(\alpha_1)$ as predicted by the simple accumulation method. (3) Length of the folding wave H versus α_1.

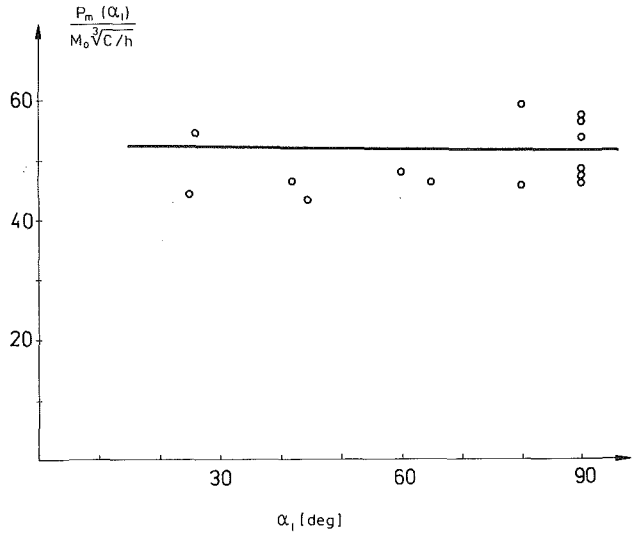


Fig. 5 Theoretical and experimental (Abramowicz et al. (1985)) mean crushing force P_m for rhomboidal columns as a function of angle α_1

section will differ from the optimum lengths for separate components and that the corresponding mean force will be larger. Indeed, the energy balance equation for a rhomboidal cross-section can be easily casted into the form of equation (23) with $A_1 = 16\ \{I_1(\psi_o) + I_1(90 - \psi_o)\}$, $A_2 + A_5 = 8\alpha_f$, $A_3 = 4\{I_3(\psi_o) + I_3(90 - \psi_o)\}$, $A_4 = 8\{I_4(\psi_o) + I_4(90 - \psi_o)\}$ and $A_6 = 2\ \{I_6(\psi_o + I_6(90 - \psi_o)\}$, respectively. It is evident from Fig. 4 that an exact numerical solution predicts a significantly larger mean force P_m from that obtained by simply adding up individual contributions of corner elements. This is especially true for α_1 smaller than 60 deg.

8 Comparison With Test Results

This section provides the result of experiments performed by one of the present authors, Abramowicz et al. (1985), on several types of multicorner mild-steel columns.

Hexagonal, square, and rhomboidal columns were manufactured from mild steel sheet strips with $\sigma_u = 243$ MN/m^2. Initially flat strips were bent along parallel lines up to desired angles, and were then joined together by a continuous weld along the middle line of two opposite walls.

Static compression tests were conducted on a standard "Instron" machine at cross-head speed, approximately 1 cm/min. In Fig. 5, experimental data for rhomboidal columns are compared with the result of numerical minimization of equation (23). We can notice a reasonble agreement of both results, even for rhomboidal columns with α_1 as small as 25 and 26 degs, which eventually close up and collapse in overall bending.

In Fig. 6, theoretical predictions for a single corner element (Fig. 2) are compared with experimental findings calculated per one folding element. In the case of hexagonal and square tube, the corresponding contributions are calculated simply by dividing the total mean force by the number of corner elements.

The global crushing resistance of a rhomboidal column is a sum of contributions of two types of corner elements. In experiments, only the total crushing force can be measured, therefore, additional information regarding the distribution of the crushing forces between the two types of elements is needed to calculate $P_m(\alpha_1)$ and $P_m(\pi/2 - \alpha_1)$. Such information can, for example, be provided by the present theoretical solution as the ratio $P_m(\alpha_1)/P_m(\pi/2 - \alpha_1)$ can always be found from Fig. 4. Therefore, experiments with rhomboidal sections provide only for an estimate on the mean crushing force per

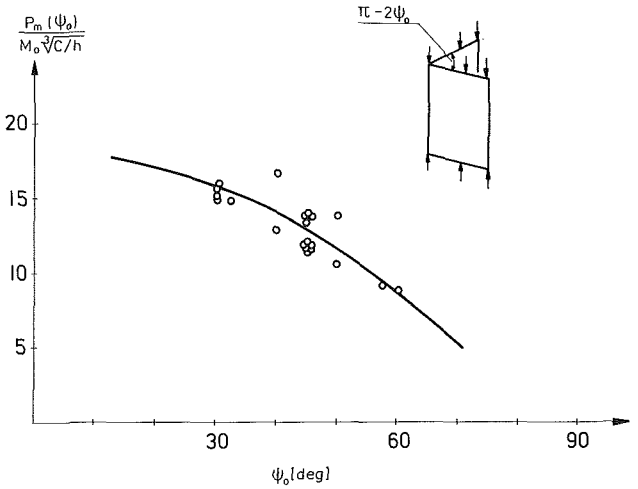


Fig. 6 Theoretical (solid line) and experimental (circles) (Abramowicz and Jones (1984), Abramowicz et al. (1985)) mean crushing force per one element as a function of angle ψ_o

one, standing alone corner element which is based on data obtained from both the experiments and theory.

9 Conclusions

The most important and new conclusion is that the plastic resistance as well as the collapse mode of a basic folding element, shown in Fig. 2, depends strongly on the central angle $(\pi/2 - 2\psi_o)$ between intersecting plates, as illustrated in Fig. 6. At the same time, the mode of deformation changes rapidly from quasi-inextensional, for acute elements, to a mixed one for obtuse elements. In obtuse elements, most of the energy dissipation are confined to extensional modes of deformation which predict 30 percent or less energy absorption than quasi-inextensional mechanisms. For corner elements with a central angle close to $\pi/2$, the quasi-inextensional and mixed modes predict similar values of mean crushing loads. One can notice, however, a significant difference in the geometry of deformed elements, as illustrated in Fig. 3. The exact determination of the deformed geometry can be especially important when assessing residual buckling strength of crushed columns, as well as in the analysis of crushing resistance of foam filled elements (Reid et al. (1986)).

Downloaded 03 May 2010 to 171.66.16.31. Redistribution subject to ASME license or copyright; see http://www.asme.org/terms/Terms_Use.cfm

The crushing resistance of a prismatic column with an even number of corners can be calculated by summing up the contributions of individual elements. However, this simple superposition method can not be applied to prismatic columns with arbitrary cross-sections. In the latter case, the crushing resistance must be calculated by optimizing equation (23) for the entire cross-section, according to the minimum condition (6).

The folding modes described in this paper have the potential of being used as "Superfolding Elements" in numerical calculations of axial crushing resistance of arbitrary prismatic columns. The work involved in the present calculations of the crush response is insignificant and requires only a few seconds of CPU time on many commercially available personal computers. Therefore, the present technique can be especially attractive for preliminary calculations and has a potential of being implemented in CAD codes. Some results along these lines have already been obtained for multicorner elements and foam filled square tubes. The results will be reported in future publications.

Acknowledgments

The authors are grateful to the M.I.T.-Industry Crashworthiness Consortium and the Center for Transportation Studies at M.I.T. for the support provided during the course of this research. We also wish to acknowledge a valuable contribution of Prof. Norman Jones of the University of Liverpool who commented on an earlier version of this manuscript.

References

Abramowicz, W., and Wierzbicki, T., 1979, "A Kinematic Approach to Crushing of Shell Structures," SAE Tech. Paper No. 790992.

Abramowicz, W., 1981, "Mechanics of the Crushing Process of Thin-Walled Structures," (in Polish), Ph.D. Thesis, Institute of Fundamental Technological Research, Report No. 35.

Abramowicz, W., 1983a, "Simplified Crushing Analysis of Thin-Walled Columns and Beams," *Engineering Transactions*, Vol. 29, pp. 5–26.

Abramowicz, W., 1983b, "The Effective Crushing Distance in Axially Compressed Thin-Walled Metal Columns," *International Journal of Impact Engineering*, Vol. 1, pp. 309–317.

Abramowicz, W., and Jones, N., 1984, "Dynamic Axial Crushing of Square Tubes," *International Journal of Impact Engineering*, Vol. 2, No. 2, pp. 179–208.

Abramowicz, W, Imielowski, S., and Wasowski, A. O., 1985, "Quasi-Static Axial Crushing of Multicorner Metal Columns," Institute of Fundamental Technological Research, Report No. 5, (in Polish).

Abramowicz, W., and Jones, N., 1986, "Dynamic Progressive Buckling of Circular and Square Tubes," *International Journal of Impact Engineering*, Vol. 4, No. 4, pp. 243–270.

Duszek, M. K., 1973, "On Optimum Principles in Finite Plasticity," *Bulletin de L'Academie Polonaise des Sciences*, Vol. XXI, No. 2, pp. 89–96.

Hayduk, R. Y., and Wierzbicki, T., 1984, "Extensional Collapse Modes of Structural Members," *Computers and Structures*, Vol. 18, No. 3, pp. 447–458.

Hill, R., 1986, "Extremal Paths of Plastic Work and Deformation," *Journal of the Mechanics and Physics of Solids*, Vol. 39, No. 5, pp. 551–523.

Jones, N., and Abramowicz, W., 1985, "Static and Dynamic Axial Crushing of Circular and Square Tubes," *Metal Forming and Impact Mechanics*, S. R. Reid, ed., Pergamon, pp. 225–247.

Martin, J. B., 1975, *Plasticity: Fundamentals and General Results*, Massachusetts Institute of Technology Press, Cambridge, Mass.

Ohokubo, Y., Akamatsu, T., and Shirasawa, K., 1979, "Mean Crushing Strength of Closed-Hat Section Members," SAE Paper No. 790060.

Reid, S. R., Reddy, T. Y., and Gray, M. D., 1986, "Static and Dynamic Axial Crushing of Foam-Filled Sheet Metal Tubes," *International Journal of Mechanical Sciences*, Vol. 28, No. 5, pp. 295–322.

Wierzbicki, T., 1983a, "Crushing Behavior of Plate Intersections," *Structural Crashworthiness*, N. Jones and T. Wierzbicki, eds., Butterworths, London, pp. 66–85.

Wierzbicki, T., and Abramowicz, W., 1983b, "On the Crushing Mechanics of Thin-Walled Structures," ASME JOURNAL OF APPLIED MECHANICS, Vol. 50, pp. 727–739.

Wierzbicki, T., and Abramowicz, W., 1989, "The Mechanics of Deep Plastic Collapse of Thin-Walled Structures," to appear in *Structural Failure*, T. Wierzbicki and N. Jones, eds., John Wiley and Sons, New York.

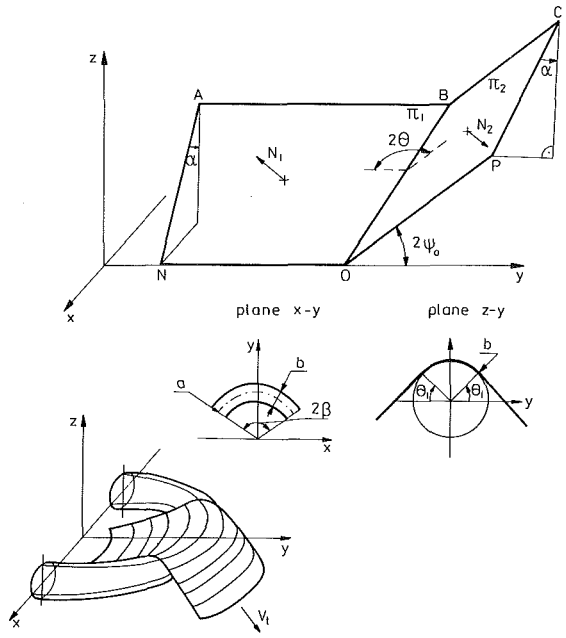


Fig. A1 Geometry of the plastic flow over a toroidal surface

APPENDIX

A detailed geometry of the folding mechanism is shown in Fig. *A*1 together with notation for toroidal surfaces. The unit normal vectors $\mathbf{N}_1$ and $\mathbf{N}_2$ to the plates π_1 and π_2 in Fig. *A*1 have the components:

$$\mathbf{N}_1 = [0;\ \cos\alpha;\ \sin\alpha] \tag{A1}$$

$$\mathbf{N}_2 = [\cos\alpha\ \sin 2\psi_o;\ \cos\alpha\cos 2\psi_o;\ -\sin\alpha] \tag{A2}$$

so that the angle $2\theta_1$ between plates π_1 and π_2, defined by the scalar product of $\mathbf{N}_1$ and $\mathbf{N}_2$ equals:

$$\cos 2\theta_1 = 2\cos^2\alpha\cos^2\psi_o - 1. \tag{A3}$$

It transpires from Fig. 1 and 2 that angel θ_1 varies with the polar ordinate Φ of the toroidal surface. The corresponding formula is:

$$\sin\theta_1 = \frac{\mathrm{tg}\psi_o}{\sqrt{\mathrm{tg}^2\psi_o + \cos^2\Phi}} \tag{A4}$$

where Φ varies in the range $-\beta(\alpha) \le \Phi \le \beta(\alpha)$.

The rate of energy dissipation associated with the plastic flow over the toroidal surface is given by equation (7), while the corresponding rate of circumferential stretching is:

$$|\dot{\lambda}_{\Phi\Phi}| = \frac{\dot{\omega} b \sin\theta}{(a + b\cos\theta)}. \tag{A5}$$

Equation (*A*9) together with (*A*4) predicts:

$$\dot{E}_1 = 4N_o bH\cos\alpha \int_o^{\beta(\alpha)} \frac{d\Phi}{\sqrt{\mathrm{tg}^2\psi_o + \cos^2\Phi}}\dot{\alpha} \tag{A6}$$

which is an energy dissipation rate at the current configuration α.

The total energy dissipation for α varying in the range $0 \le \alpha \le \bar{\alpha}$ is then:

$$\dot{E}_1 = 4N_o bH \int_o^{\bar{\alpha}} \cos\alpha \int_o^{\beta(\alpha)} \frac{d\Phi}{\sqrt{\mathrm{tg}^2\psi_o + \cos^2\Phi}}\, d\alpha \tag{A7}$$

where $\beta = \mathrm{arctg}\ \{\mathrm{tg}\alpha/\sin\psi_o\}$.

Integrating (*A*10) by parts, we finally have

Downloaded 03 May 2010 to 171.66.16.31. Redistribution subject to ASME license or copyright; see http://www.asme.org/terms/Terms_Use.cfm

$$E_1 = 16M_o\frac{Hb}{h}I_1(\psi_o,\bar{\alpha}) \tag{A8}$$

where

$$I_1(\psi_o,\bar{\alpha}) = \sin\bar{\alpha}\int_o^{\beta(\bar{\alpha})}\frac{d\Phi}{\sqrt{\mathrm{tg}^2\psi_o+\cos^2\Phi}} - \left[\frac{\pi}{2}-\psi_o-\mathrm{arctg}\left(\frac{\cos\beta(\bar{\alpha})}{\mathrm{tg}\psi_o}\right)\right]. \tag{A9}$$

In the particular case of $\bar{\alpha}=\pi/2$, the integral I_1 equals to:

$$I_1\left(\psi_o,\frac{\pi}{2}\right) = \int_o^{\pi/2}\frac{d\Phi}{\sqrt{\mathrm{tg}^2\psi_o+\cos^2\Phi}} - \left(\frac{\pi}{2}-\psi_o\right). \tag{A10}$$

At the hinge line moving with the tangential velocity V_t, the jump in the rate of rotation $[\dot{\theta}]$ is related to the change of curvature by the condition of kinematic continuity (Wierzbicki 1983b).

$$[\dot{\theta}] = V_t[\kappa] \tag{A11}$$

Downloaded 03 May 2010 to 171.66.16.31. Redistribution subject to ASME license or copyright; see http://www.asme.org/terms/Terms_Use.cfm

M. Sabag
Graduate Student.

Y. Stavsky
Gerard Swope Professor of Mechanics.

J. B. Greenberg
Senior Lecturer.

Faculty of Aeronautical Engineering,
Technion-Israel Institute of Technology,
Haifa 32 000, Israel

Buckling of Edge Damaged, Cylindrical Composite Shells

The stability of thin composite layered anisotropic cylindrical shells under axial compression is considered for the case of nonuniform boundary conditions. Such conditions are employed to model the situation where there is edge damage to the shell. The influence of weakening or a crack at an edge on the critical buckling load of a variety of single and multilayered shells is investigated. Results indicate that isotropic shells exhibit a rather sudden steep reduction in the critical buckling load for relatively small edge damage. However, some anisotropic composite shells may not be so sensitive and, in contrast, only a gradual reduction may be brought about by the edge damage. The degree of sensitivity to edge damage appears to be dependent, in some complex fashion, on the various geometric and physical shell parameters.

Introduction

In the manufacture of aircraft and space vehicles very slight flaws are sometimes to be found in the material structure and/or joint regions. The imperfections may deteriorate during inflight conditions with subsequent detrimental effects on the stability characteristics of the structure in question.

In the present paper, attention will be focused on thin cylindrical shells comprised of composite layered anisotropic materials. A typical shell will be presumed to have some damage in the region where it is connected to another portion of the craft's frame. The effects of the damage upon the critical axial buckling load that the structure can sustain will be investigated.

The pioneering work of Hoff and Soong (1967) appears to be the only attempt to tackle the problem at hand. Their work, however, considered imperfect gluing or riveting of an axially loaded *homogeneous isotropic shell* for which the imperfection was symmetric, i.e., identical at both ends of the shell. In addition, their analysis employed Donnell-type field equations. Using the examples of weakening of classical SS3 boundary conditions by SS1 conditions, and of rigid fixation (RF2) by simple support of type SS2 (see Hoff and Soong (1965), for notation) they showed that when relaxation of restraint around one-tenth of the boundary occurs the buckling stress drops by about 50 percent. In the current work the field equations are formulated based on Flügge's quasi-linear theory. Following the approach of Hoff and Soong (1967), the damaged portion of the boundary is defined using nonuniform boundary conditions. The analytic solution of the problem is developed by making use of a finite complex Fourier transform, together with a displacement function. Two types of edge damage are considered: (*i*) weakening of a portion of the shell's edge, and (*ii*) a crack over part of the shell's circumference. Both *symmetric* imperfections and the more realistic case of a flaw at one end of the shell only—*nonsymmetric imperfections*—are examined.

In the final section results are presented and discussed for a variety of single and multilayered anisotropic shells. Effects of orthotropy, geometry, and lay-up on the stability characteristics of the edge damaged shells are analyzed.

Notation

Consider a finite length circular cylindrical shell made of several layers of filament-wound composite materials whose elastic properties are thickness-dependent only. The nondimensional axial coordinate, ξ, the circumferential coordinate, θ, and the normal, ζ, to the reference surface are illustrated in Fig. 1. The winding angle of each layer (i.e., the orientation of the fiber direction to the axial direction ξ) is denoted by ϕ. A generally aeolotropic construction such as this is fairly common in structures built of filamentary composite materials.

Displacement Equilibrium Equations

For a general aeolotropic shell subjected to a constant axial

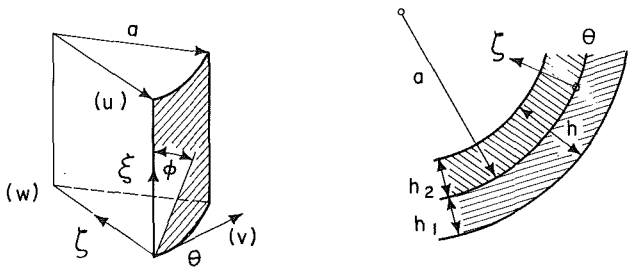


Fig. 1 Cylindrical shell notation

Contributed by the Applied Mechanics Division of THE AMERICAN SOCIETY OF MECHANICAL ENGINEERS for publication in the JOURNAL OF APPLIED MECHANICS.

Discussion on this paper should be addressed to the Editorial Department, ASME, United Engineering Center, 345 East 47th Street, New York, N.Y. 10017, and will be accepted until two months after final publication of the paper itself in the JOURNAL OF APPLIED MECHANICS. Manuscript received by ASME Applied Mechanics Division, February 25, 1988; final revision, June 15, 1988.

Copyright © 1989 by ASME

Downloaded 03 May 2010 to 171.66.16.31. Redistribution subject to ASME license or copyright; see http://www.asme.org/terms/Terms_Use.cfm

load, N_ξ^o, the displacement equilibrium equations, based on Flügge's quasi-linear theory, can be shown to be of the form:

$$\sum_{j=1}^{3} L_{ij} U_j(\xi,\theta) = 0 \quad (i=1,2,3) \tag{1}$$

where the linear, constant coefficient partial differential operators L_{ij} are given in the Appendix, and U_j $(j=1,2,3)$ are the reference surface displacements in the axial, circumferential, and normal directions, respectively. The operators L_{ii} $(i=1,2,3)$ contain the critical buckling load and, therefore, the problem at hand will be to determine the eigenvalues, N_ξ^o, of the system (1), subject to given boundary conditions.

Analytic Solution

The fact that the operators, L_{ij}, have constant coefficients, coupled with the periodicity of the displacements and their derivatives in the circumferential direction, suggests exploiting a finite complex Fourier transform to reduce the dimensionality of the problem and, hopefully, to facilitate a solution. Thus, applying the aforementioned transform, F, to the field equation (1) with respect to θ leads to:

$$F\left\{\sum_{j=1}^{3} L_{ij} U_j(\xi,\theta)\right\} = \sum_{j=1}^{3} \int_0^{2\pi} L_{ij} U_j(\xi,\theta) e^{in\theta} d\theta$$

$$= \sum_{j=1}^{3} L_{ij}^{(n)} U_j^{(n)}(\xi) = 0 \tag{2}$$

$$(n=0,1,2,\ldots;\quad i=1,2,3)$$

where the differential operators, $L_{ij}^{(n)}$ are now ordinary with possibly complex coefficients, the $U_j^{(n)}$ (ξ) $(j=1,2,3)$ are transformed displacements, n is the circumferential mode number, and i is $\sqrt{-1}$. This set of ordinary differential equations can be solved with the help of a displacement function $\Phi^{(n)}$, that is defined through the following relationships:

$$[U_1^{(n)}, U_2^{(n)}, U_3^{(n)}]$$

$$= [D_{31}^{(n)},\ D_{32}^{(n)},\ D_{33}^{(n)}]\ \Phi^{(n)}(\xi, N_\xi^0) \tag{3}$$

where $D_{ij}^{(n)}$ are certain differential operators. The displacement function is the solution of the homogeneous equation:

$$D^{(n)} \Phi^{(n)} = 0 \tag{4}$$

where the operator $D^{(n)}$ is given by:

$$D^{(n)} = \det(L_{ij}^{(n)}) \tag{5}$$

The operators, $D_{ij}^{(n)}$, of equation (3) are the minors of $D^{(n)}$. In the general case the solution of equation (4) is of the form:

$$\Phi^{(n)} = \sum_{j=1}^{8} c_j^{(n)} e^{\mu_j^{(n)}(N_\xi^0)\xi} \tag{6}$$

the upper limit of summation, 8, stemming from the order of the operator $D^{(n)}$. The $\mu_j^{(n)}(N_\xi^0)$ are the roots (assumed distinct) of the eighth-order polynomial auxiliary equation, and the $c_j^{(n)}$ are constants of integration. It is imperative to note that the roots, $\mu_j^{(n)}$, are functions of the applied axial load, N_ξ^0, in a fashion that is not expressible in analytic form. The solution for $\Phi^{(n)}$, equation (6), (and, hence, for the displacements from equation (3)) involves eight arbitrary constants which can formally be determined from the four *transformed boundary conditions* at each end of the cylinder. Application of these boundary conditions, and the requirement that the solution, equation (6), be nontrivial leads to a secular determinantal equation in which a certain determinant must vanish for particular values of N_ξ^0 only. The lowest of these values will supply the critical buckling load of the structure.

As mentioned previously, Hoff and Soong (1967) represented edge imperfections through nonuniform boundary conditions. In the current context their basic approach will be adopted and extended (*a*) to general aeolotropic composite layered shells, and (*b*) to investigate a variety of nonuniform boundary conditions, the latter being applied either at both ends of the cylinder symmetrically or, more realistically, at one end only, the other end being uniformly held.

Thus, if nonuniformity is permitted at the cylinder's edges, the transformed boundary conditions can be written as:

$$\sum_{j=1}^{3} \left[\int_0^{\theta_0(p)} e^{in\theta(p)} {}^{(p)}\alpha_{k,j} U_j(\xi,\theta) d\theta + \int_{\theta_0(p)}^{2\pi} e^{in\theta(p)} {}^{(p)}\beta_{k,j} U_j(\xi,\theta) d\theta\right]_{\xi=\pm l/2a} = 0 \tag{7}$$

$$(k=1,2,3,4;\ p=0,1;\ n=0,1,2\ldots)$$

where ${}^{(p)}\alpha_{k,j}$, ${}^{(p)}\beta_{k,j}$ are linear (often differential) operators relating to the boundary conditions applicable over the region of the circumference between 0 and $\theta_0^{(p)}$ and $\theta_0^{(p)}$ and 2π, respectively. The superscript $p=0$ for conditions at one end of the cylinder, and $p=1$ for those at the other end—the index k indicates which of the four boundary conditions necessary is applicable.

Since the actual shell displacements are given by:

$$U_j(\xi,\theta) = \mathrm{Re}\left\{\sum_{m=0}^{\infty} \frac{U_j^{(m)}(\xi)}{2\pi} e^{-im\theta}\right\} \tag{8}$$

substitution for equation (8) into equation (7) yields a set of transformed boundary conditions in terms of $U_j^{(m)}$ (ξ). Further use of equations (3) and (6) to replace $U_j^{(m)}$ enables the boundary conditions to be compactly written as:

$$\sum_{m=0}^{\infty} \sum_{s=1}^{8} c_s^{(m)} [f_{1,k}^{(p)}(s,m,n,N_\xi^0) + f_{2,k}^{(p)}(s,m,n,N_\xi^0)] = 0$$

$$(k=1,2,3,4;\quad p=0,1;\quad n=0,1,2\ldots) \tag{9}$$

where $c_s^{(m)}$ are the eight constants of integration associated with circumferential mode m (see equation (6)), and the functions f_1, f_2 are known. Note the dependence of these functions on *both* m and n, indicative of a *coupling* between the circumferential modes arising from the nonuniformity in the boundary conditions. Thus, denoting the set of elements originating from the bracketed term in equation (9) by $\mathbf{Z}^{(m,n)}$ (an 8×8 matrix) and the eight constants of mode m by $\mathbf{c}^{(m)}$ determination of the critical buckling load involves finding those values of N_ξ^0 for which the matrix equation:

$$\mathbf{Zc} = \begin{bmatrix} \mathbf{Z}^{(0,0)} & \mathbf{Z}^{(1,0)} & \cdots \\ \mathbf{Z}^{(0,1)} & \mathbf{Z}^{(1,1)} & \cdots \\ \vdots & \vdots & \ddots \end{bmatrix} \begin{bmatrix} \mathbf{c}^{(0)} \\ \mathbf{c}^{(1)} \\ \vdots \end{bmatrix} = 0 \tag{10}$$

has a nontrivial solution, i.e.,:

$$\det(\mathbf{Z}) = 0. \tag{11}$$

Boundary Conditions, Material Properties, and Computational Aspects

In the current work the sensitivity of the axial buckling load to a number of different sorts of nonuniformities in edge conditions was considered. *Weakening* of a boundary joint was described by simple support conditions SS1 or SS2, the remainder of the circumference being subjected to either classical SS3 conditions or being rigidly fixed (RF4, see Hoff and Soong (1965), for notation).

The details of the boundary conditions are as follows:

Downloaded 03 May 2010 to 171.66.16.31. Redistribution subject to ASME license or copyright; see http://www.asme.org/terms/Terms_Use.cfm

(A)

$$w = N_\xi = M_\xi = 0 \qquad (12a)$$

$$N_{\xi\theta} + \frac{M_{\xi\theta}}{a} + \frac{N_\xi^0 v_{,\xi}}{a} = 0 \qquad 0 \le \theta \le \theta_0 \qquad (12b)$$

$$v = 0 \qquad \theta_0 \le \theta \le 2\pi \qquad (12c)$$

(12*a*) and (12*b*) is SS1, (12*a*) and (12*c*) is SS3.

(B)

$$w = M_\xi = 0 \qquad (13a)$$

$$u = N_{\xi\theta} + \frac{M_{\xi\theta}}{a} + \frac{N_\xi^0 v_{,\xi}}{a} = 0 \qquad 0 \le \theta \le \theta_0 \qquad (13b)$$

$$v = N_\xi = 0 \qquad \theta_0 \le \theta \le 2\pi \qquad (13c)$$

(13*a*) and (13*b*) is SS2, (13*a*) and (13*c*) is SS3.

(C)

$$w = N_{\xi\theta} + \frac{M_{\xi\theta}}{a} + \frac{N_\xi^0 v_{,\xi}}{a} = 0 \qquad (14a)$$

$$N_\xi = M_\xi = 0 \qquad 0 \le \theta \le \theta_0 \qquad (14b)$$

$$u = w_{,\xi} = 0 \qquad \theta_0 \le \theta \le 2\pi \qquad (14c)$$

(14*a*) and (14*b*) is SS1, (14*a*) and (14*c*) is RF2.

(D)

$$u = w = 0 \qquad (15a)$$

$$M_\xi = N_{\xi\theta} + \frac{M_{\xi\theta}}{a} + \frac{N_\xi^0 v_{,\xi}}{a} = 0 \qquad 0 \le \theta \le \theta_0 \qquad (15b)$$

$$v = w_{,\xi} = 0 \qquad \theta_0 \le \theta \le 2\pi \qquad (15c)$$

(15*a*) and (15*b*) is SS2, (15*a*) and (15*c*) is RF4.

The appearance of a *crack* in a joint region was modeled by the free edge condition with the rest of the circumference assumed rigidly fixed (RF4):

(E)

$$M_{\xi,\xi} + N_\xi^0 w_{,\xi} + M_{\xi\theta,\theta} + M_{\theta,\theta} = 0 \qquad 0 \le \theta \le \theta_0 \qquad (16a)$$

$$M_\xi = N_\xi = N_{\xi\theta} + \frac{M_{\xi\theta}}{a} + \frac{N_\xi^0 v_{,\xi}}{a} = 0$$

$$w = w_{,\xi} = u = v = 0 \qquad \theta_0 \le \theta \le 2\pi \qquad (16b)$$

(16*a*) is free edge condition, (16*b*) is RF4. (In all, these boundary conditions N and M represent forces and moments, respectively, and the displacements in the axial, circumferential, and normal directions are u, v, w, respectively.)

The stability of three different shells were considered. Their material properties are given in Table 1:

Table 1 Material Properties of Cylindrical Shells

Material	E_{11}(N/m^2)	E_{22}(N/m^2)	E_{66}(N/m^2)	ν_{12}
Isotropic	7.2×10^{10}	7.2×10^{10}	5.2×10^{10}	0.3
Ultra High Modulus Graphite Epoxy (UHMG)	3.1×10^{11}	6.2×10^{9}	4.1×10^{9}	0.26
Glass Epoxy	4.3×10^{10}	8.8×10^{9}	4.5×10^{9}	0.27

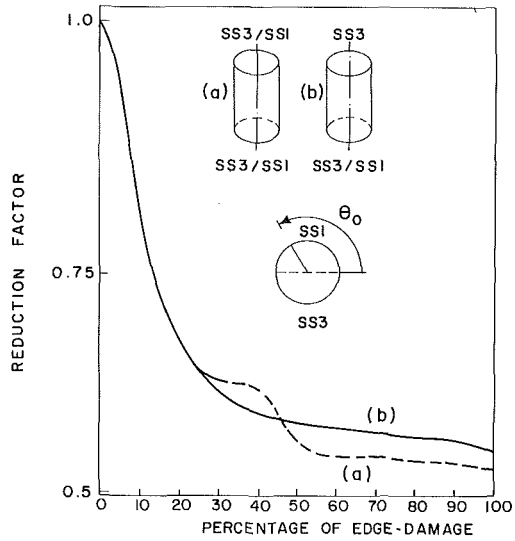


Fig. 2 Effect of nonuniform boundary conditions on axial buckling load of isotropic cylindrical shell; BCS: SS3/SS1, $l/a = 1$, $a/h = 100$

Since layered anisotropic shells were also investigated values of the transformed elastic coefficients were calculated for a given fiber angle from the above data using the transformation as given, for example, by Stavsky and Hoff (1969).

The geometric properties of the shells will be referred to specifically in the following section in which results are discussed.

For all the computations performed, 25 circumferential modes were taken into account, this being sufficient to establish a converged solution of equation (10) that is, in fact, an infinite determinantal equation. (See the next section for typical results concerning convergence.) Other salient features of the eigenvalue-search procedure have been given in detail by Greenberg, Stavsky, and Sabag (1988) and will not be discussed here.

Computed Results and Discussion

In the ensuing discussion two types of flaws in edge conditions will be referred to. The first type will be dubbed "symmetric" (S). It relates to identical nonuniformity in boundary conditions at both ends of the cylinder. The second type is probably more realistic from a practical viewpoint as it concerns a nonuniformity at *one end of the cylinder* only, the other end being subjected to some uniform boundary condition. This type will be called "nonsymmetric nonuniformity" (NS).

In addition, the term "critical load reduction factor" will refer to the ratio of the critical loads with and without edge damage.

Edge Weakening.

(*i*) *Isotropic Shells.* Consider a cylindrical shell with geometry: $l/a = 1$, $a/h = 100$. In Fig. 2 the sensitivity of the critical buckling load to weakening of SS3 boundary conditions by SS1 conditions is illustrated for both symmetric and nonsymmetric nonuniformities.

The critical load reduction factor has a lower bound of 0.52 for the symmetric case whereas for the nonsymmetric case it is about 0.55. For *both* cases the shell is very sensitive to flaws so that a weakening of one-fifth of the circumference brings about a reduction in the critical load of about 34 percent. For further weakening of the SS3 support it is interesting to contrast results for the symmetric and nonsymmetric nonuniformities. Between 20 and about 44 percent edge damage the critical load of the shell having the symmetric nonuniformity is higher than that having nonsymmetric nonuniformity.

Downloaded 03 May 2010 to 171.66.16.31. Redistribution subject to ASME license or copyright; see http://www.asme.org/terms/Terms_Use.cfm

Subsequently, for even more damage, the situation is reversed with a common buckling load for 44 percent damage.

Further results for the same shell, but subject to rigid fixation (RF4) and weakened by SS1 are listed in Table 2 (Shell I). Note that for both types of nonuniformity the reduction factor remains approximately the same until about 30 percent edge damage. Subsequently, for edge damage of more than about 55 percent the critical load of the nonsymmetrically damaged shell is some 20 percent higher than that of the symmetrically damaged one.

Additional data in Table 2 (Shell II) relates to an isotropic shell that is longer and thinner than Shell I, and that was investigated by Hoff and Soong (1967) for symmetric nonuniformities. Differences between their results and those reported here presumably stem from their use of a Donnell-type theory which predicts higher critical buckling loads than a Flügge-type theory for the present geometry but with *no* edge damage (see, e.g., Yamaki (1984)). Interestingly, for both sets of boundary conditions Shell II appears to be relatively insensitive to whether the flaw develops at one or both ends. However, for the case of the SS3/SS1 boundary conditions combination it is extremely sensitive to slight flaws whereas for the weakened rigidly fixed (RF2) case some 18 percent of the circumference must be loosened before its effect is "felt."

(*ii*) *Anisotropic Shells.* In Table 3 the effect of damage on the stability of glass epoxy cylindrical shells is summarized. For Shell III the fiber winding angle is 0 deg (i.e., fibers being like stringers along the cylinder), and for Shell IV it is 90 deg. For both shells the minimum reduction factor is about 0.68. Both shells appear to be fairly insensitive to whether damage is symmetric or nonsymmetric. Moreover they both respond qualitatively similarly to edge damage. This behavior is attributable to their geometry and low orthotropy ratio (see Table 1).

In contrast an orthotropic shell of UHMG is considered next. Its geometry is defined by $l/a = 1$, $a/h = 100$ and, in addition, its high ratio of orthotropy, 50, should be noted (see Table 1).

As an introduction to its behavior Fig. 3 should be consulted. It shows the stability response of a *uniformly* bounded (SS3) shell of UHMG as a function of the fiber winding angle, when the shell is bilayered in an antisymmetric angle ply lamina lay-up. The effect of the winding angle on the shell's stability response is quite striking with an optimal buckling load attained for a winding angle combination of +70 deg/−70 deg. The most unstable shell is that one for which the combination is at +84 deg/−84 deg, with the ratio of the extrema being 0.56. The shell having the optimal load was then permitted to develop a weakening of the boundary conditions (see Fig. 4). For symmetric nonuniformity the minimum reduction factor is 0.58 whereas for nonsymmetric nonuniformity it is 0.63. For imperfections of up to 10 percent both types of shells respond identically and the critical load drops by 1 percent. The curve for the symmetrically damaged shell falls almost linearly as the damage extends. This is not the case for the nonsymmetrically damaged shell which is *more* stable than its counterpart for damage in the range 10–50 percent,

Table 2 Effect of Nonuniform Boundary Conditions on Axial Buckling Load of Isotropic Cylindrical Shells

Shell I $l/a = 1$, $a/h = 100$; Boundary conditions: RF4/SS1								
Percent Reduction Factor		99	90	80	70	60	55	50
Percent Edge Damage	S	12.3	24	25.5	30	38.4	55	>60
	NS	12.3	24	25.5	30	55	-	-
Shell II $l/a = 5$, $a/h = 400$; Boundary conditions: SS3/SS1								
Percent Reduction Factor		99	90	80	70	60	55	53
Percent Edge Damage	S	<1	1.6	3.8	5	19.5	59	>60
	NS	<1	1.6	3.8	5	19.5	59	>60
Shell II $l/a = 5$, $a/h = 400$; Boundary conditions: RF2/SS2								
Percent Reduction Factor		99	90	80	70	60	55	50
Percent Edge Damage	S	18	21.6	24	26.6	29.5	37.5	40
	NS	18	21.6	24	26.6	29.5	38.7	40

Table 3 Effect of Nonuniform Boundary Conditions on Axial Buckling Load of Glass Epoxy Cylindrical Shells

Shell III $\phi = 0$ deg $l/a = 3$, $a/h = 100$; Boundary conditions: SS3/SS2							
Percent Reduction Factor		99	90	80	70	69	68
Percent Edge Damage	S	2.9	11.4	19.2	47.7	61.6	>65
	NS	2.9	11.4	19.2	63	>65	-
Shell IV $\phi = 90$ deg $l/a = 3$, $a/h = 100$; Boundary conditions: SS3/SS2							
Percent Reduction Factor		99	90	80	70	68	
Percent Edge Damage	S	2.2	7.2	14.7	51.8	>70	
	NS	2.2	7.2	14.7	44.4	>70	

Downloaded 03 May 2010 to 171.66.16.31. Redistribution subject to ASME license or copyright; see http://www.asme.org/terms/Terms_Use.cfm

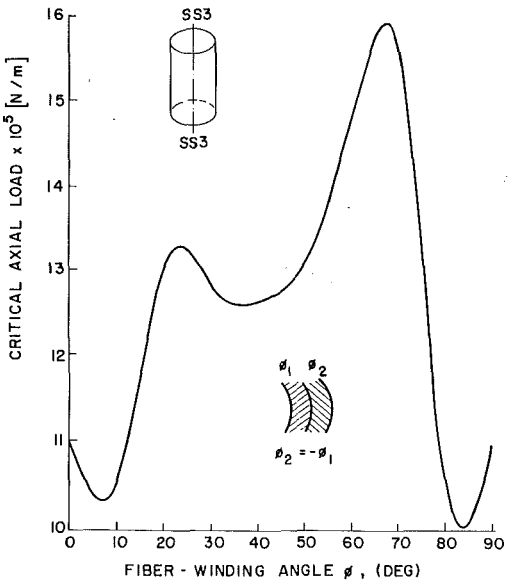


Fig. 3 Effect of fiber winding angle on axial buckling load of simply supported UHMG epoxy antisymmetric angle ply shells; *l/a* = 1, *a/h* = 100

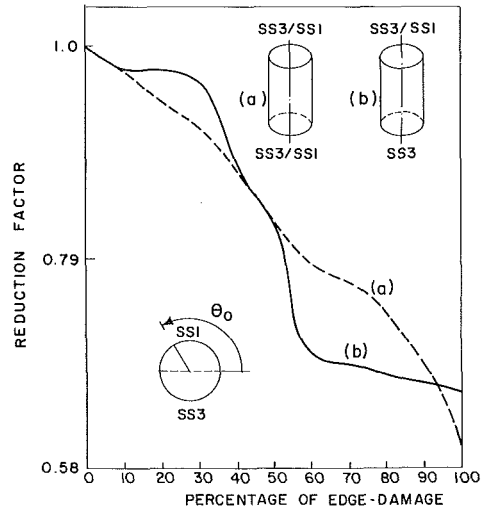


Fig. 4 Effect of nonuniform boundary conditions on axial buckling load of UHMG epoxy antisymmetric 70 deg angle ply shell; BCS: SS3/SS1, *l/a* = 1, *a/h* = 100

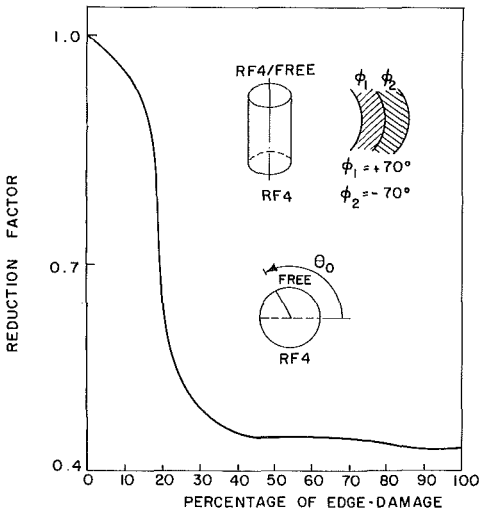


Fig. 5 Effect of nonuniform boundary conditions on axial buckling load of UHMG epoxy antisymmetric 70 deg angle ply shell; BCS: RF4/free, *l/a* = 1, *a/h* = 100

whence it becomes *less* stable for the range 50–90 percent. Finally, it ends up being more stable again than the symmetrically damaged shell. The maximum difference between the two curves occurs in the range of 60–70 percent flaws where the shell having nonuniformity at one end only buckles under a load some 11–13 percent less than that of the symmetrically damaged shell.

Cracked Edge Conditions. In this section only nonsymmetric nonuniformities will be considered in which one edge of the shell will be rigidly fixed (RF4) with the other edge having a crack around part of the circumference (free boundary condition) with the remainder rigidly fixed. Typical results will be exemplified for the particular case of the UHMG shell having the (optimal) +70 deg/−70 deg lay-up (Figs. 3 and 4).

From Fig. 5 it can be seen that the shell is sensitive to any flaw at the edge. A crack of 5 percent causes a reduction of about 4 percent in the critical load. By the time the crack has extended to three-tenths of the shell's circumference, the critical load has been further reduced by 48 percent. The lowest reduction ratio is 0.44 in this case so that any additional damage brings the stability of the shell within a few percent of that of a uniformly bounded (RF4-free) shell.

Convergence. A closing word is in place concerning the convergence of the results presented here, as a function of the number of circumferential modes participating in the modal coupling. Typical results (that speak for themselves) are shown in Table 4 for the case of the isotropic shell, considered in Fig. 2, with nonsymmetric nonuniformity and 10 percent edge damage.

Table 4 Typical Convergence Behavior

No. of Modes	15	20	25	26
Computed Buckling Load $N_\xi^0 \times 10^6$(N/m)	3.02	3.06	3.07	3.07

Conclusions

The effects on the stability characteristics of layered anisotropic cylindrical shells brought about by nonuniformities in the boundary conditions (representing edge damage) have been investigated. Although no general conclusions can be drawn, analysis of the many results indicates that isotropic shells exhibit a rather sudden steep reduction in the critical buckling load for relatively small edge damage. However, some anisotropic composite shells may not be so sensitive and, in contrast, only a gradual reduction may be brought about by the edge damage. The degree of sensitivity to edge damage appears to be dependent, in some complex fashion, on the various geometric and physical shell parameters.

Acknowledgment

The work of Y. S. was supported in part by the Fund for Promotion of Research at the Technion and in part by the Gerard Swope Chair in Mechanics. Y. S. thanks the former President of the Technion, Dr. Josef Singer, L. Shirley Tark Professor of Aircraft Structures at its Aeronautical Engineering Department, for bringing to his attention the pioneering work of N. J. Hoff and T. C. Soong (1967) and for helpful discussion of the subject matter.

Downloaded 03 May 2010 to 171.66.16.31. Redistribution subject to ASME license or copyright; see http://www.asme.org/terms/Terms_Use.cfm

References

Greenberg, J. B., Stavsky, Y., and Sabag, M., 1988, "Eigenfrequencies of Anisotropic Composite Shells of Revolution Having Nonuniform Supports," *Computer Methods in Applied Mechanics and Engineering*, Vol. 70, pp. 91–102.

Hoff, N. J., and Soong, T. C., 1965, "Buckling of Circular Cylindrical Shells in Axial Compression," *International Journal of Mechanical Sciences*, Vol. 7, pp. 489–520.

Hoff, N. J., and Soong, T. C., 1967, "Buckling of Axially Compressed Circular Cylindrical Shells with Nonuniform Boundary Conditions," *Symposium on Thin-Walled Steel Structures—Their Design and Use in Building*, University College of Swansea, Sept., pp. 61–80.

Stavsky, Y., and Hoff, N. J., 1969, "Mechanics of Composite Structures," *Composite Engineering Laminates*, A. G. H. Dietz, ed., MIT Press, Chap. 1.

Yamaki, N., 1984, *Elastic Stability of Circular Cylindrical Shells*, Elsevier Science Publishers B. V.

APPENDIX

The operators L_{ij} of equation (1) are given by:

$$
\begin{aligned}
L_{11} &= [A_{\xi\xi} - B_{\xi\xi}/a - N_\xi^0]( )_{,\xi\xi} + [2A_{\xi s}]( )_{,\xi\theta} \\
&\quad + [A_{ss} + B_{ss}/a + D_{ss}/a^2]( )_{,\theta\theta} \\
L_{12} &= [A_{\xi s} - 2B_{\xi s}/a + D_{\xi s}/a^2]( )_{,\xi\xi} \\
&\quad + [A_{ss} + A_{\xi\theta} - (B_{ss} + B_{\xi\theta})/a]( )_{,\xi\theta} \\
&\quad + A_{\theta s}( )_{,\theta\theta} \\
L_{13} &= -[B_{\xi\xi}/a - D_{\xi\xi}/a^2]( )_{,\xi\xi\xi} \\
&\quad - [3B_{\xi s}/a - D_{\xi s}/a^2]( )_{,\xi\xi\theta} \\
&\quad - [D_{ss}/a^2 + (B_{\xi\theta} + 2B_{ss})/a]( )_{,\xi\theta\theta} \\
&\quad - [B_{\theta s}/a + D_{\theta s}/a^2]( )_{,\theta\theta\theta} \\
&\quad - A_{\xi\theta}( )_{,\xi} - [A_{\theta s} + B_{\theta s}/a + D_{\theta s}/a^2]( )_{,\theta} \\
L_{21} &= L_{12} \\
L_{22} &= [A_{ss} - 3B_{ss}/a + 3D_{ss}/a^2 - N_\xi^0]( )_{,\xi\xi} \\
&\quad + [2A_{\theta s} - 4B_{\theta s}/a + 2D_{\theta s}/a^2]( )_{,\xi\theta} \\
&\quad + [A_{\theta\theta} - B_{\theta\theta}/a]( )_{,\theta\theta} \\
L_{23} &= -[B_{\xi s}/a - 2D_{\xi s}/a^2]( )_{,\xi\xi\xi} \\
&\quad - [(B_{\xi\theta} + 2B_{ss})/a - (D_{\xi\theta} + 3D_{ss})/a^2]( )_{,\xi\xi\theta} \\
&\quad - [3B_{\theta s}/a - 2D_{\theta s}/a^2]( )_{,\xi\theta\theta} - B_{\theta\theta}/a( )_{,\theta\theta\theta} \\
&\quad - [A_{\theta s} - B_{\theta s}/a]( )_{,\xi} - A_{\theta\theta}( )_{,\theta} \\
L_{31} &= L_{13} \\
L_{32} &= L_{23} \\
L_{33} &= D_{\xi\xi}/a^2( )_{,\xi\xi\xi\xi} + 4D_{\xi s}/a^2( )_{,\xi\xi\xi\theta} \\
&\quad + [2D_{\xi\theta} + 4D_{ss}]/a^2( )_{,\xi\xi\theta\theta} + 4D_{\theta s}/a^2( )_{,\xi\theta\theta\theta} \\
&\quad + D_{\theta\theta}/a^2( )_{,\theta\theta\theta\theta} + [2B_{\xi\theta}/a + N_\xi^0]( )_{,\xi\xi} \\
&\quad + [4B_{\theta s}/a + 2D_{\theta s}/a^2]( )_{,\xi\theta} \\
&\quad + [2B_{\theta\theta}/a + 2D_{\theta\theta}/a^2]( )_{,\theta\theta} \\
&\quad + [A_{\theta\theta} + B_{\theta\theta}/a + D_{\theta\theta}/a^2]( )
\end{aligned}
$$

Downloaded 03 May 2010 to 171.66.16.31. Redistribution subject to ASME license or copyright; see http://www.asme.org/terms/Terms_Use.cfm

G. Wayne Brodland
Assistant Professor.
Department of Civil Engineering,
University of Waterloo,
Waterloo, Ontario N2L 3G1 Canada

H. Cohen
Professor and Head.
Department of Civil Engineering,
University of Manitoba,
Winnipeg, Manitoba R3T 2N2 Canada

Deflection and Snapping of Ring-Loaded Spherical Caps

The axisymmetric behavior of both shallow, and deep, ring-loaded spherical caps, which are simply supported but otherwise unconstrained at their edges, is investigated using a large-strain shell theory based on a variational principle. A numerical technique is used to extract the solution. Particular attention is paid to highly nonlinear phenomena such as snapthrough, single and multiple snapback, and load-free everted states.

Introduction

The problem we address in this paper is the large, axisymmetric deformation of spherical rubber caps under the action of a vertical ring load, when the edges of the cap are simply supported but otherwise unconstrained (Fig. 1). Our objective is to determine the behavior of such caps over a wide range of deformations for various cap geometries and load placements. In particular, we seek load-deflection curves and meridian profiles. Of special interest are the location and nature of the various points of instability which are encountered on these curves as the shell is deformed back and forth between its virgin and everted states. To analyze this problem, we cast a nonlinear shell theory for hyperelastic materials in a form governed by a "stationary energy principle." The desired results are extracted by applying a numerical technique directly to this energy formulation of the problem. The analysis is an extension of recent work by Brodland and Cohen (1987) on the axisymmetric deformation of point-loaded spherical caps. It is also a variant of the numerical, small-strain, moderate-rotation study of Cagan and Taber (1986), who considered ring-loaded, spherical caps with *built-in* edges. The different boundary conditions considered in the two studies produce significantly different shell behavior. The deflection of Hookean caps has been dealt with extensively in the literature. We note, in particular, the analytical treatment of Chien and Hu (1957) and the experimental work of Evan-Iwanowski et al. (1963). References to additional pertinent background work may be found in the previously named papers.

A better understanding of the physics of rubber shells is motivated by their ever increasing use in a host of applications ranging from mechanical devices in computer equipment to major structural components in inflatable rubber dams and weirs. In particular, the problem we address here has direct application to devices which use spherical caps as a replacement for conventional spring mechanisms. Indeed, these are now used as the spring-actuator mechanisms in computer and typewriter keyboards, push-button telephones, self-banking systems, and a host of similar devices.

In addition, analyses such as that presented herein are a necessary step toward the study of many important biological problems. These include problems as diverse as mechanical aspects of critical stages of embryogenesis, and the conditions under which aneurisms swell and abate.

In the next section, we summarize the analytic apparatus utilized in formulating the problem. This is followed by a section outlining the numerical procedure used to extract the solution. The final section presents the main results of the paper. These include load-deflection curves over a broad range of cap geometries and load placements and selected details of the deformed cap shape near points of instability – points which give rise to phenomena such as snapthrough and snapback. Both phenomena can occur as the shell is taken to a state of complete eversion. The path to eversion is generally irreversible, thus giving rise to loops in the load-deflection curve. The precise number of instabilities encountered over a complete cycle from rest to eversion and back to rest is shown to depend upon the shell geometry and load location. Finally, we describe an experimental set-up used to test a ring-loaded cap, and present a comparison of the resulting experimental data with the predictions of the analysis.

The Basic Equations

Consider a spherical shell or cap of radius a and thickness h in its undeformed and unloaded state. It subtends an angle ϕ with respect to its axis of symmetry (Fig. 1). The shell midsurface $\mathcal{S}$ has meridians defined by

$$R = a \sin(S/a), \quad Z = a \cos(S/a), \quad \Psi = \Psi_0, \tag{1}$$

where (R, Z, Ψ) are the values of cylindrical polar coordinates (r, z, Ψ) on the meridian. The coordinate system has its origin at the sphere center and its z-axis along the symmetry axis of the shell. In the preceding, Ψ_0, $0 \le \Psi_0 \le 2\pi$, is a constant and S, $0 \le S \le a\phi$, is arc length along the meridian measured from the shell apex toward its edge. Let N, $|N| \le h/2$, be a coordinate measuring distance from the middle surface along the normals to $\mathcal{S}$. Then, the coordinates (S, Ψ, N) locate points in the undeformed shell.

Contributed by the Applied Mechanics Division for publication in the JOURNAL OF APPLIED MECHANICS.

Discussion on this paper should be addressed to the Editorial Department, ASME, United Engineering Center, 345 East 47th Street, New York, N.Y. 10017, and will be accepted until two months after final publication of the paper itself in the JOURNAL OF APPLIED MECHANICS. Manuscript received by ASME Applied Mechanics Division, January 28, 1988; final revision, May 30, 1988.

Copyright © 1989 by ASME

Downloaded 03 May 2010 to 171.66.16.31. Redistribution subject to ASME license or copyright; see http://www.asme.org/terms/Terms_Use.cfm

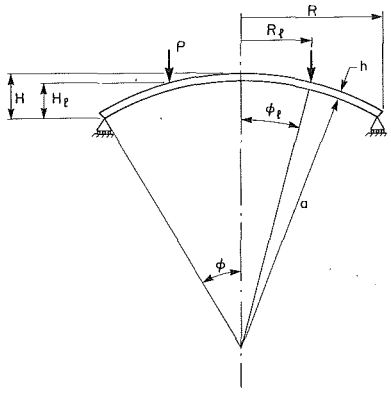


Fig. 1 Ring-loaded spherical cap

The spherical shell is loaded by a ring load p of radius $R_l = a \sin \phi_l$ centered on the z-axis. The dimension of p is force per unit length. We assume an axisymmetric deformation into a shell of revolution which takes $\mathcal{S}$ and normals to $\mathcal{S}$ into a surface $\mathcal{s}$ and its corresponding normals, respectively. Thus, the deformation is prescribed on giving the functions

$$r = r(s), \quad z = z(s), \quad \psi = \Psi, \tag{2}$$

and

$$s = s(S), \quad n = n(N). \tag{3}$$

Equation (2) defines the deformed meridians, with s measuring arc length along these from the shell apex. The coordinate n measures distance from $\mathcal{s}$ along the normals to $\mathcal{s}$. The coordinates (s, ψ, n) locate points in the deformed shell corresponding to points with coordinates (S, Ψ, N) in the undeformed shell. The assumption that normals to $\mathcal{S}$ map into normals to $\mathcal{s}$ is usually referrred to as the "relaxed" Kirchhoff hypothesis and implies the absence or neglect of transverse shear deformation. Note that, in general, $(3)_2$ does not preserve distances between points on a normal to $\mathcal{S}$ and corresponding points on a normal to $\mathcal{s}$. It follows that $\mathcal{s}$ is generally no longer the mid-surface of the deformed shell.

Straightforward computations using (1)–(3) lead to

$$v_\alpha = \lambda_\alpha (1 + k_\alpha n)/(1 + N/a), \quad v_3 = dn/dN, \tag{4}$$

where $\alpha = 1, 2$, and (v_α, v_3) are the principal stretches at arbitrary points in the shell. The quantities λ_α are the principal stretches on $\mathcal{s}$ and are given by

$$\lambda_1 = ds/dS, \quad \lambda_2 = r/R. \tag{5}$$

Clearly, the associated principal directions of stretch on $\mathcal{s}$ are along its lines of curvature, i.e., along meridians and parallel circles, respectively. The latter have principal curvatures k_α given by

$$k_1 = d\theta/ds, \quad k_2 = (\sin\theta)/r, \tag{6}$$

respectively, where θ is the angle between normals to $\mathcal{s}$ and the z-axis.

The volumetric dilatation is given by the product $v_1 v_2 v_3$. For rubber and biological materials we assume material incompressibility, i.e., $v_1 v_2 v_3 = 1$. The substitution of (4) into this condition results in a differential equation for the determination of $(3)_2$ in terms of the surface quantities λ_α, k_α, viz.,

$$dn/dN = (1 + N/a)^2/\lambda_1 \lambda_2 (1 + k_1 n)(1 + k_2 n). \tag{7}$$

We shall now restrict consideration to shells made of incompressible, hyperelastic, Mooney-Rivlin materials. For such materials, there exists a stored energy function ϵ, per unit undeformed volume, given by

$$\epsilon = C_1\{v_1^2 + v_2^2 + (v_1 v_2)^{-2}\} + C_2\{v_1^2 v_2^2 + (v_1 v_2)^{-2}(v_1^2 + v_2^2)\}, \tag{8}$$

where C_1, C_2 are material constants. If we use $(4)_1$, and $(3)_2$ obtained from (7), to eliminate v_α, n from (8), then it is easy to see the existence of a surface strain energy function $\sigma(\lambda_\alpha, k_\alpha)$, per unit area on $\mathcal{S}$, given by

$$\sigma = \int_{-h/2}^{h/2} \epsilon(\lambda_\alpha, k_\alpha, N)(1 + N/a)^2 dN. \tag{9}$$

It is the aim of shell theory to employ such surface quantities as σ in formulating the mechanics of shells in order to make shell problems tractable. Approximations common in shell theory, i.e., the neglect of sufficiently high-order terms in hk_α, allow (9) to be integrated into the explicit form

$$\begin{aligned}\sigma = {} & C_1[\{\lambda_1^2 + \lambda_2^2 + \lambda_1^{-2}\lambda_2^{-2} - 3\}h + \\ & \{a_1^2(1 + 3\lambda_1^{-4}\lambda_2^{-2}) + a_2^2(1 + 3\lambda_1^{-2}\lambda_2^{-4}) + 4a_1 a_2 \lambda_1^{-3}\lambda_2^{-3}\}h^3/12] \\ & + C_2[\{(\lambda_1^2 - a_1^2 h^2/4)^{-1} + (\lambda_2^2 - a_2^2 h^2/4)^{-1} + \lambda_1^2\lambda_2^2 - 3\}h \\ & + \{a_1^2\lambda_2^2 + 4a_1 a_2 \lambda_1 \lambda_2 + a_2^2 \lambda_1^2\}h^3/12],\end{aligned} \tag{10}$$

where

$$a_1 = (k_1/\lambda_2) - (\lambda_1/a), \quad a_2 = (k_2/\lambda_1) - (\lambda_2/a). \tag{11}$$

Similar forms of σ for Mooney-Rivlin shells have been derived by Simmonds (1986) and Taber (1985).

We assume the mechanics of the shell to be governed by a variational principle, thereby avoiding a statement of the usual laws of force and moment balance. To formulate the required principle, we need only define the total potential energy $\mathcal{W}$ by

$$\mathcal{W} = \mathcal{E} - Pw, \tag{12}$$

where

$$\mathcal{E} = 2\pi a \int_0^{a\phi} \sigma \sin(S/a) dS \tag{13}$$

is the total stored energy, and

$$P = 2\pi R_l p \tag{14}$$

is the total load, with w the vertical displacement of the ring load. Finally, we postulate that deformed shell configurations are in a state of equilibrium provided they correspond to a stationary value of $\mathcal{W}$.

The Numerical Analysis

The analytic formulation of the previous section requires that a deformed equilibrium state correspond to a stationary value of $\mathcal{W}$. To find a meridian defining this state for a given load, we proceed by a "semi-inverse" numerical method. This means we assume a trial form for the deformed meridian, which has sufficient degrees-of-freedom to allow an approximate solution of the variational problem. The degrees-of-freedom are chosen in such a fashion that the approximate numerical solution converges to the exact solution when sufficient degrees-of-freedom are used.

We now outline the numerical scheme in the form of a step-by-step procedure.

(1) Definition of Segments. We divide the undeformed meridian into m segments. The $m+1$ boundary points or "nodes" of these segments are located by their arc length coordinates S_j, $j = 0, 1, 2, \ldots, m$, where $S_0 = 0$, $S_m = a\phi$. The nodes S_j are assumed to map onto nodes on the deformed meridian on $\mathcal{s}$, located by their arc length coordinates s_j, $j = 0, 1, 2, \ldots, m$, respectively. The nodal coordinates (r_j, z_j) and segment slopes θ_j at the nodes are unknowns and constitute the $M = 3(m+1)$ degrees-of-freedom of the problem. We note (*i*) that the deformed meridian is assumed to have a continuous slope and (*ii*) that the B constraints—$r_1 = \theta_1 = 0$ at the shell apex, $z_k = w$ at the loading ring (w is the vertical deflection of the loading ring and occurs at the kth node) and z_{m+1} at the shell edge—may be regarded as constraints on the above degrees-of-freedom.

Downloaded 03 May 2010 to 171.66.16.31. Redistribution subject to ASME license or copyright; see http://www.asme.org/terms/Terms_Use.cfm

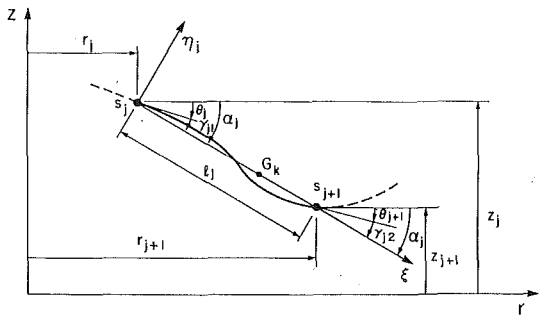


Fig. 2 Segmental representation

(2) Definition of Local Cartesians. The nodes s_j, s_{j+1}, $j = 0, 1, 2, \ldots, m$, are joined by m linear chords. At each node s_j, $j = 0, 1, 2, \ldots, (m-1)$, we construct the perpendicular line to the chords (s_j, s_{j+1}). The chords and their perpendiculars are taken to constitute m local cartesian coordinate systems (ξ_j, η_j), (Fig. 2). The ξ_j coordinate is nondimensional and normalized so that $0 \leq \xi \leq 1$. Clearly, we can now drop the subscript j from the ξ_j coordinate. The η_j coordinate has the dimension of length.

(3) Definition of Segment Shape. The shape of each of the meridian segments is assumed to be given in terms of the local coordinates (ξ, η_j) by the shape function

$$\eta_j = l_j \xi(1-\xi)\{\gamma_{j1}(1-\xi) - \gamma_{j2}\xi\}, \tag{15}$$

where the γ_{j1}, γ_{j2} are parameters and l_j is the length of the chord spanning s_j, s_{j+1}, viz.,

$$l_j = \{(r_{j+1}-r_j)^2 + (z_{j+1}-z_j)^2\}^{1/2}. \tag{16}$$

If there are a sufficient number of segments, then we can assume that the local slope $(d\eta_j/l_j d\xi) \ll 1$. Thus, $(d\eta_j/l_j d\xi)$ measures the angle γ_j between the jth shape function and the jth chord, $j = 0, 1, 2, \ldots, (m-1)$. From (15) we see immediately that γ_{j1}, γ_{j2} are the values of these angles at the nodes of the jth segment. The local angles γ_{j1}, γ_{j2} are related to θ_j, θ_{j+1}, the angles between the meridian normal at the nodes and the z-axis, by

$$\theta_j = \alpha_j - \gamma_{j1}, \quad \theta_{j+1} = \alpha_j - \gamma_{j2}, \tag{17}$$

where

$$\alpha_j = \tan^{-1}\{(z_j - z_{j+1})/(r_{j+1} - r_j)\} \tag{18}$$

defines the orientation angle α_j of the jth chord. The assumed continuity of the meridian shape requires that

$$\theta_{j+1} = \alpha_j - \gamma_{j2} = \alpha_{j+1} - \gamma_{(j+1)1}. \tag{19}$$

Because of (18) and (19) it is clear that the γ_{j1}, γ_{j2} introduce no additional degrees-of-freedom into the formulation. We point out that the function defined by (15) crosses the ξ-axis between nodes if and only if γ_{j1}, γ_{j2} are both nonzero and of the same sign. Moreover, the approximate local curvature $(d^2\eta_j/l_j^2 d\xi^2)$ may or may not change sign between the nodes and generally will be discontinuous at the nodes. Since curvature is a geometric invariant it should be obvious that the quantity $(d^2\eta_j/l_j^2 d\xi^2)$ measures the principal curvature of the deformed meridian.

(4) Meridian Shape and Geometry. The segmental shape functions have been defined in terms of the local coordinates (ξ, η_j). To utilize the concepts of step 3 we need the meridian shape in terms of the global coordinates (r, z). An easy transformation shows the meridian to be defined by

$$\begin{aligned} r_j(\xi) &= r_j(1-\xi) + r_{j+1}\xi + \eta_j(\xi)\sin\alpha_j, \\ z_j(\xi) &= z_j(1-\xi) + z_{j+1}\xi + \eta_j(\xi)\cos\alpha_j. \end{aligned} \tag{20}$$

The principal stretches (5) and principal curvatures (6) are given at any point of the jth segment by

$$\lambda_{1j} = l_j(\xi)/L_j(\xi), \quad \lambda_{2j} = r_j(\xi)/R_j(\xi), \tag{21}$$

and

$$k_{1j} = -d^2\eta_j/l_j^2 d\xi^2, \quad k_{2j} = \sin\theta_j(\xi)/r_j(\xi), \tag{22}$$

respectively, where

$$\begin{aligned} l_j(\xi) &= \{(r_j(\xi) - r_j)^2 + (z_j(\xi) - z_j)^2\}^{1/2}, \\ L_j(\xi) &= (S_{j+1} - S_j)\xi, \quad \theta_j(\xi) = \alpha_j - (d\eta_j/l_j d\xi), \\ R_j(\xi) &= a\sin\{(S_{j+1}\xi + S_j(1-\xi))/a\}. \end{aligned} \tag{23}$$

We note that the coordinate ξ is assumed to play the role of a convected coordinate in the analysis.

(5) The Potential Energy. We are now in a position to calculate the potential energy (12) in terms of the degrees-of-freedom (r_j, z_j, θ_j) of the problem formulation. We substitute (15)–(23) into (12) and use Gaussian quadrature to numerically evaluate the integral in (13). The result is an expression

$$\mathcal{W} = \mathcal{W}(r_j, z_j, \theta_j). \tag{24}$$

(6) The Critical Values. According to the variational principle, we seek stationary values of (24) in order to find the equilibrium states of the shell meridian. Obviously, the problem has been reduced to the form of a stationary value problem in M minus B variables. The values of (r_j, z_j, θ_j) at stationary $\mathcal{W}$ are called the critical values of $\mathcal{W}$. It is these that determine the solution to the problem. We remark that the values of (r_j, z_j, θ_j) will be subject to B constraints arising from the assumed boundary condition at the edge and continuity requirement at the apex. The numerical problem constitutes a standard nonlinear programming problem which can be solved by any of a number of standard numerical techniques.

The approach devised above is capable of treating fully nonlinear phenomena. *There are no restrictions on the magnitudes of strains or rotations.* Note that restrictions on the segment shape *relative to the local* (ξ, η_j) *coordinate system* in no way restrict strains or rotations.

Results and Discussion

A ring-loaded cap can be described in terms of four dimensionless parameters λ, ϕ, α and P^*. The spherical cap itself is characterized by two dimensionless parameters: the cap half-angle ϕ, and the geometric parameter λ, given by

$$\lambda^2 = [12(1-\nu^2)]^{1/2}(a/h)\sin^2\phi \tag{25}$$

which for small half-angles ϕ can be approximated by

$$\lambda^2 = [12(1-\nu^2)]^{1/2}(2H/h). \tag{26}$$

Poisson's ratio is taken as $\nu = 0.5$ since the material is assumed to be incompressible, and the constants C_1, C_2 are chosen as

$$\begin{aligned} C_1 &= 5E/24 \\ C_2 &= -E/24 \end{aligned} \tag{27}$$

to model a linear material with Young's modulus E. The height H of the cap is given by

$$H = a(1-\cos\phi) \tag{28}$$

(see Fig. 1). The parameter ϕ provides a measure of the *depth* of the shell. The shell is *shallow* when (26) holds, i.e., if $\phi \cong 2H/R$. The parameter λ^2 provides a measure of the shell *thickness*: Large λ^2 values are associated with *thin* shells. The ring load is described by its dimensionless location α and its dimensionless magnitude P^* given, respectively, by

$$\alpha = \phi_l/\phi, \quad \text{and} \quad P^* = Pa/Eh^3 \tag{29}$$

in terms of total load P.

Downloaded 03 May 2010 to 171.66.16.31. Redistribution subject to ASME license or copyright; see http://www.asme.org/terms/Terms_Use.cfm

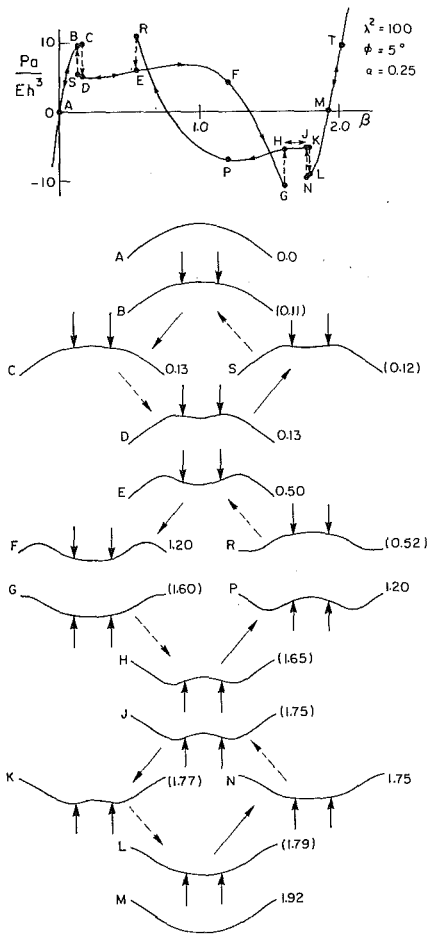


Fig. 3 Load-deflection curves and meridional contours for $\lambda^2 = 100$, $\alpha = 0.25$

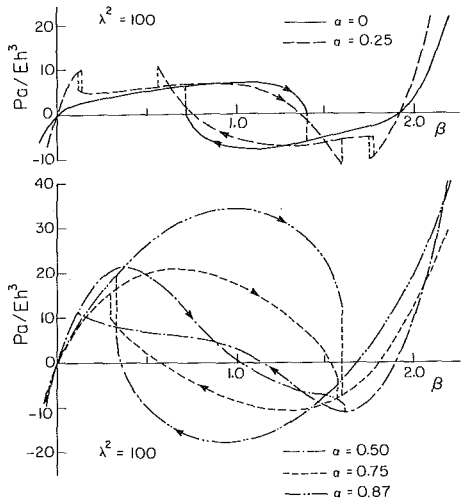


Fig. 4 Load-deflection curves for $\lambda^2 = 100$

It is convenient to nondimensionalize the vertical deflection, w, of the ring load in terms of its initial vertical distance, H_l, from the base of the shell; i.e.,

$$\beta = w/H_l \tag{30}$$

where

$$H_l = a(\cos\phi_l - \cos\phi). \tag{31}$$

Results contained herein were calculated for $\nu = 0.5$ using eight segments, each initially of equal length, to represent the meridian. The rest configuration of the shell is specified by the initial locations and slopes of its nine nodes. The properties of the shell rest configuration are then determined numerically in terms of nodal values in the same fashion as those of subsequent deformed configurations. By specifying *displacement* β rather than *load* P^* – an approach first used for analysis of spherical caps by Bueckner et al. (1967) – both stable and unstable equilibrium configurations were obtained. Unstable equilibria associated with snapback must be approached carefully using small displacement increments so that snapping does not occur prematurely.

Figure 3 shows the load-deflection curve and selected meridian contours for a thin ($\lambda^2 = 100$), shallow ($\phi = 5$ deg) spherical cap with a ring load applied near its center ($\alpha = 0.25$). As the deflection of the loaded ring is increased from the rest configuration, A, loading proceeds along the path A-B-C. Up to point C, the portion of the cap inside the ring load has essentially the same shape as it does in its rest configuration, except that the part of it close to the ring load is somewhat rotated. If *load* had been specified, a small increase in load above P_C, associated with point C, would have caused snap-through of the cap to point T, the next *stable* configuration which can support a load just higher than that carried at C. The meridian contour associated with state T is similar to that of state M, and is therefore not shown. Loads, P_C, where unstable equilibrium states first occur, are called critical loads, P_{cr}.

By specifying *deflection* instead, a wide range of stable and unstable equilibria between C and T can be investigated. When displacement is specified, an arbitrarily small further increase in displacement beyond C causes the interior portion of the cap to suddenly undergo a reversal of its curvature, called snapback, to state D. The concepts of snapthrough and snapback are discussed in some detail for the apical load case in Brodland and Cohen (1987). Further loading occurs along path D-E-F-G as the portion of the cap outside the ring load undergoes additional deformation. Just beyond G, snapback occurs to state H. This snapback involves both the inner and outer parts of the cap. Further ring displacement occurs along the path H-J-K. At K, the center of the cap again snaps to a state of reversed curvature (state L). Additional displacement produces states L-M-T, M being the load-free everted state. Thus, there are three different occurrences of snapback along the path from the rest state to the everted state. These observations are consistent with the findings of Evan-Iwanowski et al. (1963), Cagan and Taber (1986), and Wan (1984), all of which are restricted to smaller displacements and thus do not exhibit as many occurrences of snapping as observed here.

It should be noted, that most of the load-deflection path is *locally* reversible. It is possible to proceed to positions of either increasing or decreasing displacement along *any* of the *solid* curves shown in the figure. The arrows shown on the solid curves simply indicate the direction followed on going from the rest state to somewhat beyond eversion and then back to the rest state. One could proceed along the whole or any part of a path such as S-D-E-F-G in either direction. The snapback portions of the load-deflection path (shown with dashed lines), however, are *irreversible* and it is possible to proceed only in the direction shown by the arrows. It is thus possible to proceed from state G to state H, but not from H to G. Thus, it is the snapback events which give rise to the loops, such as B-C-D-S-B, in the overall load-deflection curve.

Since the shell is thin ($\lambda^2 = 100$), the ratio of membrane to bending forces is large, and the behavior of the cap is governed primarily by membrane effects. Thus, the return path to the rest state (M-L-N-J-H-P-R-E-D-S-B-A) is very similar to the loading path described above. Nonetheless, the process is seen to contain irreversible processes and thus the overall load-deflection curve contains several loops.

Downloaded 03 May 2010 to 171.66.16.31. Redistribution subject to ASME license or copyright; see http://www.asme.org/terms/Terms_Use.cfm

It is clear from symmetry arguments that snapback events in thin shells (e.g., $\lambda^2 = 100$) should occur in pairs. It is less clear why snapback events seem to always occur in pairs even in thicker caps (e.g., $\lambda^2 = 36$ or $\lambda^2 = 50$), where asymmetrical bending effects cause load-deflection and snapping behavior to be highly asymmetrical. Throughout the balance of this paper, the number of snapback occurrences, n, will refer to the number of snapback events on the path from rest to eversion, which is the same as the number on the return path from eversion to rest, and is the same as the total number of *pair* of individual snapback events.

Analysis of a few caps for which $\phi = 22.5°$ showed that the behavior of such caps is nearly indistinguishable from corresponding caps with $\phi = 5°$. This observation suggests that the behavior of *shallow* ($\phi \leq 22.5°$), ring-loaded caps is essentially independent of ϕ as is the case for *shallow* point-loaded caps (Brodland and Cohen, 1987).

Figure 4 shows the effect of ring-load location on the load-deflection behavior of thin caps ($\lambda^2 = 100$). Figure 4(*a*) shows that the behavior of a cap with a small diameter ring load ($\alpha = 0.25$) and a cap with a point load ($\alpha = 0$) are similar. As also noted by Cagan and Taber (1986), the load-deflection curve of the ring-loaded cap is initially more steep than that of a similar point-loaded cap. The ring-loaded cap exhibits two additional instances of snapback associated with the sudden formation of a dimple inside the ring load. While the center of a point-loaded cap begins to deform immediately upon application of the load, the inner portion of a thin, ring-loaded cap remains largely undeformed until it suddenly snaps through to a dimple of reversed curvature. It is this delayed center deformation which produces the additional occurrences of snapback in a ring-loaded cap. This interpretation is further supported by the similarity between the meridional contours B, D, E, F, G, J, and K for a point-loaded cap, as given in Brodland and Cohen (1987), and the corresponding contours A, F, G, H, M, P, and R given here in Fig. 3.

Figure 4(*b*) shows that the load-deflection contours change even more as the diameter of the ring load is increased. The intermediate snapping occurrence (path E-F-G-H-P-R-E in Fig. 3) vanishes for $\alpha \geq 0.5$ and the outer occurrences merge. Thus, a single occurrence of snapback occurs in the several geometries whose load-deflection curves are shown in Fig. 4(*b*). It is interesting to note, that although the load-deflection curves for $\alpha = 0.25$ and $\alpha = 0.5$ share many features, the sequence of meridional contours through which the two caps pass are very different. Conversely, although the three load-deflection curves shown in Fig. 4(*b*) for $\alpha \geq 0.5$ are quite different from each other, the sequence of meridional contours through which their respective caps pass are surprisingly similar.

Figure 5 shows the load-deflection curves of fairly thick caps ($\lambda^2 = 36$). Although the load-deflection curves shown are for caps with $\phi = 5°$, the behavior of caps for which $\phi \leq 22.5$ deg is similar. The load-deflection curves for $\alpha \leq 0.25$ show that although these caps exhibit snapping, they do not exhibit snapback. The behavior, including meridional contours, produced by a ring load of small diameter ($\alpha = 0.25$) is very similar to that produced by a point load ($\alpha = 0$). The snapping behavior and sequence of meridional contours through which caps with $\lambda^2 = 36$ and caps with $\lambda^2 = 100$ pass are very similar for $\alpha \geq 0.5$ even though their load-deflection curves are somewhat different.

It is interesting to note that the phenomenon of snapback occurs in *point-loaded* caps only when the cap is much thinner; e.g., $\lambda^2 > 64$ (Brodland and Cohen, 1987). In addition, in point-loaded caps, unlike ring-loaded caps, the load-deflection curve becomes very steep and the load approaches zero at the initiation of snapback.

Figure 6 shows the critical loads P_{cr} for caps with $\lambda^2 = 36$ and $\lambda^2 = 100$ as a function of dimensionless load location α. Centrally-loaded caps ($\alpha \leq 0.25$) with $\lambda^2 = 36$ do not exhibit snapback. Their critical loads (and load-deflection curves) are very similar to each other suggesting that the *details* of an axisymmetric central load are largely unimportant in thick caps. (See also Wan (1984).) In caps with $\lambda^2 = 36$ and large diameter ring loads ($\alpha \geq 0.5$) a single occurrence of snapback occurs. Thus, a discontinuity occurs in the P_{cr} curve for $\lambda^2 = 36$ between $\alpha = 0.25$ and $\alpha = 0.5$. In addition, as $\alpha \to 1.0$, the effect of the ring load becomes similar to that of an edge moment and the magnitude of the ring load required to produce a particular edge moment increases approximately as $1/(1-\alpha)$, as shown. Caps with $\lambda^2 = 100$ exhibit three kinds of snapping behavior (zero, one and three occurrences of snapback) and thus their P_{cr} curve has two *discontinuities*.

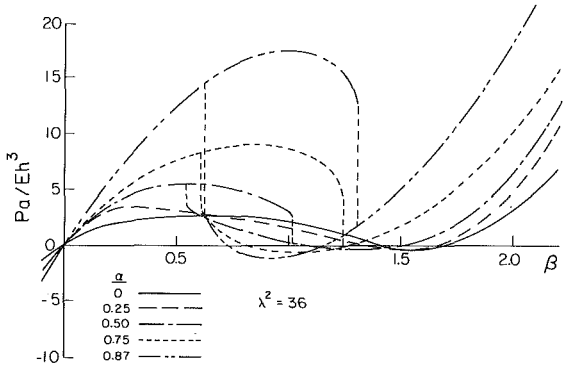


Fig. 5 Load-deflection curves for $\lambda^2 = 36$

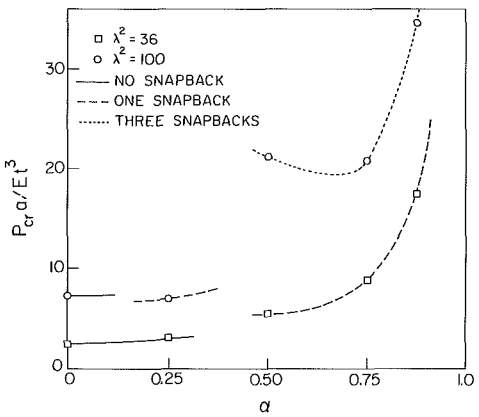


Fig. 6 Critical loads

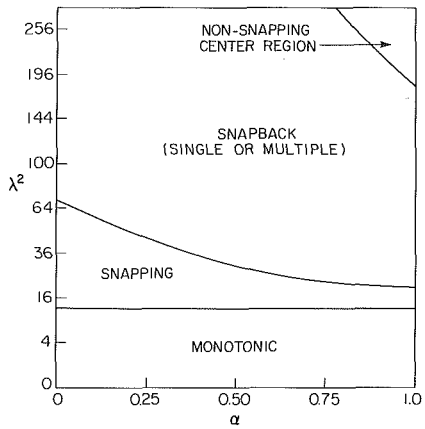


Fig. 7 Approximate behavior domains

Downloaded 03 May 2010 to 171.66.16.31. Redistribution subject to ASME license or copyright; see http://www.asme.org/terms/Terms_Use.cfm

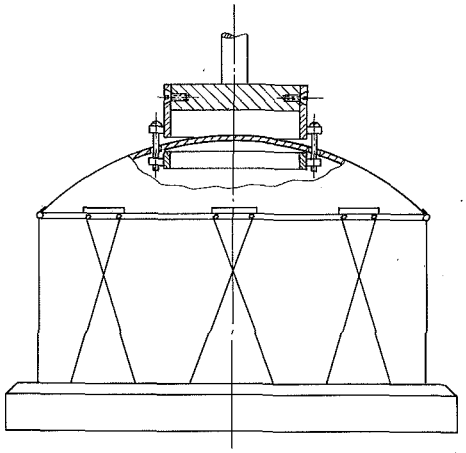


Fig. 8 Experimental apparatus

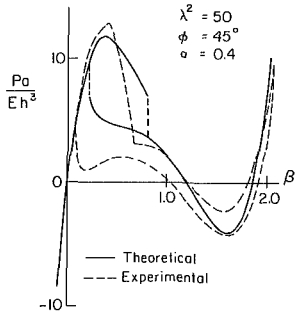


Fig. 9 Theoretical and experimental load-deflection curves for $\lambda^2 = 50$, $\phi = 45°$ and $\alpha = 0.4$

Figure 7 shows *approximate* domains of various types of behavior. The figure was constructed by supplementing the cases discussed above with snapping analyses of additional caps having different combinations of λ^2 and α. For λ^2 somewhat less than 16, load-deflection curves are monotonic for all values of α. Combinations within the small, roughly triangular region which includes $\lambda^2 = 36$, $\alpha = 0.25$ have nonmonotonic load-deflection curves and thus exhibit snapthrough. Most of the rest of the domain illustrated in the figure represents configurations which exhibit snapthrough as well as single or *multiple* snapback pair; e.g., $\lambda^2 = 36$, $\alpha = 0.5$ and $\lambda^2 = 100$, $\alpha = 0.25$, respectively. In all of the cases studied by the authors, snapback occurred in either single or triple pair. We speculate that double pair might be possible as when cap and load geometries are such that the second and third loops shown in Fig. 3 merge into one large loop E-F-G-N-L-K-J-H-P-R-E.

When a cap is sufficiently thin, as measured by λ^2, the behavior of the region inside the ring load can be largely independent of that outside of it. It is then possible to get snapback of the outer region without the inner region reversing curvature. Calculations show that this type of behavior would occur at $\lambda^2 = 256$, $\alpha = 0.78$ assuming caps this thin deform axisymmetrically.

An experiment was done using a segment of a rubber ball for which $\lambda^2 = 50$ and $\phi = 45°$ ($a = 66$ cm). The cap was supported around its perimeter using piano wire which was passed through small-diameter brass tubes. The small tubes were silver-soldered to small brass channels which were then crimped on to the edge of the cap. (See Fig. 8.) This edge-mounting arrangement proved to be more rugged than that used previously (Brodland and Cohen). Since the snapback behavior of the cap center is, in general, highly sensitive to asymmetries in the ring load, and since lateral displacements in caps with $\phi \leq 45°$ are small, a thin-walled piece of copper tubing was used to provide the ring load ($\alpha = 0.4$). Three small bolts (#2-56) passed through small holes drilled in the cap allowed a lower ring to be installed so that both upward and downward loads could be applied easily. By adjusting the spacing between the rings and by providing suitable lubrication, friction effects could be kept to a satisfactory level without introducing excessive slack.

Figure 9 shows both the theoretically predicted and experimental load-deflection curves. For the particular geometry considered, there is one occurrence of snapping. It is a form of localized snapping associated with the interior portion of the cap suddenly changing curvature. It is thus similar in kind to the outer snapping events depicted in Fig. 3. Since this cap is both thicker and deeper than those described in Figs. 3 and 4, and deeper than those described in Fig. 5, it is not surprising that bending effects are sufficient in this cap to prevent the subsequent two snapping events.

The theoretical and experimental curves are in good qualitative agreement. The discrepancies seem to be due to slight hysteresis in the rubber, and friction between the loading rings and the cap. The chief discrepancy between the two curves is on the latter part of the return path ($0 \leq \beta < 0.5$) where snapback is somewhat delayed and altered in shape. This discrepancy appears to be largely due to friction effects since its magnitude was sensitive to variations in the coefficient of friction between the rings and cap.

Acknowledgments

This research was supported by the Natural Sciences and Engineering Research Council of Canada.

References

Brodland, G. W., and Cohen, H., 1987, "Deflection and Snapping of Spherical Caps," *International Journal of Solids and Structures*, Vol. 23, No. 10, pp. 1341–1356.

Bueckner, H. F., Johnson, Jr., M. W., and Moore, R. H., 1967, "The Calculation of Equilibrium States of Elastic Bodies by Newton's Method," *Developments in Mechanics*, Vol. 3, T. C. Huang, and M. W. Johnson, Jr., eds., John Wiley, New York, pp. 201–213.

Cagan, J., and Taber, L. A., 1986, "Large Deflection Stability of Spherical Shells With Ring Loads," ASME JOURNAL OF APPLIED MECHANICS, Vol. 53, pp. 897–901.

Chien, W. Z., and Hu, H. C., 1957, "On the Snapping of a Thin Spherical Cap," *Proceedings of the 9th International Congress of Applied Mechanics*, Vol. 6, Brussels, Belgium, pp. 309–320.

Evan-Iwanowski, R. M., Loo, T. C., and Tierney, D. W., 1963, "Local Buckling of Shells," *Developments in Mechanics*, Vol. 2, S. Ostrach and R. H. Scanlan, eds., Pergamon Press, New York, pp. 221–251.

Simmonds, J. G., 1986, "The Strain-Energy Density of Rubber-Like Shells of Revolution Undergoing Torsionless, Axisymmetric Deformation (Axishells)," ASME JOURNAL OF APPLIED MECHANICS, Vol. 53, pp. 593–596.

Taber, L. A., 1985, "On Approximate Large Strain Relations for a Shell of Revolution," *International Journal of Non-Linear Mechanics*, Vol. 20, pp. 27–39.

Wan, F. Y. M., 1984, "Shallow Caps with a Localized Pressure Distribution Centered at the Apex," *Flexible Shells, Theory and Applications*, E. L. Axlerad and F. A. Emmerling, eds., Springer-Verlag, New York, pp. 124–145.

Downloaded 03 May 2010 to 171.66.16.31. Redistribution subject to ASME license or copyright; see http://www.asme.org/terms/Terms_Use.cfm

Rigid Body Collisions

Raymond M. Brach
Aerospace and Mechanical Engineering,
University of Notre Dame,
Notre Dame, IN 46556

A general approach is presented for solving the problem of the collision of two rigid bodies at a point. The approach overcomes the difficulties encountered by others on the treatment of contact velocity reversals and negative energy losses. A classical problem is solved; the initial velocities are presumed known and the final velocities unknown. The interaction process between the two bodies is modeled using two coefficients. These are the classical coefficient of restitution, e, *and the ratio,* μ, *of tangential to normal impulses. The latter quantity can be a coefficient of friction as a special case. The paper reveals that these coefficients have a much broader intepretation than previously recognized in the solution of collision problems. The appropriate choice of values for* μ *is related to the energy loss of the collision. It is shown that* μ *is bounded by values which correspond to no sliding at separation and conservation of energy. Another bound on* μ *combined with limits on the coefficient* e, *provides an overall bound on the energy loss of a collision. Examples from existing mechanics literature are solved to illustrate the significance of the coefficients and their relationship to the energy loss of collisions.*

1 Introduction

The three-dimensional problem of the collision of two rigid bodies has never been solved satisfactorily. Although the general approach using Newton's laws is certainly well known, there exist a few nagging problems involving the tangential component of the contact impulse (frequently attributed to friction) and the fact that some solutions violate energy conservation laws. These concepts are investigated and cleared up in this paper. For this problem, the term "rigid body" implies not inflexibility but rather an object whose mass moment of inertia and rotational energy are not insignificant. A classical approach is followed. Newton's laws in their integrated form involving impulse and momentum are applied directly. Coefficients such as e and μ (restitution and "friction," respectively) are used to represent material behavior and the process of interaction between bodies. Typical assumptions are made. The two main ones are that the duration of contact is short and that the interaction forces are high. These permit the further assumptions that velocity changes are nearly instantaneous, that changes in position and orientation during the contact duration are negligible and effects of other forces can be disregarded.

A third assumption, though not always valid, is made here. That is that the impact occurs at a known distinct point on each rigid body. In fact, all impact forces occur over a surface. Some surfaces such as during automobile collisions, can be quite large and the location of the point of application of the resultant impulse can be unknown. Such problems require the introduction of impulse moments and have been addressed elsewhere (see, Horak, 1948; Brach, 1984). This paper deals only with point impacts.

One reason that the rigid body collision problem has not been solved satisfactorily is an incomplete view of the coefficients e and μ. The coefficient of restitution, e, is generally viewed as an experimentally determined constant which in some way represents the effect of inelastic material behavior. Though this is true, it ignores another equally valid view of e, that of a velocity constraint parameter. In undergraduate dynamics courses, reference frequently is made of two box cars coupling upon impact. Little or no plastic deformation occurs, yet the two cars have a common final velocity. Setting e to zero here provides a way of constraining the final velocities to be equal. The definition of e is frequently given in the form of a ratio of final to initial normal velocities, i.e., a velocity constraint. This kinematic definition of e is not accidental. Many books on mechanics show a direct relationship between e^2 and kinetic energy loss. Introduction of e as a kinematic constraint implicitly introduces energy loss into the impact equations without the direct use of energy terms. The explicit use of energy terms would make the problem nonlinear in the velocity variables. Consequently, e has a dual role; it can characterize inelastic material behavior and energy loss as well as constrain velocities. Understanding of this dual role is necessary both in application of the theory and in analyzing energy loss.

Typically, the quantity μ is limited to the role of a coefficient of friction. Keller (1986) points out that incorrect solutions (Kane and Levinson (1985)), arise from an inappropriate use of μ and leads to collisions which violate conservation of energy. That is, the system of rigid bodies gains kinetic energy during an impact. While μ is almost always called a coefficient of friction, its true interpretation and role is much broader.

Contributed by the Applied Mechanics Division of THE AMERICAN SOCIETY OF MECHANICAL ENGINEERS for presentation at the Joint ASCE/ASME Applied Mechanics, Biomechanics, and Fluids Engineering Conference, San Diego, CA, July 9–12, 1989.

Discussion of this paper should be addressed to the Editorial Department, ASME, United Engineering Center, 345 East 47th Street, New York, N.Y., 10017, and will be accepted until two months after final publication of the paper itself in the JOURNAL OF APPLIED MECHANICS. Manuscript received by ASME Applied Mechanics Division, November 10, 1987; final revision, August 16, 1988.

Paper No. 89-APM-3.

Copyright © 1989 by ASME

Downloaded 03 May 2010 to 171.66.16.31. Redistribution subject to ASME license or copyright; see http://www.asme.org/terms/Terms_Use.cfm

For point collisions, it is possible to define a common, local tangent plane. The impulse between the two bodies can be broken down into two components P_n and $P_{tt'}$. These, respectively, are normal and tangent to the plane. $P_{tt'}$ is the resultant of two orthogonal impulse components P_t and $P_{t'}$, in the tangent plane itself. In this work the coefficient μ is defined simply as a constant corresponding to the ratio of the tangential impulse $P_{tt'}$ to the normal impulse P_n. As mentioned previously for e, this coefficient also plays more than one role. Values of μ control relative tangential velocity changes but also directly influence energy loss.

In addition to being a friction coefficient and a velocity constraint parameter, μ can be used in other ways. For example, when a hard object collides with a relatively soft horizontal surface, a crater is formed (either totally elastic or possibly with permanent deformation). Under these conditions, the tangential force (whose impulse is $P_{tt'}$) is formed at least partially by the horizontal component of the normal stresses acting over the crater surface. Friction can also enter into the horizontal force system. Though this is a rather complicated local mechanics problem, the rigid body velocity changes can be determined as a function of the constant μ in a rather simple fashion. Appropriate values of μ are determined analytically or experimentally. In fact, the role of μ can be examined using experimental results to determine whether the tangential force is or is not predominantly due to friction or indentation (Brach, 1988).

The procedure followed in this paper is first to present the equations corresponding to a three-dimensional impact problem of two rigid bodies. The approach to their solution is then summarized. Following this, several examples will be presented to illustrate the role of μ, how its value is determined, and the effect of e and μ on energy loss. Examples, or special cases, are used for two reasons. One is that an analytical solution of the three-dimensional problem is not available. However, a closed-form solution is available for a large class of two-dimensional problems and greater insight is gained from these rather than computerized, three-dimensional solutions. Another reason is that a certain problem, that of a falling rod (or lamina), has been solved incorrectly in at least three books. Its correct solution is presented here.

II The Three-Dimensional Collision Problem

Consider two rigid bodies with masses m_1 and m_2 which collide at a common point C. A tangent plane containing C also contains two orthogonal axes t and t' of a coordinate system with the third axis, n, being normal to the plane. Unit vectors are $\mathbf{n}$, $\mathbf{t}$, and $\mathbf{t}'$. From Newton's second law in its integrated form, linear momentum for each body provide two equations.[1]

$$m_1(\mathbf{V}_1 - \mathbf{v}_1) = \mathbf{P} \tag{1}$$

and

$$m_2(\mathbf{V}_2 - \mathbf{v}_2) = -\mathbf{P} \tag{2}$$

where

$$\mathbf{P} = P_n\mathbf{n} + P_t\mathbf{t} + P_{t'}\mathbf{t}' \tag{3}$$

is the resultant impulse. If each body's final angular momentum about its mass center is $\mathbf{H}$ then

$$\mathbf{H}_1 - \mathbf{h}_1 = \mathbf{d}_1 \times \mathbf{P} \tag{4}$$

and

$$\mathbf{H}_2 - \mathbf{h}_2 = \mathbf{d}_2 \times \mathbf{P} \tag{5}$$

where $\mathbf{d}_1$ and $\mathbf{d}_2$ are position vectors from the mass centers to point C. The coefficient of restitution can be defined as the ratio of final to initial relative normal velocity at point C and can be written as

$$\mathbf{V}_r \cdot \mathbf{n} = -e\mathbf{v}_r \cdot \mathbf{n} \tag{6}$$

where

$$\mathbf{V}_r = \mathbf{V}_2 + \Omega_2 \times \mathbf{d}_2 - \mathbf{V}_1 - \Omega_1 \times \mathbf{d}_1 \tag{7}$$

and

$$\mathbf{v}_r = \mathbf{v}_2 + \omega_2 \times \mathbf{d}_2 - \mathbf{v}_1 - \omega_1 \times \mathbf{d}_1. \tag{8}$$

Another common definition of e is the ratio of the portion of the normal impulse during restitution to the portion of the normal impulse during compression. This definition and equation (6) give the same result.

The tangential impulse is now related to the normal impulse in the following way.

$$\mathbf{P} = P_n(\mathbf{n} + \mu_t\mathbf{t} + \mu_{t'}\mathbf{t}') \tag{9}$$

The quantities μ_t and $\mu_{t'}$ are constants such that the resultant tangential impulse is written as

$$P_{tt'}{}^2 = P_t{}^2 + P_{t'}{}^2 = (\mu_t{}^2 + \mu_{t'}{}^2)P_n{}^2. \tag{10}$$

These two constants, which are presumed to be known, permit modeling of a variety of physical processes. If the tangental process is isotropic, and $P_{tt'}$ makes an angle η with the t-axis, then

$$\mu_t = \mu\cos\eta \qquad \text{and} \qquad \mu_{t'} = \mu\sin\eta \tag{11}$$

where μ is a constant. If the process or mechanism of tangential force generation is that of dry friction with a value f, then μ represents f.

The above equations represent a system of 15 linear algebraic scalar equations. These are from equations (1), (2), (4), (5), (6), and (9). Their solution provides the six final velocity components of each rigid body and the three impulse components, P_n, P_t and $P_{t'}$.

The solution of these equations requires that the coefficients e and μ (or μ_t and $\mu_{t'}$) are known. The kinematic role of the coefficient of restitution clearly illustrates that the value of e must be limited to the range $0 \le e \le 1$. The choice of appropriate values of μ is also limited by a critical value $|\mu| \le |\mu_c|$ where μ_c is yet to be determined. In the case where μ represents a friction coefficient, this limitation is noted by Keller (1986). Determination of Keller's bound on μ requires integration of the equations of motion of the colliding bodies for a (generally) unknown time interval. An advantage of using the principle of impulse and momentum for collision problems is that the solution is algebraic. Requiring integration destroys this feature. Determination of the bound on μ can be found by examining the collision's energy loss, however. As shown by Brach (1984) for point mass collisions and as shown later in this paper for planar, rigid body collisions, the kinetic energy lost during the collision, T_L, depends nonlinearly on μ. It possesses a maximum such that

$$T_{Lm} = T_L(e, \mu_m) \tag{12}$$

where μ_m is the value of μ which maximizes T_L for a given value of e. Furthermore, for a given collision,

$$(T_L)_{\max} = T_L(e = 0, \mu = \mu_{\max});\ \mu_{\max} = \mu_m\,|_{e=0} \tag{13}$$

is an overall maximum energy loss which can be viewed as an upper bound on energy loss. Furthermore, for $T_L = (T_L)_{\max}$, the final relative velocity of point C is zero. That is, no separa-

[1] Throughout this paper, final velocities and momenta are capitalized, initial quantities are written in lower case. Vectors are in bold type. The symbols V and v represent linear velocities: Ω and ω represent angular velocities.

Downloaded 03 May 2010 to 171.66.16.31. Redistribution subject to ASME license or copyright; see http://www.asme.org/terms/Terms_Use.cfm

tion occurs; Both bodies have the same final velocity at point C. It is also shown that for $|\mu| > |\mu_{\max}|$ the tangential force system must do positive work on the system which cannot occur if the tangential force is frictional in nature. Other important values of μ exist. One is the value of the impulse ratio which results with zero final relative tangential velocity at the contact point, μ_o. This value of μ depends on the coefficient of restitution; i.e., $\mu_o = \mu_o(e)$. For some collisions, $\mu_o = \mu_{\max}$. In other cases, such as for collisions of point masses, $\mu_o = \mu_m$. Another is μ_T which is the value of μ for which the energy loss becomes negative. Values of μ exceeding μ_T cause the solution to violate energy conservation.

It is hypothesized that three-dimensional collisions have the same behavior and the following solution scheme is proposed:

(1) Dry friction with coefficient f: the value of μ used in the solution is such that

$$|\mu| \le |\mu_c| = \min(f, |\mu_o|, |\mu_T|) \tag{14}$$

and

$$\text{sign}(\mu) = \text{sign}(\mu_{\max}).$$

(2) Other tangential force systems: in this case, any value of μ can be used which is consistent with the mechanism or process which generates the tangential impulse. The source of values of μ is by hypothesis or by experiment.

Equation (14) is a definition of a critical value, μ_c, of the impulse ratio, μ. The value of μ used in the solution of the impact equations derived above must not exceed μ_c if the tangential force is not to do positive net work on the system and if kinetic energy cannot be gained.

Most tangential force systems during collisions are passive, such as friction. That is, the direction of the force opposes the velocity. Under these conditions, the sign of μ would be expected to oppose the initial relative velocity such that $\mu r > 0$ $(r \neq 0)$, where

$$r = \frac{|\mathbf{v}_r - (\mathbf{v}_r \cdot \mathbf{n})\mathbf{n}|}{\mathbf{v}_r \cdot \mathbf{n}} \tag{15}$$

is the ratio of the initial relative tangential velocity to the initial relative normal velocity. However, the sign of the tangential impulse (which is determined by the sign of μ) depends upon the *net* force. Tangential velocity reversals (and force reversals) can occur due to the kinematics of the collision. Consequently, except for some special cases such as point mass collisions, the initial velocities alone cannot determine the sign of μ. If the tangential force system is elastic (for example, due to shearing deformation) a tangential restitution coefficient can be defined. Such a tangential coefficient is related directly to μ (Brach, 1988); this topic is not pursued here. If $0 \le |\mu| \le |\mu_c|$ the tangential impulse process is passive.

III Special Case and Examples

In order to demonstrate the above, a special case is presented, namely, the planar collision of two rigid bodies. Next, an example of a falling rod is presented in detail where the rod collides with a horizontal massive barrier. A second example is presented of an impact of the tip of a rigid spherical pendulum on a horizontal massive barrier.

The planar rigid body solution equations are presented because they can be obtained analytically including the energy loss expressions and the important values of μ. The example of the falling rod is chosen because incorrect or inadequate solution of this problem are presented in at least three books. Goldsmith (1960) presents a solution of the impact of a vertically falling rod with a smooth (frictionless) surface. Though the impact is frictionless, a velocity constraint is imposed of zero final tip velocity. Yet no horizontal impulse is included in order to provide the constraint. An incorrect solution is presented by Macauley (1987). In his solution, also frictionless, the horizontal velocity component of the rod's mass center is omitted from the problem. In addition, in a very unusual formulation of the problem, the angular position of the rod in included an an unknown, to be found from momentum principles. Finally, as pointed out by Keller (1986), Kilmister and Reeve (1966) solve this problem two ways, one of which is incorrect.

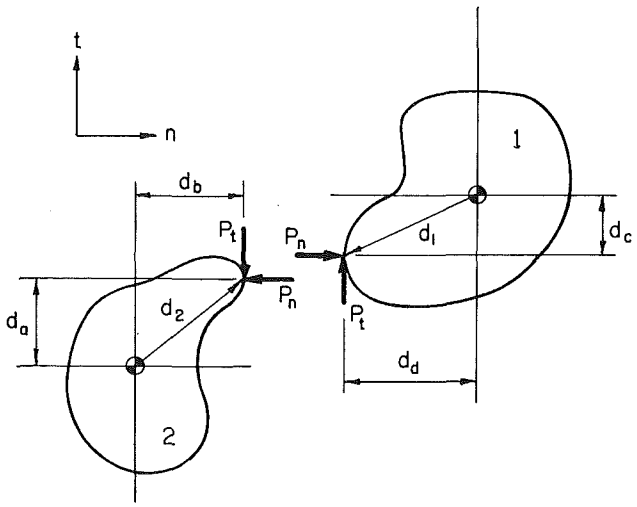


Fig. 1 Free body diagrams of bodies colliding in a plane

The final example, the rigid spherical pendulum, is presented because Keller (1986) presents some incorrect results for this problem. His equations for impact of unconstrained rigid bodies are applied inappropriately to this problem which is constrained due to the absence of linear velocity at the pivot. This same mistake is made in an earlier work on impact by Brach (1981).

A Planar Collision of Two Rigid Bodies. Figure 1 shows free body diagrams of two colliding rigid bodies (lamina). Reduction of the earlier equations to two dimensions and solution of these equations provides the following final velocity expressions:

$$V_{1n} = v_{1n} + \overline{m}(1+e)qv_{rn}/m_1 \tag{16}$$

$$V_{1t} = v_{1t} + \mu\overline{m}(1+e)qv_{rn}/m_1 \tag{17}$$

$$V_{2n} = v_{2n} - \overline{m}(1+e)qv_{rn}/m_2 \tag{18}$$

$$V_{2t} = v_{2t} - \mu\overline{m}(1+e)qv_{rn}/m_2 \tag{19}$$

$$\Omega_1 = \omega_1 + \overline{m}(1+e)d_{cd}qv_{rn}/I_1 \tag{20}$$

$$\Omega_2 = \omega_2 + \overline{m}(1+e)d_{ab}qv_{rn}/I_2 \tag{21}$$

where

$$v_{rn} = (v_{2n} - d_a\omega_2) - (v_{1n} + d_c\omega_1) \tag{22}$$

$$q = \frac{1}{1 + \dfrac{\overline{m}d_c^2}{I_1} + \dfrac{\overline{m}d_a^2}{I_2} - \mu\left(\dfrac{\overline{m}d_c d_d}{I_1} + \dfrac{\overline{m}d_a d_b}{I_2}\right)} \tag{23}$$

$$d_{cd} = d_c - \mu d_d \quad \text{and} \quad d_{ab} = d_a - \mu d_b \tag{24}$$

and

$$\overline{m} = m_1 m_2/(m_1 + m_2). \tag{25}$$

Downloaded 03 May 2010 to 171.66.16.31. Redistribution subject to ASME license or copyright; see http://www.asme.org/terms/Terms_Use.cfm

Values of P_n and P_t can be found from the momenta change and by using $P_t = \mu P_n$.

The change in kinetic energy due to the impact is written as T_L which is the initial energy minus the final. This is

$$T_L = \frac{1}{2}\,\overline{m}((1+e)qv_{rn}^2\left[2+2\mu r\right.$$

$$\left. -(1+e)q\left(1+\mu^2+\frac{\overline{m}d_{cd}^2}{I_1}+\frac{\overline{m}d_{ab}^2}{I_2}\right)\right]. \tag{26}$$

This suitably reduces to the point mass results of Brach (1984). Since T_L depends nonlinearly upon μ, its maximum[2] can be found. This is

$$\mu_m = \frac{\frac{r}{1+e}A+\frac{1}{1+e}B}{1+C+\frac{r}{1+e}B-\frac{e}{1+e}\frac{B^2}{A}} \tag{27}$$

where

$$A = 1+\frac{\overline{m}d_c^{\,2}}{I_1}+\frac{\overline{m}d_a^2}{I_2},\quad B=\frac{\overline{m}d_c d_d}{I_1}+\frac{\overline{m}d_a d_b}{I_2},$$

$$C=\frac{\overline{m}d_d^{\,2}}{I_1}+\frac{\overline{m}d_b^{\,2}}{I_2} \tag{28}$$

and

$$r=\frac{(v_{2t}+d_b\omega_2)-(v_{1t}-d_d\omega_1)}{(v_{2n}-d_a\omega_2)-(v_n+d_c\omega_1)}. \tag{29}$$

Note that, following earlier notation,

$$\mu_{\max} = \mu_m\,|_{e=0} = \frac{rA+B}{1+C+rB}. \tag{30}$$

Another important value of μ can be found, that is the value of μ which corresponds to zero final relative tangential velocity at the contact point. This is

$$\mu_o = \frac{rA+(1+e)B}{rB+(1+e)(1+C)} \tag{31}$$

Finally, μ_T is found where μ_T corresponds to the point where $T_L = 0$. Using equation (26), this is found to be

$$\mu_T(e) = \frac{rA+eB}{2rB+(1+e)(1+C)}\times$$

$$\left\{1\pm\left[1+(1-e)A\frac{2rB+(1+e)(1+C)}{(rA+eB)^2}\right]^{1/2}\right\}. \tag{32}$$

Equations (30), (31), and (32) verify the general result that

$$\mu_{\max} = \mu_o(e=0) = \mu_T(e=1). \tag{33}$$

In addition, when $B=0$, $\mu_o = \mu_m$. From equation (28) this occurs for $d_c d_d = 0$ and $d_a d_b = 0$. In practice, this typically occurs when $d_a = d_c = 0$ (see from Fig. 1) and corresponds, for example, to collisions of spheres. The case where $d_a = d_b = d_c = d_d = 0$ is, of course, when bodies are point masses. Regardless of the circumstances, when $B=0$ the critical value of μ is such that $|\mu_c| = |\mu_o|$. When $B \neq 0$, then the critical value of μ is the smaller of $|\mu_o|$ and $|\mu_T|$. This is reflected in equation (14).

B. Example of a Falling Rod. The significance of the following example is not only because it has been solved incorrectly in the past, but also because it displays a particularly troublesome frictional behavior. Figure 2 shows the rod, its geometry and coordinate system at impact. The problem solved here is for zero initial angular velocity, ω, and for dry friction at the contact point. The troublesome behavior occurs because $B \neq 0$ and

(1) for a vertical fall, $v_t = 0$, the final tip velocity V_{cf} is negative due to kinematical conditions and

(2) for a small positive initial velocity v_t, the final tip velocity V_{cf} is still negative.

Items 1 and 2 together imply sign reversal of the tip's tangential velocity over the surface at point C during the duration of contact. The dynamics of this velocity reversal are treated in great depth in Keller (1986) in an attempt to uncover the conditions in which energy is or is not conserved.

Figures 3 through 6 show the energy loss for the impact of a rod of unit mass and unit length, falling with a unit initial normal velocity $v_n = -1$. The results in Fig. 3 are for zero initial tangential velocity. Figures 4, 5 and 6 are for different initial horizontal mass center velocities. Note that $m_2 \to \infty$ and $I_2 \to \infty$ in equations (16) through (21) for this example.

For $v_t = 0$ (and $\omega = 0$), equation (29) gives $r = 0$. Furthermore, $\mu_{\max}$, $\mu_o(e)$, $\mu_T(1)$, and μ_c are all equal to 0.6. If $f \leq 0.6$, then the proper solution is for $\mu = f$. If $f > 0.6$, then the solution (equations (16) through (21)) is for $\mu = \mu_c$. Note that for

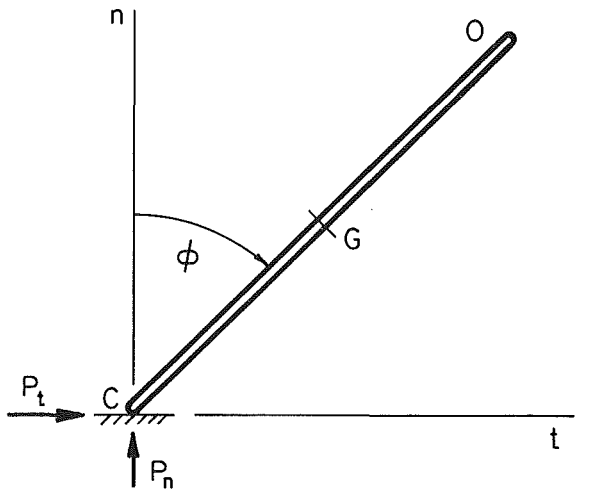


Fig. 2 Falling rod colliding with a massive, horizontal surface with friction. In all examples, mass, $m=1$; length, $2d=1$; moment of inertia, $I_G = 1/12$; $\phi = 45$ deg, initial angular velocity, $\omega = 0$; and initial normal velocity, $v_n = -1$

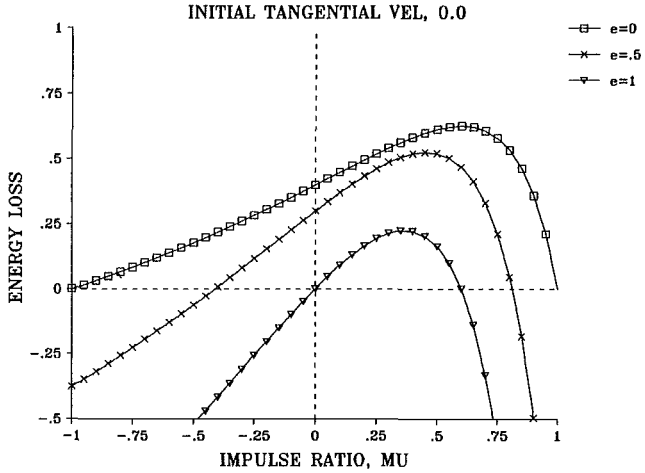


Fig. 3 Energy loss of a collision of a falling rod with a massive horizontal plane; vertical fall, $v_t = 0$

[2]The fact that this extremum is a maximum is not proven, but is arguable by considering the work of the impulses P_n and P_t when P_t opposes the tangential velocity.

Downloaded 03 May 2010 to 171.66.16.31. Redistribution subject to ASME license or copyright; see http://www.asme.org/terms/Terms_Use.cfm

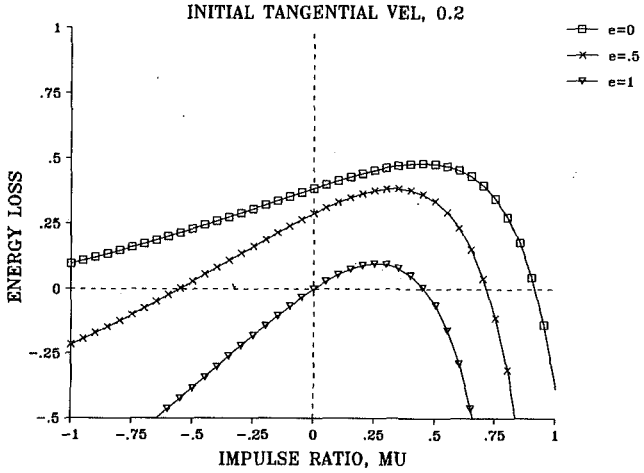


Fig. 4 Energy loss of a collision of a falling rod with a massive horizontal plane; initial horizontal velocity, $v_t = 0.2$

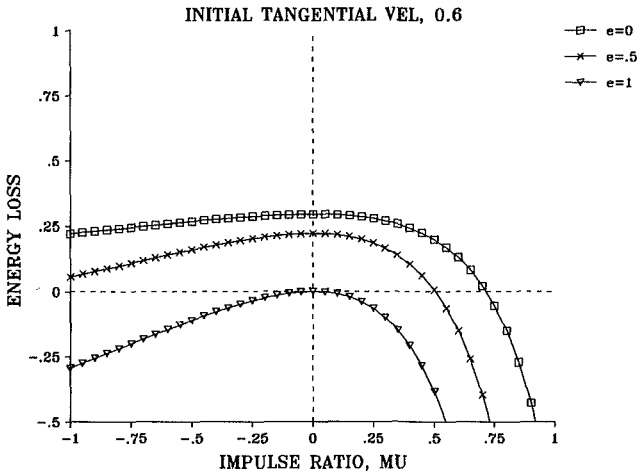


Fig. 5 Energy loss of a collision of a falling rod with a massive horizontal plane; initial horizontal velocity, $v_t = 0.6$

$e = 1$ and $\mu = \mu_{\max}$, Fig. 3 shows that the energy loss is zero. In this case this occurs because the friction is high enough to prevent the rod's tip from gaining a final tangential velocity from the impact. That is, both the initial and final tangential tip velocities are zero and so the tangential impulse does no work. This together with $e = 1$ results in no energy loss for the collision.

If (for $e = 1$) a value of $\mu > 0.6$ is used in the solution equations, energy will be gained which is a negative energy loss. In addition, the final tip velocity will be positive, opposite the direction for the frictionless case ($\mu = f = 0$).

As pointed out by Keller (1986) velocity reversals at the contact point can occur. Figure 4 shows the energy loss for the case where the initial tangential velocity, $v_t = 0.2$. Here, $\mu_{\max} = 0.45$. For all values of $\mu < \mu_o$, the final tip velocity is negative. Consequently, the tip approaches the surface with a positive tangential velocity but leaves or rebounds with a negative value. If the initial tangential velocity is 0.6 (see Fig. 5), the value of $\mu_{\max}$ is zero. For $e = 0$ the final tangential tip velocity is zero for a frictionless condition (for this initial velocity). For any value of μ other than zero, the tangential impulse will do positive work on the system. Consequently, for any value of frictional coefficient, the proper solution for $e = 0$ is found with $\mu = 0$. The use of nonzero values of μ may not cause an energy gain, but are still inappropriate since a tangential impulse, μP_n, will exist where none should. This is analogous to the collision of a ball dropped vertically onto a

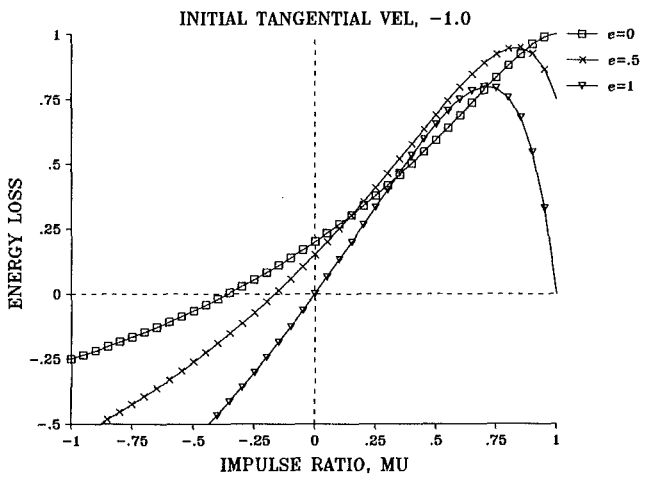


Fig. 6 Energy loss of a collision of a falling rod with a massive horizontal plane; initial horizontal velocity, $v_t = -1.0$

horizontal surface; no tangential impulse can develop, regardless of the value of the friction coefficient. For $e = 1$, $\mu_c = \mu_o = 0$ as well, and any value of μ other than zero will cause energy to be added to the system. For $0 < e < 1$, both μ_o and μ_T are greater than zero; the smaller of these may be μ_c.

The final initial conditions considered are for $v_t = v_n = -1.0$. The corresponding energy loss curves are shown in Fig. 6. This case corresponds to a javelin oriented at 45 deg, and whose tip hits a hard surface. Here, $\mu_{\max} = 1.0$. The overall maximum energy loss is 1.0, and corresponds to the kinematical conditions of zero final tip velocity and angular velocity. That is, the rod loses all of its energy. Note also that the energy loss curves in Fig. 6 intersect each other. This interesting phenomenon implies that for some values of μ, more energy can be lost by increasing the restitution coefficient, that is, making the collision more elastic. This appears to be the first time that this has ever been observed.

Of course, for these and all other initial conditions considered, μ cannot be negative since sign $(\mu) =$ sign $(\mu_{\max})$. A negative value of μ would correspond to the surface enhancing the tip velocity instead of retarding it.

C. Example of a Rigid Pendulum. A rigid spherical pendulum whose tip strikes a flat massive surface is a three-dimensional problem. The above work does not directly apply because the presence of a fixed pivot requires a velocity constraint on the rigid body, so the equations must be revised. Figure 7 shows the pendulum and associated coordinates. The x-, y-, z-axes are body axes where the x-axis lies along the pendulum. The n-axis is normal to the surface, as before. The previous three-dimensional equations could be used and constraint equations added, however, the equations are much simpler if rotation about point O is included right from the start. The system's rotational energy about the x-axis is neglected and the corresponding angular velocities ω_x and Ω_x are assumed to be zero.

The concept of restitution (equation (6)) provides

$$\boldsymbol{\Omega} \times \mathbf{d} \cdot \mathbf{n} = -e\boldsymbol{\omega} \times \mathbf{d} \cdot \mathbf{n} \tag{33}$$

The resultant tangential impulse (equation (10)) is

$$P_{tt'} = \sqrt{P_t^2 + P_{t'}^2} = \mu P_n \tag{34}$$

where $P_t = \mu_t P_n = \mu \cos\eta \; P_n$ and $P_{t'} = \mu_{t'} P_n = \mu \sin\eta \; P_n$. Equating changes in angular momentum to the moment of the impulses about the fixed point O, gives

$$I_y (\Omega_y - \omega_y) = d\mu_{t'} P_n \tag{35}$$

and

Downloaded 03 May 2010 to 171.66.16.31. Redistribution subject to ASME license or copyright; see http://www.asme.org/terms/Terms_Use.cfm

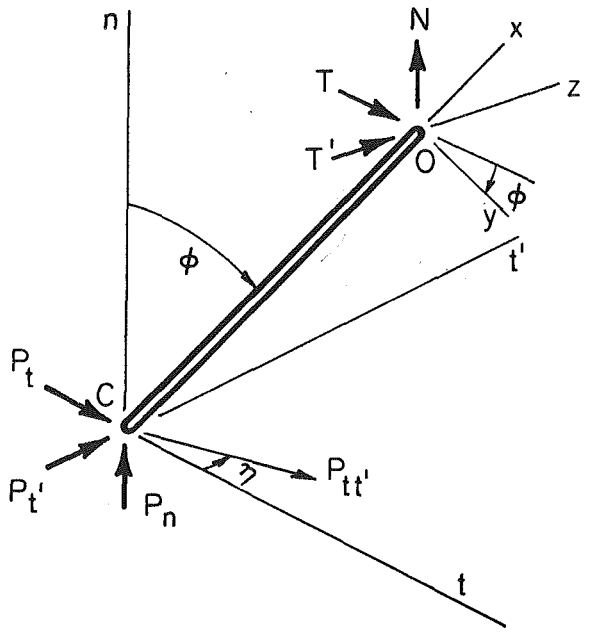


Fig. 7 Uniform rigid spherical pendulum pivoted at O and striking a massive surface at C. Mass, m; momentum of inertia, I_o; length, d; and initial angular velocities ω_y, and ω_z ($\omega_x = 0$)

$$I_z(\Omega_z - \omega_z) = d(\sin\phi - \mu_t \cos\phi)P_n. \tag{36}$$

The system has two degrees-of-freedom corresponding to the rotational velocities about the y- and z-axis, so there are four unknowns, Ω_y, Ω_z, P_n and $P_{tt'}$. Equation (33) simplifies to

$$\Omega_z = -e\omega_z. \tag{37}$$

Substitution of this into equation (36) gives

$$P_n = -\frac{(1+e)I_z\omega_z}{d(\sin\phi - \mu_t\cos\phi)}. \tag{38}$$

This, in turn, makes equation (35) become

$$\Omega_y = \omega_y - \mu_{t'}\frac{(1+e)\omega_z}{(\sin\phi - \mu_t\cos\phi)}\frac{I_z}{I_y}. \tag{39}$$

Relative motion of the pendulum's tip over the surface (i.e., sliding) can correspond only to Ω_y and not Ω_z so the resultant tangential impulse is such that $\eta = \pi/2$. The system's energy loss is

$$T_L = \frac{1}{2} I_z\omega_z^2(1+e)\left[(1-e) + \frac{2\mu}{\sin\phi}\frac{\omega_y}{\omega_z} - \mu^2\frac{(1+e)I_z}{\sin^2\phi I_y}\right]. \tag{40}$$

Setting to zero the derivative of T_L with respect to μ gives

$$\mu_m = \frac{\sin\phi}{1+e}\frac{I_y\omega_y}{I_z\omega_z} \tag{41}$$

from which for $e=0$, $\mu_{\max} = I_y\omega_y \sin\phi/I_z\omega_z$. Using equation (41) in equation (39) gives

$$\Omega_y = \omega_y(1 - \mu/\mu_m). \tag{42}$$

Equations (37) and (42) provide the solution of the rigid pendulum impact problem. The tangential tip impulse is

$$P_{tt'} = \mu P_n = -\frac{\mu I_y\omega_y}{\mu_m d}. \tag{43}$$

For the special case of a planar pendulum $\omega_y = 0$ and from equation (41), $\mu_{\max} = 0$. Here, because the pendulum is rigid and has only one degree-of-freedom, no tangential impulse can develop. These results differ from those of Keller (1986).

IV Conclusions

A complete analytical solution is provided for the planar collision of two rigid bodies, an heretofore unsolved problem in mechanics. Of particular significance to this, as well as the three-dimensional problem, is the procedure for handling the tangential impulse, particularly when it is due to the process of dry friction. The energy loss, T_L was shown to be a quadratic function of the impulse ratio μ. The maximum of T_L with respect to μ possesses some important properties. These are that

$$\mu_{\max} = \mu_m(e=0) = \mu_o(e=0) = \mu_T(e=1)$$

where μ_m is the impulse ratio which maximizes T_L, μ_o is the value of μ which causes the final relative tangential velocity at the contact point to be zero and μ_T corresponds to zero energy loss. Furthermore, in order to satisfy energy conservation principles, the value of μ used to obtain a solution for the case of dry friction must be such that

$$|\mu| \le |\mu_c| = \min(f, |\mu_o|, |\mu_T|) \quad \text{and} \quad \text{sign}(\mu) = \text{sign}(\mu_{\max})$$

where f is the coefficient of friction of the contact surfaces.

$T_L(e=0, \mu_{\max})$ provides an upper bound to the energy lost from a rigid body collision. Note that maximization of T_L is not necessary to find $\mu_{\max}$. It can found by the solution for zero final relative motion and the recognition that $\mu_{\max} = \mu_o(e=0)$.

The approach presented in this paper for the solution of rigidy body impact problems is to treat the tangential impulse as a constant fraction, μ, of the normal impulse. The energy loss is then examined as μ varies to reveal admissible values of μ and corresponding values of a friction coefficient, when appropriate. This approach avoids violation of energy conservation laws, a difficulty often encountered by other approaches.

References

Brach, R. M., 1981, "Moments Between Impacting Rigid Bodies," *J. Mech. Design*, Vol. 103, pp. 812–817.

Brach, R. M., 1984, "Friction Restitution and Energy Loss in Planar Collisions," ASME JOURNAL OF APPLIED MECHANICS, Vol. 51, pp. 164–170.

Brach, R. M., 1988, "An Impact Model with Applications to Erosion and Wear," *Int. J. of Impact Engineering*, Vol. 7, No. 1.

Goldsmith, W., 1960, *Impact*, Edw. Arnold.

Horak, Z., 1948, "Impact of a Rough Ball Spinning Round Its Vertical Diameter Onto a Horizontal Plane," *Trans. of the Faculty of Mechanical and Electrical Engineering of the Tech. Univ. of Prague*, Czechoslovakia.

Kane, T. R., and Levinson, D. A., 1985, *Dynamics: Theory and Applications*, McGraw-Hill, New York, p. 348.

Keller, J. B., "Impact with Friction," 1986, ASME JOURNAL OF APPLIED MECHANICS, Vol. 53, pp. 1-4.

Kilmister, C. W., and Reeve, J. E., 1966, *Rational Mechanics*, Longmans, London.

Macaulay, M., 1987, *Introduction to Impact Engineering*, Chapman and Hall, London.

Downloaded 03 May 2010 to 171.66.16.31. Redistribution subject to ASME license or copyright; see http://www.asme.org/terms/Terms_Use.cfm

Hui Cheng[1]
Graduate Fellow.

K. C. Gupta[2]
Professor.
Mem. ASME

Department of Mechanical Engineering,
University of Illinois at Chicago
Chicago, Ill. 60680

An Historical Note on Finite Rotations

It is shown in this paper that Euler was first to derive the finite rotation formula which is often erroneously attributed to Rodrigues, while Rodrigues was responsible for the derivation of the composition formulae for successive finite rotations and the so-called Euler parameters of finite rotation. Therefore, based upon historical facts, the following nomenclature is suggested: Euler's finite rotation formula, Rodrigues' composition formulae of finite rotations, and Euler-Rodrigues parameters. The text of the paper contains modern symbols and formula forms, while the Appendices contain brief summaries from relevant historical sources with minor alterations in symbols at the most.

I Introduction

To determine the final displacement of a point of a rigid body which undergoes a finite rotation around a fixed axis in space is a classical problem, which has attracted the attention of many researchers. Derivations of the finite rotation formula by using the different tools, such as scalars, quaternions, vectors, matrices, and tensors, etc., have been published. However, there exists some confusion about who was the first contributor of the derivation of the finite rotation formula (Goldstein, 1980, p. 165). In our opinion, the formula should be ascribed to the person who first gave the fundamental formula for finite rotation regardless of the form the formula was written in. Through our historical reference survey, we find that the finite formula is often used without an eponymic designation in textbooks and reference books; but in many cases, the formula is erroneously ascribed to the French mathematician Olinde Rodrigues (1794–1851) such as in Hamel (1949, p. 103), Hiller and Woernle (1984), and Craig (1986, p. 58). Although one can find the derivation of the finite rotation (as well as displacement) formula by using Rodrigues parameters in Rodrigues' paper (Rodrigues, 1840, pp. 403–404), the rotation formula expressed in terms of the direction cosines of the rotation axis and the rotation angle was derived by the Swiss mathematician Leonhard Euler (1707–1783) in Euler (1775b, p. 216) or Euler (Vol. 9, p. 107) and was published 65 years earlier than Rodrigues' paper as is discussed in the following section.

On the other hand, the composition formulae of rotations which are commonly given without an eponymic designation were actually derived by Rodrigues. For proper recognition of contributions, which is also the main purpose of this paper, the composition formulae of rotations should be attributed to Rodrigues.

II Euler's Finite Rotation Formula and Euler-Rodrigues Parameters

The following is Euler's theorem which is well known: *The general displacement of a rigid body with one point fixed is a rotation about some axis* (Euler, 1775a, p. 202; Euler, Vol. 9, p. 95; Goldstein, 1980, p. 158). The spatial displacement of a rigid body about a fixed point O can always be represented as a spherical rotation of a general point P described by the position vector $\mathbf{r}$ as shown in Fig. 1. According to the Euler's theorem, one can represent the spherical rotation of the vector $\mathbf{r}$ in terms of the rotation parameters: the angle of rotation ϕ and the unit vector $\mathbf{n}$ along the axis of rotation. The following vector representation of the rotation formula is commonly used (Gibbs, 1901, p. 338), (Bisshopp, 1969), (Beatty, 1977), and (Goldstein, 1980, p. 165):

$$\begin{aligned}\mathbf{r}' &= \mathbf{r}\cos\phi + (\mathbf{n}\times\mathbf{r})\sin\phi + \mathbf{n}(\mathbf{n}\cdot\mathbf{r})(1-\cos\phi)\\ &= \mathbf{r} + (\mathbf{n}\times\mathbf{r})\sin\phi + [\mathbf{n}\times(\mathbf{n}\times\mathbf{r})](1-\cos\phi),\end{aligned} \tag{1}$$

where $\mathbf{r}$ and $\mathbf{r}'$ are the initial and final positions of the vector, respectively, as is shown in Fig. 1. In order to show the similarity between the formula derived by Euler and other commonly used representations, and to try to explain how Rodrigues has been erroneously credited for the discovery of the formula (1), the following different version of the rotation formula will be discussed.

Since the rotation matrix can be treated as a linear operator, and is intuitively simple, the matrix representation of rigid body rotation is popularly used. If one defines the skew symmetrical matrix $\mathbf{N}$ corresponding to a unit vector $\mathbf{n} = [n_1, n_2, n_3]^T$ as follows

$$\mathbf{N} = \begin{bmatrix} 0 & -n_3 & n_2 \\ n_3 & 0 & -n_1 \\ -n_2 & n_1 & 0 \end{bmatrix}, \tag{2}$$

[1]Member, AMS.

[2]To whom all correspondence should be addressed.

Contributed by the Applied Mechanics Division of THE AMERICAN SOCIETY OF MECHANICAL ENGINEERS for publication in the JOURNAL OF APPLIED MECHANICS.

Discussion on this paper should be addressed to the Editorial Department, ASME, United Engineering Center, 345 East 47th Street, New York, N.Y. 10017, and will be accepted until two months after final publication of the paper itself in the JOURNAL OF APPLIED MECHANICS. Manuscript received by ASME Applied Mechanics Division, March 7, 1988; final revision, August 17, 1988.

Copyright © 1989 by ASME

Downloaded 03 May 2010 to 171.66.16.31. Redistribution subject to ASME license or copyright; see http://www.asme.org/terms/Terms_Use.cfm

then the cross product $\mathbf{n}\times\mathbf{r}$ of two vectors $\mathbf{n}$ and $\mathbf{r}$ can be expressed in matrix form as

$$\mathbf{n}\times\mathbf{r}=\mathbf{N}\mathbf{r}. \tag{3}$$

Substituting (3) into (1), we can obtain the following matrix representation of finite rotations

$$\mathbf{r}'=\mathbf{R}\mathbf{r}, \tag{4}$$

$$\mathbf{R}=\mathbf{I}+\mathbf{N}\sin\phi+\mathbf{N}^2(1-\cos\phi), \tag{5}$$

where $\mathbf{I}$ is the unit matrix, and $\mathbf{R}=\mathbf{R}(\phi)$ is the rotation matrix in terms of the direction cosines n_1, n_2, n_3 of the axis of rotation and the rotation angle ϕ.

Without losing generality, one can replace the position vector $\mathbf{r}$ and $\mathbf{r}'$ by the unit vectors $\mathbf{r}_n'$ and $\mathbf{r}_n$, respectively. Then, equation (4) becomes

$$\mathbf{r}_n'=\mathbf{R}\mathbf{r}_n. \tag{6}$$

Defining the direction cosines of unit vectors $\mathbf{n}$, $\mathbf{r}_n$, and r_n', respectively, as follows:

$$\mathbf{n}=\begin{bmatrix}\cos\alpha\\ \cos\beta\\ \cos\gamma\end{bmatrix},\ \mathbf{r}_n=\begin{bmatrix}\cos\zeta\\ \cos\eta\\ \cos\theta\end{bmatrix},\ \mathbf{r}_n'=\begin{bmatrix}\cos\zeta'\\ \cos\eta'\\ \cos\theta'\end{bmatrix}, \tag{7}$$

and substituting (5) and (7) into (6) will result in

$$\begin{aligned}
\cos\zeta' &= \cos\zeta(\cos^2\alpha+\sin^2\alpha\cos\phi)\\
&+ \cos\eta(\cos\alpha\cos\beta(1-\cos\phi)-\cos\gamma\sin\phi)\\
&+ \cos\theta(\cos\alpha\cos\gamma(1-\cos\phi)+\cos\beta\sin\phi)\\
\cos\eta' &= \cos\eta(\cos^2\beta+\sin^2\beta\cos\phi)\\
&+ \cos\theta(\cos\beta\cos\gamma(1-\cos\phi)-\cos\alpha\sin\phi)\\
&+ \cos\zeta(\cos\alpha\cos\beta(1-\cos\phi)+\cos\gamma\sin\phi)\\
\cos\theta' &= \cos\theta(\cos^2\gamma+\sin^2\gamma\cos\phi)\\
&+ \cos\zeta(\cos\alpha\cos\gamma(1-\cos\phi)-\cos\beta\sin\phi)\\
&+ \cos\eta(\cos\beta\cos\gamma(1-\cos\phi)+\cos\alpha\sin\phi).
\end{aligned} \tag{8}$$

$$\mathbf{R}=\frac{1}{1+b_1^2+b_2^2+b_3^2}\begin{bmatrix}1+b_1^2-b_2^2-b_3^2 & 2(b_1b_2-b_3) & 2(b_1b_3+b_2)\\ 2(b_1b_2+b_3) & 1-b_1^2+b_2^2-b_3^2 & 2(b_2b_3-b_1)\\ 2(b_1b_3-b_2) & 2(b_2b_3+b_1) & 1-b_1^2-b_2^2+b_3^2\end{bmatrix}. \tag{11b}$$

This form of rotation formulae was actually derived by Euler (1775b, p.216) or Euler (Vol. 9, p. 107) as is shown in Appendix [A.I.]. Therefore, the finite rotation formula (1) or (4) and (5) is nothing but a vector or matrix form of the formulae (8) obtained by Euler more than two hundred years ago. Our conclusion also seems to be supported by Cayley (1846), Benedikt (1944), and Hill (1945).

If one uses Euler angles, ϕ, θ, and ψ, the following rotation matrix can be obtained (Euler, 17??, p. 51; Euler, Vol. 9, p. 424; Goldstein, 1980, p. 147, Eq. (9)).

$$\mathbf{R}=\begin{bmatrix}\cos\psi\cos\phi-\cos\theta\sin\phi\sin\psi & -\sin\psi\cos\phi-\cos\theta\sin\phi\cos\psi & \sin\theta\sin\phi\\ \cos\psi\sin\phi+\cos\theta\cos\phi\sin\psi & -\sin\psi\sin\phi+\cos\theta\cos\phi\cos\psi & -\sin\theta\cos\phi\\ \sin\theta\sin\psi & \sin\theta\cos\psi & \cos\theta\end{bmatrix}, \tag{9}$$

where the angle ϕ, θ, and ψ are precession, nutation, and spin angles, respectively. It is noticed that the original paper about the derivation details of Euler angles was published in Euler (17??) or Euler (Vol. 9, p. 413-441) after Euler's death (1707-1783) instead of in Euler (1775a), as was erroneously referred to by Whittaker (1937, p. 9). In Euler (1775a), Euler only derived the rotation formula expressed in terms of three

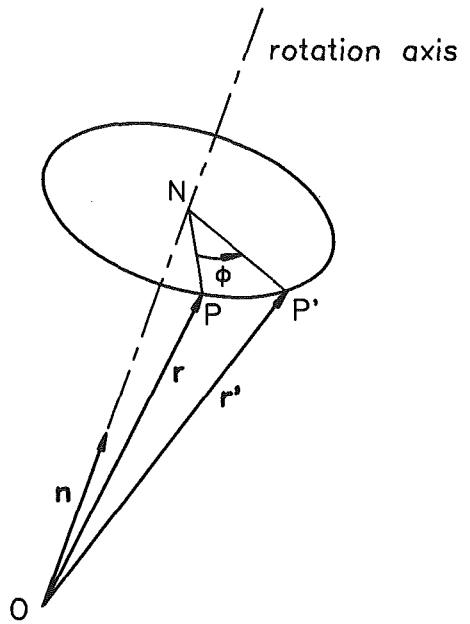


Fig. 1 The vector diagram for Euler's finite rotation formula

independent angles as is shown in Appendix C, but these angles are not what came to be known as Euler angles.

Due to the large number of trigonometric functions involved, the Euler angles are difficult to use in numerical computations for the large scale multibody mechanical systems. If one uses Rodrigues parameters (Rodrigues, 1840, p. 400; Bottema and Roth, 1979, p. 148):

$$b_1=n_1\tan\frac{\phi}{2},\ b_2=n_2\tan\frac{\phi}{2},\ b_3=n_3\tan\frac{\phi}{2}, \tag{10}$$

then the expression (1) becomes

$$\mathbf{r}'-\mathbf{r}=\frac{2(\mathbf{b}\times\mathbf{r})+2\mathbf{b}(\mathbf{b}\cdot\mathbf{r})-2(\mathbf{b}\cdot\mathbf{b})\mathbf{r}}{1+\mathbf{b}\cdot\mathbf{b}} \tag{11a}$$

where $\mathbf{b}=[b_1, b_2, b_3]^T$, and the rotation matrix (5) becomes

The corresponding rotational elements derived by Rodrigues are shown in Appendix AII. Rodrigues parameters (10) were used by the Irish mathematician Arthur Cayley (1821-1895) to study the motion of a rigid body in Cayley (1843), (1846), and (1848). One disadvantage of using Rodrigues parameters (10) is that the rotation matrix (11*b*) is singular when $\phi=\pi$.

For the general computer implementation of multibody dynamic systems, the following four parameters are extensively used:

$$e_0=\cos\frac{\phi}{2},\ e_1=n_1\sin\frac{\phi}{2},\ e_2=n_2\sin\frac{\phi}{2},\ e_3=n_3\sin\frac{\phi}{2}, \tag{12}$$

which satisfy the relation

$$e_0^2+e_1^2+e_2^2+e_3^2=1. \tag{13}$$

These four parameters are customarily called Euler

Downloaded 03 May 2010 to 171.66.16.31. Redistribution subject to ASME license or copyright; see http://www.asme.org/terms/Terms_Use.cfm

parameters (Whittaker, 1937, p. 8; Bottema and Roth, 1979, p. 150; Goldstein, 1980, p. 153; Kane et al., 1983, p. 12). Presumably, these four parameters were discussed in Euler's paper (1775b, p. 217), as was mentioned by Klein (1884 or 1914, p. 38) and Whittaker (1937, p. 8). The German mathematician Felix Klein's (1849–1925) statements may explain why Euler's name is ascribed to the parameters (12). In Klein (1914, p. 38), Klein claimed that "That it was proper, in the treatment of rotations around a fixed point, to introduce the parameters a, b, c, d of the preceding paragraph (or at least their quotients a/d, b/d, c/d), *Euler* had already found" in Euler (1775b, p. 217). The parameters a, b, c, and d in the above Klein's statements are the parameters (12) e_1, e_2, e_3, and e_0, respectively, and the parameters a/d, b/d, c/d are the so-called Rodrigues' parameters (10). But the fact is that Euler did not use these parameters to describe finite rotations explicitly in Euler (1775b, p. 217). Even half angles of the rotation which are crucial to these parameters can not be found in all of Euler's papers (Nos. 12–16) referred at the end of this paper through our historical reference survey. It was Rodrigues who defined the parameters (12) explicitly and used them to derived the composition formulae in Rodrigues (1840, p. 408) as is shown in Appendix B. Therefore, the parameters (12) should be attributed to Rodrigues instead of Euler. However, to distinguish these from Rodrigues parameters (10), the parameters (12) are called Euler-Rodrigues parameters hereafter, as is also proposed by Altmann (1986, p. 20).

If one uses Euler-Rodrigues parameters (12) and the result derived by Rodrigues (1840, p. 404), and notices that

$$\mathbf{r}=[\mathbf{R}(\phi)]^{-1}\mathbf{r}'=[\mathbf{R}(-\phi)]\mathbf{r}', \quad \mathbf{R}(\phi)=[\mathbf{R}(-\phi)]^{-1}, \tag{14}$$

where $\mathbf{r}=[x,\ y,\ z]^T$, and $\mathbf{r}'=[x',\ y',\ z']^T=[x+\Delta x,\ y+\Delta y,\ z+\Delta z]^T$ as defined in Appendix AII then, the following rotation matrix will be obtained.

$$\mathbf{R}=\begin{bmatrix} 2(e_0^2+e_1^2)-1 & 2(e_1e_2-e_0e_3) & 2(e_1e_3+e_0e_2) \\ 2(e_1e_2+e_0e_3) & 2(e_0^2+e_2^2)-1 & 2(e_2e_3-e_0e_1) \\ 2(e_1e_3-e_0e_2) & 2(e_2e_3+e_0e_1) & 2(e_0^2+e_3^2)-1 \end{bmatrix}. \tag{15}$$

The same result can be derived from equation (5) by using Euler-Rodrigues parameters (12) directly.

One of the applications of Euler-Rodrigues parameters is found in the quaternion representation of the finite rotation formula. The quaternion was conceived by the Irish mathematician and astronomer William Rowan Hamilton (1805–1865) when he was on the way to presiding a meeting of the Royal Irish Academy on Monday, October 16, 1843 (Hamilton, 1844; 1853, p. 48; Graves, 1885, Vol. II, p. 434). The number

$$q=a+bi+cj+dk \tag{16}$$

is called a quaternion with the following properties:

$$i^2=j^2=k^2=-1,$$

$$ij=-ji=k, \quad jk=-kj=i, \quad ki=-ik=j. \tag{17}$$

If one defines the following unit quaternion via Euler-Rodrigues parameters,

$$q=e_0+e_1i+e_2j+e_3k, \tag{18}$$

and the vectors $\mathbf{r}$ and $\mathbf{r}'$, which are the initial and final positions of a vector, respectively,

$$\mathbf{r}=0+x_1i+x_2j+x_3k, \tag{19}$$

$$\mathbf{r}'=0+x_1'i+x_2'j+x_3'k, \tag{20}$$

then the quaternion representation of the rotation formula will result as Cayley (1845), Hamilton (1853, p. 217; 1899, p. 359), Whittaker (1937, p. 9), and Corben and Stehle (1950, p. 171)

$$\mathbf{r}'=q\mathbf{r}q^{-1}, \tag{21a}$$

or

$$\mathbf{r}=q^{-1}\mathbf{r}'q. \tag{21b}$$

According to Cayley's note in his collected mathematical papers (1889, Vol. I, Note 20, p. 586), the quaternion formulae (21) itself was first derived by Hamilton. However, physical meaning of the quaternion form (21) in the context of finite rotation, utilizing Rodrigues parameters (10), was first discovered by Cayley [Cayley (1843)]. When expanded, the quaternion form (21) leads to formulae about which Cayley asserted in Cayley (1845) that "In fact the formulae are precisely those given for such a transformation by M. Olinde Rodrigues" in Rodrigues (1840) shown in Appendix AII.

III Rodrigues Composition Formulae of Finite Rotations

Euler in Euler (1775b) considered a single finite rotation and obtained the formula shown in the preceding section. Euler did not solve the problem of finding the resultant of successive finite rotations, although Euler's theorem affirms its existence. However, Altmann (1986, p. 19) has asserted that in Euler (1775a) "he considered the composition of two successive affine transformations (translation-rotations) and showed that the orientation of the final axes depends on six angular parameters, of which three can be eliminated algebraically, leaving three parameters only, thus determining a rotation. It must be made clear that Euler's approach is algebraic, not geometrical and that it is not constructive. That is, he does not provide closed expressions to determine the angle and axis of the resultant rotation. Euler, however, is most often credited for the solution of the existential, geometric, and constructive problems regarding the composition of two rotations." But the fact is that Euler (1775a) only discussed the representation of a single finite rotation and showed that it could be expressed by nine, and then six dependent angular parameters, and finally by three independent parameters, as is shown in Appendix C. It should be noted that the formulae (8) and (9) of a single finite rotation derived in Euler (1775b), and (17??), respectively, are much nicer in form than that in Euler (1775a).

It was Rodrigues who considered successive finite rotations (Rodrigues, 1840) and found the expressions for determining the orientation of the resultant axis of rotation and the geometrical value of the resultant angle of rotation from the given angles and axis orientations of the two rotations. Let us denote the Rodrigues parameters of the first rotation as

$$\mathbf{W}=\left[n_1\tan\frac{\phi}{2},\ n_2\frac{\phi}{2},\ n_3\tan\frac{\phi}{2}\right]^T=\mathbf{n}\tan\frac{\phi}{2}, \tag{22}$$

which is followed by the second rotation

$$\mathbf{W}'=\left[n'_1\tan\frac{\phi}{2},\ n_2'\tan\frac{\phi'}{2},\ n_3'\tan\frac{\phi'}{2}\right]^T=\mathbf{n}'\tan\frac{\phi'}{2}, \tag{23}$$

with the resultant rotation being

$$\mathbf{W}''=\left[n_1''\tan\frac{\phi''}{2},n_2''\tan\frac{\phi''}{2},n_3''\tan\frac{\phi''}{2}\right]^T=\mathbf{n}''\tan\frac{\phi''}{2}, \tag{24}$$

where $\mathbf{n}$, $\mathbf{n}'$, $\mathbf{n}''$, and ϕ, ϕ', ϕ'', are the unit vectors along the axes and the rotation angles of the first, second, and resultant

Downloaded 03 May 2010 to 171.66.16.31. Redistribution subject to ASME license or copyright; see http://www.asme.org/terms/Terms_Use.cfm

rotations, respectively. Rodrigues actually obtained the composition formula for two successive rotations (Rodrigues, 1840, p. 408), shown in Appendix B equation (B.1) which can be written in the following vector form (Gibbs, 1901, p. 345; Paul, 1963; Bisshopp, 1969),

$$\mathbf{W}'' = \frac{\mathbf{W} + \mathbf{W}' - \mathbf{W} \times \mathbf{W}'}{1 - \mathbf{W} \cdot \mathbf{W}'} = \mathbf{n}'' \tan \frac{\phi''}{2}. \tag{25}$$

The formula (25) appears in the later literature, but without an eponymic designation. Besides the formula (25) Rodrigues (1840, p. 408) also derived the composition formula (Appendix B equation (B.2)) which, by using the so-called Euler-Rodrigues parameters (12), becomes as follows:

$$\begin{cases} e_0'' = e_0 e_0' - e_1 e_1' - e_2 e_2' - e_3 e_3' \\ e_1'' = e_0 e_1' + e_1 e_0' - e_2 e_3' + e_3 e_2' \\ e_2'' = e_0 e_2' + e_1 e_3' + e_2 e_0' - e_3 e_1' \\ e_3'' = e_0 e_3' - e_1 e_2' + e_2 e_1' + e_3 e_0' \end{cases} \tag{26}$$

The four Euler-Rodrigues parameters $(e_0'', e_1'', e_2'', e_3'')$ are the resultant of two successive rotations (e_0, e_1, e_2, e_3) and (e_0', e_1', e_2', e_3'). Formula (26) can be written in the vector form as

$$\begin{cases} e_0'' = e_0 e_0' - \mathbf{e} \cdot \mathbf{e}' \\ \mathbf{e}'' = e_0 \mathbf{e}' + e_0' \mathbf{e} - \mathbf{e} \times \mathbf{e}', \end{cases} \tag{27}$$

where vectors, $\mathbf{e}$, $\mathbf{e}'$, and $\mathbf{e}''$ are defined, respectively, as follows:

$$\mathbf{e} = [e_1 e_2 e_3]^T,$$

$$\mathbf{e}' = [e_1' e_2' e_3']^T, \tag{28}$$

$$\mathbf{e}'' = [e_1'' e_2'' e_3'']^T.$$

If one defines the following quaternions,

$$q = e_0 + e_1 i + e_2 j + e_3 k,$$

$$q' = e_0' + e_1' i + e_2' j + e_3' k, \tag{29}$$

$$q'' = e_0'' + e_1'' i + e_2'' j + e_3'' k,$$

then, according to equation (21*a*),

$$\mathbf{r}'' = q' \mathbf{r}' q'^{-1} = q' q \mathbf{r} q^{-1} q'^{-1} = q'' \mathbf{r} q''^{-1}. \tag{30}$$

Therefore,

$$q'' = q' q. \tag{31}$$

Formulae (26) and (31) which constitute the theorem for the multiplication of quaternions were discovered by Hamilton according to his letter to John T. Graves dated October 17 of 1843 which was written just one day after the quaternion was conceived (Hamilton, 1844). Perhaps, Felix Klein's statements in Klein (1914, p. 38) are constructive. "It appears, however, that the formulae of composition (i.e., equation (26)) remained still unknown for a long time, till they were discovered by Rodrigues (Rodrigues, 1840). Hamilton then made the same formulae (Hamilton, 1844, p. 489) the foundation of his calculus of quaternions, without at first recognising their significance for the composition of rotations, which was soon brought to light by Cayley (Cayley, 1843, p. 141)." It is noticed that Cayley's paper was published in 1845, instead of 1843, as is referred to by Klein. Since Rodrigues first obtained the formulae (26), along with full physical meaning for combining rotations, we suggest that the formulae (25), (26), and (27) be called the Rodrigues' composition formulae for finite rotations.

IV Conclusions

From the preceding arguments, we conclude that it was Euler, not Rodrigues, who first derived the scalar form of the finite rotation formula (1). Rodrigues, on the other hand, derived the scalar form of the composition formulae (25), (26), and (27) for successive finite rotations, and was also responsible for the parameters (12).

For the terminology, we suggest that equation (1) be called as Euler's finite rotation formula; parameters (12) as Euler-Rodrigues parameters; and equations (25), (26), and (27) as Rodrigues' composition formulae for finite rotations.

V Acknowledgment

Financial support under USARO contract 24647EG/DAAL03-87-K-0041 is gratefully acknowledged.

References

Altmann, S. L., 1986, *Rotations, Quaternions, and Double Groups*, Clarendon Press, Oxford, U.K.

Beatty, M. F., 1977, "Vector Analysis of Finite Rigid Rotations," ASME, JOURNAL OF APPLIED MECHANICS, Vol. 44, pp. 501–502.

Benedikt, E. T., 1944, "On the Representation of Rigid Rotations," *J. of Applied Physics*, Vol. 15, pp. 613–615.

Bisshopp, K. E., 1969, "Rodrigues' Formula and the Screw Matrix," ASME, *Journal of Engineering for Industry*, Vol. 91, pp. 179–185.

Bottema, O., and Roth, B., 1979, *Theoretical Kinematics*, North-Holland Pub. Co., Amsterdam, The Netherlands.

Cayley, A., 1843, "On the Motion of Rotation of a Solid Body," *Cambridge Math. Journal*, Vol. III, pp. 224–232; also *The Collected Mathematical Papers*, Vol. I, pp. 28–35, (Paper No. 6), 13 Volumes plus Index, Cambridge Univ. Press, 1889.

Cayley, A., 1845, "On Certain Results Relating to Quaternions," *Phil. Mag.*, Vol. 26, pp. 141–145; also *The Collected Mathematical Papers*, Vol. I, pp. 123–126, (paper No. 20) and Note 20, p. 586, Cambridge Univ. Press, 1889.

Cayley, A., 1846, "On the Rotation of a Solid Body Round a Fixed Point," *Cambridge and Dublin Math. Journal*, Vol. I, pp. 167–173; also *The Collected Mathematical Papers*, Vol. I, pp. 237–252, (Paper No. 37), Cambridge Univ. Press, 1889.

Cayley, A., 1848, "On the Application of Quaternions to the Theory of Rotation," *Phil. Mag.*, Vol. 33, pp. 196–200; also *The Collected Mathematical Papers* Vol. I, pp. 405–409, (Paper No. 68), Cambridge Univ. Press, 1889.

Corbren, H. C., and Stehle, P., 1950, *Classical Mechanics*, John Wiley & Sons, Inc., New York.

Craig, J. J., 1986, *Introduction to Robotics, Mechanics and Control*, Addison-Wesley Pub. Co.

Euler, L., 1775a, "Formulae Generales pro Translatione Quacunque Corporum Rigidorum," *Novi Commentari Acad. Imp. Petrop.*, Vol. 20, pp. 189–207; also *Leonhardi Euleri Opera Omnia, Series Secunda, Opera Mechanica Et Astronomica*, Basileae MCMLXVIII, Vol. 9, pp. 84–98.

Euler, L., 1775b, "Nova Methodus Motum Corporum Rigidorum Determinandi," *Novi Commentari Acad. Imp. Petrop.*, Vol. 20, pp. 208–238; also *Leonhardi Euleri Opera Omnia, Series Secunda, Opera Mechanica Et Astronomica*, Basileae MCMLXVIII, Vol. 9, pp. 99–125.

Euler, L., 17??, "De Motu Corporum Circa Punctum Fixum Mobilium," *Commentatio 825 indicis ENESTROEMIANI, Opera postuma 2*, 1862, pp. 43–62; also *Leonhardi Euleri Opera Omnia, Series Secunda, Opera Mechanica Et Astronomica*, Basileae MCMLXVIII, Vol. 9, pp. 413–441.

Euler, L., *Leonhardi Euleri Opera Omnia, Series Secunda, Opera Mechanica Et Astronomica*, MCMXII–MCMLXIV, Vols. 1–8, 10–23, 25, 28–30.

Euler, J., *Leonhardi Euleri Opera Omnia, Series Tertia, Opera Physica*, Berolini, B. G. Teubneri, MCMXXVI–MCMXII, Vols. 1, 2, 3, 4.

Gibbs, J. W., 1901, *Vector Analysis*, E. B. Wilson, ed., Scribner, New York, 1901, and Yale University Press, New Haven, 1931.

Goldstein, H., 1980, *Classical Mechanics*, Addison-Wesley.

Graves, R. P., 1885, *Life of Sir William Rowan Hamilton*, Vol. I, 1882; Vol. II, 1885; Vol. III, 1889, and Arno Press, New York, 1975, Hodges, Figgis and Co., Dublin.

Hamel, G., 1949, *Theoretische Mechanik*, Springer-Verlag OHG, Berlin.

Hamilton, W. R., 1844, "On Quaternions; or on a New System of Imaginaries in Algebra (incl. letter to J. T. Graves dated October 17, 1843), *Philo. Mag.*, Supplement to Vol. 25, 3rd Series, pp. 489–495.

Hamilton, W. R., 1853, *Lectures on Quaternions*, Hodges and Smith, Dublin.

Hamilton, W. R., 1899, *Elements of Quaternions*, 2nd ed., C. J. Jolly, ed., Vol. I, 1899; Vol. II, 1901, Longmans, Green and Co., London.

Hill, E. L., 1945, "Rotation of a Rigid Body about a Fixed Point," *American J. of Physics*, Vol. 13, pp. 137–140.

Hiller, M., and Woernle, C., 1984, "A Unified Representation of Spatial Displacements," *Mechanisms and Machine Theory*, Vol. 19, No. 6, pp. 477–486.

Downloaded 03 May 2010 to 171.66.16.31. Redistribution subject to ASME license or copyright; see http://www.asme.org/terms/Terms_Use.cfm

Kane, T. R., Likins, P. W., and Levinson, D. A., 1983, *Spacecraft Dynamics*, McGraw-Hill Book Co., New York.

Klein, F., 1884, *Vorlesungen über das Ikosaeder und die Auflösung der Gleichungen vom fünften Grade*, Teubner, Leipzig. Translated as: *Lectures on the icosahedron and the solutions of equations of the fifth degree,* 2nd ed., (Trans. by G. G. Morrice), Ballantyne, Hanson Co., 1914; Dover Publications, New York, 1956.

Paul, B., 1963, "On the Composition of Finite Rotations," *American Mathematical Monthly*, Vol. 70, pp. 949–954.

Rodrigues, O., 1840, "Des lois géométriques qui régissent les déplacements d'un système solide dans l'espace, et de la variation des coordonnées provenant de ces déplacements considérés indépendamment des causes qui peuvent les produire," *J. de Mathématiques Pures et Appliquées*, Vol. 5, pp. 380–440.

Whittaker, E. T., 1937, *Analytical Dynamics of Particles and Rigid Bodies*, (1st ed., 1904), Cambridge University Press.

APPENDIX A

Euler's Rotation Formula

A.I. The Rotation Formula Derived By Euler. After defining the three orthogonal coordinates ABC with the origin at a fixed point I as shown in Fig. 2, Euler obtained the following relationship between the direction cosines $\cos\zeta'$, $\cos\eta'$, $\cos\theta'$ of the unit vector Iz (after rotation) and the direction cosines $\cos\zeta$, $\cos\eta$, $\cos\theta$ of the unit vector IZ (before rotation) as follows (Euler 1775b, p. 216; or Vol. 9, p. 107):

$$\begin{aligned}
\cos\zeta' &= \cos\zeta(\cos^2\alpha+\sin^2\alpha\cos\phi)\\
&+ \cos\eta(\cos\alpha\cos\beta(1-\cos\phi)-\cos\gamma\sin\phi)\\
&+ \cos\theta(\cos\alpha\cos\gamma(1-\cos\phi)+\cos\beta\sin\phi)\\
\cos\eta' &= \cos\eta(\cos^2\beta+\sin^2\beta\cos\phi)\\
&+ \cos\theta(\cos\beta\cos\gamma(1-\cos\phi)-\cos\alpha\sin\phi) \qquad (A.1)\\
&+ \cos\zeta(\cos\alpha\cos\beta(1-\cos\phi)+\cos\gamma\sin\phi)\\
\cos\theta' &= \cos\theta(\cos^2\gamma+\sin^2\gamma\cos\phi)\\
&+ \cos\zeta(\cos\alpha\cos\gamma(1-\cos\phi)-\cos\beta\sin\phi)\\
&+ \cos\eta(\cos\beta\cos\gamma(1-\cos\phi)+\cos\alpha\sin\phi),
\end{aligned}$$

where $\cos\alpha$, $\cos\beta$, $\cos\gamma$ were the direction cosines of the rotation axis along which the angle ϕ is rotated as is shown in Fig. 2.

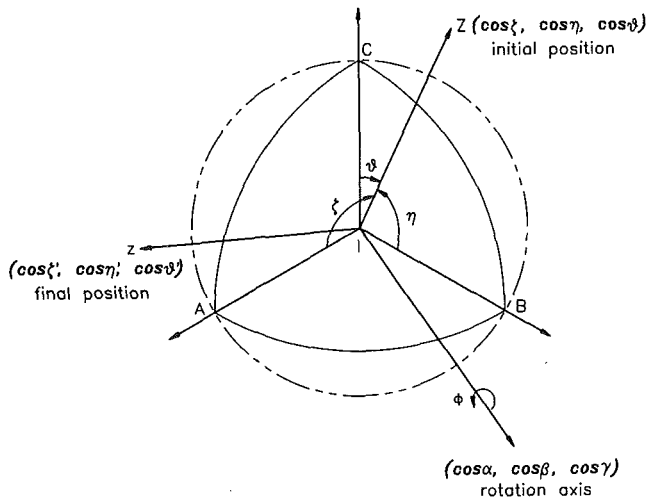


Fig. 2 The schematic diagram for the derivation of the rotation formula by Euler

A.II The Displacement Formulae Derived by Rodrigues[1]. Let the initial and the final coordinates of a point be x, y, z and x', y', z', respectively; the change between the two coordinates is defined by relations

$$x'=x+\Delta x,\quad y'=y+\Delta y,\quad z'=z+\Delta z \qquad (A.2)$$

After defining the parameters m, n, and p as follows:

$$m=2\cos\alpha\tan\frac{\phi}{2},\quad n=2\cos\beta\tan\frac{\phi}{2},\quad p=2\cos\gamma\tan\frac{\phi}{2}. \qquad (A.3)$$

Rodrigues obtained the following formulae (Rodrigues, 1840, p. 404):

$$\begin{aligned}
\Delta x &= u+\frac{py-nz+\frac{m}{2}(mx+ny+pz)-(m^2+n^2+p^2)\frac{x}{2}}{1+\frac{m^2+n^2+p^2}{4}},\\
\Delta y &= v+\frac{mz-px+\frac{n}{2}(mx+ny+pz)-(m^2+n^2+p^2)\frac{y}{2}}{1+\frac{m^2+n^2+p^2}{4}},\\
\Delta z &= w+\frac{nx-my+\frac{p}{2}(mx+ny+pz)-(m^2+n^2+p^2)\frac{z}{2}}{1+\frac{m^2+n^2+p^2}{4}},
\end{aligned} \qquad (A.4)$$

where u, v, and w were the three translational terms which were the functions of the rotation angle ϕ and the displacement t along the rotation axis with three direction cosines ($\cos\alpha$, $\cos\beta$, $\cos\gamma$) as is shown in Fig. 3. Equations (A.2) and

[1,2]In the pre-vector era, both left-handed and right-handed coordinate systems were commonly used. Rodrigues and Cayley appear to have utilized the former in their derivations which, for finite rotation formulae, has the effect of reversing the sign of convention for the rotation angle ϕ.

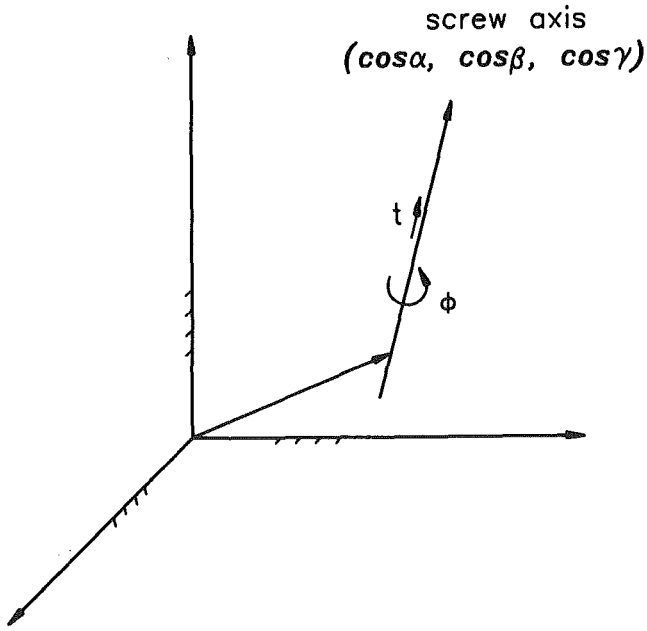


Fig. 3 The schematic diagram for the derivation of the displacement formulae by Rodrigues

Downloaded 03 May 2010 to 171.66.16.31. Redistribution subject to ASME license or copyright; see http://www.asme.org/terms/Terms_Use.cfm

(A.4) together formed the displacement formulae from the initial coordinates to the final coordinates.

An alternate form of the displacement formulae derived in Rodrigues (1840, p. 403) was

$$\Delta x = u + \sin\phi(y\cos\gamma - z\cos\beta) + 2\sin^2\frac{1}{2}\phi[\cos\alpha(x\cos\alpha + y\cos\beta + z\cos\gamma) - x],$$

$$\Delta y = v + \sin\phi(z\cos\alpha - x\cos\gamma) + 2\sin^2\frac{1}{2}\phi[\cos\beta(x\cos\alpha + y\cos\beta + z\cos\gamma) - y],$$

$$\Delta z = w + \sin\phi(x\cos\beta - y\cos\alpha) + 2\sin^2\frac{1}{2}\phi[\cos\gamma(x\cos\alpha + y\cos\beta + z\cos\gamma) - z], \qquad (A.5)$$

There are striking similarities among the rotational elements of formula (A.5) and formula (A.1).

APPENDIX B

Rodrigues' Composition Formulae of Finite Rotations[2]

Rodrigues obtained the composition formulae for the rotation from the initial coordinates to the final coordinates for two successive rotations as follows (Rodrigues, 1840, p. 408):

$$\tan\frac{1}{2}\Phi\cos A = \frac{\tan\frac{1}{2}\phi\cos\alpha + \tan\frac{1}{2}\phi'\cos\alpha' + \tan\frac{1}{2}\phi\tan\frac{1}{2}\phi'(\cos\beta\cos\gamma' - \cos\gamma\cos\beta')}{1 - \tan\frac{1}{2}\phi\tan\frac{1}{2}\phi'\cos\nu},$$

$$\tan\frac{1}{2}\Phi\cos B = \frac{\tan\frac{1}{2}\phi\cos\beta + \tan\frac{1}{2}\phi'\cos\beta' + \tan\frac{1}{2}\phi\tan\frac{1}{2}\phi'(\cos\gamma\cos\alpha' - \cos\alpha\cos\gamma')}{1 - \tan\frac{1}{2}\phi\tan\frac{1}{2}\phi'\cos\nu},$$

$$\tan\frac{1}{2}\Phi\cos\Gamma = \frac{\tan\frac{1}{2}\phi\cos\gamma + \tan\frac{1}{2}\phi'\cos\gamma' + \tan\frac{1}{2}\phi\tan\frac{1}{2}\phi'(\cos\alpha\cos\beta' - \cos\beta\cos\alpha')}{1 - \tan\frac{1}{2}\phi\tan\frac{1}{2}\phi'\cos\nu},$$

$$\cos\nu = \cos\alpha\cos\alpha' + \cos\beta\cos\beta' + \cos\gamma\cos\gamma', \qquad (B.1)$$

where ($\cos\alpha$, $\cos\beta$, $\cos\gamma$), ($\cos\alpha'$, $\cos\beta'$, $\cos\gamma'$), and (cosA, cosB, cosΓ) were the direction cosines of the first, second, and the resultant rotations with rotation angles ϕ, ϕ', and Φ, respectively.

The composition formulae which satisfy the quaternion multiplication rule was derived as follows (Rodrigues, 1840, p. 408):

$$\cos\frac{1}{2}\Phi = \cos\frac{1}{2}\phi\cos\frac{1}{2}\phi' - \sin\frac{1}{2}\phi'\sin\frac{1}{2}\phi'\cos\nu,$$

$$\sin\frac{1}{2}\Phi\cos A = \sin\frac{1}{2}\phi\cos\frac{1}{2}\phi'\cos\alpha + \sin\frac{1}{2}\phi'\cos\frac{1}{2}\phi\cos\alpha' + \sin\frac{1}{2}\phi\sin\frac{1}{2}\phi'(\cos\beta\cos\gamma' - \cos\gamma\cos\beta'),$$

$$\sin\frac{1}{2}\Phi\cos B = \sin\frac{1}{2}\phi\cos\frac{1}{2}\phi'\cos\beta + \sin\frac{1}{2}\phi'\cos\frac{1}{2}\phi\cos\beta' + \sin\frac{1}{2}\phi\sin\frac{1}{2}\phi'(\cos\gamma\cos\alpha' - \cos\alpha\cos\gamma'),$$

$$\sin\frac{1}{2}\Phi\cos\Gamma = \sin\frac{1}{2}\phi\cos\frac{1}{2}\phi'\cos\gamma + \sin\frac{1}{2}\phi'\cos\frac{1}{2}\phi\cos\gamma' + \sin\frac{1}{2}\phi\sin\frac{1}{2}\phi'(\cos\alpha\cos\beta' - \cos\beta\cos\alpha'), \qquad (B.2)$$

APPENDIX C

Euler's Displacement Transformation Formula

Euler derived the displacement transformation formula in terms of three translation parameters and three independent angular parameters, though not Euler angles, in Euler (1775a; or Vol. 9, p. 84–98). In Fig. 4, a point Z was defined by (p, q, r) with respect to the body coordinates ABC, and the same point z in the fixed coordinates could be expressed in terms of three translational parameters f, g, and h of the origin of the body coordinates ABC and the body coordinates p, q, and r via the rotational parameters F, F', F''; G, G', G''; and H, H', H''.

$$x = f + Fp + F'q + F''r,$$

$$y = g + Gp + G'q + G''r, \qquad (C.1)$$

$$z = h + Hp + H''q + H''r$$

Substituting the point $Z = (p, 0, 0)$ in the body coordinates ABC into equation (C.1) and considering the condition for the rigid body

$$|IZ| = |iz|, \qquad (C.2)$$

Downloaded 03 May 2010 to 171.66.16.31. Redistribution subject to ASME license or copyright; see http://www.asme.org/terms/Terms_Use.cfm

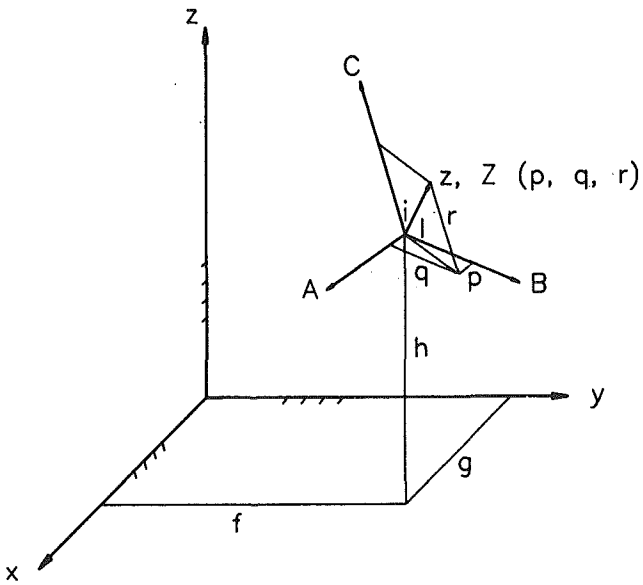


Fig. 4 The schematic diagram for the derivation of the displacement transformation formula by Euler

$$p^2=(x-f)^2+(y-g)^2+(z-h)^2=p^2(F^2+G^2+H^2), \quad (C.3)$$

one would obtain

$$F^2+G^2+H^2=1. \quad (C.4a)$$

Similarly, one could derive

$$F''^2+G'^2+H'^2=1, \quad (C.4b)$$

$$F''^2+G''^2+H''^2=1. \quad (C.4c)$$

Equation (C.4*a*) would be satisfied after defining

$$F=\sin\zeta, \quad G=\cos\zeta\sin\eta, \quad H=\cos\zeta\cos\eta. \quad (C.5a)$$

Similarly, F', G', H'; and F'', G'', H'' were defined as

$$F'=\sin\zeta', \quad G''=\cos\zeta'\sin\eta', \quad H'=\cos\zeta'\cos\eta', \quad (C.5b)$$

$$F''=\sin\zeta'', \quad G''=\cos\zeta''\sin\eta'', \quad H''=\cos\zeta''\cos\eta'', \quad (C.5c)$$

which satisfy equations (*C*.4*b*), (*C*.4*c*). In order to reduce the six dependent parameters, ζ, η, ζ', η', ζ'', and η'' to three independent parameters, substituting the point $Z=(p, q, 0)$ into equations (*C*.1) and using the conditions (*C*.2) and (*C*.4) would result

$$p^2+q^2=p^2+q^2+2pq(FF'+GG'+HH'). \quad (C.6)$$

Therefore,

$$FF'+GG'+HH'=0. \quad (C.7)$$

Similarly,

$$FF''+GG''+HH''=0, \quad (C.7b)$$

$$F'F''+G'G''+H'H''=0. \quad (C.7c)$$

After substituting *F*'s, *G*'s, and *H*'s in equation (*C*.5) into (*C*.7), one could get

$$\tan\zeta\tan\zeta'=-\cos(\eta-\eta'),$$
$$\tan\zeta'\tan\zeta''=-\cos(\eta'-\eta''), \quad (C.8)$$
$$\tan\zeta''\tan\zeta=-\cos(\eta''-\eta).$$

or,

$$\tan\zeta=-\frac{\Delta}{\cos(\eta'-\eta'')}, \quad \tan\zeta'=-\frac{\Delta}{\cos(\eta''-\eta)},$$
$$\tan\zeta''=-\frac{\Delta}{\cos(\eta-\eta')}, \quad (C.9)$$

where Δ was defined as

$$\Delta=\tan\zeta\tan\zeta'\tan\zeta''=\sqrt{-\cos(\eta-\eta')\cos(\eta'-\eta'')\cos(\eta''-\eta)}. \quad (C.10)$$

Through equation (*C*.9), one could obtain

$$\sin\zeta=-\sqrt{\cot\theta'\cot\theta''}, \quad \cos\zeta=\sqrt{1-\cot\theta'\cot\theta''}$$
$$\sin\zeta'=-\sqrt{\cot\theta''\cot\theta}, \quad \cos\zeta'=\sqrt{1-\cot\theta''\cot\theta} \quad (C.11)$$
$$\sin\zeta''=-\sqrt{\cot\theta\cot\theta'}, \quad \cos\zeta''=\sqrt{1-\cot\theta\cot\theta'}$$

where θ, θ', and θ'' were defined as

$$\theta=\eta'-\eta'', \quad \theta'=\eta''-\eta, \quad \theta''=\eta-\eta', \quad (C.12)$$

which satisfy the relation

$$\theta+\theta'+\theta''=0. \quad (C.13)$$

Defining

$$t=\cos\theta, \quad t'=\cot\theta', \quad t''=\cot\theta'' \quad (C.14)$$

would finally bring equation (*C*.1) into

$$x=f-\sqrt{t't''}p+\sin\eta\sqrt{1-t't''}q+\cos\eta\sqrt{1-t't''}r,$$

$$y=g-\sqrt{tt''}p+\sin\eta'\sqrt{1-t''}tq+\cos\eta\sqrt{1-t''}tr, \quad (C.15)$$

$$z=h-\sqrt{tt'}p+\sin\eta''\sqrt{1-tt'}q+\cos\eta''\sqrt{1-tt''}r,$$

where, t, t', and t'' were the functions of three independent rotational parameters η, η', and η'' expressed by equation (*C*.12) and (*C*.14).

The trigonometrical identity

$$\tan\theta''=-\tan(\theta+\theta')=-\frac{\tan\theta+\tan\theta'}{1-\tan\theta\tan\theta'}, \quad (C.16)$$

gives

$$tt''+t't''+tt'=1, \quad (C.17)$$

which would result in the orthogonality relations (*C*.4), (*C*.7) among the coefficients of p, q, and r in equation (*C*.15).

Downloaded 03 May 2010 to 171.66.16.31. Redistribution subject to ASME license or copyright; see http://www.asme.org/terms/Terms_Use.cfm

On Standard Eigenvalues of Variable-Coefficient Heat and Rod Equations

H. P. W. Gottlieb
Division of Science and Technology,
Griffith University,
Nathan, Queensland, 4111
Australia.

Forms of the variable-heat-conductivity coefficient function in the one-dimensional heat equation are determined which yield a standard harmonic eigenvalue sequence as in the case of homogeneity. The continuous case is found to correspond to a four-thirds power law dependence on coordinate. For the stepped case, the condition on the ratio of segmental heat conductivities in terms of the junction location is presented.

Introduction

One-dimensional eigenvalue problems arise in many physical situations and may be written in the form

$$\frac{d}{dx}\left[f(x)\frac{du}{dx}\right] = -\lambda g(x)u(x),\ 0 \le x \le L \qquad (1a)$$

where the eigenvalues λ are determined by the boundary conditions, which in this note will be taken to be the vanishing end conditions (Dirichlet Conditions)

$$u(0) = 0 = u(L). \qquad (1b)$$

The functions $f(x)$, $g(x)$ represent coordinate-dependent coefficients with appropriate physical interpretations. For the one-dimensional heat conduction equation for the temperature, the time-dependence is $\exp(-\lambda t)$, and $f(x) = \kappa(x)$ is the heat conductivity while $g(x) = c(x)$ is the heat capacity.

We are interested here in the *harmonic case* when

$$\sqrt{\lambda} \propto N; \qquad N = 1,2,3, \ldots, \qquad (2)$$

i.e., in cases when the inhomogeneous medium has standard eigenvalues indistinguishable from the homogeneous case with constant coefficients. In particular, we shall study the case of variable heat conductivity $\kappa(x)$ with constant heat capacity.

Equations (1) also govern the behavior of various structural and acoustical elements (Meirovitch, 1975; Morse, 1983). Table 1 summarizes the cases for transverse vibrations of strings, axial and torsional vibrations of rods, and acoustical horns, with customarily-used symbols; for these systems $\lambda = \omega^2$ with time-dependence $\exp(-i\omega t)$.

There is a variety of mathematical transformations changing the form of (1*a*) to other standard forms; an essential feature is that the transformed equation depends upon only one independent function, namely, the product $f(x)g(x)$. The three standard forms of (1*a*) involving one independent coefficient function and typical interpretations are:

(*A*) Constant-tension, variable-density string equation: $f = T =$ constant;

(*B*) Constant density, variable Young's modulus rod equation: $g = m =$ constant;

(*C*) (Webster) Horn equation: $f(x) \propto g(x) \propto A(x)$.

The explicit transformation from the general equation (1) to the special form (*A*) (for the heat equation) is to be found, for instance, in Horgan, Spence, and Andry (1982); the transformation from (1) to the form (*C*) may be found in Burridge (1980).

The fixed string with constant tension, case (*A*), is known to have a harmonic spectrum not only for lineal density $m =$ constant but also (Borg, 1946) when

$$m(x) \propto 1/(x + x_0)^4. \qquad (3)$$

The acoustic horn (or constant modulus, constant voluminal density axial rod), case (*C*), is known to have a harmonic spectrum not only for areal cross-section $A =$ constant but also when

$$A(x) \propto (x + x_0)^2. \qquad (4)$$

This may be demonstrated either by using the inverse transformation of that in Horgan, Spence, and Andry (1982) to pass from case (*A*) with (3) to equation (1) with $f(x) \propto g(x)$, i.e., case (*C*), hence obtaining (4); or, more conventionally, to note (Morse, 1983) that case (*C*) with (4) leads to the same formal equation as for the radial Laplacian in three-dimensions, leading to spherical waves in a conical pipe with harmonic spectrum (Lamb, 1960).

Variable Heat Conductivity

***(a)* Continuously-Varying Case.** The one remaining case, (*B*), corresponding to a variable heat conductivity medium (or a variable modulus rod), does not seem to have been discussed in this fashion. We now ask: When does such

Contributed by the Applied Mechanics Division of THE AMERICAN SOCIETY OF MECHANICAL ENGINEERS for publication in the JOURNAL OF APPLIED MECHANICS.

Discussion on this paper should be addressed to the Editorial Department, ASME, United Engineering Center, 345 East 47th Street, New York, N.Y. 10017, and will be accepted until two months after final publication of the paper itself in the JOURNAL OF APPLIED MECHANICS. Manuscript received by ASME Applied Mechanics Division, February 23, 1988; final revision, June 9, 1988.

Copyright © 1989 by ASME

Downloaded 03 May 2010 to 171.66.16.31. Redistribution subject to ASME license or copyright; see http://www.asme.org/terms/Terms_Use.cfm

a system have the same harmonic spectrum (2) as for the homogeneous case?

The answer is provided by using the inverse transformation of that given in Horgan, Spence, and Andry (1982), to pass from the known harmonic case (*A*) with (3) to equation (1) with $g(x)=c=$ constant. After appropriate calculations, we find, in the heat conduction context,

$$\kappa(x) \propto (x+x_0)^{4/3}. \tag{5}$$

An alternative procedure is to start with equation (1) with $g=$ constant and assume a power law form for $f(x)=\kappa(x)\propto(x+x_0)^p$. Solutions to (1) are then expressible in term of Bessel functions (Wylie, 1975). The requirement of a harmonic spectrum implies a simple sine term in the solution, which turns out to imply that the order of Bessel function must be equal to 1/2. This in turn leads to $p=4/3$ previously indicated.

The explicit solutions to (1) in the context of heat conduction, for heat capacity $g=c_0=$ constant and heat conductivity function $f(x)=\kappa(x)$ given by

$$\kappa(x)=k_0(x+x_0)^{4/3} \tag{6}$$

are

$$u_N(x)=(x+x_0)^{-1/3}\sin\left\{\frac{N\pi(x+x_0)^{1/3}-x_0^{1/3}}{(L+x_0)^{1/3}-x_0^{1/3}}\right\} \tag{7a}$$

with eigenvalues given by

$$\sqrt{\lambda_N}=N(\pi/3)(k_0/c_0)^{1/2}/[(L+x_0)^{1/3}-x_0^{1/3}];$$
$$N=1,2,3,\ldots, \tag{7b}$$

of the form (2) as sought.

The *equivalent homogeneous medium*, with the *same* eigenvalue sequence (7*b*), with constant heat conductivity κ_{HOM} (and the same heat capacity c_0) is given by

$$(\sqrt{\kappa})_{\text{HOM}}=(\sqrt{k_0}/3)L/[(L+x_0)^{1/3}-x_0^{1/3}]. \tag{8}$$

(b) **Stepped Case.** The condition on the ratio of densities in segments of a stepped string and piecewise constant density and uniform tension (case (*A*) stated previously), such that the complete vibration frequency spectrum is exactly harmonic, was discovered recently by the author (Gottlieb, 1986, 1987, 1988).

In the context of heat conduction, Nemat-Nasser and Lang (1979) gave the eigenfunctions for a composite of two materials in three layers (1-2-1), with exact eigenvalues computed numerically as the roots of the characteristic equation. Following on from subsection (*a*), we here analyze the case (*B*) for heat conduction in a two-part medium with common constant heat capacity c_0 and *stepped* piecewise constant heat conductivity, to determine the condition for a completely harmonic eigenvalue sequence with consequent explicit analytical expressions for mode functions.

The governing equation (1) becomes

$$\kappa_i\frac{d^2u_i}{dx^2}+\lambda c_0u_i=0,\ i=1,2;$$
$$u_i=u_1,\ \kappa_i=\kappa_1,\ 0\le x<\alpha L,$$
$$u_i=u_2,\ \kappa_i=\kappa_2,\ \alpha L\le x\le L, \tag{9}$$

where $0<\alpha<1$, and $u_1(0)=0=u_2(L)$. At the junction located at $x=\alpha L$, the interface conditions are: continuity of temperature u and of heat flux $\kappa du/dx$. Solution of this system in the usual manner leads to an eigenvalue equation for which, if the relation

$$\kappa_2/\kappa_1=[(1-\alpha)/\alpha]^2 \tag{10}$$

for the ratio of segmental heat conductivities is satisfied, the eigenvalues form an exact harmonic sequence with

$$\sqrt{\lambda_N}=N\frac{\pi}{2\alpha L}\left\{\frac{\kappa_1}{c_0}\right\}^{1/2}=N\frac{\pi}{2(1-\alpha)L}\left\{\frac{\kappa_2}{c_0}\right\}^{1/2}. \tag{11}$$

The modal functions are then given explicitly by

$$u_1^{\{N\}}(x)=A_1^{\{N\}}\sin\left[\frac{N\pi x}{2\alpha L}\right], \tag{12a}$$

$$u_2^{\{N\}}(x)=A_2^{\{N\}}\sin\left[\frac{N\pi(L-x)}{2(1-\alpha)L}\right], \tag{12b}$$

where

$$A_2^{\{N\}}/A_1^{\{N\}}=1,\ N\text{ odd}, \tag{13a}$$
$$=-\frac{\kappa_1}{\kappa_2}\frac{1-\alpha}{\alpha},\ N\text{ even}. \tag{13b}$$

If $\alpha=1/2$, the condition of harmonic eigenvalues implies complete homogeneity $\kappa_1=\kappa_2$. If $\alpha\neq1/2$, then for fixed junction location there is an inhomogeneous stepped medium given by (10) which has the standard harmonic eigenvalues. The equivalent homogeneous medium (with the same c_0) has uniform heat conductivity given by

$$(\sqrt{\kappa})_{\text{HOM}}=\sqrt{\kappa_1}/(2\alpha)=\sqrt{\kappa_2}/[2(1-\alpha)]. \tag{14}$$

The main difference between these results and analogous results for the stepped-density vibrating string (Gottlieb, 1986) is the κ_i-dependent factor in the amplitude ratio (13*b*) due to the continuity requirement for heat flux.

Summary

While the continuous variable-coefficient functions which produce standard homogeneous-type harmonic eigenvalues for the variable-density string equation and the variable cross-section acoustic horn equation are well known, the third case typified by the variable heat conductivity equation does not seem to have been discussed from this viewpoint, and this has been the principal subject of this paper. We have found that the desired effect is produced by a four-thirds power coordinate dependence for the heat conductivity, and the results are exemplified by equations (6)–(8). Such a situation also pertains, with appropriate redefinitions of variables and parameters, to longitudinal or torsional oscillations of a rod with variable appropriate modulus (see Table 1).

For a piecewise-constant heat conductivity medium with single step, equations (10)–(13) summarize the condition and results for a standard harmonic spectrum.

Conclusion

These explicit analytical results are expressions of an interesting mechanical phenomenon. In the context of the variable-coefficient heat equation, their practical utility lies in serving as exact examples against which to check the accuracy of any general numerical schemes for the one-dimensional finite inhomogeneous media.

In the case of longitudinal or torsional vibrations of a rod with variable modulus, this study also provides a reminder that, while an irregular material, in general, produces an irregular vibration spectrum, there may be instances, albeit very special, when an inhomogeneous medium is indistinguishable, as far as the values of its spectrum are concerned, from a homogeneous material.

Table 1 Physical interpretations of the coefficients

	Heat Conduction	String: Transverse	Rod: Axial	Shaft: Torsional	Horn: Acoustic
$f(x)$	$\kappa(x)$	$T(x)$	$E(x)A(x)$	$G(x)J(x)$	$A(x)$
$g(x)$	$c(x)$	$m(x)$	$m(x)$	$I(x)$	$(1/C^2)A(x)$

Downloaded 03 May 2010 to 171.66.16.31. Redistribution subject to ASME license or copyright; see http://www.asme.org/terms/Terms_Use.cfm

References

Borg, G., 1946, "Eine Umkehrung der Sturm-Liouvilleschen Eigenwertaufgabe," *Acta Mathematica*, Vol. 78, Sect. 20, pp. 1–96.

Burridge, R., 1980, "The Gelfand-Levitan, the Marchenko, and the Gopinath-Sondhi Integral Equations of Inverse Scattering Theory, Regarded in the Context of Inverse Impulse-Response Problems," *Wave Motion*, Vol. 2, pp. 305–323.

Gottlieb, H. P. W., 1986, "Harmonic Frequency Spectra of Vibrating Stepped Strings," *Journal of Sound and Vibration*, Vol. 108, pp. 63–72.

Gottlieb, H. P. W., 1987, "Multi-segment Strings with Exactly Harmonic Spectra," *Journal of Sound and Vibration*, Vol. 118, pp. 283–290.

Gottlieb, H. P. W., 1988, "Iso-spectral Operators: Some Model Examples with Discontinuous Coefficients," *Journal of Mathematical Analysis and Applications*, Vol. 132, pp. 123–137.

Horgan, C. O., Spence, J. P., and Andry, A. N., 1982, "Lower Bounds for Eigenvalues of Sturm-Liouville Problems with Discontinuous Coefficients: Integral Equation Methods," *Quarterly of Applied Mathematics*, Vol. 39, pp. 455–465.

Lamb, H., 1960, *The Dynamical Theory of Sound*, 2nd ed., Dover, New York, Sect. 84.

Meirovitch, L., 1975, *Elements of Vibration Analysis*, McGraw-Hill, New York, Chap. 5.

Morse, P. M., 1983, *Vibration and Sound*, 2nd ed., (1948), American Institute of Physics, Sect. 24.

Nemat-Nasser, S., and Lang, K.-W., 1979, "Eigenvalue Problems for Heat Conduction in Composite Materials," *Iranian Journal of Science and Technology*, Vol. 7, pp. 243–260.

Wylie, C. R., 1975, *Advanced Engineering Mathematics*, 4th ed., McGraw-Hill, New York, Sect. 9.4.

Downloaded 03 May 2010 to 171.66.16.31. Redistribution subject to ASME license or copyright; see http://www.asme.org/terms/Terms_Use.cfm

An Alternating Frequency/Time Domain Method for Calculating the Steady-State Response of Nonlinear Dynamic Systems

T. M. Cameron

J. H. Griffin
Mem. ASME

Department of Mechanical Engineering,
Carnegie-Mellon University,
Pittsburgh, PA 15213

A method is proposed for analyzing the steady-state response of nonlinear dynamic systems. The method iterates to obtain the discrete Fourier transform of the system response, returning to the time domain at each iteration to take advantage of the ease in evaluating nonlinearities there – rather than analytically describing the nonlinear terms in the frequency domain. The updated estimates of the nonlinear terms are transformed back into the frequency domain in order to continue iterating on the frequency spectrum of the steady-state response. The method is demonstrated by solving a problem with friction damping in which the excitation has multiple discrete frequencies.

1 Introduction

A variety of methods are presently available for calculating the response of nonlinear dynamic systems, (see, for example, Iwan (1974) for analytical approaches, and Press et al. (1986) for numerical approaches). The method introduced in this paper offers advantages over most other methods in its generality, efficiency, accuracy, and ease-of-use for calculating the steady-state response of forced nonlinear systems. The method involves an iterative scheme that alternates from the frequency to the time domain in order to take advantage of the convenience in performing certain tasks in each domain. Consequently, this *Alternating Frequency/Time* (AFT) method easily provides either time trajectory or frequency spectrum solutions.

The purpose of this paper is to introduce the AFT method and illustrate its utility with a friction damping problem: the response of a single degree-of-freedom (sdf) system with an elastic/perfectly-plastic friction damper subject to three discrete frequencies of excitation is calculated.

2 Alternative Spectral Methods

One of the most popular methods for approximating the frequency response of nonlinear systems is known as the *Harmonic Balance* (HB) method in the vibration literature (e.g., Nayfeh and Mook, 1979), and as the *Describing Function* (DF) approach in the control literature (e.g., Gelb and Vander Velde, 1968). This is essentially a spectral method in which the solution is assumed to have one dominant frequency component – or at most two.[1] In situations where it can be applied, and trusted to give accurate solutions (where a single harmonic description of the nonlinearity is adequate), the HB method is by far the most computationally efficient method for obtaining steady-state solutions to nonlinear dynamics problems. It has been used extensively to study friction damping (e.g., Griffin, 1980; Sinha and Griffin, 1983 and 1984; Dowell, 1983; and Jezequel, 1983). Generally, however, this method is limited to harmonically excited systems and it becomes increasingly inaccurate as higher harmonics in the expansion of the nonlinear force become significant. A fair amount of work is also required to expand the nonlinear force, although DF's for a large number of nonlinearities have been tabulated (Gelb and Vander Velde, 1968, Appendix B).

An *Incremental Harmonic Balance* (IHB) method which accommodates multiple harmonic components in the description of the nonlinear force was introduced by Lau et al. in 1982. The method was originally applied to continuous (cubic) nonlinearities (Lau et al., 1982, 1983), but Pierre et al. (1985) extended the method to analyze the rigid/perfectly-plastic friction damper problem in which the nonlinear force is discontinuous. The IHB method appears to handle strong nonlinearities well, and provides accurate solutions over a much broader range than the HB method since it accommodates multiple harmonics. The method is ideally suited to parametric studies since it can step from a known state of vibration to a neighboring state which corresponds to an incremental change in one of the governing parameters of the

Contributed by the Applied Mechanics Division for publication in the JOURNAL OF APPLIED MECHANICS.

Discussion on this paper should be addressed to the Editorial Department, ASME, United Engineering Center, 345 East 47th Street, New York, N.Y. 10017, and will be accepted until two months after final publication of the paper itself in the JOURNAL OF APPLIED MECHANICS. Manuscript received by ASME Applied Mechanics Division, October 15, 1987; final revision, June 27, 1988.

[1] The DF approach has been extended to allow two input frequencies in the case of odd, memoryless (nonhysteretic) nonlinearities (Gelb and Vander Velde, 1968, Chapter 5 and Appendix D), but the nonlinear force and the system response are described only in terms of the two input frequencies.

Copyright © 1989 by ASME

Downloaded 03 May 2010 to 171.66.16.31. Redistribution subject to ASME license or copyright; see http://www.asme.org/terms/Terms_Use.cfm

system. However, there are also significant disadvantages to the IHB method.

Computationally the IHB method is no more efficient than numerical integration, at least for the discontinuous friction damping problem (cf., Pierre et al., 1985, "Conclusions"), and the computational effort grows geometrically with the number of harmonics considered. As currently implemented, the frequencies are integer multiples of the excitation frequency, which will hide the subharmonic resonances that may occur in nonlinear systems. Another disadvantage of the IHB method is the amount of analytical work required. Functions in the equation are expanded in a first order Taylor series (which may be difficult to obtain for discontinuous functions) and substituted into the original equation to obtain a linear "incrementalized" equation. The incrementalized equation is solved by the Galerkin method, which requires further expansions and integrations. Finally, although the approach is general, the expansions are specialized, so each new dynamic system requires its own formulation and implementation.

Other numerical methods, using techniques similar to those in the AFT method, describe functions in both the frequency and time domains. In computational fluid dynamics, "Spectral" and "Pseudo-Spectral" methods (cf., Zang and Hussaini, 1985) use Fourier transform techniques to expand functions into (trigonometric or Chebyshev) polynomials. This permits derivatives and other operations on those functions to be performed with higher order accuracy than finite difference methods achieve for similar effort. Cesari (1963) appears to be the first to obtain steady-state solutions to nonlinear dynamic equations by using a trigonometric polynomial expansion, which is equivalent to a truncated Fourier series or a discrete Fourier transform. Urabe (1965) expands Cesari's results and (Urabe and Reiter, 1966) shows how the Fourier coefficients may be computed at each iteration with a discrete Fourier transform, once the nonlinear functions have been evaluated in the time domain. Urabe identifies this approach as an application of the Galerkin method. Ling and Wu (1987) use a fast Fourier transform (FFT) to implement Urabe's approach, calling it the "Fast Galerkin" (FG) method. Although there are fundamental similarities in the concepts underlying the FG and AFT methods, there are differences in how the methods are formulated and implemented. These differences are discussed later.

3 An Alternating Frequency/Time (AFT) Method

3.1 Fundamental Concepts. Frequency domain methods have long been used to analyze linear systems because the frequency content of a signal is often of greater interest than the time history and because convolution – a convenient solution method – is more efficiently accomplished in the frequency domain. In general, nonlinear forces are nonlinear functions of the past and present states of the system. Since they are not linear functions of the states or explicit functions of time, they cannot be transformed directly into the frequency domain. This makes nonlinear systems difficult to analyze in the frequency domain, as evidenced by the complicated expansions required in the frequency domain methods discussed previously. Nonlinear forces are easy to evaluate in the time domain, however, since the state history of the system is readily available. This is evidenced by the ease of implementation and greater complexity allowed by numerical integration. The AFT method employs the advantages of both domains by performing convolution (as well as filtering and convergence testing) in the frequency domain and by switching to the time domain to evaluate the nonlinear forces as functions of the state trajectory. The cost involved in this technique is the time required to switch back and forth between the frequency and time domains. A fast Fourier transform[2] algorithm makes this cost reasonable, especially in obtaining steady-state solutions to periodically excited systems.

Consider a nonlinear dynamic system in which the terms containing nonlinearities are grouped on the right hand side of the equation with the external forcing term. The equation of motion for this system may be represented by:

$$L\{x(t)\} = f(t) + N_f(x,\dot{x}) \tag{1}$$

where L is the differential operator representing the linear terms, $f(t)$ is the external forcing term, $N_f(\cdot)$ represents the nonlinear force terms, and $x(t)$ is the desired system response. These are vector functions for multi-degree-of-freedom (mdf) systems, or scalar functions for sdf systems. Taking the Fourier transform (FT) of both sides yields:

$$\Lambda(\omega)\cdot X(\omega) = F(\omega) + \eta(\omega, X(\omega)) \tag{2}$$

where $\Lambda(\omega)$, the transform of L, is a (matrix) function of the frequency, ω, $F(\omega)$ is the transform of $f(t)$, $\eta(\omega,X(\omega))$ is the transform of $N_f(\cdot)$, and $X(\omega)$ is the transform of $x(t)$. In the transform domain the nonlinear forces depend only on ω and $X(\omega)$ because derivatives of $x(t)$ transform into linearly scaled forms of $X(\omega)$:[3]

$$\begin{aligned} x(t) &\Leftrightarrow X(\omega) \\ \dot{x}(t) &\Leftrightarrow -j\omega X(\omega) \\ \ddot{x}(t) &\Leftrightarrow -\omega^2 X(\omega) \end{aligned} \tag{3}$$

("$\Leftrightarrow$" denotes a Fourier Transform pair).

Since an FFT will be used to compute and represent the frequency dependent functions, (2) is required to hold at the discrete frequencies, ω_k, introduced by the FFT. Thus, (2) becomes a system of nonlinear algebraic equations[4]:

$$\Lambda(\omega)\cdot X(\omega) = F(\omega) + \eta(\omega, X(\omega)) \tag{4}$$

where

$$\omega = \{\omega_k\} \tag{5}$$

and

$$\omega_k = \frac{2\pi k}{\Delta T \cdot N} \qquad k = 0, \ldots, \frac{N}{2}. \tag{6}$$

Here, ΔT is the sampling period and N is the number of samples in the FFT of each time domain function. In general, Λ is a matrix whose components are functions of the independent variable (ω_k), while X, F, and η are vector functions of ω_k. For example, at a given frequency, say ω_4, there will be $X_1(\omega_4), \ldots, X_m(\omega_4)$ if there are m degrees-of-freedom. Therefore, the length of $X(\omega)$ is the product of the number of frequencies in the FFT ($N/2+1$) times the number of degrees-of-freedom (m). To minimize the bandwidth of L, the equations should be ordered so that $X(\omega)$ appears as $\{X_1(\omega_0), X_2(\omega_0), \ldots, X_m(\omega_0), X_1(\omega_1), \ldots, X_m(\omega_1), \ldots, X_1(\omega_{N/2}), \ldots X_m(\omega_{N/2})\}$.

Various iterative methods are available for solving nonlinear algebraic equations, like (4). One problem facing any method is evaluation of the nonlinear term $\eta(\omega, X(\omega))$. To add it directly to $F(\omega)$ this term must be known explicitly in terms of ω, as $\eta(\omega)$, but this form is difficult to determine in

[2] "Fast Fourier transform" refers to a class of algorithms used to calculate the discrete Fourier transform (DFT – cf., Jackson, 1986, Chapter 7; and Oppenheim and Schafer, 1975, Chapter 3). The notation "FFT" will be used here to refer to the DFT as well as its implementation. The authors use an FFT subroutine from Press, et al. (1986).

[3] The Fourier Transform definition used here is $X(\omega) = \int_{-\infty}^{\infty} x(t)e^{j\omega t}\,dt$ and the inverse transform is $x(t) = 1/2\pi \int_{-\infty}^{\infty} X(\omega)e^{-j\omega t}d\omega$. Analogous definitions are employed in the FFT.

[4] The "ω" notation in (4) is for conceptual purposes. For digital implementation (4) is cast in stricter vector notation – $\Lambda(k)\cdot X(k) = F(k) + \eta(k)$ – where the kth component of each vector represents a sampled version of the corresponding continuous function at the frequency ω_k (ignoring scale factors and errors).

Downloaded 03 May 2010 to 171.66.16.31. Redistribution subject to ASME license or copyright; see http://www.asme.org/terms/Terms_Use.cfm

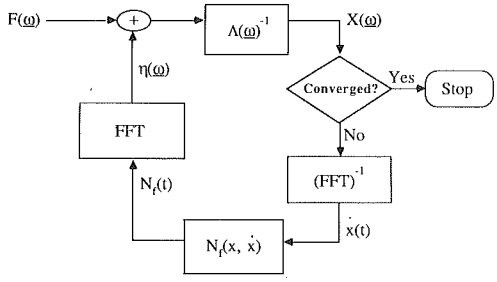


Fig. 1 Direct iteration implementation of the AFT method

the frequency domain. However, if $N_f(\cdot)$ can be expressed as an explicit function of time, $N_f(t)$, then it can be transformed to provide $\eta(\omega)$. To find $N_f(t)$, the most recent estimate of $X(\omega)$ is inverse transformed to provide an estimate of $x(t)$. Equation (3) – or the analogous FFT relationships – may be used to obtain other state variables so that $N_f(\cdot)$ may be evaluated as $N_f(t)$, and transformed to $\eta(\omega)$. For nonlinearities that involve products of time domain functions this avoids frequency domain convolution. For history-dependent nonlinearities, this procedure allows the nonlinearity to be evaluated directly from the state history as long as the time period used in the analysis is longer than the "term of memory" of the nonlinearity. With short term memory nonlinearities, values of the nonlinear terms at the beginning of the period may be obtained from periodicity requirements.

Another problem for nonlinear equation solvers is obtaining an initial estimate of the solution. An initial estimate (designated $X^0(\omega)$) may be obtained from the linear system, ignoring $\eta(\cdot)$, or from a known solution corresponding to a closely related state. For example, consider a sdf system with $f(t) = A\cos(\omega_e t)$ where a parametric study of the effect of A on the system response is desired. Once the solution, $X(\omega)$, is obtained for one value of A, it may be used as the initial estimate for a neighboring case with a slightly different value of A.

3.2 Implementation Considerations. The authors presently use two methods to solve (4). The first method, direct iteration, is an iterative implementation of (4):

$$\Lambda(\omega)\cdot X^{(i)}(\omega) = F(\omega) + \eta(\omega, X^{(i-1}(\omega)). \tag{7}$$

$\Lambda(\omega)$[5] and $F(\omega)$ are fixed by the system and the external forcing function, respectively, once the ω_k's are selected. New generations of $X^{(i)}(\omega)$ may be found by evaluating $\eta(\cdot)$, as described previously, adding it to $F(\omega)$, and multiplying by Λ^{-1}. Since Λ is a constant matrix representing the linear part of the system, it may be inverted once and saved. A flow chart of the direct iteration approach is shown in Fig. 1.

The second approach used by the authors for solving (4) is the Newton-Raphson method (cf., Stoer and Bulirsch, 1980), with a difference quotient approximation of the Jacobian. For the example problem in this paper, Newton-Raphson is more robust than direct iteration (it converges at times that direct iteration fails) and it converges in fewer iterations. However, when both methods converge, computation time is greater for Newton-Raphson than for direct iteration because of the effort required to recompute the Jacobian at each iteration. Newton-Raphson is also more difficult to implement. In some cases Newton-Raphson fails to converge, so more robust methods (cf., Wolfe, 1959; Broyden, 1969; Stoer and Bulirsch, 1980; Shacham, 1986) may be required if a solution is desired for all regions of the parameter space.

[5] Professor Alok Sinha of Pennsylvania State University has pointed out that in the absence of damping Λ may be singular. This may be remedied by adding a linear damping term to both sides of any equation at fault. The damping term may be lumped with the nonlinear term(s) on the right-hand side of an equation.

Equation (4) represents $m(1+N/2)$ equations (for m degrees-of-freedom) which for most methods is unwieldy, except for small values of N. The computational effort of the direct iteration method, $O[mN(m+\log(N)]$ multiplications per iteration, is much less affected by "N" than Newton-Raphson, which has $O[(mN)^2 \cdot \log(N)]$ multiplications per iteration. In the approach used here, rather than limiting N, which would greatly reduce the number of frequencies considered in the solution, the direct iteration approach is used first to estimate which frequency components are significant. Then, if Newton-Raphson is employed, equation (4) is implemented only for those values of k for which $X^{(i)}(\omega_k)$ is a significant component in the last estimate of the solution vector obtained from the direct iteration method, $\{X^{(i)}(\omega_o), \ldots, X^{(i)}(\omega_{N/2})\}$. This is discussed further in Section 5. This approach, by solving only the significant frequency components, keeps the number of equations and unknowns at a minimum while still allowing a full spectrum of frequencies to be considered in the solution.

There are two types of error that may corrupt FFT values. *Aliasing* error arises when the FT is nonzero for frequencies above the maximum frequency considered by the FFT ($\omega_{\max} = \pi/\Delta T$). Power at the higher frequencies is aliased or folded back and added to the FFT values for $\omega < \pi/\Delta T$. *Leakage* error occurs when the frequency values of the FFT ($k\cdot\Delta\omega$, or ω_k) do not coincide precisely with each frequency in the FT that has nonzero power. Power at a frequency not represented in the FFT is leaked to frequencies that are represented. Leakage can only be eliminated if the sampled time signal is periodic.

For the following sample problem aliasing is insignificant (as verified by taking smaller time steps), and both the excitation on the system and the system response are periodic, so no leakage will occur. Most nonlinear forces are periodic when subject to a periodic input, so the assumption of a periodic response to a periodic excitation is typically valid. Discussions of the DFT, FFT algorithms, aliasing, and leakage may be found in Jackson (1986), Oppenheim and Schafer (1975), and Press et al. (1986).

4 Sample Problem

In many mechanical applications the most significant source of vibrational damping is provided by friction. For example, friction damping occurs naturally at joints in fabricated structures, friction damping is used to control the earthquake response of buildings, and friction dampers are used in high speed turbomachinery to reduce resonant stresses in blades. An elastic/perfectly-plastic friction model may also be used to analyze the elasto-plastic behavior of materials. Interest in these applications has motivated considerable research into how friction affects the dynamic response of structures (cf., Plunkett's review of friction damping research, 1980).

In the problem considered the nonlinear element consists of a spring in series with a friction constraint (Fig. 2). The friction contact is assumed to exhibit simple Coulomb-type behavior, i.e., when slip occurs the force is constant in magnitude and directed to oppose relative motion. Since the damper force in this model depends on the history of the response, it is easiest to illustrate the damper force by example. In Fig. 2 (*b*), for instance, the damper force exhibits bilinear hysteresis, which occurs when the input to the damper is harmonic. For more complicated motion the damper force could take on any value within a similar hysteresis loop, where the upper and lower limits of the input, which represent the extreme amplitudes of motion, need not be symmetric about zero. In the sample problem the equations have been normalized so that the friction force, μC_f, is unity and does not appear explicitly.

Downloaded 03 May 2010 to 171.66.16.31. Redistribution subject to ASME license or copyright; see http://www.asme.org/terms/Terms_Use.cfm

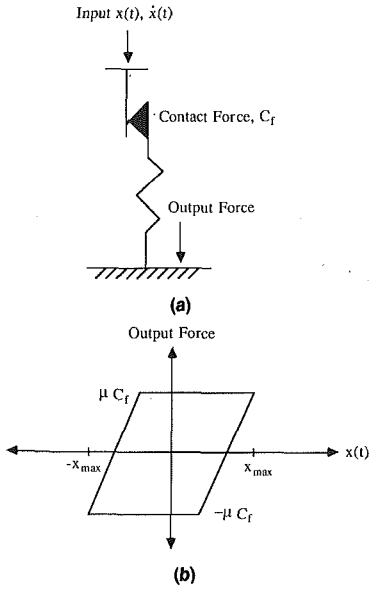


Fig. 2 Elastic/perfectly-plastic friction damper; (*a*) graphic representation and (*b*) sample output for harmonic input

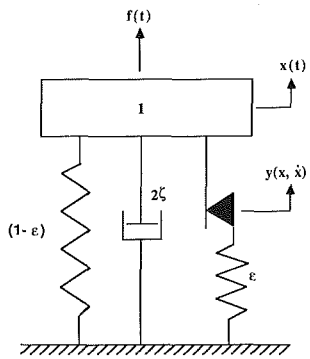


Fig. 3 Elastic/perfectly-plastic damper and system

The system used to illustrate the AFT method has only one degree-of-freedom. From the formulation in Section 3.1 it is clear that the method easily extends to multiple degrees-of-freedom (mdf). The computational savings of the AFT method over numerical integration should be even more dramatic for mdf systems since the number of frequencies to consider depends only on the excitation and the nonlinearities, not on the number of degrees-of-freedom.

4.1 An Elastic/Perfectly-Plastic Friction Damper. The sample problem was previously unsolved, although it can be solved easily by numerical integration. It would be either difficult or impossible to solve by other methods. The accuracy of the solution is judged by comparison to numerical integration. The comparison is made in the time domain to show the accuracy of the AFT method in describing both the amplitude and phase of the steady-state response.

Multiple discrete frequencies of excitation arise in high speed turbomachinery applications because as the turbine blades rotate they pass through a nonuniform, circumferentially distributed pressure field. This introduces excitation frequencies that are integer multiples of the rotation speed of the turbomachine. It is also frequently necessary to model friction dampers as having compliance, rather than being perfectly rigid. These physical considerations motivate the sdf model with an elastic/perfectly-plastic friction damper subjected to three discrete frequencies of excitation (Fig. 3). The nondimensionalized equation of motion for this system is:

$$\ddot{x}+2\zeta\dot{x}+(1-\epsilon)x=f(t)-\epsilon y(x,\dot{x}) \tag{8}$$

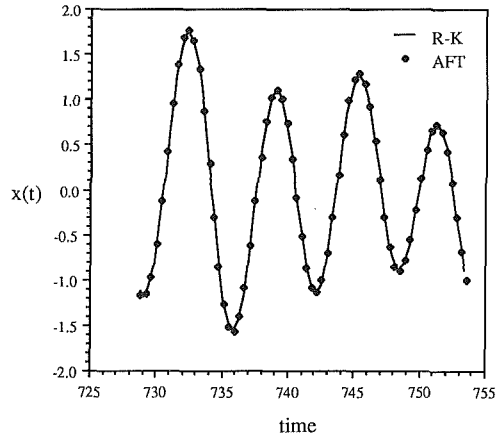


Fig. 4 Amplitude and phase comparison between AFT method and fourth-order Runge-Kutta solutions for three frequency excitation

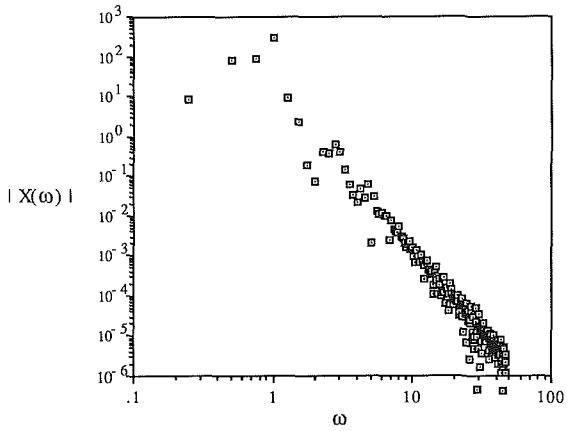


Fig. 5 Discrete Fourier transform of response for three frequency excitation

where $f(t)=0.75\ \sin\ (0.5\ t)+0.5\ \sin(0.75t)+0.375\ \sin(t)$, ζ, the fraction of critical viscous damping, is 0.01 (1 percent), and ϵ, a measure of the relative spring stiffnesses, is 0.25. The distance the mass must displace for slip of the friction damper to occur is unity. The nonlinear force on the mass is equal to the stiffness, ϵ, of the elastic friction damper times the displacement of the friction contact point, $y(\bullet)$. The contact slips when the magnitude of the friction force equals ϵ; the resulting force resists the motion. The specific excitation was chosen to provide an interesting response.

One period of the steady-state response of this system is shown in Fig. 4. The AFT and numerical integration solutions compare almost perfectly in both amplitude and phase. Since slip occurs at an amplitude of unity, there is considerable participation of the friction damper in this response. The frequency spectrum of the response (FFT) is shown in Fig. 5. This problem is used in the following section to make accuracy and efficiency comparisons between the AFT method and fourth-order Runge-Kutta integration.

4.2 Convergence, Error, and Computational Efficiency. In the absence of aliasing and leakage the FFT of a function is equivalent to a truncated Fourier series representation. Therefore, the AFT method should exhibit the convergence and error characteristics of Fourier series. Given a periodic excitation, with period Π, and assuming the time sampling is over one period, the maximum frequency in the FFT representation is:

$$\omega_{max}=\frac{\pi}{\Pi}N. \tag{9}$$

Downloaded 03 May 2010 to 171.66.16.31. Redistribution subject to ASME license or copyright; see http://www.asme.org/terms/Terms_Use.cfm

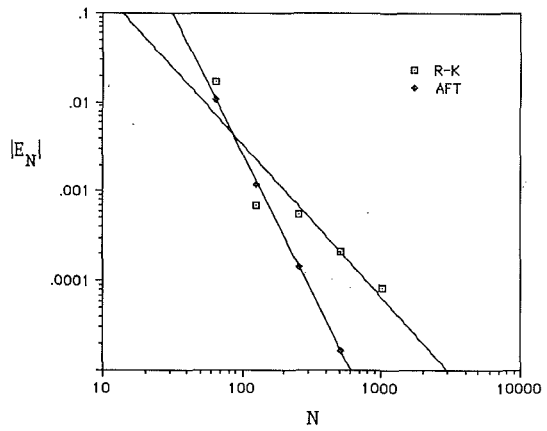


Fig. 6 Error convergence comparison between AFT and fourth-order R-K methods

Since the highest frequency is proportional to the number of samples per period, N, a continuous function which exhibits ω^{-2} convergence, like $\Lambda(\omega)^{-1}$ for second order systems, will exhibit N^{-2} convergence in its FFT components. For the sample problem, the nonlinear force on the system, $N_f(t)$, is continuous, but has a discontinuous derivative, so $\eta(\omega)$ will also converge $O(N^{-2})$. Therefore, $X(\omega)$ is expected to converge $O(N^{-4})$, which is confirmed by Fig. 5. ($F(\omega)$ has infinite order convergence so it does not affect the convergence of $X(\omega)$.)

In order to compare convergence of the time domain errors, as N increases, for the AFT and Runge-Kutta methods the error is assumed to be of the form:

$$E_N = x_N - x_{ex} = aN^c \tag{10}$$

where x_N is the value of $x(t)$ at a specified time using N sample points, x_{ex} is an extrapolated "exact" answer, E_N is the estimated error, N is the number of sample points per period, "a" is a constant, and "c" is the constant that gives the order of convergence of the error. Using three values of N gives three equations that allow the parameters x_{ex}, a, and c to be evaluated. The consistency of the error convergence is checked with two of the original three values of N, plus and an additional, fourth value. These permit another calculation of the parameters in (10).

For the AFT method, the $O(N^{-4})$ convergence of the FFT should produce similar convergence in the time domain error. This is the case if the FFT components are known precisely. However, changing N affects truncation and aliasing errors, so for different values of N the FFT components for the same frequency vary slightly. Consequently, additional errors appear in the time domain. Using $N = 64$, 128, and 256, in single precision, the AFT time domain error for equation (10) was found to be $O(N^{-3.1})$. Since the sampling period, ΔT, is Π/N, this is equivalent to $O(\Delta T^{3.1})$ convergence in the error. The error was consistent when estimated with $N = 128$, 256 and 512.

When the functions in a problem are infinitely differentiable a fourth-order Runge-Kutta (R-K) integration has error $O(\Delta T^4)$, or $O(N^{-4})$. When a function has discontinuous derivatives, like $\epsilon y(t)$ (the nonlinear force in problem 4.1), that error estimate is invalid. Since the R-K method steps progressively forward in time, accumulated roundoff error can also dominate truncation error. In fact, for this problem, no consistent error convergence (using (10)) was observed for R-K in single precision, with $N = 64$, 128, 256, 512, and 1024. Using the same values of N in double precision R-K simulations, the error was $O(\Delta T^{1.6})$, or $O(N^{-1.6})$. The error results for both R-K and AFT methods are plotted in Fig. 6.

It is impossible to make a general comparison of computational efficiency between the AFT and R-K methods. The efficiencies of both depend strongly on system parameters. Depending on damping, for example, the system may require any number of periods of oscillation before steady-state is reached. Another concern for R-K is that with complicated wave forms, like the solution to this problem (Fig. 4), it is very difficult to determine when steady-state has been achieved. The AFT method tests for convergence in the frequency domain where it is easy to discern. However, for a sample comparison, the following test was performed. This sample problem – a sdf system with three input frequencies and an elastic/perfectly-plastic friction damper – was analyzed through the 30th period of oscillation. The 30th period was selected as representative of an average number of cycles to reach steady-state. In order to achieve the same accuracy (i.e., similar error in Fig. 6) the AFT method was implemented in single precision with 256 points per period, and the R-K method was implemented in double precision with 512 points per period. In this case the AFT method took 21.7 seconds[6] and Runge-Kutta took 389 seconds on a Macintosh II, a factor of 18 difference.

5 Features of the AFT Method

Certain fundamental concepts underlying the AFT method are also employed in the FG (Fast Galerkin) method introduced by Ling and Wu (1987). Ling and Wu implement Urabe's Galerkin method with an FFT, making the method computationally efficient. In Urabe's approach the system of nonlinear equations is put into state variable form, a solution is asssumed in the form of a truncated Fourier series, and the coefficients of the Fourier series are solved for iteratively – with nonlinear terms evaluated in the time domain. Since the coefficients of the Fourier series are equivalent to the components of the DFT, the AFT and FG methods are similar in this respect. There are, however, differences in how the methods formulate and implement solutions of equations. These differences highlight some of the features of AFT method.

The first difference between the AFT and Galerkin methods lies in the form of the equations to be solved. The AFT method permits the equations to be of any order, while Urabe's formulation, which Ling and Wu repeat, assumes the equations are in first order state variable form. The AFT method only finds the linearly independent functions, thereby reducing the number of equations to be solved.

Another feature of the AFT formulation is the general manner in which it handles nonlinearities. In the problems considered by Urabe, as well as Ling and Wu, the nonlinearities are expressed analytically. In many applications, such as the elastic-plastic damper problem, the nonlinearities are hysteretic and analytical expressions may be difficult or impossible to obtain. In the AFT approach the user is provided with the full state history in order to compute the nonlinear forces in a user supplied subprogram, in a manner similar to that used in standard time integration codes.

Perhaps the most significant computational advantage of the AFT method is its technique for reducing the number of equations. As discussed previously, increasing the number of frequencies included in the solution can significantly increase

[6] It would also be possible to solve this problem using Runge-Kutta time integration in conjunction with a two point boundary value formulation. In this approach the displacement and velocity of the mass at the beginning of the period are unknowns whose values must be determined so that the solution satisfies the periodicity requirements. Such an approach requires an iterative method for solving the resulting nonlinear constraint equations (for a discussion of this approach see, for example, Press et al., 1986, Chap. 16). This procedure is less standard than time integration and, consequently, was not investigated here. However, it could be significantly more efficient than time integration and more competitive with the computational efficiency of the AFT method. Again, the outcome of such a comparison would depend on the specific physical system considered, as well as on the complexity of the frequency content of the excitation.

Downloaded 03 May 2010 to 171.66.16.31. Redistribution subject to ASME license or copyright; see http://www.asme.org/terms/Terms_Use.cfm

the computational effort, but in many problems it may be necessary to consider both low and high frequencies. The AFT implementation permits the user to include a relatively large number of frequencies and to set a "cutoff" fraction. While using direct iteration (which is computationally efficient), the algorithm scans all the frequency components to estimate which components lie above the cutoff fraction relative to the largest component. These components are considered "significant." If it becomes necessary to employ an intensive equation solver, like Newton-Raphson, only the equations corresponding to the significant components are included. This approach also makes it easy for the user to examine tradeoffs between higher accuracy (low cutoff) and lower computation time (high cutoff).

6 Concluding Remarks

In the absence of aliasing, leakage, and roundoff errors the AFT method converges uniformly to the exact answer as $N \to \infty$. Even when it cannot be eliminated, means are available for limiting the error so that good approximate solutions may be obtained. For example, in many problems the power in a signal decays asymptotically to zero as the frequency increases, so aliasing cannot be eliminated (without analog filtering). However, it is still possible to obtain exact solutions to within the precision of the computer by selecting ΔT so that power at frequencies exceeding $(\pi/\Delta T)$ cannot numerically affect the solution. In the sample problem the error in the AFT method dropped off much more quickly than the error in numerical integration.

Solutions generated by the AFT method are conveniently presented in either the frequency or time domain, or both. The AFT method also lends itself to parametric and sensitivity studies because the solution for one set of parameters supplies a good estimate of the solution for a "neighboring" set of parameters, which aids in convergence of the iterations.

Relative to other frequency domain methods, the AFT method is amenable to more general, complicated nonlinearities and excitations. By switching to the time domain to evaluate the nonlinear forces, the AFT method can use the same description of the nonlinear forces used for numerical integration. The only constraint on the excitation is that its Fourier transform can be approximated using the FFT approach.

Acknowledgment

This work was supported by the National Science Foundation, grant number MSM 8703887.

References

Broyden, C. G., 1969, "A New Method of Solving Nonlinear Simultaneous Equations," *Computer Journal*, Vol. 12, pp. 94–99.

Cesari, L., 1963, "Functional Analysis and Periodic Solutions of Nonlinear Differential Equations," *Contributions to Differential Equations*, Vol. 1, pp. 149–187.

Dowell, E. H., 1983, "The Behavior of a Linear, Damped Modal System with a Nonlinear Spring-Mass-Dry Friction Damper System Attached," *Journal of Sound and Vibration*, Vol. 89, No. 1, pp. 65–84.

Gelb, A., and Vander Velde, W. E., 1968, *Multiple-Input Describing Functions and Nonlinear System Design*, McGraw-Hill Book Co., New York.

Griffin, J. H., 1980, "Friction Damping of Resonant Stresses in Gas Turbine Engine Airfoils," ASME *Journal of Engineering for Power*, Vol. 102, pp. 329–333.

Iwan, W. D., 1974, "Application of Nonlinear Analysis Techniques," *Applied Mechanics in Earthquake Engineering*, W. D. Iwan, ed., ASME AMD Vol. 8.

Jackson, L. B., 1986, *Digital Filters and Signal Processing*, Kluwer Academic Publishers, Boston, Chapter 7.

Jezequel, L., 1983, "Structural Damping by Slip in Joints," ASME *Journal of Vibration, Acoustics, Stress, and Reliability in Design*, Vol. 105, No. 4, pp. 497–504.

Lau, S. L., Cheung, Y. K., and Wu, S. Y., 1982, "A Variable Parameter Incremental Method for Dynamic Instability of Linear and Nonlinear Elastic Systems," ASME JOURNAL OF APPLIED MECHANICS, Vol. 49, No. 4, pp. 849–853.

Lau, S. L., Cheung, Y. K., and Wu, S. Y., 1983, "Incremental Harmonic Balance Method with Multiple Time Scales for Aperiodic Vibration of Nonlinear Systems," ASME JOURNAL OF APPLIED MECHANICS, Vol. 50, No. 4, pp. 871–876.

Ling, F. H., and Wu, X. X., 1987, "Fast Galerkin Method and Its Application to Determine Periodic Solutions of Non-Linear Oscillators," *International Journal of Non-Linear Mechanics*, Vol. 22, No. 2, pp. 89–98.

Nayfeh, A. H., and Mook, D. T., 1979, *Nonlinear Oscillations*, John Wiley and Sons, New York.

Oppenheim, A. V., and Schafer, R. W., 1975, *Digital Signal Processing*, Prentice-Hall, Inc., Englewood Cliffs, N.J., Chapters 1, 3, and 6.

Pierre, C., Ferri, A. A., and Dowell, E. H., 1985, "Multi-Harmonic Analysis of Dry Friction Damped Systems Using an Incremental Harmonic Balance Method, ASME JOURNAL OF APPLIED MECHANICS, Vol. 52, No. 4, pp. 958–964.

Plunkett, R., 1980, "Friction Damping," *Damping Applications for Vibration Control*, AMD Vol. 38, P. J. Torvik, ed., ASME, New York.

Press, W. H., Flannery, B. P., Teukolsky, S. A., and Vetterling, W. T., 1986, *Numerical Recipes*, Cambridge University Press, New York, Chapters 9 and 12.

Shacham, M., 1986, "Numerical Solution of Constrained Nonlinear Algebraic Equations," *International Journal for Numerical Methods in Engineering*, Vol. 23, pp. 1455–1481.

Sinha, A., and Griffin, J. H., 1983, "Friction Damping of Flutter in Gas Turbine Engine Airfoils," *AIAA Journal of Aircraft*, Vol. 20, No. 4, pp. 372–376.

Sinha, A., and Griffin, J. H., 1984, "Effects of Static Friction on the Forced Response of Frictionally Damped Turbine Blades," ASME *Journal of Engineering for Gas Turbines and Power*, Vol. 106, No. 1, pp. 65–69.

Stoer, J., and Bulirsch, R., 1980, *Introduction to Numerical Analysis*, Springer-Verlag, New York, Chapter 5.

Urabe, M., 1965, "Galerkin's Procedure for Nonlinear Periodic Systems," *Archive for Rational Mechanics and Analysis*, Vol. 20, pp. 120–152.

Urabe, M., and Reiter, A., 1966, "Numerical Computation of Nonlinear Forced Oscillations by Galerkin's Procedure," *Journal of Mathematical Analysis and Applications*, Vol. 14, pp. 107–140.

Wolfe, P., 1959, "The Secant Method for Simultaneous Nonlinear Equations," *Communications of the ACM*, Vol. 2, pp. 12–13.

Zang, T. A., and Hussaini, M. Y., 1985, "Recent Applications of Spectral Methods in Fluid Dynamics," *Lectures in Applied Mathematics*, Vol. 22: *Large-Scale Computations in Fluid Mechanics*, edited by B. E. Engquist, S. Osher, and R. C. J. Somerville; eds., American Mathematical Society. Providence, R.I., Part 2, pp. 379–409.

Downloaded 03 May 2010 to 171.66.16.31. Redistribution subject to ASME license or copyright; see http://www.asme.org/terms/Terms_Use.cfm

On the Stability Behavor of Bifurcated Normal Modes in Coupled Nonlinear Systems

C. H. Pak
Professor.
Department of Mechanical Engineering,
Inha University,
Inchon 402-751, Republic of Korea

The stability of bifurcated normal modes in coupled nonlinear oscillators is investigated, based on Synge's stability in the kinematico-statical sense, utilizing the calculus of variations and Floquet's theory. It is found, in general, that in a generic bifurcation, the stabilities of two bifurcated modes are opposite, and in a nongeneric bifurcation, the stability of continuing modes is opposite to that of the existing mode, and the stabilities of the two bifurcated modes are equal but opposite to that of the continuing mode. Some examples are illustrated.

Introduction

Consider nonlinear conservative, holonomic systems S of two-degrees-of-freedom whose kinetic energy T may be written in the form

$$T = \tfrac{1}{2}(\dot{x}^2 + \dot{y}^2) \tag{1}$$

where x and y are generalized coordinates, and dots denote differentiation with respect to time t. The potential energy $V(x, y)$ of systems S is assumed to satisfy the following properties (Johnson and Rand, 1979; Rosenberg, 1966);

(a) $V(x, y) = V(-x, -y)$,

(b) $\nabla V = 0$ only at the origin of configuration space, and

(c) $V(x, y)$ is positive definite, and the curves $V(x, y) =$ constant form a continuum of smooth, simple closed curves surrounding the origin.

Then there is an energy integral

$$T + V(x, y) = h \tag{2}$$

where h is a constant equal to the total energy of a motion.

Rosenberg (1966) showed that in many degree-of-freedom systems the number of normal modes may exceed the degrees of freedom, called superabundant normal modes. Anand (1972) and Yen (1974) have shown that in systems S normal modes occur in pairs. Recently, Johnson and Rand (1979) have demonstrated that normal modes occur generically in pairs and the nongeneric case corresponds to the bifurcation which is divided into two types; (i) the generic bifurcation in which a normal mode B appears out of nowhere and splits into two modes B_1 and B_2, as shown in Fig. 1, and (ii) the nongeneric bifurcation in which an existing mode C_1 throws off two new modes B_1 and B_2 and continues to exist itself, as shown in Fig. 2.

The purpose of this paper is to investigate the behavior of stability of normal modes in connection with the bifurcation. In particular, we shall be concerned with the stability relation between bifurcated modes B_1 and B_2 for a generic bifurcation,

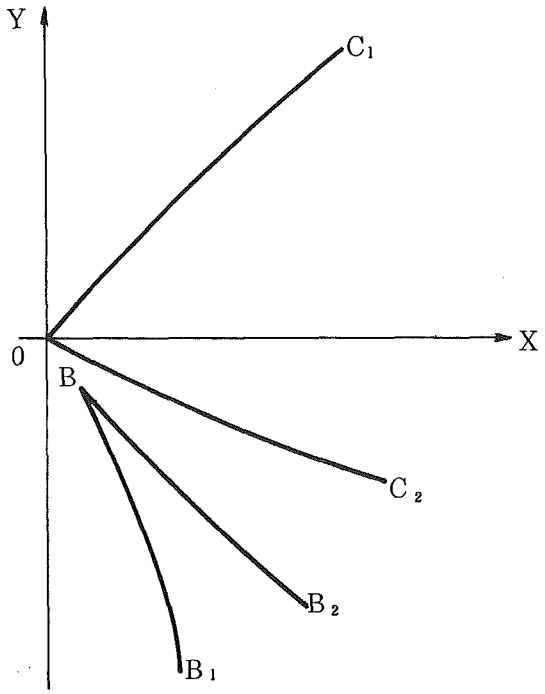


Fig. 1 An example of generic bifurcation (Shin, 1986; Yun, 1986): The loci of rest points of normal modes are drawn. Curves C_1 and C_2 represent the continuous extenstion of linearized modes. A and B appears out of nowhere and splits into two modes B_1 and B_2.

Contributed by the Applied Mechanics Division of THE AMERICAN SOCIETY OF MECHANICAL ENGINEERS for presentation at the Joint ASCE/ASME Applied Mechanics, Biomechanics, and Fluids Engineering Conference, San Diego, CA, July 9-12, 1989.

Discussion of this paper should be addressed to the Editorial Department, ASME, United Engineering Center, 345 East 47th Street, New York, N.Y. 10017, and will be accepted until two months after final publication of the paper itself in the JOURNAL OF APPLIED MECHANICS. Manuscript received by ASME Applied Mechanics Division, September 30, 1986; final revision, July 1, 1988. Paper No. 89-APM-1.

Copyright © 1989 by ASME

Downloaded 03 May 2010 to 171.66.16.31. Redistribution subject to ASME license or copyright; see http://www.asme.org/terms/Terms_Use.cfm

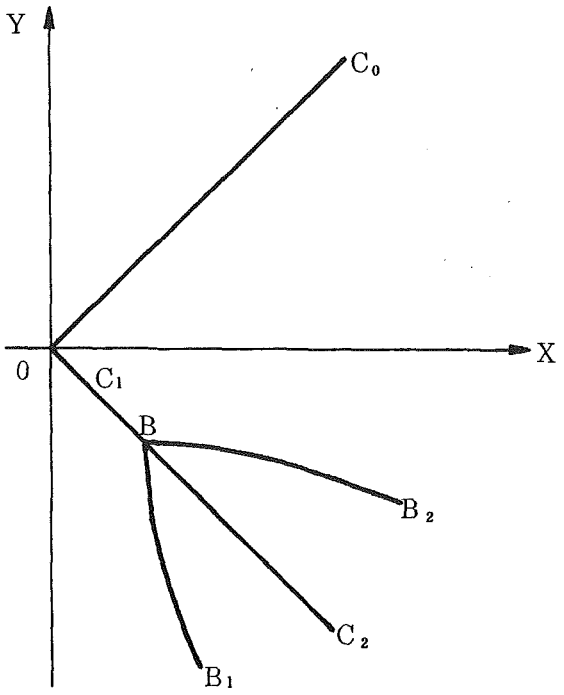


Fig. 2 An example of nongeneric bifurcation: The loci of the rest points of normal modes are drawn. The curve C_0 is the continuous extension of a linearized mode. The curve C_1 is the continuous extension of a linearized mode, but this mode throws off two new modes B_1 and B_2 at B, and continues to exist on the curve C_2.

and the stability relation among B_1, B_2, C_1 and C_2 modes for a nongeneric bifurcation.

The concept of stability is based on Synge's stability in the kinematico-statical sense (Synge, 1926; Whittaker, 1944) for a fixed energy h. Since a normal mode is a periodic motion, the governing equation for determining the stability is expressed in the form of Hill's equation and, hence, Floquet theory is applicable.

Since a system S is conservative, the equations of motion may be described by the calculus of variations. It has been shown elsewhere (Pak, to appear) that Synge's stability equation is identical with the Jacobi differential equation in the calculus of variations. The characteristic exponents for determining stability of the associated Hill's equation are estimated by utilizing the envelope theorem.

The concept of Synge's stability seems to be stronger than that of Liapunov stability because it is based on a concept reminiscent of orbital stability defined in the configuration space (Rand, 1973). The procedure for determining stability is applicable to motions of large energy, even to nonlinearizable systems, and the small divisor problem does not arise, as compared to other procedures, such as an approximate Poincaré map (Month and Rand, 1980) which is restricted to motions of small energy and depends upon the ratio of linearized frequencies.

The Stability Criterion

Let C be the normal modes whose stability is to be studied, and C^* a perturbed trajectory. Synge (1926) has defined the correspondence between configurations of C and C^* not by the condition of simultaneity but by the condition that the disturbance vector $\vec{\beta}$ shall be orthogonal to C. Then permanent smallness of $\vec{\beta}$ for every perturbed trajectory is called the stability in the kinematico-statical sense. In the case of two-degrees-of-freedom systems its magnitude β is governed by

$$\ddot{\beta} + (Kv^2 + \Sigma V_{ij} n_i n_j + 3\kappa^2 v^2)\beta + 2\kappa\, \delta h = 0 \tag{3}$$

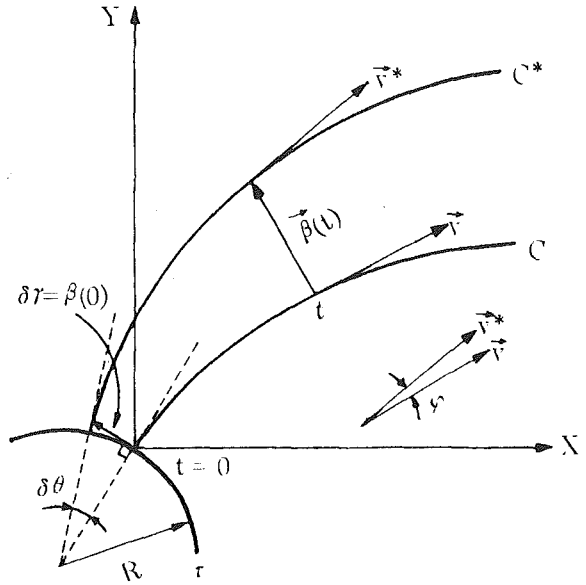


Fig. 3 Construction of a system of trajectories, each defined parametrically by a starting curve τ

where β is counted positive on one side of C, and negative on the other side (Whittaker, 1944), and

K = Gaussian curvature of the configuration space

v = velocity of the normal mode C

κ = curvature of C

$V_{ij} = \nabla\nabla V$

n_i = unit vector normal to C

δh = infinitesimal difference in energy h between C and C^*.

We shall consider the stability of C for a fixed h, $\delta h = 0$. Since the configuration space, considered here, is Euclidean, $K = 0$. Equation (3) becomes homogeneous, and it is possible to obtain geometrical insights in what follows.

Let $t = 0$ when C passes through the origin. For every perturbed trajectory C^*, one finds an initial displacement disturbance $\delta\gamma$ for the above correspondence and an initial angular disturbance $\delta\theta$, as shown in Fig. 3. Therefore, it is possible to construct a starting curve τ which is a circular arc orthogonal to the velocity vector of C passing through the origin and having radius R where $\delta\gamma = R\delta\theta$. When the initial disturbance is restricted to an angular disturbance only, the starting curve τ is shrunk to a point. Since $\delta\gamma$ and $\delta\theta$ are infinitesimal, two curves C and C^* belong to a system of curves which start orthogonally from τ and satisfy the equations of motion

$$\ddot{x} = -\frac{\partial V}{\partial x}, \quad \ddot{y} = -\frac{\partial V}{\partial y} \tag{4}$$

and the energy integral (2). Equivalently, equations (2) and (4) are written, due to Jacobi least action principle, in the variational form

$$\delta \int_{P_2}^{P_1} \sqrt{2[h - V(x, y)]}\, ds = 0 \tag{5}$$

where P_1 and P_2 are prescribed configurations, and ds is Euclidean arc length of a trajectory.

Let the starting curve τ be parametrized by α so that C and C^* correspond to $\alpha = \alpha_o$ and $\alpha = \alpha_o + \delta\alpha$, respectively. Then C and C^* may be expressed in the form

$$\begin{aligned} &C: x = x(t, \alpha_o),\ y = y(t, \alpha_o) \text{ and} \\ &C^*: x = x(t, \alpha_o + \delta\alpha),\ y = y(t, \alpha_o + \delta\alpha), \text{ respectively.} \end{aligned} \tag{6}$$

Downloaded 03 May 2010 to 171.66.16.31. Redistribution subject to ASME license or copyright; see http://www.asme.org/terms/Terms_Use.cfm

It has been shown (Pak, to appear) that equation (3), having $\delta h = 0$, is identical with Jacobi differential equation in the calculus of variations and that the disturbance $\beta(t)$ is expressed as

$$\beta(t) = z(t)\delta\alpha \tag{7}$$

where

$$z(t) = \frac{-x_\alpha y_t + y_\alpha x_t}{v} \tag{8}$$

in which subscripts denote partial derivatives. Then equation (3) is rewritten as

$$\ddot{z} + Q(t)z = 0 \tag{9}$$

where $Q(t) = \Sigma V_{ij} n_i n_j + 3\ \kappa^2\ v^2$, computed along C. Therefore, the stability of the normal mode C in the kinematico-statical sense is equivalent to the boundedness of every solution of equation (9) for all $t > 0$.

The time derivative $\dot{\beta}(t)$ of the disturbance has been geometrically shown to be

$$\dot{\beta}(t) = \pm v^* \sin\varphi \tag{10}$$

where v^* is the velocity of C^* shown in Fig. 3, φ is the angle between $\vec{v}$ and $\vec{v}^*$, the positive sign is selected when C^* tends to increase $\beta(t)$, and negative otherwise. It is noted that φ is not always infinitesimally small because the direction of C^* may differ from that of C by a finite value when C approaches to the rest point.

Let $z_1(t)$ and $z_2(t)$ be the normalized solutions of equations of equation (9) with initial conditions $z_1(0) = 1$, $\dot{z}_1(0) = 0$, and $z_2(0) = 0$, $\dot{z}_2(0) = 1$, respectively. Then the general solution of equation (9) for a perturbed trajectory C^* shown in Fig. 3 may be written as

$$\beta(t) = \delta\gamma\ z_1(t) + \sqrt{2h}\delta\theta\ z_2(t). \tag{11}$$

Let $2T$ be the period of normal mode C. Then the period of $Q(t)$ in equation (9) is T due to the property (a) of potential energy $V(x, y)$. It may be easily verified that $Q(t)$ is an even function, $Q(t) = Q(-t)$. Then the following relations are satisfied (Magnus and Winkler, 1979);

$$z_1(T) = 2\, z_1\left(\frac{T}{2}\right)\dot{z}_2\left(\frac{T}{2}\right) - 1 \tag{12a}$$

$$\dot{z}_2(T) = z_1(T) \tag{12b}$$

$$\dot{z}_1(T) = 2\, z_1\left(\frac{T}{2}\right)\dot{z}_1\left(\frac{T}{2}\right) \tag{12c}$$

$$z_2(T) = 2\, z_2\left(\frac{T}{2}\right)\dot{z}_2\left(\frac{T}{2}\right) \tag{12d}$$

where $T/2$ is the time when the normal mode C arrives at the rest point. The Wronskian determinant may be written as

$$z_1(t)\dot{z}_2(t) - \dot{z}_1(t)\ z_2(t) = 1. \tag{13}$$

As a consequence of Floquet's theorem, we express the stability criterion; a normal mode in a system S is stable in the kinematico-statical sense if and only if one of the following conditions (Magnus and Winkler, 1979)

$$|z_1(T)| < 1 \text{ or} \tag{14}$$

$$|z_1(T)| = 1 \text{ and } \dot{z}_1(T) = z_2(T) = 0 \tag{15}$$

is satisfied.

The Envelope Theorem and Bifurcation of Normal Modes

Let $C(t, \theta) = \{x(y, \theta), y(t, \theta)\}$ denote a trajectory having the total energy h which starts from the origin with an initial angle θ measured from the x-axis. In what follows, we shall consider a family of trajectories $C(t, \theta)$, $-\pi \le \theta \le \pi$, so that the disturbance $\beta(t)$ may be expressed in terms of $z_2(t)$ only in equation (11).

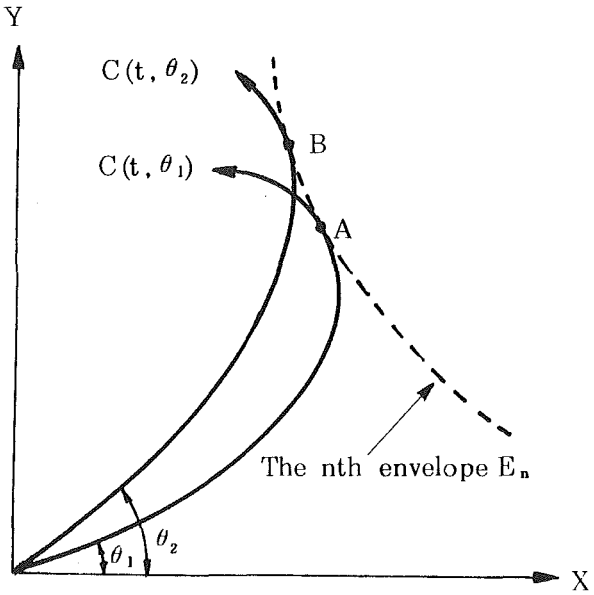


Fig. 4 The *n*th envelope of trajectories

At a conjugate point on $C(t, \theta)$, the following condition (Bolza, 1961) is satisfied;

$$-x_\theta y_t + y_\theta x_t = 0. \tag{16}$$

Since $C(\theta, t)$ remains in the bounded region expressed by equation (2), there are infinitely many conjugate points along a trajectory. Every pair of consecutive conjugate points is separated by a finite distance (Bolza, 1961). Let $t_n(\theta)$ be the time when $C(t, \theta)$ satisfies equation (16) at the nth time. Then the locus $C(t_n(\theta), \theta)$, $-\pi \le \theta \le \pi$, becomes the nth envelope E_n. And every E_n, $n = 1,2,3 \ldots$, is separated.

Since a normal mode $C(t, \theta_o)$ has two rest points where equation (16) is satisfied, there is an envelope E_n which intercepts the curve of rest points $V(x, y) = h$. Johnson and Rand (1979) considered E_1 only to demonstrate the existence and bifurcation of a special type of normal modes, called minimal normal modes. Actually, the rest point of a normal mode may be located on E_n, $n > 1$; for example, in a linear system having frequency ratio greater than two, one of the normal modes must pass through a conjugate point before it arrives at the rest point.

Let $I_n(\theta)$ be the action of a trajectory $C(t, \theta)$ defined by

$$I_n(\theta) = \int_0^{t_n(\theta)} \sqrt{2(h - V)}\sqrt{x_t^2 + y_t^2}\, dt \tag{17}$$

calculated along $C(t, \theta)$ from the origin to E_n. For given two trajectories $C(t, \theta_1)$ and $C(t, \theta_2)$, the envelope theorem (Section 33 of Bolza, 1961) may be expressed as

$$I_n(\theta_2) = I_n(\theta_1) + \int_A^B \sqrt{2(h - V)}\, d\bar{s} \tag{18}$$

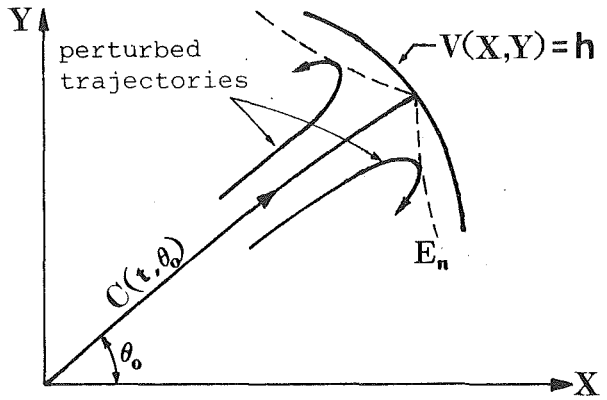
where the integration is performed along E_n, $d\bar{s}$ the Euclidean arc length of E_n, and A and B the nth conjugate points of $C(t, \theta_1)$ and $C(t, \theta_2)$, respectively, as shown in Fig. 4. The calculus of variations usually deals with E_1 only, but it is easily verified that equation (18) is valid for every E_n, $n = 1,2,3 \ldots$.

The derivative $I_n'(\theta)$ may be computed by equation (18),

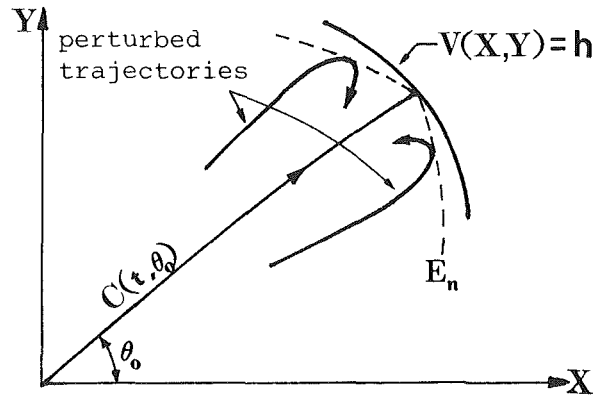
$$I_n'(\theta_1) = \left(\bar{v}\frac{d\bar{s}}{d\theta}\right)_{\theta=\theta_1} \tag{19}$$

where $\bar{v} = \sqrt{2(h - V)}$ is the velocity of $C(t, \theta_1)$ at the conjugate point. It is readily seen that there is an associated

Downloaded 03 May 2010 to 171.66.16.31. Redistribution subject to ASME license or copyright; see http://www.asme.org/terms/Terms_Use.cfm



(a) $I_n(\theta)$ has a relative minimum at $\theta=\theta_0$



(b) $I_n(\theta)$ has a relative maximum at $\theta \approx \theta_0$

Fig. 5 The extrema of $I_n(\theta)$ at a generic normal mode $C(t, \theta_0)$: E_n is the associated envelope

envelope E_n such that the function $I_n(\theta)$ is stationary at $\theta=\theta_0$ in which $C(t, \theta_0)$ is a normal mode.

In the interior region of $V(x, y)<h$, the envelope E_n is smooth except possibly at a finite numer of singular points where $d\tilde{s}/d\theta=0$. (For details of singular points, see Section 38 of Bolza (1961)). It is clear from equations (8), (11), and (16) that $z_2(t)=0$ on E_n for every trajectory in the interior region.

When a normal mode $C(t, \theta_0)$ arrives at the rest point at $t=T/2$, $z_2(T/2)$ is indeterminate by equation (8) because $x_x=y_t=v=0$ but it can be computed by solving equation (9). However, when $d\tilde{s}/d\theta=0$, it may be readily verified from the geometric viewpoint that every neighboring trajectory passes through the singular point, regardless of the condition that the singular point is located in the interior $V(x, y)<h$ or at the rest point and, hence, β vanishes. Therefore, we have the following:

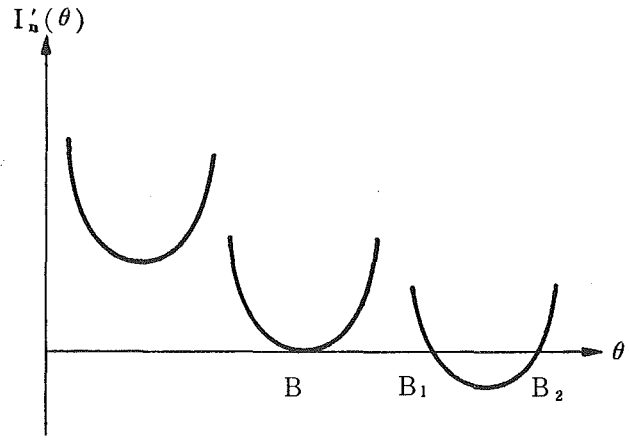
Lemma 1. Let $2T$ be the period of normal mode $C(t, \theta_0)$. If the associated envelope E_n satisfies the condition $d\tilde{s}/d\theta=0$ at $\theta=\theta_0$, then $z_2(T/2)=0$.

Consider a generic (Johnson and Rand, 1979) normal mode $C(t, \theta_0)$ in which the associated envelope E_n intercepts the curve $V(x, y)=h$ at $\theta=\theta_0$, and

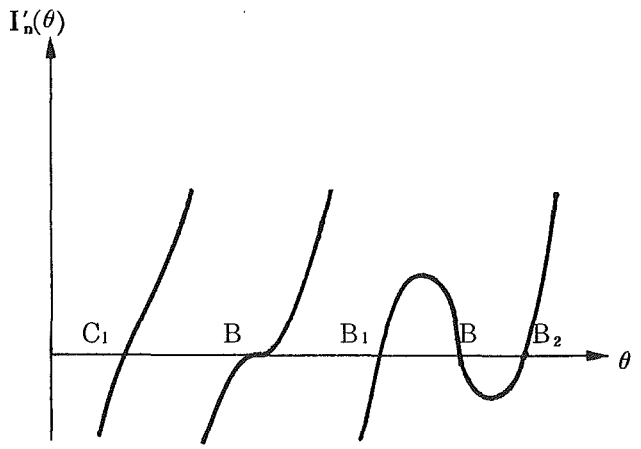
$$I_n'(\theta_0)=0 \quad I_n''(\theta_0)\neq 0. \tag{20}$$

This equation implies that the function $I_n(\theta)$ always has a relative minimum or maximum at $\theta=\theta_0$. When $I_n(\theta_0)$ is minimum (or maximum), every neighboring trajectory approaches E_n and goes away from (or comes closer to) the normal mode according to the envelope theorem, as shown in Fig. 5. Since there are $(n-1)$ conjugate points on the normal mode before it arrives at the rest point, we state the following:

Lemma 2. For a generic normal mode $C(t, \theta_0)$ in a system S $(-1)^{n-1}\dot{z}_2(T/2)>0$ if and only if $I_n(\theta)$ is minimum at $\theta=\theta_0$ $(-1)^{n-1}\dot{z}_2(T/2)<0$ if and only if $I_n(\theta)$ is maximum at $\theta=\theta_0$.



(a) Generic bifurcation



(b) Nongeneric bifurcation

Fig. 6 Generic and nongeneric bifurcations (Johnson and Rand, 1979): The point *B* is the bifurcation point, generic and nongeneric. Points *B*, B_1, and B_2 represent the respective curves in Fig. 1 and 2.

Consider a nongeneric (Johnson and Rand, 1979) normal mode $C(t, \theta_0)$ where

$$I_n'(\theta_0)=I_n''(\theta_0)=0 \tag{21}$$

and a bifurcation of normal modes occurs. The normal mode having these properties is called a bifurcation point. Since every generic normal mode $C(t, \theta_0)$ is continuously extended either from the linearized modes or from a bifurcation point, the initial angle θ_0 is a continuous function of energy h. Therefore $z_i(T/2)$ and $\dot{z}_i(T/2)$, $i=1,2$, are continuous in h.

From equation (19), $I_n''(\theta_0)$ is computed as

$$I_n''(\theta_0)=\frac{d\tilde{v}}{d\tilde{s}}\left(\frac{d\tilde{s}}{d\theta}\right)^2\Bigg|_{\theta=\theta_0} \tag{22}$$

where $\tilde{v}=0$ is utilized. Therefore, at least one of the following conditions must be satisfied at a bifurcation point;

$$\left(\frac{d\tilde{s}}{d\theta}\right)_{\theta=\theta_0}=0 \tag{23}$$

$$\left(\frac{d\tilde{v}}{d\tilde{s}}\right)_{\theta=\theta_0}=0. \tag{24}$$

The condition (23) means that $z_2(T/2)=0$ by Lemma 1. The condition (24) implies that the associated envelope E_n does smoothly touch the curve $V(x, y)=h$ at $\theta=\theta_0$. Therefore, the velocity of every neighboring trajectory vanishes at E_n. By equation (11), we have:

Downloaded 03 May 2010 to 171.66.16.31. Redistribution subject to ASME license or copyright; see http://www.asme.org/terms/Terms_Use.cfm

Lemma 3. If a normal mode in a system S has the associated envelope with the condition (24), then $\dot{z}_2(T/2)=0$.

Johnson and Rand (1979) have shown two types of bifurcation, generic and nongeneric, according $I_n'''(\theta_0)\neq 0$ and $I_n'''(\theta_0)=0$, respectively, as shown in Fig. 6. It is clear that after bifurcation, generic or nongeneric, every bifurcated mode becomes a generic normal mode which satisfies equation (20).

It is readily verified, by the Wronskian determinant (13), that conditions (23) and (24) cannot simultaneously occur at a bifurcation point. Then we shall show the following.

Lemma 4. When normal modes are bifurcated, generically or nongenerically, in a system S, we have at the bifurcation point

$$\dot{z}_2\left(\frac{T}{2}\right)=0.$$

To prove this Lemma for a generic bifurcation point suppose, on the contrary, that $\dot{z}_2(T/2)\neq 0$. Let h_0 be the energy at the bifurcation point. As h is increased from h_0 in a sufficiently small amount, two bifurcated modes split off from a generic bifurcation point. Then the function $I_n(\theta)$ has a relative minimum at one mode and maximum at the other. This implies that $\dot{z}_2(T/2)>0$ on one mode, and $\dot{z}_2(T/2)<0$ on the other by Lemma 2. This contradicts $\dot{z}_2(T/2)\neq 0$ because it is continuous in h, and proves Lemma 4 for a generic bifurcation.

From a nongeneric bifurcation point, two new modes, B_1 and B_2, and the continuing mode C_2 appear when h is increased from h_0 in a sufficiently small amount. Then the function $I_n(\theta)$ has a relative minimum at B_1 and B_2, and a maximum at C_2, or a maximum at B_1 and B_2, and a minimum at C_2 as shown in Fig. 6. This implies that the signs of $\dot{z}_2(T/2)$ are opposite on these modes by Lemma 2. The remaining part of proof is similar to that of a generic bifurcation.

The Oscillation Theorem of Hill's Equation

Since $\dot{z}_2(T/2)=0$ at a bifurcation point, by equations (12*a*) and (12*b*) we have $z_1(T)=\dot{z}_2(T)=-1$, and the solution $z_2(t)$ is periodic of period $2T$. The stability of this mode depends on the second condition of equation (15). By equation (12*d*), $z_2(T)=0$. Therefore, the stability of this mode is stable if and only if $z_1(T/2)=0$. If this condition is fulfilled, then both $z_1(t)$ and $z_2(t)$ are periodic, and every solution of solution (9) is periodic of period $2T$.

However, the value $z_1(T/2)$ may be a number, other than zero, in the continuum of real numbers. Consider a problem to determine the values of λ for which every solution of Hill's equation given in the form

$$\ddot{z}+[\lambda+Q(t)]z=0 \tag{25}$$

is stable where $Q(t)$ is the function described in equation (9). It is well known by the oscillation theorem (Magnus and Winkler, 1979) that there are stable intervals of λ and that the endpoint of stable intervals is, in general, unstable. Since $z_2(t)$ is a periodic solution of equation (25) at $\lambda=0$, it is located at the end point of a stable interval of λ. This implies:

Lemma 5. At a bifurcation point, generic or nongeneric, of a system S, $z_1(T/2)\neq 0$ in general.

Due to Lemma 4 and 5, the following theorem is asserted:

Theorem 1. In a system S, the normal mode at a bifurcation point, generic or nongeneric is, in general, unstable in the kinematico-statical sense.

The Stability Behavior of Bifurcated Modes

We shall show the stability behavior of generically bifurcated modes.

Theorem 2. If a normal mode appears out of nowhere and splits into two modes in a system S, then the stabilities of these two modes are, in general, opposite each other in the kinematico-statical sense.

Here the expression that the stabilities of two modes are opposite means that one must be stable, but the other unstable.

To prove this theorem, let h_0 be the energy at the bifurcation point where a normal mode $C(t, \theta_0)$ appears out of nowhere. As h is increased from h_0 in a sufficiently small amount, $C(t, \theta_0)$ splits into two modes. Then the function $I_n(\theta)$ has a relative minimum at one mode, and maximum at the other since the signs of $I_n''(\theta)$ are opposite each other, as depicted in Fig. 6(*a*). This implies, according to Lemma 2, that $\dot{z}_2(T/2)$ is positive at one mode, and negative at the other. But $z_1(T/2)\neq 0$ at $h=h_0$, in general, by Lemma 5. It is continuous in h, and its sign remains unchanged on two new modes. It is easily found that $z_1(T)$, computed by equation (12*a*), is smaller than -1 on one mode, and greater than -1 on the other by a sufficiently small amount. Then equation (14) may be applicable to complete the proof of Theorem 2.

Finally, the stability behavior of nongenerically bifurcation modes is to be shown in:

Theorem 3. If an existing mode in a system S throws off two new modes and continues to exist itself then, in general, the stability of continuing mode is opposite to that of existing mode, and the stabilities of the two new modes are equal but opposite to that of continuing mode in the kinematico-statical sense.

The expression that the stabilities of two modes are equal means that if one mode is stable, then the other is also stable, or if one mode is unstable, then the other is also unstable.

To prove Theorem 3, let h_0 and $C(t, \theta_0)$ be the energy and the normal mode at the bifurcation point, respectively. To prove the first assertion, notice that the sign of $I_n''(\theta_0)$ changes upon bifurcation, as depicted from Fig. 6(*b*). This implies that the function $I_n(\theta)$ has either a relative minimum at the existing mode and maximum at the continuing mode, or in the other way around. By Lemma 2, the signs of $\dot{z}_2(T/2)$ are opposite each other, and the remaining part of proof is similar to that of Theorem 2.

The second assertion may be simply demonstrated by noticing that both of bifurcated modes have the same sign of $I_n''(\theta_0)$. The third assertion may be shown by the fact that the sign of $I_n''(\theta)$ of bifurcated modes is opposite to that of continuing mode, as depicted from Fig. 6(*b*). The remaining part of proof is similar to that of Theorem 2.

Examples

Consider a system S_1 whose kinetic energy $T=1/2(\dot{x}^2+\dot{y}^2)$ and potential energy $V(x, y)$ given by

$$V(x, y)=\frac{1}{2}k_1x^2+\frac{1}{2}k_2(x-y)^2+\frac{1}{2}k_3y^2 + \frac{1}{4}\alpha_1x^4+\frac{1}{4}\alpha_2(x-y)^4+\frac{1}{4}\alpha_3y^4. \tag{26}$$

When every k_i and $\alpha_i=1,2,3$, are positive, the properties of a system S are fulfilled. It has been shown elsewhere (Shin, 1986; Yun, 1986) that the possibility of a bifurcation depends on the associated nonlinear homogeneous system S_1^* whose potential energy $V^*(x, y)$ is given by

$$V^*(x, y)=\frac{\alpha_1}{4}x^4+\frac{\alpha_2}{4}(x-y)^4+\frac{\alpha_3}{4}y^4. \tag{27}$$

If the associated homogeneous system S_1^* has four distinct similar modes, as computed by a procedure given by Rosenberg (1966), then the system S_1 has four normal modes which approach those of S_1^* when the energy h becomes suffi-

Downloaded 03 May 2010 to 171.66.16.31. Redistribution subject to ASME license or copyright; see http://www.asme.org/terms/Terms_Use.cfm

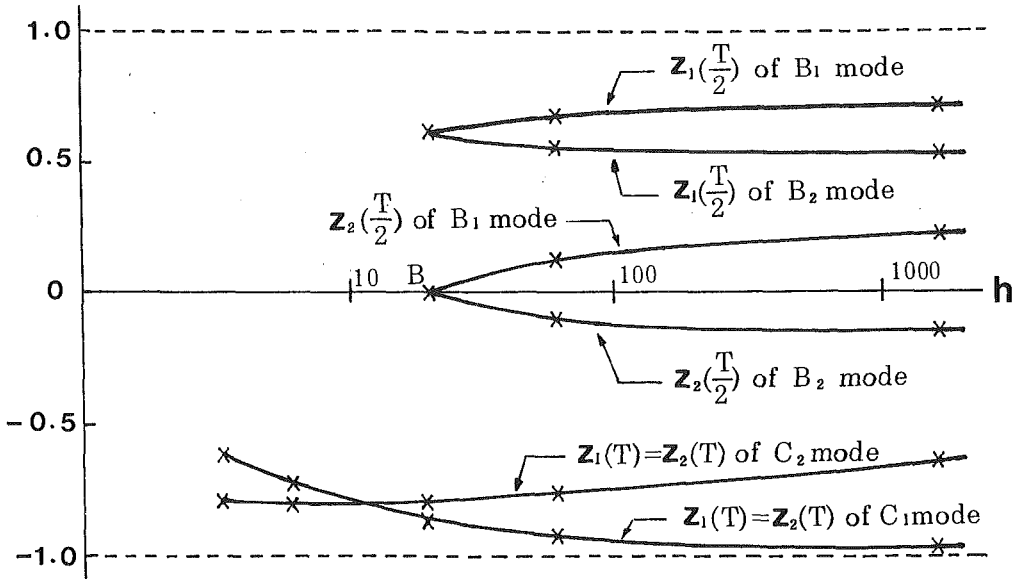


Fig. 7 Stability evaluations for a generic bifurcation (Hur, 1986): ($k_1 = 0.4$, $k_2 = 0.3$, $k_3 = 0.2$, $\alpha_1 = \alpha_3 = 1.6$ and $\alpha_2 = 0.32$). Modes B_1, B_2, C_1, and C_2 correspond to the respective curves in Fig. 1. The calculated points are marked as x.

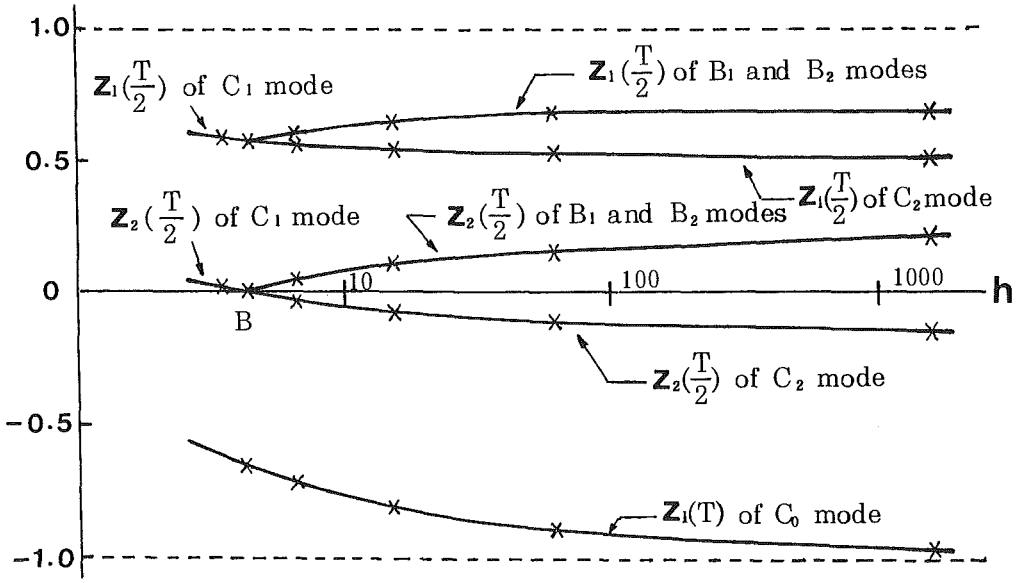


Fig. 8 Stability evaluations for a nongeneric bifurcation (Hur, 1986): ($k_1 = k_3 = 0.3$, $k_2 = 0.2$, $\alpha_1 = \alpha_3 = 1.6$ and $\alpha_2 = 0.32$). Modes B_1, B_2, C_1, and C_2 correspond to the respective curves in Fig. 2. The calculated points are marked as x.

ciently large. It has also been found that a nongeneric bifurcation occurs when the following approximate relation is satisfied;

$$(\alpha_1 + \alpha_3 - 8\alpha_2)(k_3 - k_1) + 2(\alpha_1 - \alpha_2)k_2 = 0, \tag{28}$$

and a generic bifurcation is expected, otherwise.

The exact normal modes and bifurcations are located by a personal computer. Having located them, the values of $z_i(T/2)$ and $\dot{z}_i(T/2)$, $i = 1, 2$, are calculated by equation (9) up to nine decimal points for each mode (Hur, 1986).

***(a)* Generic Bifurcation.** Choose $k_1 = 0.4$, $k_2 = 0.3$, $k_3 = 0.2$, $\alpha_1 = \alpha_3 = 1.6$ and $\alpha_2 = 0.32$. Then, the linearized modes, $h = 0$, are found at $\theta_1 = 54.2$ deg as the in-phase mode and $\theta_2 = -35.8$ deg as the out-of-phase mode. They are continuously extended to C_1 and C_2 curves as the energy h is increased, as shown in Fig. 1. As h grows infinitely large, θ_1 and θ_2 approach 45 deg and -21.3 deg, respectively.

When h reaches the value $h_0 = 21.3$, a new mode appears at $\theta_0 = -55.6$ deg and splits into two new modes, B_1 and B_2, as shown in Fig. 1, where B is the bifurcation point. It is found at B that $\dot{z}_2(T/2) = 0$ and $z_1(T/2) = 0.57 \neq 0$, illustrating Lemma 4 and 5, respectively.

As h is increased from h_0, the value $\dot{z}_2(T/2)$ grows positively on B_1 mode, and negatively on B_2 mode, but the sign of $z_1(T/2)$ remains unchanged, as shown in Fig. 7. The value of $z_1(T)$ or $\dot{z}_2(T)$ may be calculated by equation (12*a*), and it is easily concluded by equation (14) that B_1 mode is stable, but B_2 mode unstable, illustrating Theorem 2.

Downloaded 03 May 2010 to 171.66.16.31. Redistribution subject to ASME license or copyright; see http://www.asme.org/terms/Terms_Use.cfm

The values of $z_1(T)$ for C_1 and C_2 modes are similarly calculated and shown in Fig. 7. They are stable.

(b) Nongeneric Bifurcation. Choose $k_1 = k_3 = 0.2$, $k_2 = 0.3$, $\alpha_1 = \alpha_3 = 1.6$ and $\alpha_2 = 0.32$. This system is symmetric (Anand, 1972; Rosenberg, 1966) and the linearized modes are found at $\theta = \pm 45$ deg which are extended for all energy h. The $\theta = 45$ deg mode is denoted by C_0 in Fig. 2. At the energy $h_0 = 4.33$, the $\theta = -45$ deg mode throws of two new modes, B_1 and B_2. Therefore, the bifurcation point B is located at $h_0 = 4.33$ and $\theta_0 = -45$ deg. The $\theta = -45$ deg mode is divided into the existing mode C_1 and continuing mode C_2 by B as the boundary, and shown in Fig. 2.

It is found that, at the bifurcation point B, $\dot{z}_2(T/2) = 0$ and $z_1(T/2) = 0.565 \neq 0$ illustrating Lemma 4 and 5, respectively. Two bifurcated modes, B_1 and B_2, are symmetric with respect to C_2 mode. They have the same values of $z_1(T/2)$ and $z_2(T/2)$ for all $h \geq h_0$ and, hence, their stabilities are equal.

The values of $z_1(T/2)$ and $\dot{z}_2(T/2)$ are calculated at various h for B_1, C_1, and C_2 modes, and shown in Fig. 8. The values of $z_1(T/2)$ for these modes remain positive at all h. It is found that $\dot{z}_2(T/2) > 0$ for C_1 mode, and $\dot{z}_2(T/2) < 0$ for C_2 mode. Therefore, C_1 mode is stable but C_2 mode unstable. It is also found that $\dot{z}_2(T/2) > 0$ for B_1 and B_2 modes, implying that both B_1 and B_2 modes are equally stable.

The values of $z_1(T)$ for C_0 mode are similarly calculated at various h, and shown in Fig. 8. This mode is stable.

Acknowledgment

The author wishes to express his appreciation to Korea Science and Engineering Foundation for the financial support during the preparation of this paper.

References

Anand, G. A., 1972, "Natural Modes of Coupled Nonlinear Systems," *International Journal of Nonlinear Mechanics*, Vol. 7, pp. 81–91.

Bolza, O., 1961, *Lectures on the Calculus of Variations*, Dover Publications, New York, Sect. 15.

Hur, D. J., 1986, "On the Stability of Nonlinear Normal Mode Vibrations by the Geometry of Dynamics," M. S. Thesis, Inha University, Incheon, Korea.

Johnson, T. L., and Rand, R. H., 1979, "On the Existence and Bifurcations of Minimal Normal Modes," *International Journal of Nonlinear Mechanics*, Vol. 14, pp. 1–12.

Magnus, W., and Winkler, S., 1979, *Hill Equations*, Dover Publications, New York.

Month, L. A., and Rand, R. H., 1980, "An Application of Poincaré Map to the Stability of Nonlinear Normal Modes," ASME JOURNAL OF APPLIED MECHANICS, Vol. 47, pp. 645–651.

Pak, C. H., "On Geometric Insight into the Stability of Normal Modes in the Kinematico-statical Sense," to appear.

Rand, R. H., 1973, "The Geometrical Stability of Nonlinear Normal Modes in Two Degrees of Freedom Systems," *International Journal of Nonlinear Mechanics*, Vol. 8, pp. 161–168.

Rosenberg, R. M., 1966, "On Nonlinear Vibrations of Systems with Many Degrees of Freedom," *Advances in Applied Mechanics*, Vol. 9, pp. 155–242.

Shin, H. J., 1986, "On the Behaviors and Bifurcations of Nonlinear Normal Modes by Harmonic Balance Method," M. S. Thesis, Inha University, Incheon, Korea.

Synge, J. L., 1926, "On the Geometry of Dynamics," *Philosofical Transactions A*, Vol. 226, pp. 31–106.

Whittaker, E. T., 1944, *Treatise on the Analytical Dynamics of Particles and Rigid Bodies*, Dover Publications, New York, pp. 417–419.

Yen, D. H., 1974, "On the Normal Modes of Nonlinear Dual Mass Systems," *International Journal of Nonlinear Mechanics*, Vol. 9, pp. 45–53.

Yun, Y. S., 1986, "On the Nonlinear Normal Modes of Unsymmetric Systems by the Principle of Least Action," M. S. Thesis, Inha University, Inchon, Korea.

Downloaded 03 May 2010 to 171.66.16.31. Redistribution subject to ASME license or copyright; see http://www.asme.org/terms/Terms_Use.cfm

P. G. Reinhall
Department of Mechanical Engineering FU-10,
University of Washington,
Seattle, WA 98195
Assoc. Mem. ASME

T. K. Caughey
Division of Engineering and Applied Science,
California Institute of Technology,
Pasadena, CA 91125

D. W. Storti
Department of Mechanical Engineering FU-10,
University of Washington,
Seattle, WA 98195
Assoc. Mem. ASME

Order and Chaos in a Discrete Duffing Oscillator: Implications on Numerical Integration

In this paper, we study the dynamics of some two-dimensional mappings which arise when standard numerical integration schemes are applied to an unforced oscillator with a cubic stiffness nonlinearity, i.e., the Duffing equation. While the continuous time problem is integrable and is solved analytically in terms of Jacobi elliptic functions, the discrete versions of this simple system arising from standard integration schemes exhibit very complicated dynamics due to the presence of homoclinic tangles. We present an alternative scheme for discretizing the nonlinear term which preserves the integrable dynamics of the continuous system and derive analytic expressions for the orbits and invariant curves of the resulting mapping.

Introduction

It is well known from traditional numerical analysis that the numerical solution of a nonlinear ordinary differential equation converges to the exact solution as the time step is allowed to approach zero. This does not, however, guarantee accurate approximate solutions since real applications necessitate the use of a finite stepsize. The approximate solution corresponding to a small finite time step can, in some instances, as time grows large, exhibit considerably different behavior than the exact solution.

Both accuracy and stability considerations limit the size of the time step during a numerical solution process. A large amount of effort has gone into the development of efficient automatic step size control methods (Watts, 1971; Gear, 1971; Dahlquist and Bjorck, 1974). By a continuous monitoring of the step size, it is possible, in most cases, to keep the accuracy of the solution to an acceptable level. In solving nonlinear equations over long time periods, however, the situation becomes more complicated and the accuracy of the solution can no longer be taken for granted. In order to address this issue, we analyze the error due to the discretization of a nonlinear differential equation. The "structure" of the seemingly random error is discussed. This discussion is meant to introduce the role of chaotic behavior in numerical integration over long periods and the inherent differences between the continuous and discrete equations.

We consider the discrete version of the Duffing equation and show that the solution of this equation can vary significantly from the solution of the continuous Duffing equation. We indicate that the discretization process can carry the sole responsibility for the existence of very complicated or chaotic behavior.

The Discrete Duffing Equation

Let us consider the unforced, undamped Duffing equation

$$x'' + kx + \epsilon x^3 = 0 \tag{1}$$

with the initial conditions $x(0) = x_0$ and $x'(0) = v_0$. A range of direct integration methods are at our disposal to solve this initial value problem numerically. For simplicity, let us choose Euler's method:

$$x'(t_n) = \frac{x(t_n + \Delta t) - x(t_n)}{\Delta t} = \frac{x_{n+1} - x_n}{\Delta t} \tag{2}$$

where $\Delta t = t_{n+1} - t_n$ and $x(t_n) = x_n$.

Using equation (2), equation (1) becomes

$$x_{n+1} - (2 - \Delta t^2 k)x_n + x_{n-1} + \epsilon \Delta t^2 x_n{}^3 = 0 \tag{3}$$

or

$$x_{n+1} - Ax_n + Bx_{n-1} + Cx_n{}^3 = 0 \tag{4}$$

where

$$A = (2 - \Delta t^2 k), B = 1, \text{ and } C = \Delta t^2 \epsilon. \tag{5}$$

As will be discussed later, different expressions for A, B, and C are obtained for other integration schemes. We will call equation (4) the discrete Duffing equation.

After reviewing some basic theory of maps and developing familiarity with the global behavior of solutions of the difference equation, we will return for a comparison with the continuous solution.

Equation (4) can be put in the form

$$\mathbf{x}_{n+1} = \mathbf{f}(\mathbf{x}_n) \tag{6}$$

where

$$\mathbf{f}(\mathbf{x}_n) = \begin{bmatrix} x_n \\ Ax_n - Bx_{n-1} - Cx_n{}^3 \end{bmatrix}, \quad \mathbf{x}_n = \begin{pmatrix} x_{n-1} \\ x_n \end{pmatrix}. \tag{7}$$

Contributed by the Applied Mechanics Division of THE AMERICAN SOCIETY OF MECHANICAL ENGINEERS for presentation at the Joint ASCE/ASME Applied Mechanics, Biomechanics, and Fluids Engineering Conference, San Diego, Calif., July 9–12, 1989.

Discussion on this paper should be addressed to the Editorial Department, ASME, United Engineering Center, 345 East 47th Street, New York, N.Y. 10017, and will be accepted until two months after final publication of the paper itself in the JOURNAL OF APPLIED MECHANICS. Manuscript received by ASME Applied Mechanics Division, June 3, 1987; final revision, May, 1988.

Paper No. 89-APM-6.

Copyright © 1989 by ASME

Downloaded 03 May 2010 to 171.66.16.31. Redistribution subject to ASME license or copyright; see http://www.asme.org/terms/Terms_Use.cfm

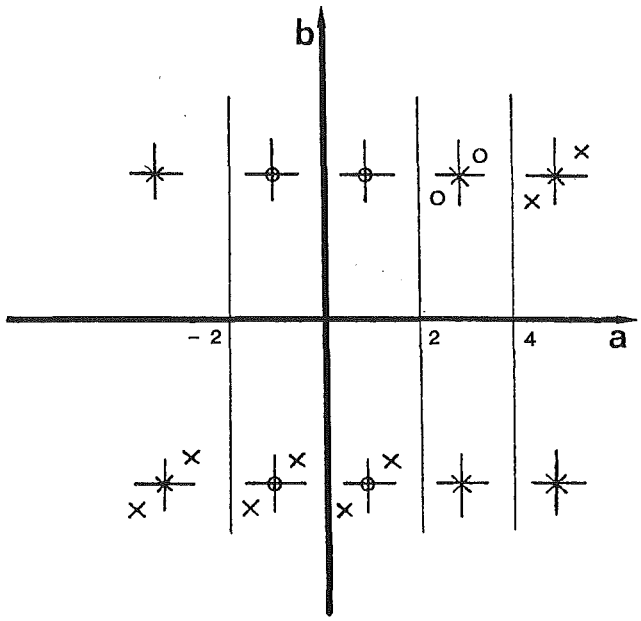


Fig. 1 Stability of the equilibrium points of the difference equation $x_{n+1} - Ax_n + Bx_{n-1} + Cx_n^3 = 0$ for $B = 1$

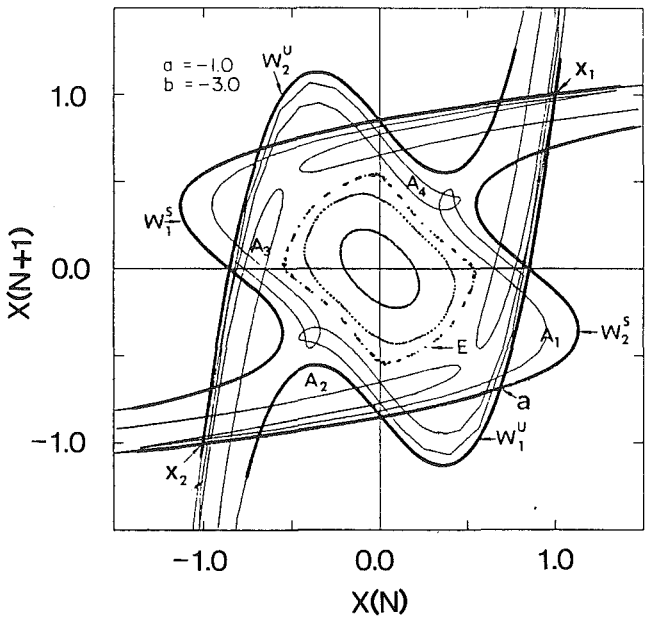


Fig. 2 Tangle of the stable and unstable manifolds (W_i^s and W_i^u, respectively) emanating from the equilibrium points x_1 and x_2 for parameter values $A = -1$, $B = 1$, and $C = -3$. Also shown are bonded trajectories encircling the center at the origin and the associated stability boundary E.

A point is p-periodic (a fixed point of order p) if p is the smallest integer such that

$$\mathbf{f}^p(x) = x. \tag{8}$$

If $p = 1$ the point is mapped onto itself at each iteration and is called an equilibrium point.

It is convenient to consider x_{n+1} versus x_n as n is changed. In order to study the behavior of the solution of equation (7) we determine the location of the equilibrium points by inserting the equilibrium condition $x_{n+1} = x_n = x_{n-1}$ into the difference equation (7) to obtain

$$x_n = x_{n+1} = \pm\sqrt{\frac{A-(1+B)}{C}} \text{ and } x_n = x_{n+1} = 0.$$

For example, let us consider the particular case $B = 1$ (which is appropriate for studying Euler's method), so that the fixed points are located at

$$x_n = x_{n+1} = \bar{x} = \pm\sqrt{\frac{A-2}{C}} \text{ and } x_n = x_{n+1} = 0. \tag{9}$$

Note that nontrivial first-order fixed points exist only when the radicand is positive (i.e., $k/\epsilon < 0$). Their stability can easily be determined by considering the behavior of the linearized map for small perturbations (δ_n) about the fixed point $\bar{x}$. Substituting $x_n = \bar{x} + \delta_n$ into equation (4) and neglecting terms of $O(\delta_n^2)$ yields

$$\begin{pmatrix} \delta_n \\ \delta_{n+1} \end{pmatrix} = \Phi \begin{pmatrix} \delta_{n-1} \\ \delta_n \end{pmatrix} = \begin{bmatrix} 0 & 1 \\ -1 & -2(A-3) \end{bmatrix} \begin{pmatrix} \delta_{n-1} \\ \delta_n \end{pmatrix}.$$

The local stability of a solution about a fixed point is determined by the eigenvalues of Φ. The stability regions in the A-C parameter plane are shown in Fig. 1. Since the determinant of Φ is unity (the map is area preserving), only two types of fixed points are possible. Either the eigenvalues occur as a complex conjugate pair on the unit circle and the fixed point is a center, or the eigenvalues are real ($\lambda_1 = 1/\lambda_2$) and the fixed point is a saddle.

Associated with each saddle point are invariant curves or stable and unstable manifolds, along which points are mapped toward or away from, respectively, the fixed point under the action of the map.

By choosing several initial points along the eigenvectors of the map linearized about the fixed points, we can trace out the unstable manifold by iterating forward in time and the stable manifold by iterating backward. The stable and unstable manifolds can be defined as follows:

$$W_i^s = \{\mathbf{y} \subset \mathbf{R}^2 : \lim_{n\to\infty} \mathbf{f}^n(\mathbf{y}) \to \mathbf{x}_i\}$$
$$W_i^u = \{\mathbf{y} \subset \mathbf{R}^2 : \lim_{n\to\infty} \mathbf{f}^{-n}(\mathbf{y}) \to \mathbf{x}_i\}$$

where $i = 1,2$ and $\mathbf{x}_i$ is the location of the ith saddle type fixed point. These manifolds are sketched and labeled in Fig. 2 which shows that the unstable manifold, W_1^u, does not simply coincide with the stable manifold, W_2^s. W_1^u crosses the stable manifold W_2^s at a heteroclinic point (Aronson et al., 1980, Birkhoff et al., 1928; Newhouse, 1980; Arnold,1978; Devaney, 1978; Holmes, 1980; Guckheimer and Holmes, 1982) and starts to oscillate around W_2^s in an increasingly violent manner. These oscillations create heteroclinic tangles which give rise to Smale horseshoes and chaotic orbits as discussed in detail in (Smale, 1963, 1967; Newhouse, 1979; Guckheimer el al., 1980; Reinhall, 1982). In Fig. 2 it can be seen that the images of the inside loops of the manifolds, A_1, A_2, etc., start to form an envelope, E, as the number of iterates grows. This closed envelope corresponds to the stability boundary for the bounded trajectories encircling the center at the origin. All points lying in the interior of the envelope are repeatedly mapped back within this region forming an "island of stability." Higher order stable fixed points are surrounded by smaller islands which are similarly enclosed by envelopes formed by the manifolds of associated higher order saddle points. Points lying outside these islands of stability eventually become unbounded under the action of the map. Therefore, the envelope, in conjunction with the heteroclinic oscillation, plays a crucial role in explaining the differences between the solution of the continuous Duffing equation and the discretized version. (Note that for parameter values where the origin is the only first-order fixed point, the envelope is formed by the manifolds of second-order saddle points.)

Downloaded 03 May 2010 to 171.66.16.31. Redistribution subject to ASME license or copyright; see http://www.asme.org/terms/Terms_Use.cfm

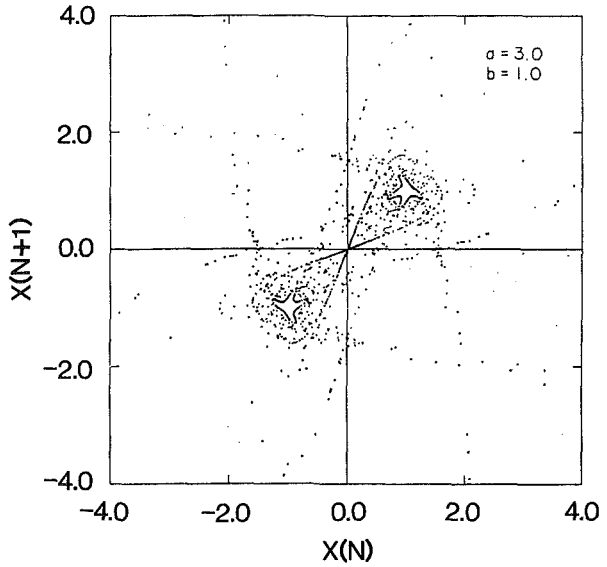


Fig. 3(a) Solution points of $x_{n+1} - 3x_n + x_{n+1} + x_n{}^3 = 0$. All of the scattered points lay on the tangling manifolds associated with the saddle point at the origin. Bounded trajectories about the centers at (−1, −1) and (1,1) are also shown.

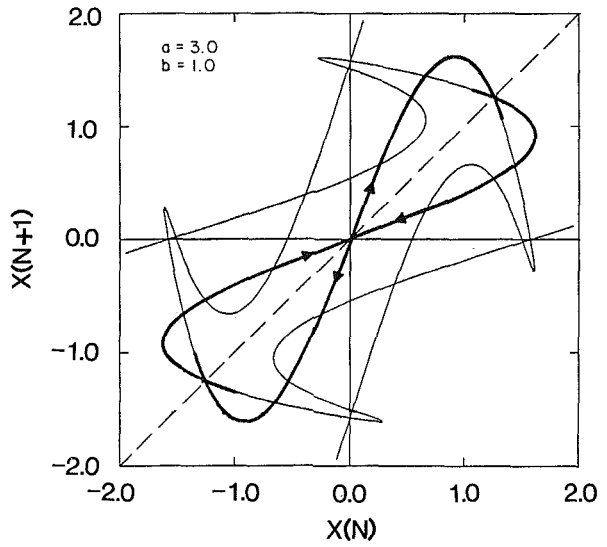


Fig. 3(b) Stable and unstable manifolds associated with the saddle point at the origin

Figure 3(*a*) shows some typical orbits for parameter values $A=3$ and $B=1$. Points surrounding the centers at (1,1) and (−1,1) lie on bounded trajectories while the remaining scattered points lie on the unstable manifold of the saddle point at the origin. The corresponding invariant manifolds are sketched in Fig. 3(*b*).

The Discrete Versus the Continuous Duffing Equation

In this section we discuss the difference between the global behavior of the solutions of the discrete (4) and continuous (1) Duffing equations. The discussion will focus on the question of when and how the correspondence between the approximate and the exact solutions is lost.

As shown earlier, the discrete Duffing equation (4) is obtained by applying a first order Euler numerical integration method to equation (1). As the time step approaches zero, we see from (5) that A approaches the value 2 from below. It is easy to show that as $\Delta t \to 0$, the solution of (4) must converge to the solution of the continuous equation (1). What is of current interest, however, is the behavior of the solution of equation (4) after a large number of finite, not infinitesimal, time steps.

The original continuous equation (1) has only one fixed point, a stable center at the origin, surrounded by a family of closed orbits (depicted in Fig. 4) which can be expressed in terms of elliptic integrals as follows. Equation (1) describes a conservative system whose phase trajectories lie on the family of invariant curves given by the Hamiltonian

$$\frac{1}{2}(x')^2 + \frac{1}{2}x^2 + \frac{1}{4}\epsilon x^4 = \frac{1}{2}a^2 + \frac{1}{4}\epsilon a^4 \tag{10}$$

where a is the constant parametrizing the family of curves. Solving for x', separating variables and integrating yields

$$t = \int_a^x \left[(a^2-\xi^2)\left\{1 + \frac{\epsilon}{2}(a^2+\xi^2)\right\}\right]^{-1/2} d\xi. \tag{11}$$

Using the trigonometric substitution $\xi = a\cos\theta$, we then obtain

$$t = \frac{1}{\sqrt{1+\epsilon a^2}} \int_0^{\phi} \frac{d\theta}{\sqrt{1-K^2\sin^2\theta}} = \frac{1}{\sqrt{1+\epsilon a^2}} F(\varphi,K) \tag{12}$$

where $F(\varphi,K)$ is the incomplete elliptic integral of the first kind. The upper limit and the modulus K are given by the following equations:

$$\phi = \cos^{-1}\left(\frac{x}{a}\right), \quad K^2 = \frac{\epsilon a^2}{2(1+\epsilon a^2)}. \tag{13}$$

From equations (12) and (13), the explicit solution or x is obtained in terms of Jacobi elliptic functions (Davis, 1962):

$$x = a\cos\phi = a\,cn[\sqrt{1+\epsilon a^2}\,t]. \tag{14}$$

The discretized equation (4), however, has an infinite set of higher order fixed points (centers and saddle points). Each saddle point, as mentioned earlier, possesses a set of stable and unstable manifolds which intersect transversely giving rise to homoclinic tangles. (While there may be special combinations of the parameters A, B, and C for which the manifolds do not have transverse intersections and tangles are not created, these would be rare and exceptional cases corresponding to special values of the stepsize.) Along the unstable manifold, the map is expanding and the nearby points separate exponentially fast. Therefore, if the initial conditions are chosen in a region where these tangles occur, there is a possibility that the approximate solution could soon deviate significantly from the true solution of the continuous equation. It would even be possible to obtain seemingly chaotic response despite the fact that the true solution of the continuous equation totally lacks such behavior. It is important to note that the existence of the chaotic behavior occurs as a result of the creation of horseshoes in the homoclinic tangles and does not arise from, or depend on, a sequence of period-doubling bifurcations as in the work of Prufer (1985). While Prufer observes interesting and rich dynamic behavior as a result of cascades of period-doublings in linear multistep methods, it is not relevant to our study since the period-doubling bifurcations begin at time steps which are much larger than those of interest for numerical integration applications. In this investigation we consider only time steps well within the traditional limits. We see that there is already interesting and complicated dynamic behavior, but it is due to the presence of homoclinic tangles and does not require the occurrence of a sequence of period-doubling bifurcations.

The effect of finite step size is illustrated in Fig. 4 which shows phase plots for a sequence of step sizes ranging from $\Delta t = 0.01$ in Fig. 4(*a*) to $\Delta t = 0.5$ in Fig. 4(*c*). The exact phase plane is shown for comparison in Fig. 4(*d*). These figures show chaotic solutions caused solely by discretization and the growth of the chaotic regions as the stepsize increases.

Downloaded 03 May 2010 to 171.66.16.31. Redistribution subject to ASME license or copyright; see http://www.asme.org/terms/Terms_Use.cfm

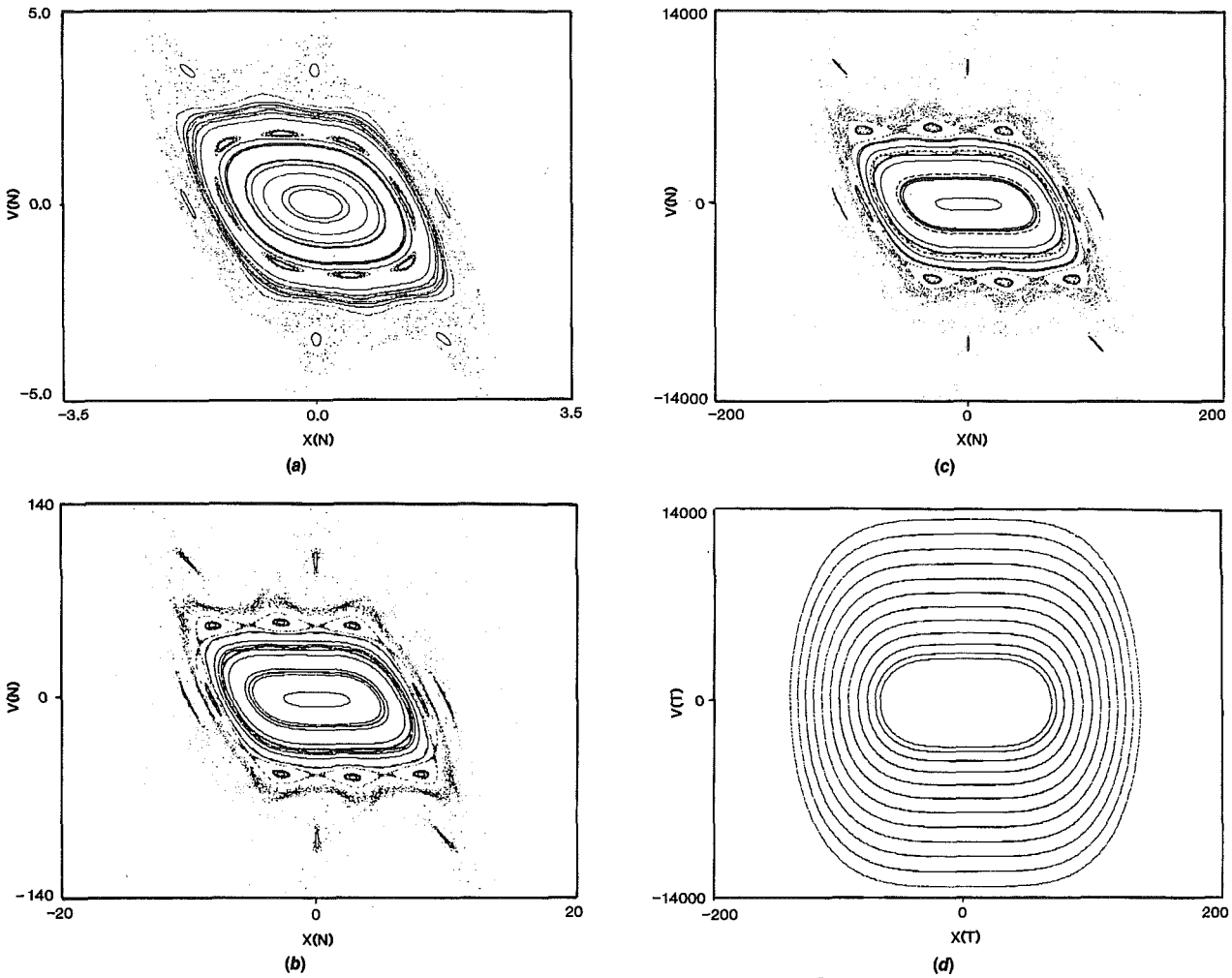


Fig. 4 Phase portraits of the Duffing equation, $x'' + x + x^3 = 0$, obtained by numerical integration using Euler's method with time step Δt; (a) $\Delta t = 0.5$, (b) $\Delta t = 0.1$, (c) $\Delta t = 0.01$, and (d) exact solution corresponding to $\Delta t \to 0$

Unstable manifolds emanating from second-order saddle points for the case when $\Delta t = 0.1$ (no first-order fixed points exist in this case) are shown in Fig. 5. The scattered points shown outside of the period -8 islands lie on the tangled second-order manifolds. Due to the heteroclinic crossings, the manifolds must encircle the origin infinitely many times. Points on the manifold can therefore be mapped around the origin many times before finally being carried off to infinity creating what can be best described as transient chaos. These manifolds are responsible for carrying solution points located outside the stability boundary to infinity. Within the stable region there are an infinite number of higher order fixed points. The tangles associated with these points are bounded by nearby simple trajectories whose existence is guaranteed by KAM theory (Guckheimer and Holmes, 1982) when Δt is sufficiently small. Points located within such a tangle are still mapped around the origin in a fashion similar to the neighboring trajectories (since the map is smooth) so that amplitudes remain close to those of the corresponding continuous problem. These bounded tangles can, however, make the solution sensitive to the initial conditions and lead to significant phase errors. As two neighboring points situated in a tangle are mapped around the origin, they will separate due to the stretching of the homoclinic loops. The significance of a tangle decreases with the increasing order of the associated fixed points. This is due to the fact that associated with an increase in the order of the fixed point there is a decrease in the area which contains the corresponding tangle. The decrease in the area increases the restrictions on the oscillating manifolds of the tangle. As the time step is made smaller, all fixed points are moved further away from the origin. For small time steps only fixed points of high order (with a small tangle area) will remain close to the origin. The errors introduced to a given elliptical orbit in the phase plane due to the tangle can therefore be made smaller by decreasing the time step. For very long simulations, however, the errors due to the higher order tangles become detrimental to the accuracy of the solution.

Higher Order Integration Methods

The structure of the discrete Duffing equation depends on the particular integration method being used. If we choose Newmark's (Newmark, 1959; Hughes, 1977, 1987) method instead of Euler's method we obtain the following equation:

$$x_{n+1} - Ax_n + Bx_{n-1} + C_1 (x_{n+1})^3 + C_2 (x_n)^3 + C_3 (x_{n-1})^3 = 0 \tag{15}$$

where

$$A = \frac{2 - \left(\gamma - 2\beta + \frac{1}{2}\right) k(\Delta t)^2}{1 + \beta k (\Delta t)^2},$$

Downloaded 03 May 2010 to 171.66.16.31. Redistribution subject to ASME license or copyright; see http://www.asme.org/terms/Terms_Use.cfm

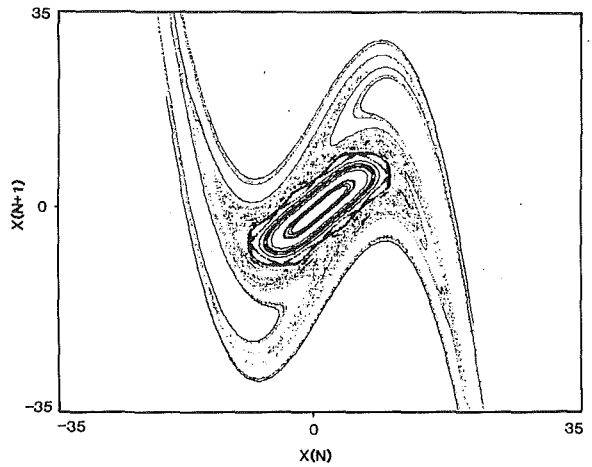


Fig. 5 Solution points of the Duffing equation discretized using Euler's method with $\Delta t = 0.1$. Bounded trajectories encircle the center at the origin. All of the scattered points lay on the tangling unstable manifolds emanating from the second-order saddle points at (20, − 20) and (− 20,20).

$$B = \frac{1 + \left(\beta - \gamma + \frac{1}{2}\right) k(\Delta t)^2}{1 + \beta k(\Delta t)^2}$$

$$C_1 = \frac{\epsilon\beta(\Delta t)^2}{1 + \beta k(\Delta t)^2}, \quad C_2 = \frac{\epsilon\left(\gamma - 2\beta + \frac{1}{2}\right)(\Delta t)^2}{1 + \beta k(\Delta t)^2},$$

$$C_3 = \frac{\frac{\epsilon}{2}\left(\beta - \gamma + \frac{1}{2}\right)(\Delta t)^2}{1 + \beta k(\Delta t)^2}.$$

Two phase planes of the Duffing equation, obtained by Newmark's method with $\beta = 1/12$ and $\gamma = 1/2$ (Fox-Goodwin method) and $\beta = 1/4$, $\gamma = 1/2$ (average acceleration method), respectively, are shown in Fig. 6. (See Hughes (1987) for a nice concise presentation of these methods.) It is seen that the Fox-Goodwin method does not produce a phase plane that significantly differs from the previous case. The average acceleration method is an unconditionally stable method. No solution points can therefore be carried to infinity by manifold oscillations. The manifolds corresponding to the higher order fixed points are confined between invariant solution curves, creating what can be described as stochastic layers (Guckheimer and Holmes, 1982).

In order to improve long time integration accuracy it is necessary to discretize the original equation such that no homoclinic or heteroclinic tangles are present in our approximate solution. Figures 4–6 indicate that none of the traditional methods considered thus far accomplishes this goal; and, in particular, the use of higher order methods does not solve the problem. As an alternative approach, we consider changing the nature of the nonlinear term in the Euler method so that the discrete problem becomes

$$x_{n+1} - A\, x_n + x_{n-1} + C\, x_{n+1} x_n x_{n-1} = 0 \tag{16}$$

and note that as $t \to 0$, $x_{n+1} x_n x_{n-1} \to x^3(t_n)$ and the new nonlinear term properly converges to that in the original Duffing equation. Moreover, we will show that this form of the nonlinearity allows us to obtain an explicit solution for the difference equation and an analytic expression for the family of invariant curves which fill the x_n, x_{n-1} plane. By analogy with the continuous solution (equation (14)), we look for a solution of the form

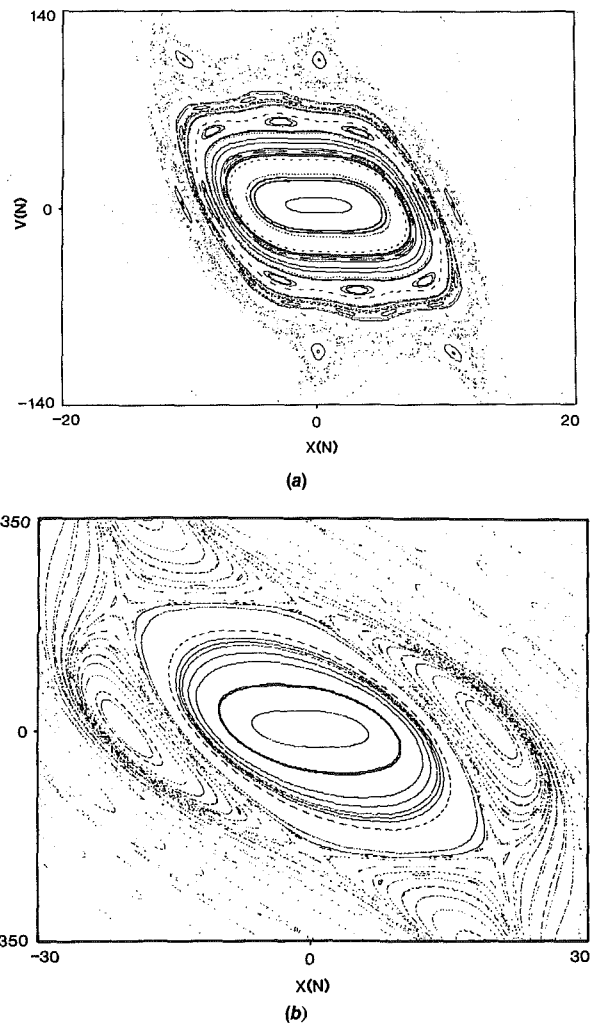


Fig. 6 Phase portraits of the Duffing equation obtained using members of the Newmark family of numerical integration methods described in equation (10); (a) Fox-Goodwin: $\gamma = 1/12$, $\beta = 1/2$, $\Delta t = 0.1$ and (b) Average acceleration: $\gamma = 1/4$, $\beta = 1/2$, $\Delta t = 0.1$

$$x_n = a\, cn(nv, m) \tag{17}$$

where v and m are to be determined. The preceding and following iterates of x are simplified using addition theorems for the Jacobi elliptic functions:

$$x_{n\pm1} = a[cn(nv)cn(v) - \pm sn(nv)dn(nv)sn(v)dn(v)]/D \tag{18}$$

where the second argument, m, of the Jacobi elliptic functions is suppressed for brevity, and the denominator D is given by

$$D = 1 - m^2 sn^2(nv) sn^2(v). \tag{19}$$

Note also that the combination $x_{n+1}x_{n-1}$ which appears in the nonlinear term can be simplified to

$$x_{n+1}x_{n-1} = a^2[cn^2(nv) - sn^2(v)dn^2(v)]. \tag{20}$$

Substituting equations (17)–(20) into (16) yields a binomial equation in $cn(nv,m)$. Requiring the coefficients to vanish (so that the equation is satisfied for all n) leads to two equations which determine v and m. After some manipulation, these can be reduced to:

$$cn(v) = \frac{1}{a^2 C}\left[-1 + \sqrt{1 + a^2 C}\right] \tag{21}$$

$$m^2 = \frac{a^2 C}{(A + a^2 C)(1 - cn^2(v))}. \tag{22}$$

This completes the solution of equation (16) in the form of

Downloaded 03 May 2010 to 171.66.16.31. Redistribution subject to ASME license or copyright; see http://www.asme.org/terms/Terms_Use.cfm

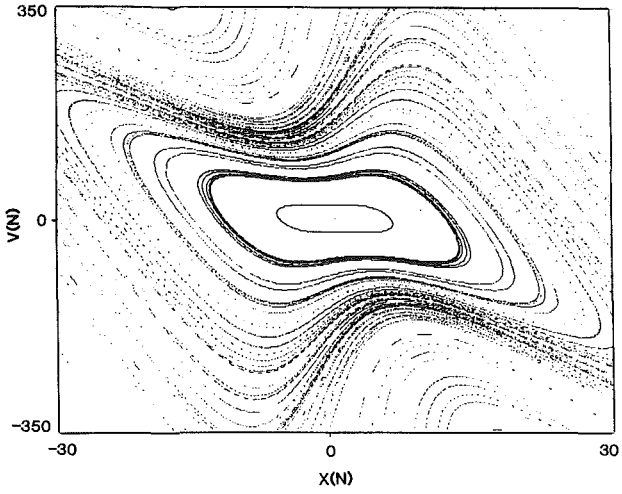


Fig. 7 Phase portrait of the Duffing equation ($k = 1$, $\epsilon = 1$) using $\Delta t = 0.1$ with a nonlinear term of the form $x_{n-1}x_n x_{n+1}$

equation (17) and indicates the existence of a family of curves which are invariant under the mapping and are parametrized by the amplitude a. Furthermore, we can find an analytic expression for the invariant curves in the x_{n-1}, x_n plane by combining our knowledge of the difference equation, its solution, and the following identities which govern the Jacobi elliptic functions.

$$sn^2(nv) + cn^2(nv) = 1 \tag{23}$$

$$cn([n+1]v) + cn([n-1]v) = \frac{2cn(nv)cn(v)}{1 - m^2 sn^2(nv) sn^2(v)} . \tag{24}$$

Solving equation (24) for $sn^2(nv)$ and substituting into equation (23) yields an expression where n appears only in terms of the form $cn(nv)$, $cn([n+1]v)$, and $cn([n-1]v)$. Replacing these by x_n, x_{n+1}, and x_{n-1} using equations (17) and (18) leaves an expression which is invariant (since the identities hold for any n). We can eliminate the x_{n+1} dependence by substituting an expression in terms of x_n and x_{n-1} obtained by solving the equation (16) directly, i.e.,

$$x_{n+1} = \frac{A\, x_n - x_{n-1}}{1 + C\, x_n x_{n-1}} . \tag{25}$$

What remains is an analytic expression for the invariant curves which, after some straightforward algebra, simplifies to

$$\frac{1 + C\, x_n x_{n-1}}{(A + C\, x_n{}^2)(A + C\, x_{n-1}{}^2)} = \text{constant}. \tag{26}$$

The existence of this family of analytic invariant curves prevents the occurrence of heteroclinic and homoclinic oscillations which were the source of the chaotic behavior in the previous examples.

Figure 7 numerically confirms that the solution of the equation with the $x_{n+1}x_n x_{n-1}$ nonlinearity does not exhibit chaotic behavior, and that all solution trajectories are invariant curves. Hence, this integration method represents the general global behavior of the exact solution more accurately than the Newmark or Euler methods. It should be noted that the integration scheme is still second-order accurate and therefore no improvement in accuracy should be expected for each small time step. However, the elimination of the tangles by an alteration of the nonlinear term substantially improves the long time integration accuracy. A measure of this improvement and a quantitative study of the significance of heteroclinic and homoclinic crossings in numerical integration will be included in a following paper.

Summary

Discretizations of a Duffing equation using the Euler and Newmark methods are shown to result in heteroclinic tangles and complicated behavior not seen in the solution of the continuous equation. This discrepancy has a significant negative impact on the accuracy of the numerical solution when long solution records are required. It is shown that tangles can be avoided and that the global behavior of the continuous equation can be preserved by a reformulation of the nonlinear term during the discretization process. Analytic expressions are given for the orbits of the new nonlinear mapping and for the associated invariant curves.

References

Arnold, V. I., 1978, *Mathematical Methods in Classical Mechanics*, Springer-Verlag, New York.

Aronson, D. G., Chory, M. A., Hall, G. R., and McGehee, R. P., 1980, "A Discrete Dynamical System with Subtly Wild Behavior," *New Approaches to Nonlinear Problems in Dynamics*, SIAM, pp. 339-359.

Birkhoff, G. D., and Smith, P. A., 1928, "Structure Analysis of Surface Transformations," *Jour. de Math. Pures and Appliques*, Vol. 9, pp. 349-379.

Dahlquist, D., and Bjorck, A., 1974, *Numerical Methods*, Prentice-Hall, Englewood Cliffs, NJ.

Davis, H. T., 1962, *Introduction to Nonlinear Differential and Integral Equations*, Dover, New York, pp. 131-150.

Devaney, R. L., 1978, "Transverse Heteroclinic Orbits in the Anisotropic Kepler Problem," *The Structure of Attractors in Dynamical Systems, Lecture Notes in Applied Mathematics*, Vol. 668, Springer-Verlag, New York, pp. 67-87.

Gear, C. W., 1971, *Numerical Initial Value Problems in Ordinary Differential Equations*, Prentice-Hall, Englewood Cliffs, NJ.

Guckheimer, J., and Holmes, P., 1982, *Nonlinear Oscillations, Dynamic Systems, and Bifurcations of Vector Fields*, Springer-Verlag, New York.

Guckenheimer, J., Moser, J., and Newhouse, S. E., 1980, "Dynamical Systems," CIME Lectures, J. Coates and S. Helgason eds., Progress in Mathematics, Vol. 8.

Holmes P., 1980, "Unfolding a Degenerate Nonlinear Oscillator: A Codimension Two Bifurcation," *Ann. NYAS*, Vol. 357, pp. 473-489.

Hughes, T. J. R., 1977, "A Note on the Stability of Newmark's Algorithm's in Nonlinear Structural Dynamics," *International Journal of Numerical Methods in Engineering*, Vol. 11, pp. 383-386.

Hughes, T. J. R., 1987, *The Finite Element Method*, Prentice-Hall, Englewood Cliffs, NJ, pp. 490-493.

Newhouse, S. E., 1979, "The Abundance of Wild Hyperbolic Sets and Non-Smooth Stable Sets for Diffeomorphisms," *Publ. Math. IHES*, Vol. 50, pp. 101-151.

Newhouse, S. E., 1980, "Asymptotic Behavior and Homoclinic Points in Nonlinear Systems," *Ann. NYAS*, Vol. 357, pp. 292-299.

Newmark, N. M., 1959, "A Method of Computation for Structural Dynamics," *Journal of the Engineering Mechanics Division*, ASCE, pp. 67-94.

Prufer, M., 1985, "Turbulence in Multistep Methods for Initial Value Problems," *SIAM Journal of Applied Mathematics*, Vol. 45, pp. 32-69.

Reinhall, P. G., 1982, "The Analysis of a Nonlinear Difference Equation Occurring in Dynamical Systems," Ph.D. Dissertation, California Institute of Technology.

Smale, S., 1963, "Diffeomorphisms with Many Periodic Points," *Differential and Combinatorial Topology*, S. S. Cairns ed., Princeton University Press, pp. 63-80.

Smale, S., 1967, "Differentiable Dynamical Systems," *Bulletin of the American Mathematical Society*, Vol. 73, pp. 63-80.

Watts, H. A., 1971, "Stepsize Control in Ordinary Differential Equation Solvers," *Transactions of the Society for Computer Simulation*, Vol. 1, pp. 15-25.

Downloaded 03 May 2010 to 171.66.16.31. Redistribution subject to ASME license or copyright; see http://www.asme.org/terms/Terms_Use.cfm

The Onset of Chaos in a Two-Degree-of-Freedom Impacting System

Jinsiang Shaw
Graduate Assistant.

Steven W. Shaw
Associate Professor,
Assoc. Mem. ASME

Department of Mechanical Engineering,
Michigan State University,
East Lansing, Mich. 48824

The dynamic response of a two-degree-of-freedom impacting system is considered. The system consists of an inverted pendulum with motion limiting stops attached to a sinusoidally excited mass-spring system. Two types of periodic response for this system are analyzed in detail; existence, stability, and bifurcations of these motions can be explicitly computed using a piecewise linear model. The appearance and loss of stability of very long period subharmonics is shown to coincide with a global bifurcation in which chaotic motions, in the form of Smale horseshoes, arise. Application of this device as an impact damper is also briefly discussed.

1 Introduction

The responses of mechanical systems having amplitude constraints when subjected to periodic excitation are inherently nonlinear and have been the subject of many investigations. Motions of systems with two-sided constraints have been studied analytically, as well as experimentally, in the context of the impact damper by several authors (see, for example, Masri, 1969, 1972; Druzhilovskaia and Neimark, 1983; Nigm and Shabana, 1983). The present work was motivated by previous work (Shaw and Rand, 1988) which considered a one-degree-of-freedom impacting oscillator similar to the system considered here.

There now exist many examples of single-degree-of-freedom systems which exhibit chaotic dynamics. However, results on multi-degree-of-freedom systems is more limited; they include simulation studies (see, for example, Dowell, 1982) and perturbations of integrable Hamiltonian systems (Holmes and Marsden, 1982). In contrast, the present example is one which is amenable to *analytical treatment* for *nonsmall* driving amplitudes and dissipation.

A schematic diagram of the system is shown in Fig. 1. The symmetrically-placed rigid stops limit the amplitude variation of the inverted pendulum from the unstable upright position, and the primary mass is subjected to periodic excitation. The unforced static rest positions correspond to the pendulum leaning against one of the walls. For small excitation amplitudes, one expects the motion to be a simple bouncing against one wall (or simply resting against one wall), and for large excitation amplitudes the pendulum will interact with both walls in some manner. The transition region contains rich dynamic behavior.

This system is modeled as piecewise linear; thus, explicit solutions of the free flight dynamic equations are known. These are matched together at impact points with an impact rule to obtain a complete solution. This type of formulation allows an implicit form of a four-dimensional Poincaré map to be obtained and, from this map, we obtain explicit results regarding the existence and stability of certain periodic motions.

The Poincaré map used herein is not the usual one which samples the phase space once per period of the driver. Instead, an "impact map" is used which can capture some types of very long period, periodic motions in a single iterate. Using this map we can also compute the condition for the onset of (possibly transient) chaotic motions using a Melnikov-type analysis and indicate how this result is linked to the long period motions.

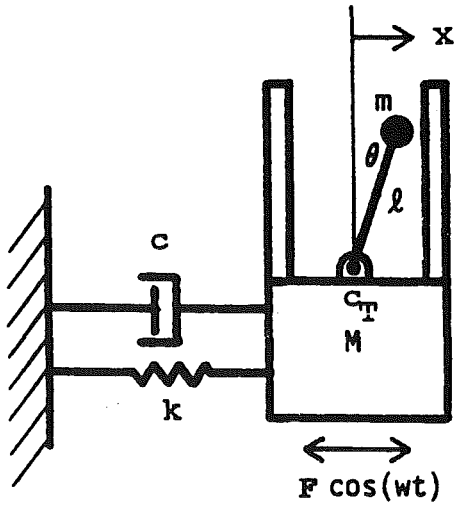


Fig. 1 The physical model

Contributed by the Applied Mechanics Division of THE AMERICAN SOCIETY OF MECHANICAL ENGINEERS for publication in the JOURNAL OF APPLIED MECHANICS.

Discussion on this paper should be addressed to the Editorial Department, ASME, United Engineering Center, 345 East 47th Street, New York, N.Y. 10017, and will be accepted until two months after final publication of the paper itself in the JOURNAL OF APPLIED MECHANICS. Manuscript received by ASME Applied Mechanics Division, March 9, 1988; final revision, July 28, 1988.

Copyright © 1989 by ASME

Downloaded 03 May 2010 to 171.66.16.31. Redistribution subject to ASME license or copyright; see http://www.asme.org/terms/Terms_Use.cfm

It is assumed that the walls are close enough so that linearization is valid during free flight. Then the equations governing motions between impacts are

$$(1+\mu)y''+\mu\psi''+2\xi_1 y'+\omega_1^2 y=\beta\cos(\Omega\tau)$$
$$y''+\psi''+2\xi_2\psi'-\psi=0,\ |\psi|<1 \tag{1}$$

where

$$\tau=\sqrt{\frac{g}{l}}t,\ \psi=\theta/\theta_o,\ y=x/l\theta_o$$

$$\mu=m/M,\ \beta=F/Mg\theta_o,\ \omega_1^2=\frac{K}{M}\frac{l}{g},\ \Omega=\omega\sqrt{\frac{l}{g}},$$

$$2\xi_1=\frac{c}{M}\sqrt{\frac{l}{g}},\ 2\xi_2=\frac{c_T}{ml^2}\sqrt{\frac{l}{g}},\ (\ )'=d/d\tau.$$

The rescaling is such that the walls are a unit distance from the vertical.

Idealizing the collision between m and the walls to be a discontinuous process, the momentum equation and the definition of the coefficient of restitution yield following impact relations:

$$\psi'\to -e\psi',\ y'\to y'+\alpha\psi',\ \text{at } |\psi|=1 \tag{2}$$

where e is the coefficient of restitution and $\alpha=\mu(1+e)\cos\theta_o/(1+\mu)$.

In much of the following analysis we will assume that impacting is the only source of energy dissipation (i.e., $\xi_1=\xi_2=0$); this is for convenience in the calculations only. Later we will require that ξ_1 and/or ξ_2 be very small, but nonzero.

The complete solution of equation (1) can be written as

$$y(\tau)=\sum_{j=1}^{4}C_j\gamma_j\exp(S_j\tau)+\mathrm{Re}\{F_1\exp(i\Omega\tau)\}$$
$$\psi(\tau)=\sum_{j=1}^{4}C_j\exp(S_j\tau)+\mathrm{Re}\{F_2\exp(i\Omega\tau)\} \tag{3}$$

where

$$S_{1,2}=\pm\lambda=\pm\left(\frac{(1+\mu-\omega_1^2)+\sqrt{(1+\mu-\omega_1^2)^2+4\omega_1^2}}{2}\right)^{1/2}$$

$$S_{3,4}=\pm\omega_n=\pm\left(\frac{\sqrt{(1+\mu-\omega_1^2)^2+4\omega_1^2}-(1+\mu-\omega_1^2)}{2}\right)^{1/2}i.$$

$$\gamma_j=\frac{1-S_j^2}{S_j^2},\ F_1=(1+\Omega^2)\beta/q,\ F_2=-\Omega^2\beta/q$$

$$q=(1+\Omega^2)\omega_1^2-(1+\Omega^2)(1+\mu)\Omega^2+\mu\Omega^4$$

C_j depends on initial conditions and $i^2=-1$.

It will be important for our later analysis to note that the eigenvalues $S_{3,4}$ are purely imaginary and correspond to an oscillatory motion of neutral stability. This is a consequence of the zero friction assumptions $\xi_1=\xi_2=0$. For ξ_1, ξ_2, or both nonzero but small and positive, $S_{3,4}$ will be displaced an amount $\mathbf{O}(\xi)$ into the left half plane resulting in the associated oscillatory motion undergoing slow exponential decay. This will be important when we discuss stability and hyperbolicity results.

2 The Poincaré Map

The notations $y_1=y$, $y_2=y'$, $y_3=\psi$, $y_4=\psi'$ and $T=2\pi/\Omega$ will be employed. Rewriting equations (1) and (2) in first-order form, the $(y_1, y_2, y_3, y_4, \phi)$ phase flow is governed by

$$\left.\begin{aligned} y_1' &= y_2\\ y_2' &= -\omega_1^2 y_1-\mu y_3+\beta\cos(\Omega\phi)\\ y_3' &= y_4\\ y_4' &= \omega_1^2 y_1+(1+\mu)y_3-\beta\cos(\Omega\phi)\\ \phi' &= 1 \end{aligned}\right\}\ \text{free flight, } |y_3|<1 \tag{4}$$

$$\left.\begin{aligned} y_4&\to -ey_4\\ y_2&\to y_2+\alpha y_4, \end{aligned}\right\}\ \text{impacts, } |y_3|=1 \tag{5}$$

where $\phi=\tau\ (\mathrm{mod}\ T)$.

The variable $y_3(=\psi)$ is restricted to $I=[-1, 1]$, ϕ is restricted to S^T (the circle of period T) and (y_1, y_2, y_4) can take on any real values. Thus, points in the five-dimensional phase space are given by $(y_1, y_2, y_3, y_4, \phi)\,\epsilon\mathbf{R}^3\times I\times S^T$. The Poincaré section is taken to be:

$$\Sigma=\{(y_1, y_2, y_3, y_4, \phi)\,|y_3=+1, y_4>0\}.$$

This section is four-dimensional and is a natural choice, prompted by the nature of the vector field given by (4) and (5). Elements in Σ are denoted by $(y_1, y_2, y_4, \phi)\,\epsilon\mathbf{R}\times\mathbf{R}\times\mathbf{R}^+\times S^T$.

Consider a point $(y_1, y_2, y_4, \phi)\epsilon\Sigma$. It is immediately mapped to $(y_1, y_2+\alpha y_4, -ey_4, \phi)\epsilon\Sigma$ under the impact rule. Then, under the flow given in equation (4), it returns to Σ after a flight of duration

$$\tilde{\tau}(y_1, y_2, y_4, \phi)=\inf\{\tau>0\,|y_3(\tau;y_1, y_2+\alpha y_4, +1, -ey_4, \phi)=+1,$$
$$y_4(\tau;y_1, y_2+\alpha y_4, +1, -ey_4, \phi)>0\}.$$

The Poincaré map is then given by

$$P(y_1, y_2, y_4, \phi)=[y_1(\tilde{\tau};y_1, y_2+\alpha y_4, +1, -ey_4, \phi),$$
$$y_2(\tilde{\tau};y_1, y_2+\alpha y_4, +1, -ey_4, \phi), y_4(\tilde{\tau};y_1, y_2+\alpha y_4, +1,$$
$$-ey_4, \phi), \tilde{\tau}(y_1, y_2, y_4, \phi)(\mathrm{mod}\ T)].$$

See Shaw and Rand (1988) and Shaw and Holmes (1983) for analyses using similarly defined maps.

Some remarks:

1 Points in Σ correspond to the pendulum at impact with the wall at $\psi=+1$ and denote the position and velocity of main mass just prior to impact (y_1 and y_2, respectively), the velocity of the pendulum (y_4), and the forcing phase at impact (ϕ). The velocities of the main mass and the pendulum just subsequent to impact are $y_2+\alpha y_4$ and $-ey_4$, respectively.

2 There is one periodic motion, given by the particular solution of (1), which is not captured by P; for $\beta<q/\Omega^2$ it is given by

$$\tilde{y}_1=F_1\cos(\Omega\tau),\ \tilde{y}_2=-\Omega F_1\sin(\Omega\tau)$$
$$\tilde{y}_3=F_2\cos(\Omega\tau),\ \tilde{y}_4=-\Omega F_2\sin(\Omega\tau)$$

This motion is a saddle-type orbit with associated eigenvalues S_i $(i=1, 2, 3, 4)$ and is the continuation for $\beta\neq 0$ of the origin in the unforced problem. Its center-stable and unstable manifolds play a central role in the birth of long-period motions and horseshoes.

3 The return time $\tilde{\tau}$ depends on the starting point and thus may be arbitrarily long if the trajectory is started close to the stable manifold of the saddle orbit. This is precisely how long-period subharmonics are captured using P.

4 While P loses information regarding the actual time of

Downloaded 03 May 2010 to 171.66.16.31. Redistribution subject to ASME license or copyright; see http://www.asme.org/terms/Terms_Use.cfm

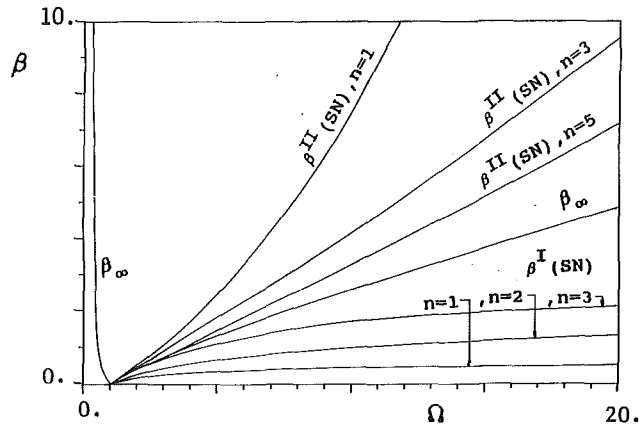


Fig. 2 Saddle-node bifucation diagram of Type I and II motions in (β,Ω) space, $e=0.8$, $\alpha=0.161$, $\mu=0.1$, $\omega_1=1$

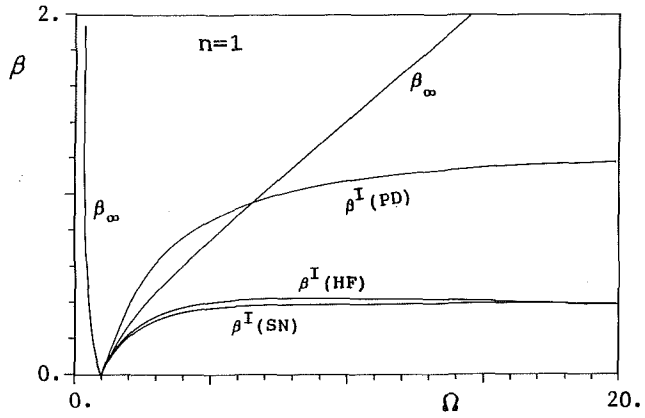


Fig. 3 The primary and secondary bifucation curves of Type I motion for $n=1$, $e=0.8$, $\alpha=0.161$, $\mu=0.1$, $\omega_1=1$

flight, due to the (mod T), this information will be carried along the analysis.

5 P is not a "nice" mapping since there are points in Σ which are mapped to $y_3=\pm 1$, $y_4=0$. These correspond to degenerate impacts which graze a wall. These can lead to discontinuities in the map.

6 P captures motions which go to $y_3=-1$ and return to $y_3=+1$, but does miss points which end up impacting only at $y_3=-1$. However, due to the symmetry of the system, P will find such a motion's antisymmetric partner which impacts only at $y_3=+1$.

7 P is known in implicit form only, the actual solution of $\bar{\tau}(y_1, y_2, y_4, \phi)$ requires finding the roots of transcendental equations.

3 Periodic Motions

There exist many possible types of periodic motions involving impacts at $\psi=+1$ and -1. (Actually, every possible combination of impact sequences is possible, as we shall show.) In this section we consider only two types of motions which are captured in a single iterate of P. Type I periodic motions correspond to the pendulum bouncing repeatedly at the $\psi=+1$ (or -1) wall with free-flight time of nT between each impact. Type II perioilic motions are symmetric and bounce back and forth between both walls with times of flight of $nT/2$ between each impact. Explicit conditions for the existence for each type can be written down and solved in closed form. Stability for these motions will be discussed in the next section.

Fixed points of P correspond to periodic motions and can be computed explicitly in a manner similar to that found in Masri and Caughey (1966), Masri (1969, 1972), and Shaw and Rand (1988). The final step involves solving a quadratic equation for the existence of periodic solutions. The main results can be summarized as follows:

Saddle-node bifurcations which result in the appearance of pairs of Type I subharmonics of order n *occur at a forcing amplitude given by*:

$$\beta_n^I(\mathrm{SN})=\frac{|A_nC_n+D_nF_n|}{[A_n^2+B_n^2D_n^2]^{1/2}}. \tag{6}$$

For $\beta>\beta_n^I(SN)$ *two pairs of such subharmonics exist.*

Saddle-node bifurcations which result in the appearance of pairs of Type II subharmonics of order n *occur at*

$$\beta_n^{II}(\mathrm{SN})=\frac{|\bar{A}_n\bar{C}_n+\bar{D}_n\bar{F}_n|}{[\bar{A}_n^2+\bar{B}_n^2\bar{D}_n^2]^{1/2}}. \tag{7}$$

For $\beta>\beta_n^{II}(\mathrm{SN})$ *one pair of such subharmonics exist.*

Where A_n, B_n, C_n, D_n, F_n (and with overbars) are functions of the system parameters. Bifurcation curves corresponding to equation (6) and (7) are presented in Fig. 2. It should be reiterated that Type I orbits exist in pairs due to symmetry, one near $\psi=+1$ and the other near -1.

4 Stability of Periodic Motions

Periodic motions of Types I and II correspond to fixed points of the Poincaré map. Hence, the stability of these periodic motions can be determined by examining the eigenvalues of the first derivative of the return map P, DP. A periodic motion is stable if and only if the moduli of all the eigenvalues of DP are less than unity. Computation of DP can be carried out by considering the dynamics of a small perturbation of the periodic motion. The analysis is lengthy; similar calculations can be found in Masri and Caughey (1966) and Shaw and Rand (1988). Here we provide only the main results of these calculations.

4.1 Type I Motions. Elements of DP depend continuously on system parameters, as do its eigenvalues. A bifurcation occurs as eigenvalues cross the unit circle in the complex plane. A saddle-node bifurcation (SN) is responsible for the birth of Type I and II steady-state motions; Figure 2 shows SN bifurcation curves for these motions. Note that the bifurcation curves accumulate onto β_∞ (discussed in the next section) as $n\to\infty$. Examinations of the eigenvalues show that one branch of the steady-state motion due to a SN bifurcation is always unstable while the others has (does not have, respectively) some stable region for $\Omega>\omega_n$ ($\Omega<\omega_n$, respectively) and undergoes secondary bifurcations. The primary and secondary bifurcation curves are shown in Fig. 3 where SN stands for saddle-node, HF for Hopf, and PD for period-doubling bifurcations. Figures 4 shows the bifurcation diagrams for $\Omega<\omega_n$ and $\Omega>\omega_n$.

As β is increased through β^I(HF) the stable Type I motion of period nT becomes unstable and new stable periodic or quasi-periodic motions appear; that is, motion on a two-dimensional torus exists; this is represented by an invariant circle for the map. As β is increased further through β^I(PD), the unstable Type I motion remains unstable and new unstable motions having period $2nT$ and two impacts per period appear.

4.2 Type II Motions. A study of the eigenvalues as parameters are varied shows that the primary and secondary bifurcations appear, as shown in Fig. 5, for this case. Note that pitchfork bifurcations can occur in this case due to the symmetry of Type II motions. (For Type II motions, period-doubling bifurcations do not occur; this also follows from symmetry).

Figure 6 shows the bifurcation diagrams for $\Omega<\omega_n$ and

Downloaded 03 May 2010 to 171.66.16.31. Redistribution subject to ASME license or copyright; see http://www.asme.org/terms/Terms_Use.cfm

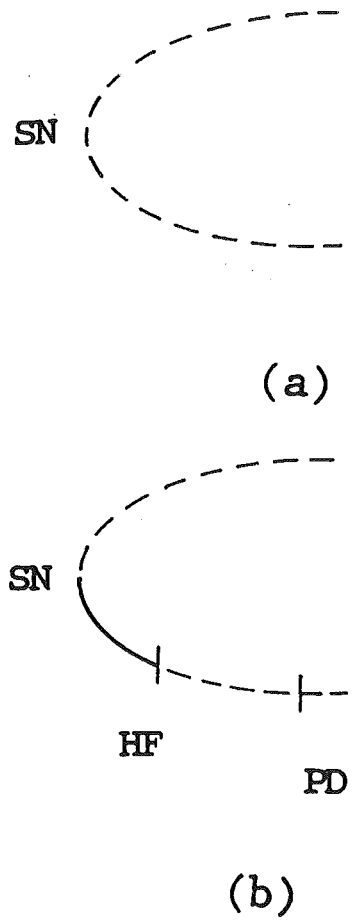


Fig. 4 Bifurcation diagrams of Type I motion; (a) $\Omega < \omega_n$, (b) $\Omega > \omega_n$

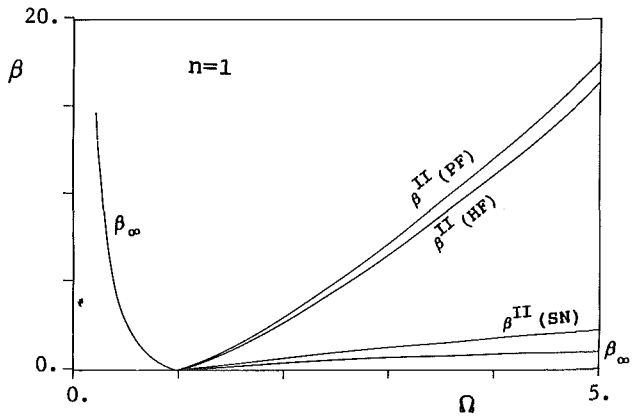


Fig. 5 The primary and secondary bifurcation curves of Type II motion for $n = 1$, $e = 0.8$, $\alpha = 0.161$, $\mu = 0.1$, $\omega_1 = 1$

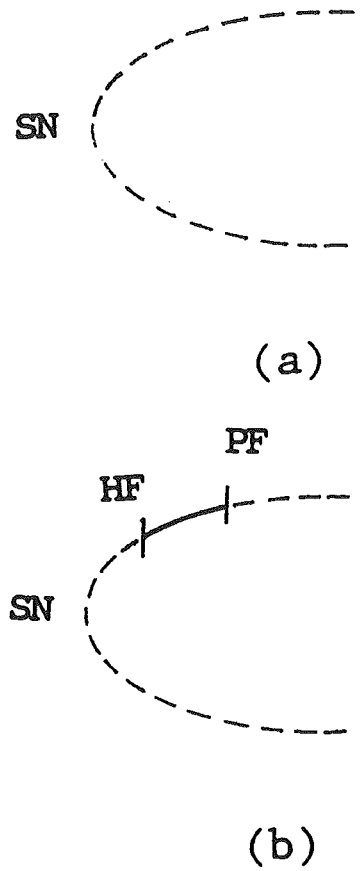


Fig. 6 Bifurcation diagrams of Type II motion; (a) $\Omega < \omega_n$, (b) $\Omega > \omega_n$

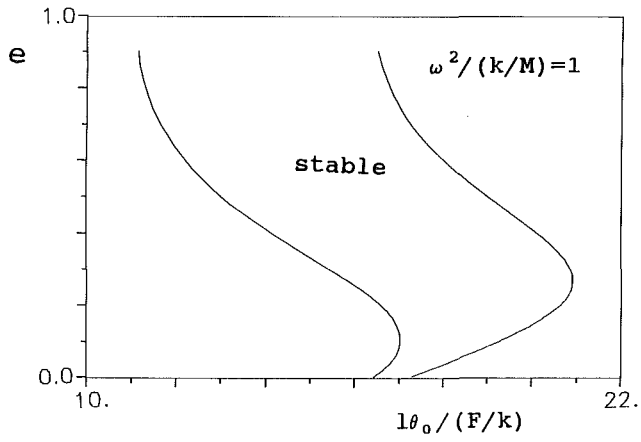


Fig. 7 Stability boundaries, $\mu = 0.1$, $\omega_1 = 1$

$\Omega > \omega_n$. Note that for $\Omega > \omega_n$, as β is increased through β^{II}(HF), the unstable Type II motion of period nT becomes stable. Also, an invariant circle for the map appears in this bifurcation. As β is increased further at β^{II} (PF) the stable motion becomes unstable and an antisymmetric pair of stable motions of period nT appear.

The stable region for Type II motions is interesting in view of application as an impact damper. As a vibration absorber, the desired forcing frequency ω is near $\sqrt{k/M}$. Figure 7 shows the stable region of Type II motions as a function of the coefficient of restitution e and the forcing amplitude β for $n = 1$ (i.e., two impacts-per-cycle) with the forcing frequency fixed at $\sqrt{k/M}$. It is seen that in the immediate vicinity of resonance (where the impact damper would normally be used), the stability boundaries enclose within them some range of system parameters which make stable symmetric two impacts-per-cycle motion realizable. However, for this system a multitude of other stable periodic (or chaotic) responses may coexist with the desired motion, rendering the absorber unreliable. For more information on the impact damper see the previously cited references.

The limit $n \to \infty$ for both the primary and secondary bifurcation curves accumulates onto β_∞ and corresponds to the appearance of arbitrarily long period periodic motions. This is now considered.

Downloaded 03 May 2010 to 171.66.16.31. Redistribution subject to ASME license or copyright; see http://www.asme.org/terms/Terms_Use.cfm

5 The Existence of Transverse Homoclinic Points and Chaos

This system can undergo chaotic motions in which the pendulum bounces back and forth between the stops in an irregular fashion. The appearance of such motions is known to be related to the saddle-type fixed point of the map which represents the nonimpacting periodic motion of the upright pendulum $(\tilde{y}_1, \tilde{y}_2, \tilde{y}_3, \tilde{y}_4)$. In particular, if its stable and unstable manifolds intersect in a transverse manner, then such chaotic dynamics are known to be possible (this follows from the Smale-Birkhoff homoclinic theorem; see Guckenheimer and Holmes, 1983).

Presented here is a calculation of the separation of the stable and unstable manifolds of the periodic orbit $(\tilde{y}_1, \tilde{y}_2, \tilde{y}_3, \tilde{y}_4)$. In the analysis that follows, we assume that there is a small amount of damping in the system (i.e., $\xi_i \neq 0, \ll 1$) for which the pair of purely imaginary eigenvalues $S_{3,4}$ move into the left side of the complex plane by an amount $\mathbf{O}(\xi_i)$. Hence, the unstable manifold, W^u, and stable manifold, W^s, of the periodic orbit $(\tilde{y}_1, \tilde{y}_2, \tilde{y}_3, \tilde{y}_4)$ are one- and three-dimensional, respectively. These invariant manifolds will be computed with $\xi_i = 0$ while assuming $\xi_i \neq 0, \ll 1$. This apparent inconsistency is used only for convenience in the calculations. The approach will result in rigorous statements regarding the existence of transverse homoclinic points, which provide a mechanism for the damper to bounce back and forth between the walls in an irregular manner, i.e., chaos.

For $\beta < q/\Omega^2$ the period T motion $(\tilde{y}_1, \tilde{y}_2, \tilde{y}_3, \tilde{y}_4)$ is not affected by impacts at $|y_3| = 1$. One branch of its unstable manifold, W^u, intersects Σ in a curve denoted by $\Phi^u(\phi)$. Its stable manifold, W^s, first reaches back to $y_3 = +1$ with $y_4 < 0$, i.e., not in Σ. Taking W^s one step further back, under the inverse of the impact rule, its intersection with Σ is given by $\Phi^s(\phi)$. The goal of this section is to determine the conditions under which $\Phi^u(\phi)$ and $\Phi^s(\phi)$ intersect transversally.

To compute $\Phi^u(\phi)$, consider trajectories starting in Σ which approach $(\tilde{y}_1, \tilde{y}_2, \tilde{y}_3, \tilde{y}_4)$ as $\tau \to -\infty$. The complete solutions for $y(\tau)$ and $\psi(\tau)$ are given in equations (3) with C_j depending on initial conditions $(y_1, y_2, y_3 = +1, y_4, \phi)$. Since S_2, S_3, S_4 are stable roots (with $0 < \xi_i \ll 1$) it must hold that $C_2 = C_3 = C_4 = 0$ in order for $(y_1^u, y_2^u + 1, y_4^u > 0, \phi)$ to be in $\Phi^u(\phi)$. Setting $C_2 = C_3 = C_4 = 0$ yields three equations which can be solved for y_1^u, y_2^u and y_4^u as functions of ϕ, resulting in an expression for $\Phi^u(\phi)$ in Σ:

$$y_1^u(\phi) = \gamma_1 + \frac{\beta}{q}(1 + \Omega^2 + \gamma_1\Omega^2)\cos(\Omega\phi)$$

$$y_2^u(\phi) = \gamma_1\lambda + \frac{\beta}{q}\lambda\Omega^2\gamma_1\cos(\Omega\phi) - \frac{\beta}{q}(\Omega + \Omega^3)\sin(\Omega\phi) \quad (8)$$

$$y_4^u(\phi) = \lambda + \frac{\beta}{q}\lambda\Omega^2\cos(\Omega\phi) + \frac{\beta}{q}\Omega^3\sin(\Omega\phi)$$

For $(\tilde{y}_1^s, \tilde{y}_2^s, +1, \tilde{y}_4^s < 0, \phi) \epsilon \Sigma$ to be in W^s, it must hold that $C_1 = 0$ since $S_1 > 0$. Setting $C_1 = 0$ one obtains

$$\left[-\tilde{y}_1^s - \tilde{y}_2^s/\lambda + \gamma_3\tilde{y}_4^s/\lambda + \gamma_3 + \frac{\beta}{q}(1 + \Omega^2 + \gamma_3\Omega^2)\cos(\Omega\phi)\right. \quad (9)$$

$$\left. - \frac{\beta}{q\lambda}(\Omega + \Omega^3 + \gamma_3\Omega^3)\sin(\Omega\phi)\right]/(\gamma_3 - \gamma_1) = 0.$$

Taking $(\tilde{y}_1^s, \tilde{y}_2^s, +1, \tilde{y}_4^s, \phi)$ under the inverse of the impact rule one obtains $(y_1^s, y_2^s + \alpha y_4^s, +1, -e y_4^s, \phi) = (\tilde{y}_1^s, \tilde{y}_2^s, +1, \tilde{y}_4^s, \phi)$ where $(y_1^s, y_2^s, y^s{}_4, \phi)\ \epsilon\Sigma$ is in $\Phi^s(\phi)$:

$$(-y_1^s - y_2^s/\lambda - (\alpha + e\gamma_3)y_4^s/\lambda + \gamma_3$$

$$+ \frac{\beta}{q}(1 + \Omega^2 + \gamma_3\Omega^2)\cos(\Omega\phi)$$

$$- \frac{\beta}{q\lambda}(\Omega + \Omega^3 + \gamma_3\Omega^3)\sin(\Omega\phi))/(\gamma_3 - \gamma_1) = 0. \quad (10)$$

In order for $\Phi^u(\phi)$ to intersect $\Phi^s(\phi)$ one requires $(y_1^s, y_2^s, y_4^s, \phi) = (y_1^u, y_2^u, y_4^u, \phi)$ at some value of ϕ. Substituting expressions (8) into equation (10) results in a condition for intersection:

$$A + \beta(B\cos(\Omega\phi) + C\sin(\Omega\phi)) = 0 \quad (11)$$

where

$$A = 2\gamma_1 + \gamma_3(e-1) + \alpha$$

$$B = (2\gamma_1 + \gamma_3(e-1) + \alpha)\Omega^2/q$$

$$C = (\alpha + \gamma_3(1+e))\Omega^3/q\lambda.$$

The main result is: *the one-dimensional manifold* $\Phi^u(\phi)$ *and three-dimensional manifold* $\Phi^s(\phi)$:

(a) Do not intersect if $\beta < \beta_\infty$.
(b) Intersect with quadratic tangencies if $\beta = \beta_\infty$.
(c) Intersect transversally if $\beta > \beta_\infty$.

where

$$\beta_\infty = \frac{|A|}{\sqrt{B^2 + C^2}}$$

$$= \frac{q\,|2\gamma_1 + \gamma_3(e-1) + \alpha|}{\Omega^2\left[(2\gamma_1 + \gamma_3(e-1) + \alpha)^2 + \dfrac{\Omega^2}{\lambda^2}(\alpha + \gamma_3(1+e))^2\right]^{1/2}}. \quad (12)$$

Remark. β_∞ can be thought of as the forcing amplitude required to push the system over the dynamic "energy hill" (represented by the unstable periodic motion) if it starts near the peak of this "hill." This condition depends on the system parameters and when $\beta > \beta_\infty$ there exists a mechanism for the pendulum to bounce from one side to the other (and back . . .) in an arbitrary fashion, that is to say, chaotically.

Proof. Equation (11) can be written in the following form

$$A + \beta(\sqrt{B^2 + C^2})\sin(\Omega\phi + \theta_1)) = 0 \quad (13)$$

where $\tan\theta_1 = B/C$. To have a solution for ϕ, we require $\beta \geq |A|/\sqrt{B^2 + C^2} = \beta_\infty$ which completes the proof for part (a). We say that two manifolds, $\Phi^s(\phi)$ and $\Phi^u(\phi)$, intersect transversally if, for every point q on $\Phi^s(\phi) \cap \Phi^u(\phi)$, we have

$$\mathrm{Dim}(T_q\Phi^s(\phi)) + \mathrm{Dim}(T_q\Phi^u(\phi)) = \mathrm{Dim}(\Sigma)$$

where $T_q\Phi$ is the tangent space of manifold Φ at q. In other words, the tangent spaces of $\Phi^s(\phi)$ and $\Phi^u(\phi)$ at q must span the Poincaré Section Σ. The tangent space of $\Phi^u(\phi)$ is represented by $(\partial y_1^u(\phi)/\partial\phi, \partial y_2^u(\phi)/\partial\phi, \partial y_4^u(\phi)/\partial\phi, \partial\phi/\partial\phi)^T$ while the tangent space of $\Phi^s(\phi)$ is spanned by

$$\left[1, 0, \frac{\partial y_4^s}{\partial y_1^s}, 0\right]^T, \left[0, 1, \frac{\partial y_4^s}{\partial y_2^s}, 0\right]^T, \left[0, 0, \frac{\partial y_4^s}{\partial\phi}, 1\right]^T.$$

These four vectors span Σ if they are linearly independent. The determinant D of the augmented matrix consisting of these four vectors is given by

Downloaded 03 May 2010 to 171.66.16.31. Redistribution subject to ASME license or copyright; see http://www.asme.org/terms/Terms_Use.cfm

$$\det\begin{vmatrix} -\frac{\beta\Omega}{q}(1+\Omega^2+\gamma_1\Omega^2)\sin(\Omega\phi) & 1 & 0 & 0 \\ -\frac{\beta}{q}\lambda\Omega^3\gamma_1\sin(\Omega\phi)-\frac{\beta}{q}\Omega(\Omega+\Omega^3)\cos(\Omega\phi) & 0 & 1 & 0 \\ -\frac{\beta}{q}\lambda\Omega^3\sin(\Omega\phi)+\frac{\beta}{q}\Omega^4\cos\Omega\phi & -\lambda/(\alpha+e\gamma_3) & -1/(\alpha+e\gamma_3) & -\frac{\beta(\Omega+\Omega^3+\gamma_3\Omega^3)}{q(\alpha+e\gamma_3)}(\lambda\sin(\Omega\phi)+\Omega\cos(\Omega\phi)) \\ 1 & 0 & 0 & 1 \end{vmatrix}$$

$$=\frac{\beta\lambda\Omega}{(\alpha+e\gamma_3)}\sqrt{B^2+C^2}\cos(\Omega\phi+\theta_1).$$

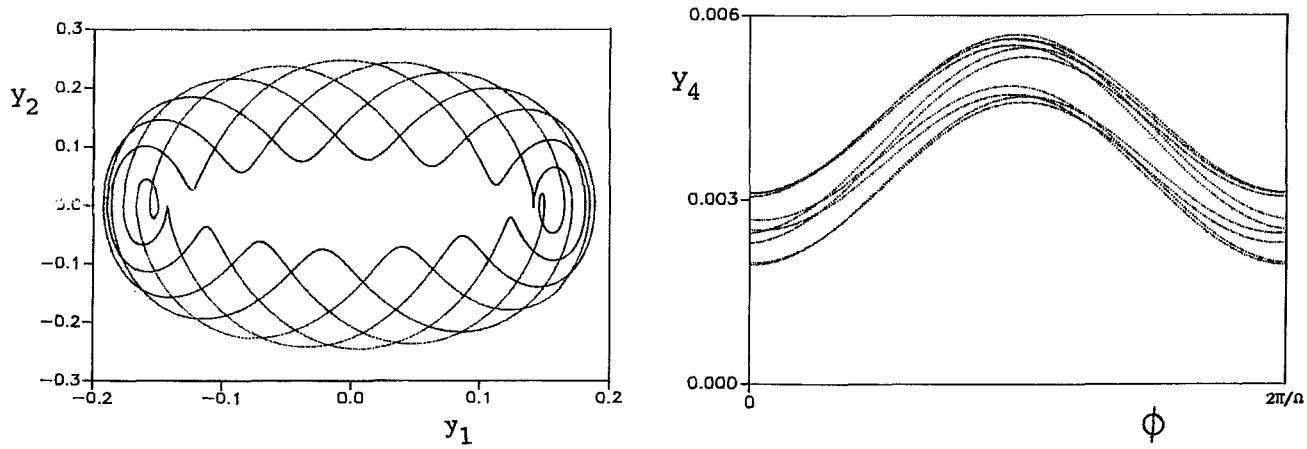
For $\beta=\beta_\infty$, we have $|\sin(\Omega\phi+\theta_1)|=1$ from equations (13) which implies $\cos(\Omega\phi+\theta_1)=0=>D=0$. This completes the proof for part (b). For $\beta>\beta_\infty$, we have $|\sin(\Omega\phi+\theta_1)|\neq 1=>\cos(\Omega\phi+\theta_1)\neq 0$, hence, $D\neq 0$ which completes the proof for part (c).

Remarks

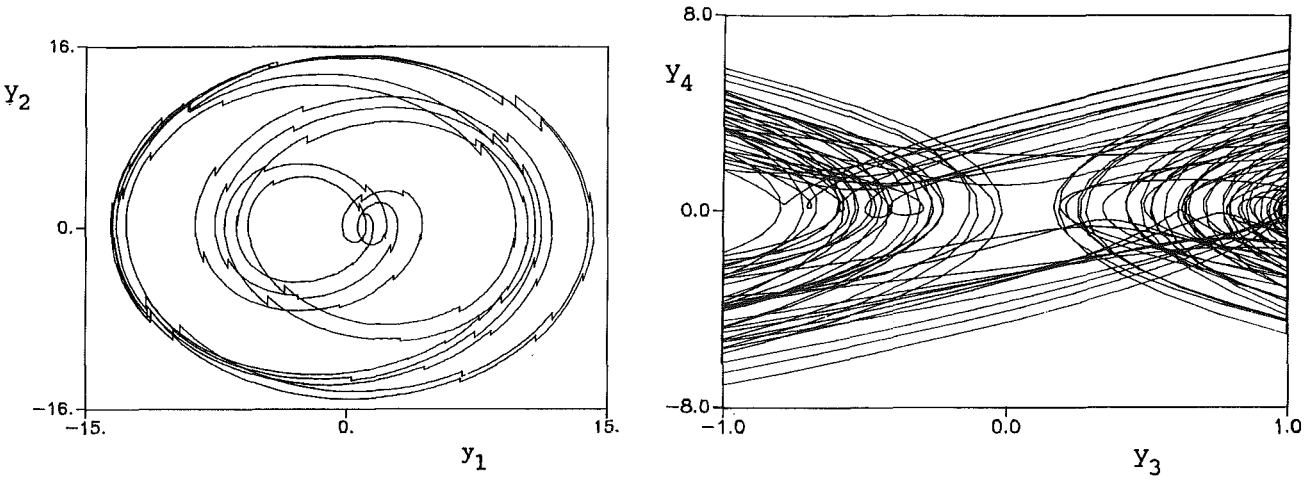
1 The three-dimensional manifold expressed by $\Phi^s(\phi)$ is actually a *center stable* manifold for $\xi_i=0$. Chaos *may or may not* exist when an unstable manifold intersects with a center-stable manifold, and conditions must be carefully checked in individual cases (Wiggins, 1988). In the present situation we use the fact that this manifold is *normally hyperbolic* (Hirsch et al. 1977) and thus will persist for $0<\xi_i\ll 1$. In fact, the continuation of the $\xi_i=0$ center-stable manifold for $0<\xi_i\ll 1$ will be within $\mathbf{O}(\xi_i)$ of the given expression for $\Phi^s(\phi)$ where it first intersects Σ. Then, since the intersection between $\Phi^s(\phi)$ and $\Phi^u(\phi)$ is transversal, it cannot be broken by small perturbations and it will also persist for some ξ_i, $0<\xi_i\ll 1$. The Smale-Birkhoff homoclinic theorem can be used directly then, and equation (12) will give the intersection point to within $\mathbf{O}(\xi_i)$.

2 This recaptures, by another method, the appearance of nonperiodic motions in the system; that is $n\to\infty$.

3 For $\beta>\beta_\infty$ complicated dynamics may be expected for this system. Specifically, the existence of Smale horseshoes (cf., Guckenheimer and Holmes, 1983, Chap. 5) implies that periodic motions of all periods and nonperiodic motions exist



(a) quasi-periodic motion after Hopf Bifurcation as seen in Σ, $\beta=0.35$, $\Omega=4$



(b) apparently chaotic motion, $\beta=4$, $\Omega=1.2$

Fig. 8 Simulations, $e=0.8$, $\alpha=0.161$, $\mu=0.1$, $\omega_1=1$

Downloaded 03 May 2010 to 171.66.16.31. Redistribution subject to ASME license or copyright; see http://www.asme.org/terms/Terms_Use.cfm

for $\beta > \beta_\infty$. These motions are unstable but are at the heart of the observable chaotic dynamics.

4 Stable Type II motions exist for $\beta > \beta_\infty$. Thus $\beta \geq \beta_\infty$ is not a sufficient condition for sustained chaotic motions, or strange attractors, to occur.

6 Simulations

The known solutions of the linear equations, the impact rule, and a simple root solving technique are combined to form the simulation routine. The simulation is used here to demonstrate some of the analytical results of the previous sections.

Figure 8(a) indicates the result of a Hopf bifurcation of a Type I motion, this is an invariant circle when depicted in Σ. The corresponding time response is quasi-periodic (or of very long period) in nature. A motion resulting from a period doubling bifurcation of a Type I motion is not presented here since these are unstable and not physically important. Figure 8(b) shows a strange attractor type motion, for $\beta > \beta_\infty$, in the phase space. Results for saddle-node bifurcations of motions of Types I and II, as well as those for pitchfork bifurcations of Type II motions were determined but are not included here; the reader is referred to Shaw and Rand (1988) for simulations of a similar system.

7 Discussion

For $\mu \ll 1$ the system can be treated as a one-degree-of-freedom system which has been well explored in Shaw and Rand (1988) and the analytical results presented here carry through in the limit $\mu \to 0$.

The *unperturbed* system is taken to be the unforced, undamped system ($\beta = 0$, $\xi_i = 0$, $e = 1$). It is nonintegrable and possesses chaotic dynamics for some initial conditions (without forcing!). This is in contrast with single-degree-of-freedom systems which are integrable when unforced and undamped; in such cases, one can proceed with an usual Melnikov approach to detect chaotic motions. In this example, no "unperturbed homoclinic orbit" exists from which one can carry out such an asymptotic analysis. The present analysis proceeds by an *explicit* compulation of the stable and unstable manifolds; this is not generally possible to do.

The *damped*, unforced problem is nonchaotic; motions simply settle to one of the two static rest configurations. The forced system without damping is potentially the most dynamically rich case since a four-dimensional, volume-preserving map can exhibit Arnold diffusion (see Wiggins, 1988).

The condition $\beta = \beta_\infty$ represents a lower bound for the existence of chaos (or of fractal basin boundaries which may separate two attractors, one bouncing at the left wall only, and one at the right) in this case.

The complexity of the response of this simple system indicates the need to carry out a thorough search for possible motions in nonlinear systems. We have gone only the first step in the present case and there is much that remains to be explored. For example, various bifurcations examined may be degenerate for some parameter values, leading to very subtle dynamics for nearly parameter values. A search for such situations was carried out by looking for simultaneous simple bifurcations (e.g., Hopf and period-doubling), but none were found in the parameter regions explored; however, they may well exist. Also, the invariant circles born in Hopf bifurcations can develop in a variety of ways, including "quasi-periodic breakdown" which results in chaotically modulated motions.

In conclusion, it should be pointed out that inverted pendulum (or any other system) with a unstable central position should be used as an absorber only with great care since the parameter range of desired motions can potentially possess several possible steady-states, including chaos. This is less critical if one designs the system so that the forcing amplitude is much larger than that required to push the pendulum over the dynamic energy hill, that is $\beta \gg \beta_\infty$.

Acknowledgment

Support for this work from the National Science Foundation (contract MSM-8613294) and from DARPA is gratefully acknowledged.

References

Dowell, E. H., 1982, "Flutter of a Buckled Plate as an Example of Chaotic Motion of a Deterministic Autonomous System," *Journal of Sound and Vibration*, Vol. 85, pp. 333–344.

Druzhilovskaia, T. Iu., and Neimark, Iu. I., 1983, "Stochastic Auto-Oscillations of a Non-Linear Oscillator with Impact Energy Absorber," *Prikl. Matem. Mekhan.*, Vol. 46, No. 6, pp. 741–745.

Guckenheimer, J., and Holmes, P., 1983, *Nonlinear Oscillations, Dynamical Systems and Bifurcations of Vector Fields*, Springer-Verlag, New York.

Hirsch, M. W., Pugh, C. C., and Shub, M., 1977, "Invariant Manifolds," *Springer Lecture Notes in Mathematics*, Vol. 583, Springer-Verlag, New York, Heidelberg, and Berlin.

Holmes, P., and Marsden, J., 1982, "Horseshoes in Perturbations of Hamiltonians with Two Degree of Freedom," *Communications in Mathematical Physics*, Vol. 82, pp. 523–544.

Masri, S. F., 1969, "Analytical and Experimental Studies of Multiple-Unit Impact Dampers," *Journal of the Acoustical Society of America*, Vol. 45, No. 5, pp. 1111–1117.

Masri, S. F., 1972, "Theory of the Dynamic Vibration Neutralizer with Motion-Limiting Stops," ASME JOURNAL OF APPLIED MECHANICS, Vol. 39, pp. 563–568.

Masri, S. F., and Caughey, T. K., 1966, "On the Stability of the Impact Damper," ASME JOURNAL OF APPLIED MECHANICS, Vol. 33, pp. 586–592.

Nigm, M. M., and Shabana, A. A., 1983, "Effect of an Impact Damper on a Multi-Degree-of-Freedom System," *Journal of Sound and Vibration*, Vol. 89, No. 4, pp. 541–557.

Shaw, S. W., and Holmes, P., 1983, "A Periodically Forced Piecewise Linear Oscillator," *Journal of Sound and Vibration*, Vol. 90, pp. 129–155.

Shaw, S. W., and Rand, R. H., 1988, "The Transition to Chaos in a Simple Mechanical System," *International Journal of Nonlinear Mechanics*, to appear.

Wiggins, S., 1988, *Chaos and Global Bifucations: Analytical Methods*, Springer-Verlag, New York.

Downloaded 03 May 2010 to 171.66.16.31. Redistribution subject to ASME license or copyright; see http://www.asme.org/terms/Terms_Use.cfm

Almost-Sure Stability of Some Linear Stochastic Systems

S. T. Ariaratnam
Solid Mechanics Division,
Faculty of Engineering,
University of Waterloo,
Waterloo, Ontario, Canada, N2L 3G1.

B. L. Ly
Civil Engineering Branch,
Atomic Energy of Canada Limited,
Mississauga, Ontario, Canada, L5K 1B2

The almost-sure stability of linear second-order systems which are parametrically excited by ergodic, "nonwhite," random processes is studied by an extension of the method of Infante. In this approach, a positive-definite quadratic function of the form $V = x'Px$ *is assumed and a family of stability boundaries depending on the elements of the matrix* P *is obtained. An envelope of these boundaries is then solved for by optimizing the stability boundary with respect to the elements of* P. *It is found that the optimum matrix* P *in general depends not only on the system constants but also on the excitation intensities. This approach is, in principle, applicable to study systems involving two or more random processes. The results reported in previous investigations are obtained as special cases of the present study.*

Introduction

The study of stability of solutions of differential equations with randomly varying coefficients has attracted considerable interest. A substantial amount of literature has been published dealing with this subject. Stability analysis of stochastic systems depends to a large extent on the nature of the excitation processes. The systems studied can be broadly divided into two groups, namely, systems described by stochastic differential equations with "nonwhite noise" coefficients, and those described by Itô equations, respectively. Analysis of the former class of equations can be carried out by the ordinary rules of calculus since the coefficient processes are well defined with well-behaved sample functions. On the other hand, Itô's equations have to be handled by the rules of Itô's calculus because solutions to Itô equations are Markov diffusion processes.

In investigation of stochastic systems, one is generally most interested in the almost-sure (a.s.) sample behavior of the solution process, as the results thus obtained hold true with probability one (w.p.1) for almost all sample systems. In what follows here, conditions that guarantee the a.s. stability of the trivial solution of the following differential equation

$$\dot{x}_i = \sum_j [a_{ij} + b_{ij}(t)]x_j, \text{ w.p.1, } (i, j = 1,2), \tag{1}$$

where a_{ij} are constants and $b_{ij}(t)$ are ergodic "nonwhite" random processes, are obtained by an extension of the method of Infante (1968). Investigations of almost-sure stability of Itô equations, which are outside the scope of our study, can be found in the works of, for example, Khas'minskii (1964), Kozin and Prodromou (1971), and Mitchell (1972).

Contributed by the Applied Mechanics Division for publication in the JOURNAL OF APPLIED MECHANICS.

Discussion on this paper should be addressed to the Editorial Department, ASME, United Engineering Center, 345 East 47th Street, New York, N.Y. 10017, and will be accepted until two months after final publication of the paper itself in the JOURNAL OF APPLIED MECHANICS. Manuscript received by ASME Applied Mechanics Division, October 29, 1987; final revision, June 24, 1988.

A. S. Stability by Infante's Method

The a.s. stability of systems governed by differential equations of the form

$$\dot{x} = Ax + \xi(t)Bx,$$

where A, B are constants and $\xi(t)$ a nonwhite, zero mean, ergodic random process was first studied by Kozin (1963).

His approach was based on the Gronwall-Bellman lemma. Under the assumption that the unperturbed system is stable, i.e., all eigenvalues of the matrix A have negative real parts, and $\xi(t)$ ergodic, he found that there exists a constant $\alpha > 0$ depending on the eigenvalues of A such that

$$\sigma_\xi^2 < \alpha$$

implies that the equilibrium solution is asymptotically stable w.p.1.

The sufficient condition derived by Kozin was improved by Ariaratnam (1966), Caughey and Gray (1965), Infante (1968), and Kozin and Wu (1973).

The most significant improvement was due to Infante (1968), who considered linear systems of the form

$$\dot{x} = Ax + B(t)x$$

with A a constant matrix whose eigenvalues have negative real parts, and $B(t)$ a square matrix, the nonzero elements of which are nonwhite ergodic processes.

Defining the norm of x, $\|x\|$ by

$$\|x\|^2 = V = x'Px,$$

where x' denotes the transpose of the vector x and P is a positive-definite matrix to be determined, and by means of the min-max properties of pencils of quadratic forms, he showed that

$$\omega(t) \le \frac{\dot{V}}{V} \le \Omega(t),$$

where $\dot{V}$ is evaluated along the trajectories, and $\omega(t)$ and $\Omega(t)$ are the minimum and the maximum eigenvalues, respectively, of the matrix

Copyright © 1989 by ASME

Downloaded 03 May 2010 to 171.66.16.31. Redistribution subject to ASME license or copyright; see http://www.asme.org/terms/Terms_Use.cfm

$$\{(A'+B')P+P(A+B)\}P^{-1}.$$

Consequently,

$$V_0\exp\left[\int_{t_0}^{t}\omega(s)ds\right]\le V(t)\le V_0\exp\left[\int_{t_0}^{t}\Omega(s)ds\right],$$

where $V_0=V[x(t_0)]$.

Since $\lim_{t\to\infty}\frac{1}{t}\int_0^t\Omega(s)ds=E[\Omega(t)]$ w.p.1, a sufficient condition for a.s. asymptotic stability was obtained as

$$E[\Omega(t)]<-\epsilon,\ \epsilon>0.$$

The matrix P is now chosen so as to achieve the largest possible stability domain.

Solving for $E[\Omega(t)]$ is generally difficult. Without any further information other than the mean and the variance of the excitation processes, Infante applied the Schwarz inequality to estimate a bound for $E[\Omega(t)]$. This naturally makes his sufficient condition further conservative. If more information about the excitation processes is known, obviously the stability domain can be improved. Recognizing this, Kozin and Wu (1973) solved for $E[\Omega(t)]$ for a Gaussian process and a periodic noise. In this way, they obtained results that are much sharper than Infante's.

Extension of Infante's Method

When $B(t)$ contains two or more random processes, Infante did not obtain a sufficient stability condition that would be simultaneously optimum for the individual excitations. He stated that unless the excitation processes were related, there existed no optimum matrix P. However, it will be shown in the following that, by allowing P to depend not only on the system parameters but also on the excitation intensities, an optimum matrix P can, in fact, be constructed.

For a linear second-order system as described by (1), let us assume for V a positive-definite function of the form

$$V=x'\begin{bmatrix}a & b\\ b & 1\end{bmatrix}x,\quad a>0,\quad a-b^2>0.$$

With $\dot V$ evaluated along the trajectories of equation (1) and use made of Infante's method, a sufficient condition for a.s. asymptotic stability of the trivial solution is given by

$$E[\Omega(t)]<-\epsilon,\ \epsilon>0,$$

where $E[\Omega(t)]$ denotes the expected value of $\Omega(t)$.

Let us denote $F=E[\Omega(t)]$. The relation $F=F(a,\ b;\ c_1,\ c_2,\ \ldots;\ \sigma_f,\ \sigma_g,\ \ldots)=0$, where $c_1, c_2, \ldots$ are constants of the system and $\sigma_f, \sigma_g, \ldots,$ are the excitation intensities, represents a family of stability boundaries that depend on the parameters a and b. The envelope to the family of stability boundaries, if it exists, is obtained by eliminating a, b from the following equations:

$$F=0,\ \frac{\partial F}{\partial a}=0,\quad \frac{\partial F}{\partial b}=0,$$

with a and b subjected to the conditions $a>0$, $a-b^2>0$.

In solving for the envelope, one has also optimized the quadratic function V at the same time.

In the study of the stability of Itô equations, Kushner (1965) has suggested a method of construction of stochastic Lyapunov functions. It is interesting to note that the Lyapunov functions thus obtained by Kushner also depend on the excitation intensities.

For higher order systems, Infante's method has not met with much success since the optimization of the quadratic function and the evaluation of the maximum eigenvalue $\Omega(t)$ become exceedingly cumbersome.

In order to be able to compare with some of the existing results, the stability of a mass-spring-dashpot model with random fluctuation in both the stiffness coefficient and the damping coefficient is considered. In this case, sufficient stability conditions are obtained for arbitrary ergodic processes as well as ergodic Gaussian processes.

Systems Under Arbitrary Ergodic Excitation

Consider the following state equation

$$\dot x=\begin{bmatrix}0 & 1\\ -\xi(t) & -2\eta(t)\end{bmatrix}x, \tag{2}$$

where

$$\xi(t)=1+\sigma_g g(t),\ \eta(t)=\beta+\sigma_f f(t),$$

and $f(t)$, $g(t)$ are *independent* ergodic processes with zero mean values and unit variances.

Equation (2) is the state equation of a mass-spring-dashpot model described by

$$\ddot q+2\eta(t)\dot q+\xi(t)q=0$$

with the state vector x given by $\{q,\ \dot q\}$.

Following the procedure as outlined in the previous section, the maximum eigenvalue $\Omega(t)$ is obtained as

$$\Omega(t)=-2\eta+[4\eta^2-G/(a-b^2)]^{1/2},$$

where $G=4b\xi(2\eta-b)-(a-\xi-2b\eta)^2$.

The stability condition is given by setting $E[\Omega(t)]<0$ which in turn yields

$$E[\{4\eta^2-G(/a-b^2)\}^{1/2}]<2\beta. \tag{3}$$

If no further information than the mean values and the variances of the processes $f(t)$ and $g(t)$ are available, one can apply the Schwarz inequality to equation (3) to obtain a stability boundary:

$$F=4a\sigma_f^2+(a-1)^2+\sigma_g^2-4b\beta(a+1)+4b^2(\beta^2+1)=0. \tag{4}$$

Now, the conditions $\partial F/\partial a=\partial F/\partial b=0$ give

$$a-2\beta b=1-2\sigma_f^2, \tag{5}$$

$$-\beta a+2(\beta^2+1)b=\beta, \tag{6}$$

which when solved for a and b give

$$a=2\beta^2+1-2\sigma_f^2(\beta^2+1), \tag{7}$$

$$b=\beta(1-\sigma_f^2). \tag{8}$$

It is seen that a and b are dependent on σ_f.

Substitution of a and b into equation (4) yields

$$\sigma_g^2-4\beta^2(1-\sigma_f^2)[1-(1+\beta^2)\sigma_f^2/\beta^2]=0, \tag{9}$$

which represents the optimized stability boundary when both $f(t)$ and $g(t)$ are present.

When $\sigma_f=0$, i.e., no fluctuation in the damping coefficient, the stability boundary is given by

$$\sigma_g^2=4\beta^2, \tag{10}$$

and when $\sigma_g=0$, i.e., no fluctuation in the stiffness coefficient, equation (9) is reduced to

$$\sigma_f^2=\frac{\beta^2}{1+\beta^2}, \tag{11}$$

with $\sigma_f^2=1$ as the asymptote.

Downloaded 03 May 2010 to 171.66.16.31. Redistribution subject to ASME license or copyright; see http://www.asme.org/terms/Terms_Use.cfm

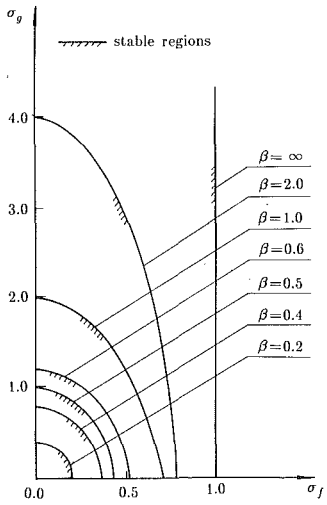


Fig. 1 Regions of almost-sure asymptotic stability for $\ddot{x}+2[\beta+f(t)]\dot{x}+[1+g(t)]x=0$ via Schwarz inequality

Both results stated in equations (10) and (11) were obtained by Infante (1968), which are here special cases of equation (9).

It is now necessary to show that V is postive-definite in the stability region, i.e.,

$$\Delta_1 = a > 0,\ \Delta_2 = a - b^2 > 0.$$

Since, within the stability domain,

$$\sigma_f^2 < \frac{\beta^2}{\beta^2+1},$$

by substituting into equations (7) and (8), it can be seen that

$$a > 2\beta^2 + 1 - \frac{2\beta^2}{\beta^2+1}(\beta^2+1) = 1 > 0,$$

and, similarly,

$$\begin{aligned} a - b^2 &= \beta^2 + 1 - 2\sigma_f^2 - \beta^2\sigma_f^4 \\ &= \beta^2 + 1 + \frac{1}{\beta^2} - \beta^2\left(\sigma_f^2 + \frac{1}{\beta^2}\right)^2 \\ &> \frac{\beta^4+\beta^2+1}{\beta^2} - \frac{1}{\beta^2}\left(\frac{\beta^4+\beta^2+1}{\beta^2+1}\right)^2 \\ &= \frac{\beta^4+\beta^2+1}{(\beta^2+1)^2} > 0, \end{aligned}$$

thus concluding the proof.

The stability boundaries given by equation (9) are plotted for various values of β in Fig. 1.

Systems Under Ergodic Gaussian Excitation

Kozin and Wu (1973) showed that, if the probability density of the excitation process is known, $E[\Omega(t)]$ can be explicitly evaluated without recourse to the Shwarz inequality. They illustrated this idea by solving for a Gaussian process and a periodic noise.

Here use is made of this concept to solve for $E[\Omega(t)]$ when the excitation processes $f(t)$ and $g(t)$ are Gaussian with the joint probability density given by

$$p_{fg} = \frac{1}{2\pi}\exp\left(-\frac{f^2+g^2}{2}\right).$$

Before solving for the general case when both $f(t)$ and $g(t)$ are present, the cases when (i) $\eta(t)\equiv\beta$, and (ii) $\xi(t)\equiv 1$ are considered first.

In the following analysis, let

$$\begin{aligned} H &= [4\eta^2(a-b^2) - G]^{1/2}, \\ G &= 4b\xi(2\eta - b) - (a - \xi - 2b\eta)^2, \\ F &= E[H] - 2\beta(a-b^2)^{1/2}. \end{aligned}$$

(i) When $f(t)\equiv 0$, one has $\eta(t)\equiv\beta$. In this case H becomes

$$H = [4\beta^2(a-b^2) + (a-\xi-2b\beta)^2 - 4\xi(2b\beta - b^2)]^{1/2}.$$

Now $\partial F/\partial a = 0$ gives

$$E\left[\frac{2\beta^2 + (a-\xi-2b\beta)}{H}\right] - \frac{\beta}{(a-b^2)^{1/2}} = 0, \tag{12}$$

and $\partial F/\partial b = 0$ gives

$$E\left[\frac{2\xi(b-\beta) - \beta(a-\xi-2b\beta) - 2\beta^2 b}{H}\right] + \frac{b\beta}{(a-b^2)^{1/2}} = 0. \tag{13}$$

Comparison of equation (12) with equation (13) yields $b=\beta$ which, when substituted in equation (3) leads to

$$E[\,|a-\xi|\,] - 2\beta(a-\beta^2)^{1/2} = 0. \tag{14}$$

Differentiating equation (14) with respect to a gives

$$E[\mathrm{sgn}(a-\xi)] - \frac{\beta}{(a-\beta^2)^{1/2}} = 0, \tag{15}$$

Equations (14) and (15) are used to solve for a and σ_g.

It might be noted that equation (14) was obtained by Kozin and Wu (1973) by a somewhat different approach.

(ii) When $g(t)\equiv 0$, one has $\xi(t)\equiv 1$. Let

$$H^* = \frac{H}{\sqrt{a}} = \left[4\eta^2 + \frac{(a-1)^2 - 4b\eta + 4b^2}{a} - 4b\eta\right]^{1/2},$$

$$F^* = E[H^*] - 2\beta(1 - b^2/a)^{1/2} = 0.$$

Again, $\partial F^*/\partial a = 0$ gives

$$E\left[\frac{a^2 - 1 + 4b\eta - 4b^2}{2H^*}\right] - b^2\beta\left(\frac{a}{a-b^2}\right)^{1/2} = 0, \tag{16}$$

and $\partial F^*/\partial b = 0$ gives

$$E\left[\frac{2b - \eta(a+1)}{H^*}\right] + b\beta\left(\frac{a}{a-b^2}\right)^{1/2} = 0. \tag{17}$$

From equations (16) and (17), one obtains

$$(a-1)E\left[\frac{a+1-2b\eta}{H}\right] = 0,$$

so that $a=1$. Then, with $a=1$, equations (3) and (16) become

$$E[\,|b-\eta|\,] - \beta(1-b^2)^{1/2} = 0, \tag{18}$$

$$E[\mathrm{sgn}(b-\eta)] - \frac{b\beta}{(1-b^2)^{1/2}} = 0. \tag{19}$$

The quantities b and σ_f can now be obtained by solving equations (18) and (19) simultaneously. Again, equation (18) was obtained by Kozin and Wu (1973) in a different manner.

(iii) The case when both $f(t)$ and $g(t)$ are not identically zero is now considered. The stability boundary in this case is given by

$$F = E[H] - 2\beta(a-b^2)^{1/2} = 0,$$

and the optimization conditions $\partial F/\partial a = 0$ and $\partial F/\partial b = 0$ give

$$Q = E\left[\frac{2\eta^2 + a - \xi - 2b\eta}{H}\right] - \frac{\beta}{(a-b^2)^{1/2}} = 0,$$

$$R = E\left[\frac{2b\xi - a\eta - \xi\eta}{H}\right] + \frac{b\beta}{(a-b^2)^{1/2}} = 0.$$

For fixed β and a given σ_f, the above equations constitute three simultaneous nonlinear algebraic equations for a, b, and

Downloaded 03 May 2010 to 171.66.16.31. Redistribution subject to ASME license or copyright; see http://www.asme.org/terms/Terms_Use.cfm

σ_g. Solutions for a, b, and σ_g can be obtained numerically by the Newton-Raphson method as follows.

The method is one of successive approximation. Let the step-by-step approximation be denoted by

$$\{a,b,\sigma_g\}_{k+1} = \{a,b,\sigma_g\}_k + \{\Delta a,\Delta b,\Delta\sigma_g\}_k \quad (k=1,2,3,\ldots,). \tag{20}$$

With an initial value assumed for $\{a,b,\sigma_g\}_{k=1}$, the Jacobian matrix $[\partial(F,Q,R)/\partial(a,b,\sigma_g)]_{k=1}$ and the vector $\{F,Q,R\}_{k=1}$ are evaluated.

The correction term $\{\Delta a,\Delta b,\Delta\sigma_g\}_{k=1}$ is then obtained by solving

$$\left[\frac{\partial(F,Q,R)}{\partial(a,b,\sigma_g)}\right]_{k=1} \cdot \begin{bmatrix}\Delta a\\ \Delta b\\ \Delta\sigma_g\end{bmatrix}_{k=1} = -\begin{bmatrix}F\\ Q\\ R\end{bmatrix}_{k=1}. \tag{21}$$

Substituting the correction term into (20) gives $\{a,b,\sigma_g\}_{k=2}$. The procedure is repeated until a desired degree of accuracy is reached, and

$$\{a,b,\sigma_g\} = \lim_{k\to\infty} \{a,b,\sigma_g\}_k, \tag{22}$$

if the sequences converge.

Numerical results for $\beta = 0.2$, 0.4, 0.5, 0.6, 1.0, and 2.0 are plotted in Fig. 2. The positive-definiteness of V is checked by computing the quantities a and $(a-b^2)$. Within the stability domain, V is indeed found to be always positive definite.

Conclusions

Infante's method has been extended to study the a.s. stability of solutions of some two-dimensional linear state equations, the coefficients of which are ergodic nonwhite random processes. The extension is achieved by obtaining, first, a family of stability boundaries by means of the extremum properties of the eigenvalues associated with pencils of quadratic forms, and then an evelope to these boundaries. It is found that the matrix defining the norm of the response, in general, depends on both the system parameters and the excitation intensities. The method presented here is quite straightforward and can be used to study systems excited by two or more random processes. The results reported in earlier investigations can be obtained as special cases of the present study.

In principle, the method used here is applicable to study systems of higher order. However, in such cases, results in analytical form are generally very difficult to obtain, and the investigation will have to be carried out numerically.

Kozin and Milstead (1979) have presented an approach, also based on Infante's (1968) idea, for studying the stochastic stability of higher order linear systems with several independent random coefficient processes. This method was applied to the stability of a moving elastic strip, whose equations of motion consist of a pair of coupled second-order linear differential equations. It seems difficult to find a connection between the approach of Kozin and Milstead (1979) and that of the present paper, although both methods yield the same stability boundaries for the second-order system considered here. It is felt that the method presented in this paper is more direct and easier to apply for second-order systems.

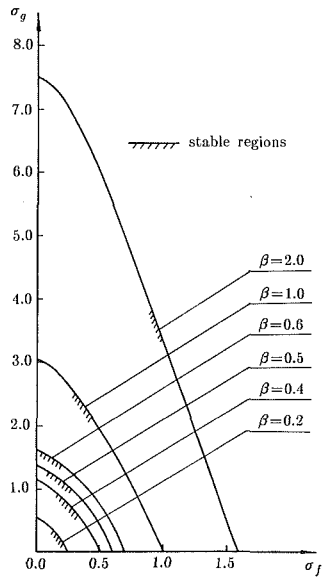


Fig. 2 Regions of almost-sure asymptotic stability for $\ddot{x} + 2[\beta + f(t)]\dot{x} + [1 + g(t)]x = 0$; ($f(t)$, $g(t)$ Gaussian)

Acknowledgment

The research for this paper was supported (in part) by the National Sciences and Engineering Research Council of Canada through grant No. A-1815.

References

Ariaratnam, S. T., 1967, "Dynamic Stability of a Column under Random Loading," *Dynamic Stability of Structures*, G. Herrmann, ed. Pergamon Press, New York, pp. 267–284.

Caughey, T. K., and Gray, Jr., A. H., 1965, "On Almost Sure Stability of Linear Dynamic Systems with Stochastic Coefficients," ASME JOURNAL OF APPLIED MECHANICS, Vol. 32, pp. 365–372.

Infante, E. F., 1968, "On the Stability of Some Linear Nonautonomous Random Systems," ASME JOURNAL OF APPLIED MECHANICS, Vol. 35, pp. 7–12.

Khas'minskii, R. Z., 1967, "Necessary and Sufficient Conditions for the Almost-Sure Asymptotic Stability of Linear Stochastic Systems," *Theory Prob. Appl.*, Vol. 12, No. 1, pp. 144–147, (English Translation).

Kozin, F., 1963, "On Almost Sure Stability of Linear Systems with Random Coefficients," *J. Math. Phys.*, Vol. 42, pp. 59–67.

Kozin, F., and Milstead, R. M., 1979, "The Stability of a Moving Elastic Strip Subjected to Random Parametric Excitation," ASME JOURNAL OF APPLIED MECHANICS, Vol. 46, pp. 404–410.

Kozin, F., and Prodromou, S., 1971, "Necessary and Sufficient Conditions for Almost-Sure Sample Stability of Linear Itô Equations," *SIAM J. Appl. Math.*, Vol. 21, pp. 413–424.

Kozin, F., and Wu, C. M., 1973, "On the Stability of Linear Stochastic Differential Equations," ASME JOURNAL OF APPLIED MECHANICS, Vol. 40, pp. 87–92.

Kushner, H. J., 1965, "On The Construction of Stochastic Lyapunov Functions," *IEEE Trans. Automatic Control*, Vol. AC-10, pp. 477–478.

Mitchell, R. R., 1972, "Sample Stability of Second-Order Stochastic Differential Equations with Non-Singular Phase Diffusion," *IEEE Trans. Automatic Control*, Vol. AC-17, pp. 706–707.

Downloaded 03 May 2010 to 171.66.16.31. Redistribution subject to ASME license or copyright; see http://www.asme.org/terms/Terms_Use.cfm

Methods and Gaussian Criterion for Statistical Linearization of Stochastic Parametrically and Externally Excited Nonlinear Systems[1]

R. J. Chang
Associate Professor,
Department of Mechanical Engineering,
National Chong Kung University,
Tainan, Taiwan 70101

G. E. Young
Associate Professor,
School of Mechanical and
Aerospace Engineering,
Oklahoma State University
Stillwater, OK 74078
Mem. ASME

The methods of Gaussian linearization along with a new Gaussian Criterion used in the prediction of the stationary output variances of stable nonlinear oscillators subjected to both stochastic parametric and external excitations are presented. The techniques of Gaussian linearization are first derived and the accuracy in the prediction of the stationary output variances is illustrated. The justification of using Gaussian linearization a priori *is further investigated by establishing a Gaussian Criterion. The non-Gaussian effects due to system nonlinearities and/or large noise intensities in a Duffing oscillator are also illustrated. The validity of employing the Gaussian Criterion test for assuring accuracy of Gaussian linearization is supported by performing the Chi-square Gaussian goodness-of-fit test.*

1 Introduction

The techniques of using statistical linearization for the dynamic analysis of nonlinear stochastic systems are very effective. Since Booton (1954) and Caughey (1959) independently extended the equivalent linearization method (Krylov and Bogoliubov, 1943) to statistical linearization, the techniques have been widely used for the dynamic analysis and controller design of stochastic externally excited nonlinear systems (Gelb and Vander Velde, 1968). However, when the nonlinear systems are subjected to both stochastic parametric and external excitations, the applications of statistical linearization have not been fully investigated (Young and Chang, 1987b). In the applications of the linearization approach, the simple and useful jointly Gaussian distribution is usually applied to the evaluation of expectations of certain nonlinear functions of states. Although Gelb concluded that there was little difference in a linearizing gain when either a non-Gaussian distributed signal including uniform and triangular distributed signal or a Gaussian distributed signal was passed through a saturating element (Gelb, 1974), a quantitative measure of the effects of large nonlinearities on Gaussian linearization of external noise excited nonlinear systems has not been established. Some studies are only to compare the output variance of the linearization solution with that of the exact solution of some solvable nonlinear oscillators (Crandall, 1980; Hedrick, 1980). When nonlinear systems are subjected to both stochastic parametric and external excitations, the density function of states is usually far from a jointly Gaussian distribution. For example, the stationary probability density function of the states of a simple second-order stochastic parametrically and externally excited linear system is not a jointly Gaussian distribution (Dimentberg, 1982). Thus, in the applications of statistical linearization for stochastic parametrically and externally excited stable nonlinear systems, a non-Gaussian density needs to be applied for the linearization or a jointly Gaussian distribution can still be used if the system parameters and noise intensities can satisfy certain Gaussian criteria.

In this paper, the methods of Gaussian linearization of stable nonlinear stochastic parametrically and externally exicted systems are presented along with the derivation of a new Gaussian criterion. The techniques of Gaussian linearization of these systems are first derived. A parametric and external noise excited oscillator with cubic nonlinear spring is then selected to illustrate these applications. The non-Gaussian linearization is illustrated through implementation of a non-Gaussian density which is derived by using the concepts of equivalent external excitation (Young and Chang, 1987a). By following these concepts and their extensions, a Gaussian criterion is further proposed. A stochastic parametrically and externally excited Duffing oscillator is selected to illustrate the applications of the Gaussian Criterion for the justification of employing Gaussian linearization *a priori*. The validity of us-

[1]Presented at the 1988 ASME Winter Annual Meeting as Paper No. WA/DSC-9.

Discussion on this paper should be addressed to the Editorial Department, ASME, United Engineering Center, 345 East 47th Street, New York, N.Y. 10017, and will be accepted until two months after final publication of the paper itself in the JOURNAL OF APPLIED MECHANICS. Manuscript received by ASME Applied Mechanics Division, June 23, 1987; final revision, April 5, 1988.

Copyright © 1989 by ASME

Downloaded 03 May 2010 to 171.66.16.31. Redistribution subject to ASME license or copyright; see http://www.asme.org/terms/Terms_Use.cfm

ing the Gaussian Criterion for assuring accurate prediction of the stationary output variance of a stable nonlinear stochastic system by employing Gaussian linearization is supported by performing the Chi-square Gaussian goodness-of-fit test (Bendat and Piersol, 1971).

2 Statistical Linearization of Stochastic Parametrically and Externally Excited Nonlinear Systems

Consider a second-order stochastic parametrically and externally excited stable nonlinear system described by

$$\ddot{x}+\sum_{i=1}^{n}(a_i+\alpha_i)H_i(x,\dot{x})=W' \tag{1}$$

where the a_i are constants and the α_i and W' are mutually independent zero-mean Gaussian white noises with intensities $E[\alpha_i(t)\alpha_i(s)]=2q_{ii}\,\delta(t-s)$ and $E[W'(t)W'(s)]=2q_{n+1\,n+1}\,\delta(t-s))$, respectively. The equivalent linearization system of (1) is expressed as

$$\ddot{x}+\sum_{i=1}^{n}(a_i+\alpha_i)(g_i\dot{x}+f_ix)=W' \tag{2}$$

where $f_i=f_i(m_{20}, m_{02})$, $g_i=g_i(m_{20}, m_{02})$ and m_{ij} is defined as the expected value of $x_1^i x_2^j$ with $x_1=x$ and $x_2=\dot{x}$. The equation difference between the left-hand side of (1) and (2) is given by

$$e'=\sum_{i=1}^{n}(a_i+\alpha_i)[H_i-(g_i\dot{x}+f_ix)]=\sum_{i=1}^{n}(a_i+\alpha_i)e_i \tag{3}$$

where e_i is defined as an error and given by

$$e_i=H_i-g_i\dot{x}-f_ix \tag{4}$$

Thus, the techniques of statistical linearization which were originally derived for nonlinear systems subjected to stochastic external excitation are now extended to include the parametric noise excited terms if the error of equation difference between (1) and (2) is defined as e_i rather than e', which is an error usually defined for nonlinear systems subjected to stochastic external excitation. By following the usual concepts of statistical linearization (Caughey, 1959; Krylov and Bogoliubov, 1943), f_i and g_i are selected such that the mean-square error of e_i will be minimized. Utilizing the following equations,

$$\frac{\partial E[e_i^2]}{\partial f_i}=0 \tag{5a}$$

$$\frac{\partial E[e_i^2]}{\partial g_i}=0 \tag{5b}$$

and substituting e_i from (4), f_i and g_i are then derived as

$$f_i=\frac{m_{02}E[x\cdot H_i(x,\dot{x})]-m_{11}E[\dot{x}\cdot H_i(x,\dot{x})]}{m_{20}m_{02}-m_{11}^2} \tag{6a}$$

$$g_i=\frac{m_{20}E[\dot{x}\cdot H_i(x,\dot{x})]-m_{11}E[x\cdot H_i(x,\dot{x})]}{m_{20}m_{02}-m_{11}^2} \tag{6b}$$

By applying Ito's differential rule to (1), $\dot{m}_{20}$ is derived as (Young and Chang, 1987a)

$$\dot{m}_{20}=2m_{11} \tag{7}$$

If stationary, (6*a*) and (6*b*) are further simplified by substituting $m_{11}=0$ to yield

$$f_i=\frac{E[x\cdot H_i(x,\dot{x})]}{m_{20}} \tag{8a}$$

$$g_i=\frac{E[\dot{x}\cdot H_i(x,\dot{x})]}{m_{02}} \tag{8b}$$

The equivalent linearization system (2) is then rewritten as

$$\ddot{x}+(\zeta_0+\zeta')\dot{x}+(\mu_0+u')x=W' \tag{9}$$

where

$$\zeta_0=\sum_{i=1}^{n}a_ig_i$$

$$\mu_0=\sum_{i=1}^{n}a_if_i$$

$$\begin{aligned}E[\zeta'(t)\zeta'(s)] &= 2S\delta(t-s)\\ &= \Big(\sum_{i=1}^{n}2q_{ii}g_i^2\Big)\delta(t-s)\\ E[\mu'(t)\mu'(s)] &= 2R\,\delta(t-s)\\ &= \Big(\sum_{i=1}^{n}2q_{ii}f_i^2\Big)\delta(t-s)\end{aligned} \tag{10}$$

The stationary output variances of x and $\dot{x}$ of (9) can be derived from the moment equations with diffusional correction term as (Young and Chang, 1987a)

$$m_{20}=m_{02}/\mu_0 \tag{11a}$$

$$=q_{n+1\,n+1}/\zeta_0\mu_0-R-2S\mu_0 \tag{11b}$$

By substituting (10) into (11*a*) and (11*b*), two simultaneous algebraic equations with unknown m_{20} and m_{02} are then derived to yield

$$m_{02}-\Big(\sum_{i=1}^{n}a_if_i\Big)m_{20}=0 \tag{12a}$$

$$\Big(\sum_{i=1}^{n}a_ig_i\Big)\Big(\sum_{i=1}^{n}a_if_i\Big)m_{20}-\Big(\sum_{i=1}^{n}q_{ii}f_i^2\Big)m_{20}$$

$$-2\Big(\sum_{i=1}^{n}q_{ii}g_i^2\Big)\Big(\sum_{i=1}^{n}a_if_i\Big)m_{20}-q_{n+1\,n+1}=0 \tag{12b}$$

Thus, m_{20} and m_{02} are readily obtained by solving (12*a*) and (12*b*) with f_i and g_i derived by using the Gaussian or non-Gaussian density function in (8*a*) and (8*b*), respectively. When the Gaussian (non-Gaussian) density function is applied to evaluate f_i and g_i from (8*a*) and (8*b*), the statistical linearization approach is called the Gaussian (non-Gaussian) linearization approach.

The non-Gaussian densities of the states of (9) under certain conditions can be derived through the Fokker-Planck-Kolmogorov (FPK) equaton. For $R=\mu_0 S$, Dimentberg (1982) has solved the stationary joint probability density of the states to (9) as

$$p(x_1, x_2)=\frac{(\beta-1)\alpha^{\beta-1}}{\pi\sqrt{\mu_0}}\,\frac{1}{(\alpha+x_2^2/\mu_0+x_1^2)^{\beta}} \tag{13}$$

where $\alpha=q_{n+1\,n+1}/R$ and $\beta=(\zeta_0/S+1)/2$, $\beta>1$. From (13), it is seen that the stationary states of x_1 and x_2 are not independent in spite of $m_{11}=0$ from (7). Thus, the highly non-Gaussian effects in the linearization of stochastic parametrically and externally excited nonlinear systems need to be considered. One approach of the non-Gaussian linearizations of stochastic parametrically and externally excited nonlinear systems as proposed is implemented by first deriving the non-Gaussian probability density from the concepts of equivalent external excitation (Young and Chang, 1987a). Then, the equivalent linear gains f_i and g_i are readily obtained by using the density function in (8*a*) and (8*b*), respectively. The applications of the non-Gaussian linearization are il-

Downloaded 03 May 2010 to 171.66.16.31. Redistribution subject to ASME license or copyright; see http://www.asme.org/terms/Terms_Use.cfm

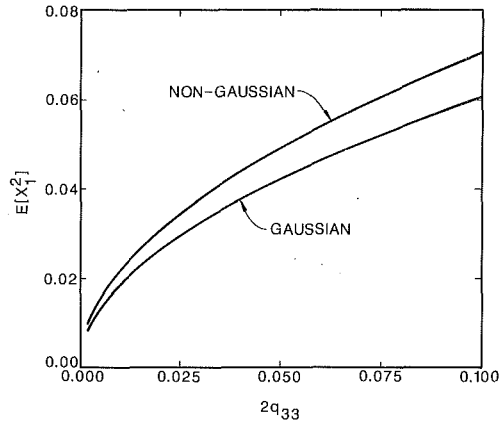


Fig. 1 The comparisons of output mean-square displacement by (21*a*) and (23*a*) using $\mu_0 = 5.0$, $\zeta_0 = 1.0$, $2q_{11} = 5.0$, $2q_{22} = 0.0$, and with varying $2q_{33}$

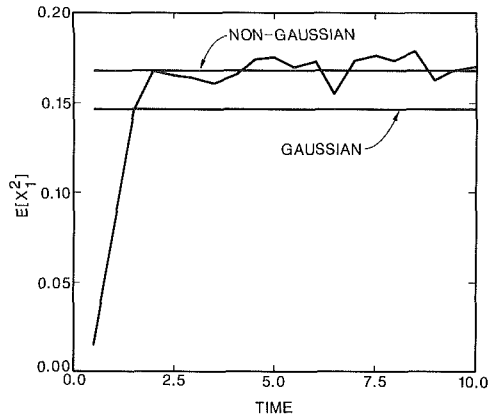


Fig. 2 The comparisons of output mean-square displacement by (21*a*), (23*a*), and 1000-run Monte Carlo simulation using $\mu_0 = 5.0$, $\zeta_0 = 1.0$, $2q_{11} = 5.0$, $2q_{22} = 0.0$, and $2q_{33} = 0.5$

lustrated by using the following Duffing-type nonlinear oscillator.

Example 1

A stochastic parametrically and externally excited stable nonlinear system is described by (Young and Chang, 1987a)

$$\ddot{x} + (\zeta_0 + \zeta')\dot{x} + (\mu_0 + \mu')x^3 = W' \tag{14}$$

where $E[\mu'(t)\mu'(s)] = 2q_{11}\,\delta(t-s)$, $E[\zeta'(t)\zeta'(s)] = 2q_{22}\,\delta(t-s)$, and $E[W'(t)W'(s)] = 2q_{33}\,\delta(t-s)$. From (2) and (6*a*), the equivalent linearization system of (14) is written as

$$\ddot{x} + (\zeta_0 + \zeta')\dot{x} + (\mu_0 + \mu')f_1 x = W' \tag{15}$$

where

$$f_1 = m_{40}/m_{20} \tag{16}$$

The applications of non-Gaussian linearization are first illustrated. By following the concepts of equivalent external excitation and using the FPK equation, $p(x_1)$ and $p(x_2)$ are derived to yield (Young and Chang, 1987a)

$$p(x_1) = \frac{2k_1^{1/4}}{\Gamma(1/4)} \exp(-k_1 x_1^4),\ k_1 = \frac{(\zeta_0 - q_{22})\mu_0}{2Q} > 0 \tag{17a}$$

$$p(x_2) = \sqrt{\frac{k_2}{\pi}} \exp(-k_2 x_2^4),\ k_2 = \frac{2k_1}{\mu_0} \tag{17b}$$

where $\Gamma(\cdot)$ is the Gamma function and $Q = 2q_{11}m_{60} + 2q_{22}m_{02} + 2q_{33}$. By employing (17*a*) to evaluate m_{20} and m_{40}, respectively, to derive

$$m_{20} = \frac{\Gamma(3/4)}{\Gamma(1/4)} \cdot \frac{1}{k_1^{1/2}} \tag{18a}$$

$$m_{40} = \frac{1}{4k_1} \tag{18b}$$

then (16) becomes

$$f_1 = \frac{\Gamma(1/4)}{4\Gamma(3/4)} \cdot \frac{1}{k_1^{1/2}} \tag{19}$$

From (18*a*) and by substituting $k_1^{1/2}$ into (19), then (19) is expressed as

$$f_1 = 2.188\, m_{20} \tag{20}$$

By using (12*a*) and (12*b*) with f_1 given by (20), one derives

$$4.787\, q_{11}m_{20}^3 + (4.376\, q_{22}\,\mu_0 - 2.188\,\mu_0\zeta_0)m_{20}^2 + q_{33} = 0 \tag{21a}$$

$$m_{02} = 2.188\,\mu_0 m_{20}^2 \tag{21b}$$

Hence, the stationary output variances of the states x_1 and x_2 are derived by solving (21*a*) and substituting m_{20} into (21*b*) to obtain m_{02}. Next, the Gaussian linearization approach is applied to derive f_1. From (16), one obtains

$$f_1 = 3.0 m_{20} \tag{22}$$

Thus, following the derivations of (21*a*) and (21*b*), the stationary output variances of x_1 and x_2 can be derived from

$$9q_{11}m_{20}^3 + (6q_{22}\mu_0 - 3\zeta_0\mu_0)m_{20}^2 + q_{33} = 0 \tag{23a}$$

$$m_{02} = 3\mu_0 m_{20}^2 \tag{23b}$$

The comparisons of (21*a*) and (23*a*) by choosing $\mu_0 = 5.0$, $\zeta_0 = 1.0$, $2q_{11} = 5.0$, and $2q_{22} = 0.0$, with varying q_{33} are shown in Fig. 1. When $2q_{33}$ equals 0.5, a 1000-run Monte Carlo simulation to (14) is given to compare the results derived by using (21*a*) and (23*a*) as shown in Fig. 2. From Figs. 1 and 2, it is seen that the Gaussian linearization approach predicts lower variance of x_1 than that by the non-Gaussian linearization approach. Also, better prediction of the stationary output variance of x_1 is obtained by utilizing the present non-Gaussian linearization approach. Although the present non-Gaussian linearization approach can be developed through the non-Gaussian density derived by using the concepts of equivalent external excitation, this approach is applied only for some practical nonlinear stochastic systems. Actually, if the Gaussian assumption is deemed appropriate *a priori* by using a quantitative measure, the simple and effective Gaussian linearization approach can be applied with high confidence in the resulting solution. As a result, a quantitative measure called the Gaussian criterion will be derived to help in determining when the application of Gaussian linearization is appropriate.

3 Gaussian Criterion (GC)

The determination of using Gaussian linearization for the accurate prediction of stationary output variance of stable nonlinear stochastic systems has not been investigated by establishing a concrete Gaussian measure. The successful applications of Gaussian linearization for stochastic externally excited "weak" nonlinear oscillators are only supported by comparing the linearization solution with the exact solution of some solvable examples, e.g., the Duffing oscillator. When stable nonlinear systems are subjected to both stochastic parametric and external excitations, the non-Gaussian effects of parametric noise have not been investigated although one may give some vague physical interpretations such as "When the noise intensity is increased, the output densities become 'less' Gaussian." Thus, a concrete mathematical criterion needs to be established for the investigation of the non-Gaussian effects of system nonlinearities and noise intensities. For a stochastic parametric and external noise excited stable

Downloaded 03 May 2010 to 171.66.16.31. Redistribution subject to ASME license or copyright; see http://www.asme.org/terms/Terms_Use.cfm

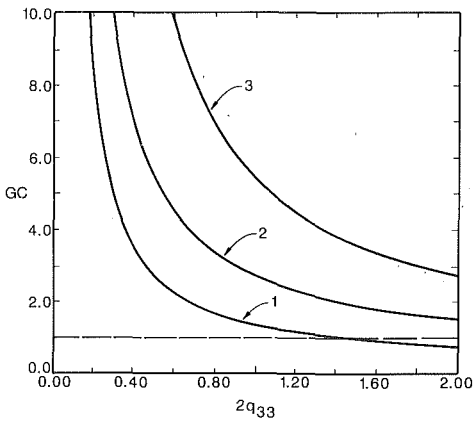


Fig. 3 The non-Gaussian effects of μ_0 and ζ_0 for the stochastic externally excited Duffing oscillator, $1-\zeta_0=0.5$, $\mu_0=1.0$, $2-\zeta_0=1.0$, $\mu_0=2.0$, $3-\zeta_0=1.0$, $\mu_0=1.0$

nonlinear system described by (1), the GC is established by the following arguments.

Let (1) be rewritten as

$$\ddot{x}+\sum_{i=1}^{n} a_i H_i(x,\dot{x})=W'-\sum_{i=1}^{n}\alpha_i H_i(x,\dot{x}) \tag{24}$$

By following the concepts of equivalent external excitation, the stochastic parametrically excited term $\alpha_i H_i(x,\dot{x})$ in (24) can be interpreted as an equivalent external noise excited term with intensity $2q_{ii}\,E[H_i^2(x,\dot{x})]$. Thus, the stationary output response of (24) will be dominated by the external noise term W' if

$$\sum_{i=1}^{n} 2q_{ii}E[H_i^2(x,\dot{x})]\ll 2q_{n+1\,n+1} \tag{25}$$

The inequality (25) provides the relationship between system parameters and noise intensities such that (24) becomes a nonlinear system excited solely by an external noise. Since it is well known that the output variance of stochastic externally excited nonlinear systems predicted by the Gaussian linearization method are accurate within ten percent error in some cases in spite of rather strong system nonlinearities (Hedrick, 1980), the non-Gaussian effects of parametric noise can be investigated by using (25) without considering the effects of system nonlinearities. If the effects of system nonlinearities are considered, the strength of system nonlinearities needs to be quantified by certain mathematical expressions. One may interpret the strength of system nonlinearities in (24) as $\sum_{i=1}^{n} a_i^2 E[H_i^2(x,\dot{x})]$, which may give an overestimate (underestimate) of the strength of system nonlinearities when a_i is large (small), then (25) is modified to

$$\sum_{i=1}^{n}(2q_{ii}+a_i^2)E[H_i^2(x,\dot{x})]\ll 2q_{n+1\,n+1} \tag{26}$$

For the convenient use of (26), the Gaussian criterion is defined as

$$\mathrm{GC}=2q_{n+1\,n+1}\Big/\sum_{i=1}^{n}(2q_{ii}+a_i^2)E[H_i^2(x,\dot{x})] \tag{27}$$

Since the higher-order moment terms are required to express $E[H_i^2(x,\dot{x})]$ in (27), certain approximate estimates need to be applied. In considering the derivation of (27), it is based on physical interpretation that the output response will be dominated by the linear part of a system equation if the intensity of both system nonlinearities and parametric noise excitations can be suppressed by that of external noise. Thus, the intensity of the nonlinear term $H_i(x,\dot{x})$ is replaced by that of the equivalent linear term $g_i\,\dot{x}+f_i\,x$ as given by

$$E[H_i^2(x,\dot{x})]=f_i^2 m_{20}+g_i^2 m_{02} \tag{28}$$

By substituting (28) into (27), the GC is finally obtained as

$$\mathrm{GC}=2q_{n+1\,n+1}\Big/\sum_{i=1}^{n}(2q_{ii}+a_i^2)(f_i^2 m_{20}+g_i^2 m_{02}) \tag{29}$$

In (29), the unknown m_{20} and m_{02} are derived by solving (12*a*) and (12*b*) and f_i and g_i are obtained by using (8*a*) and (8*b*), respectively. Hence, from (26) and (27), the Gaussian linearization approach is appropriate if

$$\mathrm{GC}\gg 1.0 \tag{30}$$

Here, 1.0 is given as the critical value of the GC (CVGC). The applications of the GC are illustrated by using the following stochastic Duffing oscillator.

Example 2

For a stochastic parametrically and externally excited stable Duffing oscillator described as

$$\ddot{x}+(\zeta_0+\zeta')\dot{x}+x+(\mu_0+\mu')x^3=W' \tag{31}$$

the GC is established from (29) and given as

$$\mathrm{GC}=2q_{33}/((2q_{11}+\mu_0^2)(f_1^2 m_{20})+2q_{22}m_{02}) \tag{32}$$

where f_1 is given by (22). By substituting (22) into (32), one obtains

$$\mathrm{GC}=2q_{33}/((2q_{11}+\mu_0^2)(9m_{20}^3)+2q_{22}m_{02}) \tag{33}$$

In considering that the non-Gaussian effects due to system parametric noises and nonlinearities are interpreted as an equivalent intensity in the sense of the second-order moments (Young and Chang, 1987a), a simple and practical Gaussian linearization approach would be appropriate in deriving the approximate unknown m_{02} and m_{20}. By using (12*a*) and (12*b*), one obtains

$$m_{02}-(3\mu_0 m_{20}+1)m_{20}=0 \tag{34a}$$

$$\zeta_0(3\mu_0 m_{20}+1)m_{20}-(q_{11}9m_{20}^2)m_{20} \tag{34b}$$
$$-2(q_{33})(3\mu_0 m_{20}+1)m_{20}-q_{33}=0$$

Thus, the GC (33) is evaluated by substituting m_{02} and m_{20} which are derived from solving (34*a*) and (34*b*).

The applications of the GC are illustrated by first plotting (33) as a function of system parameters or noise intensities. Then, the GC test is performed by using the criterion (30). The non-Gaussian effects of μ_0 and ζ_0 for the stochastic externally excited Duffing oscillator are shown in Fig. 3. It is seen that the non-Gaussian effects due to the decreasing of the damping coefficient are much stronger than the effects due to the increasing of the nonlinear-spring coefficient. In addition, the Gaussian linearization approach can be applied to a nonlinear system subjected to a rather strong external noise excitation if the nonlinear system is not lightly damped. The non-Gaussian effects of $2q_{11}$ and $2q_{22}$ for the stochastic parametrically and externally excited Duffing oscillator are shown in Fig. 4. It is seen that the non-Gaussian effects of noise intensity in the damping term are much stronger than that of the noise intensity in the spring term. Also, when a nonlinear system is subjected to both stochastic parametric and external excitations, the increasing of external noise intensity can easily drive the system response into an almost non-Gaussian region. Thus, the applications of the GC provide a good insight into the non-Gaussian sensitivity of system parameters and/or noise intensities. The CVGC which is used to help assure the accuracy of Gaussian linearization *a priori* is further investigated by using the Chi-square Gaussian goodness-of-fit test.

Downloaded 03 May 2010 to 171.66.16.31. Redistribution subject to ASME license or copyright; see http://www.asme.org/terms/Terms_Use.cfm

4 Chi-Square Gaussian Goodness-of-Fit (CSGGF) Test

The applications of the GC and its critical value for assuring accuracy of Gaussian linearization are further supported by performing the CSGGF test. Here, the CSGGF test is used as a measure of the discrepancy between the output non-Gaussian process of a nonlinear stochastic dynamic system and the Gaussian density function.

The CSGGF test for a random dynamic system subjected to Gaussian white noise excitations is first simulated and investigated by collecting 5000 weakly stationary random data from the system response of states and arranging them into 25 groups of 200 data each. The test of normality then follows an equal frequency procedure with 16 class intervals under 5 percent level of significance (Bendat and Piersol, 1971). Since the random data are collected from the stationary response of a dynamic system excited by a pseudo-random number generator, the 25 groups' Chi-square value calculated by using 200 random data each will fluctuate. Thus, it is proposed that the hypothesis of Gaussian distribution is accepted if the average Chi-square value of the 25 groups is less than 22.36 (Bendat and Piersol, 1971) and if at least one half of the number of groups have Chi-square values less than 22.36 (i.e., 13 in this case). Before the CSGGF test is performed on the stochastic Duffing oscillator, the output of a pseudo-random number generator which simulates the Gaussian white noise and the output of the states of a second-order linear system excited externally by the pseudo-random number generator are first tested as shown in Fig. 5. It is seen that the output of both pseudo-random number generator and state $\dot{x}$ satisfies the Gaussian hypothesis at 5 percent level of significance but the output of state x does not satisfy the above hypothesis test. This phenomenon contradicts the fact that the Gaussian distribution after being transformed by a linear transformation including the differential operator should still be Gaussian. This phenomenon has not been reported to the authors knowledge and can be interpreted as the effects of numerical integration of inexact Gaussian noise which amplify the discrepancy between the output process x and the Gaussian density function. Since the number of numerical integrations used to obtain the output process x from the pseudo-random number generator is one more than that used to derive the output process $\dot{x}$, the output distribution of the process x will be "less" Gaussian than that of the process $\dot{x}$. This interpretation is further supported by using a third-order linear system excited externally by the pseudo-random number generator. For the third-order system, by following the above interpretation, the selection of state $\ddot{x}$ is better than $\dot{x}$ and $\dot{x}$ is better than x in performing the CSGGF test. The above interpretations are verified by the simulated results as given in Table 1 which includes the maximum and average values of 25 groups' Chi-square value, number of Chi-square values which is greater than 22.36, and Gaussian (G) or non-Gaussian (N-G) distribution which is classified by using the above simulated Chi-square results and following the present Gaussian hypothesis test. Hence, the following CSGGF test for the second-order stochastic Duffing oscillator will be performed by using state $\dot{x}$.

Although the purpose of the establishment of GC is for assuring accurate prediction of stationary output variance when the Gaussian linearization approach is employed, the non-Gaussian sensitivity due to system parameters and noise excitations in some practical nonlinear stochastic systems can be investigated through the GC test. The non-Gaussian effects and the CVGC for the external noise excited Duffing oscillator are first investigated by using both the CSGGF and GC tests. The simulated results are given in Table 2 which is divided into three groups with each group arranged in the increasing order

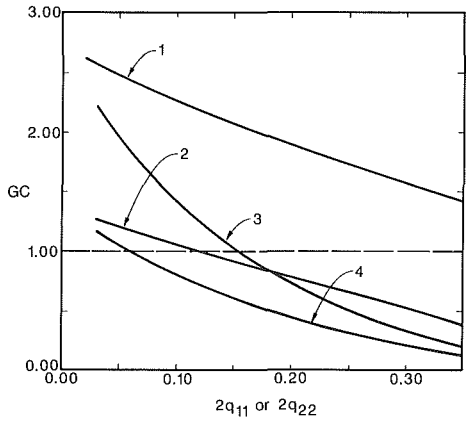


Fig. 4 The non-Gaussian effects of parametric noise $2q_{11}$ and $2q_{22}$ for the stochastic parametrically and externally excited Duffing oscillator with $\mu_0 = 1.0$ and $\zeta_0 = 0.5$, 1 – x-axis represents $2q_{11}$, $2q_{22} = 0.0$, $2q_{33} = 0.5$, 2 – x-axis represents $2q_{11}$, $2q_{22} = 0.0$, $2q_{33} = 1.0$, 3 – $2q_{11} = 0.0$, x-axis represents $2q_{22}$, $2q_{33} = 0.5$, 4 – $2q_{11} = 0.0$, x-axis represents $2q_{22}$, $2q_{33} = 1.0$

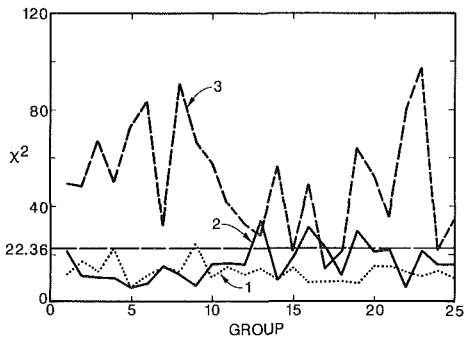


Fig. 5 The Chi-square Gaussian goodness-of-fit test for a second-order linear system subjected to externally Gaussian white noise excitation with $\mu_0 = 1.0$ and $\zeta_0 = 1.0$, 1 – Output of a pseudo-random number generator, 2 – Output process of velocity, 3 – Output process of displacement

Table 1 The CSGGF test for the second-order and third-order linear systems subjected to externally Gaussian white noise excitation

Systems	Distribution of χ^2	Maximum value of χ^2	Average value of χ^2	No. of χ^2 values >22.36	Gaussian or Non-Gaussian
Second-order linear system	x	97.66	50.65	21	N-G
	$\dot{x}$	34.81	17.14	5	G
Third-order linear system	x	138.74	67.65	24	N-G
	$\dot{x}$	107.01	51.98	25	N-G
	$\ddot{x}$	38.71	20.03	9	G

Downloaded 03 May 2010 to 171.66.16.31. Redistribution subject to ASME license or copyright; see http://www.asme.org/terms/Terms_Use.cfm

Table 2 The CSGGF and GC tests for the stochastic externally excited Duffing oscillator

Group Case		μ_0	ζ_0	$2q_{33}$	GC	Max. value of χ^2	Avg. value of χ^2	No. of χ^2 values >22.36	Gaussian or Non-Gaussian
	1	100	0.5	1.0	0.06	48.32	18.60	5	G
	2	50	0.5	1.0	0.09	61.48	22.22	9	G
1	3	10	0.5	1.0	0.24	43.00	19.74	8	G
	4	1	0.5	1.0	1.36	52.51	21.27	12	G
	5	0.1	0.5	1.0	21.27	43.58	20.75	8	G
	1	1.0	0.5	100	0.06	48.32	18.60	5	G
	2	1.0	0.5	50	0.09	61.48	22.22	9	G
2	3	1.0	0.5	10	0.24	43.00	19.74	8	G
	4	1.0	0.5	1.0	1.36	52.50	21.27	12	G
	5	1.0	0.5	0.1	21.27	43.58	20.75	8	G
	1	0.5	0.1	10.0	0.03	148	40.50	16	N-G
	2	0.5	0.1	2.0	0.08	117	41.78	19	N-G
3	3	1.0	0.2	2.0	0.15	89.5	27.54	12	N-G
	4	0.2	0.2	1.0	1.08	59.8	30.94	15	N-G
	5	0.2	0.2	0.2	8.51	40.4	27.49	18	N-G

Table 3 The CSGGF and GC tests for the stochastic parametrically and externally excited Duffing oscillator

Case	μ_0	ζ_0	$2q_{11}$	$2q_{22}$	$2q_{33}$	GC	Max. value of χ^2	Avg. value of χ^2	No. of χ^2 values >22.36	Gaussian or Non-Gaussian
1	1.	.5	0.00	0.35	1.0	0.14	59.4	25.0	13	N-G
2	1.	.5	0.00	0.24	1.0	0.34	81.0	25.3	12	N-G
3	1.	.5	0.00	0.25	0.5	0.51	108.3	24.9	10	N-G
4	1.	.5	0.00	0.15	1.0	0.60	62.0	24.2	14	N-G
5	1.	.5	0.20	0.00	1.0	0.78	42.4	22.2	11	G
6	1.	.5	0.00	0.05	1.0	1.05	39.7	21.6	8	G
7	1.	.5	0.00	0.00	1.0	1.36	52.5	21.3	12	G
8	1.	.5	0.34	0.00	0.5	1.46	38.5	20.7	10	G
9	1.	.5	0.00	0.09	0.5	1.50	56.5	21.9	8	G
10	1.	.5	0.00	0.00	0.5	2.70	45.7	21.8	12	G

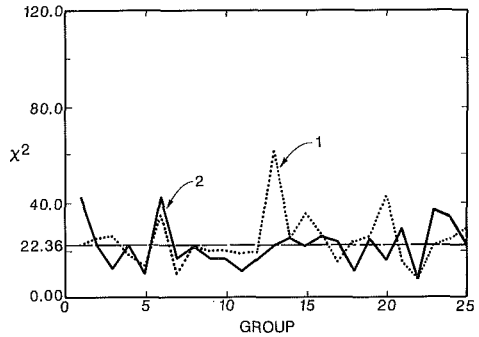


Fig. 6 The Chi-square Gaussian goodness-of-fit test for the stochastic parametrically and externally excited Duffing oscillator with $\mu_0 = 1.0$ and $\zeta_0 = 0.5$, 1 – $2q_{11} = 0.0$, $2q_{22} = 0.15$, $2q_{33} = 1.0$ (GC = 0.60), 2 – $2q_{11} = 0.2$, $2q_{22} = 0.0$, $2q_{33} = 1.0$ (GC = 0.78)

of GC. The first group is simulated with $\zeta_0 = 0.5$, $2q_{33} = 1.0$, and with varying μ_0. It is seen that the output response of the moderately damped Duffing oscillator can be considered as a Gaussian distribution from the CSGGF test even if the strength of nonlinearity varies over a wide range. The decreasing of μ_0 from 100 to 0.1 results in a nonlinear system with "weak" strength of system nonlinearity. This fact is reflected in the increasing of GC from 0.06 to 21.27 but not in the decreasing of the Chi-square value. Thus, it implies that the CSGGF test cannot be used for sensitivity studies of the non-Gaussian effects of system parameters; however, it can be studied by using the GC test as shown in Fig. 3. For the selection of CVGC, the value of 1.0 gives a conservative Gaussian boundary in classification because even though GC is equal to 0.06, the CSGGF test still confirms the acceptance of Gaussian hypothesis. This phenomenon is due to the fact that $9\mu_0^2 m_{20}^3$ gives an overestimate of the strength of system nonlinearity. However, in considering the applications of the Gaussian linearization approach, when the GC is greater than 1.0, it implies that the strength of system nonlinearity is weak. Hence, the accurate prediction of output variance by employing the linearization approach is guaranteed if the GC is greater than 1.0. The non-Gaussian effects of $2q_{33}$ are simulated and given in the second group. It is interesting to note that the increasing of $2q_{33}$ plays the same role as that of μ_0 to drive the output response of the nonlinear stochastic system into a "less" Gaussian region. The simulated results show that the Chi-square characteristics are exactly the same if one interchanges the values of μ_0 and ζ_0 between the first and second groups for each Chi-square test. The simulated results of an underdamped stochastic Duffing oscillator are given in the third group. From cases 1 to 3 in this group, it is seen that if the GC is less than one, the hypothesis of Gaussian distribution is rejected. From cases 4 and 5, it is seen that although the GC is greater than one, the hypothesis of Gaussian distribution is still rejected. This phenomenon is owing to the fact that $9\mu_0^2 m_{20}^3$ not gives an underestimate of the strength of system nonlinearity. Thus, by applying the GC test to determine whether the Gaussian linearization can be used to predict accurate output variance, it is applicable to a nonlinear system when its coefficients of system nonlinearities are greater than one. When the coefficients of system nonlinearities are less than one, the accurate output variance can be predicted by using the Gaussian linearization approach if the system is not lightly damped as seen from the Gaussian and non-Gaussian response of the moderately damped oscillator in Group 1, case 5 and the lightly damped oscillator in Group 3, case 4, respec-

Downloaded 03 May 2010 to 171.66.16.31. Redistribution subject to ASME license or copyright; see http://www.asme.org/terms/Terms_Use.cfm

tively. Next, the non-Gaussian effects and the CVGC for the stochastic parametrically and externally excited Duffing oscillator are investigated. The simulated results are given in Table 3 with cases 4 and 5 also shown in Fig. 6. It is seen that the combined effects of both parametric and external noise excitations will easily drive the system response into a non-Gaussian region. Also, the non-Gaussian effects of damping noise is stronger than that of spring noise as shown in Fig. 4. Here, in applying the GC test, the CVGC is defined as 1.0 which is also acceptable to help in determining whether Gaussian linearization can predict accurate output variance.

5 Conclusions

The methods and criterion of Gaussian linearization of nonlinear stochastic parametrically and externally excited nonlinear oscillators have been developed in this paper. The simulated results show that the applications of Gaussian linearization for the nonlinear oscillator provide an underestimate of output variance. By using a non-Gaussian linearization approach, the accurate prediction of stationary output variance can be obtained; however, it is applicable to certain classes of practical nonlinear stochastic systems. Thus, by the extension of the concepts of equivalent external excitation, the Gaussian criterion is established to determine when the accurate prediction of stationary output variance can be obtained by employing the Gaussian linearization techniques. The applications of the present GC test are illustrated by using a stochastic parametrically and externally excited stable Duffing oscillator. First, it provides the understanding of the strong non-Gaussian effects of the system damping coefficient and of combined system damping and external noise. Then, in the determination of using Gaussian linearization for the accurate prediction of output variance, the present GC test is simply performed by testing whether the GC is greater than the CVGC. The simulated results, by using the GC test and CSGGF test which is performed at 5 percent level of significance for the state $\dot{x}$, show that the CVGC can be defined as 1.0 when the coefficients of system nonlinearities are greater than one. With better understanding of the non-Gaussian effects in employing the Gaussian linearization approach *a priori*, the accurate prediction of the stationary output variances can be assured by this simple and practical technique.

References

Bendat, J. S., and Piersol, A. G., 1971, *Random Data: Analysis and Measurement Procedures*, John Wiley, New York, pp. 119–122.

Booton, R. C., 1954, "The analysis of nonlinear control systems with random inputs, Circuit Theory," *IRE Trans.*, Vol. 1, pp. 32–34.

Caughey, T. K., 1959, "Response of nonlinear string to random loading," ASME JOURNAL OF APPLIED MECHANICS, Vol. 26, pp. 341–344.

Crandall, S. H., 1980, *On statistical linearization for nonlinear oscillators, Nonlinear System Analysis and Synthesis: Vol. 2*, ASME, New York, pp. 199–209.

Dimentberg, M. F., 1982, "An exact solution to a certain non-linear random vibration problem," *Int. J. Non-Linear Mechanics*, Vol. 17, pp. 231–236.

Gelb, A., and Vander Velde, W. E., 1968, *Multiple-input Describing Functions and Nonlinear System Design*, McGraw-Hill, New York.

Gelb, A., 1974, *Applied Optimal Estimation*, MIT Press, MA., pp. 220–222.

Hedrick, J. K., 1980, *Nonlinear System Response: Quasi-linearization Methods, Nonlinear System Analysis and Synthesis: Vol. 1*, ASME, New York, pp. 97–124.

Krylov, N., and Bogoliubov, N., 1943, *Introduction to Nonlinear Mechanics*, Princeton University Press, Princeton, N.J.

Young, G. E., and Chang, R. J., 1987a, "Prediction of the response of nonlinear oscillators under stochastic parametric and external excitations," *Int. J. Non-Linear Mechanics*, Vol. 22, pp. 151–160.

Young, G. E., and Chang, R. J., 1987b, "Optimal Control of Stochastic Parametrically and Externally Excited Nonlinear Control Systems," *Journal of Dynamic Systems, Measurement, and Control*, Vol. 110, No. 2, pp. 114–119.

Downloaded 03 May 2010 to 171.66.16.31. Redistribution subject to ASME license or copyright; see http://www.asme.org/terms/Terms_Use.cfm

Statistical Identification of Nonlinear Random Vibration Systems

Tohru Ozaki
The Institute of Statistical Mathematics,
4-6-7 Minami Azabu,
Minato-Ku Tokyo, Japan 106

A statistical method for the identification of nonlinear random vibration systems is presented. The first step in the identification process is to obtain a discrete time version of a random vibration model using a local linearization approach. It is shown that the discrete time version thus obtained may be utilized in the identification of original random vibration model. The method is applied to some real ship engineering data.

1 Introduction

Recently it was pointed out (Ozaki, 1985) that continuous-time stochastic dynamical system models and amplitude-dependent nonlinear time series models are closely related by a time discretization scheme for deterministic dynamical systems, called local linearization. The idea of local linearization was extended to the multivariate situation and was applied to the modeling of nonlinear random vibration systems described by a second-order nonlinear stochastic differential equation (Ozaki, 1986).

The purpose of the present paper is to present a statistical identification method of these nonlinear random vibration system models based on the maximum likelihood method for discrete time models. The application of the method to simulated data is shown. Statistical analysis of ship dynamics data is also discussed with numerical results obtained by applying the present method.

2 Locally Linearized Model

We consider how to obtain a discrete time version of a continuous time stochastic nonlinear differential equation model for the nonlinear random vibration system,

$$\ddot{x}+g_1\ (x|\ \mathbf{a})\dot{x}+g_2(x|\ \mathbf{b})x=n(t) \tag{1}$$

where $n(t)$ is a continuous-time Gaussian white noise defined by Caughey (1971)

$$E[n(t)]=0,$$
$$E[n(t)n(s)]=\sigma^2\delta(t-s).$$

$E[\ ]$ means the expectation and $\delta(t)$ is the Dirac delta function. The model (1) is expressed by the following continuous time bivariate stochastic dynamical system model,

$$\dot{\mathbf{z}}=\mathbf{f}(\mathbf{z}|\ \mathbf{a},\ \mathbf{b})+\mathbf{n}(t) \tag{2}$$

where

$$\dot{\mathbf{z}}=(\dot{x},\ x)',$$
$$\mathbf{f}(\mathbf{z}|\ \mathbf{a},\ \mathbf{b})=(-g_1(x|\ \mathbf{a})\ \dot{x},\ -g_2(x|\ \mathbf{b}))\ x'$$

and

$$\mathbf{n}(t)=(n(t),0)'.$$

Here the notation $(A)'$ indicates the transpose of a vector or a matrix A. It is shown in Ozaki (1986) that when we assume that the dynamical system is locally linear, i.e., the Jacobian matrix

$$\left[\frac{\partial\mathbf{f}\ (\mathbf{z}|\ \mathbf{a},\ \mathbf{b})}{\partial\mathbf{z}}\right]_{\mathbf{z}=\mathbf{z}_t}=\mathbf{J}_t$$

is constant on each short interval $(t,\ t+\Delta t)$, we have, from **(2)**, the following discrete time model,

$$\mathbf{z}_{t+\Delta t}=\mathrm{Exp}\ (K_t\Delta t)\mathbf{z}_t+\mathbf{w}_{t+\Delta t} \tag{3}$$

where

$$\mathbf{w}_{t+\Delta t}=\int_t^{t+\Delta t}\mathrm{Exp}\ \{K_t(t+\Delta t-u)\}\mathbf{n}(u)du,$$

$$K_t=\frac{1}{\Delta t}\ \mathrm{Log}\ A_t,$$

$$A_t=I+J_t^{-1}\ \{\mathrm{Exp}\ (J_t\Delta t)-I\}F_t.$$

I is a unit matrix and F_t is a matrix satisfying $F_t\ \mathbf{z}=\mathbf{f}(\mathbf{z}_t|\ \mathbf{a},\ \mathbf{b})$ Exp $(K_t\Delta t)$ and Log A_t are matrices defined, respectively, by

$$\mathrm{Exp}(K_t\Delta t)=1+\sum_{i=1}^{\infty}\frac{(K_t\Delta t)^i}{i!},$$

$$\mathrm{Log}\ A_t=\sum_{i=1}^{\infty}\frac{(-1)^i}{i!}\ (A_t-I)^i.$$

The variance-covariance matrix Σ_d of the discrete time white noise $\omega_{t+\Delta t}$ is given by

$$\Sigma_d=\sigma^2\ \Sigma_t,$$

Contributed by the Applied Mechanics Division of THE AMERICAN SOCIETY OF MECHANICAL ENGINEERS for publication in the JOURNAL OF APPLIED MECHANICS.

Discussion on this paper should be addressed to the Editorial Department, ASME, United Engineering Center, 345 East 47th Street, New York, N.Y. 10017, and will be accepted until two months after final publication of the paper itself in the JOURNAL OF APPLIED MECHANICS. Manuscript received by ASME Applied Mechanics Division, July 21, 1986; final revision, March 15, 1988.

Copyright © 1989 by ASME

Downloaded 03 May 2010 to 171.66.16.31. Redistribution subject to ASME license or copyright; see http://www.asme.org/terms/Terms_Use.cfm

where the elements $\sigma_{i,j}$ of Σ_t are functions of $\mathbf{z}_t$ and are given by

$$\sigma_{1,1}=\frac{1}{(\mu_1-\mu_2)^2}\left\{\frac{\mu_1}{2}E_1-\frac{2\mu_1\mu_2}{\mu_1+\mu_2}E_{1,2}+\frac{\mu_2}{2}E_2\right\}$$

$$\sigma_{2,2}=\frac{1}{(\mu_1-\mu_2)^2}\left\{\frac{1}{2\mu_1}E_1-\frac{2}{\mu_1+\mu_2}E_{1,2}+\frac{1}{2\mu_2}E_2\right\},$$

$$\sigma_{1,2}=\frac{1}{(\mu_1+\mu_2)^2}\left\{\frac{1}{2}E_1-E_{1,2}+\frac{1}{2}E_2\right\},$$

$\sigma_{2,1}=\sigma_{1,2}$,

$E_1=-\exp(2\mu_1\Delta t)-1$,

$E_2=\exp(2\mu_2\Delta t)-1$,

$E_{1,2}=\exp\{(\mu_1+\mu_2)\Delta t\}-1$,

μ_1 and μ_2 are eigenvalues of K_t and are also functions of $\mathbf{z}_t$. We note that, although the variance-covariance matrix Σ_c of the continuous-time white noise $\mathbf{n}(t)=(n(t),0)'$ has rank one, the variance-covariance matrix Σ_d of the discrete time white noise $\mathbf{w}_{t+\Delta t}$ has full rank 2 as a result of integration over $[t, t+\Delta t)$. Σ_t is decomposed as follows,

$$\Sigma_t=U_t\begin{bmatrix}\lambda_1 & 0\\ 0 & \lambda_2\end{bmatrix}U_t' \tag{4}$$

using a unitary matrix U_t whose elements $u_{1,1}$, $u_{1,2}$, $u_{2,1}$, and $u_{2,2}$ are obtained by

$$u_{1,1}=\frac{\sigma_{1,2}}{\sqrt{\sigma_{1,2}^2+(\lambda_1-\sigma_{1,1})^2}},$$

$$u_{2,2}=\frac{\sigma_{1,2}}{\sqrt{\sigma_{1,2}^2+(\lambda_2-\sigma_{2,2})^2}},$$

$$u_{1,2}=\frac{(\lambda_1-\sigma_{1,1})}{\sqrt{\sigma_{1,2}^2+(\lambda_1-\sigma_{1,1})^2}}$$

$u_{2,1}=-u_{1,2}$.

Eigenvalues, λ_1 and λ_2, of Σ_t are also functions of $\mathbf{z}_t$ and are given as the roots of the polynomial,

$$\lambda^2-(\sigma_{1,1}+\sigma_{2,2})\lambda+\sigma_{1,1}\sigma_{2,2}-\sigma_{1,2}^2=0.$$

From (3) and (4), we have the following nonlinear Markovian state space representation,

$$\begin{aligned}\mathbf{z}_{t+\Delta t}&=A_t\mathbf{z}_t+B_t\mathbf{n}_{t+\Delta t},\\ x_t&=C\mathbf{z}_t\end{aligned} \tag{5}$$

where

$$A_t=\mathrm{Exp}(K_t\Delta t),$$

$$B_t=U_t\begin{bmatrix}\sqrt{\lambda_1} & 0\\ 0 & \sqrt{\lambda_2}\end{bmatrix},$$

$$C=(0,1),$$

and $\mathbf{n}_t$ is a discrete time bivariate white noise of variance-covariance matrix $\sigma^2 I$. When the vibration system is linear, A_t is constant and the model (5) has an ARMA time series model representation (Akaike, 1974a). When the vibration system is nonlinear, A_t and B_t are functions of $\mathbf{z}_t$ and we can calculate them using the above relations. For example, for the following hard spring-type nonlinear vibration system,

$$\ddot{x}+0.25\dot{x}+14.8x+4x^3=n(t), \tag{6}$$

we have $A(\mathbf{z}_t)$ and $B(\mathbf{z}_t)$ whose eigenvalues, μ, $\bar{\mu}$, λ_1 and λ_2, are functions of x_t. The figures of functions, arg $(\mu(x_t))$, $|\mu(x_t)|$, $\lambda_1(x_t)$ and $\lambda_2(x_t)$ are shown in Fig. 1. From the figures we can see that $|\mu|$, λ_1 and λ_2 look almost constant for

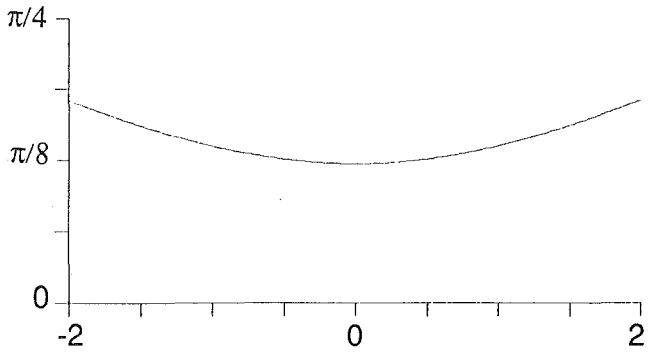


Fig. 1(*a*) Argument of the eigenvalues μ and $\bar{\mu}$ of $A(\mathbf{z}_t)$ for (9)

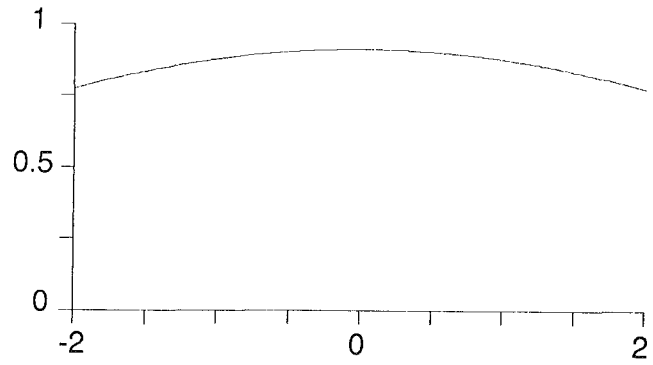


Fig. 1(*b*) Absolute value of eigenvalues μ and $\bar{\mu}$ of $A(\mathbf{z}_t)$ for (9)

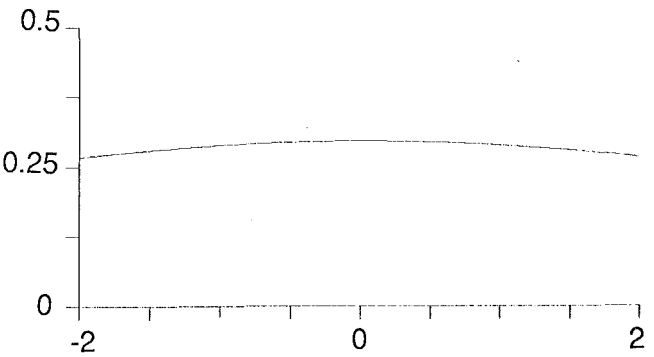


Fig. 1(*c*) An eigenvalue of $B(\mathbf{z}_t)$ for (9)

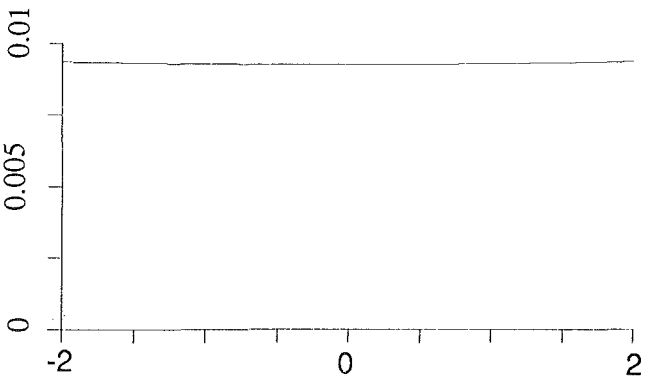


Fig. 1(*d*) An eigenvalue of $B(\mathbf{z}_t)$ for (9)

Downloaded 03 May 2010 to 171.66.16.31. Redistribution subject to ASME license or copyright; see http://www.asme.org/terms/Terms_Use.cfm

$|x_t| < 2$, while arg (μ) does not. It becomes larger when $|x_t|$ increases, i.e., the instantaneous characteristic frequency becomes higher for large $|x_t|$. This phenomenon is called hard spring-type amplitude-dependent frequency shift, which is one of the typical nonlinear phenomena observed in Duffing type vibration system (6).

3 Estimation and Identification

To identify a stochastic dynamical system model (2) for the random vibration system (1), we first try to estimate the following discrete time model,

$$\mathbf{z}_{t+1} = A(\mathbf{z}_t \mid \mathbf{a}, \mathbf{b})\,\mathbf{z}_t + B(\mathbf{z}_t \mid \mathbf{a}, \mathbf{b})\mathbf{n}_{t+1} \tag{7}$$

$$A(\mathbf{z}_t \mid \mathbf{a},\mathbf{b}) = e^{K(\mathbf{z}_t \mid \mathbf{a},\mathbf{b})\Delta t},$$

$$B(\mathbf{z}_t \mid \mathbf{a},\mathbf{b}) = U_t \begin{bmatrix} \sqrt{\lambda_1} & 0 \\ 0 & \sqrt{\lambda_2} \end{bmatrix},$$

$$K(\mathbf{z}_t \mid \mathbf{a},\mathbf{b}) = \frac{1}{\Delta t} \operatorname{Log}\,[1 + J(\mathbf{z}_t \mid \mathbf{a},\mathbf{b})^{-1}\,\{e^{J(\mathbf{z}_t \mid \mathbf{a},\mathbf{b})\Delta t} - I\}F(\mathbf{z}_t\,\mathbf{a},\mathbf{b})],$$

$$J(\mathbf{z}_t \mid \mathbf{a},\mathbf{b}) = \left[\frac{\partial f(\mathbf{z} \mid \mathbf{a},\mathbf{b})}{\partial \mathbf{z}}\right]_{\mathbf{z}=\mathbf{z}_t},$$

from the data $\mathbf{z}_1, \mathbf{z}_2, \ldots, \mathbf{z}_N$ where $\mathbf{z}_t = (\dot{x}_t, x_t)'$ and $\mathbf{n}_{t+1}$ is a bivariate Gaussian white noise with variance-covariance matrix $\sigma^2 I$. $F(\mathbf{z}_t \mid \mathbf{a}, \mathbf{b})$ is a matrix which satisfies

$$F(\mathbf{z}_t \mid \mathbf{a}, \mathbf{b})\mathbf{z}_t = \mathbf{f}(\mathbf{z}_t \mid \mathbf{a}, \mathbf{b}).$$

U_t, λ_1, and λ_2 and functions of the eigenvalues of $K_t(\mathbf{z}_t \mid \mathbf{a}, \mathbf{b})$ and are given by (4) and (5). The data are supposed to be sampled at equally-spaced time points, $t, t+\Delta t, t+2\Delta t, \ldots$ from a continuous time bivariate process $\mathbf{z}(t) = (\dot{x}(t), x(t))'$, generated from the model (2). Then, using the estimated discrete time model, we try to identify the original continuous time model (2). The log likelihood of the model (7) is given as follows.

$$\begin{aligned}
&\log p(\mathbf{z}_1, \mathbf{z}_2, \ldots, \mathbf{z}_N \mid \mathbf{a},\mathbf{b},\sigma^2) \\
&= \log p(\mathbf{z}_2, \mathbf{z}_3, \ldots, \mathbf{z}_N \mid \mathbf{z}_1, \mathbf{a}, \mathbf{b}, \sigma^2) + \log p(\mathbf{z}_1 \mid \mathbf{a},\mathbf{b}, \sigma^2) \\
&= \log p(\mathbf{n}_2,\mathbf{n}_3, \ldots, \mathbf{n}_N \mid z_1, \mathbf{a}, \mathbf{b}, \sigma^2) + \log J(\mathbf{z},\mathbf{n}) \\
&\qquad + \log p(\mathbf{z}_1 \mid \mathbf{a}, \mathbf{b}, \sigma^2) \\
&= -\sum_{t=2}^{N} \frac{\|B(\mathbf{z}_t \mid \mathbf{a},\mathbf{b})^{-1}\{\mathbf{z}_{t+1} - A(\mathbf{z}_t \mid \mathbf{a},\mathbf{b})\mathbf{z}_t\}\|^2}{2\sigma^2} \\
&\qquad - \frac{N-1}{2} \log |\sigma^2 I| \\
&- \frac{N-1}{2} \log 2\pi - \sum_{t=2}^{N} \log \det |B(\mathbf{z}_t \mid \mathbf{a}, \mathbf{b})| \\
&\qquad + \log p(\mathbf{z}_1 \mid \mathbf{a}, \mathbf{b}, \sigma^2),
\end{aligned}$$

where $J(\mathbf{z},\mathbf{n})$ is the Jacobian of the transformation from $(\mathbf{z}_2, \mathbf{z}_3, \ldots, \mathbf{z}_N)$ to $(\mathbf{n}_2, \ldots, \mathbf{n}_N)$. $\|\bullet\|$ means the Euclidian norm. For large N, the last term is negligibly small compared with the rest and can be ignored. Since the maximum likelihood estimate $\hat{\sigma}^2_N$ satisfies

$$\left[\frac{\partial \log p(\mathbf{z}_1, \mathbf{z}_2, \ldots, \mathbf{z}_N \mid \mathbf{a}, \mathbf{b}, \sigma^2)}{\partial \sigma^2}\right]_{\sigma^2 = \hat{\sigma}^2_N} = 0,$$

we have

$$\hat{\sigma}^2_N = \operatorname*{Min}_{\mathbf{a},\mathbf{b}}\ \sigma^2(\mathbf{a},\mathbf{b} \mid \mathbf{z})$$

where

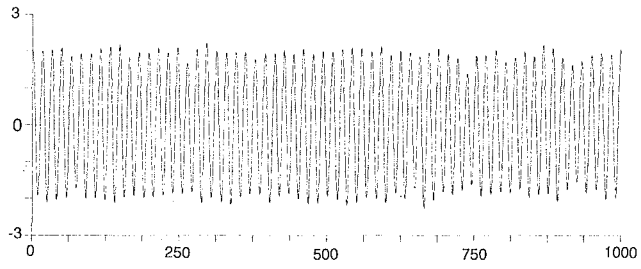


Fig. 2(a) Simulated data of the model (8)

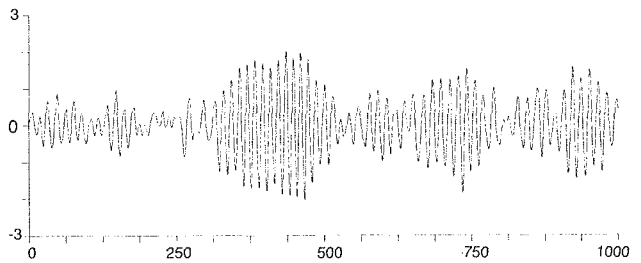


Fig. 2(b) Simulated data of the model (9)

$$\sigma^2(\mathbf{a},\mathbf{b} \mid \mathbf{z}) = \frac{1}{2(N-1)} \sum_{t=2}^{N} \|B(\mathbf{z}_t \mid \mathbf{a}, \mathbf{b})^{-1}\{\mathbf{z}_{t+1} - A(\mathbf{z}_t \mid \mathbf{a}, \mathbf{b})\mathbf{z}_t\}\|^2.$$

To minimize $\sigma^2(\mathbf{a}, \mathbf{b} \mid \mathbf{z})$ with respect to $\mathbf{a}$ and $\mathbf{b}$, some nonlinear numerical optimization procedure is needed (see, Fletcher and Powell, 1963.

The maximum likelihood estimates, $\hat{\sigma}_{N,\Delta t} = (\hat{\mathbf{a}}, \hat{\mathbf{b}}, \hat{\sigma}^2_N)$, thus obtained are known to be consistent and asymptotically normal under some regularity conditions (Billingsley, 1961). However, this is under the assumption that the data is generated from the discrete-time Markov chain model (7) with true parameters $\theta_0 = (\mathbf{a}, \mathbf{b}, \sigma^2)'$. In the present case, since the data is generated from the continuous time model (1), the maximum likelihood estimate tends not to $\theta_{d,\Delta t}(=\theta_0)$ for $N \to \infty$ but to some value $\theta_{c,\Delta t}$ which is characterized by the property

$$E_c[\log p(\mathbf{z},\theta) - \log p(\mathbf{z},\theta_{c,\Delta t})] < 0$$

for any $\theta \neq \theta_{c,\Delta t}$ (Huber, 1967). Here, E_c means the expectation with respect to the probability measure defined by the continuous-time ergodic process (8), and $p(\mathbf{z}, \theta)$ is a likelihood function of θ for the given data $\mathbf{z}$. For the nonlinear case, $\theta_{c,\Delta t}$ is not necessarily equal to $\theta_{d,\Delta t}$. However, the difference between them tends to zero, i.e., $|\theta_{c,\Delta t} - \theta_{d,\Delta t}| \to 0$, for $\Delta t \to 0$. This is because, as is seen from the definition of the locally linearized model, the ergodic process defined by (7) converges, for $\Delta t \to 0$, to the ergodic process defined by (2) (Gikhman and Skorohod (1965), Chap 9). Therefore, the above procedure is consistent in the sense that $\hat{\theta}_{N,\Delta t}$ converges to θ_0 for $\Delta t \to 0$ and $N\Delta t \to \infty$.

To check if the maximum likelihood method actually works numerically, we performed some numerical experiments. We simulated two data sets: one from a locally linearized model, obtained from

$$\ddot{x} + g_1(x)\dot{x} + 14.8x = n(t) \tag{8}$$

$$g_1(x) = x^2 - 1$$

$$\sigma^2 = 1.0$$

and another from a locally linearized model obtained from

Downloaded 03 May 2010 to 171.66.16.31. Redistribution subject to ASME license or copyright; see http://www.asme.org/terms/Terms_Use.cfm

$$\ddot{x}+0.25\dot{x}+g_2(x)x=n(t) \tag{9}$$

with

$$g_2(x)=14.8+4x^2$$
$$\sigma^2=4.0$$

where Δt is taken to be 0.1. The first example (8) is a van der Pol-type random vibration system which is known to produce limit cycles when the random input is suppressed. When the random input is present, it produces perturbed limit cycles, as in Fig. 2, whose phase and amplitude are random variables. The vibration of the second example (9) is a hard spring-type vibration system whose restoring force becomes stronger than for the linear case when $|x|$ becomes larger.

The two sets of generated output data ($N=1000$), one from model (8) and another from model (9), are shown in Fig. 2. For the first example, we fit the model (7) with $g_1(x\,|\,\mathbf{a})=a_1+a_2x+a_3x^2$ and $g_2(x\,|\,b)=b$. The estimates obtained are $\hat{a}_1=-0.9742$, $\hat{a}_2=-0.1120\times10^{-1}$, $\hat{a}_3=0.9878$, $\hat{b}=14.8520$ and $\hat{\sigma}^2=1.0141$. The estimated function $g_1(x\,|\,\hat{a})$ is quite close to the original function used in the simulation. For the data from the second example, we fit the model (7) with

$$g_1(x\,|\,a)=a$$

and

$$g_2(x\,|\,\mathbf{b})=b_1+b_2x+b_3x^2.$$

The maximum likelihood estimates obtained for this model are $\hat{a}=0.1589$, $\hat{b}_1=14.9385$, $\hat{b}_2=0.3551$, $\hat{b}_3=3.7954$ and $\hat{\sigma}^2=4.0270$.

Another possible method of identifying $g_2(x)$ is, instead of giving a continuous-time parametric model (2), to give a discrete time model parameterization, thus

$$\mathbf{z}_{t+\Delta t}=A_{\Delta t}(\mathbf{z}_t\,|\,\varphi)\mathbf{z}_t+B_{\Delta t}(\mathbf{z}_t\,|\,\varphi)\mathbf{n}_{t+\Delta t} \tag{10}$$

where $A_{\Delta t}(z_t\,|\,\varphi)$ is some matrix function, with parameter vector $\varphi=(\varphi_1,\varphi_2,\ldots,\varphi_k')$. This type of direct modelling in discrete time is useful when the analysts have no idea of the functional form of $\mathbf{f}(\mathbf{z}_t\,|\,\mathbf{a},\mathbf{b})$. $B_{\Delta t}(\mathbf{z}_t\,|\,\varphi)$ is determined from $A_{\Delta t}\,|\,\varphi)$ as follows,

$$B_{\Delta t}(\mathbf{z}_t\,|\,\varphi)=U(\mathbf{z}_t\,|\,\varphi)\begin{bmatrix}\sqrt{\lambda_1(\mathbf{z}_t\,|\,\varphi)} & 0\\ 0 & \sqrt{\lambda_2(\mathbf{z}_t\,|\,\varphi)}\end{bmatrix}.$$

$U(\mathbf{z}_t\,|\,\varphi)$ and $\lambda_1(\mathbf{z}_t\,|\,\varphi)$ and $\lambda_2(\mathbf{z}_t\,|\,\varphi)$ are functions of $\sigma_{i,j}(\mathbf{z}_t\,|\,\varphi)$ which, in turn, are functions of the eigenvalues $\mu_1(\mathbf{z}_t\,|\,\varphi)$ and $\mu_2(\mathbf{z}_t\,|\,\varphi)$ of the matrix $\mathrm{Log}\,A_{\Delta t}(\mathbf{z}_t\,|\,\varphi)$ as in Section 2. We note $\mathrm{Log}\,A_{\Delta t}(\mathbf{z}_t\,|\,\varphi)$ is well defined when $\|A_{\Delta t}(\mathbf{z}_t\,|\,\varphi)-I\|$ is sufficiently small, which always occurs when the data is sampled from the original continuous-time process with a sufficiently small sampling interval. One example of such a parameterization is

$$A_{\Delta t}^{(i,j)}(\mathbf{z}_t\,|\,\varphi)=\varphi_1^{(i,j)}+\{\varphi_2^{(i,j)}+\varphi_3^{(i,j)}x_t+\ldots+\varphi_k^{(i,j)}x_t^{k-2}\}e^{-rx_t^2}. \tag{11}$$

and another example is

$$A_{\Delta t}^{(i,j)}(\mathbf{z}_t\,|\,\varphi)=\begin{cases}\varphi_1^{(i,j)}+\varphi_2^{(i,j)}x_t+\ldots+\varphi_k^{(i,j)}x_t^{k-1} & \text{for } |x_t|<T\\ \varphi_1^{(i,j)}+\varphi_2^{(i,j)}T+\ldots+\varphi_k^{(i,j)}T^{k-1} & \text{for } |x_t|\geq T\end{cases} \tag{12}$$

where $A^{(i,j)}(\mathbf{z}_t\,|\,\varphi)$ is (i,j)th element of $A_{\Delta t}(\mathbf{z}_t\,|\,\varphi)$. We call the model (10) with (11) or (12), an *amplitude-dependent time series model*. This type of parameterization is a bivariate generalization of the parameterization introduced in nonlinear time series analysis by Ozaki (1981) and Haggan and Ozaki (1981).

We can obtain, from $A_{\Delta t}(\mathbf{z}\,|\,\varphi)$ of the model (10), a function vector $\mathbf{f}_{\Delta t}(\mathbf{z}\,|\,\varphi)$ whose local linearization is equal to $A_{\Delta t}(\mathbf{z}\,|\,\varphi)$, i.e., the function vector which satisfies the local linearization relationship,

$$\mathbf{f}_{\Delta t}(\mathbf{z}\,|\,\varphi)=\left[\mathrm{Exp}\left\{\frac{\partial\mathbf{f}_{\Delta t}(\mathbf{z}\,|\,\varphi)}{\partial\mathbf{z}}\Delta t\right\}-I\right]^{-1}\left\{\frac{\partial\mathbf{f}_{\Delta t}(\mathbf{z}\,|\,\varphi)}{\partial\mathbf{z}}\right\}\{A_{\Delta t}(\mathbf{z}\,|\,\varphi)-I\}\mathbf{z}. \tag{13}$$

In general, we cannot give an explicit form for $\mathbf{f}_{\Delta t}(\mathbf{z}\,|\,\varphi)$. Instead we can obtain $\mathbf{f}_{\Delta t}(\mathbf{z}\,|\,\varphi)$ by the following numerical iterative procedure,

$$\mathbf{f}_{\Delta t}^{(k+1)}(\mathbf{z}_{i,j}\,|\,\varphi)=(1-\Delta s)\,\mathbf{f}_{\Delta t}^{(k)}(\mathbf{z}_{i,j}\,|\,\varphi)+\Delta s\{\mathrm{Exp}\,(J_{i,j}\Delta t)-I\}^{-1}\{A_{\Delta t}(\mathbf{z}_{i,j}\,|\,\varphi)-I\}\mathbf{z}_{i,j} \tag{14}$$

for each point $\mathbf{z}_{i,j}=(x_i,\dot{x}_j)'$ $(i=1,2,\ldots,j=1,2,\ldots)$ on any finite region. This is because $\mathbf{f}_{\Delta t}(\mathbf{z}\,|\,\varphi)$ can be considered as a limiting function $\mathbf{f}_{\Delta t}(\mathbf{z},\infty\,|\,\varphi)$, characterizd by

$$\frac{\partial\mathbf{f}_{\Delta t}(\mathbf{z},s|\varphi)}{\partial s}=0,$$

of a deterministic spatial process $\mathbf{f}_{\Delta t}(\mathbf{z},s\,|\varphi)$ defined by the partial differential equation,

$$\frac{\partial\mathbf{f}_{\Delta t}(\mathbf{z},s\,|\,\varphi)}{\partial s}=-\mathbf{f}_{\Delta t}(z,s\,|\varphi)\times\left[\mathrm{Exp}\left\{\frac{\partial\mathbf{f}_{\Delta t}(\mathbf{z},s\,|\,\varphi)}{\partial\mathbf{z}}\Delta t\right\}-I\right]^{-1}\{A_{\Delta t}(\mathbf{z}\,|\,\varphi)-I\}\mathbf{z}.$$

$J_{i,j}$ is a matrix obtained by approximating the Jacobian matrix

$$\left[\frac{\partial\mathbf{f}_{\Delta t}\mathbf{z}\,|\,\varphi)}{\partial\mathbf{z}}\right]_{z=(x_i,\dot{x}_j)'}$$

by some numerical differencing method with $\Delta\mathbf{z}=(\Delta x,\Delta\dot{x})'$. We have $\mathbf{f}_{\Delta t}^{(k+1)}\to\mathbf{f}_{\Delta t}(\mathbf{z}\,|\,\varphi)$ for $k\to\infty$ if Δs of (14) is sufficiently small compared with Δx and $\Delta\dot{x}$. For the initial function of the above iteration, the following function,

$$\mathbf{f}_{\Delta t}^{(0)}(\mathbf{z}\,|\,\varphi)=\frac{1}{\Delta t}\{A_{\Delta t}(\mathbf{z}\,|\,\varphi)-I\}\mathbf{z},$$

which is obtained from the local linearization relationship (13) by employing the approximation,

$$\mathrm{Exp}\left[\left\{\frac{\partial f_{\Delta t}(\mathbf{z}\,|\,\varphi)}{\partial\mathbf{z}}\right\}\Delta t\right]\doteqdot I+\left\{\frac{\partial\mathbf{f}_{\Delta t}(\mathbf{z}\,|\,\varphi)}{\partial\mathbf{z}}\right\}\Delta t$$

will be useful.

Of course, the function $\mathbf{f}_{\Delta t}(\mathbf{z}\,|\,\mathbf{a},\mathbf{b})$ obtained from $\mathbf{f}(\mathbf{z}\,|\,\mathbf{a},\mathbf{b})$ through the locally linearized $A_{\Delta t}(\mathbf{z}\,|\,\mathbf{a},\mathbf{b})$ using

$$A_{\Delta t}(\mathbf{z}|\,\mathbf{a},\mathbf{b})=I+\left\{\frac{\partial\mathbf{f}(\mathbf{z}|\,\mathbf{a},\mathbf{b})}{\partial\mathbf{z}}\right\}^{-1}\times\left[\mathrm{Exp}\left\{\frac{\partial\mathbf{f}(\mathbf{z}|\,\mathbf{a},\mathbf{b})}{\partial\mathbf{z}}\Delta t\right\}-I\right]F(\mathbf{z}|\,\mathbf{a},\mathbf{b})$$

is not equal to the original $\mathbf{f}(\mathbf{z}\,|\,\mathbf{a},\mathbf{b})$ since the local linearity approximation is used in deriving $A_{\Delta t}(\mathbf{z}\,|\,\mathbf{a},\mathbf{b})$ from $\mathbf{f}(\mathbf{z}\,|\,\mathbf{a},\mathbf{b})$. We can easily see how fast $\mathbf{f}_{\Delta t}(\mathbf{z}\,|\,\mathbf{a},\mathbf{b})$ approaches the true $\mathbf{f}(\mathbf{z}|\,\mathbf{a},\mathbf{b})$ for $\Delta t\to0$ by employing the above numerical procedure. Figure 3 shows $\mathbf{f}(\mathbf{z}\,|\,\mathbf{a},\mathbf{b})$ and $\mathbf{f}_{\Delta t}(\mathbf{z}\,|\,\mathbf{a},\mathbf{b})$ for example 1 for different Δt's for the model (9).

To choose a model among several candidate models parameterized either in the continuous time domain as in (2) or the discrete time domain as in (10) we can use the minimum AIC procedure (Akaike, 1974b) based on Akaike's entropy maximization principle (Akaike, 1977), which suggests choos-

Downloaded 03 May 2010 to 171.66.16.31. Redistribution subject to ASME license or copyright; see http://www.asme.org/terms/Terms_Use.cfm

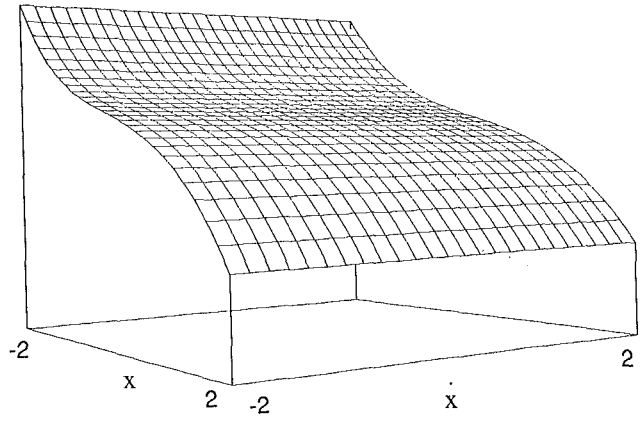


Fig. 3(a) True function f(z | a, b) of the model (9)

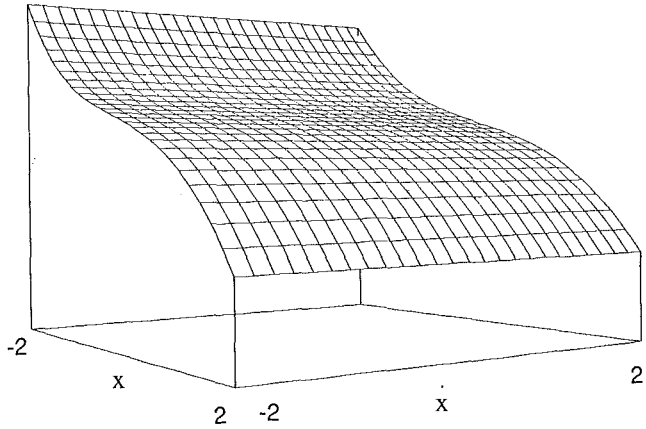


Fig. 3(c) $f_{\Delta t}(z \mid a, b)$ for f (z | a, b) of (9) where $\Delta t = 0.03$

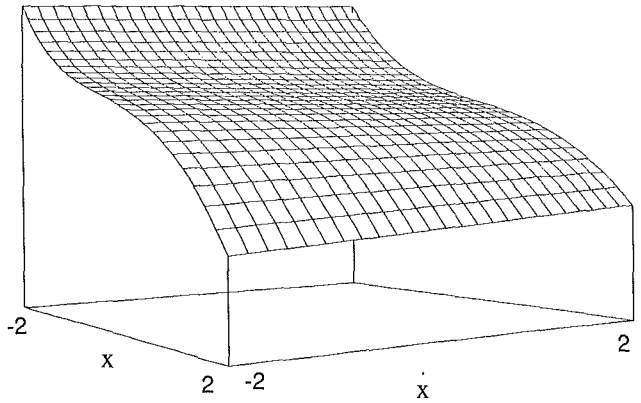


Fig. 3(b) $f_{\Delta t}$ (z | a, b) for f(z | a, b) of (9) where $\Delta t = 0.1$

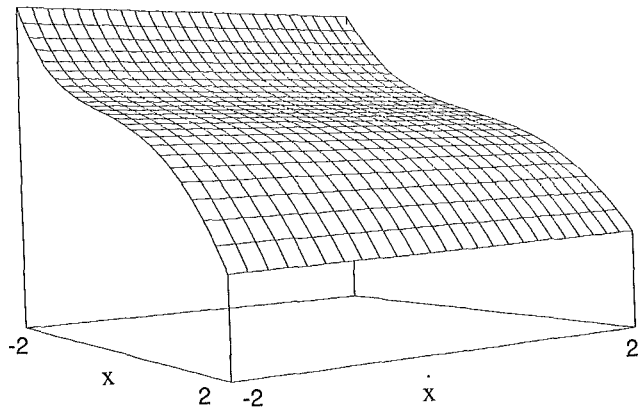


Fig. 3(d) $f_{\Delta t}$ (z | a, b) for f (z | a, b) of (9) where $\Delta t = 0.01$

ing that model which has minimum AIC value among the candidate models.

4 Application to Data Analysis

To see if the identification procedure discussed in a previous section is useful in the analysis of real nonlinear oscillation data, we apply the procedure to pitching data for a ship moored in the sea (see Fig. 4). The data was sampled with $\Delta t = 0.06$ second. Since the ship is moored by a rope to some fixed point, the dynamics of the pitching of the ship is an asymmetric type of oscillation.

A well-known mathematical model for the dynamics of the moored vessel is the following stochastic differential equation model,

$$\ddot{x} + a\dot{x} + bx = n(t) - T(x) \tag{15}$$

where $T(x)$ is a force function to pull the ship back when the pitching angle is x. $T(x)$ is usually zero for $x < 0$. For $x \geq 0$ some polynomial function is used for $T(x)$. Then, from (15) we have the following nonlinear random vibration model for the pitching motion,

$$\ddot{x} + a\dot{x} + \left\{b + \frac{T(x)}{x}\right\}x = n(t).$$

The problem is how to estimate a, b, and $T(x)$ from the data. We applied a locally linearized model (3), parameterized in a continuous-time domain by

$$\ddot{x} + a\dot{x} + g(x \mid \mathbf{b})x = n(t) \tag{16}$$

with

$$g(x \mid \mathbf{b}) = b_1 + b_2\ [x^2]_+$$

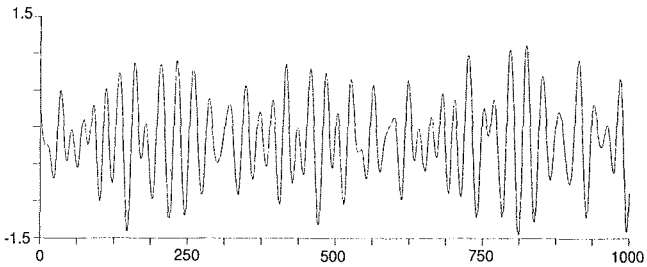


Fig. 4 Pitching data of a moored ship

where

$$[x^2]_+ = \begin{cases} x^2 & \text{for } x > 0 \\ 0 & \text{for } x \leqq 0. \end{cases}$$

We take $\Delta t = 0.1$ in the estimation procedure. The choice of Δt in the estimation procedure affects only the scale of function $g_2(x \mid \mathbf{b})$ and does not affect the estimation results. The estimated parameters are $\hat{a} = 0.4659$, $\hat{b}_1 = 14.6819$ $\hat{b}_2 = 5.9752$ and $\hat{\sigma}^2 = 9.3055$. Using the estimated parameters, we can easily simulate the model (16) and can see that the estimated model produces similar asymmetric behavior of the dynamics of pitching motion.

The present method can be applied to any system, $\dot{\mathbf{v}} = \mathbf{f}(\mathbf{v}) + \mathbf{n}(t)$, where $\mathbf{f}(\mathbf{v})$ is analytic and so its Jacobian $\mathbf{J}(\mathbf{v})$ can be calculated, since the A matrix and B matrix of (7) are obtained from $\mathbf{f}(\mathbf{v})$ and $\mathbf{J}(\mathbf{v})$. Calculation of the B matrix may look complicated for higher order degree-of-freedom systems but it all depends on the diagonalization of the K_t matrix, which is needed to calcuate the variance-covariance matrix of

Downloaded 03 May 2010 to 171.66.16.31. Redistribution subject to ASME license or copyright; see http://www.asme.org/terms/Terms_Use.cfm

the discrete time white noise $w_{t+\Delta t}$ of (3), and we see not special difficulty in principle for carrying this out in higher degree-of-freedom systems.

The present method can be extended, without much complication, to the case where the vibration system is excited by some other nonwhite random force. One example of such an extension is given in Oda, Ozaki, and Yamanouchi (1988).

References

Akaike, H., 1974a, "Markovian Representation of Stochastic Processes and its Application to the Analysis of Autoregressive and Moving Average Process," *Ann. Inst. Statist. Math.*, Vol. 26, pp. 363–387.

Akaike, H., 1974b, "A New Look at the Statistical Model Identification," *IEEE Trans. Auto. Control,* Vol. AC-19, pp. 716–723.

Akaike, H., 1977, "On Entropy Maximization Principle," *Application of Statistics,* P. R. Krishnaiah, ed., North-Holland, Pub. Co., Amsterdam, The Netherlands.

Billingsley, P., 1961, *Statistical Inference for Markov Processes*, Holt, New York.

Caughey, T. K., 1971, "Nonlinear Theory of Random Vibrations" *Advances in Applied Mechanics*, Vol. 11, Chia-Shun Yih eds., Academic Press, New York and London, pp. 209–253.

Gikhman, I. I., and Skorohod, A. V., 1965, *Introduction to the Theory of Random Processes* (translated by Scripta Technica, Inc.) W. B. Saunders Company.

Fletcher, R., and Powell, M. J. D., 1963, "A Rapidly Convergent Descent Method for Minimization," *Computer J.*, Vol. 6, pp. 163–168.

Haggan, V., and Ozaki, T., 1981, "Modelling Nonlinear Random Vibrations Using an Amplitude-Dependent Autoregressive Time Series Model," *Biometrika*, Vol. 68, pp. 189–196.

Huber, P. J., 1967, "The Behavior of the Maximum Likelihood Estimates under Nonstandard Conditions," *Proc. 5th Berkeley Symp. Math. Statist. Prob.*, Vol. 1, pp. 221–233.

Oda, H., Ozaki, T., and Yamanouchi, Y., 1988, "A Nonlinear System Identification in the Analysis of Offshore Structure Dynamics in Random Waves," *Nonlinear Stochastic Dynamic Engineering Systems, IUTAM Symposium*, Innsburck/Igls, Austria, June 21–26, 1987, F. Ziegler and G. I. Schueller, eds., Springer-Verlag, pp. 87–100.

Ozaki, T., 1981, "Non-linear Phenomena and Time Series Models," Invited Paper, 43rd Session of the International Statistical Institute. Buenos Aires, Argentina, *Bulletin of the International Statistical Institute*, Vol. 49, Book 3, pp. 1193–1210.

Ozaki, T., 1986, "Local Gaussian Modelling of Stochastic Dynamical Systems in the Analysis of Nonlinear Random Vibrations," *Essays in Time Series and Allied Processes*, Festschrift in honour of Prof. E. J. Hannan, Applied Probability Trust, pp. 241–255.

Ozaki, T., 1985, "Non-linear Time Series Models and Dynamical Systems," *Handbook of Statistics*, Vol. 5, E. J. Hannan et al., eds., North-Holland, pp. 25–83.

Downloaded 03 May 2010 to 171.66.16.31. Redistribution subject to ASME license or copyright; see http://www.asme.org/terms/Terms_Use.cfm

Response and Stability of a Random Differential Equation: Part I—Moment Equation Method

H. Benaroya
Mem. ASME

M. Rehak[1]
Applied Science Division,
Weidlinger Associates,
333 Seventh Avenue,
New York, N.Y. 10001

A linear stochastic differential equation of order N *excited by an external random force and whose coefficients are white noise random processes is studied. The external force may be either white or colored noise random process. Given the statistical properties of the coefficients and of the force, equivalent statistics are obtained for the response.*

The present solution method is based on the derivation of the equation governing the response autocorrelation function. The simplifying assumption that the response is stationary when the coefficients and input force are stationary is introduced. Another simplification occurs with the assumption that the response is uncorrelated from the random coefficients. Closed-form solutions for the response autocorrelation function and spectral density are derived in conjunction with a stability bound.

1 Introduction

The linear stochastic differential equation of order N with white noise random coefficients has been investigated by Samuels (1960) for a nonstationary case and by Caughey and Dienes (1962) when only one coefficient is random. First- and second-order equations with parametric uncertainties have been the object of a large number of studies (Kozin, 1986). A frequently used method to estimate output probabilities is the Fokker-Planck equation method, which requires that the parametric uncertainties be white nose or filtered white noise processes. A survey of systems with random parametric excitations can be found in Ibrahim (1985).

In the present paper, the assumption that the response is stationary is introduced and the resulting simplifications lead to expressions for the statistics of the response. A stability limit is also derived. Furthermore, all coefficients (system parameters) are random processes. In Caughey and Dienes (1962), where both stability limits and autocorrelation function are derived, only the coefficient of the lowest order term is random. Although the method used in this paper differs from that in Caughey and Dienes (1962), where the Fokker-Planck equation is derived, results of this paper reduce to those, for the particular case where only the coefficient of the lowest order term is random.

This work on linear stochastic differential equations of order N is in two parts:

(i) Part 1 derives the response autocorrelation function, spectral density, and stability bound when the coefficients are assumed to be white noise processes,

(ii) Part 2 derives approximations for the response autocorrelation, and spectral density when the coefficients are assumed to be colored noise random processes.

The expansion method used in Part 2 is also applied when the coefficients are assumed white noise, in order to verify results of Part 1. This expansion method is used to prove that when the random coefficients are white noise; they are uncorrelated from the response. This property is essential in deriving resultings of Part 1.

A third paper (Rehak and Benaroya, 1987) proves that when the coefficients and random input are stationary processes, the response is also stationary. This property is assumed in both Parts 1 and 2.

2 Governing Equation

Consider a differential equation of the form:

$$x^{(N)}(t) + \sum_{j=0}^{N-1} (a_j + b_j(t)) x^{(j)}(t) = F(t),$$

$$x^{(j)}(t) \equiv \frac{d^j x(t)}{dt^j}, \tag{1}$$

where a_j are deterministic coefficients, $b_j(t)$ are uncorrelated zero mean white noise processes, and $F(t)$ is a stationary random process defined by its spectral density. It is assumed that $b_j(t)$ and $F(t)$ are uncorrelated. The autocorrelation function for $b_j(t)$ is:

$$R_{b_j b_j}(\tau) = D_j \delta(\tau), \tag{2}$$

and, thus, its Fourier transform, the spectral density is:

[1] Presently at Brookhaven National Laboratories.

Contributed by the Applied Mechanics Division of THE AMERICAN SOCIETY OF MECHANICAL ENGINEERS for publication in the JOURNAL OF APPLIED MECHANICS.

Discussion on this paper should be addressed to the Editorial Department, ASME, United, Engineering Center, 345 East 47th Street, New York, 10017, and will be accepted until two months after final publication of the paper itself in the JOURNAL OF APPLIED MECHANICS. Manuscript received by ASME Applied Mechanics Division, June 23, 1986; final revision, May 11, 1987.

Copyright © 1989 by ASME

Downloaded 03 May 2010 to 171.66.16.31. Redistribution subject to ASME license or copyright; see http://www.asme.org/terms/Terms_Use.cfm

$$S_{b_j b_j}(\omega) = D_j; \tag{3}$$

here, D_j are the intensities and $\delta(\tau)$ is the Dirac-delta function. If differential equation (1) is written in operator notation, it would not be possible to invert this random operator. It is therefore useful to combine all random components on the right-hand side, and all deterministic components on the left-hand side, of equation (1):

$$x^{(N)}(t) + \sum_{j=0}^{N-1} a_j x^{(j)}(t) = F(t) - \sum_{j=0}^{N-1} b_j(t) x^{(j)}(t). \tag{4}$$

It is reasonable to expect that it is possible to invert the deterministic operator

$$L \equiv \sum_{j=0}^{N-1} a_j x^{(j)}(t),\ a_N = 1. \tag{5}$$

Denoting the inverse of L by L^{-1}, we have

$$x(t) = x_0(t) - \sum_{j=0}^{N-1} L^{-1}(b_j(t) x^{(j)}(t)), \tag{6}$$

where $x_0(t)$ represents the solution to the respective problem without random coefficients:

$$x_0(t) = L^{-1}(F(t)). \tag{7}$$

3 Autocorrelation Function

In this section, the equation governing second-order moments of the response $x(t)$ is derived. Equation (6) is, of course, only a formal solution and, since $b_j(t)$ are random, it is only possible to obtain random measures of $x(t)$.

Equation (6) is rewritten as

$$x(t) = x_0(t) - \sum_{j=0}^{N-1} \int_{-\infty}^{\infty} h(t-t_0) b_j(t_0) x^{(j)}(t_0) dt_0, \tag{8}$$

where the impulse response, $h(t)$, has the following properties:

$$L(h(t)) = \delta(t), \quad h(t) = 0 \quad \text{for } t < 0$$

$$h^{(i)}(0) = 0, \quad i = 1, \ldots, N-2$$

$$h^{(N-1)}(0) = 1, \quad h^{(N)}(0) = -a_{N-1}. \tag{9}$$

If $x(t)$ is a stationary process, its autocorrelation is defined as

$$R_{xx}(\tau) = \langle x(t) x(t+\tau) \rangle, \tag{10}$$

where $\langle\ \rangle$ denotes the mathematical expectation. The validity of this assumption, that $x(t)$ is stationary when the coefficients and input are stationary, is derived in Rehak and Benaroya (1987). Upon substitution of equation (8) for $x(t)$ in equation (10), one has

$$\begin{aligned} R_{xx}(\tau) = {} & \langle x_0(t) x_0(t+\tau) \rangle \\ & + \sum_{i=0}^{N-1} \left\langle \int_{-\infty}^{\infty} x_0(t+\tau) h(t-t_1) b_i(t_1) x^{(i)}(t_1) dt_1 \right\rangle \\ & + \sum_{j=0}^{N-1} \left\langle \int_{-\infty}^{\infty} x_0(t) h(t+\tau-t_2) b_j(t_2) x^{(j)}(t_2) dt_2 \right\rangle \\ & + \sum_{i=0}^{N-1} \sum_{j=0}^{N-1} \left\langle \int_{-\infty}^{\infty} h(t-t_1) b_i(t_1) x^{(i)}(t_1) dt_1 \right. \\ & \left. \int_{-\infty}^{\infty} h(t+\tau-t_2) b_j(t_2) x^{(j)}(t_2) dt_2 \right\rangle. \end{aligned} \tag{11}$$

4 Implicit Equation For the Autocorrelation

In order to simplify this last equation, it is necessary to use the property that $x(t)$ and $b_j(t)$ are uncorrelated. A proof of this assumption can be found in Samuels (1960). The derivation is quite involved since it is performed for the general case of a nonstationary problem. An alternate proof appears in the companion paper by the authors (1989). Using, in addition, the properties that $b_j(t)$ are zero mean and uncorrelated processes, one has

$$\langle b_i(t) x^{(i)}(t) \rangle = \langle b_i(t) \rangle \langle x^{(i)}(t) \rangle = 0 \tag{12}$$

$$\begin{aligned} & \langle b_i(t_1) b_j(t_2) x^{(i)}(t_1) x^{(j)}(t_2) \rangle \\ & \quad = \langle b_i(t_1) b_i(t_2) \rangle \langle x^{(i)}(t_1) x^{(i)}(t_2) \rangle. \end{aligned} \tag{13}$$

The single sums in equation (11) are thus equal to zero. We note that the expected value of $x(t)$ is $\langle x_0(t) \rangle$. The term with the double sum in equation (11) is rewritten using equation (13) as

$$\begin{aligned} & \sum_{i=0}^{N-1} \sum_{j=0}^{N-1} \int_{-\infty}^{\infty} dt_1 \int_{-\infty}^{\infty} dt_2 h(t+\tau-t_2) h(t-t_1) \\ & \quad \langle b_i(t_1) x^{(i)}(t_1) b_i(t_2) x^{(i)}(t_2) \rangle, \end{aligned} \tag{14}$$

where the product of the two integrals is replaced by a multiple integral of order two. Using equations (13), and (2), and the assumption that $x(t)$ is stationary, one obtains for the above expectation

$$\begin{aligned} & \langle b_i(t_1) b_i(t_2) x^{(i)}(t_1) x^{(i)}(t_2) \rangle \\ & \quad = D_i \delta(t_2 - t_1) R_{x^{(i)} x^{(i)}}(t_2 - t_1). \end{aligned} \tag{15}$$

The delta function reduces by one the order of the multiple integral. Equation (11) thus becomes

$$R_{xx}(\tau) = R_{x_0 x_0}(\tau) + \rho(\tau) \sum_{i=0}^{N-1} D_i m_i, \tag{16}$$

where

$$\begin{aligned} m_i &= R_{x^{(i)} x^{(i)}}(0) \\ \rho(\tau) &= \int_0^{\infty} h(t+\tau) h(t) dt. \end{aligned} \tag{17}$$

m_i is the variance of $x^{(i)}(t)$. $\rho(\tau)$ is the autocorrelation of the response of the determinstic system (i.e., when $b_j(t) = 0$ for all j) to a white noise forcing function of intensity 1 (Papoulis, 1965).

5 Variances

Equation (16) is not explicit since the variances m_i are so far unknown. A system of equations that can be solved for these unknowns is set up in this section.

$R_{x^{(j)} x^{(j)}}(t)$ is related to $R_{xx}(t)$ by (Papoulis, 1965):

$$R_{x^{(j)} x^{(j)}}(\tau) = (-1)^j \frac{d^{2j} R_{xx}(\tau)}{d\tau^{2j}}. \tag{18}$$

Equation (16) is differentiated $2j$ times with respect to τ:

$$R_{x^{(j)} x^{(j)}}(\tau) = R_{x_0^{(j)} x_0^{(j)}}(\tau) + (-1)^j \frac{d^{2j} \rho(\tau)}{d\tau^{2j}} \sum_{i=0}^{N-1} D_i m_i. \tag{19}$$

Setting $\tau = 0$ in the above, an equation relating the variances is obtained

$$m_j = m_j^0 + n_j^0 \sum_{i=0}^{N-1} D_i m_i, \tag{20}$$

where the following notation has been introduced for simplicity:

Downloaded 03 May 2010 to 171.66.16.31. Redistribution subject to ASME license or copyright; see http://www.asme.org/terms/Terms_Use.cfm

$$m_j^0 = R_{x_0^{(j)} x_0^{(j)}}(0),\ n_j^0 = (-1)^j \frac{d^{2j}\rho(0)}{d\tau^{2j}}. \tag{21}$$

m_i^0 is the variance of $x_0^{(i)}(t)$ for colored or white $F(t)$, and n_i^0 is the variance of $x_0^{(i)}(t)$ when $F(t)$ is white noise of intensity 1. It is recalled that m_j are the unknowns while m_j^0, n_j^0 are known quantities.

A system of equations in the N unknowns m_i is formed by letting j vary in equation (20) from 0 to $N-1$. The system of equations is

$$[\mathbf{A}](\mathbf{m}) = (\mathbf{m}^0), \tag{22}$$

where [A] is an $N \times N$ matrix with coefficients

$$a_{ij} = \delta_{ij} - D_j n_i^0, \tag{23}$$

(m) is the vector

$$(\mathbf{m}) = [m_0, m_1, \ldots, m_{N-1}]^T, \tag{24}$$

and δ_{ij} denotes the Kronecker delta.

Upon inversion of [A] (under conditions which will be subsequently examined), equation (22) is solved in terms of (m)

$$(\mathbf{m}) = [\mathbf{A}]^{-1}(\mathbf{m}^0) = [\mathbf{C}](\mathbf{m}^0). \tag{25}$$

It can be verified (Rehak et al., 1987) that the coefficients of $[\mathbf{C}] = [\mathbf{A}]^{-1}$ denoted by c_{ij}, are given by

$$c_{ij} = D_i n_j^0 / \mathrm{Det}[\mathbf{A}],\ i \neq j \tag{26}$$

$$c_{ii} = \mathrm{Det}[\mathbf{A}]_{D_i=0} / \mathrm{Det}[\mathbf{A}], \tag{27}$$

$$\mathrm{Det}[\mathbf{A}] = 1 - \sum_{i=0}^{N-1} D_i n_i^0. \tag{28}$$

6 Explicit Expression for the Autocorrelation

Using equations (25) to (27), we find the components of vector (m):

$$m_i = m_i^0 + n_i^0 \frac{\Sigma_{j=0}^{N-1} D_j m_j^0}{\mathrm{Det}[\mathbf{A}]}. \tag{29}$$

Since m_i appear in equation (16) as part of the sum $\Sigma_{i=0}^{N-1} D_i m_i$, we evaluate this expression by performing some algebraic manipulations on equation (29)

$$\sum_{i=0}^{N-1} D_i m_i = \frac{\Sigma_{i=0}^{N-1} D_i m_i^0}{\mathrm{Det}[\mathbf{A}]}. \tag{30}$$

The explicity expression for the autocorrelation is then given by equation (16) as

$$R_{xx}(\tau) = R_{x_0 x_0}(\tau) + \rho(\tau) \frac{\Sigma_{i=0}^{N-1} D_i m_i^0}{\mathrm{Det}[\mathbf{A}]}, \tag{31}$$

where Det [A] is given in equation (28). In the frequency domain, with $H(j\omega)$ denoting the Fourier transform of $h(t)$, the spectral density is

$$S_{xx}(\omega) = S_{x_0 x_0}(\omega) + |H(j\omega)|^2 \frac{\Sigma_{i=0}^{N-1} D_i m_i^0}{\mathrm{Det}[\mathbf{A}]}. \tag{32}$$

These results reduce to those obtained by Caughey and Dienes (1962) for the case where the only random parameter is $b_0(t)$ and $b_j(t) = 0$, $j = 1, \ldots, N-1$.

Equation (31) indicates that the solution is the linear superposition of the autocorrelation for the deterministic system $R_{x_0 x_0}(\tau)$, and of a correction term accounting for the randomness in the system. The detailed form of this correction term reveals that it is the response of the same deterministic system to an effective white noise of intensity $\Sigma_{i=0}^{N-1} D_i m_i^0 / \mathrm{Det}[\mathbf{A}]$. Introducing random coefficients in the deterministic equation is equivalent to adding an external white noise forcing function to $F(t)$.

7 Conditions For Existence For a Solution

The conditions under which it is possible to solve equation (22) for (m) are established next. It is recalled that m_i, m_i^0, n_i^0, D_i are variances and therefore positive semidefinite quantities. The values of c_{ij} could be such that [C] ($\mathbf{m}^0$) is a vector with some negative components. In this case we can no longer say that negative components represent variances. The following question naturally arises: What are the conditions on the parameters of this problem such that each component of [C]($\mathbf{m}^0$) is positive? It will be demonstrated next that a necessary and sufficient condition is that Det [A] be positive.

Equations (26) and (27) defining the coefficients of [C], indicate that

$$\mathrm{Det}[\mathbf{A}] > 0 \Leftrightarrow c_{ij} > 0, \quad \forall (i,j) \in [0,1, \ldots, N-1]. \tag{33}$$

Thus, since the components of ($\mathbf{m}^0$) are all positive, Det [A] >0 is a necessary and sufficient condition for [C]($\mathbf{m}^0$) to have positive components.

8 Stability

Stability in the mean-square sense is defined as (Samuels, 1960):

$$\lim_{t \to \infty} R_{xx}(t) < C. \tag{34}$$

Inspection of equation (31) reveals that the only possibility for $R_{xx}(t)$ to become unbounded arises when $\mathrm{Det}[\mathbf{A}] = 0$. The other terms entering in the definition of $R_{xx}(t)$ are the autocorrelations of the response of the deterministic system, which is stable. It can be verified that for a second-order equation, one has

$$\lim_{\tau \to \infty} R_{x_0 x_0}(\tau) = 0. \tag{35}$$

Instability is implied by:

$$\lim_{\mathrm{Det}[\mathbf{A}] \downarrow 0} R_{xx}(t) = \infty. \tag{36}$$

Since the autocorrelation function becomes unbounded as Det[A] approaches zero from above, Det [A] >0 is a stability limit in the mean square sense. It is noted that stability in the mean square sense is necessary but not sufficient condition for stability since higher order moments may be unbounded and the system may still be unstable. Another result of interest is given by examining equation (29), where m_i is equal to m_i^0 plus an additional term which is always positive. Thus,

$$m_i \geq m_i^0, \forall i \in [0,1, \ldots, N-1]. \tag{37}$$

The variance of the random system response and of its derivatives is larger than the corresponding variances when no randomness is present in the system. It is therefore concluded, as Caughey and Dienes (1962) have done earlier, that it is impossible to stabilize a system by introducing white noise parametric excitation.

9 Example

To demonstrate the application of the above theory, we consider the harmonic oscillator governed by

$$\ddot{x}(t) + (2\zeta + Z(t))\dot{x}(t) + (1 + K(t))x(t) = F(t), \tag{38}$$

where $K(t)$, $Z(t)$ are white noise processes with respective intensities D_0, D_1.

The following quantities related to the deterministic counterpart of equation (38) are needed: $h(t)$, $\rho(t)$, n_0^0, n_1^0, m_0^0, m_1^0. To evaluate these, we begin with the deterministic system equation

$$\ddot{x}_0(t) + 2\zeta \dot{x}_0(t) + x_0(t) = F(t). \tag{39}$$

Downloaded 03 May 2010 to 171.66.16.31. Redistribution subject to ASME license or copyright; see http://www.asme.org/terms/Terms_Use.cfm

The impulse response corresponding to this equation is

$$h(t) = e^{-\zeta t}\frac{\sin(\zeta_1 t)}{\zeta_1},\ \zeta_1 = \sqrt{1-\zeta^2},\ \zeta < 1,\ t > 0, \tag{40}$$

$$h(t) = 0,\ t \le 0. \tag{41}$$

From equation (17)

$$\rho(\tau) = e^{-\zeta\tau}\frac{[\zeta_1 \cos(\zeta_1 \tau) + \zeta \sin(\zeta_1 \tau)]}{4\zeta\zeta_1}. \tag{42}$$

From equation (24),

$$n_0^0 = n_1^0 = \frac{1}{4\zeta} \tag{43}$$

and assuming the spectral density for $F(t)$ to be of the form:

$$S_{FF}(\omega) = \frac{2\alpha}{\alpha^2 + \omega^2} \tag{44}$$

along with the relations (Papoulis, 1965)

$$m_i^0 = \frac{1}{2\pi}\int_{-\infty}^{\infty} \omega^{2i} S_{x_0 x_0}(\omega)\, d\omega, \tag{45}$$

$$S_{x_0 x_0}(\omega) = S_{FF}(\omega)\, |H(i\omega)|^2, \tag{46}$$

one obtains,

$$m_0^0 = \frac{2\zeta + \alpha}{2\zeta(1 + \alpha^2 + 2\alpha\zeta)}, \tag{47}$$

$$m_1^0 = \frac{\alpha}{2\zeta(1 + \alpha^2 + 2\alpha\zeta)}. \tag{48}$$

Using equation (23) we have

$$[\mathbf{A}] = \begin{bmatrix} 1 - \dfrac{D_0}{4\zeta} & -\dfrac{D_1}{4\zeta} \\ \dfrac{D_0}{4\zeta} & 1 - \dfrac{D_1}{4\zeta} \end{bmatrix}. \tag{49}$$

Our desired result is obtained from equation (31) which becomes

$$R_{xx}(\tau) = R_{x_0 x_0}(\tau) + \rho(\tau)\frac{4\zeta(D_0 m_0^0 + D_1 m_1^1)}{4\zeta - D_0 - D_1}. \tag{50}$$

The stability condition is:

$$D_0 + D_1 < 4\zeta. \tag{51}$$

When $D_1 = 0$, i.e., the stiffness only is random, this reduces to the stability criterion found in the literature (Ibrahim, 1985),

$$D_0 < 4\zeta. \tag{52}$$

10 Conclusions

In this paper, a closed-form expression for the autocorrelation function of the response of linear differential equation of order N, whose coefficients are white noise processes, has been derived. It is demonstrated that a solution exists only when the variances of the coefficients satisfy the inequality Det $[\mathbf{A}] > 0$, which is the stability limit of the system. It is also demonstrated that it is not possible to stabilize a system by introducing white noise parametric excitation.

Acknowledgments

This paper has been written as part of research sponsored by the Air Force Office of Scientific Research (AFSC), under Contract No. F49620-84-C-0009. Dr. Anthony Amos of the Air Force Office of Scientific Research is sincerely thanked for financial support as well as for his encouragement of this continuing effort. Prof. F. DiMaggio, Dr. G. Goldstein, and Prof. J. Wright are thanked for their comments.

References

Benaroya, H., and Rehak, M., 1989, "Response and Stability of a Random Differential Equation, Part 2: Iterative Method," Weidlinger Associates Technical Report No. 7, Air Force Office of Scientific Research, Contract No. F4620-84-C-0009; ASME JOURNAL OF APPLIED MECHANICS, Vol. 55, pp. 196-201.

Caughey, T. K., and Dienes, J. K., 1962, "The Behavior of Linear Systems With Random Parametric Excitation," *Journal of Mathematics and Physics*, Vol. 41.

Ibrahim, R. A., 1985, *Parametric Random Vibration*, Research Studies Press, London.

Kozin, F., 1986, "Some Results of Stability of Stochastic Dynamical Systems," *Probalistic Engineering Mechanics*, Vol. 1, No. 1.

Papoulis, A., 1965, *Probability, Random Variables and Stochastic Processes*, McGraw-Hill, New York.

Rehak, M., and Benaroya, H., 1987, "Stationary and Stochastic Differential Equations," ASME JOURNAL OF APPLIED MECHANICS, in progress.

Rehak, M., DiMaggio, F., Benaroya, H., and Elishakoff, I., 1987, "Random Vibrations With MACSYMA," *Computer Methods in Applied Mechanics and Engineering*, Vol. 61, pp. 61-70.

Samuels, J. C., 1960, "On the Stability of Random Systems and the Stabilization of Deterministic Systems With Random Noise," *Journal of the Acoustical Society*, Vol. 33, No. 6.

Downloaded 03 May 2010 to 171.66.16.31. Redistribution subject to ASME license or copyright; see http://www.asme.org/terms/Terms_Use.cfm

Response and Stability of a Random Differential Equation: Part II—Expansion Method

H. Benaroya
Mem. ASME

M. Rehak[1]

Applied Science Division,
Weidlinger Associates,
333 Seventh Avenue,
New York, N. Y. 10001

A linear stochastic differential equation of order N *with colored noise random coefficients and random input is studied. An approximate expression for the autocorrelation of the response is derived in terms of the statistical properties of the random coefficients and input. This is achieved by using an expansion method known as the Born expansion (Feynman, 1962). Feynman diagrams are used as a short hand notation.*

In the particular case where the coefficients are white noise processes, the expansion method yields identical results to those obtained using an alternate method in a companion paper (Benaroya and Rehak, 1989). The expansion method is also used to demonstrate that white noise coefficients are statistically uncorrelated from the response.

1 Introduction

The methodology used in this paper is known as the Born expansion (Feynman, 1962). This method provides correction terms to the solution obtained when randomness in the system is neglected. When only the first correction term is considered, it is known under the name Born approximation. This approach, investigated by Samuels and Eringen (1959), is further elaborated here with the additional assumption that the problem is stationary.

After introducing the method, approximations for the response autocorrelation function when the coefficients are colored noise are derived. Next, Feynman diagrams, which are of help here in the case where the coefficients are white noise, are introduced. The particular case of white noise coefficients is addressed in the last section.

2 The Expansion Method

The governing equation is

$$x^{(N)}(t)+\sum_{j=0}^{N-1}(a_j+b_j(t))x^{(j)}(t)=F(t),$$

$$j=0,1,\ldots,N-1. \tag{1}$$

One is referred to the companion paper (Benaroya and Rehak, 1989) for definitions and properties of the above terms. The only difference from this reference is that $b_j(t)$ are colored noise random processes, uncorrelated from each other. Thus, it is also no longer possible to use the simplifying assumption that the response $x(t)$ is uncorrelated from the coefficients $b_j(t)$ as is the case with white noise coefficients. One must, therefore, use approximate methods. The expansion method consists in seeking a solution to equation (1) of the form

$$x(t)=\sum_{i=0}^{\infty}x_i(t), \tag{2}$$

where

$$x_0(t)=L^{-1}F(t), \tag{3}$$

and where the general term of the series is

$$x_i(t)=-L^{-1}\sum_{j=0}^{N-1}b_j(t)x_{i-1}^{(j)}(t). \tag{4}$$

When all the terms of the series in (2) are available, this is an exact solution. The approximation occurs when the series is truncated. We wish to find the mean value $\langle x(t)\rangle$ and the autocorrelation $R_{xx}(\tau)=\langle x(t)x(t+\tau)\rangle$ of $x(t)$. The validity of the assumption that $x(t)$ is stationary, introduced here by writing its autocorrelation function as function of time difference only, is studied in depth in Rehak and Benaroya (1987). It follows from equation (2) that

$$\langle x(t)\rangle=\sum_{i=0}^{\infty}\langle x_i(t)\rangle \tag{5}$$

and

$$R_{xx}(\tau)=\sum_{i,k=0}^{\infty}R_{x_ix_k}(\tau). \tag{6}$$

3 Colored Noise Coefficients Case

If the convergence of the series it sufficiently rapid, the first

[1] Presently at Brookhaven National Laboratories.

Contributed by the Applied Mechanics Division of THE AMERICAN SOCIETY OF MECHANICAL ENGINEERS for publication in the JOURNAL OF APPLIED MECHANICS.

Discussion on this paper should be addressed to the Editorial Department, ASME, United Engineering Center, 345 East 47th Street, New York, N. Y. 10017, and will be accepted until two months after final publication of the paper itself in the JOURNAL OF APPLIED MECHANICS. Manuscript received by ASME Applied Mechanics Division, June 23, 1986; final revision, May 11, 1988.

Copyright © 1989 by ASME

Downloaded 03 May 2010 to 171.66.16.31. Redistribution subject to ASME license or copyright; see http://www.asme.org/terms/Terms_Use.cfm

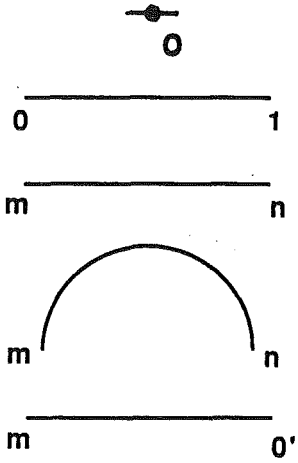


Fig. 1

two terms may be representative of the exact solution. $x(t)$ can then be approximated by

$$x(t) \simeq x_0(t) + x_1(t), \tag{7}$$

where $x_0(t)$ is defined in equation (3) and $x_1(t)$ is obtained by letting $i=1$ in equation (4)

$$x_1(t) = -L^{-1} \sum_{j=0}^{N-1} (b_j(t) x_0^{(j)}(t)). \tag{8}$$

Due to the fact that convolutions in the time domain become products in the frequency domain, it is advantageous to work with spectral densities. The Fourier transform of equation (6) is

$$S_{xx}(\omega) = \sum_{i,k=0}^{\infty} S_{x_i x_k}(\omega). \tag{9}$$

Following equation (7), this expression is approximated by

$$S_{xx}(\omega) \simeq S_{x_0 x_0}(\omega) + S_{x_1 x_1}(\omega). \tag{10}$$

The cross terms $S_{x_0 x_1}(\omega)$ and $S_{x_1 x_0}(\omega)$ are equal to zero because they contain odd moments in $b_j(t)$ which are equal to zero. The first term of this equation is the product of the input spectral density, $S_{FF}(\omega)$, and the squared system transfer function complex modulus, $H(i\omega)$.

$$S_{x_0 x_0}(\omega) = S_{FF}(\omega)\, |H(i\omega)|^2. \tag{11}$$

From equation (8), it appears that $S_{x_1 x_1}(\omega)$ can be interpreted as the output spectral density of the same system when the input force is $G = \Sigma_{j=0}^{N-1} b_j(t) x_0^{(j)}(t)$, thus,

$$S_{x_1 x_1}(\omega) = S_{GG}(\omega)\, |H(i\omega)|^2. \tag{12}$$

In order to compute $S_{GG}(\omega)$, some preliminary steps are needed. By taking the Fourier transform of

$$\langle b_j(t_0) x_0^{(j)}(t_0) b_j(t_0^\wedge) x_0^{(j)}(t_0^\wedge) \rangle$$

$$= \langle b_j(t_0) b_j(t_0^\wedge) \rangle \langle x_0^{(j)}(t_0) x_0^{(j)}(t_0^\wedge) \rangle, \tag{13}$$

one finds

$$S_{(b_j x_0^{(j)})(b_j x_0^{(j)})}(\omega) = \frac{1}{2\pi} (S_{b_j b_j}(\omega) \bigstar S_{x_0^{(j)} x_0^{(j)}}(\omega)), \tag{14}$$

where a star denotes a convolution. Using the relation

$$S_{x_0^{(j)} x_0^{(j)}}(\omega) = \omega^{2j} S_{x_0 x_0}(\omega), \tag{15}$$

and the fact that $b_j(t)$ are uncorrelated, we finally obtain

$$S_{x_1 x_1}(\omega) = \frac{1}{2\pi} \sum_{j=0}^{N-1} (S_{b_j b_j}(\omega) \bigstar \omega^{2j} S_{x_0 x_0}(\omega))\, |H(i\omega)|^2. \tag{16}$$



Fig. 2



Fig. 3

A comparison study with a Monte-Carlo simulation for an oscillator with random stiffness indicates that this one term approximation is adequate for certain ranges of parameter values (Rehak and Benaroya, 1988).

4 Feynman Diagrammatical Representation

The present section introduces a symbolism (Dence and Spence, 1973) which will prove helpful in representing $\langle x_i(t) \rangle$ and $R_{x_i x_k}(\tau)$, in particular when the coefficients are white noise processes. Define —●— as the vertex over which integration is implied, 0 1 represents $h(t_0 - t_1)$, $\overline{m \quad n}$ represents $h^{(j)}(t_m - t_n)$, $\widehat{m\ n}$ represents the correlation $\langle b_j(t_m) b_j(t_n) \rangle$, and $\overline{m \quad 0'}$ represents a terminator $x_0^{(j)}(t_m)$ (Fig. 1).

Times are ordered according to indices: $t_0 \geq t_1 \geq t_2 \ldots \geq t_0'$.

4.1 Mean Values. From equation (8), the explicit expression for $x_1(t)$ is:

$$x_1(t_0) = \int_{-\infty}^{\infty} dt_1 h(t_0 - t_1) \sum_{j=0}^{N-1} b_j(t_1) x_0^{(j)}(t_1). \tag{17}$$

The mean value of $x_1(t)$ is represented diagrammatically in Fig. 2.

$x_2(t)$ is expressed in terms of $x_0(t)$ using the representation of $x_1(t)$ in terms of $x_0(t)$:

$$x_2(t_0) = \int_{-\infty}^{\infty} dt_1 h(t_0 - t_1) \sum_{j=0}^{N-1} b_j(t_1)$$

$$\int_{-\infty}^{\infty} dt_2 h^{(j)}(t_1 - t_2) \sum_{k=0}^{N-1} b_k(t_2) x_0^{(k)}(t_2). \tag{18}$$

When taking the expected value of $x_2(t_0)$, the expression $\langle b_j(t_1) b_k(t_2) \rangle$ is equal to zero unless $j=k$ because $b_j(t)$, $j=1, \ldots, N-1$ are uncorrelated processes. This property is used throughout to simplify expressions. The mean value of $x_2(t)$ is represented by Fig. 3.

This diagram is equivalent to

$$\langle x_2(t_0) \rangle = \int_{-\infty}^{\infty} dt_1 h(t_0 - t_1) \int_{-\infty}^{\infty} dt_2$$

$$\sum_{j=0}^{N-1} h^{(j)}(t_1 - t_2) \langle b_j(t_1) b_j(t_2) \rangle \langle x_0^{(j)}(t_2) \rangle. \tag{19}$$

We now assume that the coefficients $b_j(t)$ have Gaussian distributions in order to take advantage of a useful property of moments of Gaussian process: the moments of order $2i$ can be expressed as $n = (2i)!/i!2^{2i}$ products of second-order moments. It is noted that odd order moments are equal to zero since $b_j(t)$ are zero mean processes.

$x_4(t)$ contains one moment of order 4 in $b_j(t)$ which breaks up into the sum of three second-order moment products:

$$\langle b_j(t_1) b_j(t_2) b_j(t_3) b_j(t_4) \rangle = \langle b_j(t_1) b_j(t_2) \rangle \langle b_j(t_3) b_j(t_4) \rangle$$

$$+ \langle b_j(t_1) b_j(t_3) \rangle \langle b_j(t_2) b_j(t_4) \rangle + \langle b_j(t_1) b_j(t_4) \rangle \langle b_j(t_2) b_j(t_3) \rangle. \tag{20}$$

Downloaded 03 May 2010 to 171.66.16.31. Redistribution subject to ASME license or copyright; see http://www.asme.org/terms/Terms_Use.cfm

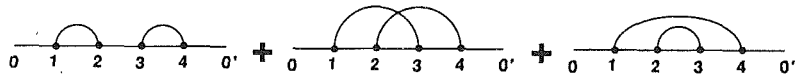


Fig. 4

$\langle x_4(t)\rangle$ is represented in Fig. 4.

4.2 Correlation Functions. The same notation can now be used to represent autocorrelation functions. There are now two families of dummy indices: $t_0 \geq t_1 \geq t_2 \ldots \geq t_0'$, $t_0^\wedge \geq t_1^\wedge \geq t_2^\wedge \ldots \geq t_0^{\wedge\prime}$. With τ defined by $t_0^\wedge = \tau + t_0$, we have

$$R_{x_0x_0}(\tau) = \langle x_0(t_0)x_0(t_0^\wedge)\rangle, \tag{21}$$

or, substituting for $x_0(t_0)$,

$$R_{x_1x_1}(\tau) = \int_{-\infty}^{\infty} dt_1 h(t_0 - t_1)\int_{-\infty}^{\infty} dt_1^\wedge h(t_0^\wedge - t_1^\wedge)$$

$$\sum_{j=0}^{N-1} \langle x_0^{(j)}(t_1)x_0^{(j)}(t_1^\wedge)\rangle\langle b_j(t_1)b_j(t_1^\wedge)\rangle. \tag{22}$$

which is represented in Fig. 5.

Examples of cross terms containing even moments in $b_j(t)$ are $R_{x_0x_2}(\tau)$ and $R_{x_2x_0}(\tau)$, which are depicted in Fig. 6.

Cross terms containing odd moments in $b_j(t)$ are equal to zero since $b_j(t)$ has a zero mean value.

$R_{x_2x_2}(\tau)$ contains a moment of order four in b_j, which is expressed in terms of second-order moments according to equation (20). The algebraic expression for $R_{x_2x_2}(\tau)$ is

$$R_{x_2x_2}(\tau) = \int_{-\infty}^{\infty} dt_1 h(t_0 - t_1)\int_{-\infty}^{\infty} dt_2 \sum_{j=0}^{N-1} h^{(j)}(t_1 - t_2)$$

$$\int_{-\infty}^{\infty} dt_1^\wedge h(t_0^\wedge - t_1^\wedge)\int_{-\infty}^{\infty} dt_2^\wedge h^{(j)}(t_1^\wedge - t_2^\wedge)$$

$$[\langle b_j(t_1)b_j(t_1^\wedge)\rangle\langle b_j(t_2)b_j(t_2^\wedge)\rangle + \langle b_j(t_1)b_j(t_2)\rangle$$

$$\langle b_j(t_1^\wedge)b_j(t_2^\wedge)\rangle + \langle b_j(t_1)b_j(t_2^\wedge)\rangle\langle b_j(t_2)b_j(t_1^\wedge)\rangle]$$

$$\langle x_0^{(j)}(t_2)x_0^{(j)}(t_2^\wedge)\rangle. \tag{23}$$

This is identical to Fig. 7.

The next term in the series is $R_{x_3x_3}(\tau)$, which is the sum of 15 terms resulting from the breakup of the moment of order 6 in $b_j(t)$ (see Fig. 8).

5 White Noise Coefficients Case

The purpose of this section is to demonstrate the use of the Feynman diagrammatical method when the general term of the infinite series of autocorrelation functions is available. When the random coefficients are white noise parameters, we can compare the results of this method with those in the companion paper (Benaroya and Rehak, 1989).

5.1 Autocorrelation Function. The particular case where the coefficients are white noise processes is now considered. Substituting

$$\langle b_j(t_1)b_j(t_1^\wedge)\rangle = D_j\delta(t_1 - t_1^\wedge) \tag{24}$$

in equation (22) we find

$$R_{x_1x_1}(\tau) = \int_{-\infty}^{\infty} dt_1 h(t_0 - t_1)$$

$$\times h(t_0^\wedge - t_1^\wedge)\sum_{j=0}^{N-1} D_j R_{x_0^{(j)}x_0^{(j)}}(0). \tag{25}$$

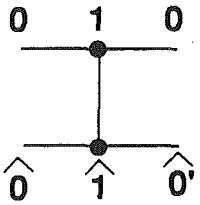


Fig. 5

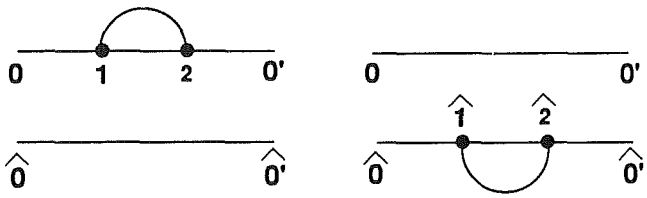


Fig. 6

Figure 5 indicates that a connection between two dots, here at times t_1 and $t_1^\wedge$, implies that those two quantities are equal.

For clarity, the same notation as in Benaroya and Rehak (1989) is used:

$$m_j^0 = R_{x_0^{(j)}x_0^{(j)}}(0), \quad n_j^0 = (-1)^j\rho(0)^{(2j)},$$

$$\rho(\tau) = \int_0^{\infty} dt h(t+\tau)h(t). \tag{26}$$

Equation (25) becomes

$$R_{x_1x_1}(\tau) = \rho(\tau)\sum_{j=0}^{N-1} D_j m_j^0. \tag{27}$$

Each of the three diagrams comprising $R_{x_2x_2}(\tau)$ in Fig. 7 is reexamined for the white noise case:

(*i*) In the first diagram, which we will call element 1, equation (24) implies that $t_1 = t_1^\wedge$, $t_2 = t_2^\wedge$.

(*ii*) In the second diagram of Fig. 7, or element 2, equation (24) implies that $t_1 = t_2^\wedge$, $t_1^\wedge = t_2$. These equalities, with $t_1 \geq t_2$ and $t_1^\wedge \geq t_2^\wedge$, are simultaneously satisfied only when $t_1 = t_2 = t_1^\wedge = t_2^\wedge$. However, due to the causality of the system, $h^{(j)}(t_1 - t_2) = h^{(j)}(0) = 0$. Diagrams containing temporal crossings of correlations are equal to zero.

(*iii*) In the third diagram, equation (24) implies that $t_1 = t_2$, $t_1^\wedge = t_2^\wedge$. The corresponding algebraic equation contains the expression $h^{(j)}(t_1 - t_2) = h^{(j)}(0) = 0$. Diagrams containing correlations within the same family of indices are also equal to zero. This is a very general result and it can be verified that correlations between dots on the same family of indices results in an expression which is equal to zero. Indeed, if $t_i = t_{i+1}$, then $h^{(j)}(t_{i+1} - t_i) = h^{(j)}(0) = 0$. If $t_i = t_k$, when i and k are not adjacent, the resulting expression is also equal to zero, as is demonstrated next with $k = i+2$. This expression contains $h^{(j)}(t_{i+2} - t_{i+1})h^{(j)}(t_{i+1} - t_i)$, but the equality $t_i = t_k$ can be only when $t_{i+2} = t_{i+1} = t_i$, thus, we find again $h^{(j)}(t_{i+1} - t_i) = h^{(j)}(0) = 0$.

For instance, the cross term $R_{x_0x_2}(\tau)$ is equal to zero as can be seen from Fig. 6. All other cross terms of the series of equation (6) are also equal to zero.

Equation (23) reduces to

$$R_{x_2x_2}(\tau) = \rho(\tau)\Big(\sum_{j=0}^{N-1} D_j m_j^0\Big)\Big(\sum_{j=0}^{N-1} D_j n_j^0\Big). \tag{28}$$

Downloaded 03 May 2010 to 171.66.16.31. Redistribution subject to ASME license or copyright; see http://www.asme.org/terms/Terms_Use.cfm

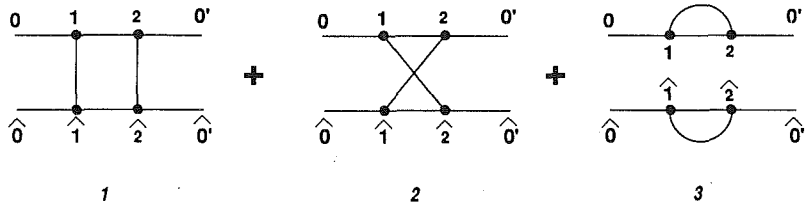


Fig. 7

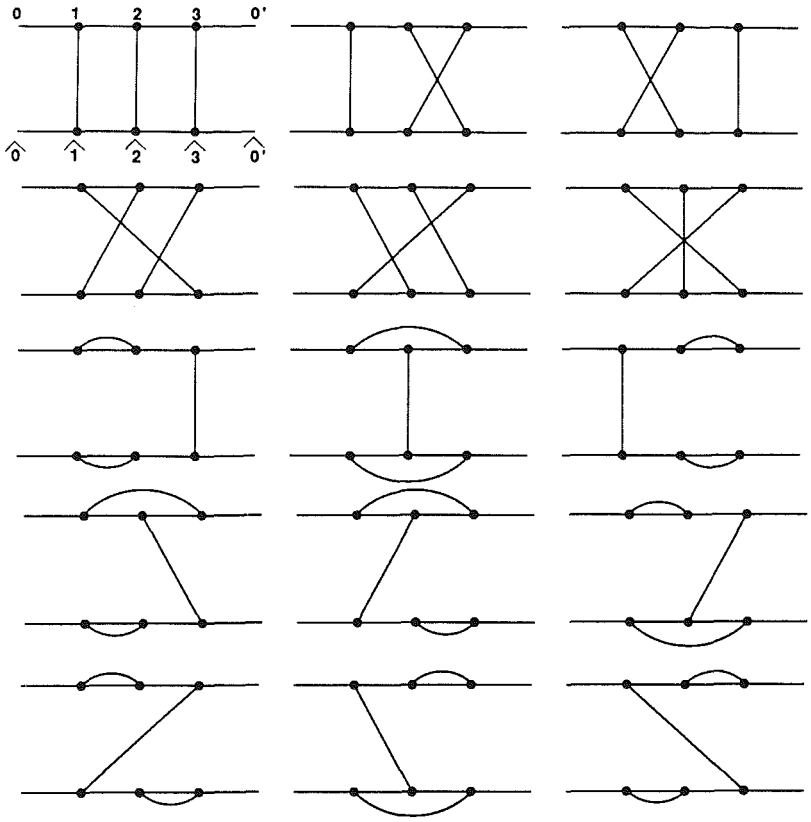


Fig. 8

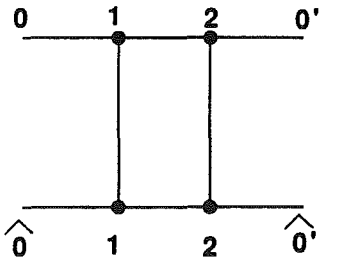


Fig. 9

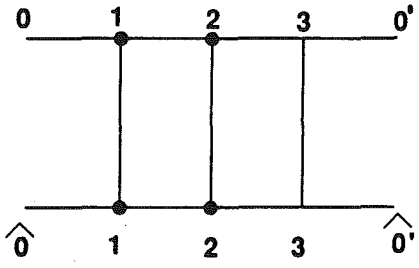


Fig. 10

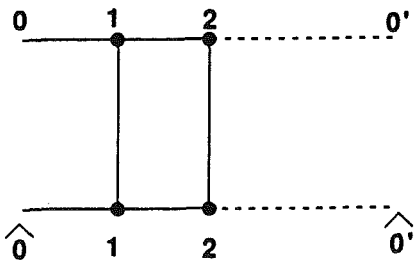


Fig. 11

Using a diagram where $t_1 = t_1^{\wedge}$ and $t_2 = t_2^{\wedge}$, one has to refer to Fig. 9.

The next term in the series, $R_{x_3x_3}(\tau)$, was illustrated in Fig. 8 for the colored noise case as the sum of 15 terms. Using the same reasoning as for $R_{x_2x_2}(\tau)$, the only nonzero contribution comes from the first term of this sum (i.e., Fig. 10). with $t_1 = t_1^{\wedge}$, $t_2 = t_2^{\wedge}$, $t_3 = t_3^{\wedge}$. $R_{x_3x_3}(\tau)$ is therefore equal to

$$R_{x_3x_3}(\tau) = \rho(\tau)\left(\sum_{j=0}^{N-1} D_j m_j^0\right)\left(\sum_{j=0}^{N-1} D_j n_j^0\right)^2. \tag{29}$$

From Fig. 8, it is apparent that diagrams representing $R_{x_ix_i}(\tau)$ contain combinations of elements 1, 2, and 3 only. But for white noise coefficients, only element 1 is nonzero. It can be

Downloaded 03 May 2010 to 171.66.16.31. Redistribution subject to ASME license or copyright; see http://www.asme.org/terms/Terms_Use.cfm

deduced by induction that, of all the elementary diagrams composing $R_{x_i x_i}(\tau)$, only the diagram which does not contain elements 2 or 3 is nonzero. This component can be evaluated analytically (see Fig. 11).

The general expression for $R_{x_i x_i}(\tau)$ is now apparent from Fig. 11 or equivalently from equations (28) and (29):

$$R_{x_i x_i}(\tau) = \rho(\tau)\Big(\sum_{j=0}^{N-1} D_j m_j^0\Big)\Big(\sum_{j=0}^{N-1} D_j n_j^0\Big)^{i-1}. \tag{30}$$

The final expression for $R_{xx}(\tau)$ is obtained by performing the infinite summation over the index i provided the series converges. The convergence condition for the series of autocorrelations is

$$\sum_{j=0}^{N-1} D_j n_j^0 < 1. \tag{31}$$

Using the identity

$$\sum_{i=0}^{\infty}\Big(\sum_{j=0}^{N-1} D_j n_j^0\Big)^{i-1} = \frac{1}{1-\sum_{j=0}^{N-1} D_j n_j^0}, \tag{32}$$

and the definition

$$m_j = m_j^0 \sum_{i=0}^{\infty}\Big(\sum_{j=0}^{N-1} D_j n_j^0\Big)^{i-1}, \tag{33}$$

one has

$$R_{xx}(\tau) = R_{x_0 x_0}(\tau) + \rho(\tau)\sum_{j=0}^{N-1} D_j m_j. \tag{34}$$

This result is identical to that of the companion paper (Benaroya and Rehak, 1989).

5.2 Interpretation of Results. Some insight is obtained by comparing equation (34) to the governing equation (1) in the form:

$$x(t) = x_0(t) - \sum_{j=0}^{N-1} b_j(t)x^{(j)}(t). \tag{35}$$

By comparing these two equations term by term, the following correspondence between random processes and their autocorrelations can be observed:

$$x(t) \leftrightarrow R_{xx}(\tau)$$

$$x_0(t) \leftrightarrow R_{x_0 x_0}(\tau)$$

$$b_j(t)x^{(j)}(t) \leftrightarrow \rho(\tau)D_j m_j.$$

It is recalled that $\rho(\tau)$ is a particular case of $R_{x_0 x_0}(\tau)$ when the external forcing function $F(t)$ is white noise of intensity 1. This indicates that the parametric excitation $b_j(t)x^{(j)}(t)$ acts as an external white noise forcing function on the deterministic system with effective variance $D_j m_j$.

Equation (31) gives the criterion for convergence of the series. A comparison with the stability condition in the companion paper (Benaroya and Rehak, 1989) reveals that these two conditions are identical. Therefore, convergence of the series of the autocorrelation (or spectral density) and stability in the mean square sense are equivalent.

5.3 Statistical Correlation of Response and Coefficients. Using the expansion method, we presently prove that the response (and its derivatives $x^{(j)}(t)$) and the coefficients are uncorrelated when these are white noise processes. This assumption was made in the companion paper (Benaroya and Rehak, 1989).

The response is expanded according to equation (2), and it is demonstrated by induction that each term of the series $x_i^{(j)}(t)$ is uncorrelated from $b_i(t)$, i.e.,

$$\langle x_i^{(j)}(t_0)x_i^{(j)}(t_0^\wedge)b_j(t_0)b_j(t_0^\wedge)\rangle$$

$$= \langle x_i^{(j)}(t_0)x_i^{(j)}(t_0^\wedge)\rangle\langle b_j(t_0)b_j(t_0^\wedge)\rangle. \tag{36}$$

Starting with $i=0$, equation (3) indicates that $x_0^{(j)}(t)$ depends only on $F(t)$, and is therefore uncorrelated with $b_j(t)$. Equation (36) is valid when $i=0$.

We now wish to verify equation (36) when $i=1$. Using equation (17) we have

$$\langle x_1^{(j)}(t_0)x_1^{(j)}(t_0^\wedge)b_j(t_0)b_j(t_0^\wedge)\rangle$$

$$= \int_{-\infty}^{\infty} dt_1 h(t_0-t_1)\int_{-\infty}^{\infty} dt_1^\wedge h(t_0^\wedge - t_1^\wedge)\sum_{j=0}^{N-1}$$

$$\langle x_0^{(j)}(t_1)x_0^{(j)}(t_1^\wedge)b_j(t_1)b_j(t_1^\wedge)b_j(t_0)b_j(t_0^\wedge)\rangle. \tag{37}$$

As in the derivation of $R_{x_2 x_2}(\tau)$, it can be verified that only one term, $\langle b_j(t_1)b_j(t_1^\wedge)\rangle\ \langle b_j(t_0)b_j(t_0^\wedge)\rangle$, amounts to a nonzero contribution. Therefore,

$$\langle x_0^{(j)}(t_1)x_0^{(j)}(t_1^\wedge)b_j(t_1)b_j(t_1^\wedge)b_j(t_0)b_j(t_0^\wedge)\rangle$$

$$= \langle x_0^{(j)}(t_1)x_0^{(j)}(t_1^\wedge)\rangle\langle b_j(t_1)b_j(t_1^\wedge)\rangle\langle b_j(t_0)b_j(t_0^\wedge)\rangle. \tag{38}$$

Substituting the above in equation (37), taking the term $\langle b_j(t_0)b_j(t_0^\wedge)\rangle$ out of the integral, we obtain

$$\langle x_1^{(j)}(t_0)x_1^{(j)}(t_0^\wedge)b_j(t_0)b_j(t_0^\wedge)\rangle = \langle b_j(t_0)b_j(t_0^\wedge)\rangle$$

$$\int_{-\infty}^{\infty} dt_1 h(t_0-t_1)\int_{-\infty}^{\infty} dt_1^\wedge h(t_0^\wedge - t_1^\wedge)\sum_{j=0}^{N-1}$$

$$\langle x_0^{(j)}(t_1)x_0^{(j)}(t_1^\wedge)\rangle\langle b_j(t_1)b_j(t_1^\wedge)\rangle. \tag{39}$$

Rewriting $\langle x_0^{(j)}(t_1)x_0^{(j)}(t_1^\wedge)\rangle\ \langle b_j(t_1)b_j(t_1^\wedge)\rangle$ as $\langle x_0^{(j)}(t_1)x_0^{(j)}(t_1^\wedge)b_j(t_1)b_j(t_1^\wedge)\rangle$ in equation (39), we obtain equation (36) with $i=1$ when the definition of $x_1(t)$ is invoked.

This procedure is generalized to $x_i^{(j)}(t)$ where the relevant expression contains a moment of order $2i$ in $b_j(t)$, which can be expressed as a product of second-order moments. As only one of those products contributes to the final expression, it can be verified that equation (36) holds for any value of i. Upon summation with respect to i, equation (36) is also correct when $x(t)$ is used instead of $x_i(t)$.

6 Conclusions

The expansion method provides a formal solution for the autocorrelation and spectral density functions of the response. In practice, it is possible to evaluate only terms containing second-order moments in $b_j(t)$, only because of the complexity of higher order terms. However, if the parameters governing the convergence of the series (variances of the random coefficients in particular) are small, then considering only one correction term is an acceptable approximation since terms of order i are multiplied by variances to the power $2i$. Thus, higher order corrections become small by comparison. The complete theoretical equations defining the general term of the series are nevertheless available. These may prove to be useful if assumptions such as "weak correlations" are possible.

The case where the coefficients are white noise is an example where it is possible to evaluate the general term of the autocorrelation series. With the help of Feynman diagrams, the expansion method yields the analytic expression of the companion paper (Benaroya and Rehak, 1989). This method is also used to prove that the response and the coefficients are uncorrelated when these are white noise processes.

Downloaded 03 May 2010 to 171.66.16.31. Redistribution subject to ASME license or copyright; see http://www.asme.org/terms/Terms_Use.cfm

Acknowledgments

This paper has been written as part of research sponsored by the Air Force Office of Scientific Research (AFSC), under Contract No. F49620-84-C-0009. Dr. Anthony Amos of the Air Force Office of Scientific Research is sincerely thanked for financial support as well as for his encouragement of this continuing effort. Prof. F. DiMaggio, Dr. G. Goldstein, and Prof. J. Wright are thanked for their discussions regarding this paper.

References

Benaroya, H., and Rehak, M., 1989, "Response and Stability of a Random Differential Equation, Part 1: Moment Equation Method," Weidlinger Associates Technical Report No. 6, Air Force Office of Scientific Research, Contract No. F4620-84-C-0009, ASME JOURNAL OF APPLIED MECHANICS, Vol. 55, pp. 192–195.

Dence, D., and Spence, J. E., 1973, "Wave Propagation in Random Anisotropic Media," *Probabilistic Methods in Applied Mathematics*, Vol. 3, Academic Press, New York.

Feynman, R., 1962, *Quantum Electrodynamics*, W. A. Benjamin, Inc.

Rehak, M., and Benaroya, H., 1988, "Simulation of a Random Differential Equation," *AIAA Journal of Guidance, Control, and Dynamics*, Vol. 11, No. 2, pp. 173–178.

Rehak, M., and Benaroya, H., 1987, "Stationarity and Stochastic Differential Equations," ASME JOURNAL OF APPLIED MECHANICS, in progress.

Samuels, J. C., and Eringen, A., 1959, "On Stochastic Linear Systems," *J. Mathematics and Physics*, Vol. 38, pp. 83–103.

Downloaded 03 May 2010 to 171.66.16.31. Redistribution subject to ASME license or copyright; see http://www.asme.org/terms/Terms_Use.cfm

Probability Distribution of the Eigenvalues of the Random String Equation

R. N. Iyengar
Professor.

C. S. Manohar
Research Scholar.

Department of Civil Engineering,
Indian Institute of Science,
Bangalore 560 012, India

The probability distribution of the eigenvalues of a second-order stochastic boundary value problem is considered. The solution is characterized in terms of the zeros of an associated initial value problem. It is further shown that the probability distribution is related to the solution of a first-order nonlinear stochastic differential equation. Solutions of this equation based on the theory of Markov processes and also on the closure approximation are presented. A string with stochastic mass distribution is considered as an example for numerical work. The theoretical probability distribution functions are compared with digital simulation results. The comparison is found to be reasonably good.

Introduction

Some amount of uncertainty is unavoidable in the determination of the mass and stiffness of engineering structures. If one wants to study the effect of uncertainties in structural parameters on the system response, it is necessary to model the system statistically. Consequently, eigenvalue problems such as the determination of the natural frequencies or the buckling loads become probabilistic in nature. This means that the eigenvalues are no longer deterministic numbers but are now random variables. Several attempts have been made in the past to tackle such problems. Scheidt and Purkert (1983) in their book on random eigenvalue problems have presented an extensive review of the topic along with a useful bibliography. Significant contributions to the field have been made by Boyce and his co-workers (1970, 1985). Several techniques including variational methods, perturbation methods, iterative methods, closure techniques, etc., have been studied by Boyce (1970). In general, these methods are capable of including correlation among random quantities and lead to bounds on the moments of the eigenvalues. Scheidt and Purkert (1983) have chiefly dealt with expansion methods to compute the moments of the eigenvalues and the eigenfunctions of random operators. Also, when the random quantities are weakly correlated, they show that the limiting probability distribution function (PDF) of the eigenvalues and eigenfunctions, as the correlation length goes to zero, tend to be Gaussian. Soong and Bogdanoff (1963) have demonstrated the sensitivity of higher natural frequencies of a linear chain to system disorders. They have used an approach based on transfer matrix scheme coupled with the perturbation technique. Based on the concept of mean square systems developed earlier by Bogdanoff (1965) and Schiff and Bogdanoff (1972) have suggested a simple estimator for the upper bound of the standard deviation of the natural frequencies of complex systems with small disorders. Hoshiya and Shah (1971) have employed a perturbation scheme to study the free vibration of stochastic beam columns. A similar technique is used by Huang (1982) to estimate the natural frequencies of a random periodic structure. Monte Carlo simulation studies have been carried out to examine the limitation of the perturbation methods by Shinouzuka and Astill (1971) for the case of beam columns. The variance of the eigenvalues of a random matrix can be estimated by perturbing the random eigenvalue about the mean matrix eigenvalues. Such an approach, with several variations, has been used by Collins and Thomson (1969), Hassleman and Hart (1972), and Hart (1973) for finding the eigenvalues of large scale disordered systems. Many of these studies primarily aim at estimating the first two moments of the eigenvalues and often end up establishing bounds on them.

In the present study we address ourselves to the problem of the eigenvalues of a string with stochastic properties. Previously, Iyengar and Athreya (1975) have considered this problem. They have shown that the problem can be converted into an initial value problem. This allows one to bring in the powerful concepts of diffusion processes to derive a differential equation for the PDF of the eigenvalues. This was, however, only a formal equation in the sense that no solution could be obtained. The present paper is an extension of the above work to study a few cases where the solutions to the PDF of eigenvalues can be obtained and compared with digital simulations.

The Problem

The second-order eigenvalue problem in structural mechanics arises in the vibration of strings, shear beams, soil layers, and bars with stochastic properties. In general, one has to find the solution of the boundary value problem

Contributed by the Applied Mechanics Division of THE AMERICAN SOCIETY OF MECHANICAL ENGINEERS for publication in the JOURNAL OF APPLIED MECHANICS.

Discussion on this paper should be addressed to the Editorial Department, ASME, United Engineering Center, 345 East 47th Street, New York, N.Y. 10017, and will be accepted until two months after final publication of the paper itself in the JOURNAL OF APPLIED MECHANICS. Manuscript received by ASME Applied Mechanics Division, February 12, 1987; final revision, May 24, 1988.

Copyright © 1989 by ASME

Downloaded 03 May 2010 to 171.66.16.31. Redistribution subject to ASME license or copyright; see http://www.asme.org/terms/Terms_Use.cfm

$$\frac{d}{dx}\left[(1+\delta g(x))\frac{dy}{dx}\right]+\lambda^2[1+\epsilon f(x)]y=0. \tag{1}$$

$$y(0)=y(1)=0. \tag{2}$$

Here, g and f are known random processes which are bounded in mean square sense and δ and ϵ are parameters such that $(1+\delta g)$ and $(1+\epsilon f)$ are positive. λ is the associated eigenvalue, the distribution of which is the prime concern here. Even when g and f arise as Markov processes, one cannot immediately use Ito calculus to further analyze equation (1). First, it is necessary to pose the problem as an initial value problem so as to write down a diffusion equation for the probabilities.

Initial Value Approach

We consider equation (1) with the initial conditions

$$y(0)=0;\ y'(0)=1 \tag{3}$$

Now, from Sturm-Liouville theory if for any given λ, $y^*(x,\lambda)$ is the solution of equations (1) and (3). Then the zeros of $y^*(x,\lambda)$ denoted by $Z_n(\lambda)$ are countable and nondecreasing in λ. Also those λ's for which

$$Z_n(\lambda)=1 \tag{4}$$

are the eigenvalues associated with equations (1) and (2). At this stage it would be convenient to introduce an amplitude and a phase through the equations.

$$y=r\sin\phi \tag{5}$$

$$(1+\delta g)\frac{dy}{dx}=r\lambda\cos\phi. \tag{6}$$

The equation for r and ϕ get uncoupled resulting in

$$\frac{d\phi}{dx}=\lambda\left[\frac{\cos^2\phi}{(1+\delta g)}+(1+\epsilon f)\sin^2\phi\right] \tag{7}$$

$$\frac{dr}{dx}=0.5\ \lambda r\ \sin 2\phi\left[\frac{1}{(1+\delta g)}-(1+\epsilon f)\right] \tag{8}$$

with initial conditions

$$\phi(0)=0;\ r(0)=1. \tag{9}$$

It is observed that the zeros of $y^*(x,\lambda)$ are the roots of

$$\phi(x,\lambda)=n\pi \tag{10}$$

and, hence, $Z_n(\lambda)$ are the random variables satisfying

$$\phi[Z_n(\lambda),\lambda]=n\pi. \tag{11}$$

It is evident from equation (7) that ϕ is nondecreasing in x and since $Z_n(\lambda)$ is nonincreasing in λ, the following string of probability statements are true:

$$\begin{aligned}P[\lambda_n \leqq \lambda] &= P[Z_n(\lambda) \leqq 1]\\ &= P[\phi(Z_n(\lambda),\lambda) \leqq \phi(1,\lambda)]\\ &= P[n\pi \leqq \phi(1,\lambda)].\end{aligned} \tag{12}$$

Thus, in order to find the PDF of λ_n, it is sufficient to solve equations (7) and (9) for every value of λ.

It may be mentioned here that the idea of computing the eigenvalues of Sturm-Liouville equations via a phase function as in equation (7) has been used previously by Bailey (1966) in the context of deterministic problems.

For further work, the phase process is redefined as

$$\phi(x,\lambda)=\theta(x,\lambda)+\lambda x. \tag{13}$$

Accordingly, equations (7) and (9) become, respectively,

$$\frac{d\theta}{dx}=\lambda\left[\frac{\cos^2(\theta+\lambda x)}{(1+\delta g)}+(1+\epsilon f)\sin^2(\theta+\lambda x)-1\right] \tag{14}$$

$$\theta(0)=0. \tag{15}$$

It may be noted that with $\delta=0$ and $\epsilon=0$, one gets $\theta=0$ and thus $\phi=\lambda x$, which is the solution for the deterministic case. Thus, $\theta(x)$ may be interpreted as the change in ϕ due to randomness in the system. Further, it is clear that whenever f and g arise as filtered white noise processes, $\theta(x)$ is a Markov process and, hence, the Fokker-Planck equation for the joint probability density function can be obtained. For example, let $\delta=0, f=w^2$ and

$$\frac{dw}{dx}+\alpha w=\xi(x) \tag{16}$$

where $\xi(x)$ is a stationary white noise process with strength I. The Fokker-Planck equation for the transition probability density function $q(\theta w, x\,|\theta_o, w_o, x_o)$ is

$$\frac{\partial q}{\partial x}=-\epsilon\lambda w^2\frac{\partial}{\partial\theta}[\sin^2(\theta+\lambda x)q] + \alpha\frac{\partial}{\partial w}(wq)+0.5I\frac{\partial^2 q}{\partial w^2}. \tag{17}$$

The knowledge of q at $x=1$ for any λ will lead to the distribution function for the random eigenvalues through equation (12). However, the solution of the above equation, even for simple cases, is extremely difficult.

A Special Case

When f and g are such that

$$\frac{1}{(1+\delta g)}=1+\epsilon f \tag{18}$$

the problem is simple. It follows that

$$\frac{d\theta}{dx}=\epsilon\lambda f \tag{19}$$

and, hence,

$$\theta(1,\lambda)=\epsilon\lambda\int_o^1 f(x)dx. \tag{20}$$

Equation (18) implies that the mass and the stiffness are inversely proportional to each other. Even though this case may not be physically very significant, this, perhaps, is the only case wherein a closed-form solution for the probability density of the eigenvalues is possible. Thus, the effort is reduced to that of finding the PDF of the integral of the random process $f(x)$. Further, for mathematical expedience, if $f(x)$ is taken as the square of a stationary Gaussian random process, the Karhunen-Loeve expansion can be used, following Slepian (1958), to find the PDF of $\theta(1,\lambda)$. Otherwise a quick and good approximation to $p(\theta;\lambda)$, the probability density function of $\theta(1,\lambda)$, can be obtained in terms of a Lagurre series as shown by Deutsch (1962). This gives

$$p(\theta,\lambda)=\frac{\beta}{\sigma^2\Gamma(\beta^2/\sigma^2)}(\beta\theta/\sigma^2)^{\left(\frac{\beta^2}{\sigma^2}-1\right)}\exp(-\beta\theta/\sigma^2). \tag{21}$$

This is a gamma density function with parameters β^2/σ^2 and β/σ^2. Here, β and σ^2 are the mean and the variance of $\theta(1,\lambda)$, which are in terms of the autocorrelation function of $f(x)$. From equation (12) the PDF of the nth eigenvalue is given as

$$\begin{aligned}P[\lambda_n \leq \lambda] &= 1-P[\phi(1,\lambda)\leq n\pi]\\ &= 1-P[\{\theta(1,\lambda)+\lambda\}\leq n\pi]\\ &= 1-\int_o^{(n\pi-\lambda)} p(\theta;\lambda)d\theta.\end{aligned} \tag{22}$$

Downloaded 03 May 2010 to 171.66.16.31. Redistribution subject to ASME license or copyright; see http://www.asme.org/terms/Terms_Use.cfm

Discrete Markov Chain

For further work, it will be assumed that $\delta = 0$. This corresponds to a string with only the mass being randomly distributed along the length. The initial value problem to be solved reduces to

$$\frac{d\theta}{dx} = \epsilon\lambda f(x)\sin^2(\theta + \lambda x) \tag{23}$$

$$\theta(0) = 0. \tag{24}$$

In vibration problems it is common practice to discretize a continuous system. In the present context this would amount to rewriting the above equation as

$$\theta_{i+1} = \theta_i + \epsilon\lambda f_i \Delta \sin^2(\theta_i + i\lambda\Delta);\ (i = 1,2,\ \ldots\ ,N-1). \tag{25}$$

Here f_i denotes $f(x_i) = f(i\Delta)$. Since our interest is at $x = 1$, the discretization will be done such that $N\Delta = 1$. If $f(x)$ has short correlation length, much less than Δ, then it is reasonable to assume that f_i is a sequence of independent random variables. Now θ_{i+1} depends on θ_i and f_i and, hence, is a discrete parameter Markov chain. If f_i is a discrete random variable, θ_i becomes a Markov chain with finite number of states. As before, the aim is to find the PDF of θ_N for any value of λ. Denoting by D_i the set of values taken by the random variable θ_i and noting that $P[\theta_o = 0] = 1$, the following can be written based on the Kolmogorov-Smoulchowski equation

$$P[\theta_i = k_i; k_i \epsilon D_i] = \sum_{k_{i-1}\epsilon D_{i-1}} P[\theta_i = k_i \mid \theta_{i-1}$$

$$= k_{i-1}]P[\theta_{i-1} = k_{i-1}] = \sum_{k_{i-1}\epsilon D_{i-1}} \cdots \sum_{k_1 \epsilon D_1} P[\theta_i = k_i \mid \theta_{i-1}$$

$$= k_{i-1}]. \ . \ . P[\theta_2 = k_2 \mid \theta_1 = k_1]P[\theta_1 = k_1]. \tag{26}$$

Starting with $i = 2$, the sets D_i and $P[\theta_i = k_i]$ can be recursively computed using equation (26) for $i = 2,3,\ \ldots\ ,N$.

A Closure Approximation

When the exact PDF is difficult to obtain one likes to obtain at least the moments. With nonlinear equations, even this is quite difficult. This is due to the fact that the lower moments get linked up with still unknown higher order moments. This is the well-known closure problem. In the literature there are a variety of ad hoc approaches available for closing the hierarchy of moment equations. A simple closure approximation can be obtained in the present problem by taking the process $\theta(x)$ to be Rayleigh distributed as

$$p(\theta;x) = (\theta/c^2)\exp(-0.5\theta^2/c^2) \tag{27}$$

with an unknown parameter $c(x)$. Further at the same point x, the process $f(x)$ and $\theta(x)$ are assumed to be statistically independent. Now taking averages throughout on equation (23) we get

$$\frac{d\langle\theta\rangle}{dx} = \epsilon\lambda\langle f(x)\rangle\langle\sin^2(\theta + \lambda x)\rangle. \tag{28}$$

Since θ is assumed to be Rayleigh distributed, it follows that $\langle\theta\rangle = c(\pi/2)^{1/2}$ and

$$\langle\sin^2(\theta + \lambda x)\rangle = \int_o^\infty \left(\frac{\theta}{c^2}\right)\exp(-0.5\theta^2/c^2)\sin^2(\theta + \lambda x)d\theta. \tag{29}$$

This integral can be further simplified following Gradshteyn and Ryzhik (1980) to get

$$\frac{dc}{dx} = \epsilon\lambda m_f\left[\frac{1}{\sqrt{2\pi}}(1 - \cos 2\lambda x) + \frac{c}{\sqrt{\pi}}\cos 2\lambda x \sum_{k=0}^{\infty} \frac{(-1)^k k!}{(2k+1)!}(2\sqrt{2}c)^{(2k+2)} + c\sin 2\lambda x \exp(-2c^2)\right] \tag{30}$$

$$c(0) = 0. \tag{31}$$

This equation can be solved numerically for all real λ to find $c(1,\lambda)$, which in turn is sufficient to characterize the PDF of $\theta(1,\lambda)$ and through this the PDF of the nth eigenvalue.

Stochastic Averaging

An approximate solution to equation (23) which is valid for small ϵ can be obtained using an asymptotic method due to Stratonovich (1967). For this purpose f is rewritten as

$$f(x) = m_f + \bar{f}(x) \tag{32}$$

Here, m_f is a constant and $\bar{f}(x)$ is a zero-mean stationary random process such that its correlation length is small compared to $1/\epsilon\lambda$. Equation (23) can now be written as

$$\frac{d\theta}{dx} = \epsilon\lambda m_f \sin^2(\theta + \lambda x) + \epsilon\lambda\bar{f}\sin^2(\theta + \lambda x). \tag{33}$$

For small values of ϵ, $\theta(x)$ will be a slowly varying random process. The trigonometric terms present in the right side of the above equation give rise to rapid oscillations of small magnitude in θ. Thus, equation (33) may be approximately replaced by an averaged equation in which these rapid oscillations are suitably eliminated. For this purpose a two-stage averaging procedure as outlined by Stratonovich (1967) can be used. First, the term not containing $\bar{f}$ is replaced by its spatial average over the interval $(0,2\pi/\lambda)$ to get

$$\frac{d\theta}{dx} = 0.5\epsilon\lambda m_f + \epsilon\lambda\bar{f}\sin^2(\theta + \lambda x). \tag{34}$$

Since $\bar{f}$ is a broad band process, θ and $\bar{f}$ in equation (34) are correlated and, as such, $\theta(x)$ is not a Markov process. In the next stage of averaging, which is based on the assumption that the band width of $\bar{f}$ is much greater than that of θ, equation (34) is replaced in an asymptotic sense such that $\theta(x)$ can be approximated by a Markov process. This procedure is widely used in random vibration studies and the various applications are well documented in a review by Roberts and Spanos (1986). The new equation corresponding to equation (34) for further analysis is found to be

$$\frac{d\theta}{dx} = A + BW(x) \tag{35}$$

where

$$\langle W(x_1)W(x_2)\rangle = \delta(x_1 - x_2)$$

$$A = 0.5\epsilon\lambda m_f - 0.25\epsilon^2\lambda^2\gamma$$

$$B^2 = 0.125\epsilon^2\lambda^2[2.0S_f(0) + S_f(2\lambda)]$$

$$\gamma = \int_o^\infty R_f(x)\sin 2\lambda x\, dx \tag{36–39}$$

Here S_f and R_f are, respectively, the power spectral density and autocorrelation functions of the random process $\bar{f}(x)$. It follows from equation (35) that $\theta(1,\lambda)$ is a Gaussian random variable with mean A and variance B^2. Accordingly, the PDF of λ_n is given by

$$P[\lambda_n \le \lambda] = 1 - P[\theta(1,\lambda) \le n\pi - \lambda]$$

$$= 0.5 - \mathrm{erf}[(n\pi - \lambda - A)/B]. \tag{40}$$

Downloaded 03 May 2010 to 171.66.16.31. Redistribution subject to ASME license or copyright; see http://www.asme.org/terms/Terms_Use.cfm

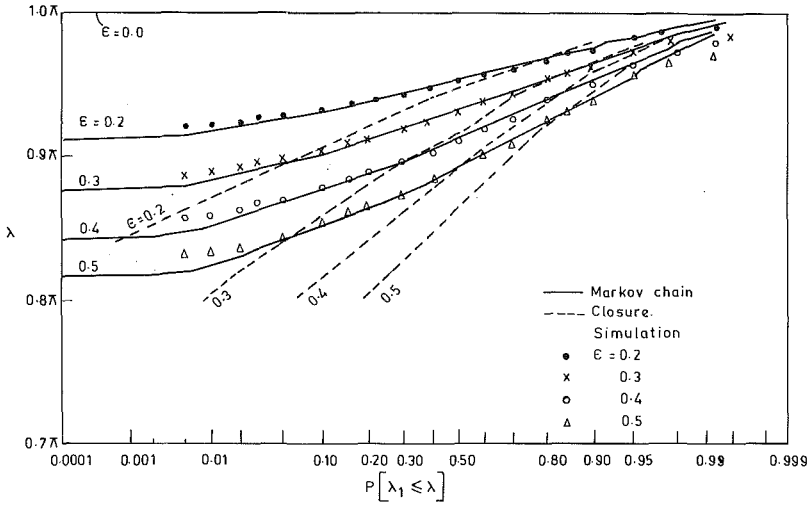


Fig. 1 Probability distribution of the first eigenvalue: example 1

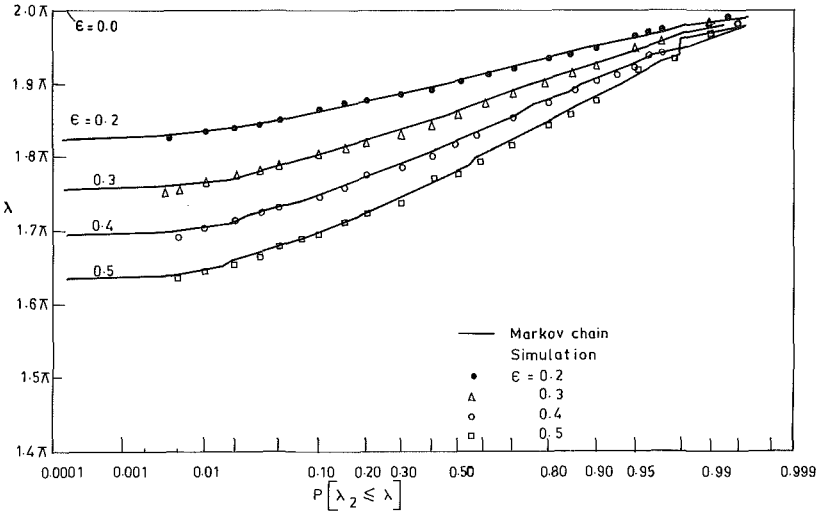


Fig. 2 Probability distribution of the second eigenvalue: example 1

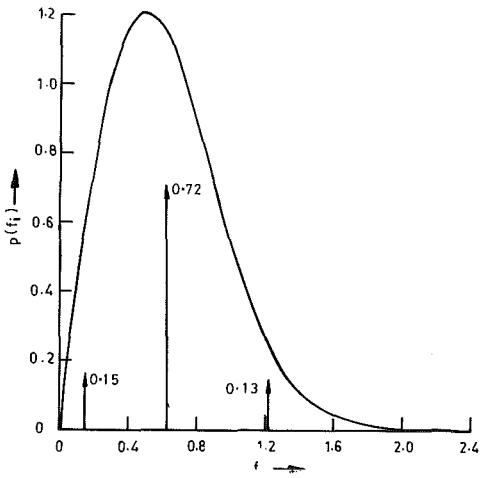


Fig. 3 Discretization of state space of Rayleigh random variable: example 2

Numerical Results

Limited numerical results have been generated to illustrate the above theoretical results. First the string is divided into ten divisions in ($0 \leqq x \leqq 1$) with $N = 10$. Two cases are considered for the process $f(x)$.

Example 1: $f(x)$ is a (0,1) process with equal probability, varying over the parameter index $i = 1,2, \ldots ,10$. The distribution function for the first two eigenvalues of the string are obtained from equation (12) and shown in Figs. 1 and 2. The mean of $f(x)$ in this case is $m_f = 0.5$. With this the solution of equation (30) yields the closure approximation which is also shown in these figures. These results are further compared with the digital simulation results obtained by taking a ten term Galerkin series solution

$$y(x) = \sum_{j=1}^{10} a_j \sin j\pi x. \tag{41}$$

For every sample of $f(x)$ this leads to a sample realization of the eigenvalues and eigenfunctions. Two hundred such samples are obtained for the first two eigenvalues to construct the probability distribution functions which are shown in Figs. 1 and 2 for different values of ϵ.

Example 2: f_i is distributed as a Rayleigh variable

$$p(f_i) = (f_i/a^2)\exp(-0.5f_i^2/a^2). \tag{42}$$

This case is theoretically amenable for a solution as per equation (25). However, one has to evaluate multiple integrals which become cumbersome. On the other hand, a simple discretization of the probability density function of the variable f_i to postulate a finite number of states can be done as

Downloaded 03 May 2010 to 171.66.16.31. Redistribution subject to ASME license or copyright; see http://www.asme.org/terms/Terms_Use.cfm

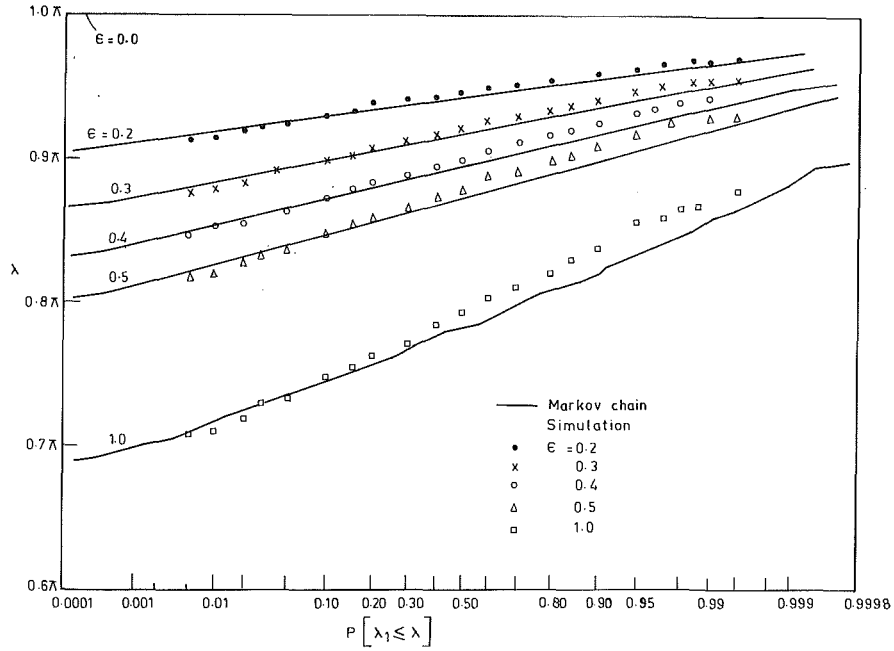


Fig. 4 Probability distribution of the first eigenvalue: example 2

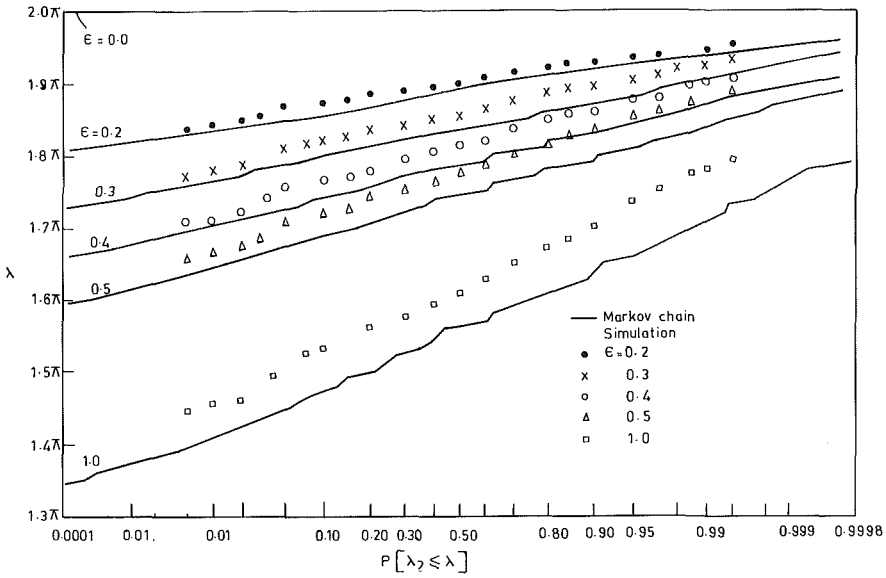


Fig. 5 Probability distribution of the second eigenvalue: example 2

depicted in Fig. 3. Here, for $a = 0.5$, these are defined through the relation

$$P[f_i = 0.15] = 0.15$$

$$P[f_i = 0.62] = 0.72$$

$$P[f_i = 1.21] = 0.13; (i = 1,2, \ldots, N = 9). \quad (43\text{-}45)$$

It may be mentioned here that this discretized random variable and the random variable in equation (42) have nearly the same mean and variance. The corresponding PDF of the first two eigenvalues through the Markov chain formulation are compared in Figs. 4 and 5 with a 200 sample numerical simulation using equation (41). In the digital solution the actual Rayleigh density function is used without discretizing the state space.

Discussion and Conclusions

The eigenvalue problem of a string with random mass and stiffness distribution has remained unsolved. In the present study, the main thrust has been, essentially, to consider particular kinds of uncertainties which would be amenable for study through the techniques of Markov processes and chains. Thus, it is shown that when the aforementioned parameters are filtered white noise processes, the eigenvalue probabilities can be characterized indirectly, through an associated Fokker-Planck equation. However, even with simple process models an exact solution of this equation looks unlikely. There are two alternative approaches available. The first is to try to solve the Fokker-Planck equation approximately through a numerical discretization scheme. The second approach is to discretize the input process and the domain of interest so as to gain the advantage of dealing with a discrete Markov chain rather than a continuous process. The latter approximation has been adopted in the present work. The theoretical results and the results of digital simulation of the problem using 200 samples, compare very well even for large values of ϵ. The simulation has been done by solving every sample problem through the Galerkin procedure. It is noted that the simulation

Downloaded 03 May 2010 to 171.66.16.31. Redistribution subject to ASME license or copyright; see http://www.asme.org/terms/Terms_Use.cfm

does not require the discretization of either the state space or the parameter space. Thus, it can be expected that the discretization adopted in the theoretical solution will not influence the probability distribution of the eigenvalue.

The closure approximation is an ad hoc approach for arriving at closed equations for the moments of the variables of interest. Here equation (27) is such an ad hoc probability density function for θ. This immediately leads to equation (30), which is a nonlinear equation for the parameter $c(x)$. In the illustrative example this equation has been solved numerically using a fourth-order Runge-Kutta method. The infinite series that appears in the equation was found to converge with ten terms. As can be seen from the results of Fig. 1 for the first eigenvalue, the present closure solution is a poor approximation.

A limitation of the Markov chain approach is that autocorrelation in the mass variables cannot be effectively considered. This can be overcome by the stochastic averaging technique. But a penalty is paid by getting a Gaussian approximation to the phase process $\theta(x)$. This would mean that there will be a small but finite probability of negative $\theta(x)$ which, as per equation (23) for positive $f(x)$, is inadmissible.

In conclusion, it is observed that the Markov process formulation is a very powerful approach for studying the random eigenvalue problem of a string. Further extension to more complicated systems like a chain with random stiffness and mass and beams is currently under investigation.

References

Bailey, P. B., 1966, "Sturm-Liouville Eigenvalues Via a Phase Function," *SIAM Journal of Applied Mathematics*, Vol. 14, pp. 242–249.

Bogdanoff, J. L., 1965, "Mean Square Approximate Systems and Their Application in Estimating Response in Complex Disordered Linear Systems," *Journal of Accoustical Society of America*, Vol. 38, pp. 244–252.

Boyce, W., 1970, "Random Eigenvalue Problems," *Probabilistic Methods in Applied Mathematics*, Vol. 2, A. T. Bharucha Reid, ed., Academic Press, New York, pp. 1–73.

Boyce, W., and Xia Ning-Mao, 1985, "Upper Bounds for the Means of Eigenvalues of Random Boundary Value Problems with Weakly Correlated Coefficients," *Quarterly of Applied Mathematics*, Vol. 43, pp. 435–454.

Collins, J. D., and Thomson, W. T., 1969, "The Eigenvalue Problem for Structural Systems with Statistical Properties," *AIAA Journal*, Vol. 7, pp. 642–649.

Deutsch, R., 1962, *Nonlinear Transformations of Random Processes*, Prentice-Hall Inc., Englewood Cliffs, N.J., 1962.

Gradshteyn, I. S., and Ryzhik, I. M., 1980, *Table of Integrals, Series and Products*, Academic Press, New York.

Hart, G. C., 1973, "Eigenvalue Uncertainty in Stressed Structures," *Journal of Engineering Mechanics Division*, ASCE, Vol. 98, pp. 561–579.

Hassleman, T. K., and Hart, G. C., 1972, "Model Analysis of Random Structural Systems," *Journal of Engineering Mechanics Division*, ASCE, Vol. 98, pp. 561–579.

Hoshiya, M., and Shah, H. C., 1971, "Free Vibration of Stochastic Beam Column," *Journal of Engineering Mechanics Division*, ASCE, Vol. 97, pp. 1239–1255.

Huang, W., 1982, "Vibration of Some Structures with Random Parameters," *AIAA Journal*, Vol. 20, pp. 1001–1008.

Iyengar, R. N., and Athreya, K. B., 1975, "A Diffusion Process Approach to a Random Eigenvalue Problem," *Journal of Indian Institute of Science*, Vol. 57, pp. 185–191.

Roberts, J. B., and Spanos, P. D., 1986, "Stochastic Averaging: An Approximate Method of Solving Random Vibration Problems," Invited Review No. 1, *International Journal of Nonlinear Mechanics*, Vol. 21, pp. 111–134.

Scheidt, J., and Purkert, G. M., 1983, *Random Eigenvalue Problems*, North Holland, New York.

Schiff, A. J., and Bogdanoff, J. L., 1972, "An Estimator for the Standard Deviation of a Natural Frequency—Part I," ASME JOURNAL OF APPLIED MECHANICS, Vol. 39, pp. 535–538.

Shinouzuka, M., and Astill, J., 1971, "Random Eigenvalue Problems in Structural Analysis," AIAA 9th Aerospace Sciences Meeting, No. 71-149, New York.

Slepian, D., 1958, "Fluctuation of Random Noise Power," *The Bell System Technical Journal*, Vol. 37, pp. 163–184.

Soong, T. T., and Bogdanoff, J. L., 1963, "On the Natural Frequencies of a Disordered Linear Chain of N-Degree of Freedom," *International Journal of Mechanical Science*, Vol. 5, pp. 237–265.

Stratonovich, R. L., 1967, *Topics in the Theory of Random Noise*, Vol. 2, Gordon and Breach, New York.

Downloaded 03 May 2010 to 171.66.16.31. Redistribution subject to ASME license or copyright; see http://www.asme.org/terms/Terms_Use.cfm

An Integral Variational Equation for Transport Processes in a Moving Fluid[1]

E. S. Geskin
New Jersey Institute of Technology,
Newark, N.J. 07102

An integral variational equation can adequately describe heat, mass, and momentum transfer in a moving chemically reactive fluid. The Euler-Lagrange equations corresponding to the suggested variational equation are identical to the equations of entropy, momentum, angular momentum, and mass balance. The constructed Lagrangian density relates energy change in the system to the work and energy dissipation of the system. For steady-state processes, the Lagrangian density includes convective energy flow through the system boundary, energy dissipation in the system, and work of the system. The proposed variational equation is equivalent to the expansion of the principle of minimum energy dissipation.

Introduction

Variational equations for describing irreversible transport processes in a fluid was suggested by Gyarmati (1970, 1974) and modified by Geskin et al. (1970a, 1970b) and Geskin (1980, 1987). These equations are based on the use of the rate of entropy production and dissipative functions.

The presented paper is concerned with the construction of a more general variational equation applicable to both reversible and irreversible transport processes.

A variational equation describing heat, mass, and momentum transfer in a chemically reactive rotating fluid is suggested. The proposed Lagrangian includes process variables, their material, time and space derivatives, and the rate of entropy production. The substitution of the presented Lagrangian into the Euler-Lagrange equation results in the construction of mass, entropy, and momentum balances. By the use of thermodynamic identities, the physical meaning of this equation is determined and its possible applications are discussed.

Statement of a Variational Problem

The transport processes in a moving, rotational and compressible, chemically-reactive Newtonian fluid can be described by the variational equation

$$\delta\int_V L dV = 0 \tag{1}$$

where Lagrangian density L is given by the relation

$$L = \rho T\frac{ds}{dt} + \Sigma\rho\mu\frac{dc_1}{idt} + \mathbf{v}\cdot\frac{d\mathbf{v}}{dt} + \rho\theta\omega\cdot\frac{d\omega}{dt}$$
$$-\rho\nabla\cdot\mathbf{v} - \rho\mathbf{v}\cdot\mathbf{F} + T\sigma_s + \frac{1}{2}\left(\eta_v - \frac{2}{3}\eta\right)(\nabla\cdot\mathbf{v})^2$$
$$+\frac{1}{2}\eta_r(\nabla\times\mathbf{v} - 2\omega)^2 + \eta[(\nabla\mathbf{v})^s:(\nabla\mathbf{v})^s] + \frac{1}{2}1_{ss}(\nabla T)^2$$
$$+\sum_i 1_{is}(\nabla T)\cdot(\nabla\mu_i) + \frac{1}{2}\sum_{ij}1'_{ij}\mu_i\mu_j$$
$$+\sum_{ij}1_{ij}(\nabla\mu_i)\cdot(\nabla\mu_j). \tag{2}$$

It is assumed that the process variables are fixed at the boundary of the system; coefficients 1_{ij}, $1'_{ij}$, η_v, η and η_r do not depend on Γ and $\nabla\Gamma$ and reciprocal Onsager's equations $1_{ij} = 1_{ji}$, and $1_{si} = 1_{si}$ are valid.

The Derivation of Balance Equations

The Euler-Lagrange equation corresponding to equations (1) and (2) has the form

$$\rho\frac{ds}{dt} - \sigma_s - \nabla\cdot[1_{ss}(\nabla T)] - \nabla\cdot\sum_i[1_{is}(\nabla\mu_i)] = 0 \tag{3}$$

if T is a variable;

$$\rho\frac{dc_i}{dt} + \sum_j 1'_{ij}\mu_j - \nabla\cdot\left[\sum_j 1_{ij}(\nabla\mu_j)\right] - \nabla\cdot[i_{is}(\nabla T)] = 0 \tag{4}$$

if μ is a variable;

$$\rho\frac{d\mathbf{v}}{dt} - \rho\mathbf{F} + \nabla p - \eta\Delta\mathbf{v} - \left(\frac{\eta}{3} + \eta_v\right)\nabla(\nabla\cdot\nu)$$
$$-\eta_r\nabla\times(2\omega - \nabla\times\mathbf{v}) = 0 \tag{5}$$

[1]This paper was presented at the Symposium on Computer-Aided Engineering of Energy Systems during the 1986 Winter Annual Meeting of THE AMERICAN SOCIETY OF MECHANICAL ENGINEERS, Anahiem, Calif.

Contributed by the Applied Mechanics Division of THE AMERICAN SOCIETY OF MECHANICAL ENGINEERS for publication in the JOURNAL OF APPLIED MECHANICS.

Discussion on this paper should be addressed to the Editorial Department, ASME, United Engineering Center, 345 East 47th Street, New York, N.Y. 10017, and will be accepted until two months after final publication of the paper itself in the JOURNAL OF APPLIED MECHANICS. Manuscript received by ASME Applied Mechanics Division, January 27, 1987; final revision, January 20, 1988.

Copyright © 1989 by ASME

Downloaded 03 May 2010 to 171.66.16.31. Redistribution subject to ASME license or copyright; see http://www.asme.org/terms/Terms_Use.cfm

if $\mathbf{v}$ is a variable; and

$$\rho\theta \frac{d\omega}{dt} - 2\eta_r(\nabla \times \mathbf{v} - 2\omega) = 0 \tag{6}$$

if ω is a variable.

In the course of applying the transformation resulting in equations (3)–(6) the time derivatives, rate of entropy production and coefficients η, η_v and η_r are assumed to be constant. To construct equation (5), for example, the Euler–Lagrange equation is presented in the form

$$\frac{\partial L}{\partial v_\beta} - \sum_{\alpha=1}^{3} \frac{\partial}{\partial x_\alpha} \frac{\partial L}{\partial\left(\frac{\partial v_\beta}{\partial x_\alpha}\right)} = 0 \ (\beta = 1,2,3). \tag{7}$$

After transformation we obtain

$$\frac{\partial L}{\partial v_\beta} = \frac{dv_\beta}{dt} - \rho \cdot F_\beta \tag{8}$$

and

$$\sum_{\alpha=1}^{3} \frac{\partial}{\partial x_\alpha} \frac{\partial L}{\partial\left(\frac{\partial v_\beta}{\partial x_\alpha}\right)} = \frac{\partial p}{\partial x_\beta} - \left(\eta_v + \frac{\eta}{3}\right) \frac{\partial}{\partial x_\beta} (\nabla \cdot \mathbf{v})$$
$$- \eta \nabla v_\beta - \eta_r [\nabla \times (2\omega - \nabla \times \mathbf{v})]_\beta \ (\beta = 1,2,3). \tag{9}$$

Constructed relatianships yield equation (5). Constructing equations (3), (4), and (6) is similar.

It is convenient to rewrite equations (3) and (4) in a more conventional form. Using the definition of the thermodynamic fluxes, (Katchalsky and Curran, 1965), we can present the current densities of entropy and mass of substance "i" and the rate of chemical and phase transformation in the form:

$$\mathbf{J}_s = -[1_{ss}(\nabla T) + 1_{si}(\nabla \mu_i)] \tag{10}$$

$$\mathbf{J}_i = -\left[1_{si}(\nabla T) + \sum_{ij} 1_{ij}(\nabla \mu_j)\right] \tag{11}$$

$$\sigma_i = -\sum_j 1'_{ij} \mu_j \tag{12}$$

Substituting (10) into (3) we obtain

$$\rho \frac{ds}{dt} - \sigma_s = -\nabla \cdot \mathbf{J}_s. \tag{13}$$

Equations (10), (11), and (12) yield

$$\rho \frac{dc_i}{dt} - \sigma_i = -\nabla \cdot \mathbf{J}_i. \tag{14}$$

Equations (13) and (14) are the routine expression of the entropy and mass balances while equations (5) and (6) determine the balances of the momentum and angular momentum.

Particular Cases

For different specific processes, equations (2) can be simplified. For example, heat conduction in a homogeneous solid is determined by the Lagrangian density.

$$L = \rho T \frac{\partial s}{\partial t} - T\sigma_s + \frac{1}{2} 1_{ss} (\nabla T)^2. \tag{15}$$

For diffusion in a nonreactive solid, the Lagrangian density has the form

$$L = \rho \sum_i \mu_i \frac{\partial c_i}{\partial t} + \frac{1}{2} \sum_{ij} 1_{ij} (\nabla \mu_i) \cdot (\nabla \mu_j). \tag{16}$$

Isothermal irrotational flow of an one-component, inviscid fluid is given by the equation

$$L = \rho \tilde{v} \cdot \frac{d\mathbf{v}}{dt} - \rho \nabla \cdot \mathbf{v} - \rho \mathbf{v} \cdot \mathbf{F} \tag{17}$$

The equation

$$L = \rho \mathbf{v} \cdot \frac{d\mathbf{v}}{dt} + \eta [(\nabla \mathbf{v})^s : (\nabla \mathbf{v})^s] - \rho \nabla \cdot \mathbf{v} \tag{18}$$

determines the Lagranigan density for the motion of an incompressible and irrotational fluid.

The resulting balance equations can be obtained by the substitution of the above Lagrangian densities in the Euler–Lagrange equation. For example, the Lagrangian (17) results in the equation

Nomenclature

a = specific value of a generalized field variable
A = surface area
c_i = mass concentration of the material "i"
$\frac{d}{dt}$ = material time derivative
e = $u + k$
$\mathbf{F}$ = external force
$\mathbf{J}_i$ = current density of a material "i"
$\mathbf{J}_s$ = entropy current density
k = specific kinetic energy
L = Lagrangian density
l_{ii}, l_{is}, l_{ij}, l'_{ij} = phenomenological coefficients
p = static pressure
s = specific entropy
t = time
T = temperature
u = specific internal energy
$\mathbf{v}$ = velocity
$(\nabla \mathbf{v})^s$ = symmetric part of the tensor $(\nabla \mathbf{v})$
V = volume
w = rate of work per unit of volume
x_α, x_β = space coordinates (α, $\beta = 1,2,3$)
Γ = intensive property
Δ = ∇^2
θ = inertia momentum of the unit of mass
η_r = rotational viscosity coefficient
η_v = volume viscosity coefficient
η = viscosity coefficient
μ = specific chemical potential
ν = specific volume
ρ = density
σ_a = rate of production of property "a" per unit of volume
ω = angular velocity
ψ = specific dissipative function (specific rate of energy dissipation)
ϕ = $w + \psi$

Subscripts

a = property a
i = substance i
j = substance j
m = property m
n = property n
s = entropy
α = projection on axis α
β = projection on axis β

Downloaded 03 May 2010 to 171.66.16.31. Redistribution subject to ASME license or copyright; see http://www.asme.org/terms/Terms_Use.cfm

$$\rho \frac{d\mathbf{v}}{dt} = -\nabla \rho + \mathbf{F} \tag{19}$$

which expresses the momentum balance for invisid fluid flow.

Alternative Expression of the Variational Equation

The expression of the Lagrangian density can be rearranged by the use of the identities

$$\frac{du}{dt} = T\frac{ds}{dt} = \rho \frac{dv}{dt} + \sum_i \mu \frac{dc_i}{dt} \tag{20}$$

$$\frac{dk}{dt} = \mathbf{v} \cdot \frac{d\mathbf{v}}{dt} + \theta\omega \cdot \frac{d\omega}{dt} \tag{21}$$

$$\rho \frac{d\bar{v}}{dt} = \nabla \cdot \mathbf{v} \tag{22}$$

$$\psi = \frac{1}{2}\sum_{n,m} L_{nm}(\nabla\Gamma_n)\cdot(\nabla\Gamma_m) + \frac{1}{2}\sum_{i,j} 1'_{i,j}\mu_i\mu_j \tag{23}$$

$$w = -\mathbf{F}\cdot\bar{\mathbf{v}}. \tag{24}$$

Substituting equations (20)–(24) into equation (2) results in

$$L = \rho \frac{d(u+k)}{dt} + w - T\sigma_s + \Psi. \tag{25}$$

Equation (25) can be written as

$$L = \rho \frac{de}{dt} - T\sigma_s + \phi. \tag{26}$$

The function ϕ determines the thermodynamic cost of the process characterized by the work of the system and the energy dissipation in the system.

Equation (26) relates energy change in a system with energy degradation and work.

Steady-State

The balance of a property "a" is determined as:

$$\rho \frac{da}{dt} = \frac{\partial(\rho a)}{\partial t} + \nabla \cdot (\rho a \mathbf{v}). \tag{27}$$

For steady processes equation (27) takes the form

$$\rho \frac{da}{dt} = \nabla \cdot (a\mathbf{v}\rho) \tag{28}$$

From the Gauss theorem it follows:

$$\int_V \nabla \cdot (\rho a \mathbf{v}) dV = \int_A (\rho a \mathbf{v}) \cdot dA. \tag{29}$$

The right part of equation (29) is a convective flux through a system boundary.

Using equations (27)–(29) we can rewrite equation (26) in the form of

$$\int_V (w - T\sigma_s + \psi) dV + \int_A (\rho e \mathbf{v}) dA = 0. \tag{30}$$

Equations (30) relates the convective energy flow through the system boundary with energy dissipation in the system and work of the system. For steady-state conditions the energy of a system is constant. Consequently, for an adiabatic system we obtain

$$\int_A (pe\mathbf{v}) dA + \int_V w dV = 0 \tag{31}$$

and equation (30) takes the form

$$\delta\left[\int_V (\psi - T\sigma_s) dV\right] = 0. \tag{32}$$

This equation holds also for $\mathbf{v} = 0$. Equation (32) is the expression of the principle of minimum energy dissipation (Gyarmati, 1974).

Concluding Remarks

The suggested variational equation enables us to describe transport processes in a system with constant boundary variables. This equation can be used to derive the element equation needed when applying the finite element method to transport processes. Furthermore, due to the generality of equation (2) its application to a specific transport process merely involves elimination of irrelevant terms in the equation. The proposed technique simplifies the application of the finite element method to coupled processes, to process involving conduction and convection as well as to some other more complicated transport processes.

The proposed technique can also be used for qualitative analysis of systems with fixed boundary variables. In this case several terms of equation (25), such as de/dt, σ_s, ψ and w are to be approximated by simplified functions of process variables and the extreme value of the integral $\int_V L dV$ is to be then estimated. This estimation enables us to determine the proper relationships among process variables.

Acknowledgments

The author would like to express his appreciation of Prof. R. Mazo, University of Oregon, Eugene, Drs. L. Schmidt, National Bureau of Standards for their review of the paper, and Dr. P. Astor, and Mrs. M. Eddings, New Jersey Institute of Technology for the assistance in the preparation of the manuscript.

References

Geskin, E. S., Goldfarb, E. M., and Kotylar, B. D., "A Variational Method of Derivation of Transport Equations for Dissipative Systems with Arbitrary Boundary Conditions," *Russian Journal of Physical Chemistry*, Vol. 44, pp. 543–544.

Geskin, E. S., Goldfarb, E. M., 1970, "Application of the Pontryagin's Principle of the Maximum to Non-Equilibrium Thermodynamics," *Russian Journal of Physical Chemistry*, Vol. 44, p. 1509.

Geskin, E. S., 1987, "A Simplified Variational Technique for Description of Heat and Fluid Flow," *Proceedings of the Fourth International Symposium on the Second Law Analysis of Thermal Systems*, Rome, Italy, M. J. Moran and E. Scuiba, eds., ASME, New York, pp. 25–29.

Gyaramati, I., 1970, *Non-Equilibrium Thermodynamics*, Springer-Verlag, New York, p. 133.

Gyarmati, I., 1974, *Generalization of the Governing Principle of Dissipative Processes to Complex Scalar Fields, Annalen der Physik*, Vol. 7, pp. 18–21.

Katchalsky, A., and Curran, P. F., 1965, *Nonequilibrium Thermodynamics in Biophyics*, Harvard University Press, pp. 60–70.

Downloaded 03 May 2010 to 171.66.16.31. Redistribution subject to ASME license or copyright; see http://www.asme.org/terms/Terms_Use.cfm

Boundary Integral Analysis of the Creeping Flow of Long Bubbles in Capillaries

M. J. Martinez

K. S. Udell

Department of Mechanical Engineering,
University of California,
Berkeley, CA 94720

A boundary integral analysis of the creeping motion of a long inviscid bubble in a liquid filled tube is presented. The effects of interfacial surface tension are included in the stress balance across the liquid-bubble interface. Velocities, stresses, and the bubble profile are obtained as a function of the capillary number. Computed values of the thickness of the liquid film between the bubble and tube wall are in excellent agreement with published experimental measurements. The results are of interest in exposing the role of surface tension in multiphase flow in capillary tubes and porous materials.

Introduction

The flow of bubbles of negligible viscosity in an otherwise liquid filled tube is of interest in understanding two phase flow through porous media. Examples include the immiscible displacement of a viscous oil by a less viscous pusher fluid from within the porous rock of an oil-wet reservoir and the displacement of water from a natural gas reservoir during gas production. Bubble flow in tubes is also relevant to the rheology of emulsions and foams, and to biological fluid mechanics; one of the earliest studies of blood flow involved the flow of air bubbles in a tube as a model for the motion of blood cells in capillaries (Prothero and Burton, 1961).

Experimental studies of bubble flow in capillaries have been conducted by Fairbrother and Stubbs (1935), Taylor (1961), Cox (1962), Goldsmith and Mason (1963), and more recently by Schwartz et al. (1986). Fairbrother and Stubbs were concerned with the use of an indicator bubble flowing in a liquid filled tube as a means of estimating the flow rate. By dimensional analysis, they reasoned that the amount by which the bubble exceeds the average liquid velocity depends on only one dimensionless group, the capillary number, $Ca = \mu U/\gamma$, where μ is the suspending fluid viscosity, U is the bubble speed, and γ is the surface tension. Goldsmith and Mason established experimentally that there is a liquid film of uniform thickness between the leading and trailing menisci and that the film is at rest with respect to the tube.

Bretherton (1961) analyzed the problem for vanishing capillary number using essentially the method of matched asymptotic expansions. He assumed that the bubble profile is of constant curvature except very near the wall where the meniscus is deformed by viscous forces. The transition region between the film of uniform thickness and the undeformed spherical profile was analyzed using lubrication theory. Bretherton also performed experiments to verify his theory and found reasonable agreement for $Ca > 10^{-4}$ but found that the measured values of film thickness exceed the theoretical predictions for smaller capillary number. Schwartz et al. also observed this discrepancy for effectively infinitely long bubbles but surprisingly found agreement with Bretherton's theory for $Ca < 10^{-4}$ and bubbles between 5 and 15 tube diameters long. The explanation of this behavior is, as yet, incomplete. The difficulties with the nonlinear stress conditions on the unknown bubble surface have prevented further analytical analysis and solutions for larger capillary number have been obtained numerically. Shen and Udell (1985) using finite elements and Reinelt (1984) using finite differences have considered the displacement of viscous liquid from a tube by a semi-infinite inviscid bubble, i.e., they consider the leading meniscus only.

In the present study we consider the flow of a long inviscid bubble suspended in a viscous fluid flowing in a tube of uniform cross section using a boundary integral method. Several authors have successfully applied the boundary integral equation method to study the deformation of drops and bubbles (Youngren and Acrivos, 1976; Rallison and Acrivos, 1978; Rallison, 1981) and the deformation of a fluid interface due to an approaching sphere (Lee and Leal, 1982; Geller et al., 1986), both in unbounded fluid. The application to flows with a fluid interface in the presence of bounding walls apparently has not been previously examined. In this problem the interface between the bubble and fluid is a free surface of unknown shape and has constant surface tension along its length. The shape is determined through use of the kinematic condition which identifies the interface as a material surface. This work generalizes that of Shen and Udell (1985) and Reinelt (1984) since we consider both the leading and trailing menisci and also extend the capillary number range to values approaching the infinite capillary number asymptote. The ef-

Contributed by the Applied Mechanics Division for publication in the JOURNAL OF APPLIED MECHANICS.

Discussion on this paper should be addressed to the Editorial Department, ASME, United Engineering Center, 345 East 47th Street, New York, N.Y. 10017, and will be accepted until two months after final publication of the paper itself in the JOURNAL OF APPLIED MECHANICS. Manuscripts received by ASME Applied Mechanics Division, October 29, 1987; final revision, June 18, 1988.

Copyright © 1989 by ASME

Downloaded 03 May 2010 to 171.66.16.31. Redistribution subject to ASME license or copyright; see http://www.asme.org/terms/Terms_Use.cfm

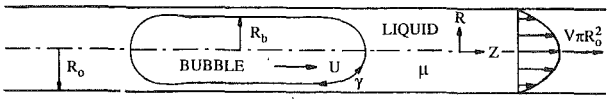


Fig. 1 Steady translation of an inviscid bubble in a liquid filled tube

fects of capillary number on the bubble profiles, flow fields, and pressure drop across the entire bubble are examined.

Problem Statement and Integral Formulation

Consider the creeping motion of a long inviscid bubble translating steadily with speed U in a capillary tube filled with an incompressible fluid of viscosity μ as illustrated in Fig. 1. The interfacial tension, γ, is taken as constant. The suspending fluid preferentially wets the tube wall and flows at constant discharge with a steady Poiseuille distribution far ahead and behind the bubble. The Bond number, the ratio of buoyancy to surface tension forces, is assumed small so that gravity forces can be neglected.

Because the bubble is inviscid, the stress in the bubble is approximated by a uniform pressure p_b. The velocity and pressure for the suspending fluid are governed by continuity and the Stokes approximation for momentum balance;

$$\nabla \cdot \mathbf{u} = 0, \ \nabla \cdot \sigma = \mathbf{0} \tag{1a,b}$$

$$\sigma(\mathbf{u}) = -p\mathbf{I} + \mu[\nabla \mathbf{u} + (\nabla \mathbf{u})^T] \tag{2}$$

where $\mathbf{u}$ is the velocity vector, σ is the Newtonian stress tensor, and p is the pressure. As assumed by Bretherton (1961) and verified experimentally by Goldsmith and Mason (1963), a film of uniform thickness is left on the tube wall between the leading and trailing menisci, the thickness of which is determined by the leading meniscus. Furthermore, the film is at rest with respect to the wall since no tangential stresses can be exerted by the inviscid bubble. Thus, the leading meniscus can be analyzed independently of the trailing meniscus to determine the film thickness, flow field and stresses for a particular capillary number. The analysis of the trailing meniscus can be completed in a separate calculation using the previously determined film thickness left by the leading meniscus for the same capillary number.

In the equations to follow, distances are nondimensionalized by the tube radius R_0, velocity components by the bubble speed U, pressure and viscous stress by $\mu U/R_0$, and time by R_0/U. The only parameter in the problem is the capillary number, $Ca = \mu U/\gamma$, arising from the jump in normal stress across the interface due to the surface tension exerted along the interface. The capillary number is a measure of the ratio of viscous to surface tension forces. Thus, the bubble shape, flow field, and pressure distribution depend only on the capillary number.

In a reference frame fixed to the bubble, the boundary conditions for the leading meniscus are the following:

$$\begin{aligned} \mathbf{u} &= [2r_b^2(1-r^2)-1]\mathbf{e}_z, \text{ as } z \to \infty, \\ \mathbf{u} &= -\mathbf{e}_z, \text{ as } z \to -\infty, \\ \mathbf{u} &= -\mathbf{e}_z, \text{ on } r = 1, \\ \mathbf{t} &= \sigma \cdot \mathbf{n} = \left(\frac{\kappa}{Ca} - p_b\right)\mathbf{n} \text{ on } \Gamma_b, \end{aligned} \tag{3}$$

where r_b is the asymptotic bubble radius, κ is the surface curvature, $\mathbf{n}$ is the outward unit normal with respect to the suspending fluid domain, and Γ_b designates the bubble-liquid interface. The bubble pressure, p_b, is arbitrary and is set to zero in the analysis. The kinematic condition requires that the interface move normal to itself at the local normal velocity,

$$\frac{\partial \mathbf{Y}}{\partial t} \cdot \mathbf{n} = \mathbf{u} \cdot \mathbf{n} \tag{4}$$

where $\mathbf{Y}(\mathbf{X},t)$ is the position vector of a point on the interface and $\mathbf{X}$ is a reference configuration for the bubble. The boundary conditions for the trailing meniscus are the same as above if the conditions at $z = \pm\infty$ are interchanged.

The problem is nonlinear because the interface shape is unknown *a priori* and must be found as part of the solution. The shape enters nonlinearly through the normal stress condition (3) and the film thickness, $1 - r_b$, through the boundary condition for the discharge as $z \to \infty$.

Ladyzhenskaya (1963) gives a solution to (1) and (2) in an arbitrary domain Ω by superposing a distribution of hydrodynamic potentials over the boundary surface, Γ. In normalized variables, the solution is

$$u_k(\mathbf{x}) = \int_\Gamma T_{ik}(\mathbf{x},\mathbf{y}) u_i(\mathbf{y}) d\Gamma(\mathbf{y}) - \int_\Gamma U_{ik}(\mathbf{x},\mathbf{y}) t_i(\mathbf{y}) d\Gamma(\mathbf{y}), \ \mathbf{x} \in \Omega, \tag{5}$$

$$U_{ik}(\mathbf{x},\mathbf{y}) = -\frac{1}{8\pi}\left[\frac{\delta_{ik}}{|\mathbf{x}-\mathbf{y}|} + \frac{(x_i - y_i)(x_k - y_k)}{|\mathbf{x}-\mathbf{y}|^3}\right],$$

$$T_{ik}(\mathbf{x},\mathbf{y}) = -\frac{3}{4\pi}\frac{(x_i - y_i)(x_j - y_j)(x_k - y_k)}{|\mathbf{x}-\mathbf{y}|^5} n_j(\mathbf{y}).$$

The integral equation involves both the velocity, $\mathbf{u}$, and traction, $\mathbf{t} = \sigma \cdot \mathbf{n}$, on the boundary. In a well-posed boundary value problem, either the velocity, traction, or a component of each is specified on the boundary and the other is to be determined. Thus, to effect a solution the identity (5), valid for $\mathbf{x} \in \Omega$, is converted to a boundary integral equation (BIE) by taking the limit as $\mathbf{x}$ tends to a boundary point (Ladyzhenshaya, 1963). The resulting BIE is

$$C_{ki} u_i(\mathbf{x}) + \int_\Gamma T_{ik}(\mathbf{x},\mathbf{y}) u_i(\mathbf{y}) d\Gamma(\mathbf{y}) - \int_\Gamma U_{ik}(\mathbf{x},\mathbf{y}) t_i(\mathbf{y}) d\Gamma(\mathbf{y}) \tag{6}$$

where the tensor $\mathbf{C}$ includes the principal value from the jump in the stress kernel, $\mathbf{T}$, as $\mathbf{x}$ passes from the interior to the boundary. The value of $\mathbf{C}$ depends upon the smoothness of the boundary at the point in question. In particular, $\mathbf{C} = -\frac{1}{2}\mathbf{I}$ at a smooth boundary point, defined as a point having a continuous local tangent plane. The integral equation, (6), is formally valid for $\mathbf{x} \in \Omega$ by setting $\mathbf{C} = -\mathbf{I}$.

For the axisymmetric motion considered here, the integral equation, after transformation to cylindrical coordinates, can be integrated with respect to the azimuthal angle, thus reducing the surface integrals to line integrals along the generating curve in a meridional plane (Youngren and Acrivos, 1975). The BIE generally cannot be solved explicitly but is readily solved numerically.

The major advantage of the BIE is the reduction in dimension; the axisymmetric problem becomes a vector line integral. This feature is particularly attractive for the free surface problem in a numerical sense in that dynamic shape evolution is more manageable than with domain type methods (finite difference or finite element) which require remeshing of the domain rather than merely redistributing the boundary nodes.

Numerical Analysis

The numerical solution of the integral equation (6) involves approximation by a linear system to be solved for the unknown stresses on the tube wall and velocities on the bubble-liquid interface. The boundary is discretized into M elements, each with n_s geometrical boundary points and n_b basis nodes. Two unknown components of velocity or traction

Downloaded 03 May 2010 to 171.66.16.31. Redistribution subject to ASME license or copyright; see http://www.asme.org/terms/Terms_Use.cfm

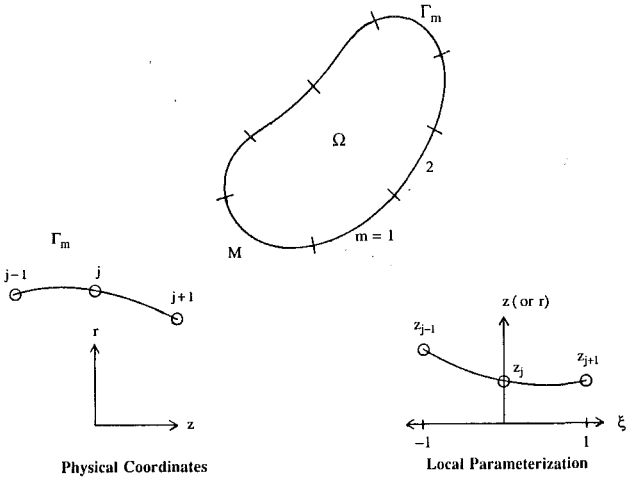


Fig. 2 Schematic of boundary discretization and parameterization

are to be determined per basis node; the total number of basis nodes in the mesh is N. Each curvilinear boundary element is mapped into the local coordinate system as shown in Fig. 2 using the transformation,

$$\begin{bmatrix} z \\ r \end{bmatrix} = \sum_{j=1}^{n_s} \psi_j(\xi) \begin{bmatrix} z_j \\ r_j \end{bmatrix} \tag{7}$$

where (z_j, r_j) are the cylindrical coordinates of the jth node. The velocity and traction components are also referred to a basis defined on the boundary as in the finite element method,

$$\begin{bmatrix} u \\ v \end{bmatrix} = \sum_{j=1}^{n_b} \phi_j(\xi) \begin{bmatrix} u_j \\ v_j \end{bmatrix}, \tag{8a}$$

$$\begin{bmatrix} t_z \\ t_r \end{bmatrix} = \sum_{j=1}^{n_b} \phi_j(\xi) \begin{bmatrix} t_{zj} \\ t_{rj} \end{bmatrix}. \tag{8b}$$

On each element, either linear or quadratic basis functions ψ can be used to describe the geometry, and constant, linear or quadratic basis functions ϕ can be specified for $\mathbf{u}$ and $\mathbf{t}$.

Applying the BIE to each basis node and using the approximations (7) and (8), a full $2N \times 2N$ matrix system results,

$$\mathbf{Gt} = \mathbf{Hu} \tag{9}$$

where, for example, the contribution to $\mathbf{G}$ from the nodes i and j is,

$$\begin{bmatrix} G_{2i-1,2j-1} & G_{2i-1,2j} \\ G_{2i,2j-1} & G_{2i,2j} \end{bmatrix} = \int_\Gamma \begin{bmatrix} U_{zz}(\mathbf{x}_i) & U_{zr}(\mathbf{x}_i) \\ U_{rz}(\mathbf{x}_i) & U_{rr}(\mathbf{x}_i) \end{bmatrix} \phi_j 2\pi\, r\, ds$$

and similarly for $\mathbf{H}$ which includes the contribution from $\mathbf{C}$. The quadratures are performed numerically over elements Γ_m when $\mathbf{x}_i \notin \Gamma_m$. The kernels are improper on elements where $\mathbf{x}_i$ is included and the integration is performed on these elements by extracting the singular part, integrating it analytically, and summing with the numerical integral of the remainder. Applying the known boundary conditions to the system (9) and rearranging, the usual linear system, $\mathbf{Ax} = \mathbf{f}$, results and is solved by Gaussian elimination with partial pivoting.

The condition on the velocity as $z \to \pm\infty$, the no-slip condition on the tube wall, and the stress jump condition on the interface are used as the known quantities in (6). These are sufficient to close the boundary value problem if the shape of the free surface is given. The present scheme solves the full problem as an initial value problem for the history of the coordinates on the free surface by specifying an initial shape, solving the system (9) for the velocity on the bubble surface, and using the kinematic condition (4) to evolve the shape in time. Thus, the kinematic condition generates a system of ordinary differential equations (ODE's), $\mathbf{Y}' = \mathbf{F}(\mathbf{Y}, t)$, for the position of the basis nodes on the interface. Evaluation of the derivative functions, $\mathbf{F}$, involves the solution of the boundary integral equation for a given bubble shape. The ODE's are integrated in time using a variable step forward Euler formula in conjunction with a comparison backward Euler step for estimating the local truncation error (without taking the corrector step). The step size for each succeeding time interval is selected such that a user specified truncation error tolerance is met. Further details can be found in Martinez (1987).

We find that the present scheme for determining the free surface shape as part of the solution is suitably reliable in that the steady solution is independent of the given initial shape, assuming that the initial shape is reasonable. The number of steps (or equivalently the adjustment time) required to reach the steady solution from the initial shape is, however, directly proportional to the difference in their shapes. Unfortunately, the ODE's become quite stiff for small capillary number, due to large variations in time constants among the component equations. The explicit variable step solver is not designed for stiff systems and can only respond by reducing the step size, and thereby increasing the number of steps required to achieve a steady-state. As a result, solutions have been computed only for $Ca \geq 0.01$. The convergence behavior itself is reasonable, and the scheme is expected to be viable for small capillary number if used with a stiff ODE solver. For example, in the analysis of the leading meniscus for $Ca = 0.025$, near steady-state the L_2 norm of the normal velocity on the interface behaved as

$$\| \mathbf{u} \cdot \mathbf{n} \| \approx 0.807 e^{-1.75t}$$

however, the ODE solver was using step sizes $\delta t \approx 0.006$ in order to satisfy a requested absolute truncation error tolerance of 10^{-4}. The exponential approach to vanishing normal velocity is typical of the behavior of this scheme. Small truncation error tolerances are required to enable the explicit solver to integrate the equations in the presence of stiffness.

For $Ca > 0.1$, between 20 and 60 steps were required to achieve a steady-state, defined by $\| \mathbf{u} \cdot \mathbf{n} \| < 0.01$. The solution for the current value of capillary number was used as the initial condition for the next value for increments in capillary number of about 0.1. Solutions for smaller Ca required an increasing number of steps to attain a steady-state. The solution for $Ca = 0.025$, using the shape from $Ca = 0.05$ as the initial shape, required about 200 steps. The nominal adjustment time to achieve steady-state was approximately 2 to 3 units of Ut/R_0 or about the time required to travel one tube diameter. The mesh extent was one tube diameter ahead (behind) of the leading (trailing) meniscus and up to 1.25 diameters into the film side of the meniscus. The larger mesh length was needed for large capillary number where the adjustment length increased from the nominal tube diameter which was normally sufficient for small capillary number. The results presented were computed with 40 to 50 basis nodes on the entire boundary for $Ca \geq 0.1$; results for smaller Ca were computed on an 83-node mesh. Selected comparisons with solutions using the 83-node mesh showed less than 1 percent difference in results. For example, the solution to the leading meniscus problem at $Ca = 0.05$ resulted in $r_b = 0.878$ for the 45-node mesh and in $r_b = 0.880$ for the 83-node mesh. Occasionally, it was useful to generate a new mesh of nodes to maintain a proper discretization. This was accomplished by fitting a cubic spline to the shape and redistributing the nodes to predetermined locations.

The simulations required about 45 seconds of CPU per time step for a 50-node mesh on a Digital Equipment Corporation

Downloaded 03 May 2010 to 171.66.16.31. Redistribution subject to ASME license or copyright; see http://www.asme.org/terms/Terms_Use.cfm

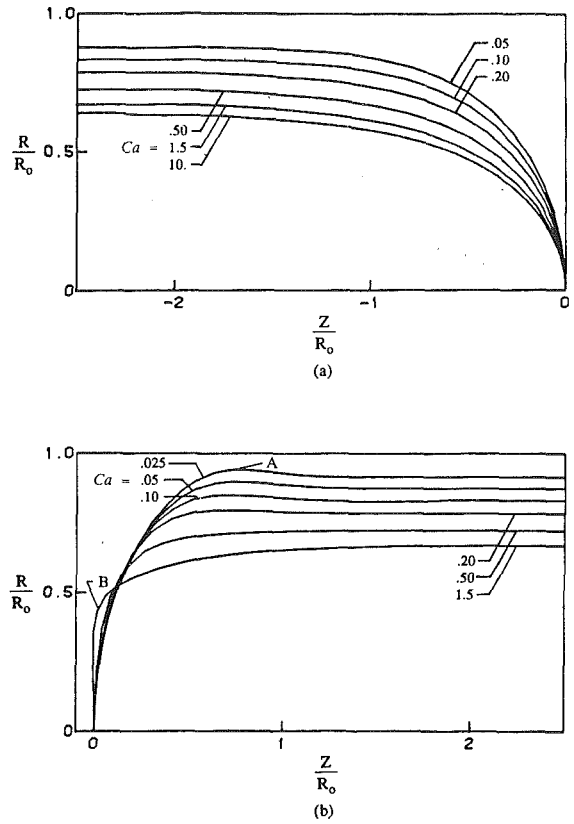


Fig. 3 Bubble profiles as a function of capillary number for the (a) leading and (b) trailing menisci

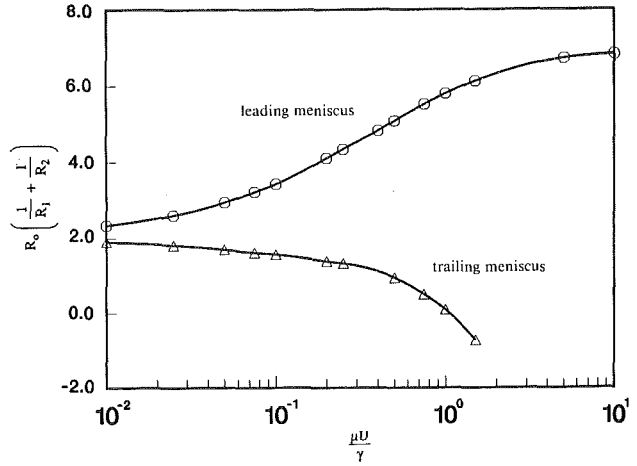


Fig. 4 Bubble-liquid interface curvature on the tube centerline for the leading and trailing menisci

μVAX II minicomputer operating in single precision. Comparison of selected single precision solutions with those from a double precision version of the code indicated four significant figures of precision in the former.

Results and Discussion

Profile shapes of the leading and trailing menisci are shown in Fig. 3 for various values of the capillary number. Generally, the film of suspending fluid left on the tube wall thins as the capillary number decreases, presumably until disjoining or conjoining pressures result in either an equilibrium thickness independent of capillary number or complete drying of the film thickness (point A of Fig. (3*b*)) occurs for values of capillary number less than about 0.2. Goldsmith and Mason (1963) observed wave disturbances preceding the rear of 0.37 for capillary numbers in excess of 10. The leading meniscus is blunt at low capillary number where stresses induced by surface tension are dominant except for the thin film region near the wall where viscous forces are always important. The profile becomes more slender, accompanied by increased interfacial curvature, with increasing capillary number as viscous stresses become important and finally dominant as $Ca \to \infty$.

The trailing meniscus has a more interesting dependence on the capillary number than the leading meniscus. A minimum film thickness (point A of Fig. (3*b*)) occurs for values of capillary number less than about 0.2. Goldsmith and Mason (1963) observed wave disturbances preceding the rear meniscus for low capillary number and Bretherton's (1961) analysis of the transition region also gives a minimum film thickness. This interface profile results in a curvature maximum and, hence, a local fluid pressure minimum directly behind the minimum film thickness. The difference between the film pressure and the minimum fluid pressure is responsible for setting the stationary film in motion behind the bubble. The local thinning of the film is also necessary to accommodate an increase in curvature from $1/R_b$, the value in the uniform film thickness region, to a maximum (e.g., point A of Fig. (3*b*)) and then a decrease towards the centerline to a value less than $2/R_0$. This condition is illustrated in Fig. 4 which shows the interface curvature on the tube centerline for the leading and trailing menisci as a function of the capillary number. As $Ca \to 0$, the leading meniscus curvature approaches $2/R_0$ from above while the trailing meniscus curvature approaches from below, both in agreement with the asymptotic analysis of Bretherton. At large values of the capillary number, the minimum disappears and the film thickness actually increases slightly along the back of the bubble until the interface turns sharply towards the tube centerline. This transition region, labeled B in Fig. (3*b*), increases dramatically in curvature with increasing capillary number and results in large viscous stresses. The centerline curvature simultaneously decreases towards zero. Goldsmith and Mason reported that for large capillary number some bubbles developed a reentrant cavity of suspending fluid at the rear of the bubble. The numerical solutions develop negative curvature on the centerline of the trailing meniscus, attaining a value of $-0.71/R_0$ for $Ca = 1.5$ as shown in Fig. 4. The large curvature at the transition prevented solutions for larger capillary number; however, the negative curvature perhaps signals the onset of the reentrant cavity for capillary numbers slightly larger than one.

Flow fields, in a frame fixed to the bubble, for a small and large value of capillary number are shown in Fig. 5. As surmised by Taylor (1961), a core of recirculation is apparent in this reference frame for $Ca < 0.5$. The radial location of the stagnation ring moves towards the tube centerline with increasing capillary number and is slightly higher on the trailing meniscus than on the leading meniscus. The solutions for the interfacial velocity indicate the recirculating core disappears for $Ca \approx 0.7$.

The recirculation could be of significance if surface active impurities are present in the suspending fluid. A nonuniform concentration of surfactant on the bubble surface, and therefore a variable surface tension, results in a tangential stress opposing the flow along the interface as well as a variation in the normal stress. The distribution of surfactant on the surface is a result of convection and diffusion in the fluid and will be influenced by the recirculation. Surface tension induced stress gradients would likely modify the bubble profile, film thickness and pressure drop.

The computed film thickness, in terms of the parameter

Downloaded 03 May 2010 to 171.66.16.31. Redistribution subject to ASME license or copyright; see http://www.asme.org/terms/Terms_Use.cfm

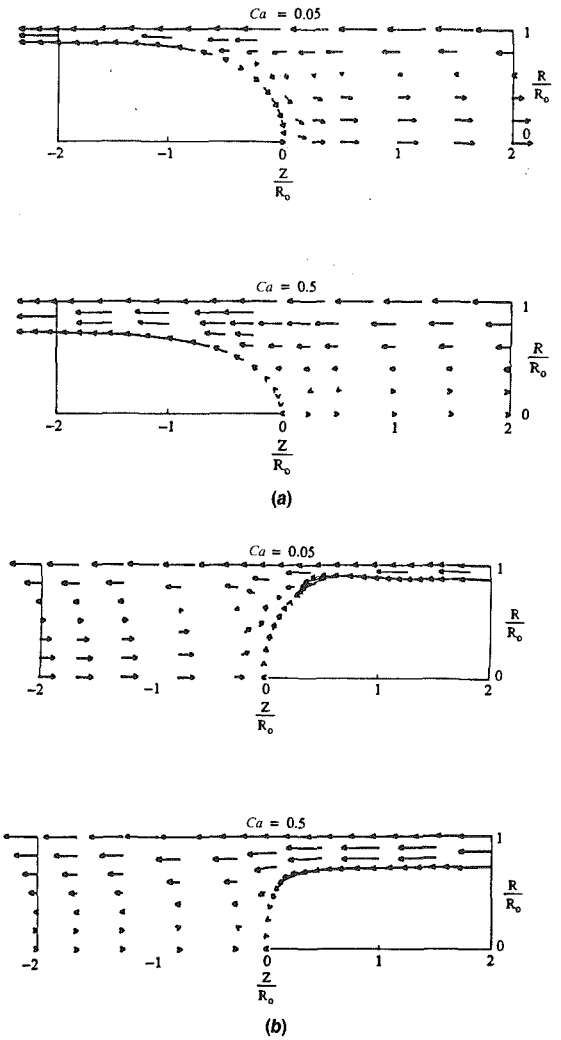


Fig. 5 Velocity vector field about the (a) leading meniscus and (b) trailing meniscus

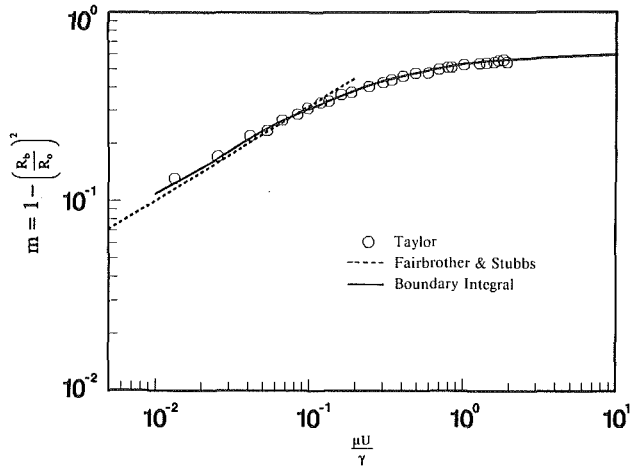


Fig. 6 Film thickness parameter, m, for various values of capillary number

$m = 1 - r_b^2$, as a function of capillary number is compared to the data of Taylor (1961) and to the empirical correlation of Fairbrother and Stubbs (1935), $m = Ca^{1/2}$, in Fig. 6. The thickness parameter, which is the volume fraction of suspending fluid left on the tube wall by the passage of a semi-infinite bubble, asymptotes to a value of about 0.60 according to the experiments conducted by Cox (1962); we compute a value of 0.59 at $Ca = 10$. The present results are in excellent agreement with Taylor's data and show Fairbrother and Stubbs' correlation to be accurate for $Ca < 0.1$. Comparison with Bretherton's asymptotic result, $m = 1.29(3Ca)^{2/3}$, is not possible since his analysis is valid for $Ca \leq 0.005$. For values of capillary number greater than about two we found oscillatory solutions for the leading meniscus profile near the uniform film thickness region. The oscillations dampled out toward the nose of the bubble. The amplitude of the oscillation in bubble radius was about 0.005 R_0 with period about 0.75 R_0/U for $Ca = 5$. It is not clear whether these oscillations are phenomenological or numerical in origin.

The pressure difference between the leading meniscus and the film, the trailing meniscus and the film, and across the entire bubble are shown in Fig. 7 for two different forms of scaling. The quantities computed in the boundary integral formulation are the components of the stress vector on the surface of the bubble, the normal component of which includes both pressure and viscous normal stresses. Although the pressure field can be computed explicitly once the boundary values have been obtained (Ladyzhenskaya, 1963), this entails an additional quadrature over the surface. We are content here with an approximate though economical alternative. The normal stress component on the surface with outward normal $\mathbf{n}$ is

$$t_n = -p + 2\frac{\partial u_n}{\partial n}.$$

Using continuity in a local $n-s$ coordinate system (Happel & Brenner, 1965) and the element mapping, we can express the normal stress on the bubble surface as

$$t_n = -p - \frac{2}{r}\left(\frac{ds}{d\xi}\right)^{-1}\frac{d(r\,u_s)}{d\xi},$$

which is true on any surface with zero normal velocity. In this form the viscous component can be easily computed by taking the numerical derivative of the tangential velocity component u_s along the bubble surface. For the range of capillary number computed, the film is always at a pressure higher than the nose value, p_f, shown in the inset of Fig. 7(a). The pressure in the film is also higher than the value on the tube centerline of the trailing meniscus, p_t, provided $Ca < 0.45$. For larger capillary number the pressure at the trailing end of the bubble is higher than in the film. The different scaling in Figs. 7(a) and (b) reflects the dominant mechanism operating in the regimes of small and large capillary number as implied by its interpretation as a measure of the viscous stresses to surface tension induced stresses. At small capillary number the latter is dominant and the pressure scales well with γ/R_0 (Fig. 7(a)). This scaling was used by Bretherton (1961) in his asymptotic analysis for vanishing capillary number. For large capillary number the "film" is thick and the stresses are everywhere of $O(\mu U/R_0)$ and this scale eliminates the pressure difference as is evident in Fig. 7(b). The different scales give the appearance of asymptotes to unbounded pressure difference when applied in an inappropriate capillary number regime.

The quantity of most practical interest is probably the additional pressure drop in the presence of the bubble. Following the work of Brenner (1971), the extra pressure drop, ΔP^+, is defined as the pressure drop in excess of the Poiseuille pressure drop for the same discharge and over the same distance along the tube. This excess pressure drop, over a distance sufficiently ahead of and behind the bubble, has contributions from the leading and trailing menisci and also depends on the length of the bubble, since the region of constant film thickness is at rest on the tube and therefore has zero pressure drop. Thus, there will always be less pressure drop than the Poiseuille value if the bubble is long enough. In order to eliminate the effect of the length of the bubble, the

Downloaded 03 May 2010 to 171.66.16.31. Redistribution subject to ASME license or copyright; see http://www.asme.org/terms/Terms_Use.cfm

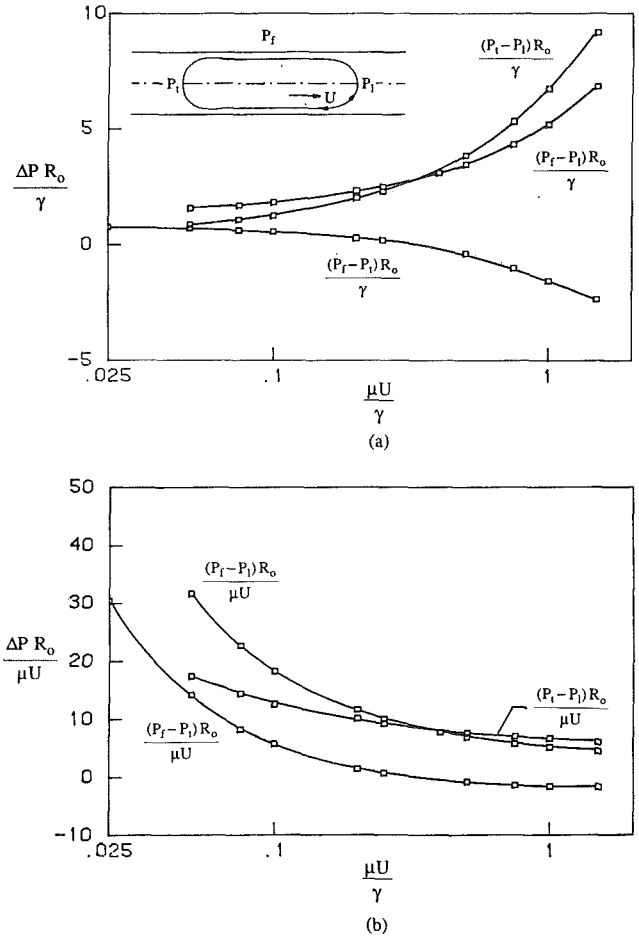


Fig. 7 Pressure difference across the menisci for (a) surface tension scaling, and (b) viscous scaling

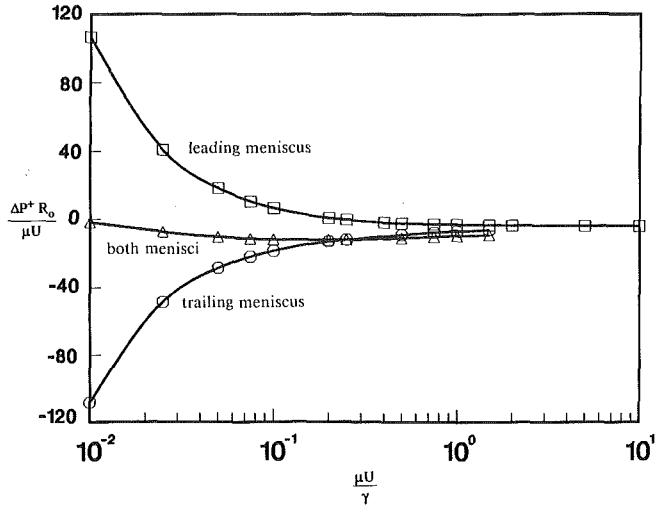


Fig. 8 Extra pressure drop as a function of capillary number

pressure difference is given here over one tube diameter behind and ahead of the intersection of the bubble with the tube centerline for both leading and trailing menisci. This distance nominally encompasses the adjustment length on either side of the meniscus for most of the Ca range considered. Thus ΔP^+, for either meniscus, is the computed pressure drop over a tube diameter on either side of the meniscus minus $32r_b^2$, the nondimensional Poiseuille value over the same distance. The extra pressure drop versus capillary number across the leading and trailing menisci is shown in Fig. 8. The viscous scaling is used in this case since we are comparing the pressure drop to the Poiseuille value. The pressure drop across the trailing meniscus is always negative, i.e., less than the Poiseuille value. The extra pressure drop across the leading meniscus changes sign at $Ca \approx 0.25$. For lower values of the caillary number, the pressure drop is greater than the Poiseuille value; most of it is due to surface tension as $Ca \to 0$. At larger values of the capillary number, the extra pressure drop is less than the Poiseuille value. Less pressure drop when surface tension is not important can also be understood in that a substantial volume fraction of the fluid about the leading meniscus is inviscid and, hence, the bulk volume has proportionately less dissipation. The sum of the ΔP^+ over both menisci is also indicated in Fig. 8. Subtracting $8r_b^2(L/R_0 - 4)$ from this sum gives the nondimensional extra pressure drop over one tube diameter ahead and behind a bubble of length L. The sum of the ΔP^+ is negative for $Ca \geq 0.01$, but appears to turn positive for smaller values, in agreement with Bretherton's analysis which gives

$$\frac{\Delta P^+ R_0}{\mu U} = \frac{13.56}{(3Ca)^{1/3}} - 32r_b^2, \; Ca \leq 0.005$$

assuming Poiseuille flow along the distance of one tube diameter on either side of the menisci. For small capillary number, the extra pressure drop required to displace the viscous fluid by the passage of a semi-infinite bubble is remarkably large and provides the impetus for current studies of the use of foam as a mobility control mechanism in immiscible displacement in porous media (Ransohoff et al., 1987). The extra pressure drop associated with an entire bubble, however, is positive only if $Ca < 0.01$.

Conclusions

In this work we have analyzed the flow of a long inviscid bubble in a liquid filled tube at low Reynolds number using the boundary integral method. The bubble profiles, flow field, and pressure distribution depend only on the capillary number, $\mu U/\gamma$. The results obtained are of interest in understanding the role of surface tension forces in two phase flow through porous media and in capillary tubes.

Computed values of the film thickness are in excellent agreement with the data of Taylor and the correlation of Fairbrother and Stubbs for $Ca < 0.1$. The displacement efficiency of the bubble is best at small capillary number when the leading meniscus leaves only a thin film on the tube wall. The film thickens with increasing capillary number, attaining a value of about 0.36 tube radii at $Ca = 10$; Cox reports a value of 0.37 for $Ca > 10$. This thickness for $Ca = 10$ indicates the leading meniscus displaces only 40 percent of the liquid originally in the tube and the ratio of bubble speed to the average fluid speed is about 2.5.

The curvature on the trailing meniscus at the tube centerline becomes negative for $Ca > 1$. A similar condition was reported by Goldsmith and Mason (1963) who observed a reentrant cavity at the trailing meniscus for large capillary number.

The dominant mechanism responsible for bubble deformation in the regions of small and large capillary number is reflected in the scale for pressure difference between the menisci and the uniform film on the tube wall. At small capillary number, surface tension resists bubble deformation and the pressure difference is $O(\gamma/R_0)$. At large capillary number, viscous forces overcome the surface tension and the pressure difference is $O(\mu U/R_0)$.

For $Ca > 0.01$ the total additional pressure drop, ΔP^+, due to the presence of the bubble is negative, i.e., the pressure drop in the tube is less than the Poiseuille value for the same discharge of suspending fluid alone. The pressure drop varies

Downloaded 03 May 2010 to 171.66.16.31. Redistribution subject to ASME license or copyright; see http://www.asme.org/terms/Terms_Use.cfm

nonlinearly with the discharge and so constitutes a mechanism for non-Newtonian behavior of the bulk flow. The extra pressure drop across the leading meniscus only is positive if $Ca < 0.25$ and negative for greater values. The extra pressure drop across the trailing meniscus is always negative.

Acknowledgments

This study was performed with financial support from Sandia National Laboratories under the Doctoral Studies Program.

References

Brenner, H., 1971, "Pressure Drop Due to the Motion of Neutrally Buoyant Particles in Duct Flows. II. Spherical Droplets and Bubbles," *Ind. & Eng. Chem. Fund.*, Vol. 10, No. 4, pp. 537–543.

Bretherton, F. P., 1961, "The Motion of Long Bubbles in Tubes," *J. Fluid Mech.*, Vol. 10, pp. 166–188.

Cox, B. G., 1962, "On Driving a Viscous Fluid Out of a Tube," *J. Fluid Mech.*, Vol. 14, pp. 81–98.

Fairbrother, F., and Stubbs, A., 1935, "Studies in Electroendosmosis. Part VI. The Bubble-Tube Methods of Measurements," *J. Chem. Sci.*, Vol. 1, pp. 527–529.

Geller, A. S., Lee, S. H., and Leal, L. G., 1986, "The Creeping Motion of a Spherical Particle Normal to a Deformable Interface," *J. Fluid Mech.*, Vol. 169, pp. 27–69.

Goldsmith, H. L., and Mason, S. G., 1963, "The Flow of Suspensions Through Tubes: II Single Large Bubbles," *J. Colloid Sci.*, Vol. 18, pp. 237–261.

Happel, J., and Brenner, H., 1965, *Low Reynolds Number Hydrodynamics*, Prentice-Hall, Englewood Cliffs, N.J.

Ladyzhenskaya, O. A., 1963, *The Mathematical Theory of Viscous Incompressible Flow*, Gordon and Breach, New York.

Lee, S. H., and Leal, L. G., 1982, "The Motion of a Sphere in the Presence of a Deformable Interference," *J. Coll. Interf. Sci.*, Vol. 87, pp. 81–106.

Martinez, M. J., 1987, "Viscous Flow of Drops and Bubbles in Straight and Constricted Tubes," Ph.D. Thesis, University of California, Berkeley.

Prothero, J., and Burton, A. C., 1961, "The Physics of Blood Flow in Capillaries," *J. Biophysics*, Vol. 2, pp. 525–572.

Rallison, J. M., 1981, "A Numerical Study of the Deformation and Burst of a Viscous Drop in General Shear Flows," *J. Fluid Mech.*, Vol. 109, pp. 465–482.

Rallison, J. M., and Acrivos, A., 1978, "A Numerical Study of the Deformation and Burst of a Viscous Drop in an Extensional Flow," *J. Fluid Mech.*, Vol. 89, pp. 191–200.

Ransohoff, T. C., Gauglitz, P. A., and Radke, C. J., 1987, "Snap-Off of Gas Bubbles in Smoothly Constricted Noncircular Capillaries," *AIChE J.*, Vol. 33, pp. 753–765.

Reinelt, D. A., 1984, "The Penetration of a Finger into a Viscous Fluid," Ph.D. Thesis, Calif. Inst. of Tech., Pasadena, CA.

Schwartz, L. W., Princen, H. M., and Kiss, A. D., 1986, "On the Motion of Bubbles in Capillary Tubes," *J. Fluid Mech.*, Vol. 172, pp. 259–275.

Shen, E. I., and Udell, K. S., 1985, "A Finite Element Study of Low Reynolds Number Two-Phase Flow Cylindrical Tubes," ASME JOURNAL OF APPLIED MECHANICS, Vol. 52, pp. 253–256.

Taylor, G. I., 1961, "Deposition of a Viscous Fluid on the Wall of a Tube," *J. Fluid Mech.*, Vol. 10, pp. 161–165.

Teletzke, G. F., 1983, "Thin Liquid Films: Molecular and Hydrodynamic Implications," Ph.D. Thesis, University of Minnesota, Minneapolis, MN.

Youngren, G. K., and Acrivos, A., 1975, "Stokes Flow Past a Particle of Arbitrary Shape: A Numerical Method of Solution," *J. Fluid Mech.*, Vol. 69, pp. 377–403.

Youngren, G. K., and Acrivos, A., 1976, "On the Shape of a Gas Bubble in a Viscous Extensional Flow," *J. Fluid Mech.*, Vol. 76, pp. 433–442.

Downloaded 03 May 2010 to 171.66.16.31. Redistribution subject to ASME license or copyright; see http://www.asme.org/terms/Terms_Use.cfm

A Similar Flow Between Two Disks in the Presence of a Magnetic Field

E. A. Hamza
School of Mathematical Sciences,
University of Khartoum,
Khartoum, Sudan

A similarity solution may be obtained for a flow between two parallel disks which, at time t^*, *are spaced a distance* $H(1-\alpha t^*)^{1/2}$ *apart and a magnetic field proportional to* $B_0(1-\alpha t^*)^{-1/2}$ *is applied perpendicular to the disks. Approximate analytic solutions are given and a numerical solution to the resulting nonlinear ordinary differential equations is presented. The effects of the magnetic forces on the velocity profiles and on the normal forces which the fluid exerts on the disks are studied. It has been found that by increasing the magnetic force a considerable increase in the load can be achieved.*

1 Introduction

The similarity solution to the governing equations of the motion of a thin film of fluid squeezed between two planes is of special interest in the theory of hydrodynamic lubrication due to its value in the study of other, less tractable, cases. The remarkable simplification which has resulted from the reduction of the partial differential equations to ordinary differential equations, has made possible an in-depth study of the nature of the flow. Ishizawa (1966) appears to have been the first to derive a similarity solution to the case of the unsteady laminar flow between two parallel disks. His solution requires the distance of separation of the disks to be proportional to $(1-\alpha t^*)^{1/2}$, where α^{-1} denotes a representative time. Ten years later, Wang (1976) derived a similarity solution to the two-dimensional and axisymmetric cases, and obtained a full numerical solution to the resulting ordinary differential equation. Recently, Tichy and Bourgin (1986) found that a similarity solution does exist for the steady flow in a narrow channel of a gap width varying as $(a+bx)^m$, where a, b, and m are constants. The transformation, which reduces the partial differential equations to a coupled pair of ordinary differential equations in the case of a viscous incompressible fluid contained between two parallel disks which at time t^*, are spaced a distance $H(1-\alpha t^*)^{1/2}$, where H denotes a representative length, and are rotating with angular velocities proportional to $\Omega(1-\alpha t^*)^{-1}$, where Ω denotes a representative angular velocity, was recognized by Hamza and MacDonald (1984).

Magnetic effects in lubrication have received considerable attention due to the important roles they play in many industrial applications. Authors who have investigated the magnetohydrodynamic lubrication phenomenon include Hughes and Elco (1962), Kuzma, Maki, and Donnelly (1964), Krieger, Day, and Hughes (1967), Kamiyama (1969), and Hamza (1988). The first four authors considered the magnetic force term but they neglected some or all the inertia terms in the Navier-Stokes equations. In the last paper all inertia terms are retained.

The present paper is concerned with the case where a fluid is contained between two parallel disks which at time t^*, are spaced a distance $H(1-\alpha t^*)^{1/2}$ apart and a magnetic field proportional to $B_0(1-\alpha t^*)^{-1/2}$, where B_0 denotes a representative magnetic field, is applied perpendicular to the disks. A similarity solution, which will be used to examine the way in which the flow pattern and the load change with the squeeze Reynolds number Re and Hartmann number M, is obtained.

2 Mathematical Formulation

Consider axisymmetric incompressible flow between two parallel infinite disks which are spaced a distance $h(t^*)$ apart, where t^* denotes time. A magnetic field $B(t^*)$ is applied perpendicular to the two disks, and the upper disk is moving with velocity $h'(t^*)$ towards the lower disk which is fixed. Select cylindrical polar coordinates (r^*, θ^*, z^*) and denote by u^* and w^*, the velocity components in the radial (r^*), and axial (z^*) directions. Suppose the lower disk is at $z^*=0$ and the upper one is at $z^*=h(t^*)$, where $h(0)=H$.

On the assumption that

$$u^*=\frac{\alpha r^*}{2(1-\alpha t)}f'(y),\quad w^*=-\frac{\alpha H}{\sqrt{1-\alpha t}}f(y),\quad B=\frac{B_0}{\sqrt{1-\alpha t}}$$

where

$$y=\frac{z^*}{H\sqrt{1-\alpha t}},\quad r=r^*,\quad t=t^*$$

the mass conservation equation is satisfied, and from the momentum equations, the radial and axial pressure gradients may be expressed in the form

Contributed by the Applied Mechanics Division of THE AMERICAN SOCIETY OF MECHANICAL ENGINEERS for publication in the JOURNAL OF APPLIED MECHANICS.

Discussion on this paper should be addressed to the Editorial Department, ASME, United Engineering Center, 345 East 47th Street, New York, N.Y. 10017, and will be accepted until two months after final publication of the paper itself in the JOURNAL OF APPLIED MECHANICS. Manuscript received by ASME Applied Mechanics Division, September 4, 1987; final revision, May 15, 1988.

Copyright © 1989 by ASME

Downloaded 03 May 2010 to 171.66.16.31. Redistribution subject to ASME license or copyright; see http://www.asme.org/terms/Terms_Use.cfm

$$\frac{1}{r}\frac{\partial P^*}{\partial r}=\frac{\rho\alpha^2}{4(1-\alpha t)^2}\left\{\frac{1}{\mathrm{Re}}f'''-yf''-2f'\right.$$

$$\left.-(f')^2+2ff''-M^2f'\right\}\equiv P_1(y,\,t) \tag{1}$$

$$\frac{\partial P^*}{\partial y}=-\frac{\rho\alpha^2H^2}{2(1-\alpha t)}\left\{\frac{1}{\mathrm{Re}}f''-yf'-f+2ff'\right\}\equiv P_2(y,\,t) \tag{2}$$

where $\mathrm{Re}=\rho\alpha H^2/2\mu$ and $M^2=B_0^2\sigma/\mu$ (ρ denotes density, μ denotes viscosity, and σ denotes fluid electrical conductivity). Further, equations (1) and (2) show that

$$\frac{1}{r}\frac{\partial P^*}{\partial r}=P_1(t).$$

Whence differentiation of equation (1) with respect to y leads to the equation

$$\mathrm{Re}\{yf'''+3f''-2ff'''\}+M^2f''=f^{iv}. \tag{3}$$

The boundary conditions under which equation (3) is to be integrated follow from the conditions

$u^*=0,\quad w^*=0\quad$ on $z^*=0$
$u^*=0,\quad w^*=h',\quad$ on $z^*=h(t^*)$.

Thus,

$$f(0)=0,\qquad f'(0)=0, \tag{4}$$
$$f(1)=1/2,\qquad f'(1)=0. \tag{5}$$

In the limiting case when $M^2/\mathrm{Re}\to 0$, equations (3)–(5) at once reduce to the equations which govern the unsteady flow between two disks at a distance $h(t) = H\sqrt{1-\alpha t}$ apart and moving towards (or away from) each other with relative velocity h'. This case was studied by Ishizawa and Wang.

The Normal Force. By integrating equations (1) and (2), the fluid pressure P^* may be written in the form

$$P^*(r,\,y,\,t)=\frac{1}{2}r^2P_1(t)+\int_0^y P_2(y,\,t)dy+P(t),$$

where

$$P_1(t)=\frac{\rho\alpha^2}{4\mathrm{Re}(1-\alpha t)^2}f'''(0),$$

$$\int_0^y P_2(y,\,t)dy=-\frac{\rho\alpha^2H^2}{2(1-\alpha t)}\left[\frac{1}{\mathrm{Re}}f'-yf+(f)^2\right]$$

and $P(t)$ is an arbitrary function of t. Thus,

$$P^*(r,\,1,\,t)=P(t)+\frac{\rho\alpha^2H^2}{8(1-\alpha t)}+\frac{\rho\alpha^2r^2}{8\mathrm{Re}(1-\alpha t)^2}f'''(0)$$

If the disks are assumed to be of finite radius a and of negligible thickness, the normal force or load W^*, which the fluid exerts on the disks, is given by

$$W^*=2\pi\int_0^a r\left[P^*(r,\,1,\,t)-P_0^*\right]dr$$

where $P_0^*=P_0^*(a,\,1,\,t)$.
Thus,

$$W^*=-\frac{\rho\alpha^2\pi a^4}{16\mathrm{Re}(1-\alpha t)^2}f'''(0)$$

or

$$W=-\frac{1}{6\ \mathrm{Re}}f'''(0)$$

where

$$W=\frac{8W^*(1-\alpha t)^2}{3\rho\alpha^2\pi a^4}.$$

3 Approximate Analytic Solutions

To solve the full nonlinear equation (3), a numerical approach is necessary. Before discussing the numerical solution, we describe approximate analytical results which can be obtained for $\mathrm{Re}=o(1)$ and $M=o(1)$.

When $\mathrm{Re}=o(1)$ and $M=o(\mathrm{Re})$ the radial and axial velocity profiles, and the normal forces which are exerted by the fluid on the disks, are approximately equal to the values they assume when the magnetic field is absent.

When $M=O(\mathrm{Re})$ and when $M=O(\mathrm{Re}^{1/2})$ f may, for $\mathrm{Re}=o(1)$, be expanded in the form

$$f=f_0+\mathrm{Re}\,f_1+O(\mathrm{Re}^2)$$

where f_0, f_1 satisfy the conditions

$$f_0(0)=f_0'(0)=0, f_0(1)=1/2, f_0'(1)=0;$$
$$f_1(0)=f_1'(0)=0, f_1(1)=f_1'(1)=0.$$

Case (*i*). For $M=0(\mathrm{Re})$, the functions f_0, f_1, satisfy the equations

$$f_0^{iv}=0$$

$$f_1^{iv}=yf_0'''+3f_0''-2f_0f_0'''+\frac{M^2}{\mathrm{Re}}f_0''$$

we find

$$f_0=y^2(3/2-y)$$

$$f_1=\frac{y^2(1-y)^2}{280}\left\{19-40y+6y^2-4y^3+\frac{7M^2}{\mathrm{Re}}(1-2y)\right\}$$

and the load W is given by the equation

$$W=\frac{1}{\mathrm{Re}}\left\{1+\frac{\mathrm{Re}}{6}\left(\frac{117}{70}+\frac{3}{5}\frac{M^2}{\mathrm{Re}}\right)+O(\mathrm{Re}^2)\right\}. \tag{6}$$

Case (*ii*). For $M=O(\mathrm{Re}^{1/2})$, the equations satisfied by f_0, f_1 are

$$f_0^{iv}-M^2f_0''=0$$

$$f_1^{iv}-M^2f_1''=yf_0'''+3f_0''-2f_0f_0'''.$$

We obtain

$$kf_0=g+My-\beta,$$
$$6Mk^3f_1=6kk_1\mathrm{sech}^2(M/2)\sinh^2(My/2)+6Mk\beta gy(1-y)$$
$$+k(1+g')(18My-6\beta y-3\beta-g)$$
$$+4\beta^2\{2k_2(\beta-g)-Mk_3y\},$$

where

$$g(y)=\beta\cosh My-\sinh My,$$
$$k=2M-4\beta,\ k_1=3M-2\beta,\ k_2=4M-3\beta,\ k_3=9M-8\beta$$

and

$$\beta=\tanh(M/2).$$

The load W is found to be

$$W=\frac{M}{18k^3\mathrm{Re}}\left\{3k^2M^2+\mathrm{Re}\left[57M^2\right.\right.$$
$$\left.\left.+2\beta^2(17\beta M+54)-28\beta M(\beta M+6)\right]+O(\mathrm{Re}^2)\right\}. \tag{7}$$

Downloaded 03 May 2010 to 171.66.16.31. Redistribution subject to ASME license or copyright; see http://www.asme.org/terms/Terms_Use.cfm

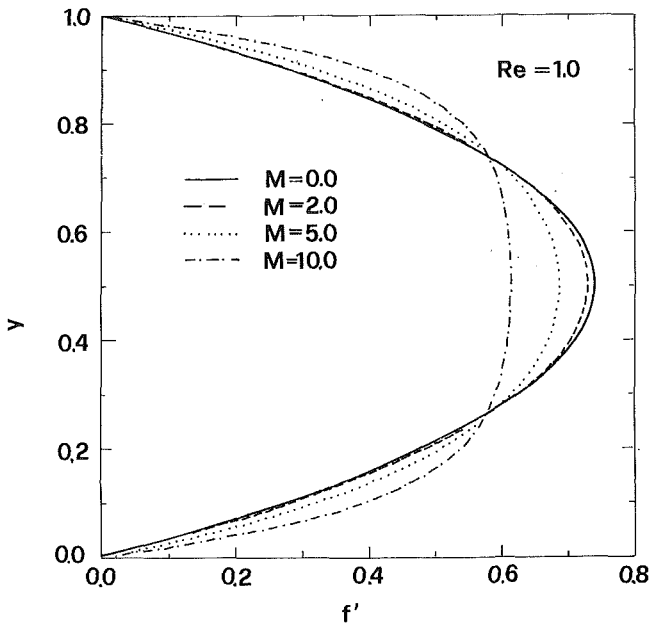


Fig. 1 Variation of dimensionless function f' with M when Re = 1.0

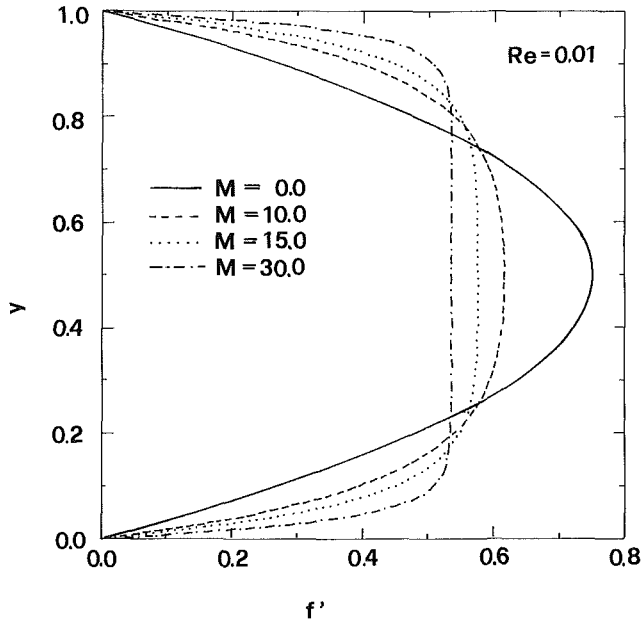


Fig. 2 Variation of dimensionless function f' with M when Re = 0.01

4 Numerical Solution

To test the accuracy of the perturbation solution of Section 3 and to obtain reliable information on the nature of the flow for values of Re and M, which are not small, a numerical solution of the governing equations is necessary. For wide ranges of Re and M the two point, boundary value problem, expressed by equations (3)–(5), can be integrated by applying a shooting and matching technique.

The equations were integrated by use of the Numerical Algorithm Group (NAG) routine (DO2AGF) which solves the two point, boundary value problem for a system of ordinary differential equations, using initial value techniques (DO2ABF) and Newton iteration. The DO2AGF subroutine requires initial estimates for the unknown boundary conditions at $y=0$ and $y=1$. For $\mathrm{Re}=o(1)$ and $M=o(1)$, these were

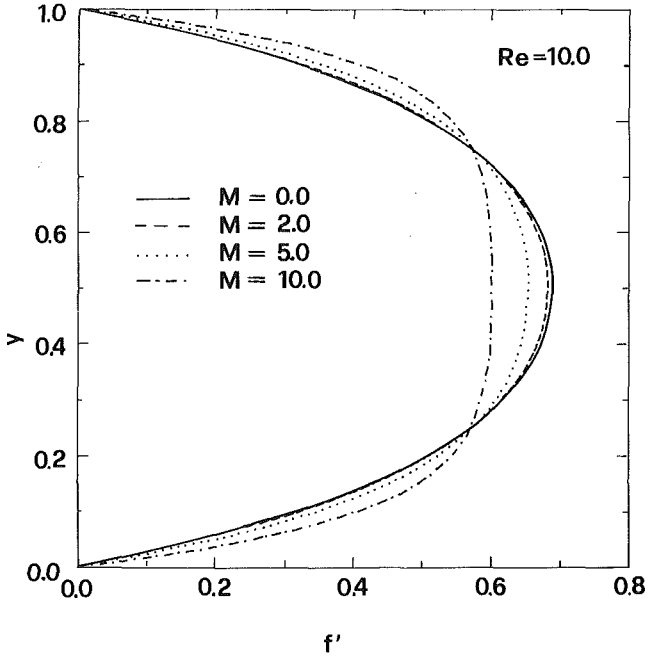


Fig. 3 Variation of dimensionless function f' with M when Re = 10.0

provided by the regular perturbation results of Section 3. This being successful, results for larger values of Re and M can be obtained by progressively increasing Re and M by small amounts and estimating the unknown boundary conditions from the previously computed set of results.

The calculations were performed on a CDC 7600 machine which retained 15 significant figures for values of Re and M in the ranges $0.01 \le \mathrm{Re} \le 10$ and $0 \le M \le 30$. As a first check the program was run for $M=0$. The results were in full agreement with those obtained by Wang (1976). Furthermore, comparison of the regular perturbation results and the full numerical results over a wide range of Re and M indicates satisfactory agreement.

5 Results and Discussion

We present and discuss the case where a thin film of fluid is squeezed between two parallel disks in the presence of a perpendicular magnetic field. In the following, we shall be concerned with the combined effects of magnetic forces and squeezing on the velocity profiles, and the normal force which the fluid exerts on the upper disk.

The Velocity Field: For $\mathrm{Re}=o(1)$ and $M=o(\mathrm{Re})$, the behavior of the flow may be described by the perturbation results of Section 3. If $M=o(\mathrm{Re})$, we note that the motion is well approximated by the solution relevant to squeezing with zero magnetic field. Since $\mathrm{Re}=o(1)$, the dimensionless functions f and f', which give components of velocity in the axial and radial directions, are approximately given by the zero-order perturbation results, i.e., by

$$f=y^2(3/2-y), \quad f'=3y(1-y).$$

Thus, we have the usual parabolic distribution in the radial direction.

If $M=O(\mathrm{Re})$, the effects of magnetic forces are equal in importance to squeezing, and from the perturbation solution we observe that with an increase in M, with Re held fixed, there is a slight increase in the radial velocity profile near the disks and a slight decrease in the region of the midplane $y=1/2$. This increase (decrease) becomes more pronounced with more increase in M, and the radial velocity profiles in the interior region become more flat – features which are common to all values of Re quoted in Figs. 1-3. On the other hand, for fixed

Downloaded 03 May 2010 to 171.66.16.31. Redistribution subject to ASME license or copyright; see http://www.asme.org/terms/Terms_Use.cfm

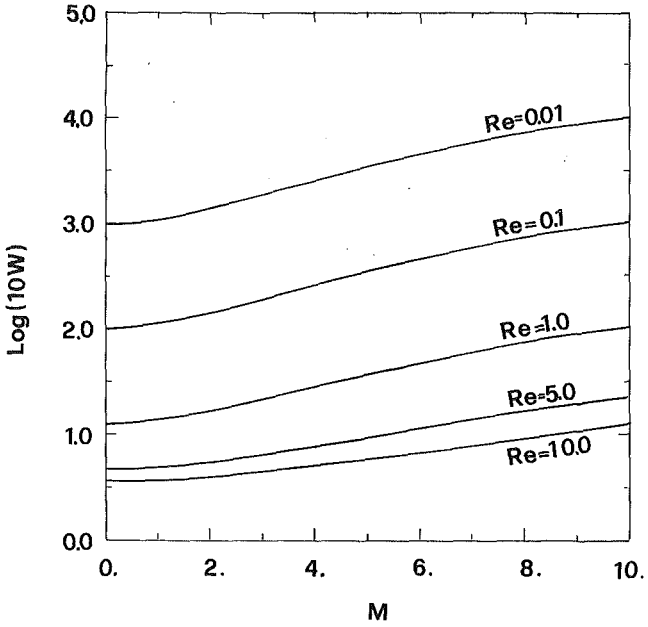


Fig. 4 Normal force, or load, variation with M

values of M the magnitude of the radial flow decreases with increase of Re.

The case of slight squeezing with a slight and moderate magnetic field is demonstrated in Fig. 1, while the case of slight squeezing with a large magnetic field is exhibited in Fig. 2. In Fig. 2 we notice the remarkable change in the radial flow for values of $M/\mathrm{Re} >> 1$. Figure 3 presents the case of moderate squeezing with slight and moderate magnetic forces.

The Load. Of particular interest is the response of the radial pressure gradient (or equivalently, the load) to changes in the squeeze Reynolds number and Hartmann number. When magnetic field is absent, the normal force, or load W, which is exerted on the upper surface, is large and positive and decreases with increase of the squeeze Reynolds number. By applying a perpendicular magnetic field, the results of this study indicate that a remarkable increase in the load can be obtained. These are in agreement with the experimental results.

Figure 4 shows for values of $\mathrm{Re} = 0.01$, 0.1, 1.0, 5.0, and 10.0, the way in which W varies with M. We observe that the load increases with increase of M, while, for a fixed value of M, W decreases with increase of Re.

Acknowledgments

The author would like to thank Prof. Abdus Salam, the International Atomic Energy Agency, and UNESCO for hospitality at the International Centre for Theoretical Physics, Trieste.

References

Hamza, E. A., and MacDonald, D. A., 1984, "A Similar Flow Between Two Rotating Disks," *Quarterly of Applied Mathematics*, Vol. 41, pp. 495–511.

Hamza, E. A., 1988, "The Magnetohydrodynamic Squeeze Film," ASME *Journal of Tribology*, Vol. 110, No. 2, pp. 375–377.

Hughes, W. F., and Elco, R. A., 1962, "Magnetohydrodynamic Lubrication Flow Between Parallel Rotating Disks," *Journal of Fluid Mechanics*, Vol. 13, pp. 21–32.

Ishizawa, S., 1966, "The Unsteady Laminar Flow Between Two Parallel Disks with Arbitrarily Varying Gap Width," *Bull. of the J.S.M.E.*, Vol. 9, No. 35, pp. 533–550.

Kamiyama, S., 1969, "Inertia Effects in MHD Hydrostatic Thrust Bearing," ASME *Journal of Lubrication Technology*, Vol. 91, No. 4, pp. 589–596.

Krieger, R. J., Day, H. J., and Hughes, W. F., 1967, "The MHD Hydrostatics Thrust Bearing—Theory and Experiments," *Journal of Lubrication Technology*, Trans. ASME, Series F, Vol. 89, pp. 307–313.

Kuzma, D. C., Maki, E. R., and Donnelly, R. J., 1964, "The Magnetohydrodynamic Squeeze Film," *Journal of Fluid Mechanics*, Vol. 19, pp. 395–400.

Tichy, J. A., and Bourgin, P., 1986, "A Similarity Solution for Flow in a Narrow Channel of Varying Gap," ASME JOURNAL OF APPLIED MECHANICS, Vol. 53, pp. 943–946.

Wang, C. Y., 1976, "The Squeezing of a Fluid Between Two Plates," ASME JOURNAL OF APPLIED MECHANICS, Vol. 43, pp. 579–583.

Downloaded 03 May 2010 to 171.66.16.31. Redistribution subject to ASME license or copyright; see http://www.asme.org/terms/Terms_Use.cfm

Journal of Applied Mechanics

Brief Notes

A Brief Note is a short paper that presents a specific solution of technical interest in mechanics but which does not necessarily contain new general methods or results. A Brief Note should not exceed 1500 words *or equivalent* (a typical one-column figure or table is equivalent to 250 words; a one line equation to 30 words). Brief Notes will be subject to the usual review procedures prior to publication. After approval such Notes will be published as soon as possible. The Notes should be submitted to the Technical Editor of the JOURNAL OF APPLIED MECHANICS. Discussions on the Brief Notes should be addressed to the Editorial Department, ASME, United Engineering Center, 345 East 47th Street, New York, N. Y. 10017, or to the Technical Editor of the JOURNAL OF APPLIED MECHANICS. Discussions on Brief Notes appearing in this issue will be accepted until two months after publication. Readers who need more time to prepare a Discussion should request an extension of the deadline from the Editorial Department.

On Immobile Kinematic Chains and a Fallacious Matrix Analysis

E. N. Kuznetsov[1]

Immobile Chains

When formulating a stiffness criterion for pin-bar systems, Maxwell noticed the existence of peculiar exceptional assemblies: Having fewer independent constraints than necessary to be geometrically invariant, such systems are underconstrained and yet kinematically immobile. An analytical treatment, due to Levi-Civita and Amaldi (1930), stems from the fact that the kinematic properties of assemblies are fully determined by a compatible set of constraint equations

$$F_i(X_1, \ldots X_n, \ldots X_N) = 0, \quad i = 1,2, \ldots I \tag{1}$$

The functions F_i relate the N generalized coordinates X_n to the implicitly present geometric parameters of the system (member sizes). Equations (1) linearized at the solution point $X_n = X_n^o$ involve infinitesimal virtual displacements x_n:

$$F_{in}^o x_n = 0 \quad (F_{in} = \partial F_i / \partial X_n). \tag{2}$$

Here and below a repeated subscript denotes summation. By employing the principle of virtual work, homogeneous equilibrium equations in generalized constraint reactions, Λ_i, are obtained from (2):

$$F_{in}^o \Lambda_i = 0 \tag{3}$$

When the rank r of the Jacobian F_{in}^o is $r < I$, equations (3) admit at least one set of $\Lambda_i \neq 0$. This set is used to form a linear combination of constraint equations expanded in power series

$$\Lambda_i[F_{in}^o x_n + (1/2)F_{imn}^o x_m x_n + \ldots] = 0. \tag{4}$$

On multiplying out and employing equations (2) the first product vanishes and the remaining quadratic form is rewritten in r independent displacements. If the resulting form is definite, all $x_n = 0$, and $X_n = X_n^o$ is an isolated solution of equation (1); the system lacks kinematic mobility and possesses a unique configuration. When the form is indefinite the system is a finite mechanism. In the case of semi-definiteness, higher-order terms in the above expansion must be considered. The presence of third-order terms indicates mobility while their absence calls for the evaluation of next-order terms.

Example. For the system in Fig. 1(*a*), $I = 3$, $N = 4$, and the constraint equations are

$$X_1^2 + X_2^2 - l_1^2 = 0$$
$$(X_3 - X_1)^2 + (X_4 - X_2)^2 - l_2^2 = 0$$
$$(l - X_3)^2 + X_4^2 - l_3^2 = 0.$$

The Jacobian F_{ni} is given in Table 1 (omitting the factor 2)

Table 1

X_1	$X_1 - X_3$	0
X_2	$X_2 - X_4$	0
0	$X_3 - X_1$	$X_3 - l$
0	$X_4 - X_2$	X_4

Table 2

l_1	$-l_2$	0
0	0	0
0	l_2	$-l_3$
0	0	0

Table 3

l_1	$-l_2$	0
0	0	0
0	l_2	l_3
0	0	0 .

For an ordinary configuration of the system, the Jacobian rank is 3 and equations (2) allow a nonzero solution x_n indicating kinematic mobility.

For the exceptional configuration in Fig. 1(*b*), $X_1^o = l_1$, $X_2^o = X_4^o = 0$, $X_3^o = l_1 + l_2$ and the Jacobian is given in Table 2. The rank drops to 2 and equilibrium equations (3) allow a nontrivial solution

$$\Lambda_1 = \Lambda/l_1, \ \Lambda_2 = \Lambda/l_2 \ \Lambda_3 = \Lambda/l_3.$$

Taking displacements x_2 and x_4 as independent yields $x_1 = x_3 = 0$ and the quadratic form in independent variables becomes

$$\Lambda[x_2^2/l_1 + (x_2 - x_4)^2/l_2 + x_4^2/l_3] = 0.$$

The form is positive definite, hence, $x_2 = x_4 = 0$ and the system is immobile.

Table 3 is the Jacobian for the system in Fig. 1(*c*). Again, $\Lambda_i \neq 0$ exist:

$$\Lambda_1 = \Lambda/l_1, \ \Lambda_2 = \Lambda/l_2, \ \Lambda_3 = -\Lambda/l_3$$

but the corresponding quadratic form

$$\Lambda[x_2^2/l_1 + (x_2 - x_4)^2/l_2 - x_4^2/l_3] = 0$$

is indefinite, and the system is a finite mechanism.

Physically, the existence of a nontrivial solution to homogeneous equilibrium equations indicates statical possibility of initial forces (self-stress). The leading term in (4) is the lowest-order differential of the work done by the initial forces on virtual displacements compatible with the constraint conditions. If this work is strictly positive the state of self-

[1]Department of General Engineering, University of Illinois, Urbana, Ill. 61801.

Manuscript received by the ASME Applied Mechanics Division, March 18, 1988; final revision, August 3, 1988.

Copyright © 1989 by ASME

Downloaded 03 May 2010 to 171.66.16.31. Redistribution subject to ASME license or copyright; see http://www.asme.org/terms/Terms_Use.cfm

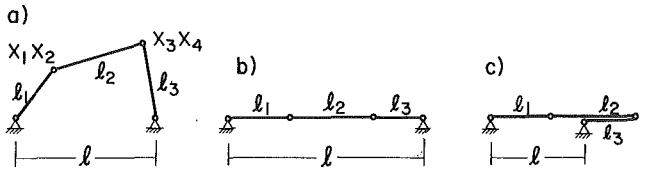


Fig. 1 Geometric configurations of a "four-bar" chain; (a) finite mechanism, (b) immobile kinematic chain (infinitesimal mechanism), and (c) finite mechanism in a degenerate ("dead center") configuration

stress is stable. Thus, an underconstrained system allowing a stable self-stress is kinematically immobile.

A few subtle but important points require clarification.

(1) As is readily seen, it is just the *statical possibility* (and not the actual state) of a stable self-stress that constitutes the statical criterion of immobility. Indeed, just the formal existence of a set of numbers $\Lambda_i \neq 0$ satisfying the above criterion is sufficient for immobility. In cases where $r < I-1$, the required set may be one of the several existing linearly independent sets or their linear combination.

(2) The stability in question is of *kinematic*, or geometric nature, since the constraints (structural members) were assumed ideal and the foregoing reasoning does not involve any notion of elasticity. Thus, the system is only *kinematically immobile* and is an infinitesimal mechanism; if made of a real material, it allows first-order displacements at the expense of second- or higher-order extensions of the structural members.

(3) Elimination of dependent displacements from (4) is not always completed by solving *linearized* constraint equations (2). For example, when analyzing a kinematic chain containing the system in Fig. 1(*b*) as a subassembly (Fig. 2), displacements $x_2 = x_4 = 0$ are evaluated from a *quadratic form*; nevertheless, coordiantes X_2 and X_4 in all constriant equations can be fixed. If, as a result, the rest of the chain becomes immobile, this signals a corresponding increase in the order of the infinitesimal mechanism. Curiously, this algorithmic nuance is the only sign of the increased order for the cases where expansion (4) does not contain higher-order terms (for example, for pin-bar systems, the expansion terminates with quadratic terms).

(4) The established analytical criterion (sign definiteness of the lowest-order form in linear combination (4)) represents a *sufficient* condition for an immobile kinematic chain. In mathematical terms, the problem consists of formulating necessary and sufficient conditions for a known real solution $X_n = X_n^o$ to simultaneous nonlinear equations (1) to be isolated. To the best of the author's knowledge, the necessary condition is unknown.

Tarnai's Questions

The foregoing analysis is closely related to two questions posed by Tarnai (1980):

(1) What criterion determines whether self-stress stiffens an assembly which is both statically and kinematically indeterminate?

(2) How can matrix methods be used to decide whether kinematical indeterminacy takes the form of an infinitesimal or a finite mechanism?

To take advantage of the above analysis, note that, for an assembly defined by N generalized coordinates and I constraints, the degrees of statical and kinematic indeterminacy are, respectively, $(I-r)$ and $(N-r)$ where r is the rank of Jacobian F_{in}^o in a given configuration $X_n = X_n^o$. Statical indeterminacy implies (and, strictly speaking, is defined by) the existence of a nontrivial solution to the homogeneous system of equilibrium equations (3).

As an answer to the first question, *stability* of self-stress is the sought criterion. In a certain sense, stability of self-stress and its stiffening effect are very close, if not synonymous,

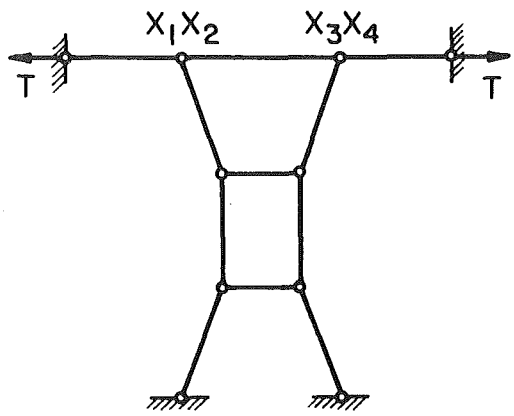


Fig. 2 Infinitesimal mechanism of second order

concepts: Both imply resistance to perturbations. Accordingly, a self-stress which does not stiffen the assembly, is either neutral or unstable and, in the latter case, physically unrealizable. Analytically, the stability criterion requires the existence of a linear combination of expanded constraint equations (1) with a sign-definite lowest-order form in independent displacements. This condition for an infinitesimal mechanism provides an answer to the second of Tarnai's questions except that the Levi-Civita procedure does not entirely qualify as a matrix method. However, in light of the key role of the stability aspect of the problem, and taking a clue from the general theory of stability, it can be conjectured that the necessary analysis, as a rule, cannot be confined to linear matrix operations.

A Matrix Attempt

A different approach was taken by Pellegrino and Calladine (1984, 1986) who claim that their method "enables us to answer for the first time Tarnai's questions." The method employs a "generalized equilibrium matrix," $\mathbf{A}'$, which is comprised of r independent columns of the original equilibrium matrix and $(N-r)$ "product-force vectors," i.e., perturbation forces corresponding to each of the independent internal mechanisms of the assembly. The major premise of the proposed matrix test is: "When we allow the assembly to distort in its inextensional modes, it will be able, after all, to support a completely *arbitrary* set of loads . . . if the matrix $\mathbf{A}'$ is of full rank."

The premise is devoid of any notion of stability thus emasculating the proposed matrix test: It fails to recognize the system in Fig. 1(*c*) as a finite mechanism. This system was not discussed in the report (1984) that was later presented at the 1984 IUTAM Congress. However, when the report was published as a paper (1986), the system was addressed prompting the following correction:

"It is thus clear that our matrix test . . . must be supplemented in general by a check that the scalar product of *all* mechanisms with the corresponding product forces are positive."

Unfortunately, the suggested "supplemental check" of all (in this case, two) internal mechanisms is also inadequate: the system in Fig. 1(*c*) still passes the check (both scalar products are positive) provided that $l_3 > l_2$. To verify stability in this way, it would be necessary to check all *linear combinations* of mechanisms, but that would require an infinite number of operations. If the authors indeed intended to check stability, surely a more feasible method of analysis could be suggested.

Aside from this critical flaw, the reader should be wary of some other misconceptions in the paper. Following are a few examples.

"If the product force vector does not lie in the column space of $\mathbf{A}$, then the corresponding mechanism is infinitesimal, of

Downloaded 03 May 2010 to 171.66.16.31. Redistribution subject to ASME license or copyright; see http://www.asme.org/terms/Terms_Use.cfm

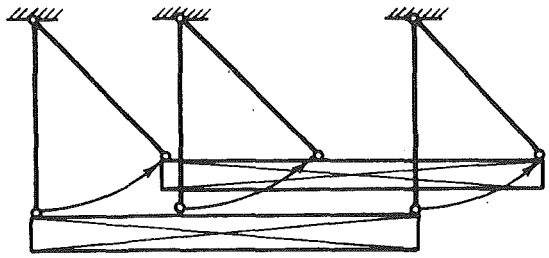


Fig. 3 Statically indeterminate finite mechanism

first order." —Not so (Fig. 1(*c*) is a counterexample). "But if it does lie in the column space we cannot distinguish between a higher-order infinitesimal mechanism and a finite mechanism." —This is a case when equation (4) is satisfied identically indicating that, in the absence of higher-order terms (pin-bar assemblies), constraint equations (1) are globally dependent; the assembly is a finite mechanism which is globally statically indeterminate (e.g., Fig. 3) so that the self-stress is unstable and unrealizable. "This assembly is evidently of a type not envisaged by Maxwell: Its key feature is one of symmetry." —Although the assembly (Tarnai's ring) possesses an interesting symmetry, it is nothing but a globally statically indeterminate finite mechanism conceptually similar to the system in Fig. 3. While it is arguable what Maxwell did or did not envisage, it is certain that symmetry is not the key feature of a statically indeterminate finite mechanism. Another certainty is that such a mechanism cannot be in a state of self-stress and retain its kinematic mobility: these two features are incompatible. In particular, Tarnai's ring cannot be prestressed in any of its kinematically possible configurations.

Conclusions

(1) A sufficient analytical criterion for an immobile kinematic chain is the existence of a linear combination of expanded constraint equations with a sign-definite lowest-order form in independent displacements. The physical meaning of this condition—the statical criterion of immobility—is the statical possibility of stable self-stress.

(2) Most of the claims of the paper by Pellegrino and Calladine (1986) including the central one ("We have succeeded in giving a matrix test . . . ") are invalid. The matrix analysis as conceived and used in the paper (i.e., "unsupplemented" with the stability check) is erroneous. If "supplemented" with a feasible check of stability, the analysis is unnecessary: The stability check alone is sufficient. The authors (borrowing their own comment on p. 412 about another paper) "ended up in a state of confusion."

References

Levi-Civita, T., and Amaldi, U., 1930, *Lezioni di Meccanica Razionale*, (in Italian), Vol. 1, Part 2, 2nd ed., Bologna.

Pellegrino, S., and Calladine, C. R., 1984, "Matrix Analysis of Statically and Kinematically Indeterminate Frameworks," Dept. of Engineering, University of Cambridge, Report CUED/D-Struct/TR110; 1986, *Int. Journ. Solids Structures*, Vol. 22, No. 4, pp. 409-428.

Tarnai, T., 1980, "Problems Concerning Spherical Polyhedra and Structural Rigidity," *Struct. Topology*, Vol. 4, pp. 61-66.

A Way of Accurately Estimating Eigenvalues

Robert Schmidt[2]

Introduction

During the early decades of this century, Timoshenko (1936) and Temple and Bickley (1956) demonstated (by solving many examples) the efficacy of the combination of Rayleigh's method with the method of successive approximation in the estimation of buckling loads and fundamental frequencies. Herein we show how to obtain remarkably accurate estimates of such eigenvalues by combining the two aforementioned methods in a somewhat different way, viz., by using generating shape functions with an adjustable exponent, refining them by the method of successive approximations, and then employing a set of formulas obtained via the Rayleigh-Ritz method or the Temple inequalities.

A Formulation of the Technique

For brevity, let us limit ourselves to eigenvalue problems of the Sturm-Liouville type (Kline, 1972; Courant and Hilbert, 1931), viz.,

$$(py')' + kqy = 0, \quad y' = dy/dx, p(x) > 0, q(x) > 0, \tag{1a}$$

$$y'(a) - h_1 y(a) = 0, y'(1) + h_2 y(1) = 0, a < 1, \tag{1b}$$

or (Finlayson, 1972),

$$S = \int_a^1 [p(y')^2 - kqy^2]dx, \ \delta S = 0. \tag{2}$$

Equation (1*a*) is the Euler equation corresponding to (2).

Let us approximate the solution of (1) by (Collatz, 1948)

$$y = Au(x) + Bv(x), \tag{3}$$

where u and v are some simple functions satisfying the essential (boundary) conditions; substitute (3) in the integral of (2); and apply $\partial S/\partial A = \partial S/\partial B = 0$. In this way, we obtain

$$(P_{uu} - kQ_{uu})A + (P_{uv} - kQ_{uv})B = 0, \tag{4a}$$

$$(P_{uv} - kQ_{uv})A + (P_{vv} - kQ_{vv})B = 0, \tag{4b}$$

where

$$P_{uu} = \int pu'^2 dx, P_{uv} = \int pu'v' dx, P_{vv} = \int pv'^2 dx, \tag{5a}$$

$$Q_{uu} = \int qu^2 dx, Q_{uv} = \int quv dx, Q_{vv} = \int qv^2 dx, \tag{5b}$$

the limits on the integrals being $x = a$ and $x = 1$. The determinant of the coefficients of A and B must vanish, hence,

$$\alpha k^2 - \beta k + \gamma = 0, \tag{6}$$

where

$$\alpha = Q_{uu}Q_{vv} - Q_{uv}^2,$$

$$\beta = P_{uu}Q_{vv} + P_{vv}Q_{uu} - 2P_{uv}Q_{uv}, \tag{7}$$

$$\gamma = P_{uu}P_{vv} - P_{uv}^2.$$

The solutions k_1 and k_2 of (6) are

$$k_1 = [\beta - (\beta^2 - 4\alpha\gamma)^{1/2}]/2\alpha, \quad k_2 = \gamma/\alpha k_1. \tag{8}$$

The formulas,

$$k_{uu} = P_{uu}/Q_{uu}, \ k_{uv} = P_{uv}/Q_{uv}, k_{vv} = P_{vv}/Q_{vv}, \tag{9}$$

obtained from (4) with $B = 0$ and $A = 0$, successively, also yield approximate values of the lowest eigenvalue k_1. (There are several different ways of obtaining these quotients.)

If v is obtained by one full cycle of successive approximations (Temple and Bickley, 1956) from an assumed generating function u, then $k_{uu} \geq k_{uv} \geq k_{vv}$, which are the same as the Schwarz and Rayleigh quotients $\mu_n \geq \mu_{n+1} \geq \mu_{n+2}$ given by Temple and Bickley (1956), and Collatz (1948).

In order to examine the accuracy of the results obtainable by this procedure, let us solve a few specific problems.

[2]Professor of Engineering Mechanics, College of Engineering and Science, University of Detroit, Detroit, Mich. 48221-9987. Mem. ASME.

Manuscript received by ASME Applied Mechanics Division, April 11, 1988; final revision, August 22, 1988.

Downloaded 03 May 2010 to 171.66.16.31. Redistribution subject to ASME license or copyright; see http://www.asme.org/terms/Terms_Use.cfm

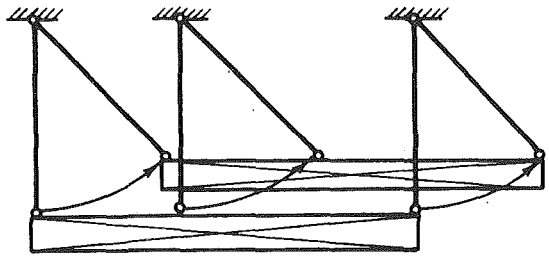


Fig. 3 Statically indeterminate finite mechanism

first order." —Not so (Fig. 1(*c*) is a counterexample). "But if it does lie in the column space we cannot distinguish between a higher-order infinitesimal mechanism and a finite mechanism." —This is a case when equation (4) is satisfied identically indicating that, in the absence of higher-order terms (pin-bar assemblies), constraint equations (1) are globally dependent; the assembly is a finite mechanism which is globally statically indeterminate (e.g., Fig. 3) so that the self-stress is unstable and unrealizable. "This assembly is evidently of a type not envisaged by Maxwell: Its key feature is one of symmetry." —Although the assembly (Tarnai's ring) possesses an interesting symmetry, it is nothing but a globally statically indeterminate finite mechanism conceptually similar to the system in Fig. 3. While it is arguable what Maxwell did or did not envisage, it is certain that symmetry is not the key feature of a statically indeterminate finite mechanism. Another certainty is that such a mechanism cannot be in a state of self-stress and retain its kinematic mobility: these two features are incompatible. In particular, Tarnai's ring cannot be prestressed in any of its kinematically possible configurations.

Conclusions

(1) A sufficient analytical criterion for an immobile kinematic chain is the existence of a linear combination of expanded constraint equations with a sign-definite lowest-order form in independent displacements. The physical meaning of this condition—the statical criterion of immobility—is the statical possibility of stable self-stress.

(2) Most of the claims of the paper by Pellegrino and Calladine (1986) including the central one ("We have succeeded in giving a matrix test . . . ") are invalid. The matrix analysis as conceived and used in the paper (i.e., "unsupplemented" with the stability check) is erroneous. If "supplemented" with a feasible check of stability, the analysis is unnecessary: The stability check alone is sufficient. The authors (borrowing their own comment on p. 412 about another paper) "ended up in a state of confusion."

References

Levi-Civita, T., and Amaldi, U., 1930, *Lezioni di Meccanica Razionale*, (in Italian), Vol. 1, Part 2, 2nd ed., Bologna.

Pellegrino, S., and Calladine, C. R., 1984, "Matrix Analysis of Statically and Kinematically Indeterminate Frameworks," Dept. of Engineering, University of Cambridge, Report CUED/D-Struct/TR110; 1986, *Int. Journ. Solids Structures*, Vol. 22, No. 4, pp. 409-428.

Tarnai, T., 1980, "Problems Concerning Spherical Polyhedra and Structural Rigidity," *Struct. Topology*, Vol. 4, pp. 61-66.

A Way of Accurately Estimating Eigenvalues

Robert Schmidt[2]

Introduction

During the early decades of this century, Timoshenko (1936) and Temple and Bickley (1956) demonstated (by solving many examples) the efficacy of the combination of Rayleigh's method with the method of successive approximation in the estimation of buckling loads and fundamental frequencies. Herein we show how to obtain remarkably accurate estimates of such eigenvalues by combining the two aforementioned methods in a somewhat different way, viz., by using generating shape functions with an adjustable exponent, refining them by the method of successive approximations, and then employing a set of formulas obtained via the Rayleigh-Ritz method or the Temple inequalities.

A Formulation of the Technique

For brevity, let us limit ourselves to eigenvalue problems of the Sturm-Liouville type (Kline, 1972; Courant and Hilbert, 1931), viz.,

$$(py')' + kqy = 0, \quad y' = dy/dx, p(x) > 0, q(x) > 0, \tag{1a}$$

$$y'(a) - h_1 y(a) = 0, y'(1) + h_2 y(1) = 0, a < 1, \tag{1b}$$

or (Finlayson, 1972),

$$S = \int_a^1 [p(y')^2 - kqy^2]dx, \ \delta S = 0. \tag{2}$$

Equation (1*a*) is the Euler equation corresponding to (2).

Let us approximate the solution of (1) by (Collatz, 1948)

$$y = Au(x) + Bv(x), \tag{3}$$

where u and v are some simple functions satisfying the essential (boundary) conditions; substitute (3) in the integral of (2); and apply $\partial S/\partial A = \partial S/\partial B = 0$. In this way, we obtain

$$(P_{uu} - kQ_{uu})A + (P_{uv} - kQ_{uv})B = 0, \tag{4a}$$

$$(P_{uv} - kQ_{uv})A + (P_{vv} - kQ_{vv})B = 0, \tag{4b}$$

where

$$P_{uu} = \int pu'^2 dx, P_{uv} = \int pu'v' dx, P_{vv} = \int pv'^2 dx, \tag{5a}$$

$$Q_{uu} = \int qu^2 dx, Q_{uv} = \int quv dx, Q_{vv} = \int qv^2 dx, \tag{5b}$$

the limits on the integrals being $x = a$ and $x = 1$. The determinant of the coefficients of A and B must vanish, hence,

$$\alpha k^2 - \beta k + \gamma = 0, \tag{6}$$

where

$$\alpha = Q_{uu}Q_{vv} - Q_{uv}^2,$$
$$\beta = P_{uu}Q_{vv} + P_{vv}Q_{uu} - 2P_{uv}Q_{uv}, \tag{7}$$
$$\gamma = P_{uu}P_{vv} - P_{uv}^2.$$

The solutions k_1 and k_2 of (6) are

$$k_1 = [\beta - (\beta^2 - 4\alpha\gamma)^{1/2}]/2\alpha, \quad k_2 = \gamma/\alpha k_1. \tag{8}$$

The formulas,

$$k_{uu} = P_{uu}/Q_{uu}, \ k_{uv} = P_{uv}/Q_{uv}, k_{vv} = P_{vv}/Q_{vv}, \tag{9}$$

obtained from (4) with $B = 0$ and $A = 0$, successively, also yield approximate values of the lowest eigenvalue k_1. (There are several different ways of obtaining these quotients.)

If v is obtained by one full cycle of successive approximations (Temple and Bickley, 1956) from an assumed generating function u, then $k_{uu} \geq k_{uv} \geq k_{vv}$, which are the same as the Schwarz and Rayleigh quotients $\mu_n \geq \mu_{n+1} \geq \mu_{n+2}$ given by Temple and Bickley (1956), and Collatz (1948).

In order to examine the accuracy of the results obtainable by this procedure, let us solve a few specific problems.

[2]Professor of Engineering Mechanics, College of Engineering and Science, University of Detroit, Detroit, Mich. 48221-9987. Mem. ASME.

Manuscript received by ASME Applied Mechanics Division, April 11, 1988; final revision, August 22, 1988.

Copyright © 1989 by ASME

Downloaded 03 May 2010 to 171.66.16.31. Redistribution subject to ASME license or copyright; see http://www.asme.org/terms/Terms_Use.cfm

Buckling of a Heavy Slender Cone

We assume that this vertical, elastic, conical pole of length L and weight W is built-in at the bottom and free at its tip. We place the origin of coordinates at the top, direct the ξ-axis downward and the η-axis horizontally to the left, and assume that the buckling pole deflects to the right, its tip carrying the nonrotating coordinate axes with it. The small deflection of the buckled pole is governed by the eigenvalue formulation

$$(x^4\theta')' + kx^3\theta = 0,\ \theta(1) = 0,\ x^4\theta' = 0 \text{ at } x = 0, \tag{10}$$

where $x = \xi/L$, $\theta' = d\theta/dx$, θ is the angle of rotation of the line element $d\xi$, and $k = WL^2/EI_m$, EI_m being the maximal bending stiffness (at the base). The differential equation in (10) is the Euler equation corresponding to the integral (2) with $y = \theta$, $p = x^4$, and $q = x^3$.

Now let us assume that, approximately,

$$\theta = y = u = 1 - x^n, \tag{11}$$

where n is an adjustable exponent (it is not easy to surmise the nearly best value of n, in this case). Substituting (11) into (5) and (2), and using the Rayleigh condition $S = 0$ (which is identical with $\delta S = 0$ for Cu, in this case), we obtain

$$k_{uu} = P_{uu}/Q_{uu} = 4(n+2)(n+4)/(2n+3). \tag{12}$$

According to Rayleigh (1945), n is determined from $dk/dn = 0$, which yields $n^2 + 3n + 1 = 0$, so that $n = -0.3819660113$ and, by (12), $k_{uu} = 10.47213595$, as compared with the exact value $k_E = 10.17661$. (The approximate values of k usually are not very sensitive to small changes in n, nor are they much improved by using other k's in the condition $dk/dn = 0$.) (The second root of the quadratic equation does not result in convergence of the successive approximations.)

Next, we rewrite the differential equation in (10) in the form $(x^4\theta_1')' = -kx^3\theta = -kx^3u = -kx^3(1-x^n)$, and, after two successive integrations, obtain

$$v = 4(n+1)(n+4)\theta_1/k = n(n+5) - (n+1)(n+4)x + 4x^{n+1} \tag{13}$$

after satisfying the boundary conditions of (10) and dropping an inconsequential constant multiplier. Substituting the calculated value of $n = -0.3819660113$ into (11) and (13), and then these into (5), (7), (8), and (9), we arrive at

$$Q_{uu} = 0.006230590, \qquad P_{uu} = 0.06524758,$$
$$Q_{uv} = 0.005443215, \qquad P_{uv} = 0.05572809,$$
$$Q_{vv} = 0.004777343, \qquad P_{vv} = 0.04868560,$$
$$\alpha = 0.0000001370755,$$
$$\beta = 0.000008370125,$$
$$\gamma = 0.00007099755,$$

as well as

$$k_{uu} = 10.47214 > k_{uv} = 10.23808 > k_{vv} = 10.19094 > k_1 = 10.17913 > k_E = 10.17661.$$

We see that the error in k_1 is less than 0.025 percent.

A rough (but rather definite) lower bound k_L can be obtained by the well-known formula (Schreyer and Shih, 1973)

$$k_L = k_{vv} - [k_{vv}(k_{uv} - k_{vv})]^{1/2} = 9.498.$$

The formula

$$k_E > k_{HM} = k_{vv} - \left[\frac{1}{3}\, k_{vv}(k_{uv} - k_{vv})\right]^{1/2},$$

recommended by Hanna and Michalopoulos (1979), yields the lower-bound value of 9.791. A tighter (but only very likely) lower bound k_{LL} may be estimated by a simple empirical formula,

$$k_{LL} = k_{vv}^2/k_{uv} = 10.144.$$

Buckling of a Uniformly Compressed Circular Plate

For a buckled clamped circular plate of radius a, Langhaar (1962) gives the governing equations in the form

$$r^2\phi_{rr} + r\phi_r + (\alpha^2 r^2 - 1)\phi = 0, \quad \phi(0) = \phi(a) = 0, \tag{14}$$

where r is the radial coordinate; ϕ the angle of rotation of a radial line element dr; $\phi_r = d\phi/dr$; and $\alpha^2 = N/D = K/a^2$, N being the uniform compressive edge force and D the bending stiffness. With the notation $x = r/a$, $y = x\phi$, we obtain equation (1a) with $p = q = 1/x$, and $k = K = a^2N/D$, and the boundary conditions $y(1) = 0$, $y(0) = 0$.

Now let us assume that, approximately (Schmidt, 1982), $\phi = x - x^n$, or,

$$y = x\phi = u = x^2 - x^{n+1}. \tag{15}$$

Substituting (15) into (2) and proceeding as described in the preceding section, we obtain

$$K_{uu} = 2(n+1)(n+3)/n, \tag{16}$$

$$n^2 - 3 = 0,\ n = 1.732050808,\ K_{uu} = 14.9282032,$$

$$v = (n-1)(n+5)x^2 - (n+1)(n+3)x^4 + 8x^{n+3}, \tag{17}$$

so that

$$K_{uu} = 14.928203 > K_{uv} = 14.713844 > K_{vv} = 14.686661 > K_1 = 14.682723 > K_E = 14.6820. \tag{18}$$

Thus, we see that the error in K_1 is about 0.005 percent.

Graetz's Problem

Shah and London (1978) presented

$$(xy')' + \kappa(x - x^3)y = 0, \quad 0 \le x \le 1, \tag{19a}$$

$$y(1) = 0, \quad y'(0) = 0. \tag{19b}$$

Hence, by (1a), $p = x$, $q = x - x^3$. Assuming $y = u = 1 - x^n$, as in (11), and proceeding as before, we obtain

$$\kappa_{uu} = 2(n+1)(n+2)(n+4)/n(n+7), \tag{20}$$

$$n^4 + 14n^3 + 35n^2 - 16n - 56 = 0, \tag{21}$$

$$n \approx 1.2,\ \kappa_{uu} = 7.4406504,$$

$$v = 3.429375 - 6.76x^2 + 2.640625x^{3.2} + 1.69x^4 - x^{5.2}, \tag{22}$$

$$\kappa_{uu} = 7.4406504 > \kappa_{uv} = 7.3206672 > \kappa_{vv} = 7.3140784 > \kappa_1 = 7.3136959 > \kappa_E = 7.3135869, \tag{23}$$

where κ_E denotes the exact eigenvalue. The error in κ_1 is circa 0.0015 percent.

Remarks

The procedure for calculating the lowest eigenvalue presented herein makes use of the original Rayleigh method, which had been largely neglected until resurrected and expanded by Schmidt (1981, 1982, 1985) and Bert (1984); a modified two-term Ritz approach; and the method of successive approximations. A considerable number of buckling and vibration problems (other than the three presented in this brief note) have been solved approximately by the author with the aid of this technique and, in all cases, results of remarkable ac-

Downloaded 03 May 2010 to 171.66.16.31. Redistribution subject to ASME license or copyright; see http://www.asme.org/terms/Terms_Use.cfm

curacy have been obtained with a moderate expenditure of labor (the technique can also be applied to eigenvalue problems governed by higher-order differential equations obtainable by the calculus of variations).

Whenever the function $k_{uu}=f(n)$ is not easily differentiable, we can estimate the minimal k_{uu} and, hence, the best value of n, by performing a few trial calculations and observing the trend of their results.

It might be of interest to note that equating the two expressions involving k_E in $k_{E2} \le k_{vv}(k_{uv}-k_E)/(k_{vv}-k_E) \le k_{uv}(k_{uu}-k_E)/(k_{uv}-k_E)$ (which formulas can be deduced from the main rigorous result given by Temple and Bickley (1956)), and replacing k_E by k, we obtain a quadratic equation whose roots k_1 and k_2 numerically coincide with those of equation (6)!

We may also state here that *all* lower-bound formulas mentioned herein are a direct consequence of Temple's inequality, $k_E \ge k_{vv}(k_{E2}-k_{uv})/(k_{E2}-k_{vv}) \ge k_{uv}(k_{E2}-k_{uu})/(k_{E2}-k_{uv})$, (Temple and Bickley, 1956), and hence, knowledge of the second eigenvalue k_{E2} or its (rough) lower bound is a precondition for their *definite* validity. Nevertheless, these formulas are very useful, since, in practice, the second eigenvalue k_{E2} is usually larger than $2k_E$ (Temple and Bickley, 1956).

References

Bert, C. W., 1984, "Improved Technique for Estimating Buckling Loads," *ASCE Journal of Engineering Mechanics*, Vol. 110, pp. 1655–1665.

Collatz, L., 1948, *Eigenwertprobleme und Ihre Numerische Behandlung*, Chelsea Publishing Co., New York.

Courant, R., and Hilbert, D., 1931, *Methoden der Mathematischen Physik*, Vol. 1, Verlag von Julius Springer, Berlin.

Finlayson, B. A., 1972, *The Method of Weighted Residuals and Variational Principles*, Academic Press, New York.

Hanna, S. Y., and Michalopoulos, C. D., 1979, "Improved Lower Bounds for Buckling Loads and Fundamental Frequencies of Beams," ASME JOURNAL OF APPLIED MECHANICS, Vol. 46, pp. 696–698.

Kline, M., 1972, *Mathematical Thought from Ancient to Modern Times*, Oxford Unversity Press, New York.

Langhaar, H. L., 1962, *Energy Methods in Applied Mechanics*, John Wiley and Sons, New York.

Rayleigh, J. W. S., 1945, *The Theory of Sound*, Vol. 1, 2nd ed., Dover Publications, New York.

Schmidt, R., 1981, "A Variant of the Rayleigh-Ritz Method," *Industrial Mathematics*, Vol. 31, pp. 37–46.

Schmidt, R., 1982, "Estimation of Buckling Loads and Other Eigenvalues via a Modification of the Rayleigh-Ritz Method," ASME JOURNAL OF APPLIED MECHANICS, Vol. 49, pp. 639–640.

Schmidt, R., 1985, "Towards Resurrecting the Original Rayleigh Method," *Industrial Mathematics*, Vol. 35, pp. 69–73.

Schreyer, H. L., and Shih, P.-Y., 1973, "Lower Bounds to Column Buckling Loads," *Journal of the Engineering Mechanics Division, Proc. ASCE*, Vol. 99, pp. 1011–1022.

Shah, R. K., and London, A. L., 1978, *Laminar Flow Forced Convection in Ducts*, Academic Press, New York.

Temple, G., and Bickley, W. G., 1956, *Rayleigh's Principle*, Dover Publications, New York (a reprint of the 1933 edition).

Timoshenko, S., 1936, *Theory of Elastic Stability*, McGraw-Hill Book Co., New York.

Thermodynamical Inequalities, Reciprocal Relations, and Mixtures

A. E. Green[3] and P. M. Naghdi[4]

A thermodynamical inequality is obtained for mixtures of interacting continua; it represents the analogue of a corresponding inequality for single phase media contained in a paper of Green and Naghdi (1984) and is less restrictive than one proposed earlier (1978b). Also, the use of such inequalities in conjunction with the so-called reciprocal relations is briefly discussed.

1 Introduction

Some statements of the Second Law of Thermodynamics and a thermodynamical inequality for single-phase continua were previously discussed by Green and Naghdi (1978a) and these were subsequently extended in a paper which also accounts for electromagnetic effects (Green and Naghdi, 1984). Our purpose here is to provide a parallel extension (in the absence of electromagnetic effects) to mixtures of thermodynamical statements and inequality for single-phase media contained in Green and Naghdi (1984). At the same time, we take this opportunity to clarify some misinterpretations pertaining to the use of such inequalities (Green and Naghdi, 1977; 1978a,b) in conjunction with the Onsager reciprocal relations. For further background we recall that in a recent paper, Woods (1980, pp. 238–240) has criticized one of the thermodynamical inequalities used by Green and Naghdi (1977, 1978a, b) on the grounds that it suppresses thermal diffusion in a diffusing fluid mixture. This is not because the inequality alone suppresses thermal diffusion—it certainly does not do so—but because Woods claims that the (Onsager) reciprocal relations, used in conjunction with the inequality, demand this restriction. Evidently Woods regards the reciprocal relations as a necessary part of the thermodynamics—a view shared by a number of authors—so that he never considers the alternative possibility that the reciprocal relations may be too restrictive. Nevertheless, the status of these relations is still unclear. For a detailed discussion, see Truesdell (1969). Without entering into this controversial question, we observe that the derivation of reciprocal relations usually depends on the existence of a nonnegative quadratic function associated with the local rate of production of entropy, together with additional assumptions; see, for example, Woods (1975, Sections 40.2, 42.3). Green and Naghdi use a number of inequalities which are closely related to physical requirements of the Second Law of Thermodynamics and which are summarized in the form of statements, mostly for cyclic motions (see Truesdell, 1976; Green and Naghdi, 1978a) and only one of these involves the rate of production of entropy. This is

$$-\int_I \int_{B_t} \xi \, dm \, dt = \int_I \left[\int_{B_t} \frac{r}{\theta} dm - \int_{\partial B_t} \frac{\mathbf{q}\cdot n}{\theta} da \right] dt \le 0 \quad (1)$$

for all *cyclic* motions where the time integral is over a closed interval of time I and the volume and surface integrals are over the whole body B_t and its boundary ∂B_t. Here r is the external rate of supply of heat per unit mass, $\mathbf{q}$ is the heat conduction vector, θ (≥ 0) is the absolute temperature, and ξ is the internal rate of production of entropy per unit mass. Such an inequality cannot, in general, yield a local inequality of the type used by Woods so that in this context there is no basis for his form of reciprocal relation. The Green-Naghdi inequality $\mathbf{w}^* \ge 0$ to which Woods refers (see Green and Naghdi, 1978a, inequality (30)) is a local inequality and following his method, could be used as a basis for deriving reciprocal relations. The inequality $w^* \ge 0$ does not involve the heat conduction vector $\mathbf{q}$, so that reciprocal relations obtained from it would, in turn, not involve $\mathbf{q}$. If such relations were then used with the Green-Naghdi inequality, thermal diffusion would not be suppressed. We are not advocating such inequalities, but merely wish to point out that in the context of the development of

[3]Mathematical Institute, University of Oxford, Oxford OXl 3LB, U.K.

[4]Department of Mechanical Engineering, University of California, Berkeley, Calif. 94720. Honorary Member ASME.

Manuscript received by the ASME Applied Mechanics Division, June 10, 1988; final revision, August 29, 1988.

Downloaded 03 May 2010 to 171.66.16.31. Redistribution subject to ASME license or copyright; see http://www.asme.org/terms/Terms_Use.cfm

curacy have been obtained with a moderate expenditure of labor (the technique can also be applied to eigenvalue problems governed by higher-order differential equations obtainable by the calculus of variations).

Whenever the function $k_{uu}=f(n)$ is not easily differentiable, we can estimate the minimal k_{uu} and, hence, the best value of n, by performing a few trial calculations and observing the trend of their results.

It might be of interest to note that equating the two expressions involving k_E in $k_{E2} \le k_{vv}(k_{uv}-k_E)/(k_{vv}-k_E) \le k_{uv}(k_{uu}-k_E)/(k_{uv}-k_E)$ (which formulas can be deduced from the main rigorous result given by Temple and Bickley (1956)), and replacing k_E by k, we obtain a quadratic equation whose roots k_1 and k_2 numerically coincide with those of equation (6)!

We may also state here that *all* lower-bound formulas mentioned herein are a direct consequence of Temple's inequality, $k_E \ge k_{vv}(k_{E2}-k_{uv})/(k_{E2}-k_{vv}) \ge k_{uv}(k_{E2}-k_{uu})/(k_{E2}-k_{uv})$, (Temple and Bickley, 1956), and hence, knowledge of the second eigenvalue k_{E2} or its (rough) lower bound is a precondition for their *definite* validity. Nevertheless, these formulas are very useful, since, in practice, the second eigenvalue k_{E2} is usually larger than $2k_E$ (Temple and Bickley, 1956).

References

Bert, C. W., 1984, "Improved Technique for Estimating Buckling Loads," *ASCE Journal of Engineering Mechanics*, Vol. 110, pp. 1655–1665.

Collatz, L., 1948, *Eigenwertprobleme und Ihre Numerische Behandlung*, Chelsea Publishing Co., New York.

Courant, R., and Hilbert, D., 1931, *Methoden der Mathematischen Physik*, Vol. 1, Verlag von Julius Springer, Berlin.

Finlayson, B. A., 1972, *The Method of Weighted Residuals and Variational Principles*, Academic Press, New York.

Hanna, S. Y., and Michalopoulos, C. D., 1979, "Improved Lower Bounds for Buckling Loads and Fundamental Frequencies of Beams," ASME JOURNAL OF APPLIED MECHANICS, Vol. 46, pp. 696–698.

Kline, M., 1972, *Mathematical Thought from Ancient to Modern Times*, Oxford Unversity Press, New York.

Langhaar, H. L., 1962, *Energy Methods in Applied Mechanics*, John Wiley and Sons, New York.

Rayleigh, J. W. S., 1945, *The Theory of Sound*, Vol. 1, 2nd ed., Dover Publications, New York.

Schmidt, R., 1981, "A Variant of the Rayleigh-Ritz Method," *Industrial Mathematics*, Vol. 31, pp. 37–46.

Schmidt, R., 1982, "Estimation of Buckling Loads and Other Eigenvalues via a Modification of the Rayleigh-Ritz Method," ASME JOURNAL OF APPLIED MECHANICS, Vol. 49, pp. 639–640.

Schmidt, R., 1985, "Towards Resurrecting the Original Rayleigh Method," *Industrial Mathematics*, Vol. 35, pp. 69–73.

Schreyer, H. L., and Shih, P.-Y., 1973, "Lower Bounds to Column Buckling Loads," *Journal of the Engineering Mechanics Division, Proc. ASCE*, Vol. 99, pp. 1011–1022.

Shah, R. K., and London, A. L., 1978, *Laminar Flow Forced Convection in Ducts*, Academic Press, New York.

Temple, G., and Bickley, W. G., 1956, *Rayleigh's Principle*, Dover Publications, New York (a reprint of the 1933 edition).

Timoshenko, S., 1936, *Theory of Elastic Stability*, McGraw-Hill Book Co., New York.

Thermodynamical Inequalities, Reciprocal Relations, and Mixtures

A. E. Green[3] and P. M. Naghdi[4]

A thermodynamical inequality is obtained for mixtures of interacting continua; it represents the analogue of a corresponding inequality for single phase media contained in a paper of Green and Naghdi (1984) and is less restrictive than one proposed earlier (1978b). Also, the use of such inequalities in conjunction with the so-called reciprocal relations is briefly discussed.

1 Introduction

Some statements of the Second Law of Thermodynamics and a thermodynamical inequality for single-phase continua were previously discussed by Green and Naghdi (1978a) and these were subsequently extended in a paper which also accounts for electromagnetic effects (Green and Naghdi, 1984). Our purpose here is to provide a parallel extension (in the absence of electromagnetic effects) to mixtures of thermodynamical statements and inequality for single-phase media contained in Green and Naghdi (1984). At the same time, we take this opportunity to clarify some misinterpretations pertaining to the use of such inequalities (Green and Naghdi, 1977; 1978a,b) in conjunction with the Onsager reciprocal relations. For further background we recall that in a recent paper, Woods (1980, pp. 238–240) has criticized one of the thermodynamical inequalities used by Green and Naghdi (1977, 1978a, b) on the grounds that it suppresses thermal diffusion in a diffusing fluid mixture. This is not because the inequality alone suppresses thermal diffusion—it certainly does not do so—but because Woods claims that the (Onsager) reciprocal relations, used in conjunction with the inequality, demand this restriction. Evidently Woods regards the reciprocal relations as a necessary part of the thermodynamics—a view shared by a number of authors—so that he never considers the alternative possibility that the reciprocal relations may be too restrictive. Nevertheless, the status of these relations is still unclear. For a detailed discussion, see Truesdell (1969). Without entering into this controversial question, we observe that the derivation of reciprocal relations usually depends on the existence of a nonnegative quadratic function associated with the local rate of production of entropy, together with additional assumptions; see, for example, Woods (1975, Sections 40.2, 42.3). Green and Naghdi use a number of inequalities which are closely related to physical requirements of the Second Law of Thermodynamics and which are summarized in the form of statements, mostly for cyclic motions (see Truesdell, 1976; Green and Naghdi, 1978a) and only one of these involves the rate of production of entropy. This is

$$-\int_I \int_{B_t} \xi \, dm \, dt = \int_I \left[\int_{B_t} \frac{r}{\theta} dm - \int_{\partial B_t} \frac{\mathbf{q}\cdot n}{\theta} da \right] dt \le 0 \quad (1)$$

for all *cyclic* motions where the time integral is over a closed interval of time I and the volume and surface integrals are over the whole body B_t and its boundary ∂B_t. Here r is the external rate of supply of heat per unit mass, $\mathbf{q}$ is the heat conduction vector, θ (≥ 0) is the absolute temperature, and ξ is the internal rate of production of entropy per unit mass. Such an inequality cannot, in general, yield a local inequality of the type used by Woods so that in this context there is no basis for his form of reciprocal relation. The Green-Naghdi inequality $\mathbf{w}^* \ge 0$ to which Woods refers (see Green and Naghdi, 1978a, inequality (30)) is a local inequality and following his method, could be used as a basis for deriving reciprocal relations. The inequality $w^* \ge 0$ does not involve the heat conduction vector $\mathbf{q}$, so that reciprocal relations obtained from it would, in turn, not involve $\mathbf{q}$. If such relations were then used with the Green-Naghdi inequality, thermal diffusion would not be suppressed. We are not advocating such inequalities, but merely wish to point out that in the context of the development of

[3]Mathematical Institute, University of Oxford, Oxford OXl 3LB, U.K.

[4]Department of Mechanical Engineering, University of California, Berkeley, Calif. 94720. Honorary Member ASME.

Manuscript received by the ASME Applied Mechanics Division, June 10, 1988; final revision, August 29, 1988.

Copyright © 1989 by ASME

Downloaded 03 May 2010 to 171.66.16.31. Redistribution subject to ASME license or copyright; see http://www.asme.org/terms/Terms_Use.cfm

Green-Naghdi (1978a), any possible reciprocal relations would not be the same as those used by Woods, and would not cause undue restrictions in thermal diffusion.

In a later paper, which included electromagnetic effects for a single phase media, Green and Naghdi (1984) established the inequality (1) as a necessary and sufficient condition for the satisfaction of a number of statements. These statements represent various ideas concerning irreversibilities which occur in nature and which are usually known as the Second Law of Thermodynamics. They then raised the question as to whether or not one of the statements (numbered 3), namely that "It is impossible completely to reverse a process (not necessarily cyclic) in which mechanical work is transformed into heat by friction," had been interpreted by Green and Naghdi (1978a) in a too restrictive way. They rephased Statement 3 more precisely as "in any process and reverse process the total mechanical work done on the body is nonnegative provided the body has returned to its same state." To summarize the consequences of the latter statement in the absence of electromagnetic forces, consider a single-phase continuum and recall that the terminology of a *process* refers to a sequence of values of the deformation[5] $\mathbf{x}(t)$ and the temperature $\theta(t)$ throughout the body in the time interval $0 \le t \le \sigma$, while, for a *reverse process*, the deformation and temperature must satisfy $\mathbf{x}(t) = \mathbf{x}(2\sigma - t)$, $\theta(t) = \theta(2\sigma - t)$ in the interval $\sigma \le t \le 2\sigma$. Then, if the process is such that the body is in the same state at $t = 0$ and $t = 2\sigma$, $\mathbf{v} \cdot \mathbf{v}$ is continuous at $t = \sigma$ and has the same value at $t = 0$ and $t = 2\sigma$, application of the foregoing statement to any part P of the body yields the condition

$$\int_o^\sigma \int_P \mathbf{T}(t) \cdot \mathbf{D}(t) dv\, dt + \int_\sigma^{2\sigma} \int_P \mathbf{T}(t) \cdot \mathbf{D}(t) dv dt \ge 0, \tag{2}$$

where $\mathbf{T}$ is the stress tensor and $\mathbf{D}$ the rate of deformation tensor. Since, in the interval $\sigma \le t \le 2\sigma$, $\mathbf{D}(t) = -\mathbf{D}(2\sigma - t)$ and the mass density $\rho(t) = \rho(2\sigma - t)$, the inequality (2) may be expressed in the form

$$\int_o^\sigma \int_P \{\mathbf{T}(t) - \mathbf{T}(2\sigma - t)\} \cdot \mathbf{D}(t) dv\, dt$$

$$= \int_P \rho\, dv \int_o^\sigma \rho^{-1}(t) \{\mathbf{T}(t) - \mathbf{T}(2\sigma - t)\} \mathbf{D}(t) dt \ge 0, \tag{3}$$

which must hold for all P. Then, under sufficient smoothness, assumptions (more drastic assumptions have already been made in deriving field equations of motion), it follows from (3) that

$$\int_o^\sigma \rho^{-1}(t) \{\mathbf{T}(t) - \mathbf{T}(2\sigma - t)\} \cdot \mathbf{D}(t) dt \ge 0. \tag{4}$$

2 Inequalities for Mixtures

Changes corresponding to the various inequalities in Section 1 (including $w^* \ge 0$) would be necessary in mixture theory (Green and Naghdi, 1978b) which we indicate briefly here, using the notation of that paper. First, we apply the statements which resulted in the inequality (1), as developed in detail by Green and Naghdi (1984), to the whole mixture contained in some region R of space at time t. Then, with $\theta_\alpha\ (>0)$ being the absolute temperature of the constituent C_α, r_α the external rate of supply of heat to C_α per unit mass and $-\mathbf{q}_\alpha$ the heat flux vector for C_α, we are led to the inequality

$$\sum_{\alpha=1}^{\nu} \int_I \left[\int_R \frac{\rho_\alpha r_\alpha}{\theta_\alpha} dv - \int_{\partial R} \frac{\mathbf{q} \cdot \mathbf{n}}{\theta_\alpha} da \right] dt \le 0 \tag{5}$$

for all cyclic motions in which the time integral is over the closed interval of time T. The inequality (5) may be reduced to

$$\sum_{\alpha=1}^{\nu} \int_I \left[\frac{d}{dt} \int_R \rho_\alpha \eta_\alpha dv - \int_{\partial R} \rho_\alpha \xi_\alpha dv \right] dt \le 0 \tag{6}$$

or, since the motion is cyclic, to

$$\sum_{\alpha=1}^{\nu} \int_I \int_R \rho_a \xi_\alpha dv\, dt \ge 0, \tag{7}$$

where η_α is the partial entropy density per unit mass and ξ_α the partial internal rate of production of entropy per unit mass.

In a similar way, Statement 3, as recorded in Section 1, when applied to the mixture as a whole, i.e., to any parts P_α $(\alpha = 1, 2, \ldots \nu)$ which coincide with P in the present configuration at time t, leads to

$$\sum_{\alpha=1}^{\nu} \int_o^\sigma \left[\int_{P_\alpha} \rho_\alpha \mathbf{b}^\alpha \cdot \mathbf{v}^\alpha dv + \int_{\partial P_\alpha} \mathbf{t}^\alpha \cdot \mathbf{v}^\alpha da \right] dt$$

$$+ \sum_{\alpha=1}^{\nu} \int_\sigma^{2\sigma} \left[\int_{P_\alpha} \rho_\alpha \mathbf{b}^\alpha \cdot \mathbf{v}^\alpha dv + \int_{\partial P_\alpha} \mathbf{t}^\alpha \cdot \mathbf{v}^\alpha da \right] dt \ge 0, \tag{8}$$

where $\mathbf{v}^\alpha$ is the velocity vector, $\mathbf{b}^\alpha$ the externally applied force per unit mass, and $\mathbf{t}^\alpha$ the partial contact force vector per unit area, all for the constituent C_α. With the help of the equations of motion for each constituent, the inequality (8) can be rewritten as

$$\sum_{\alpha=1}^{\nu} \int_o^\sigma \left[\frac{d}{dt} \int_{P_\alpha} \frac{1}{2} \rho_\alpha \mathbf{v}^\alpha \cdot \mathbf{v}^\alpha dv \right.$$

$$+ \int_{P_\alpha} \left(\frac{1}{2} m_\alpha \mathbf{u}^\alpha \cdot \mathbf{u}^\alpha + \boldsymbol{\mu}^\alpha \cdot \mathbf{v}^\alpha \right.$$

$$\left. \left. + \mathbf{T}^\alpha \cdot \mathbf{L}^\alpha \right) dv \right] dt + \sum_{\alpha=1}^{\nu} \int_\sigma^{2\sigma} \left[\frac{d}{dt} \int_{P_\alpha} \frac{1}{2} \rho_\alpha \mathbf{v}^\alpha \cdot \mathbf{v}^\alpha dv \right.$$

$$\left. + \int_{P_\alpha} \left(\frac{1}{2} m_\alpha \mathbf{u}^\alpha \cdot \mathbf{u}^\alpha + \boldsymbol{\mu}^\alpha \cdot \mathbf{v}^\alpha + \mathbf{T}^\alpha \cdot \mathbf{L}^\alpha \right) dv \right] dt \ge 0, \tag{9}$$

where $\mathbf{L}^\alpha = \operatorname{grad} \mathbf{v}^\alpha$, $\mathbf{T}^\alpha$ the partial stress tensor, $\boldsymbol{\mu}^\alpha$ the internal diffusive force, $\mathbf{u}^\alpha = \mathbf{v}^\alpha - \mathbf{v}$ with $\mathbf{v}$ being the barycentric or mean velocity of the mixture, and m_α the rate at which mass is supplied to C_α. Then, if the process is such that the mixture is in the same state at $t = 0$ and $t = 2\sigma$, $\mathbf{v}^\alpha \cdot \mathbf{v}^\alpha$ is continuous at $t = \sigma$ and has the same values at $t = 0$ and $t = 2\sigma$, the inequality (9) reduces to

$$\sum_{\alpha=1}^{\nu} \int_o^\sigma \{ [\boldsymbol{\mu}^\alpha(t) - \boldsymbol{\mu}^\alpha(2\sigma - t)] \cdot \mathbf{v}^\alpha(t)$$

$$+ [\mathbf{T}^\alpha(t) - \mathbf{T}^\alpha(2\sigma - t)] \cdot \mathbf{L}^\alpha(t) \} dt \ge 0, \tag{10}$$

where, in obtaining (10), we have also made use of the fact that in the interval

$$\sigma \le t \le 2\sigma,\ \mathbf{v}^\alpha(t) = -\mathbf{v}^\alpha(2\sigma - t),\ \mathbf{L}^\alpha(t) = -\mathbf{L}^\alpha(2\sigma - t),$$

$$\rho_\alpha(t) = \rho_\alpha(2\sigma - t),\ m_\alpha(t) = -m_\alpha(2\sigma - t).$$

It should be noted that the inequality (7), which is directly related to some statements of the Second Law, is not contained in the previous paper (Green and Naghdi 1978b) on mixtures. The special inequality (5.14) of that paper, which is valid only for equilibrium, can be derived from (7). The inequality (10) is slightly less restrictive than (5.9) of Green and Naghdi (1978b), although in many applications, yields the same results. In the case of the mixture of inviscid fluids discussed in Sections 4 and 6 of Green and Naghdi (1978b), the inequality (10) reduces to

$$\int_o^\sigma [\bar{\boldsymbol{\mu}}''(t) - \bar{\boldsymbol{\mu}}''(2\sigma - t)] \cdot \mathbf{a}(t) dt \ge 0, \tag{11}$$

[5] Quantities such as $\mathbf{x}$, θ, and other variables all are functions of both position $\mathbf{X}$ and t, although only dependence on time is emphasized here.

Downloaded 03 May 2010 to 171.66.16.31. Redistribution subject to ASME license or copyright; see http://www.asme.org/terms/Terms_Use.cfm

after use is made of invariance conditions under superposed rigid body motions. Also, in (11), $\mathbf{a}=\mathbf{v}^1-\mathbf{v}^2$ is the difference of the velocities of the mixture of two inviscid fluids and $\bar{\mu}''=0$ when $\mathbf{a}=0$. Now if $\bar{\mu}''$ is a linear function of $\mathbf{a}$, for example

$$\bar{\mu}''=\mathbf{A}\mathbf{a}, \tag{12}$$

where $\mathbf{A}$ is a tensor function of ρ_1, ρ_2, θ_1, θ_2, grad ρ_1, grad ρ_2. grad θ_1, grad θ_2, independent of $\mathbf{a}$, then (11) becomes

$$\int_o^\sigma \mathbf{A}(t)\mathbf{a}\cdot\mathbf{a}dt\geq 0. \tag{13}$$

For given arbitrary values of ρ_1, ρ_2, θ_1, θ_2, grad ρ_1, grad ρ_2, grad θ_1, grad θ_2, independent of time, (13) yields

$$\mathbf{A}\cdot\int_o^\sigma a\otimes\mathbf{a}dt\geq 0, \tag{14}$$

so that $\mathbf{A}$ is a positive semi-definite function of its arguments. This last result is then true for all values of its arguments, time-dependent or not, and is the same as that which follows from (6.11) of Green and Naghdi (1978b).

Continuing with a mixture of two inviscid fluids as in Section 6 of Green and Naghdi (1978b), the inequality (7)—after using also (6.9) and (6.11) of that paper—becomes

$$\int_I\int_R [-\mathbf{p}^1\cdot\text{grad }\theta_1-\mathbf{p}^2\cdot\text{grad }\theta_2+\bar{\mu}''\cdot\mathbf{a}]dv\,dt\geq 0, \tag{15}$$

where $\mathbf{p}^1$, $\mathbf{p}^2$, $\bar{\mu}''$ depend on ρ_1, ρ_2, θ_1, θ_2, grad ρ_1, grad ρ_2, grad θ_1, grad θ_2, $\mathbf{a}$ and $\bar{\mu}''$ vanishes when $\mathbf{a}=0$. To exploit (15), it is necessary to consider particular constitutive equations for $\mathbf{p}^1$, $\mathbf{p}^2$, $\bar{\mu}''$. It can be shown that (15) does not prevent $\mathbf{p}^1$, $\mathbf{p}^2$ from depending on $\mathbf{a}$, although it may be in a nonlinear manner.

Finally, turning to one other remark by Woods (1980, p. 239) which is somewhat misleading, the main purpose of the example of heat conduction in Green and Naghdi (1977, p. 268) was to show that before any other criteria are used, the Clausius-Duhem inequality demands behavior which is in complete opposition to that required by other thermodynamical concepts. In fact, as pointed out by Green and Naghdi (1978a, Sec. 5), the dissipation inequality they finally used in that paper ruled out this kind of heat conduction. Alternatively, the combined use of (1) together with another inequality in Green and Naghdi (1977, equation (4.11)) again ruled out this conductor and reduced it to the usual type of heat conductor.

Acknowledgment

The work of one of us (P.M.N.) was supported by the U.S. Office of Naval Research under Contract N00014-84-K-0264, Work Unit 4324-436 with the University of California, Berkeley.

References

Green, A. E., and Naghdi, P. M., 1977, "On Thermodynamics and the Nature of the Second Law," *Proc. R. Soc. Lond.*, Vol. A357, pp. 253–270.

Green, A. E., and Naghdi, P. M., 1978a, "The Second Law of Thermodynamics and Cyclic Processes," ASME JOURNAL OF APPLIED MECHANICS, Vol. 45, pp. 487–492.

Green, A. E., and Naghdi, P. M., 1978b, "On Thermodynamics and the Nature of the Second Law for Mixtures of Interacting Continua," *Quart. J. Mech. Appl. Math.*, Vol. 31, pp. 265–293.

Green, A. E., and Naghdi, P. M., 1984, "Aspects of the Second Law of Thermodynamics in the Presence of Electromagnetic Effects," *Quart. J. Mech. Appl. Math.*, Vol. 37, pp. 179–193.

Truesdell, C., 1969, *Rational Thermodynamics*, McGraw-Hill, New York.

Truesdell, C., 1976, "Irreversible Heat Engines and the Second Law of Thermodynamics," *Letters in Heat and Mass Transfer*, Vol. 3, pp. 267–290.

Woods, L. C., 1975, *The Thermodynamics of Fluid Systems*, Oxford University Press.

Woods, L. C., 1980, "On the Thermodynamics of Nonlinear Constitutive Relations in Gas Dynamics," *J. Fluid Mech.*, Vol. 101, pp. 225–242.

Vibration of Beams and Plate Strips With Three-Dimensional Flexibility

Manuel Stein[6]

Studies making use of higher vibration modes and frequencies have indicated a need for a more accurate beam theory. Equations of motion are developed here that give a more accurate representation of the dynamic behaivor of a beam than conventional beam theory. Results are obtained using these equations for the natural vibrations of simply-supported aluminum beams of rectangular cross-sections. These results are compared to results from conventional beam theory, and they are examined to identify where various effects are important.

Introduction

Classical (one-dimensional) beam equations may be obtained from three-dimensional theory by assuming for the deformations terms which are arbitrary in one direction and have prescribed coefficients which are functions of the other coordinates. In addition, assumptions are made on forces. Both sets of assumptions are based on the idea that the depth of a beam or plate strip is small compared with its length and that simple deformations occur across the width. More deformation terms and few assumptions on forces may be included to specify a more accurate theory. Equations known as the Timoshenko beam equations are available in the literature and are generally more accurate than the classical beam equations. In classical beam theory, elements of the beam have motion associated with uniform translation and rotation but the translation and rotation are coupled because the transverse shear strain is set equal to zero according to the Kirchoff assumption. In Timoshenko beam theory, elements have the additional motion associated with uncoupled rotation. Thus, Timoshenko beam theory allows additional deformation due to shearing.

For certain applications, such as the studies of structural noise transmission, flutter or sonic fatigue, the higher vibration modes and frequencies are needed. For higher modes and frequencies, the accuracy of Timoshenko theory has been in doubt. To assess the accuracy of the equations for beams or plate strips, comparisons may be made with experimental results or with three-dimensional theory. If the equations are suspect for higher modes and frequencies, three-dimensional theory should be used since dependable experimental results are difficult to obtain in this frequency range. To address some of these limitations a new theory is developed in this paper, which retains the convenience of a one-dimensional theory but has accuracy approaching that of three-dimensional theory. The present theory involves three more unknowns than Timoshenko theory. Cross-sectional elements of the beam or plate strip have the additional motion associated with cross-sectional warping. Also, by adding a trigonometric rotation term, more complicated deformation due to shearing is allowed.

A purpose of this paper is to present one-dimensional equations for the dynamic analysis of beams, plate strips, and columns that include motions of uniform translation and rotation, or cross-sectional warping and translation, and of additional trigonometric rotation. Vibration results are obtained for aluminum beams using these equations and the results identify the natural frequencies for which cross-sectional effects or nonuniform rotation effects are more important.

[6]Senior Aerospace Engineer, Structural Mechanics Division, NASA Langley Research Center, Hampton, Va. 23665.

Manuscript received by the ASME Applied Mechanics Division, November 10, 1987; final revision, April 4, 1988.

Downloaded 03 May 2010 to 171.66.16.31. Redistribution subject to ASME license or copyright; see http://www.asme.org/terms/Terms_Use.cfm

after use is made of invariance conditions under superposed rigid body motions. Also, in (11), $\mathbf{a}=\mathbf{v}^1-\mathbf{v}^2$ is the difference of the velocities of the mixture of two inviscid fluids and $\bar{\mu}''=0$ when $\mathbf{a}=0$. Now if $\bar{\mu}''$ is a linear function of $\mathbf{a}$, for example

$$\bar{\mu}''=\mathbf{A}\mathbf{a}, \tag{12}$$

where $\mathbf{A}$ is a tensor function of ρ_1, ρ_2, θ_1, θ_2, grad ρ_1, grad ρ_2. grad θ_1, grad θ_2, independent of $\mathbf{a}$, then (11) becomes

$$\int_o^\sigma \mathbf{A}(t)\mathbf{a}\cdot\mathbf{a}dt\geq 0. \tag{13}$$

For given arbitrary values of ρ_1, ρ_2, θ_1, θ_2, grad ρ_1, grad ρ_2, grad θ_1, grad θ_2, independent of time, (13) yields

$$\mathbf{A}\cdot\int_o^\sigma a\otimes\mathbf{a}dt\geq 0, \tag{14}$$

so that $\mathbf{A}$ is a positive semi-definite function of its arguments. This last result is then true for all values of its arguments, time-dependent or not, and is the same as that which follows from (6.11) of Green and Naghdi (1978b).

Continuing with a mixture of two inviscid fluids as in Section 6 of Green and Naghdi (1978b), the inequality (7)—after using also (6.9) and (6.11) of that paper—becomes

$$\int_I\int_R [-\mathbf{p}^1\cdot\text{grad }\theta_1-\mathbf{p}^2\cdot\text{grad }\theta_2+\bar{\mu}''\cdot\mathbf{a}]dv\,dt\geq 0, \tag{15}$$

where $\mathbf{p}^1$, $\mathbf{p}^2$, $\bar{\mu}''$ depend on ρ_1, ρ_2, θ_1, θ_2, grad ρ_1, grad ρ_2, grad θ_1, grad θ_2, $\mathbf{a}$ and $\bar{\mu}''$ vanishes when $\mathbf{a}=0$. To exploit (15), it is necessary to consider particular constitutive equations for $\mathbf{p}^1$, $\mathbf{p}^2$, $\bar{\mu}''$. It can be shown that (15) does not prevent $\mathbf{p}^1$, $\mathbf{p}^2$ from depending on $\mathbf{a}$, although it may be in a nonlinear manner.

Finally, turning to one other remark by Woods (1980, p. 239) which is somewhat misleading, the main purpose of the example of heat conduction in Green and Naghdi (1977, p. 268) was to show that before any other criteria are used, the Clausius-Duhem inequality demands behavior which is in complete opposition to that required by other thermodynamical concepts. In fact, as pointed out by Green and Naghdi (1978a, Sec. 5), the dissipation inequality they finally used in that paper ruled out this kind of heat conduction. Alternatively, the combined use of (1) together with another inequality in Green and Naghdi (1977, equation (4.11)) again ruled out this conductor and reduced it to the usual type of heat conductor.

Acknowledgment

The work of one of us (P.M.N.) was supported by the U.S. Office of Naval Research under Contract N00014-84-K-0264, Work Unit 4324-436 with the University of California, Berkeley.

References

Green, A. E., and Naghdi, P. M., 1977, "On Thermodynamics and the Nature of the Second Law," *Proc. R. Soc. Lond.*, Vol. A357, pp. 253–270.

Green, A. E., and Naghdi, P. M., 1978a, "The Second Law of Thermodynamics and Cyclic Processes," ASME JOURNAL OF APPLIED MECHANICS, Vol. 45, pp. 487–492.

Green, A. E., and Naghdi, P. M., 1978b, "On Thermodynamics and the Nature of the Second Law for Mixtures of Interacting Continua," *Quart. J. Mech. Appl. Math.*, Vol. 31, pp. 265–293.

Green, A. E., and Naghdi, P. M., 1984, "Aspects of the Second Law of Thermodynamics in the Presence of Electromagnetic Effects," *Quart. J. Mech. Appl. Math.*, Vol. 37, pp. 179–193.

Truesdell, C., 1969, *Rational Thermodynamics*, McGraw-Hill, New York.

Truesdell, C., 1976, "Irreversible Heat Engines and the Second Law of Thermodynamics," *Letters in Heat and Mass Transfer*, Vol. 3, pp. 267–290.

Woods, L. C., 1975, *The Thermodynamics of Fluid Systems*, Oxford University Press.

Woods, L. C., 1980, "On the Thermodynamics of Nonlinear Constitutive Relations in Gas Dynamics," *J. Fluid Mech.*, Vol. 101, pp. 225–242.

Vibration of Beams and Plate Strips With Three-Dimensional Flexibility

Manuel Stein[6]

Studies making use of higher vibration modes and frequencies have indicated a need for a more accurate beam theory. Equations of motion are developed here that give a more accurate representation of the dynamic behaivor of a beam than conventional beam theory. Results are obtained using these equations for the natural vibrations of simply-supported aluminum beams of rectangular cross-sections. These results are compared to results from conventional beam theory, and they are examined to identify where various effects are important.

Introduction

Classical (one-dimensional) beam equations may be obtained from three-dimensional theory by assuming for the deformations terms which are arbitrary in one direction and have prescribed coefficients which are functions of the other coordinates. In addition, assumptions are made on forces. Both sets of assumptions are based on the idea that the depth of a beam or plate strip is small compared with its length and that simple deformations occur across the width. More deformation terms and few assumptions on forces may be included to specify a more accurate theory. Equations known as the Timoshenko beam equations are available in the literature and are generally more accurate than the classical beam equations. In classical beam theory, elements of the beam have motion associated with uniform translation and rotation but the translation and rotation are coupled because the transverse shear strain is set equal to zero according to the Kirchoff assumption. In Timoshenko beam theory, elements have the additional motion associated with uncoupled rotation. Thus, Timoshenko beam theory allows additional deformation due to shearing.

For certain applications, such as the studies of structural noise transmission, flutter or sonic fatigue, the higher vibration modes and frequencies are needed. For higher modes and frequencies, the accuracy of Timoshenko theory has been in doubt. To assess the accuracy of the equations for beams or plate strips, comparisons may be made with experimental results or with three-dimensional theory. If the equations are suspect for higher modes and frequencies, three-dimensional theory should be used since dependable experimental results are difficult to obtain in this frequency range. To address some of these limitations a new theory is developed in this paper, which retains the convenience of a one-dimensional theory but has accuracy approaching that of three-dimensional theory. The present theory involves three more unknowns than Timoshenko theory. Cross-sectional elements of the beam or plate strip have the additional motion associated with cross-sectional warping. Also, by adding a trigonometric rotation term, more complicated deformation due to shearing is allowed.

A purpose of this paper is to present one-dimensional equations for the dynamic analysis of beams, plate strips, and columns that include motions of uniform translation and rotation, or cross-sectional warping and translation, and of additional trigonometric rotation. Vibration results are obtained for aluminum beams using these equations and the results identify the natural frequencies for which cross-sectional effects or nonuniform rotation effects are more important.

[6]Senior Aerospace Engineer, Structural Mechanics Division, NASA Langley Research Center, Hampton, Va. 23665.

Manuscript received by the ASME Applied Mechanics Division, November 10, 1987; final revision, April 4, 1988.

Copyright © 1989 by ASME

Downloaded 03 May 2010 to 171.66.16.31. Redistribution subject to ASME license or copyright; see http://www.asme.org/terms/Terms_Use.cfm

Analysis

Equations of motions for beams or plate strips are developed in this section of the paper following the work of Mindlin (1951) using total energy. These equations are then applied to the natural vibration of simply-supported rectangular cross-section aluminum beams.

In three-dimensional theory the strain-energy density is given by

$$S=\frac{1}{2}\left(\sigma_x\epsilon_x+\sigma_y\epsilon_y+\sigma_z\epsilon_z+\tau_{yz}\gamma_{yz}+\tau_{xz}\gamma_{xz}+\tau_{xy}\gamma_{xy}\right)$$

and the kinetic energy per unit volume is given by

$$K=\frac{\rho}{2}\left(u_{,t}^2+v_{,t}^2+w_{,t}^2\right)$$

where ρ is the density of the material. The total energy Π at time t, neglecting body and surface forces, may be written as

$$\Pi=\int\int\int_{t_o}^{t}(S+K)_{,t}dtdxdydz+\Pi_o. \tag{1}$$

To get equations more accurate than those of classical or Timoshenko theory, let the displacements be represented by

$$u=\frac{z}{h}u^1(x,t)+\sin\frac{\pi z}{h}u^s(x,t)$$

$$v=\frac{yz}{bh}v_1^1(x,t)$$

$$w=w_o(x,t)+\frac{y^2}{b^2}w_2(x,t) \tag{2}$$

where the coordinates x, y, z are measured along the length, chord, and depth, respectively, and u^1 and w_o are the uniform rotation and deflection terms which appear in Timoshenko theory (1937). If u^1 is set equal to $-w_{o,x}$ in Timoshenko theory only the one unknown w_o is involved and theory based on this one unknown is called classical theory. If v_1^1 and w_2 are included in Timoshenko theory, then the first effects of cross-sectional warping and bending are included. If u_s is included, then a nonuniform additional (trigonometric) rotation is included. To help explain what each of the displacement terms mean the following sketches are presented:

The linear strain-displacement relations of three-dimensional theory and their corresponding values in terms of the present displacements are

$$\begin{Bmatrix}\epsilon_x\\ \epsilon_y\\ \epsilon_z\\ \gamma_{yz}\\ \gamma_{xz}\\ \gamma_{xy}\end{Bmatrix}=\begin{Bmatrix}u_{,x}\\ v_{,y}\\ w_{,z}\\ v_{,z}+w_{,y}\\ u_{,z}+w_{,x}\\ u_{,y}+v_{,x}\end{Bmatrix}$$

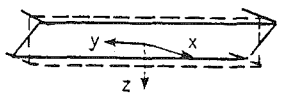
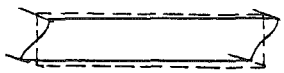
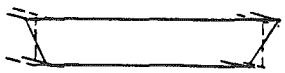
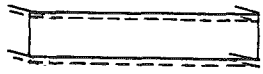
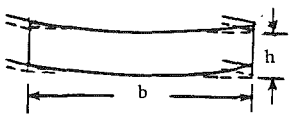
$$=\begin{Bmatrix}\frac{z}{h}u_{,x}^1+\sin\frac{\pi z}{h}u_{,x}^s\\ \frac{z}{bh}v_1^1\\ 0\\ \frac{y}{bh}v_1^1+\frac{2y}{b^2}w_2\\ \frac{1}{h}u^1+\frac{\pi}{h}\cos\frac{\pi z}{h}u^s+w_{o,x}+\frac{y^2}{b^2}w_{2,x}\\ \frac{yz}{bh}v_{1,x}^1\end{Bmatrix}. \tag{3}$$

The strain-displacement relations are substituted into the total energy and the integration over y and z is done.

After integration by parts (in x), the total energy becomes

$$\Pi=\int_0^L\int_{t_o}^{t}\left[\left(-M_{x,x}+N_{xz}+\rho^1\frac{1}{h}u_{,tt}^1+\rho^s\frac{1}{h}u_{,tt}^s\right)\frac{1}{h}u_{,t}^1\right.$$

$$\left.+\left(-M_{xs,x}+N_{xzc}+\rho^s\frac{1}{h}u_{,tt}^1+\rho^{ss}\frac{1}{h}u_{,tt}^s\right)\frac{1}{h}u_{,t}^s\right.$$

Term	Sketch of Cross-Section	Motion
$u=\frac{z}{h}u^1(x,t)$		Uniform Rotation
$u=\sin\frac{\pi z}{h}u^s(x,t)$		Trigonometric Rotation
$v=\frac{yz}{bh}v_1^1(x,t)$		Anticlastic Warping
$w=w_o(x,t)$		Uniform Translation
$w=\frac{y^2}{b^2}w_2(x,t)$		Anticlastic Translation

___ Undeformed

___ Deformed

Downloaded 03 May 2010 to 171.66.16.31. Redistribution subject to ASME license or copyright; see http://www.asme.org/terms/Terms_Use.cfm

$$+\left(-L_{xy,x}+M_y+M_{yz}+\frac{p_1^1}{bh}v_{1,tt}^1\right)\frac{1}{bh}v_{1,t}^1$$

$$+\left(-N_{xz,x}+\rho_o\, w_{o,tt}+\frac{\rho^2}{b^2}w_{2,tt}\right)w_{o,t}$$

$$+\left(-K_{xz,x}+2M_{yz}+\rho_2\, w_{o,tt}\right.$$

$$\left.+\frac{\rho_{22}}{b^2}w_{2,tt}\right)\frac{1}{b^2}w_{2,t}\Big]dtdx+\Pi_o$$

$$+\int_{t_o}^{t}\left(M_x\frac{1}{h}u_{,t}^1+M_{xs}\frac{1}{h}u_{,t}^s+L_{xy}\frac{1}{bh}v_{1,t}^1\right.$$

$$\left.+N_{xz}w_{o,t}+K_{xz}\frac{1}{b^2}w_{2,t}\right)_0^L dt \tag{4}$$

where

$$M_x=\int\int\sigma_x z\,dydz \quad M_{xs}=h\int\int\sigma_x\sin\frac{\pi z}{h}\,dydz$$

$$M_y=\int\int\sigma_y z\,dydz \quad M_{yz}=\int\int\tau_{yz}y\,dydz$$

$$N_{xz}=\int\int\tau_{xz}dydz \qquad N_{xzc}=\pi\int\int\tau_{xz}\cos\frac{\pi z}{h}\,dydz$$

$$K_{xz}=\int\int\tau_{xz}y^2dydz \qquad L_{xy}=\int\int\tau_{xy}yz\,dydz$$

$$\rho^1=\rho\int\int z^2dydz \qquad \rho^s=\rho h\int\int z\sin\frac{\pi z}{h}\,dydz$$

$$\rho^{ss}=\rho h^2\int\int\sin^2\frac{\pi z}{h}\,dydz \qquad \rho_1^1=\rho\int\int y^2z^2dydz \tag{5}$$

$$\rho_o=\rho\int\int dydz \qquad \rho_2=\rho\int\int y^2dydz \qquad \rho_{22}=\rho\int\int y^4dydz$$

and the differential equations of motion corresponding to the assumed displacements (2) are

$$M_{x,x}-N_{xz}=\frac{1}{h}(\rho^1u_{,tt}^1+\rho^su_{,tt}^s)$$

$$M_{xy,x}-N_{xzc}=\frac{1}{h}(\rho^su_{,tt}^1+\rho^{ss}u_{,tt}^s)$$

$$L_{xy,x}-M_y-M_{yz}=\frac{1}{bh}\rho^1v_{1,tt}$$

$$N_{xz,x}=\rho_o w_{o,tt}+\frac{1}{b^2}\rho_2 w_{2,tt} \tag{6}$$

$$K_{xz,x}-2M_{yz}=\rho_2 w_{o,tt}+\frac{1}{b^2}\rho_{22}w_{2,tt}.$$

Consistent boundary conditions are those which cause the integral over time at the boundaries $x=0$ and $x=L$ in equation (6) to vanish. Usually this is accomplished by either prescribing the stress resultants or the corresponding time derivative of the displacement components. If the stress results are constant in time, the displacement components may be prescribed instead. With Hooke's law given by

$$\begin{Bmatrix}\sigma_x\\ \sigma_y\\ \sigma_z\\ \tau_{yz}\\ \tau_{xz}\\ \tau_{xy}\end{Bmatrix}=\begin{bmatrix}C_{11}&C_{12}&0&0&0&0\\ C_{12}&C_{22}&0&0&0&0\\ 0&0&C_{33}&0&0&0\\ 0&0&0&C_{44}&0&0\\ 0&0&0&0&C_{55}&0\\ 0&0&0&0&0&C_{66}\end{bmatrix}\begin{Bmatrix}\epsilon_x\\ \epsilon_y\\ \epsilon_z\\ \gamma_{yz}\\ \gamma_{xz}\\ \gamma_{xy}\end{Bmatrix}. \tag{7}$$

For natural vibrations of an untapered simply supported beam of length, L, the equations of motion (6) are satisfied by

$$u^1=U\cos\frac{m\pi x}{L}\sin\omega t$$

$$u^s=U_s\cos\frac{m\pi x}{L}\sin\omega t$$

$$v_1^1=V\sin\frac{m\pi x}{L}\sin\omega t \tag{8}$$

$$w_o=W\sin\frac{m\pi x}{L}\sin\omega t$$

$$w_2=W_2\sin\frac{m\pi x}{L}\sin\omega t.$$

The results of the present paper are determined by obtaining the natural frequencies ω for a rectangular cross-section untapered beam of length of L, width b, and thickness h by substitution of equations 8 into equations 6 and using the expressions for the the integrals in equation 5.

Results and Discussion

Equations of motion are developed for a beam or plate strip that give more accurate dynamic behavior. Exact dynamic behavior is given by three-dimensional theory. Approximate dynamic behavior can be studied by the energy method where more terms taken in a series guarantee that as good or more accurate behavior will be obtained. More accurate theory is obtained here by starting with the displacements for anticlastic bending of the cross-section suggested by the "exact" solution for pure bending of bars from elasticity in three dimensions (see Timoshenko and Goodier, 1970). More complicated (trigonometric) rotations are also included (a relaxation of the assumption of uniform rotation). Body and surface forces have not been included. From the energy method, five differential equations of motion (equations 6) are derived with consistent boundary conditions. These equations include motions of

- Uniform translation
- Uniform rotation
- Anticlastic warping
- Anticlastic translation
- Trigonometric rotation

The last three motions named are not present in classical or Timoshenko theory.

To determine if these additional motions are important, vibration results are obtained for aluminum beams (plate strips) of rectangular cross-section. Natural frequencies have been calculated for simply-supported beams of square cross-section ($b/h=1$) and for $b/h=5$ and 10 using the present theory and for all b/h using classical and Timoshenko theories. The results are plotted in Fig. 1 using

$$C_{11}=C_{22}=E/(1-\nu^2)$$
$$C_{12}=\nu E/(1-\nu^2)$$
$$C_{44}=C_{55}=C_{66}=G=E/[2(1+\nu)]$$

Downloaded 03 May 2010 to 171.66.16.31. Redistribution subject to ASME license or copyright; see http://www.asme.org/terms/Terms_Use.cfm

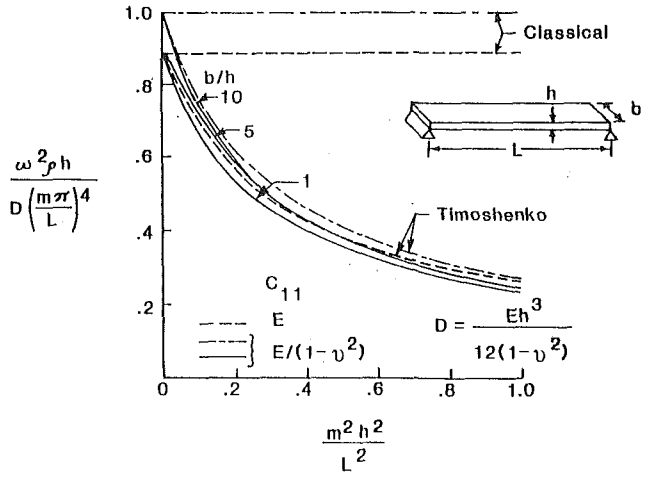


Fig. 1 Natural frequencies for an aluminum beam

Table 1 Calculated frequencies

$\left(\frac{mh}{L}\right)^2$	.16	1.		
	.8889	.8889	Classical	$C_{11} = E$
	.6127	.2539	Timoshenko	
$\frac{\omega^2 \rho h}{D\left(\frac{m\pi}{L}\right)^4}$	.6704	.2668	Timoshenko	$C_{11} = E/(1-\upsilon^2)$
	.6285	.2580	U W V	
	.6180	.2554	U W V W_2	
	.5893	.2331	U W V W_2 U_s	

where

$$\upsilon = .33$$

$$E = 10.7 \times 10^6 \text{psi}.$$

In this figure, the frequency ω is plotted versus the ratio of the thickness h to half wave length L/m in terms of dimensionless parameters. If consideration is restricted to the material parameter C_{11} given by the value $C_{11} = E/(1-\nu^2)$, then the present theory gives the lowest frequencies, Timoshenko theory gives the next lowest frequencies, and classical theory gives the highest frequencies. The present results are, therefore, the most accurate. Often the value of $C_{11} = E$ is used for the classical and Timoshenko theoretical calculations of natural frequency, and using $C_{11} = E$ gives good results for the lower frequencies of narrow strips using Timoshenko theory. There is no usual way of studying the elasticity of beam in three dimensions with this value of C_{11}. For larger values of the ratio of thickness to half wavelength, the present theory gives much lower frequencies than Timoshenko theory, no matter which value of C_{11} is used, and is expected to always be better based on the discussion at the beginning of this section for the same C_{11}.

Another comparison is presented in Table 1 for the square cross-section aluminum beam to identify where the various new effects of the present theory are important. Values of the frequency parameter are given from classical and Timoshenko theories for a low value of the ratio $m^2h^2/L^2 = 0.16$ and for a high value $m^2h^2/L^2 = 1.0$. These results are obtainable from the present theory if only the U and W coefficients are nonzero; that is, if only the displacement terms u^1 and w_o are nonzero. Other results in Table 1 for the values of the ratio 0.16 and 1.0 and presented for cases where U, W, and V are nonzero; U, W, V, and W_2 are nonzero; and where all the terms U, W, V, W_2, and U_s are nonzero. A study of the frequency parameter values in this table reveals that anticlastic effects (V and W_2) are important for lower natural frequencies and more complicated (trigonometric) rotations (U_s) are important for higher natural frequencies.

Concluding Remarks

Equations of motion have been derived for beams and plate strips which are more accurate than conventional classical or Timshenko theories. Besides the usual motion of uniform translation and rotation, motions of anticlastic bending the (trigonometric) nonuniform rotation are allowed.

Vibration results are obtained for aluminum beams which show that the present theory is more accurate than conventional transverse shearing theory.

Anticlastic effects are important for lower natural frequencies. Nonuniform rotation (trigonometric) effects are important for higher natural frequencies.

References

Mindlin, R. D., 1951, "Influence of Rotatory Inertia and Shear on Flexural Motions of Isotropic, Elastic Plates," ASME JOURNAL OF APPLIED MECHANICS,, pp. 31-38.

Timoshenko, S., 1937, *Vibration Problems in Engineering*. Second ed., D. Van Nostrand Co., Inc., New York, p. 337.

Timoshenko, S. P., and Goodier, J. N., 1970, *Theory of Elasticity*. Third ed., McGraw-Hill Book Co., New York, p. 284.

Two-Dimensional Singularity Solutions in the Presence of an Elliptical Hole

M. Denda[7]

Introduction

Important two-dimensional singularity solutions in an infinite isotropic medium with an elliptical hole are identified and derived systematically based on the solutions of a point force and of a Volterra dislocation in the same medium. (Although the fundamental solutions for a point force and a Volterra dislocation were presented previously by Vitek and Hirth (1977), their solutions contain some errors which are corrected in this note.) These solutions have important applications, not only in the micromechanical studies of defects around the crack, but also in the formulation of the complex variable boundary element method (Denda, 1988) for problems involving a single crack.

In plane problems of elasticity there are other important singularities than a point force and a Volterra dislocation. These are a force dipole, a dislocation dipole, and a plastic source. While a dislocation dipole is an infinitesimal line segment over which a displacement discontinuity is specified, a plastic source (Denda, 1987a) in two dimensions is an infinitesimal region which undergoes a stress-free transformation. Each of them is represented by a certain linear combination of force dipoles resulting in a double couple without moment. Although the three-dimensional versions of these singularities are well known (Mura, 1983), a simple reduction of the dimension in the three-dimensional solutions does not always lead to the correct two-dimensional solutions, as demonstrated by Denda (1987a) for the case of a plastic source. All the existing treatments of the two-dimensional stress-free transformation (or eigenstrain) problems in plane strain (Mura,

[7]Department of Mechanics and Materials Science, College of Engineering, Rutgers University, Piscataway, NJ 08895-0909.

Manuscript received by the ASME Applied Mechanics Division, October 19, 1987; final revision, April 7, 1988.

Downloaded 03 May 2010 to 171.66.16.31. Redistribution subject to ASME license or copyright; see http://www.asme.org/terms/Terms_Use.cfm

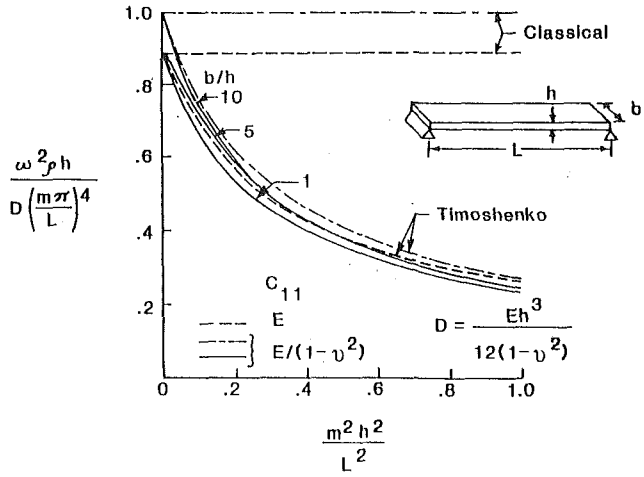


Fig. 1 Natural frequencies for an aluminum beam

Table 1 Calculated frequencies

$\left(\frac{mh}{L}\right)^2$	.16	1.		
$\frac{\omega^2 \rho h}{D\left(\frac{m\pi}{L}\right)^4}$	.8889	.8889	Classical	$C_{11} = E$
	.6127	.2539	Timoshenko	
	.6704	.2668	Timoshenko	$C_{11} = E/(1-\upsilon^2)$
	.6285	.2580	U W V	
	.6180	.2554	U W V W_2	
	.5893	.2331	U W V W_2 U_s	

where

$$\upsilon = .33$$

$$E = 10.7 \times 10^6 \text{psi}.$$

In this figure, the frequency ω is plotted versus the ratio of the thickness h to half wave length L/m in terms of dimensionless parameters. If consideration is restricted to the material parameter C_{11} given by the value $C_{11} = E/(1-\nu^2)$, then the present theory gives the lowest frequencies, Timoshenko theory gives the next lowest frequencies, and classical theory gives the highest frequencies. The present results are, therefore, the most accurate. Often the value of $C_{11} = E$ is used for the classical and Timoshenko theoretical calculations of natural frequency, and using $C_{11} = E$ gives good results for the lower frequencies of narrow strips using Timoshenko theory. There is no usual way of studying the elasticity of beam in three dimensions with this value of C_{11}. For larger values of the ratio of thickness to half wavelength, the present theory gives much lower frequencies than Timoshenko theory, no matter which value of C_{11} is used, and is expected to always be better based on the discussion at the beginning of this section for the same C_{11}.

Another comparison is presented in Table 1 for the square cross-section aluminum beam to identify where the various new effects of the present theory are important. Values of the frequency parameter are given from classical and Timoshenko theories for a low value of the ratio $m^2h^2/L^2 = 0.16$ and for a high value $m^2h^2/L^2 = 1.0$. These results are obtainable from the present theory if only the U and W coefficients are nonzero; that is, if only the displacement terms u^1 and w_o are nonzero. Other results in Table 1 for the values of the ratio 0.16 and 1.0 and presented for cases where U, W, and V are nonzero; U, W, V, and W_2 are nonzero; and where all the terms U, W, V, W_2, and U_s are nonzero. A study of the frequency parameter values in this table reveals that anticlastic effects (V and W_2) are important for lower natural frequencies and more complicated (trigonometric) rotations (U_s) are important for higher natural frequencies.

Concluding Remarks

Equations of motion have been derived for beams and plate strips which are more accurate than conventional classical or Timshenko theories. Besides the usual motion of uniform translation and rotation, motions of anticlastic bending the (trigonometric) nonuniform rotation are allowed.

Vibration results are obtained for aluminum beams which show that the present theory is more accurate than conventional transverse shearing theory.

Anticlastic effects are important for lower natural frequencies. Nonuniform rotation (trigonometric) effects are important for higher natural frequencies.

References

Mindlin, R. D., 1951, "Influence of Rotatory Inertia and Shear on Flexural Motions of Isotropic, Elastic Plates," ASME JOURNAL OF APPLIED MECHANICS,, pp. 31-38.

Timoshenko, S., 1937, *Vibration Problems in Engineering*. Second ed., D. Van Nostrand Co., Inc., New York, p. 337.

Timoshenko, S. P., and Goodier, J. N., 1970, *Theory of Elasticity*. Third ed., McGraw-Hill Book Co., New York, p. 284.

Two-Dimensional Singularity Solutions in the Presence of an Elliptical Hole

M. Denda[7]

Introduction

Important two-dimensional singularity solutions in an infinite isotropic medium with an elliptical hole are identified and derived systematically based on the solutions of a point force and of a Volterra dislocation in the same medium. (Although the fundamental solutions for a point force and a Volterra dislocation were presented previously by Vitek and Hirth (1977), their solutions contain some errors which are corrected in this note.) These solutions have important applications, not only in the micromechanical studies of defects around the crack, but also in the formulation of the complex variable boundary element method (Denda, 1988) for problems involving a single crack.

In plane problems of elasticity there are other important singularities than a point force and a Volterra dislocation. These are a force dipole, a dislocation dipole, and a plastic source. While a dislocation dipole is an infinitesimal line segment over which a displacement discontinuity is specified, a plastic source (Denda, 1987a) in two dimensions is an infinitesimal region which undergoes a stress-free transformation. Each of them is represented by a certain linear combination of force dipoles resulting in a double couple without moment. Although the three-dimensional versions of these singularities are well known (Mura, 1983), a simple reduction of the dimension in the three-dimensional solutions does not always lead to the correct two-dimensional solutions, as demonstrated by Denda (1987a) for the case of a plastic source. All the existing treatments of the two-dimensional stress-free transformation (or eigenstrain) problems in plane strain (Mura,

[7]Department of Mechanics and Materials Science, College of Engineering, Rutgers University, Piscataway, NJ 08895-0909.

Manuscript received by the ASME Applied Mechanics Division, October 19, 1987; final revision, April 7, 1988.

Copyright © 1989 by ASME

Downloaded 03 May 2010 to 171.66.16.31. Redistribution subject to ASME license or copyright; see http://www.asme.org/terms/Terms_Use.cfm

1983; Jaswon and Bhargava, 1961) consider only the in-plane components $\epsilon''_{\alpha\beta}$ ($\alpha, \beta, = 1, 2$) of the eigenstrain but does not consider the out-of-plane component ϵ''_{33}. Obviously, if the eigenstrain represents the plastic strain, the neglect of the component ϵ''_{33} violates the requirement of incompressibility, unless Poisson's ratio $\nu = 0.5$ in isotropic solids. Denda (1987a) overcame this inconsistency by introducing a fictitious eigenstrain called the plane inelastic strain which includes the component ϵ''_{33} and gave a double-couple representation of a plastic source. In this paper we derive these basic singularity solutions in an infinite medium with an elliptical hole in terms of the complex potential functions $\phi(z)$ and $\psi(z)$ of a complex variable $z = x + iy$ (Muskhelishvili, 1958).

Plane Inelastic Strain

Given inelastic strain components ϵ''_{11}, ϵ''_{22}, ϵ''_{12}, and ϵ''_{33} either in plane stress or in plane strain, the stress-strain relations for in-plane components are given by

$$\sigma_{\alpha\beta} = C^*_{\alpha\beta\gamma\delta}(\epsilon_{\gamma\delta} - \epsilon^*_{\gamma\delta}), \tag{1}$$

in terms of the total strain $\epsilon_{\alpha\beta}$ and a fictitious inelastic strain quantity

$$\epsilon^*_{\alpha\beta} = \epsilon''_{\alpha\beta} \text{ (plane stress)}, \quad \epsilon^*_{\alpha\beta} = \epsilon''_{\alpha\beta} + \nu\epsilon''_{33}\delta_{\alpha\beta} \text{ (plane strain)}, \tag{2}$$

which is called the plane inelastic strain (Denda, 1987a). The elastic modulus tensor $C^*_{\alpha\beta\gamma\delta}$ in two dimensions is given by

$$C^*_{\alpha\beta\gamma\delta} = \lambda^*\delta_{\alpha\beta}\delta_{\gamma\delta} + \mu(\delta_{\alpha\gamma}\delta_{\beta\delta} + \delta_{\alpha\delta}\delta_{\beta\gamma}), \tag{3}$$

where λ^* is given by $\lambda^* = 2\lambda\mu/(\lambda + 2\mu)$ in plane stress and $\lambda^* = \lambda$ in plane strain in terms of Lamé constants λ and μ. The out-of-plane components are given by

$$\epsilon_{33} = -\frac{1}{2\mu}\frac{\nu}{\nu+1}\sigma_{\kappa\kappa} + \epsilon''_{33} \text{ (plane stress)},$$

$$\sigma_{33} = \nu\sigma_{\kappa\kappa} - E\epsilon''_{33} \text{ (plane strain)}, \tag{4}$$

where ν is Poisson's ratio and E is Young's modulus.

Singularity Solutions

Consider a point force $f = f_1 + if_2$ (per unit thickness) or a Volterra dislocation with the Burgers vector $b = b_1 + ib_2$ located at ξ in an infinite isotropic medium. The complex potential functions (or the Green's functions) are given (Denda, 1987a) by

$$\phi_s(z) = -\gamma\log(z-\xi), \quad \psi_s(z) = -k\bar{\gamma}\log(z-\xi) + \gamma\frac{\bar{\xi}}{z-\xi}, \tag{5}$$

where

$$k = -\kappa, \gamma = \frac{f}{2\pi(\kappa+1)} \quad \text{(for point force)},$$
$$k = 1, \gamma = \frac{i\mu b}{\pi(\kappa+1)} \quad \text{(for dislocation)}, \tag{6}$$

and $\kappa = (3 - \nu)/(1 + \nu)$ in plane stress and $\kappa = 3 - 4\nu$ in plane strain. When an elliptical hole with semi-axes a and b in the x and y directions, respectively, is present, additional image terms in the complex potential functions are required to produce zero tractions on the hole surface. They are obtained by the use of the conformal mapping

$$z = M(w) = R\left(w + \frac{m}{w}\right); \quad R = \frac{1}{2}(a+b), \quad m = \frac{(a-b)}{(a+b)}, \tag{7}$$

and the method of Cauchy integrals with the result:

$$\phi_I(w) = \phi_{I1}(w)\gamma + \phi_{I2}(w)\bar{\gamma},$$

$$\psi_I(w) = \psi_{I1}(w)\gamma + \psi_{I2}(w)\bar{\gamma} - \frac{w(1+mw^2)}{w^2-m}\frac{d}{dw}\phi_I(w), \tag{8}$$

where

$$\phi_{I1}(w) = \log\left(w - \frac{m}{\rho}\right) + k\log\left(w - \frac{1}{\bar{\rho}}\right) - (1+k)\log w,$$

$$\phi_{I2}(w) = -\frac{\rho(1+m\bar{\rho}^2) - \bar{\rho}(m+\rho^2)}{\rho\bar{\rho}(\bar{\rho}^2-m)}\frac{1}{w-\frac{1}{\bar{\rho}}},$$

$$\psi_{I1}(w) = -\frac{\bar{\rho}(m^3+\rho^2) - m\rho(m+\bar{\rho}^2)}{\rho\bar{\rho}(\rho^2-m)}\frac{1}{w-\frac{m}{\rho}},$$

$$\psi_{I2}(w) = \log\left(w - \frac{1}{\bar{\rho}}\right) + k\log\left(w - \frac{m}{\rho}\right) - (1+k)\log w,$$

where ρ is the transform of the source point ξ due to (7).

A force dipole (or a dislocation dipole) is defined by a pair of point forces f and $-f$ (or a pair of Volterra dislocations with the Burgers vectors b and $-b$) located at $\xi + d\xi$ and ξ, respectively. While a force dipole represents a couple, a dislocation dipole represents a displacement discontinuity over an infinitesimal line segment $d\xi$. The complex potential functions for a force dipole (or a dislocation dipole) are derived from those for a point force (or a Volterra dislocation) by applying a total differential operator (Denda, 1987a)

$$d = \frac{\partial}{\partial\xi}d\xi + \frac{\partial}{\partial\bar{\xi}}d\bar{\xi} = \frac{\partial}{\partial\rho}d\rho + \frac{\partial}{\partial\bar{\rho}}d\bar{\rho}, \tag{9}$$

while treating the coefficient γ constant, where $d\rho = \partial\rho/\partial\xi d\xi$. The result is given by

$$\phi^{(d)} = -\gamma\frac{\partial}{\partial\xi}\{\log(z-\xi)\}d\xi + \phi_I^{(d)}, \tag{10}$$

$$\psi^{(d)} = -\frac{\partial}{\partial\xi}\{\log(z-\xi)\}(k\bar{\gamma}d\xi + \gamma d\bar{\xi}) + \gamma\frac{\partial}{\partial\xi}\left\{\frac{\bar{\xi}}{z-\xi}\right\}d\xi + \psi_I^{(d)},$$

where

$$\phi_I^{(d)} = \phi_{I1}^{(d)}\gamma + \phi_{I2}^{(d)}\bar{\gamma}, \quad \psi_I^{(d)} = \psi_{I1}^{(d)}\gamma + \psi_{I2}^{(d)}\bar{\gamma} - \frac{w(1+mw^2)}{w^2-m}\frac{d}{dw}\phi_I^{(d)}, \tag{11}$$

with

$$\phi_{I1}^{(d)} = \frac{\partial}{\partial\rho}\log\left(w - \frac{m}{\rho}\right)d\rho + k\frac{\partial}{\partial\bar{\rho}}\log\left(w - \frac{1}{\bar{\rho}}\right)d\bar{\rho},$$

$$\phi_{I2}^{(d)} = -\frac{\partial}{\partial\rho}\left\{\frac{\rho(1+m\bar{\rho}^2) - \bar{\rho}(m+\rho^2)}{\rho\bar{\rho}(\bar{\rho}^2-m)}\right\}\frac{1}{w-\frac{1}{\bar{\rho}}}d\rho$$

$$-\frac{\partial}{\partial\bar{\rho}}\left\{\frac{\rho(1+m\bar{\rho}^2) - \bar{\rho}(m+\rho^2)}{\rho\bar{\rho}(\bar{\rho}^2-m)}\frac{1}{w-\frac{1}{\bar{\rho}}}\right\}d\bar{\rho},$$

$$\psi_{I1}^{(d)} = -\frac{\partial}{\partial\rho}\left\{\frac{\bar{\rho}(m^3+\rho^2) - m\rho(m+\bar{\rho}^2)}{\rho\bar{\rho}(\rho^2-m)}\frac{1}{w-\frac{m}{\rho}}\right\}d\rho$$

$$-\frac{\partial}{\partial\bar{\rho}}\left\{\frac{\bar{\rho}(m^3+\rho^2) - m\rho(m+\bar{\rho}^2)}{\rho\bar{\rho}(\rho^2-m)}\right\}\frac{1}{w-\frac{m}{\rho}}d\bar{\rho},$$

Downloaded 03 May 2010 to 171.66.16.31. Redistribution subject to ASME license or copyright; see http://www.asme.org/terms/Terms_Use.cfm

$$\psi_{J2}^{(d)} = \frac{\partial}{\partial \bar{\rho}} \log\left(w - \frac{1}{\bar{\rho}}\right) d\bar{\rho} + \mathrm{k} \frac{\partial}{\partial \rho} \log\left(w - \frac{m}{\rho}\right) d\rho.$$

The complex potential functions for a plastic source located at ξ are obtained by using those for a force dipole in its double-couple representation (Denda, 1987a) with the result:

$$\phi^* = -\tau^* \frac{\partial}{\partial \xi} \log(z-\xi) dA + \phi_I^*,$$

$$\psi^* = (\kappa - 1)\sigma^* \frac{\partial}{\partial \xi} \log(z-\xi) dA + \tau^* \frac{\partial}{\partial \xi} \left\{\frac{\bar{\xi}}{z-\xi}\right\} dA + \psi_I^*, \quad (12)$$

where

$$\phi_I^* = \left\{ \left(\tau^* \frac{\partial \phi_{I1}}{\partial \rho} + \sigma^* \frac{\partial \phi_{I2}}{\partial \rho}\right) \frac{1}{M'(\rho)} + \left(\sigma^* \frac{\partial \phi_{I1}}{\partial \bar{\rho}} + \bar{\tau}^* \frac{\partial \phi_{I2}}{\partial \bar{\rho}}\right) \frac{1}{\overline{M'(\rho)}} \right\} dA,$$

$$\psi_I^* = \left\{ \left(\tau^* \frac{\partial \psi_{I1}}{\partial \rho} + \sigma^* \frac{\partial \psi_{I2}}{\partial \rho}\right) \frac{1}{M'(\rho)} + \left(\sigma^* \frac{\partial \psi_{I1}}{\partial \bar{\rho}} + \bar{\tau}^* \frac{\partial \psi_{I2}}{\partial \bar{\rho}}\right) \frac{1}{\overline{M'(\rho)}} \right\} dA - \frac{w(1+mw^2)}{w^2-m} \frac{d}{dw} \phi_I^*, \quad (13)$$

with $M'(\rho) = dM(\rho)/d\rho$ and dA is the infinitesimal area (in the original z-plane) of the plastic source. The coefficients σ^* and τ^* are given by

$$\sigma^* = \frac{1}{2\pi(\kappa+1)} C^*_{\gamma\gamma\alpha\beta} \epsilon^*_{\alpha\beta},$$

$$\tau^* = \frac{1}{2\pi(\kappa+1)} (C^*_{11\alpha\beta} - C^*_{22\alpha\beta} + 2iC^*_{12\alpha\beta}) \epsilon^*_{\alpha\beta}. \quad (14)$$

Concluding Remarks

First, for the solutions of a point force and Volterra dislocation the following corrections in Vitek and Hirth (1977) should be made: The last term in equation (1), i.e., $\bar{\delta} \overline{z_d}/(z - z_d)$, and terms $\frac{\delta}{\bar{\gamma}}$ and $\frac{\bar{\delta}}{\gamma}$ in equation (3) in Vitek and Hirth (1977) should be eliminated.

According to a physical interpretation (Eshelby, 1969) of Somigliana's identity, the displacement field in a finite cracked body R whose boundary ∂R is subject to a traction t_α and a displacement u_α is the same as it would be if the region R is embedded in an infinite medium and ∂R (which now is simply a line marked out in the infinite medium) is covered by a continuous distribution of point forces with density t_α and by a continuous distribution of dislocation dipoles with the Burgers vector u_α. This interpretation provides the basis for the formulation of the complex variable boundary element method for finite cracked plates (Denda, 1988) in which the solutions for a point force and a dislocation dipole, obtained in this note, serve as kernel functions for their continuous distributions. Further, when inelastic deformation is present around a crack, Denda (1987b) has shown that its contribution is represented by a continuous distribution of plastic sources in the infinite cracked body. In such representation, the use of the fictitious inelastic strain quantity $\epsilon^*_{\alpha\beta}$ enables us to give the correct and a common representation of the domain integrals for plane strain and plane stress without changing the form of the kernel functions. In comparison, Mukherjee (1977) has obtained the correct representation in plane strain by amending the kernel functions while using the true inelastic strain $\epsilon''_{\alpha\beta}$.

References

Jaswon, M. A., and Bhargava, R. D., 1961, "Two-dimensional Elastic Inclusion Problems," *Proc. Camb. Phil. Soc.*, Vol. 57, pp. 669–680.

Denda, M., 1987a, "A Complex Variable Green's Function Representation of Plane Inelastic Deformation in Isotropic Solids," *Acta Mechanica*, Vol. 72, pp. 205–221.

Denda, M., 1987b, "A Complex Variable Approach to Inelastic Boundary Value Problems," *Advances in Design and Analysis in Pressure Vessel Technology*, H. Chung, et al., eds., ASME PVP-130 and NE-2, pp. 23–32.

Denda, M., 1988, "The Complex Variable Boundary Element Method for Cracked Isotropic Plates," submitted for publication.

Eshelby, J. D., 1969, "The Elastic Field of a Crack Extending Non-uniformly under General Anti-plane Loading," *J. Mech. Phys. Solids*, Vol. 17, pp. 177–199.

Mukherjee, S., 1977, "Corrected Boundary Integral Equations in Planar Thermoelastoplasticity," *Int. J. Solids Structures*, Vol. 13, pp. 331–335.

Mura, T., 1982, *Micromechanics of Defects in Solids*, Martinus Nijhoff, The Hague.

Muskhelishvili, N. I., 1958, *Some Basic Problems of Mathematical Theory of Elasticity*, Noordhoff, Groningen.

Vitek, V., and Hirth, J. P., 1977, "Line Singularity Fields in the Presence of a Crack of Elliptical Cross-Section," *Scripta Metallurgica*, Vol. 11, pp. 339–340.

Downloaded 03 May 2010 to 171.66.16.31. Redistribution subject to ASME license or copyright; see http://www.asme.org/terms/Terms_Use.cfm

Journal of Applied Mechanics

Discussion

Determining the Stress Distributions in Wound Reels of Magnetic Tape Using a Nonlinear Finite-Difference Approach[1]

Z. Hakiel.[2] I would like to clarify that the approach and key results of this work had been established previously by me in an article presented at the 1986 TAPPI Finishing and Converting Conference and included in the conference proceedings and subsequently published in the May 1987 issue of the TAPPI Journal. The main essence of the work by Willett and Poesch is the solution of the wound reel stress problem in the case of nonlinear orthotropic stack properties and with the use of a central difference technique. This is precisely what is described in the TAPPI publications. In fact, the development of the solution and the experimental verification of the results is very similar in the two papers. It is unfortunate that the authors overlooked the TAPPI publications.

Authors' Closure

We have carefully reviewed the comments by Mr. Hakiel concerning our paper and wish to clarify several points. First, considering the matter of precedence (which was never a major concern to us), the technique we presented in our paper was fully developed as early as July 1985, and the paper which was to appear in *Journal of Applied Mechanics* was completed in May 1986. We did not "overlook" Mr. Hakiel's paper; we were merely finished with our work a year before his analysis appeared.

Mr. Hakiel also seems to imply that the methods presented in the two papers are identical. This is incorrect. Mr. Hakiel makes three simplifying assumptions in his analysis that we chose not to incorporate in our model. First, to quote from his paper, "winding is modeled as the incremental process of adding tensioned hoops of web onto the roll. During the adding of any single hoop, the elastic properties of the roll, including E_r (the radial elastic modulus), are assumed to be constant." This assumption simplifies the numerical procedure because E_r is no longer a function of interlayer pressure within the roll, allowing for the explicit calculation of the pressure distribution in one step. We incorporated a more realistic model wherein this functional dependence on pressure is maintained. This necessitated the use of an implicit, iterative solution technique and differs greatly from that used in Mr. Hakiel's work. In fact, this is the distinguishing feature of our analysis.

Secondly, because the roll at a particular radial station is assumed to have constant elastic properties, the assumption of linear orthotropy can be made. This allows a simple relation between elastic constants to be written as

$$\frac{\nu_r}{E_r} = \frac{\nu_t}{E_t}.$$

Again, because the radial stiffness, E_r, within a roll is really a function of interlayer pressure, this relationship is approximate at best, because the material is not truly orthotropic.

And, finally, the radial Poisson's ratio, ν_r, which we precisely measured for our model is *assumed* to be zero in Mr. Hakiel's analysis. We performed many sensitivity studies using our analysis and found ν_r to be a very important parameter in determining the interlayer pressure distribution (which is why we decided to measure it). In fact, for ν_r values in the range of 0.0 to 0.3, we found that the interlayer pressures could vary by as much as a factor of four!

We appreciate Mr. Hakiel's comments, but, for the reasons outlined above, we must point out that the two techniques are essentially different.

[1] By M. S. Willet and W. L. Poesch, published in the June 1988 issue of the ASME JOURNAL OF APPLIED MECHANICS, Vol. 55, pp. 365-371.

[2] Technical Leader, MR&E-Coating Technologies Division, Kodak Park Site, Eastman Kodak Company, 1669 Lake Avenue, Rochester, N. Y. 14650.

Copyright © 1989 by ASME

Downloaded 03 May 2010 to 171.66.16.31. Redistribution subject to ASME license or copyright; see http://www.asme.org/terms/Terms_Use.cfm

Journal of Applied Mechanics

Book Reviews

Propagation of Transient Elastic Waves in Stratified Anisotropic Medium, by J.H.M.T. Van der Hijden. North Holland, Amsterdam, 1987. 288 pages.

REVIEWED BY S. K. DATTA[1]

In recent years there has been renewed interest in wave propagation in anisotropic elastic media because of current developments in composite materials and seismology. Although this book is written with emphasis on seismology, it will be of general interest also to those interested in understanding guided waves in laminated composite media.

The book has seven chapters and five appendices. Its focus is on calculations of wave fields radiated by transient point sources in stratified anisotropic (and isotropic) media. It is assumed that the media are horizontally stratified such that each layer is a homogeneous anisotropic solid. Even in this context not all the methods that have been found useful in analyzing this problem are discussed. The aim of this monograph is to present the Cagniard-de Hoop technique combined with a generalized ray theoretic approach. Thus, it is rather narrow in its scope. Furthermore, no experimental results are presented. Even so, it gives a fairly thorough exposition of the generalized ray technique and the Cagniard-de Hoop method. So the book will be of use to those interested in analyzing and understanding pulse propagation in anisotropic media.

The author lays out the scope of this book in the first chapter, which is followed by a general derivation in Chapter 2 of the generalized ray wave constituents in a stratified medium. Here the matrix formalism for expressing the motion-stress vector in any layer is succinctly developed.

Chapter 3 deals with the source problem for a horizontally stratified isotropic medium. The general equations derived in Chapter 2 are specialized for the isotropic case in this chapter.

Cagniard-de Hoop technique is illustrated in Chapter 4 by an application to the calculation of the transient wave field in an infinite isotropic medium due to a time dependent point source. Chapter 5 deals with the extension to transient motion in a stratified isotropic medium. Numerical results in the form of synthetic seismograms are presented for a four-layered case. Different source and receiver locations are considered. Finally, transient wave propagation in an unbounded homogeneous and a layered anisotropic medium is solved in Chapters 6 and 7, respectively. Numerical results are presented for transversely isotropic media.

Appendices deal with some theoretical concepts like the slowness, upward and downward propagating waves, and transversely isotropic medium.

Overall, this monograph is a welcome addition to the literature on wave propagation in elastic media.

[1]University of Colorado, Campus Box 427, Boulder, CO 80309.

Dynamics of Multibody Systems, by R. E. Roberson and R. Schwertassek. Springer-Verlag, New York, 1988.

REVIEWED BY RONALD L. HUSTON[2]

The authors define a "multibody system" as: "a system of interconnected mechanical bodies, individually rigid or gyrostatic, possibly together with a control system." They observe that a wide variety of mechanical systems can be described in these terms. The objective of the book is to present a general procedure for studying such systems.

This is the the setting for one of the most comprehensive and detailed accounts to date on this fascinating and rapidly growing subject. The reviewer believes the book will become a classic. The authors are to be commended for their efforts in compiling this treatise.

The book itself is divided into four parts with the first part containing two chapters providing introductory material and mathematical preliminaries. The second part discusses kinematics. The focus is upon a single rigid body. The notions of orientation, angular velocity, and constraints are discussed in three chapters. The third part reviews the principles of rigid body dynamics. This part is divided into two chapters devoted to inertia and dynamical equations.

Finally, in Part IV the authors discuss multibody systems. This part, consuming over half the book, is divided into seven chapters discussing the foundations, formalisms, kinematics, dynamics, equation development and simplification, and numerical analysis of multibody systems. In the reviewer's opinion a major contribution to the field is presented in these chapters. Such diverse subjects as connection configurations, use of graph theory, barycentric vectors, tree systems, closed loops, recursive computation, linearized equations, and robotic systems are discussed.

The book concludes with a series of appendices providing a summary of notation and an extensive bibliography. (The bibliography itself may be worth the price of the book – containing 257 citations.)

It is difficult to write such a book without having many

[2]Department of Mechanical and Industrial Engineering, University of Cincinnati, Cincinnati, OH 45221-0072.

Copyright © 1989 by ASME

Downloaded 03 May 2010 to 171.66.16.31. Redistribution subject to ASME license or copyright; see http://www.asme.org/terms/Terms_Use.cfm

topics whose treatment may be less complete than might be desired by a given reader. (For example, the reviewer found the discussion on angular velocity to be a bit too brief.) Nevertheless, the reviewer strongly recommends the book to students and practitioners working in any of the many areas of multibody systems. The book is carefully written and reasonably complete. It should be accessible to those with only a modest background. Indeed, the authors assume only a knowledge of vector analysis and linear algebra. In summary, the book will likely be of interest and use to a wide community of scholars for many years.

Die Methode der Finiten Elemente, Band III: Einfürung in die Dynamik (in German), by John Argyris, F.R.S. and Hans-Peter Mlejnek. Friedr. Vieweg and Sohn, Braunschweig/Wiesbaden, 1988. 946 pages, with 490 Figures.

REVIEWED BY K. APPA[3]

This masterpiece on finite element methods is organized in three volumes. Professor Argyris, the pioneer in the finite element method, envisioned the power of computing machines early in the 1940s and then started an evolutionary finite element approach in computational mechanics. This treatise shares his 40 years of research experience in an easy to understand, mathematical treatment.

The first two volumes deal with the force and displacement methods employed in structural analysis, including nonlinear computational methods. The third volume is devoted to linear and nonlinear dynamic analyses. This review mainly concerns the third volume. The third volume begins with the 14th chapter and continues through Chapter 26. Half of the book is devoted to linear dynamics and other half to nonlinear dynamics. The first chapter covers the basic introduction to dynamics with exclusive use of illustrations. The next chapter highlights the understanding of kinematics in inertial and moving coordinate systems. Subsequently, virtual work principle is introduced to derive element mass matrices. Chapter 16 demonstrates the application of these principles to develop element mass matrices for triangular and beam elements.

Chapter 17 describes in great detail the eigenvalue analysis methods of large scale systems, which may include singular mass or stiffness matrices and multiple eigenvalues. This chapter also includes an interesting Appendix describing the computation of orthogonal vectors with respect to a given mass matrix. Chapter 18 summarizes economical methods of eigenvalue analysis, such as modal techniques and dynamic reductions.

The response analysis of damped and undamped systems are discussed in Chapters 19 and 20. Many examples are used to describe the characteristics of responses due to various types of excitations. The authors present statistical analysis in Chapter 21, using easily understandable mathematical notations. Important statistical definitions are tabulated for ready references. A sufficient number of examples are also included.

Chapter 22 treats special eigenvalue solution methods, such as the modified Jacobi and Eberlein, as applied to systems with nonproportional damping. In Chapter 23, the authors extend the finite element formulation in space and time coordinates. A vivid discussion on basic principles of direct integration methods is covered in the first few sections of this chapter. In subsequent sections stability and accuracy of Newmark's β-γ method and a cubic Hermitian method, developed by Argyris and his collaborators, are discussed in great detail.

A fascinating presentation of nonlinear dynamics is offered in Chapter 24. Nearly 150 pages are devoted to this complex topic. The aspects of nonlinear phenomena are illustrated by means of the classical Duffings' equation. Following this introduction, advanced numerical integration methods are described in sufficient detail. The cubic Hermitian and Newmark's methods are again applied to solve highly nonlinear problems; such as the displacement-dependent forces, and the crashworthiness studies. In all these test cases, the cubic Hermitian method has shown excellent computational stability and robustness, even when large time steps were used. This chapter also includes an interesting example of modeling dynamics of celestial bodies by finite element methods.

The study of chaos has been an attractive topic among mathematicians and physicists. In recent years, because of the availability of high speed computing machines, this study has been extended to engineering sciences to understand the phenomena of irregular motion based on nonlinear deterministic equations. Some of the dynamical systems, under particular initial conditions, exhibit strange behaviors. For example, a mass point as a nonlinear system may have more than one equilibrium position, which may be unpredictable in time. This complex phenomenon can not be explained in simple mathematical terms. However, the authors succeed in describing the basic principles of chaotic motions in Chapter 25, in a simple language, but remembering the famous quotation from Albert Einstein, "Everything should be made as simple as possible, but not simpler." The first few sections review the definitions of commonly used terms such as: casuality, point attractor, limit cycles, Lorenz attractor, Poincaré mapping, Hénon portrait and invariant manifolds with ample amount of examples and illustrations. In the subsequent sections the well-known KAM (Kolomogorov-Arnold-Moser) theory and the criteria for the existence of chaotic motions are presented together with a number of color photographs depicting the fractals of chaotic motions.

Having discussed the linear and nonlinear dynamic phenomena, the authors conclude this volume with the study of aeroelasticity in Chapter 26. The aeroelastic phenomena is an interaction of aerodynamic, elastic, and inertial forces. The stability of a system is judged by the balance of energy in a cycle of oscillation, and can broadly be classified as static or dynamic in nature. The authors highlight various types of instabilities with reference to the aeroelastic triangle used by Professor Collar. In the first few sections an excellent introduction to the characteristics of steady and unsteady flow and the work done by air loads is presented. In the next few sections, classical two-dimensional aeroelastic problems, such as bending and torsional divergences, aileron effectiveness, aileron reversal speed, and flutter are reported. In subsequent sections, linear and nonlinear panel flutter analyses in supersonic flow are discussed. Application of the finite element methods to determine unsteady air loads is also outlined. The reader will observe interesting discussions on nonlinear characteristics of stall flutter, both in bending and torsional modes.

Following the introduction to flutter mechanisms, practical flutter solution methods such as the V-g method and the CT method by Wittmeyer are described. In the next section the authors introduce some advanced studies such as active flutter suppression and optimum design, with some examples.

Finally, the authors conclude this chapter with some valuable outline on computational fluid dynamics (CFD) by finite element methods (FEM). In the published literature,

[3]Senior Technical Specialist, Structural Dynamics and Loads Department, Northrop Aircraft, CA 90250.

Copyright © 1989 by ASME

Downloaded 03 May 2010 to 171.66.16.31. Redistribution subject to ASME license or copyright; see http://www.asme.org/terms/Terms_Use.cfm

Professor Argyris has demonstrated the feasibility of applying the finite element methods for determining transient aerodynamic loads for applications in flutter analyses and simulation of flight vehicles. In this development, full Navier-Stoke's equations, in compressible and incompressible media including hypersonic flow regimes, are employed. It appears the CFD analysis by the FEM may find distinct advantage over the finite difference method.

Each chapter in this book contains extensive literature references, lucid mathematical developments, and intriguing examples. The reader will appreciate the authors' effort in maintaining systematic definitions, symbols, and notations for easy reading. This book will serve the engineering community as a valuable reference as well as a text on finite element methods. Therefore the reviewer recommends the addition of this book (in three volumes) in every library and also as a personal copy to students, practicing engineers, and researchers.

Downloaded 03 May 2010 to 171.66.16.31. Redistribution subject to ASME license or copyright; see http://www.asme.org/terms/Terms_Use.cfm